METALLURGICAL SOCIETY CONFERENCES

VOLUME 51

ELECTRON AND ION BEAM SCIENCE AND TECHNOLOGY

VOLUME 1

Proceedings of the
Second International Conference on
Electron and Ion Beam
Science and Technology,
sponsored by the
Institute of Metals Division
The Metallurgical Society of AIME
and
Electrothermics and Metallurgy Division
The Electrochemical Society, Inc.

NEW YORK, NEW YORK APRIL 1966

Edited by: ROBERT BAKISH
Bakish Materials Corporation
Englewood, New Jersey
and
Fairleigh Dickinson University
Teaneck, New Jersey

AMERICAN INSTITUTE OF MINING, METALLURGICAL,
AND PETROLEUM ENGINEERS
NEW YORK

ELECTRON AND ION BEAM SCIENCE AND TECHNOLOGY

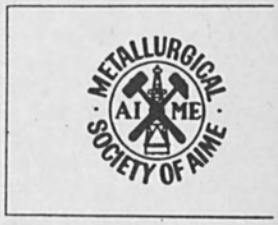

A NOTE TO THE READER

"The material herein was prepared for the June, 1966 conference. However, during the various stages of preparation of this volume, complex production problems and disputes have arisen which have made it economically impractical for Gordon and Breach Science Publishers, Incorporated to meet their usual high standards of publication. The publisher and the Society request the reader's indulgence for the typographical errors and format irregularities herein. These deficiencies should not be construed as a reflection on the authors and editors hereof.

Of course, as is their usual practice, The Metallurgical Society of AIME does not vouch for the scientific accuracy of the data or statements in these materials."

METALLURGICAL SOCIETY CONFERENCES VOLUME 51

ELECTRON AND ION BEAM SCIENCE AND TECHNOLOGY

VOLUME 1

Proceedings of the
Second International Conference on
Electron and Ion Beam
Science and Technology,
sponsored by the
Institute of Metals Division
The Metallurgical Society of AIME
and
Electrothermics and Metallurgy Division
The Electrochemical Society, Inc.

NEW YORK, NEW YORK APRIL 1966

Edited by: ROBERT BAKISH
Bakish Materials Corporation
Englewood, New Jersey
and
Fairleigh Dickinson University
Teaneck, New Jersey

AMERICAN INSTITUTE OF MINING, METALLURGICAL,
AND PETROLEUM ENGINEERS
NEW YORK

Distributed by

GORDON AND BREACH, Science Publishers, Inc.,
150 Fifth Avenue, New York, N.Y. 10011

Library of Congress Catalog Card Number: 67-28243

Editorial office for Great Britain:

Gordon and Breach, Science Publishers Ltd.
8 Bloomsbury Way
London W.C.1, England

Editorial office for France:

Gordon & Breach
7-9 rue Emile Dubois
Paris 14e

Distributed in Canada by:

The Ryerson Press
299 Queen Street West
Toronto 2B, Ontario

Printed in the United States of America

Preface

This volume is the record of the Second International Conference on Electron and Ion Beams in Science and Technology. It is the result of the combined effort and cooperation of the conference committee, the contributors to this event, their employers, and the ECS and the AIME which co-sponsored the event.

As the person who was responsible for much of the activities which led to this conference, I wish to take the opportunity to express my sincere thanks to all those who made the event a reality. Let me also say that it was both a privilege and a pleasure to work with all of you. I believe that I speak for all responsible for the conference organization by saying that we aimed to establish the state of this technology as revealed by events in the spring of 1966. It is my opinion that this record offers a very comprehensive insight into this technology. It is a fitting sequence to the proceedings of the First International Conference on Electron and Ion Beams in Science and Technology published by John Wiley & Sons, N. Y.

Inasmuch as many who would be reading this volume were not at the conference. I regret to say that not all that transpired there is on record. Two particularly exciting round table discussions devoted to electron beam welding defects and electron and ion beams in micro electronics respectively are the most serious omission from the record. Several of the papers presented at the meeting are also missing; their authors having failed to meet the publication deadline. Further, I have assumed my prerogative as the editor, and rearranged the presentations with the hope to produce a more coherent volume. With this in mind I have also preceded several of the sections dealing with specific aspects of the technology with short introductory remarks and limited bibliographic references. I feel that in this manner a newcomer to the field can effect an easier transition from his role as outsider to that of a competent insider.

Tremendous strides have been made to date and I am confident that this progress will continue. Future conferences as those in the past will continue to help the dissemination of this valuable information. This will enable all those who suspect possibilities related to their own work to establish this for certain either personally, or through encounters with individuals who can definitely assist them to do so. As to all who participated in this event, let me say that our next "get together" is scheduled for May 6–9, 1968, at the Statler Hotel in Boston. I hope to have the opportunity to greet you again on the occasion of the Third International Conference on Electron and Ion Beams in Science and Technology for another exciting event devoted to this dynamic area of scientific endeavor.

I have just looked over the preface and it occurs to me that I almost forgot to thank the person who really helps me most, my dear wife, Ellen.

R. Bakish,

Englewood, New Jersey.

TABLE OF CONTENTS

VOLUME I

I. PHYSICS OF ELECTRON AND ION BEAMS

II. ELECTRON BEAMS IN MELTING AND REFINING-BASIC

VOLUME 2

VI. ION PROPULSION

VII. ELECTRON BEAMS IN RECORDING AND INFORMATION STORAGE

VII. ELECTRON BEAMS IN MICRO ELECTRONICS

CONTRIBUTORS

Conference Chairman:

R. Bakish, Bakish Materials Corporation, Englewood, New Jersey, and Fairleigh Dickinson University, Teaneck, New Jersey, U.S.A.

Conference Committee and Sessions Chairmen:

M. von Ardenne, Institute M. von Ardenne, Dresden, East Germany
E. Bas, Swiss Federal Polytech. Inst., Zurich, Switzerland
F. Benesowski, Metalwerk Plansee, Reutte/Tyrol, Austria
M. Boston, Esq., Torvac Ltd., Histon, Cambridge, England
J. Cabelka, International Institute of Welding, Bratislava, Czechoslovakia
R. Castaing, University of Paris, Orsay (S.-et-O), France
W. Dietrich, W. C. Heraeus, Hanau/Main, West Germany
G. W. A. Dummer, Esq., Royal Radar Establishment, Great Malvern, England
T. Everhart, University of California, Berkeley, California, U. S. A.
T. Forrester, University of California, Irvine, California, U. S. A.
L. Habraken, CNRM, Liege, Belgium
C. Hayashi, Japan Vacuum Engineering Co. Ltd., Yokohama, Japan
A. E. Jenkins, University of New South Wales, N. S. W., Australia
A. Lawley, Drexel Institute, Philadelphia, Pennsylvania, U. S. A.
G. Molenstedt, University of Tubingen, Tubingen, West Germany

E. C. Muly, Jr. N. R. C., Newton Highlands, Massachusetts, U. S. A.
S. Namba, The Institute of Physical & Chemical Research, Tokyo, Japan
N. A. Olshanski, Moscow Power Institute, Moscow, U. S. S. R.
B. Paton, Institute for Electro-Welding, Kiev, U. S. S. R.
E. Rexer, Institute for Applied Physics of Pure Metals, Dresden, East Germany
B. W. Schumacher, Ontario Research Foundation, Toronto 5, Canada
J. G. Siekman, Philips Research Laboratories, Eindhoven, Holland
C. Spitzer, Ampex Corp., Redwood City, California, U. S. A.
J. A. Stohr, Centre d'Etudes Nucleaires, Saclay, France
F. Lincoln Vogel, University of Pennsylvania, Philadelphia, Pennsylvania, U. S. A.
O. Winkler, Balzers AG, Balzers, Lichtenstein

CONTRIBUTORS OF PRESENTATIONS

Anderson, J. R., Hughes Research Laboratories, Malibu, California
von Ardenne, M., Research Institute M. von Ardenne, Dresden, East Germany
Barrekette, IBM, Watson Research Center, Yorktown Heights, New York
Bas, E. B., Department of Industrial Research, Swiss Federal Institute of Technology, Zurich, Switzerland
Beer, A. F., Mullard Research Laboratories, Redhill, Surrey, England
Bernheim, M., Faculty of Science, Orsay, France
Brody, M. D., M.I.T., Cambridge, Massachusetts
Castaing, R., Faculty of Science, Orsay, France
Crawford, C. K., M.I.T., Cambridge, Massachusetts
Cremosnik, G., Dept. of Industrial Research, Swiss Federal Institute of Technology, Zurich, Switzerland
Cullum, D. G., IBM, Research Center, Yorktown Heights, New York
Davies, I. G. A., Dept. of Materials Science, U. C. N. W., Bangor, Caerns, United Kingdom
Davis, J. M., United Aircraft Research Lab., East Hartford, Connecticut
Dove, J. F., Rome Air Development Center, Rome, N. Y.
Dubbe, R. F., Minnesota Mining and Manufacturing Co., St. Paul, Minnesota
Duffy, J. A., IBM, Watson Research Center, Yorktown Heights, New York
Eckhardt, W. O., Hughes Research Laboratories, Malibu, California
Einstein, P. A., Vickers Research Establishment, Ascot, England

Everhart, T. E., University of California, Berkeley, California
Foti, E., Centrel Research Institute for Physics, Budapest, Hungary
Friedler, V. E. B., Edelstahl Werk, Freital, East Germany
Garasi, L. A., Electro Optical Systems Inc., Pasadena, California
Gerken, J. M., TRW Equipment Laboratories, Cleveland, Ohio
Glotin, P., Centre of Nuclear Studies, Grenoble, France
Gibbons, J. F., Stanford Electronics Lab., Stanford University, Stanford, California
Gonzales, A. J., University of California, Berkeley, California
Grapa, J., National Institute for Scientific Investigation, France
Groves, M. T., TRW Equipment Laboratories, Cleveland, Ohio
Heil, H., Hughes Research Laboratories, Malibu, California
Hessig, U., Research Institute M. von Ardenne, Dresden, East Germany
Hill, G. W., Semi Conductor and Thin Film Dept., British Scientific Assoc., South Hill, Chislehurst, Kent, England
Hughes, K. A., Dept. of Materials Science, U. C. N. W., Bangor, Caerns, United Kingdom
d' A. Hunt, C., Temescal Metallurgical Corp., Berkeley, California
Husmann, O. K., formerly Hughes Research Laboratories, Malibu, California
James, J. A., Sciaky Bros., Chicago, Illinois
Jensen, A. S., Aerospace Div., Westinghouse Defense and Aerospace Center, Baltimore, Maryland
Kaye, S., Electro Optical Systems, Inc., Pasadena, California
Kelley, J., Mullard Research Laboratories, Redhill, Surrey, England
King, H., Hughes Research Laboratories, Malibu, California

King, H. N. G., Mullard Research Laboratories, Redhill, Surrey, England
Kretizer, N. H., IBM Research Center, Yorktown Heights, New York
Kothe, A., Institute for Metal Physics and Pure Metals, Dresden, East Germany
Large, L. N., Services Electronics Research Laboratory, Baldock, England
Lawley, A., Drexel Institute, Philadelphia, Pennsylvania
Koch, F., Central Welding Institute, Halle, East Germany
Lenk, P., Research Institute M. von Ardenne, Dresden, East Germany
Liberman, I., Westinghouse Research Lab., Pittsburgh, Pennsylvania
Limansky, I. S., Westinghouse Defense and Aerospace Center, Baltimore, Maryland
Manchester, K. E., Sprague Electric Co., North Adams, Massachusetts
Masek, T. D., J. P. L., California Institute of Technology, Pasadena, California
Medved, B., Electro Optical Systems, Inc., Pasadena, California
Mesharekov, V. M., Moscow Power Engineering Institute, Moscow, U. S. S. R.
Meier, J. M., Hamilton Standard, Windsor Locks, Connecticut
Miller, K., Metals Joining Corp., Redondo Beach, California
Muelemans, M., Centre for Nuclear Studies, Mol, Belgium
Neve, N. F. B., Dept. of Materials Science, U. C. N. W., Bangor, Caerns, United Kingdom
Norris, Jr. C. B., Stanford Electric Lab., Stanford University, Stanford, California
Olshansky, N. A., Moscow Power Engineering Institute, Moscow, U. S. S. R.
Oman, R. M., ASD Litton Industries, Inc., Minneapolis, Minnesota
Panzer, J., Research Institute M. von Ardenne, Dresden, East Germany
Paton, B. E., E. O. Paton Institute for Welding, Kiev, U. S. S. R.

Pease, R. F. W., Dept. of Electrical Engineering, University of Calif., Berkeley, California
Peisach, M., Southern Universities Nuclear Institute Faure, C. P., South Africa
Pinsley, E. A., United Aircraft Research Lab., East Hartford, Connecticut
Poole, Darrell O., Southern Universities Nuclear Institute Faure, C. P., South Africa
Prekel, H. L., Franklin Institute, Philadelphia, Pennsylvania
Reed, E. W., Minnesota Mining and Manufacturing Co., St. Paul, Minnesota
Reed, R. E., Oak Ridge National Laboratory, Oak Ridge, Tennessee
Reininger, W. G., Aerospace Div., Westinghouse Electric Co.
Rexer, E., Institute for Metal Physics and Pure Metals, Dresden, East Germany
Roberts Jr. A. S., School for Engineering, Old Dominion College, Norfolk, Virginia
Roberts, E. D., Mullard Research Laboratories, Redhill, Surrey, England
Rose, R. M., M.I.T., Cambridge, Massachusetts
Rolick, G. P., Electro Optical Systems, Inc., Pasadena, California
Ruth, R. P., Autonetics Div., North American Aviation, Inc., Anaheim, California
Schiller, S., Research Institute M. von Ardenne, Dresden, East Germany
Schlat, F., Institute for Metal Physics and Pure Metals, Dresden, East Germany
Schofield, J. M. S., Mullard Research Laboratories, Redhill, Surrey, England
Schonberg, H. V. E. B. L. E. W. Henningsdorf, East Germany
Schwartz, M., Advanced Manufacturing Technology, Martin-Baltimore, Maryland
Scott, B. W., Hughes Research Laboratories, Malibu, California
Shaw, A., Dept. of Materials Science, U. C. N. W., Bangor, Caerns, United Kingdom

Siekman, J. G., Philips Research Laboratories, N. V. Philips Gloelampenfabrieken, Eindhoven, Netherlands
Smith, H. R., Temescal Metallurgical Corp., Berkeley, California
Skinner, L. G., M.I.T., Cambridge, Massachusetts
Stevens, H., Dept. of Ind. Research, Swiss Federal Institute of Technology, Zurich, Switzerland
Soloman, J., Sciaky Bros., Chicago, Illinois
Stohr, J. A., French Atomic Energy Commission, Saclay, France
Sulway, D. V., Department of Materials Science, U. C. N. W., Bangor, Caerns, United Kingdom
Thieme, O., Research Institute M. von Ardenne, Dresden, East Germany
Thomas, R. N., Department of Industrial Research, Swiss Federal Institute of Technology, Zurich, Switzerland
Thornton, P. R., Dept. of Materials Science, U. C. N. W., Bangor, Caerns, United Kingdom
Varek, C. J., Westinghouse Molecular Electronics Div., Elk Ridge, Maryland
Walsh, A. P., United Aircraft Research Lab., East Hartford, Connecticut
Wayte, R. C., Dept. of Materials Science, U. C. N. W., Bangor, Caerns, United Kingdom
Wehe, H. G., Bell Telephone Lab., Murray Hill, New Jersey
Wiedmer, H. B., Institute of Technology, Zurich, Switzerland
Wolf, P. A., Bell Telephone Laboratories, Inc., Murray Hill, New Jersey
Zeheb, D., IBM Research Center, Yorktown Heights, New York

Pease, R. F. W., Dept. of Electrical Engineering, University of Calif., Berkeley, California
Peisach, M., Southern Universities Nuclear Institute Faure, C. P., South Africa
Pinsley, E. A., United Aircraft Research Lab., East Hartford, Connecticut
Poole, Darrell O., Southern Universities Nuclear Institute Faure, C. P., South Africa
Prekel, H. L., Franklin Institute, Philadelphia, Pennsylvania
Reed, E. W., Minnesota Mining and Manufacturing Co., St. Paul, Minnesota
Reed, R. E., Oak Ridge National Laboratory, Oak Ridge, Tennessee
Reininger, W. G., Aerospace Div., Westinghouse Electric Co.
Rexer, E., Institute for Metal Physics and Pure Metals, Dresden, East Germany
Roberts Jr. A. S., School for Engineering, Old Dominion College, Norfolk, Virginia
Roberts, E. D., Mullard Research Laboratories, Redhill, Surrey, England
Rose, R. M., M.I.T., Cambridge, Massachusetts
Rolick, G. P., Electro Optical Systems, Inc., Pasadena, California
Ruth, R. P., Autonetics Div., North American Aviation, Inc., Anaheim, California
Schiller, S., Research Institute M. von Ardenne, Dresden, East Germany
Schlat, F., Institute for Metal Physics and Pure Metals, Dresden, East Germany
Schofield, J. M. S., Mullard Research Laboratories, Redhill, Surrey, England
Schonberg, H. V. E. B. L. E. W. Henningsdorf, East Germany
Schwartz, M., Advanced Manufacturing Technology, Martin-Baltimore, Maryland
Scott, B. W., Hughes Research Laboratories, Malibu, California
Shaw, A., Dept. of Materials Science, U. C. N. W., Bangor, Caerns, United Kingdom

Siekman, J. G., Philips Research Laboratories, N. V. Philips Gloelampenfabrieken, Eindhoven, Netherlands
Smith, H. R., Temescal Metallurgical Corp., Berkeley, California
Skinner, L. G., M.I.T., Cambridge, Massachusetts
Stevens, H., Dept. of Ind. Research, Swiss Federal Institute of Technology, Zurich, Switzerland
Soloman, J., Sciaky Bros., Chicago, Illinois
Stohr, J. A., French Atomic Energy Commission, Saclay, France
Sulway, D. V., Department of Materials Science, U. C. N. W., Bangor, Caerns, United Kingdom
Thieme, O., Research Institute M. von Ardenne, Dresden, East Germany
Thomas, R. N., Department of Industrial Research, Swiss Federal Institute of Technology, Zurich, Switzerland
Thornton, P. R., Dept. of Materials Science, U. C. N. W., Bangor, Caerns, United Kingdom
Varek, C. J., Westinghouse Molecular Electronics Div., Elk Ridge, Maryland
Walsh, A. P., United Aircraft Research Lab., East Hartford, Connecticut
Wayte, R. C., Dept. of Materials Science, U. C. N. W., Bangor, Caerns, United Kingdom
Wehe, H. G., Bell Telephone Lab., Murray Hill, New Jersey
Wiedmer, H. B., Institute of Technology, Zurich, Switzerland
Wolf, P. A., Bell Telephone Laboratories, Inc., Murray Hill, New Jersey
Zeheb, D., IBM Research Center, Yorktown Heights, New York

Introductory Remarks

Ladies and Gentlemen:

It gives me great pleasure to welcome you on behalf of the AIME and ECS here in New York on the occasion of the Second International Conference on Electron and Ion Beams in Science and Technology. I hope that all of you who are here today, and those who will be coming for specific sessions of the conference in the days to follow, will find this event in accordance with your expectation and that you will have a profitable and pleasant conference.

At this time I must take the opportunity to express my most sincere thanks to the conference committee members and session chairmen for their effort in organizing the conference program. Thanks and deep appreciation are also due to all the speakers who have traveled extensive distances to be with us for the event and to share with you the findings of their work in this dynamic technology. Thanks also are due to both the AIME and the ECS, the sponsoring societies, for the effort which they invested so that this event might become a reality.

Electron and Ion Beams in their many ramifications are exerting a powerful influence in our modern technology. We are seeing here, as in other areas of scientific endeavor, an increasing pace in the move of findings from the research laboratory to the production line. Science itself advances more rapidly than ever before and yet it is in the engineering accomplishment and the reduction of advanced scientific thought to practice that ultimately advances the welfare of our society. The subject matter of the conference covers the spectrum from fundamental studies through industrial applications. The two years which expired since the first conference have seen much excitement take place. I look with great confidence to the future and the even greater influence that electron and ion beams will play in shaping of industrial progress.

The conference sessions will essentially follow the outlined program and your sessions chairman will advise you of minor program changes which might take place. In view of all the material that we intend to cover here, I wish to request that the speakers do not forget that others will speak after them. I would be deeply grateful if they will adhere to the speech duration time allotted to them by the session chairman. Every morning at the author's breakfast each speaker will be notified of the time allotted for his presentation.

But you did not come to listen to me talk. Have a pleasant stay in our city and do try to take in at least some of its many exciting sites and activities to complement the scientific exposure provided by the conference.

R. Bakish,

New York, April 17, 1966.

PHYSICS OF ELECTRON AND ION BEAMS

PHYSICS OF ELECTRON
AND ION BEAMS

Physics of Electron and Ion Beams

This common to the technology area is one of considerable activities. As a consequence the few papers in this section are but an insignificant sampling of the type of work that is being carried out today throughout the world. This area of electron and ion beam related work is the most painstaking and critical. It is the backbone work for progress here. It is work imposing most stringent requirements on the individuals involved in it. On many occasions it does not even provide the material rewards that often go hand in hand with those who successfully resolve problems of more applied nature, those who attempt to translate the results of work done here to the commercial products or ultimate profitable processes. Every seemingly non consequential contribution made by the theoretical or experimental physicist here in the ultimate brings further the technological development. It is then only natural that these papers will be in the first and introductory section of this volume.

The papers here are not very much related except for the fact that they deal with physical aspects of electron and ion beam related phenomena. The first paper is also pertinent to this technology because of the increased importance of plasmas and their relation to corpuscular beams. The two papers on electron gun design are a good example to illustrate recent work to this aim. It is this writer's feeling that progress here will be increasingly more difficult to achieve in the future and will only be brought about as in the past by effort of increased intensity and superior competence.

In closing I would suggest that for neophites with interest in the physics of electron and ion beams little success will be in the offing unless concerted effort is exerted to narrow the scope of their interest before proceeding to seek information here. It will be virtually impossible to

provide general bibliography here, but consulting references in the specific areas of interest given with many of the papers presented here and in the proceedings of the first conference volume should be an adequate point of departure.

(Editor)

Plasmas in Solids*

P. A. Wolff

Bell Telephone Laboratories, Inc.
Murray Hill, New Jersey

I. INTRODUCTION

Plasmas are gas-like media whose constituents are highly mobile, charged particles. Their most characteristic feature is the ease with which they respond to electric or magnetic forces. Generally speaking this response is collective in nature--involving relatively small, coherent motions of many particles in the system. The study of such collective behavior is the central theme of plasma physics.

The most familiar example of a plasma is, of course, an ionized gas. However, any other medium whose constituents are both mobile and charged must also exhibit plasma-like properties. One such is the gas of current carrying electrons in a conducting crystal. These charge carriers are often highly mobile, and will then respond collectively to external stimuli. The study of the collective behavior of such systems is a relatively new, and rapidly expanding, branch of solid state physics. It is the aim of this article to review some of the recent work in this field of solid state plasmas.

Solid state plasma research is generally concerned with one or the other of two problems: that of electromagnetic wave propagation in plasmas under equilibrium

*This was one of the plenary presentations at the opening session of the conference.

conditions; or that of plasma stability under non-equilibrium conditions. In this article we will review work on the wave propagation problem. It is the better understood of the two problems and, to date, has been the more fruitful in illuminating the fundamental features of plasmas in solids. Important work is also being done on instabilities, however, and may ultimately lead to devices based on solid state plasma effects.

The study of waves in solid state plasmas began about twenty years ago with the observation, by Ruthemann [1] and Lang [2], of plasma oscillations in metals. These oscillations, which are probably the most characteristic feature of a plasma, are high frequency density waves in the gas of conduction electrons. In most experiments they are excited by an energetic electron beam. The earliest measurements established the existence of plasma oscillations in metals and determined their frequencies. More recently it has been possible, from a careful study of the energy and angular distribution of the scattered electrons, to infer the frequency, dispersion and damping of these waves in considerable detail. This information is fundamental to our understanding of the structure of the electronic medium in metals.

Lately it has also been realized that, in the presence of a DC magnetic field, low frequency electromagnetic waves (as contrasted to the high frequency plasma waves, which are driven by electrostatic forces) will propagate in solid state plasmas. These waves can be excited with standard electrical techniques and have been studied, in a variety of materials, at frequencies ranging from audio to microwave. Under optimum conditions they can be transmitted through bulk samples of solid conductors.

The two wave types described above are, at present, the best tools we have for probing the structure of plasmas in solids. In most cases the behavior of the waves is well understood, and measurements of their characteristics can be used to determine important plasma parameters or other features of the crystals in which they occur. We will discuss the two types of waves in turn, indicating their physical origin, the sort of experiments used to observe them and the kind of information they give us about plasmas in solids. Plasma waves are treated in Section III; electro-

magnetic waves in Section IV. Section II is devoted to a brief description of a few of the important solid state plasma materials.

II. TYPES OF SOLID STATE PLASMAS

Before discussing the experiments which have been used to study solid state plasmas, it is useful to classify these plasmas and to consider some of the parameters which characterize them. All plasmas are alike in supporting high frequency charge density (plasma) oscillations, and in being able to screen low-frequency electric fields. These phenomena only occur in media whose constituents are charged. Indeed, it could well be said that their occurrence distinguishes a plasma from an ordinary gas of neutral particles. The plasma oscillations are electron density waves driven by the Coulomb forces between the charged particles in the medium. Their frequency is given by the formula (derived in the next section)

$$\omega_p = \sqrt{\frac{4\pi n e^2}{m}} , \qquad (1)$$

where n is the electron density, e its charge and m the mass. ω_p is a measure of the speed at which a plasma can respond to an external perturbation. Electrostatic fields of frequency lower than ω_p are screened by a plasma, but it has relatively little effect on higher frequency ones.

In metals, because of the large electron density, plasma frequencies are very high--typically of the order of 10^{16} radians/sec. Quantum effects play a considerable role in their behavior. In particular, the quantum of plasma oscillation (called a plasmon) has an energy, $h\omega_p$, which is about ten electron volts. This energy is several orders of magnitude greater than kT at room temperature, so we do not ordinarily expect plasmons to be excited in metals. To observe them it is necessary to supply energy to the metal from an outside source. When this is done the metal does not absorb energy continuously, but in discrete multiples of the plasma quantum, $h\omega_p$. We shall see presently that the electron beam is an ideal tool for supplying this energy in a controlled way.

Electron densities in semiconductors usually lie in the range 10^{14} - 10^{18} /cc., as contrasted to about 10^{22} /cc in metals. Consequently, their plasma frequencies are in the microwave or far infrared regions. The plasma properties of such materials have been studied with microwave resonance techniques [3] and by far infrared spectroscopy [4].

The second distinguishing feature of a plasma is its ability to screen external electric fields. For example, if a positive charge q is placed in a plasma it attracts the electrons in its vicinity and repels ions. As a consequence, the medium is polarized and the Coulomb potential, q/r, that would be associated with the charge if it were in free space, is replaced by a screened potential, $(q/r)e^{-r/\lambda_D}$. The parameter λ_D is known as the Debye length, and is a measure of the distance to which external electrostatic fields will penetrate the plasma. The Debye length is related to the plasma frequency by the formula

$$\lambda_D = \sqrt{\frac{\langle v^2 \rangle}{3\omega_p^2}} \qquad (2)$$

where $\langle v^2 \rangle$ is the average of the electron velocity squared. Two types of electron velocity distributions commonly occur in solids--the Maxwellian in dilute plasmas (such as those in semiconductors), and the Fermi-Dirac distribution in denser ones. The formula given above is correct in both cases. In metals the latter applies and the length, λ_D, is usually called the Fermi-Thomas length. It is very small; typically 10^{-8} cm. Debye lengths in semiconductors are considerably larger; between 10^{-4} and 10^{-6} cm. These lengths give some measure of the size of space charge regions at semiconductor--vacuum interfaces or at junctions in these materials.

Plasmas as a whole are electrically neutral. The manner in which this neutrality is achieved, however, can be different in various types of solid state plasmas. A gas plasma is generally composed of electrons and ions, both of which are mobile. This is an example of a <u>two-component</u> plasma. Two-component plasmas also occur in solids. In an intrinsic semiconductor at finite tempera-

ture electrons and holes are present in equal numbers, and both are mobile. The semi-metal bismuth is another example of a two-component solid state plasma. A pure bismuth crystal contains 10^{18} mobile electrons and holes per cc. even at absolute zero temperature.

It is also possible to have single component plasmas in solids. Consider, for example, the simple metal potassium. It contains a dense sea of conduction electrons whose charge is neutralized by that of the K^+ ions. These ions, however, are fixed in the crystal lattice and are immobile at ordinary temperatures. Thus, the plasma has a single mobile component. An extrinsic (doped) semiconductor is another example of a single component plasma since the donors, whose charge neutralizes that of the mobile electrons, are fixed in the crystal lattice.

The variety of solid state plasmas is enormous. A gas plasma is made up of electrons and ions whose masses and charges, which determine the dynamics of the particles, are known and unchangeable. In a solid, on the other hand, the dynamical behavior of a conduction electron is determined by the periodic crystal field through which it moves. As a consequence, there are as many different types of electron dynamics as there are conducting solids. Crystals exist in which electrons have an "effective" mass as small as .01 times that of the free electron. In other materials the mass is anisotropic--the electrons being easy to accelerate in one direction and hard to accelerate in another. Each solid state plasma material is, in this sense, peculiar and interesting in its own special way.

In Table I we have listed a few important solid state plasma materials with the parameters that characterize them. The list is far from exhaustive. Materials were chosen that have been extensively studied and illustrate some of the experimental techniques we will discuss in succeeding sections. Solid state plasma experiments have been done in many other crystals, but space prevents us from discussing their properties.

III. PLASMA OSCILLATIONS IN SOLIDS

Plasma oscillations in metals are generally studied in an experiment of the type illustrated in Fig. 1. Here an

Table 1. Parameters Characterizing a few Solid State Plasma Materials.

Material	Plasmon Energy (in ev)	Carrier Density cm^{-3}	Effective mass (in units of free electron mass)	Type of Plasma
Aluminum	15.0	1.8×10^{23}	1.0	Single component
Potassium	3.9	1.3×10^{22}	1.2	Single component
Bismuth	.025	n=p $=2 \times 10^{17}$	anisotropic, varies from .006 to 1.3	Two component
Indium Antimonide (intrinsic)	~.01	$\sim 10^{16}$	.013	Two component

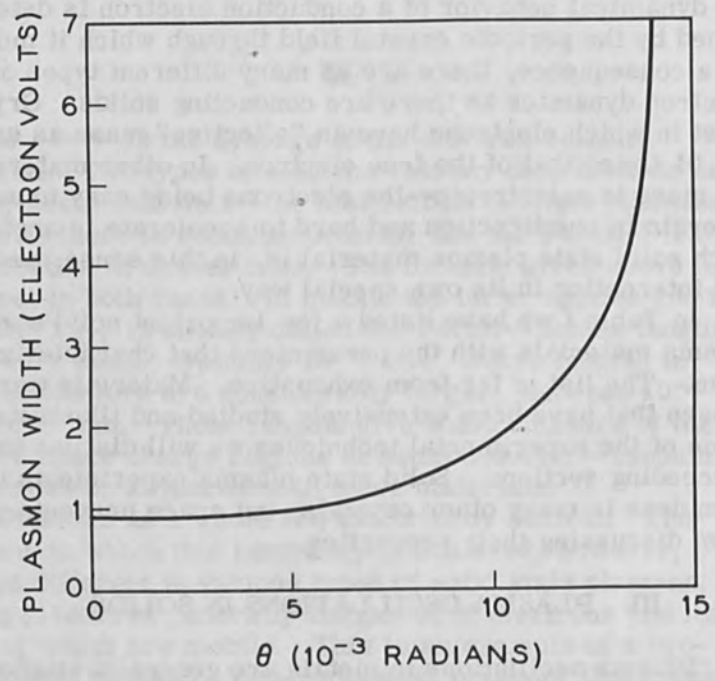

Figure 1. Schematic Diagram of Characteristic Energy Loss Experiment.

electron beam is fired through a very thin foil, usually less than 500 Å thick, of the metal being investigated. The beam is monoenergetic, to within an electron volt, and generally has an energy of several kilovolts or greater. After the electrons have passed through the foil their energy spectrum is carefully measured, again to within a volt. A typical characteristic energy loss spectrum (number of electrons vs. energy lost) is shown in Fig. 2. These data are for an aluminum foil about 300 Å thick and are taken from the original work of Lang. It is immediately clear from this figure that the electrons lose energy in integral multiples of a basic quantum which, in aluminum, turns out to be 15 electron volts. This is also the value one calculates from Eq. (1), using for n the valence electron density. Thus, there seems little question that what is being observed in the characteristic energy loss experiments is multiple excitation of plasma quanta in the metal film by the fast electron beam. From the film thickness and number of peaks observed in the experiment it is also possible to infer the mean free path for plasmon excitation. In aluminum it is 200 Å at an electron energy of 10 kilovolts, and varies approximately linearly with energy.

Since the classic work of Ruthemann and Lang, the characteristic energy loss experiment has been repeated many times on a wide variety of materials. [5] Loss data are now available for several dozen elements. In many metals the characteristic energy loss agrees with that predicted from Eq. (1) using for n the valence electron density. Exceptions occur in elements such as copper or silver which have large numbers of d-electrons. These deviations are fairly well understood in some cases. [6]

A more sophisticated version of the characteristic energy loss experiment is that in which loss spectra are measured as a function of scattering angle (the angle θ in Fig. 1). Experiments of this kind were first performed by Watanabe [7] and have been further refined in recent work of Kunz, [8] Swanson and Powell, [9] and Ninham, Powell and Swanson. [10] The great advantage of this type of experiment is that it enables one to measure the energy of plasma oscillations as a function of their momentum or wave-vector. In other words, it determines the dispersion relation of the plasma waves. Figure 3 illustrates the

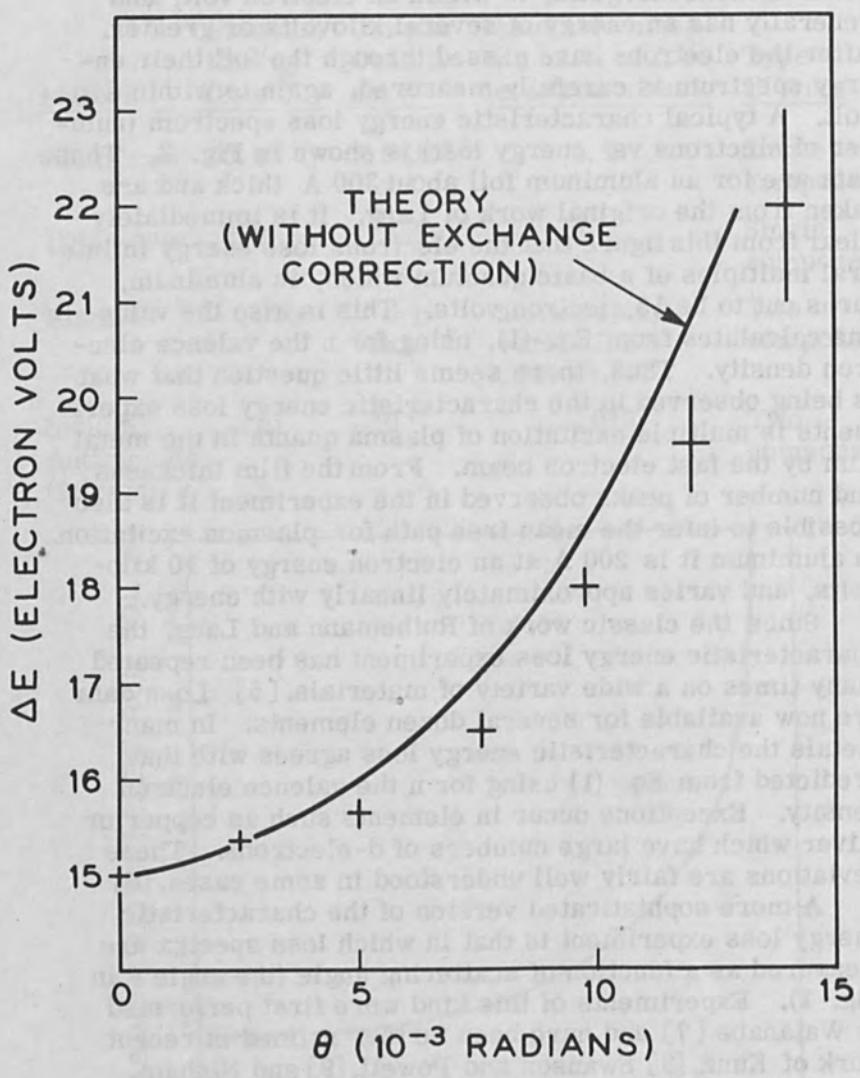

Figure 2. Electron Beam Intensity vs. Energy Loss for Aluminum (after Lang).

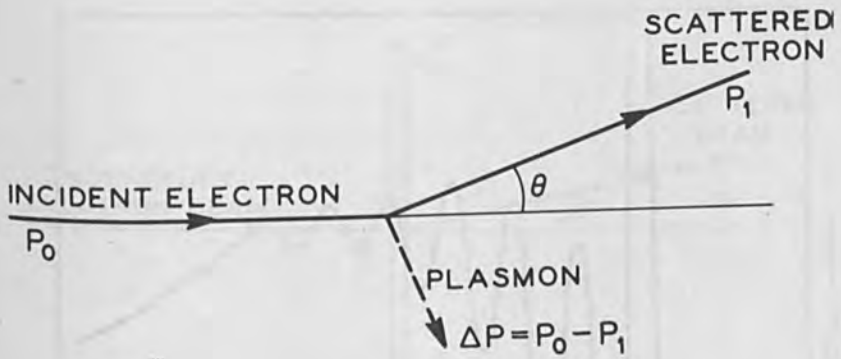

Figure 3. Kinetics of Plasmon Excitation by an Electron Beam.

basic plasmon excitation process in which energy and momentum must be conserved. Here a fast electron, of momentum p_o , excites a plasmon, losing to it some energy and momentum, and is left with momentum p_1 . The momentum difference, $\Delta p = p_o - p_1$, is carried off by the plasmon. The conservation laws imply that $\Delta p \simeq p_o \sin\theta \simeq p_o \theta$. Thus, a measurement of the characteristic energy loss at an angle θ gives the energy of the plasmon with momentum $p_o \theta$. A series of such measurements, at different scattering angles, permits one to track out the whole plasmon dispersion relation. Figure 4 shows the dispersion relation of plasma oscillations in aluminum, as measured in this way by Kunz. [8] Notice that the energy of the plasmon varies as θ^2 --that is, as the square of its momentum. We will discuss the reason for this dispersion presently. The plasmon dispersion relation terminates at a certain critical scattering angle. Just before this point the loss peaks rather abruptly broaden, and then disappear. This behavior is illustrated in Fig. 5 which shows the width of the loss peak, in aluminum, as a function of the scattering angle. We see that the line width, γ, of the plasmon is a quite smooth function of θ except near the critical angle, θ_c, where it appears to diverge. Since the width is related to the lifetime, τ , of the plasmon

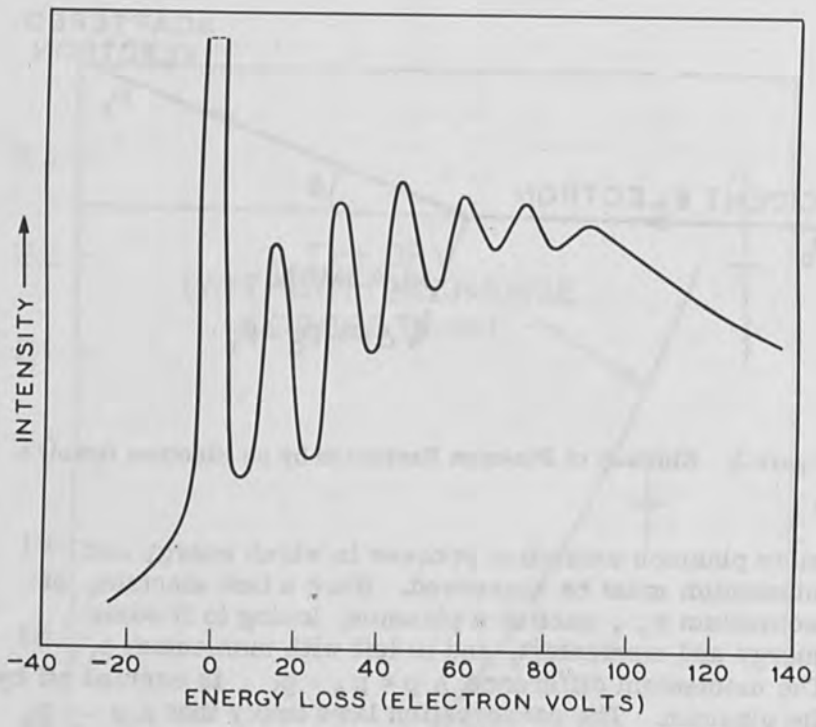

Figure 4. Dispersion of Characteristic Energy Loss in Aluminum (after Kunz).

through the uncertainty principle $\tau \sim h/\gamma$, we may also interpret the data shown in Fig. 5 as indicating a plasmon lifetime that decreases with the momentum of the plasmon. The rapid rise in γ near θ_c suggests that some new process, which heavily damps the plasma oscillation, has its onset at this point. For plasmon momenta larger than that at the critical angle, the oscillation is so heavily damped that it no longer is a well defined excitation of the medium. It is then natural that the dispersion relation should terminate at this point. For the moment these ideas are speculative, but we will see below that they are entirely consistent with our theoretical understanding of plasmon behavior. In simple metals, such as aluminum,

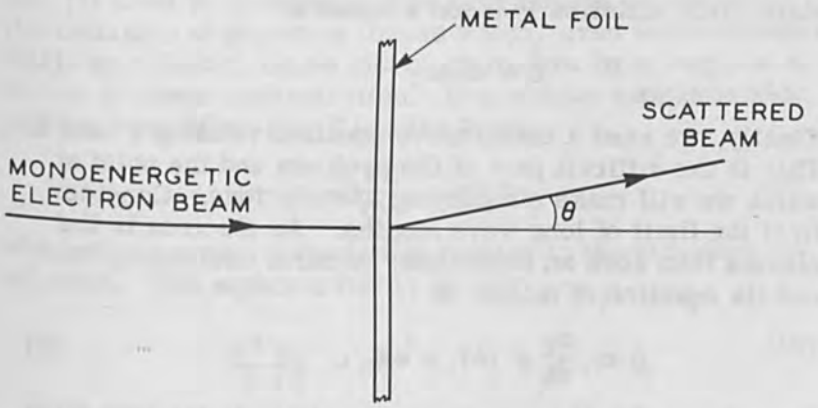

Figure 5. Variation of Plasmon Line Width with Angle in Aluminum (after Kunz).

there is even detailed quantitative agreement between the theory, and data such as that shown in Figs. 4 and 5.

The problem of plasmon behavior in metals, particularly the simpler ones, has been extensively studied theoretically (see Reference 5 and other references therein). We will make no attempt to develop the complete theory here, but merely discuss the key ideas in a qualitative way. Our aim is to explain the important features of the data shown in Figs. 4 and 5.

As mentioned earlier, the plasmon is a space charge wave in the electron gas of a metal. We assume that the density fluctuation is relatively small and write

$$n(r, t) = n_o + n_1 (r, t) \tag{3}$$

where $n(r, t)$ is the electron density at position r and time t, and $|n_1| / n_o \ll 1$. This perturbation produces electrostatic fields which cause particle currents to flow in the plasma. $\Gamma (r, t)$, the particle current, must obey the continuity equation

$$\frac{\partial n_1}{\partial t} + \nabla \circ \Gamma = 0 \tag{4}$$

to conserve electron number. In addition, the electrostatic field satisfies Poisson's equation

$$\nabla \cdot E = 4\pi e n_1 \tag{5}$$

Finally, we need a constitutive equation relating Γ and E. This is the difficult part of the problem and the point at which we will make simplifying assumptions. Consider first the limit of long wave lengths. An electron in the plasma then sees an essentially uniform oscillating field, and its equation of motion is

$$m \frac{dv}{dt} = m\dot{v} = eE \quad . \tag{6}$$

Since $\Gamma \simeq n_0 v$, the constitutive equation in the long wave length limit is

$$\frac{\partial \Gamma}{\partial t} = \frac{n_0 eE}{m} \quad . \tag{7}$$

By combining Eq. (4-7) we may now obtain the harmonic oscillator equation

$$\frac{\partial^2 n_1}{\partial t^2} + \omega_p^2 n_1 = 0 \tag{8}$$

which describes the electron density fluctuation in a long wave length plasmon. We have derived this result in a casual way but, in the long wave length limit, it can be shown to be rigorously correct even if one takes into account electron-electron scattering (which is ignored above). The physical origin of the oscillation is also fairly clear. If there is a density perturbation in the plasma electrostatic fields are produced (Eq. 5). The fields cause currents to flow (Eq. 7) in such a direction as to smooth out the original perturbation. However, because of the electrons' inertia (Eq. 6) this process tends to "overshoot"--regions which were originally negatively charged (electron excess) become positively charged and vice versa. The process then reverses and the net result is the oscillation described by Eq. (8). From this description we see that the spring constant of this oscillator is caused by the Coulomb forces between electrons, and its inertia is just their mass density.

When the plasma oscillation has a finite wave length Eq. (7) must be modified. The first change necessary is the inclusion of pressure forces which, even in the absence of electric fields, cause electrons to flow from regions of higher to lower concentration. In a simple approximation, pressure modifies Eq. (7) to the form

$$\frac{\partial \Gamma}{\partial t} = \frac{n_o eE}{m} - \alpha \nabla n \tag{9}$$

where the quantity α is closely related to the diffusion coefficient. The equation for n_1 is now

$$\frac{\partial^2 n_1}{\partial t^2} - \alpha \nabla^2 n_1 + \omega_p^2 n_1 = 0, \tag{10}$$

and the traveling wave solution $n_1 (rt) = n_1 e^{i(k \cdot r - \omega t)}$ has the dispersion relation

$$\omega^2 = \omega_p^2 + \alpha k^2 , \tag{11}$$

where $k = 2\pi/\lambda$ is the wave vector. The pressure forces aid the electric field in driving the plasma towards uniformity. As a consequence, the restoring force in the plasma oscillation is larger and its frequency higher than in their absence. Equation (11) has the correct wave vector (or momentum) variation to explain the dispersion observed in characteristic energy loss experiments. Detailed calculations, [11] including corrections for electron interaction, yield values of α which are also in quantitative agreement with the measured values for simple metals. Thus, in such metals the plasmon dispersion is well accounted for by the theory.

Let us now consider the damping of plasma oscillations in metals. Here a crucial parameter is the ratio of the phase velocity of the plasma wave to the average electron velocity. The phase velocity is given by the usual formula

$$v_\varphi \equiv (\omega/k) = \sqrt{(\omega_p^2/k^2) + \alpha} \tag{12}$$

Notice that v_φ is very large at long wavelengths (small k) and gradually decreases as k becomes bigger. At some critical value of k, v_φ becomes equal to the velocity of the

fastest electron in the plasma*. In the frame of reference of such an electron the wave appears to be stationary. The electron, therefore, experiences a constant electrostatic field which continuously accelerates it. Energy is transferred from the wave to the electron and the former is heavily damped. This synchronous process, which is the reverse of that which occurs in traveling wave tubes, was first discussed in connection with plasmas by L. D. Landau, [12] and is therefore called Landau damping. It is responsible for the large damping and subsequent disappearance of plasma oscillations in metals beyond the critical momentum (or scattering angle). For simple metals, the value of the critical momentum is also correctly predicted by the theory. [13]

Finally, it remains to explain the rather small, and smoothly varying, damping of longer wavelength plasma oscillations. This effect is, in some ways, the most intriguing result of the characteristic energy loss experiments. In the simple theory which leads to Eq. (8) the electron gas is essentially treated as an electrical fluid of mass density ρ = nm and charge density σ = ne. (Notice that ω_p is a function only of ρ and σ, and not of e, m and n separately). The particulate nature of the plasma plays no role in Eq. (8). But electrons in metals certainly are particles, and this fact must eventually manifest itself in the behavior of the plasma oscillation. The simplest example of such an effect is the Landau damping described above. In this process the energy and momentum of the plasma wave are transferred to a single electron traveling at the phase velocity of the wave. The velocity matching condition ensures the conservation of energy and momentum in this process. In metals, the matching condition is satisfied by plasma waves of sufficiently short wave

*Here the fact that the electrons are in a Fermi-Dirac, rather than Maxwellian, distribution plays an important part. The Fermi distribution has a sharp upper bound (the Fermi velocity), whereas the Maxwellian tails off smoothly at large velocities. Landau damping of plasma oscillations also occurs in Maxwellian distributions, but its onset is not quite as abrupt as it is in the Fermi-Dirac case.

length. Such waves are heavily Landau damped, whereas plasmons of longer wave length are unaffected by the Landau mechanism--essentially because it is impossible to conserve energy and momentum in any process in which they decay by exciting a single electron. However, it is possible to satisfy the conservation laws if the plasmon decays by exciting two electrons. Such a process, which can only occur during the time the electrons in question are scattering from one another, is responsible for the damping of long wave length plasmons in metals. Recent detailed calculations[10] have shown that this process will quantitatively account for the damping of such plasmons in aluminum. This damping is one of the few effects observed in metals whose existence specifically requires electron-electron correlation.

To summarize the work outlined above, we may say that there is quantitative agreement between theory and experiment as regards the behavior of plasmons in a simple metal such as aluminum. This is encouraging, but much work remains to be done. On the theoretical side it is puzzling that the theory of plasmon behavior works as well as it does. The theory treats electron-electron interaction by a perturbation theory which does not converge well. One expects the theory to be best for aluminum and it may not be surprising, therefore, that agreement is obtained in this case. Other simple metals are available, however, in which the theory should be much nearer the ragged edge of non-convergence. The extreme example is the metal cesium which contains an almost pathologically dilute (by metal standards) electron gas. It would be fascinating to have detailed data on plasmon behavior in this metal. Since cesium is a violently reactive material with a consistency, at room temperature, about the same as butter, it is clear that considerable experimental ingenuity will be required to perform this ultimate plasmon experiment in metals.

IV. ELECTROMAGNETIC WAVES IN SOLIDS

The plasma oscillations described in the previous section are longitudinal waves driven by Coulomb forces. It is also possible to propagate transverse (or partially

$$\rho \frac{\delta^2 u_y}{\delta t^2} - \frac{neB}{c} \frac{\delta u_x}{\delta t} - T \frac{\delta^2 u_y}{\delta z^2} = 0 , \tag{16}$$

where u_x and u_y are displacements in two directions normal to B. For simplicity we have again assumed that the wave is propagating parallel to B. In the low frequency limit the inertial terms in these equations are small. The wave is driven by the Lorentz force and the tension, $B^2/4\pi$. It is circularly polarized and hence is known as a helicon wave.

The propagating solution of Eq. (16) is a wave of the form

$$\begin{pmatrix} u_x \\ u_y \end{pmatrix} = u_o \begin{pmatrix} 1 \\ i \end{pmatrix} e^{i(kz-\omega t)} \tag{17}$$

where k and ω satisfy the helicon dispersion relation

$$\frac{c^2 k^2}{\omega^2} = \frac{4\pi nec}{\omega B} . \tag{18}$$

$\left(\frac{ck}{\omega}\right)^2 \equiv \epsilon$ is the effective dielectric constant of the medium for this wave. In metals it can be exceedingly large; greater than 10^{16}. Helicon waves therefore travel quite slowly in metals, typically at speeds between 10^2 and 10^5 cm/sec. It is also important to notice that there is strong dispersion of the helicon wave. Helicon waves are the solid state analogue of "whistlers" observed in the ionosphere.

In deriving Eq. (15) and Eq. (18), which describe Alfven and helicon wave propagation, we have focused our attention on the magnetic lines, and assumed that the particles are tied to them. This assumption can only be correct, however, if the particles have a relatively small chance of suffering a collision in going around a cyclotron orbit. If τ is the collision time, this requirement can be expressed in the form $\omega_c \tau >> 1$. This is a necessary condition for obtaining low-loss waves. For helicon waves it is also sufficient--the loss per wave length of such waves is $(\omega_c \tau)^{-1}$. Large values of τ are best achieved in pure crystals at low (4°K) temperatures. Collision times greater than 10^{-10} sec are attainable. Fields of

10 kilogauss or greater are then required to make the helicon relatively lossless.

For Alfven waves, the condition for achieving low loss is more stringent than that for helicons. It is $\omega\tau \gg 1$, rather than $(\omega_c \tau) \gg 1$. For this and other reasons, Alfven waves have only been observed in a few materials.

The experiment which broke open the field of electromagnetic wave propagation in solid state plasmas was the observation of helicon waves by Bowers, Legendy and Rose. [18] The material used was pure sodium metal at 4°K. A field of 10,000 gauss produced an $(\omega_c \tau)$ of about 20. In the first version of this experiment a sample of the sodium was wound with primary and secondary coils; one observed the voltage in the secondary as a function of time, after a discontinuous change of current in the primary. Without a magnetic field the secondary current decays monotonically, but it show damped oscillations when a field is present. These oscillations are caused by helicon waves bouncing back and forth inside the sample. A more graphic demonstration of this fact is provided by a slightly different experiment in which one measures the voltage in the secondary coil as a function of the frequency of the current in the primary. The response is large when the frequency coincides with one of the cavity resonances of the helicon wave inside the sodium crystal. Figure 6 shows data taken in this way by Bowers and his co-workers. The peaks occur at cavity resonances; their width is a measure of the Q. In these measurements the wave travels quite slowly, about 100 cm/sec, and the effective dielectric constant is about 10^{17} !

In the experiment described above the crystal forms a cavity, and one looks for resonances of the helicon wave within it. It is also possible to do transmission experiments with electromagnetic waves in solid state plasmas. The first experiment of this type was done by Williams [19] to demonstrate Alfven wave propagation in solids. The material used was a single crystal of bismuth (remember that this element contains a two-component plasma and therefore supports Alfven waves). Microwaves (at 18 kMc) were incident on a plate shaped sample about 3 mm thick, and a detector was placed on the other side of the sample. In the presence of a magnetic field the crystal transmits

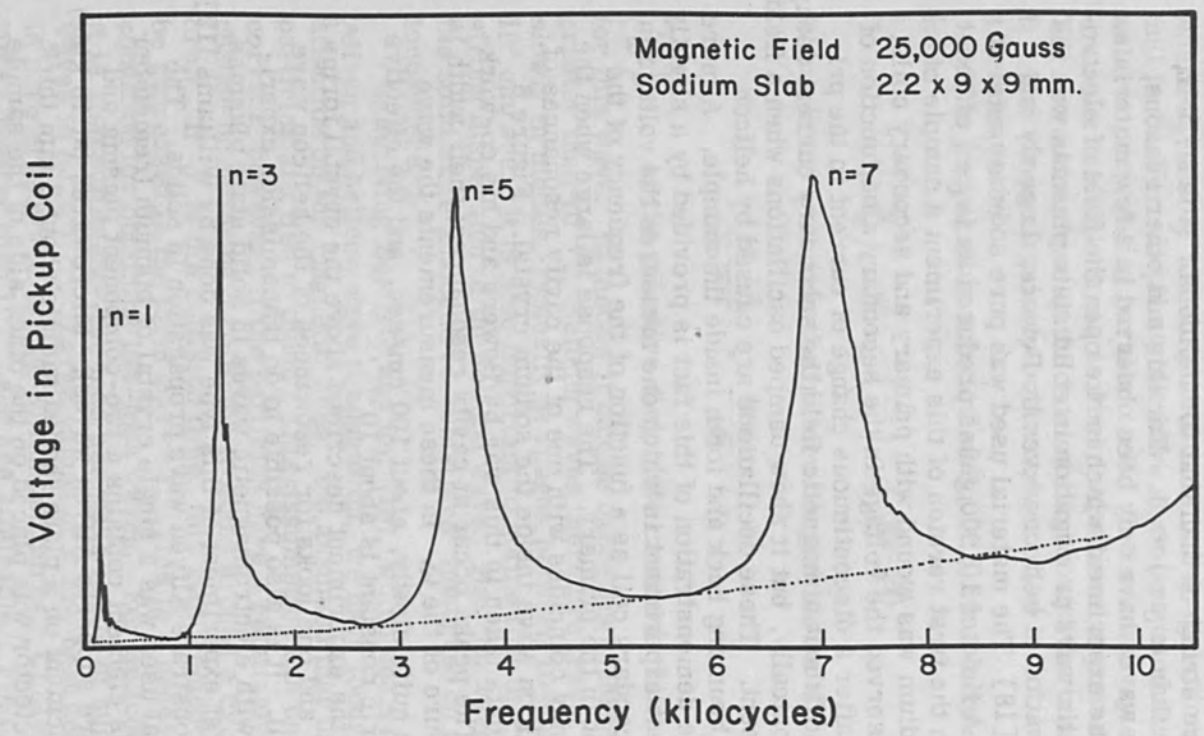

Figure 6. Helicon Resonances in a Sodium Slab (after Bowers).

radiation as Alfven waves. In addition, a small fraction of the microwave power leaks around the sample. The detector sees the sum, with proper phases, of the transmitted and "leakage" signals. The optical thickness of the sample depends, via Eq. (15) on the magnetic field. Thus, as the field is changed, the phase of the transmitted signal varies relative to that of the leakage signal. The result is a series of beats from which one can infer the effective dielectric constant of the slab. Data taken in this way by Williams are shown in Fig. 7. Many beats between the two signals are visible.

An experiment, similar in principle to that of Williams, has also been done with helicon waves by Grimes. [20] Grimes, however, works at frequencies near 1 Mc/sec. This is possible with helicons since their damping is determined by $\omega_c \tau$ (rather than $\omega \tau$ as for Alfven waves). Figure 8 shows the sort of data Grimes obtains. The "leakage" fringes are clearly visible and can be analyzed to determine the dispersion relation with high precision.

What parameters of a solid state plasma can be studied with wave experiments of the sort outlined above? To date, the most fruitful work has been done with helicon waves. In the first helicon experiments the dispersion relation was confirmed (Eq. 18) and the electron density measured. As expected, this quantity is given by the number of valence electrons/cc in simple metals such as Na, K and Al. In these measurements one is essentially determining the high field Hall constant, R, of the crystal (the combination nec that appears in Eq. (18) is just 1/R). The helicon experiments give the most accurate values of this constant that have been obtained. It is also possible to use the damping of the helicon wave to measure transverse magnetic-resistance. This technique has recently been exploited by Bowers [21] to determine the magnetoresistance of alkali metals. The results show a disagreement with theory that has not yet been resolved.

In another application, helicon waves have been used to obtain information about the dynamical behavior of electrons in metals. Certain metals (such as Cu or Ag) support a class of electron trajectories in which the electrons have a net velocity across the magnetic field. This behavior is entirely different from that of electrons in free

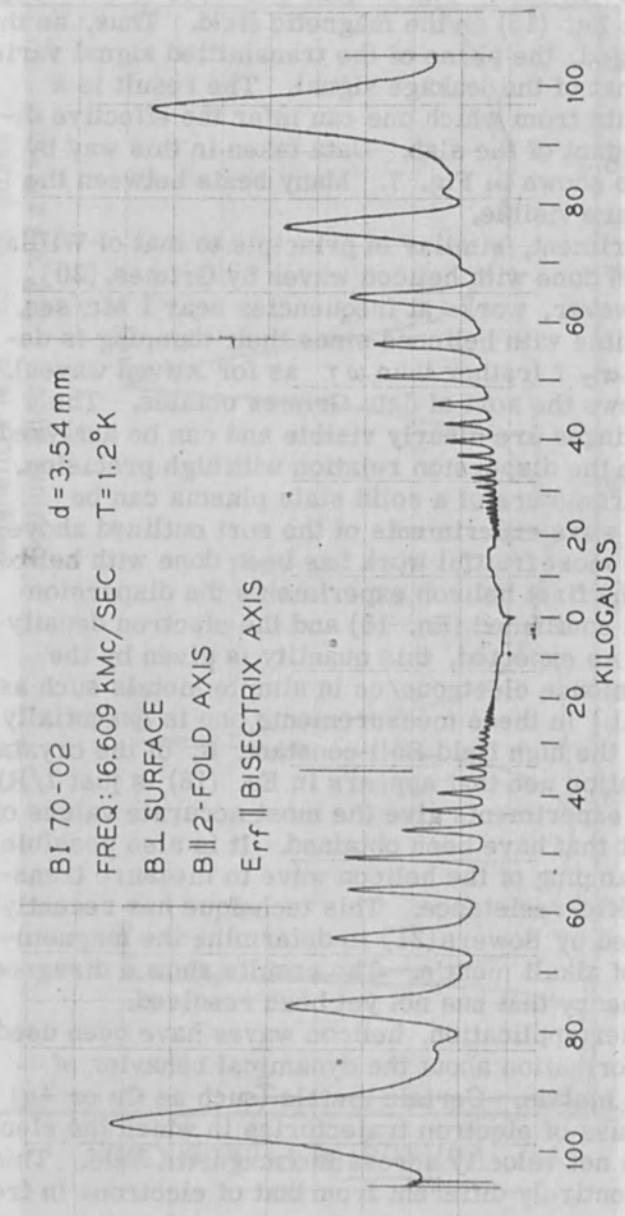

Figure 7. Interference Fringes due to Alfven Wave Propagation through a Bismuth Slab (after Williams).

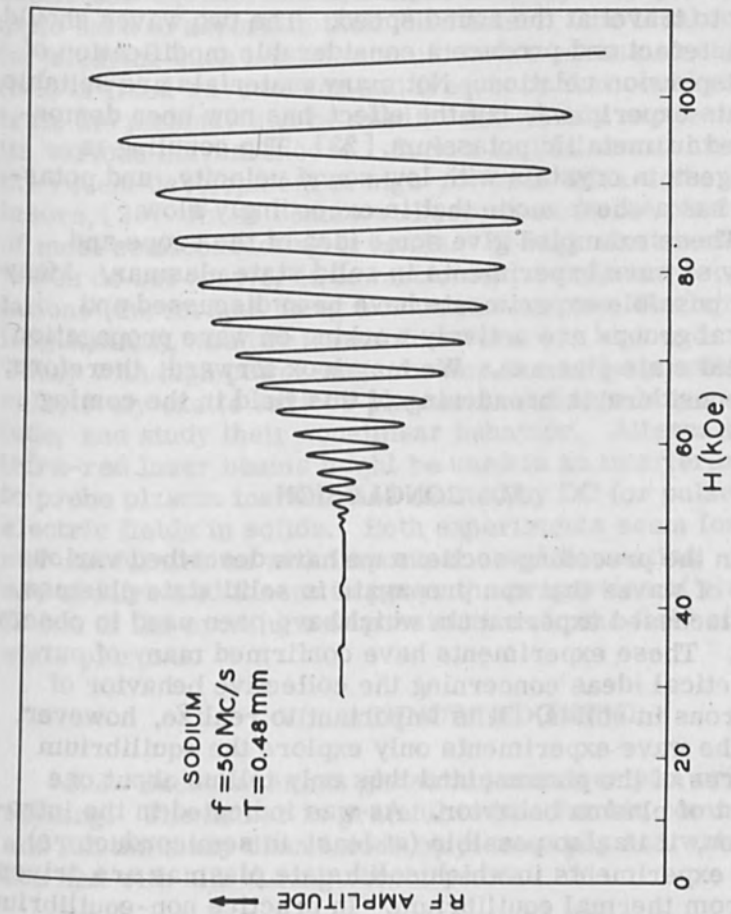

Figure 8. Helicon Wave Interference Fringes in a Sodium Slab (after Grimes).

space, whose motion is confined in directions normal to the field. These special trajectories are called open orbits, and have been detected in Ag [22] by the additional damping of the helicon wave that they produce. This technique is still in its infancy, but may ultimately prove as powerful as magnetoresistance methods which have hitherto been used to detect such phenomena.

As mentioned earlier, helicons are slow waves. Sound waves in solids also travel relatively slowly. Thus, a natural experiment to attempt is one in which helicons are made to travel at the sound speed. The two waves should then interact and produce a considerable modification of the dispersion relation. Not many materials are suitable for this experiment, but the effect has now been demonstrated in metallic potassium. [23] The coupling is strongest in crystals with low sound velocity, and potassium has a shear mode that is exceedingly slow.

These examples give some idea of the scope and utility of wave experiments in solid state plasmas. Many other possible experiments have been discussed and several groups are actively working on wave propagation in solid state plasmas. We may look forward, therefore, to a considerable broadening of this field in the coming years.

V. CONCLUSION

In the preceding sections we have described various types of waves that can propagate in solid state plasmas, and discussed experiments which have been used to observe them. These experiments have confirmed many of our theoretical ideas concerning the collective behavior of electrons in solids. It is important to realize, however, that the wave experiments only explore the equilibrium features of the plasma, and thus only tell us about one aspect of plasma behavior. As was indicated in the introduction, it is also possible (at least in semiconductors) to do experiments in which solid state plasmas are driven far from thermal equilibrium. In practice non-equilibrium situations are usually produced by the application of large electric fields, and often result in some sort of an instability in the plasma. A good deal of research has been devoted

to the study of such instabilities and many interesting results have been obtained. [24] It is still fair to say, however, that our understanding of the non-equilibrium properties of plasmas in solids is very much less complete than our understanding of equilibrium ones.

One difficulty in the study of non-equilibrium properties is the fact that the major experimental tool (large, usually pulsed, electric fields) is not a particularly delicate or selective one. Moreover, once such fields are used to excite non-equilibrium situations in a crystal, it is often quite hard to ascertain their character. The ideal tool for studying such behavior would be an intense electric field of fixed wave vector and frequency that could penetrate the plasma, and be used to selectively excite or probe its various normal modes. Such a tool is now at hand with the recent development of high-powered infra-red lasers, [25] whose beams will propagate in the plasmas of most semiconducting crystals. Though electromagnetic waves do not couple, in lowest order, to plasma oscillations (the former being a transverse wave, the latter longitudinal), the two waves do interact in high orders. Thus, with high power laser beams it may be possible to selectively excite various plasma modes to a large amplitude, and study their non-linear behavior. Alternatively, infra-red laser beams might be used in an interferometer to probe plasma instabilities excited by DC (or pulsed) electric fields in solids. Both experiments seem feasible and can furnish us with important new information. The use of infra-red lasers to probe the properties of plasmas is one of the exciting new possibilities in the field of solid state plasmas.

VI. ACKNOWLEDGMENT

S. J. Buchsbaum has given this manuscript a critical reading. The author is grateful to him for his comments, and for the many discussions on plasma physics which he has had with him during recent years.

REFERENCES

1. G. Ruthemann, Ann. Phys. 2, 113 (1948).
2. W. Land, Optik 3, 233 (1948).
3. See, for example, Dresselhaus, Kip and Kittel, Phys. Rev. 100, 618 (1955); Smith, Hebel and Buchsbaum, Phys. Rev. 129, 154 (1963).
4. Examples are: W. S. Boyle and K. F. Rodgers, Phys. Rev. Letts. 2, 338 (1959); B. Lax and G. B. Wright, Phys. Rev. Letts. 4, 16 (1960); W. S. Boyle and A. D. Brailsford, Phys. Rev. 120, 1943 (1960); L. C. Hebel and P. A. Wolff, Phys. Rev. Letts. 11, 368 (1963).
5. The data are reviewed in an article by H. Raether, Ergebnisse der exakten Naturwissenschaffen, Vol. 38 (Springer-Verlag, Berlin 1965).
6. H. Ehrenrich and H. R. Philipp, Phys. Rev. 128, 1622 (1962).
7. H. Watanabe, J. Phys. Soc. Japan 11, 112 (1956).
8. C. Kunz, Z. Physik 167, 53 (1962).
9. N. Swanson and C. J. Powell, Phys. Rev. (in press).
10. B. W. Ninham, C. J. Powell and N. Swanson, Phys. Rev. (in press).
11. D. Bohm and D. Pines, Phys. Rev. 92, 609 (1953); R. A. Ferrell, Phys. Rev. 107, 450 (1957); D. Pines, Physica 26, Suppl. 103 (1960).
12. L. Landau, J. Phys. USSR 10, 25 (1946).
13. R. A. Ferrell, Phys. Rev. 107, 450 (1957).
14. O. V. Konstantinov and V. I. Perel, Soviet Phys. JETP, 11, 117 (1960).
15. P. Aigrain, Proceedings of the International Conference on Semiconductor Physics, Prague, 1960 (Czechoslovak Academy of Science, Prague, 1961). p. 224.
16. S. J. Buchsbaum and J. K. Galt, Phys. of Fluids, 4, 1514 (1961).
17. The experimental situation is reviewed in an article by R. Bowers, Plasma Effects in Solids (Dunod, Paris, 1964).
18. R. Bowers, C. Legendy and F. Rose, Phys. Rev. Letts. 7, 339 (1961).

19. G. A. Williams, Bull. Am. Phys. Soc. 7, 409 (1962) and 8, 205 (1963); G. A. Williams and G. E. Smith, I. B. M. Journal of Research, 8, 276 (1964).
20. C. C. Grimes, Bull. Am. Phys. Soc. 9, 239 (1964); C. C. Grimes, Plasma Effects in Solids (Dunod, Paris, 1964).
21. P. A. Penz and R. Bowers, Bull. Am. Phys. Soc. 11, 92 (1966).
22. S. J. Buchsbaum and P. A. Wolff, Phys. Rev. Letts. 15, 406 (1965), C. C. Grimes, G. Adams and P. H. Schmidt, Phys. Rev. Letts. 15, 409 (1965).
23. C. C. Grimes and S. J. Buchsbaum, Phys. Rev. Letts. 12, 357 (1964).
24. Work on instabilities in solid state plasmas is reviewed in an article by M. Glicksman, Plasma Effects in Solids (Academic Press - Dunod, Paris 1964). See also A. G. Chynoweth and S. J. Buchsbaum, Physics Today, November 1965.
25. C. K. N. Patel, Proceedings of the International Conference on the Physics of Quantum Electronics, edited by P. L. Kelly, B. Lax and P. E. Tannenwald (McGraw-Hill Book Company, Inc., New York, 1965).

REFERENCES

1. G. Ruthemann, Ann. Phys. 2, 113 (1948).
2. W. Land, Optik 3, 233 (1948).
3. See, for example, Dresselhaus, Kip and Kittel, Phys. Rev. 100, 618 (1955); Smith, Hebel and Buchsbaum, Phys. Rev. 129, 154 (1963).
4. Examples are: W. S. Boyle and K. F. Rodgers, Phys. Rev. Letts. 2, 338 (1959); B. Lax and G. B. Wright, Phys. Rev. Letts. 4, 16 (1960); W. S. Boyle and A. D. Brailsford, Phys. Rev. 120, 1943 (1960); L. C. Hebel and P. A. Wolff, Phys. Rev. Letts. 11, 368 (1963).
5. The data are reviewed in an article by H. Raether, Ergebnisse der exakten Naturwissenschaffen, Vol. 38 (Springer-Verlag, Berlin 1965).
6. H. Ehrenrich and H. R. Philipp, Phys. Rev. 128, 1622 (1962).
7. H. Watanabe, J. Phys. Soc. Japan 11, 112 (1956).
8. C. Kunz, Z. Physik 167, 53 (1962).
9. N. Swanson and C. J. Powell, Phys. Rev. (in press).
10. B. W. Ninham, C. J. Powell and N. Swanson, Phys. Rev. (in press).
11. D. Bohm and D. Pines, Phys. Rev. 92, 609 (1953); R. A. Ferrell, Phys. Rev. 107, 450 (1957); D. Pines, Physica 26, Suppl. 103 (1960).
12. L. Landau, J. Phys. USSR 10, 25 (1946).
13. R. A. Ferrell, Phys. Rev. 107, 450 (1957).
14. O. V. Konstantinov and V. I. Perel, Soviet Phys. JETP, 11, 117 (1960).
15. P. Aigrain, Proceedings of the International Conference on Semiconductor Physics, Prague, 1960 (Czechoslovak Academy of Science, Prague, 1961). p. 224.
16. S. J. Buchsbaum and J. K. Galt, Phys. of Fluids, 4, 1514 (1961).
17. The experimental situation is reviewed in an article by R. Bowers, Plasma Effects in Solids (Dunod, Paris, 1964).
18. R. Bowers, C. Legendy and F. Rose, Phys. Rev. Letts. 7, 339 (1961).

19. G. A. Williams, Bull. Am. Phys. Soc. 7, 409 (1962) and 8, 205 (1963); G. A. Williams and G. E. Smith, I. B. M. Journal of Research, 8, 276 (1964).
20. C. C. Grimes, Bull. Am. Phys. Soc. 9, 239 (1964); C. C. Grimes, Plasma Effects in Solids (Dunod, Paris, 1964).
21. P. A. Penz and R. Bowers, Bull. Am. Phys. Soc. 11, 92 (1966).
22. S. J. Buchsbaum and P. A. Wolff, Phys. Rev. Letts. 15, 406 (1965), C. C. Grimes, G. Adams and P. H. Schmidt, Phys. Rev. Letts. 15, 409 (1965).
23. C. C. Grimes and S. J. Buchsbaum, Phys. Rev. Letts. 12, 357 (1964).
24. Work on instabilities in solid state plasmas is reviewed in an article by M. Glicksman, Plasma Effects in Solids (Academic Press - Dunod, Paris 1964). See also A. G. Chynoweth and S. J. Buchsbaum, Physics Today, November 1965.
25. C. K. N. Patel, Proceedings of the International Conference on the Physics of Quantum Electronics, edited by P. L. Kelly, B. Lax and P. E. Tannenwald (McGraw-Hill Book Company, Inc., New York, 1965).

A Quasi-Fluid Treatment for Intense Electron Beam Flow

A. S. Roberts, Jr.*

I. INTRODUCTION

A wealth of literature is accumulating which reports the results of experimental and analytical investigations on the internal structure of high ($> 1 \times 10^{-6}$ amp-volt$^{-3/2}$) and low perveance electron beams. Yet to be developed, however, is the generalized flow theory which will describe in the first order the spatial evolution of the beam from source to collector and in the second order include beam aberrant conditions. Each worker then uses a beam theory which is adequate for his problem or experiment.

A most intriguing beam flow problem involves the electromagnetic possibility that a beam generating device might be constructed where careful control of counterbalancing processes would allow the magnetostatic forces, which accompany an intense current filament, to constrain the beam against dispersive effects. The beam generated plasma can, under proper experimental conditions (Ginzton and Wadia [1], Wadia [2], provide positive ions to neutralize beam space-charge. The neutralization process is available in principle without the use of excessive pressures ($< 10^{-4}$ torr). The self-focusing forces become important when space-charge is neutralized. This type of beam flow has been analyzed from the standpoint of free charged particle dynamics and paraxial analysis (Roberts, [3]).

*School of Engineering, Old Dominion College, Norfolk, Virginia, 23508

Magnetostatic effects are interesting mainly for high current ($\sim$ 1 amp) and high perveance beams ($\sim 2 \times 10^{-6}$ amp-volt$^{-3/2}$), where the radii are about 1 mm; in this parameter range experimentation is difficult. Furthermore, the present and past [3] analyses limit beam drift energy to 3000 kev so that relativistic effects are negligible. These are none-the-less high current density beams and as such present the possibility of electron-electron collision times (Spitzer [4]) becoming similar in magnitude to transition times for electrons through a Laboratory tube drift space. These collective beam particle interactions give rise to pressure or temperature-like behavior in a kinetic theory sense. Conceptually, the beam flow problem is stationary in the laboratory frame of reference but is also a highly non-equilibrium situation. So it is the purpose of this analysis to formulate and solve beam flow equations which have theoretical basis in the principles of statistical mechanics. Moments of the Boltzman transport equation are taken and the resulting conservation laws allow a quasi-fluid treatment of electron beam flow, where collective electron-electron interactions are manifested through a simple kinetic stress tensor. A beam surface trajectory equation is finally gotten under two major constraining conditions, (1) adiabatic beam flow with elastic collisions between electrons, and (2) application of the Bennett [5] critical current relation, which relates beam current and thermal energy for self-focused beam flow.

Certain significant beam flow analyses which are found in the literature warrant comment. It would be remiss not to mention the text by Pierce [6], which consolidated earlier work in electron beam analysis; recently beam envelope trajectory equations have been solved by Walsh [7] and Roberts [3] where cognizance of non-zero angular momentum is taken. The spectre of laminarity haunts most analytic efforts; however, Herrmann [8] has apparently eliminated this assumption with his beam optical model. A rather general theory of axi-symmetric beams has been presented by Kirstein [9] which accounts for thermal effects, but the results are not simply applied.

In the succeeding sections of this paper a quasi-fluid analysis is developed. In section II the analytic model is constructed, governing equations are presented and important constraining conditions are discussed. Presentation of the beam envelope trajectory equation is made in section III, trajectory solutions which include self-magnetostatic and thermal effects are gotten in section IV, and section V is the summary of results.

II. THE ANALYTIC MODEL

An intense beam of electrons can be extracted from a plasma source and focused on an aperture which initiates an electrically and magnetically shielded drift space (see Fig. 1). This technique allows the non-accelerated beam to be studied as it travels under influence of its intrinsic electromagnetic field forces. Behavior of the beam in the drift space will be subject to source conditions; in the case of a duoplasmatron source (Froehlich [10]), plasma temperature and applied magnetic induction will impose initial conditions on beam particles as they enter the drift space. In a previous paper [3] Newton's second law was written with the Lorentz force, and the beam trajectory equation in the drift space was cast as an initial value problem. The beam electrons were supposed to move under influence of classical field forces, and the "granular" nature of the force fields due to electron-electron collisions was ignored. The trajectory equation for a test particle in the beam envelope or edge was solved. These first order electron-electron collisional effects appear naturally by considering a particle balance in an elemental volume of a six-dimensional phase space. The result is the Boltzman transport equation,

$$\frac{\partial f}{\partial t} + \vec{\nu} \cdot \vec{\nabla}_r f + \frac{\vec{F}}{m} \cdot \vec{\nabla}_\nu f = \left(\frac{\partial f}{\partial t} \right)_c \qquad (1)$$

where $f(\vec{\nu}, \vec{r}; t)$, the distribution function, measures the probability of finding a beam electron at $(\vec{r}, \vec{\nu})$ in phase space within an elemental volume $d\vec{r}\, d\vec{\nu}$. For the beam particles $\vec{F}$ is the Lorentz force, $\vec{\nu}$ the particle velocity,

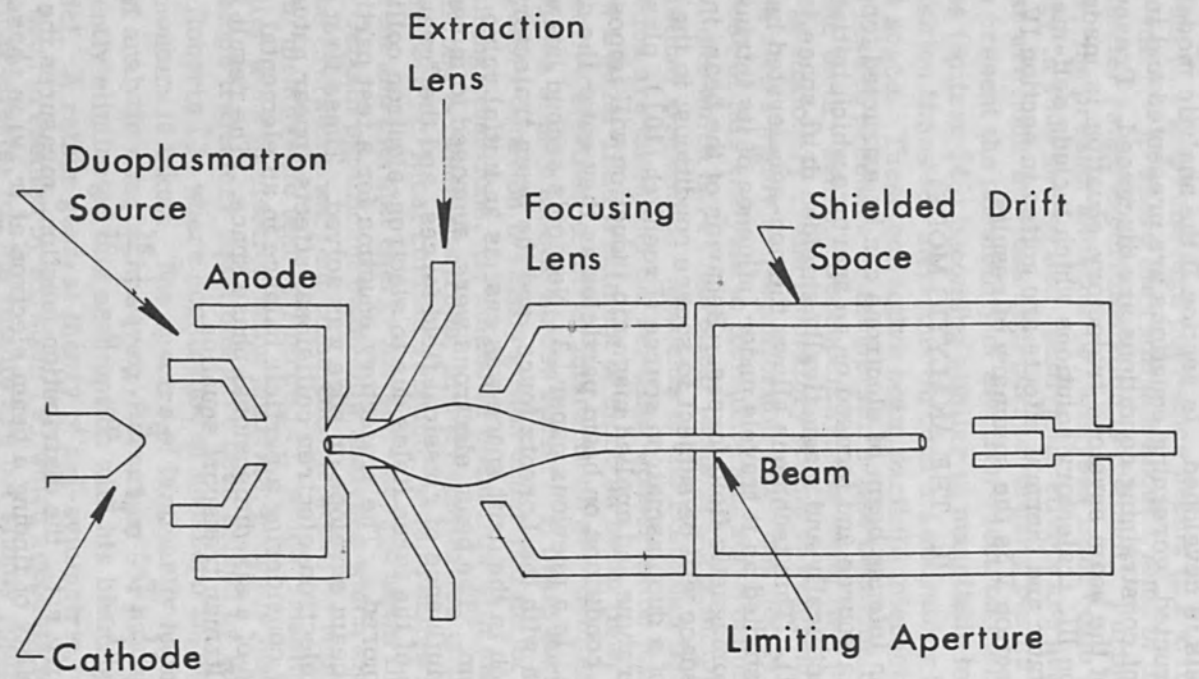

Figure 1. Tube Schematic for Generation of Intense, Undriven Electron Beams.

and $(\partial f/\partial t)_c$ accounts for inelastic collisions of the electrons or for production of beam particles.

Assuming elastic collisions only among the beam electrons, the first three moments of the transport equation lead to equations for conservation of mass, momentum, and energy respectively,

$$\frac{\partial n}{\partial t} + \vec{\nabla}_r \cdot (n\vec{\bar{\nu}}) = 0 \tag{2}$$

$$\frac{d\vec{\nu}}{dt} = \frac{1}{mn} \vec{\nabla} \cdot \vec{P} - \frac{|e|}{m} \overline{(\vec{E} + \vec{\nu} \times \vec{B})} \tag{3}$$

$$\frac{\partial}{\partial t}\left(\frac{nm}{2}\overline{\nu^2}\right) + \vec{\nabla}_r \cdot \left(\frac{nm}{2}\overline{\vec{\nu}\nu^2}\right) = \vec{j} \cdot \vec{E} \tag{4}$$

The "barred" quantities are averaged over all velocities, n is number density, m is the electron mass (also $\eta = |e|/m$), spatial and velocity gradient operators are subscripted with r and v, j is the beam current density, and $\vec{P}$ is the kinetic stress tensor which replaces the familiar scalar pressure when moments of the transport equation are taken. Note that particle velocity, $\vec{\nu}$, has been decomposed into an average drift velocity and random velocity components (see Rose and Clark [11]),

$$\vec{\nu} = \vec{\bar{\nu}} + \vec{\nu}_r \tag{5}$$
$$\vec{\nu}^2 = \nu^2 \text{ (scalar)}$$

Equation (2), (3), and (4) apply when the following conditions exist:

1. $(\partial f/\partial t)_c = 0$, elastic collisions among single species
2. $\vec{\nabla}_\nu \cdot \vec{F} = 0$ (true for Lorentz force)
3. adiabetic beam flow
4. non-relativistic velocities

Note that the governing equations are not limited to cases where the distribution function is isotropic, i. e.,

$$f(\nu) = f(\nu_r) \cdot f(\nu_\theta) \cdot f(\nu_z)$$

can be anisotropic while the component distribution functions (if separable) can each display piece-wise isotropy.

The discrete particle concept which easily lends itself to paraxial analysis is abandoned here. However, beam surface trajectories may still be calculated by associating with the "average" particle in the beam edge a drift velocuty $\vec{v}$; in the equation of motion, (3), the random velocity components are contained in $\vec{P}$. The velocity decomposition of equation (5) should be kept in mind.

A. The Kinetic Stress Tensor and Consequences

The fluid equations (2), (3), and (4), which imply adiabetic and non-dissipative motion, can be combined with the relevent Maxwell's equations to form a surface electron trajectory equation. The thermal effects are manifested through the kinetic stress tensor term; so, it is expedient to select a physically reasonable anisotropic tensor to represent the non-equilibrium flow problem. Since the beam motion is highly ordered along the axis in a cylindrically symmetric configuration, i. e.,

$$V_z \gg (v_r, v_\theta),$$

the inference is made that the longitudinal spread in random energy, through the particle v_{rz} values, is uncoupled from transverse random modes. The v_{rz} values might seek one equilibrium configuration, while the transverse random components seek an independent one. The contention is also supported by the absense of electron-ion, electron-neutral collisions for the high vacuum beam. Furthermore, it is assumed that the two random transverse modes are coupled and seek a mutual equilibrium configuration. The allowed anisotropy can then be expressed through the tensor,

$$\vec{P} = \begin{bmatrix} P_\perp & O & O \\ O & P_\perp & O \\ O & O & P_\parallel \end{bmatrix} \qquad (6)$$

where

$$P_{\perp} = 1/2\ mn\ \overline{v_{\perp}^2} \tag{7}$$

$$P_{||} = nm\ \overline{v_{rz}^2} \tag{8}$$

and,

$$\overline{v_{\perp}^2} = \overline{v_{rx}^2} + \overline{v_{ry}^2} = 2\overline{v_{r\alpha}^2}. \tag{9}$$

This same tensor is valid when a high B_z induction is impressed along the axis of flow. In the present case beam "rigidity" is gained through careful focusing of the fast beam in a plane which initiates the drift space. It is also essential that the beam space charge be eliminated as the beam enters the drift space; this point will be discussed further in section III.

With the tensor [6], equations (2), (3), and (4) can be combined with object of relating $P_{||}$ and $P_{\perp}$. This bit of vector algebra is facilitated by using the velocity decomposition [5] and by separating vector quantities into perpendicular ($\perp$) and parallel ($||$) components with respect to the z-axis. Such a reduction of the energy equation (4) yields,

$$\begin{aligned} nm\vec{\bar{\nu}} \cdot \frac{\partial \vec{\nu}}{\partial t} + \frac{\partial P_{\perp}}{\partial t} + \frac{1}{2}\frac{\partial P_{||}}{\partial t} + \frac{1}{2} nm\vec{\bar{\nu}} \cdot \vec{\nabla}\vec{\bar{\nu}}^2 + 2\left(P_{\perp} + \frac{P_{||}}{4}\right)\vec{\cdot}\,\vec{\bar{\nu}}_{\perp} \\ + 2\vec{\bar{\nu}}_{\perp} \cdot \vec{} \left(P_{\perp} + \frac{P_{||}}{4}\right) + (3/2\, P_{||} + P_{\perp})\vec{\nabla} \cdot \vec{\bar{\nu}}_{||} \\ + \vec{\bar{\nu}}_{||} \cdot \vec{\nabla}\ (3/2\ P_{||} + P_{\perp}) = \vec{j} \cdot \vec{E} \end{aligned} \tag{10}$$

where mass continuity, equation (2) was used to eliminate two terms. The scalar product of $mn\vec{\nu}$ taken through equation (3) gives the result,

$$\begin{aligned} nm\vec{\bar{\nu}} \cdot \frac{\partial \vec{\nu}}{\partial t} + nm\vec{\bar{\nu}} \cdot (\vec{\bar{\nu}} \cdot \vec{\nabla})\vec{\bar{\nu}} + \vec{\bar{\nu}} \cdot \vec{\nabla}_{\perp} P_{\perp} \\ + \vec{\bar{\nu}} \cdot \vec{\nabla}_{||} P_{||} = nq\vec{\bar{\nu}} \cdot \vec{E} \end{aligned} \tag{11}$$

After subtracting (11) from (10), grouping terms, using mass continuity again, and recognizing total derivatives, the following ordinary differential equation is obtained.

$$\frac{d}{dt}\left(P_{\perp} + \frac{P_{||}}{2}\right) - 2\left(P_{\perp} + \frac{P_{||}}{4}\right)\frac{1}{n}\frac{dn}{dt} = \left(P_{\perp} - P_{\parallel}\right)\vec{\nabla}_{||}\cdot\bar{\vec{\nu}}_{||} \tag{12}$$

Through a similar reduction of the first three moment equations Delcroix [12] obtained the result,

$$\left.\begin{aligned} \frac{dP_{\perp}}{dt} + 2P_{\perp}\vec{\nabla}_{\perp}\cdot\bar{\vec{\nu}}_{\perp} + P_{\perp}\vec{\nabla}_{||}\cdot\bar{\vec{\nu}}_{||} &= 0 \\ \frac{dP_{||}}{dt} + 3P_{||}\vec{\nabla}_{||}\cdot\bar{\vec{\nu}}_{||} + P_{||}\vec{\nabla}_{\perp}\bar{\vec{\nu}}_{\perp} &= 0 \end{aligned}\right\} \tag{13}$$

using the notation of the present paper. A summation of equations (13) produces the identical result, equation (12), found in the present analysis after eliminating some velocity divergence terms using equation (2).

When the mean square random velocity terms become equal (Maxwellian equilibrium), $P_{\perp} = P_{||}$, and equation (12) reduces to a familiar relation which yields the adiabetic gas law,

$$p\nu^{5/3} = C \tag{14}$$

The corresponding abiabetic law for the present problem, involving an anisotropic kinetic stress tensor, can be derived by algebraically combining equations (2) and (13) to completely eliminate the velocity divergences. This result is,

$$2P_{||}\frac{dP_{\perp}}{dt} + P_{\perp}\frac{dP_{||}}{dt} - \frac{5}{n}\frac{dn}{dt}P_{||}P_{\perp} = 0 \tag{15}$$

which immediately integrates to,

$$\frac{P_{\perp}^{2}P_{||}}{n^{5}} = C \tag{16}$$

For a scalar pressure equation (16) reduces to the conventional adiabetic law, equation (14).

The paradox of the interesting result given as equation (16) is that there are now two unknown "pressure" terms, $P_{\perp}$ and $P_{\parallel}$; knowledge of one defines the other. Another condition is needed which will enable $P_{\perp}$ or $P_{\parallel}$ to be written in terms of variables which are found in the trajectory problem, defined through the equation of motion, equation (3).

B. The Critical Current Condition

A critical current condition exists due to Bennett [5] which relates undriven beam current to transverse random or thermal energy and beam particle density. This criterion for beam current,

$$I^2 = \frac{8\pi k T_{\perp} N}{\mu_o} \tag{17}$$

establishes a necessary condition for magnetic self-focusing of a space-charge neutralized electron beam. In (17) k is Boltzmans constant, N is the linear density of electrons, and μ_o is the permeability of free space. The transverse thermal energy is measured by $T_{\perp}$ so that by considering two degrees of freedom in the kinetic theory sense,

$$kT_{\perp} = \frac{1}{2} m \overline{v_{\perp}}^2 \tag{18}$$

From equation (7) an association for $P_{\perp}$ is made, viz. ,

$$P_{\perp} = nkT_{\perp} . \tag{19}$$

Some algebraic manipulation of equation (19) and (17) yields

$$P_{\perp} = \frac{\mu_o I^2}{8\pi^2 r^2} \tag{20}$$

with r the beam radius, a function of axial displacement, z. The terms of the kinetic stress tensor are now defined for use in equation (3).

Prior to reduction of the equation of motion, it is instructive to consider the divergence of the stress tensor in cylindrical coordinates, viz.,

$$\begin{aligned}\vec{\nabla} \cdot \vec{P} = \vec{e}_r &\left(\frac{1}{r}\frac{\partial}{\partial r} r\, P_{rr} + \frac{1}{r}\frac{\partial}{\partial \theta} P_{r\theta} - \frac{P_{\theta\theta}}{r} + \frac{\partial}{\partial z} P_{rz}\right) \\ + \vec{e}_\theta &\left(\frac{1}{r}\frac{\partial}{\partial r} r\, P_{\theta r} + \frac{1}{r}\frac{\partial}{\partial \theta} P_{\theta\theta} + \frac{1}{r} P_{r\theta} + \frac{\partial}{\partial z} P_{\theta z}\right) \\ + \vec{e}_z &\left(\frac{1}{r}\frac{\partial}{\partial r} r P_{zr} + \frac{1}{r}\frac{\partial}{\partial \theta} P_{z\theta} + \frac{\partial}{\partial z} P_{zz}\right)\end{aligned} \tag{21}$$

Due to the absense of off-diagonal terms in equation (6) and $P_{rr} = P_{\theta\theta} = P_\perp$, $P_{zz} = P_{||}$, equation (21) becomes,

$$\vec{\nabla} \cdot \vec{P} = \vec{e}_r \left(\frac{\partial P_\perp}{\partial r} + \frac{P_\perp}{r} - \frac{P_\perp}{r}\right) + \vec{e}_\theta \left(\frac{1}{r}\frac{\partial P_\perp}{\partial \theta}\right) + \vec{e}_z \left(\frac{\partial P_{||}}{\partial z}\right) \tag{22}$$

Now take the beam density and longitudinal random energy distributions to be functions of z only, i. e.

$$\left.\begin{aligned} n &= n(z) \\ P_{||} &= P_{||}(z) \end{aligned}\right\} \tag{23}$$

then from equation (16),

$$P_\perp = P_\perp(z) \tag{24}$$

which is compatible with equation (20). The stress tensor divergence, equation (22), reduces to,

$$\vec{\nabla} \cdot \vec{P} = \vec{e}_z \frac{\partial P_{||}}{\partial z} . \tag{25}$$

III. DEVELOPMENT OF TRAJECTORY EQUATION

The analytic model has been sufficiently developed in section II so that the beam envelope trajectory can now be calculated from equation (3),

$$\frac{d\vec{\nu}}{dt} = -\vec{e}_z \frac{1}{mn} \frac{\partial P_{||}}{\partial z} - \eta (\vec{E} + \vec{\nu} \times \vec{B}) \tag{26}$$

where use was made of equation (25). The averaging over velocity space indicated in equation (3) has effectively separated random and drift components of the velocity, so in equation (26) is the translational or drift velocity. Using equation (20) and the current relation,

$$I = |e| \eta(z) \nu_z \pi r^2(z) \tag{27}$$

equation (16) can be solved for $P_{||}$. After some manipulation the result

$$\frac{\partial P_{||}}{\partial z} = -\frac{384\, CI}{\pi \mu_o^2 (|e| \nu_z)^5} \frac{1}{r^7} \frac{dr}{dz} \tag{28}$$

is obtained. The parameter, I, is the total enclosed beam current. Equation (26) is now cast in cylindrical coordinates to give,

$$\ddot{r} - r\dot{\theta}^2 = -\eta (E_r - \dot{z} B_\theta) \tag{29}$$

$$m(r\ddot{\theta} + 2\dot{r}\dot{\theta}) = 0 \tag{30}$$

$$\ddot{z} = -\frac{1}{mn} \frac{\partial P_{||}}{\partial z} - \eta (E_z + \dot{r} B_\theta) \tag{31}$$

where dotted quantities indicate differentiation with respect to time. The B_r and B_z components are not included due to symmetry and the absence of axially impressed magnetic induction; E_θ is taken as zero in the absence of net azimuthal charge separation.

The reduction procedure which transforms equations (29), (30) and (31) into an (r, z) space is treated in another paper [3]; the pressure-like term in equation (31) carries through in a straight-forward manner. However, before describing the trajectory equation it is well to summarize the important assumptions which simplify the analysis:

(i) A first-order space-charge correction, f, is unity in the present analysis, being the ratio of positive ion density to electron density.

(ii) The analysis is non-relativistic.

(iii) Particle densities and longitudinal electron velocities are independent of beam radius.

(iv) Electron-ion and electron-neutral collisions are ignored.

(v) The transverse velocity of beam electrons is small compared with their longitudinal velocity.

(vi) Secondary electrons are expelled rapidly in infrequent gas ionizing events.

(vii) A magnetic induction is present as fast beam particles pass through the stationary positive ion background.

Some of these assumptions have already been introduced, and the balance of them are needed for the formation and solution of the trajectory equation.

The pertinent Maxwells' equations are combined with equations (29), (30), and (31) to obtain the undriven beam envelope trajectory equation,

$$r'' + \underline{\overline{K}}^* \frac{(r')^2}{r} + \frac{T(r')}{I} = \frac{Q}{r^3} + \frac{\overline{\underline{K}}}{r} \tag{32}$$

where

$$\underline{\overline{K}}^* = \frac{\sqrt{2\eta}\,\mu_0 I}{4\pi V^{1/2}} \tag{33}$$

$$\overline{\underline{K}} = -\underline{\overline{K}}^* \tag{34}$$

$$Q = \frac{P_\theta^2}{2\eta m^2 V} \tag{35}$$

$$T = \frac{96\pi^2 V\left(V_T/V\right)^3 r_1^4}{\mu_o \eta I^2}, \quad V_T = \frac{kT_o}{|e|} \tag{36}$$

The primes on r indicate derivatives with respect to z, r_1 is the beam radius at the entrance of the drift space, V is the beam drift potential, T_o is an assigned value of beam temperature at entrance to the drift space, and P_θ is the test particle angular momentum, considering equation (30), and is a constant in the drift space. The angular momentum is dependent on source properties and can be considered as a parameter in the problem; the same can be said for T_o.

IV. SOLUTION OF THE TRAJECTORY EQUATION

The solution of equation (32) is facilitated by employing a normalization procedure, whereby,

$$R = r/r_1 \tag{37}$$

and as a result, equation (32) becomes,

$$R'' + \underline{\overline{K}} * \frac{(R')^2}{R} + T_1 \frac{(R')^2}{R^5} = \frac{Q_1}{R^3} + \frac{\underline{\overline{K}}_1}{R} . \tag{38}$$

Equation (38) is cast as an initial value problem to trace the path of a surface electron in the drift space. The initial conditions are:

$$R(0) = 1, \; R'(0) = \sigma \tag{39}$$

and the re-defined parameters become,

$$T_1 = \frac{T}{r_1^4} \tag{40}$$

$$\underline{\overline{K}}_1 = \frac{\underline{\overline{K}}}{r_1^2} \tag{41}$$

$$Q_1 = \frac{Q}{r_1^4} \tag{42}$$

For the general problem at hand the above parameters are further characterized as being,

$$\left.\begin{array}{r} \overline{\underline{K}}^*,\ Q_1,\ T_1 > 0 \\ \sigma \gtreqless 0 \\ \overline{\underline{K}}_1 < 0 \end{array}\right\} \tag{43}$$

The physical sense of the problem also requires the variables R and z to be positive over all interesting ranges of variation.

A closed-form analytic solution has not been obtained for the ordinary, non-linear differential equation (38). Solutions to the initial value problem were obtained by numerical methods, and some of these results are discussed in the next section. The order of integration in equation (38) can be reduced by an assiduous change of variable, so that,

$$z = \int_1^R \frac{dR}{P(R)} \tag{44}$$

where,

$$P^2 = \left(\frac{dR}{dz}\right)^2 = -\frac{Q_1}{2} R^{-a} e^{\frac{T_1}{2} R^{-4}} \int_1^{R^{-4}} \frac{e^{-\frac{T_1}{2} x}\, dx}{x^{\frac{2+a}{4}}} + \frac{2\overline{\underline{K}}_1}{a}\left[R^{-a} - 1\right] + \sigma^2 e^{-\frac{T_1}{2}} \qquad (a = 2\overline{\underline{K}}^*) \tag{45}$$

Since the beam radius does not go to zero (trajectory does not cross axis) due to the invariance of angular momentum (see equation (30)), the integral in (45) is well-behaved. Integration of equation (44) with (45) proceeds between

integrand singularities, a domain outside of which imaginary integrals result. The function P(R) has only two zeros, and careful scrutiny of the behavior of the trajectory equation (39) in a (P, R) space indicates that a closed curve is traced there for increasing z-values; this result implies periodicity of R in z. One period of the beam envelope trajectory is determined and plotted in Figures 2 and 3 for the numerical cases considered.

Variation of the parameters in (43) over selected values would constitute a parametric study of the trajectory equation. Under conditions of the problem the free parameters are beam current I, initial angular momentum P_θ, initial beam radius r_1, and initial beam thermal energy kT_0. The beam drift potential is assumed held at an arbitrary limit above which relativistic effects would be important. Changes in free parameters interact to give the numerical cases shown in Table I.

V. DISCUSSION OF RESULTS

The three cases listed in Table I were studied in order to (1) compare trajectories with and without the temperature effect--free particle model versus quasi-fluid model, and (2) observe effect of changing electron source temperature.

Figure 2 compares primarily the magnetically self-focused trajectories for the free particle case (Case 1) and the quasi-fluid case (Case 2) on a semi-logarithmic plot. The analysis for Case 1 was treated in a previous paper [3]. The differences in depth of approach toward the axis and in the period are analytically a result of including the beam thermal energy term in equation (38). Physically speaking another degree of freedom is included in the equations of motion, the effect of which is to cause the trajectory turn-about point to occur at a larger radius; as a consequence the period is also slightly shortened.

In Fig. 3 results of calculations are presented which compare cases where only the electron source temperature is varied, i. e., for kT = 2ev and for kT = .2ev (see Table I). The lower temperature source effects a smaller residual angular momentum in Case 3, and the result is

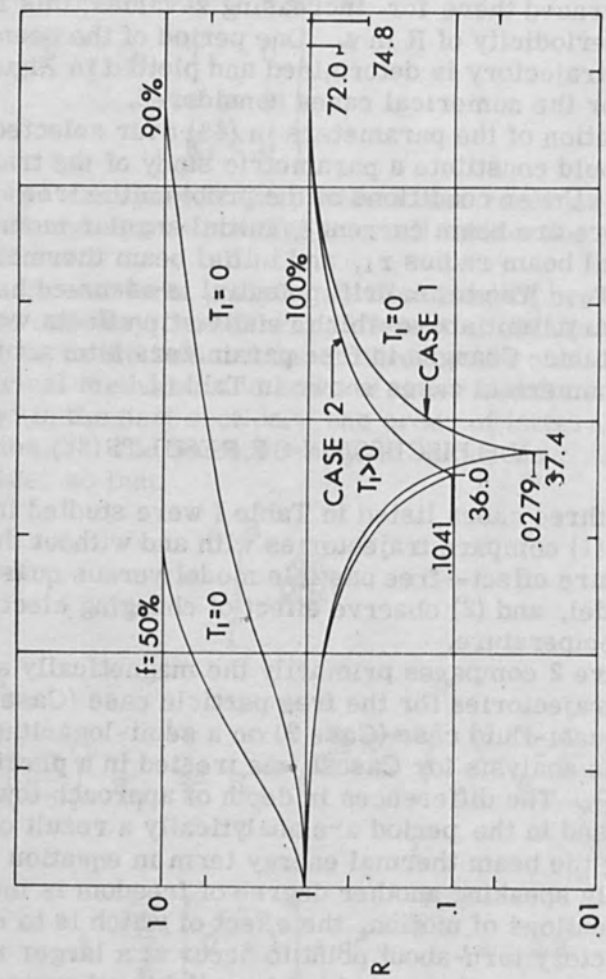

Figure 2. Surface Electron Trajectories Showing Temperature Effect for Space-Charge Neutralized Beam (f = 100%) and Space-charge Divergence in Free Particle Cases (f = 50%, 90%).

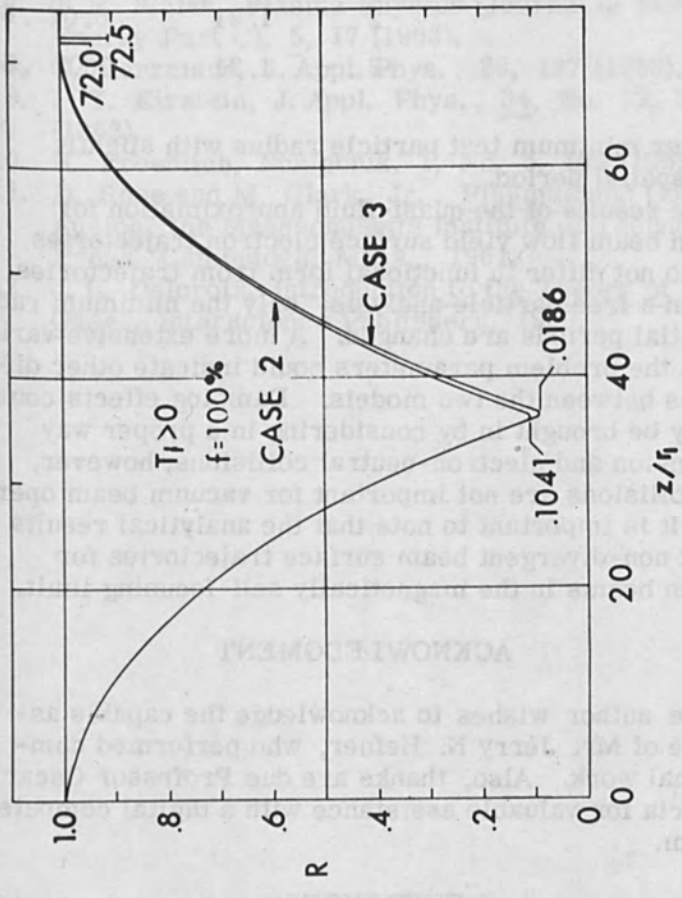

Figure 3. One Period of Surface Electron Trajectories Comparing Variation in Source Temperature (see Table I).

Table I. Self-focused Beam Conditions; Only Parameter Changes are Indicated.

					Source					
	I	V	σ	r_1	kt	B_z	kT_o	$\bar{K}_1$	Q_1	T_1
CASE	(amp)	(kv)	(m^{-1})	(m)	(ev)	(G)	(ev)	(m^{-2})	(m^{-2})	
1	1	3	0	.001	2	500	0	-1085	6.07	0
2					2		1.21		6.07	$.667 \times 10^{-3}$
3					.2		1.21		.0607	$.667 \times 10^{-3}$

a smaller minimum test particle radius with slightly larger spatial period.

The results of the quasi-fluid approximation for electron beam flow yield surface electron trajectories which do not differ in functional form from trajectories gotten in a free particle analysis; only the minimum radii and spatial periods are changed. A more extensive variation in the problem parameters could indicate other differences between the two models. Damping effects could possibly be brought in by considering in a proper way electron-ion and electron-neutral collisions; however, these collisions are not important for vacuum beam operation. It is important to note that the analytical results suggest non-divergent beam surface trajectories for undriven beams in the magnetically self-focusing limit.

ACKNOWLEDGMENT

The author wishes to acknowledge the capable assistance of Mr. Jerry N. Hefner, who performed computational work. Also, thanks are due Professor Oscar N. Garcia for valuable assistance with a digital computer program.

REFERENCES

1. E. L. Ginzton and B. H. Wadia, Proc. IRE, 42, No. 10, 1548 (1954).
2. B. W. Wadia, J. Electron. Control, 6, No. 4, 307 (1959).

3. A. S. Roberts, Jr., Plasma Phys. (Journal of Nuclear Energy Part C), 8, 53 (1966).
4. L. Spitzer, Jr., Physics of Fully Ionized Gases, Interscience Publishers, 1962.
5. W. H. Bennett, Phys. Rev., 45, No. 12, 890 (1934).
6. J. R. Pierce, Theory and Design of Electron Beams, Van Nostrand Co., Inc., Princeton, N. J., 1954.
7. T. R. Walsh, Plasma Physics (Journal of Nuclear Energy Part C), 5, 17 (1963).
8. G. Herrmann, J. Appl. Phys., 29, 127 (1958).
9. P. T. Kirstein, J. Appl. Phys., 34, No. 12, 3479 (1963).
10. H. Froehlich, Nukleonik, 1, No. 5, 183 (1959).
11. D. Rose and M. Clark, Jr., Plasmas and Controlled Fusion, the Massachusetts Institute of Technology Press, Cambridge, Mass., 1961.
12. J. L. Delcroix, Introduction to the Theory of Ionized Gases, Interscience Publishers, 1960.

Phase Space Representations of Charged Particle Beams

C. K. Crawford and M. D. Brody

Massachusetts Institute of Technology
Cambridge, Massachusetts

INTRODUCTION

The intent of this paper is to extol the virtues of a well known but not often used technique of studying charged particle motion, that of plotting their trajectories in phase space. The advantage of this method over the use of ordinary real-space plots is two-fold. First, a phase-space plot provides a complete description of the motion; second, certain conservation relations directly apply. As a result, it is easier to visualize what is going on, and easier to see the effects of fundamental limitations. For example, the effects produced by initial thermal velocities and lens aberations are directly visible.

The method has seen limited use in the past for several reasons. In spite of the fact that the basic ideas are presented in many books, [1-11] many designers are unfamiliar with it, partly perhaps because the mathematical formalism is time-consuming to understand. Several of the most common books concerning electron optics ignore it. In addition, the study of phase-space trajectories often requires the visualization of motion in more than three dimensions, which is abstract and awkward. Finally, the construction of a phase-space plot usually follows, rather than precedes, the complete algebraic solution of the problem; hence it is likely to be regarded as an additional time-consuming procedure, to be undertaken after a solution has already been found. We would like to suggest that the mathematics need not be complicated, that three spatial dimensions are often sufficient (and where a higher

number is required, projections into three dimensions may be used), and that even though an algebraic solution has been found, very useful insight can usually be obtained from a phase-space plot. In problems solved on a computer, the use of phase space is a particularly appropriate way of presenting output data. [11]

ELEMENTARY EXAMPLES

Two types of phase space are well-known, Γ space and μ space. Γ space has 2f coordinate axes, where f is the number of degrees of freedom in the system under study. One axis corresponds to the position and one to the momentum for each degree of freedom. The state of a system is described by a single point, and the behavior of the system as a function of time is represented by a single trajectory. Γ space is most often used to study ensembles of identical systems in statistical mechanics.

If the system under study is composed of a large number of individual identical non-interacting particles, then it is easier to describe the motion in μ space, which has only six axes, three for position and three for momentum. Here the state of the system is described by a cloud of points, one of which gives the position and momenta of each particle. The motion of the system through time is given by the set of trajectories which represent the motion of each point. While the μ space representation is less general than a Γ space representation, which for example allows exact treatment of space-charge, it is easier to visualize and is the most useful representation for studying charged-particle optics.

An interesting feature which may be observed about trajectories in either type of phase space is that if the forces do not depend explicitly on time, then no two trajectories ever intersect. This is a consequence of the completeness of the phase-space representation. The specification of an initial position and an initial momentum specifies the motion of a particle for all time (because Newton's Second Law is a second-order differential equation). If two trajectories did cross, we could pick the intersection as a possible set of initial conditions, whereupon the particle would have to move off in two directions

at once, an obvious impossibility. Thus particles must move in phase space with a kind of laminar flow; one-dimensional motion of this kind is shown in Fig. 1. What is not obvious, but may be shown, is that under certain broad restrictions, namely that the force on any particle be independent of its momentum component in the direction of the force (other types of time-varying forces are allowed), the theorem of Liouville holds. This theorem states that the density of phase-space points in the neighborhood of any individual point is constant. Thus for cases like that shown, where a fixed number of particles is released with a uniform density in phase space, the phase space volume occupied by the particles (a two-dimensional area in this case) remains constant.

That this is true may be seen directly for the case of motion of particles in a force-free region, Fig. 2. If there is no force, momentum is conserved and each particle moves horizontally from left to right with a constant velocity equal to its momentum divided by its mass. Given an initial distribution of particles spread uniformly over a parallelogram, we find that the parallelogram distorts but that its area remains constant, because its base and height are fixed. Figure 3 shows two other simple cases which are easily plotted, that of a harmonic oscillator with its elliptical trajectories, and that of a force equal to a positive constant times displacement, which results in hyperbolic trajectories.

For general motion in three dimensions, the conserved phase-space volume is six-dimensional. However, if the equations of motion separate, then this volume is the product of three separately conserved two-dimensional areas, or, if they only partially separate, one two-dimensional area and one four-dimensional volume.

APPLICATION TO CHARGED-PARTICLE OPTICS

The application to charged-particle optics is straightforward, and a number of such applications have been made. [7-17] Most of them have concerned the matching of injection systems to high-energy particle accelerators. [9-11, 13-16]

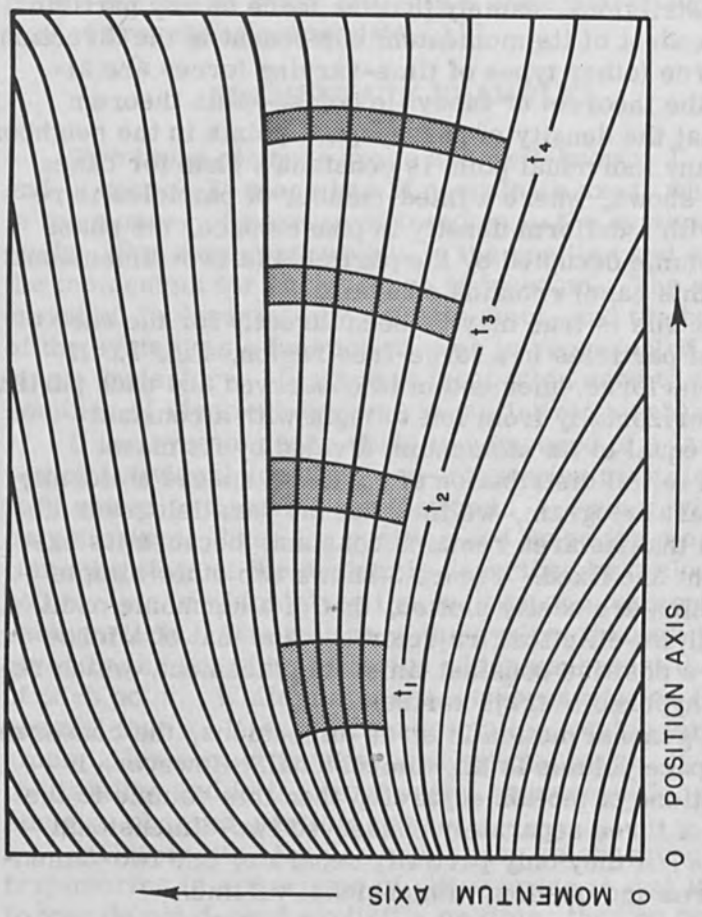

Figure 1. Trajectories for one-dimensional motion in μ space. A uniform distribution of particles released at t_1 occupies the same area at any later time.

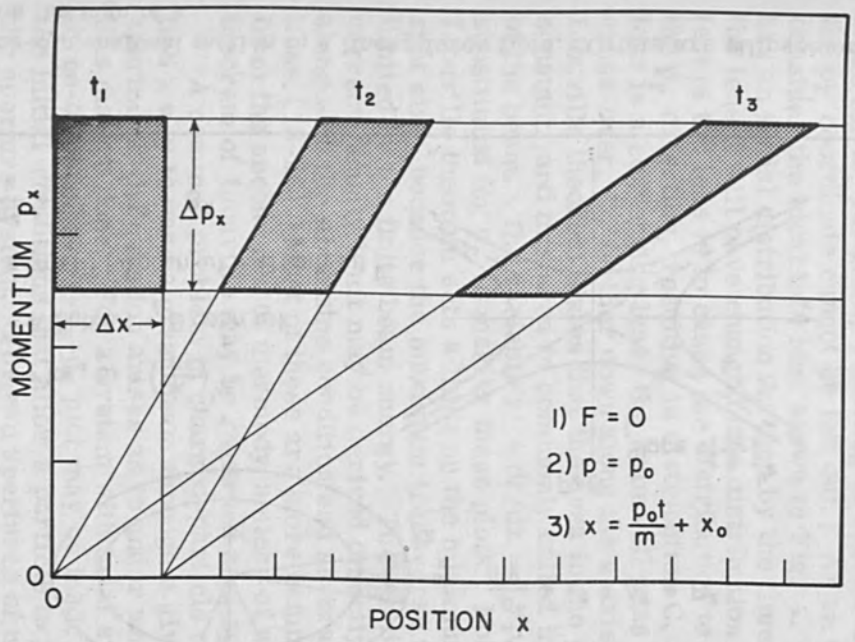

Figure 2. Motion in a force-free region. The area of the parallelogram, base times height, remains fixed, but the parallelogram gradually stretches out because the particles with lower momentum move slower.

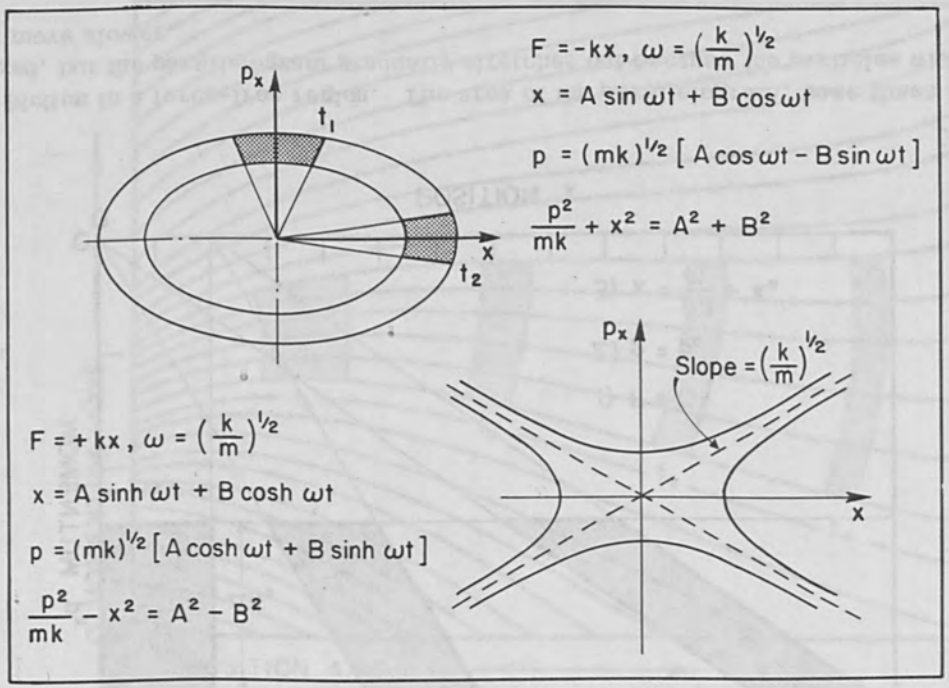

Figure 3. One-dimensional motion in a linear force field. Orbits are ellipses or hyperbolas, depending upon the sign of k.

Consider the paths of paraxial rays in an axially-symmetric optical system. If we assume that the momentum in the axial direction, p_z, remains approximately constant, and we ignore the usually unimportant variables p_θ and θ, only three phase-space coordinates, p_r, r, and z, are needed to describe the motion. The particles move as a group along the z axis. (Note that if p_z is not the same for all particles, resulting in chromatic aberation, the p_z coordinate cannot be left out.) As an example, consider the ideal thin lens shown in Fig. 4. If the beam has an initial distribution A, then by the time it reaches the lens it will have changed into distribution B. The effect of the lens is to cause the distribution to slew along the p_r direction, resulting in distribution C. Because the lens is a converging lens, the beam will pass through a cross-over, D, farther down along the z axis. The Liouville theorem states that the area in the p_r-r plane is constant, and this area is commonly called the emittance of the beam. The variable $r' = dr/dz = p_r/p_z$ is often substituted for p_r in making these plots. Note that the Liouville theorem sets a limit on the minimum obtainable spot size, because the maximum transverse momentum is limited by the finite beam energy. The familiar Langmuir current-density limit may be derived directly from this, along with the Abbe sine condition and several other relations. [18-20] Most of these are more commonly derived from the second law of thermodynamics, of which the theorem of Liouville may be regarded as a special case.

A common problem in charged-particle optics is to find a way to pass a given beam through a given series of apertures; the question arises as to under what conditions this may be done. For a system with axial symmetry, a three-dimensional r-p_r-p_z plot may be made which shows the initial conditions that allow a particle to pass through the aperture system. For two apertures of unequal size this plot is most conveniently made at the position $z = z_a$ of the first aperture, as shown in Fig. 5. If the axial momenta of all the particles in the beam are fixed at $p_z = p_{zo}$, then an area of allowable r and p_r is defined in r-p_r space. This area is called the acceptance of the aperture system. In general, if the beam emittance is less than the aperture system acceptance, a lens system

Figure 4. Focusing action of an ideal thin lens for paraxial rays. Liouville's Theorem limits the minimum spot size, and thus effectively limits the maximum current density.

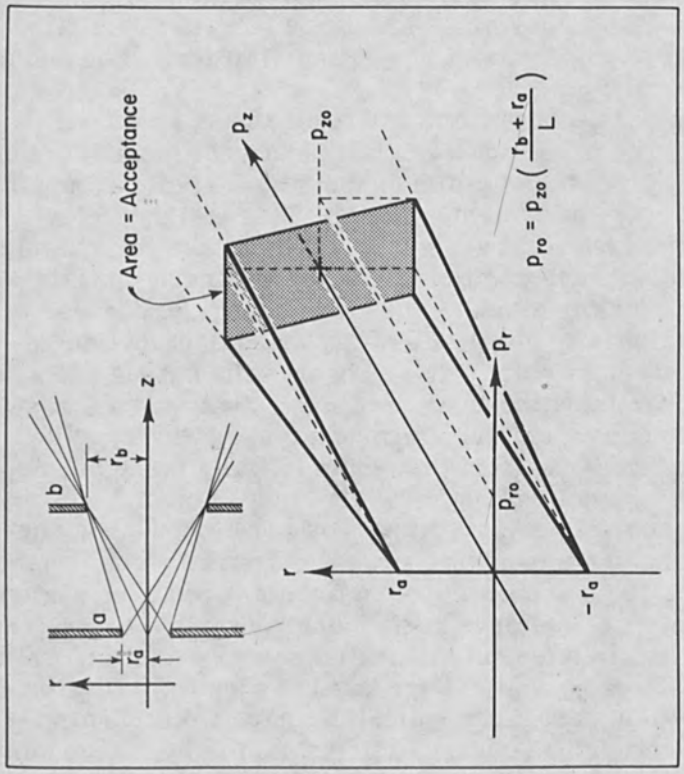

Figure 5. Skew-wedge shaped volume which defines the allowable acceptance conditions for two circular apertures of unequal size.

can presumably be found which will cause the entire beam to pass through the aperture system. If, on the other hand, the beam emittance is greater than the system acceptance, some of the beam must be lost. If the aperture system contains lenses as well as apertures, the same analysis may be made by optically transforming all the apertures into a region of lens-free space. [21] Though it is not normally done, these techniques could be generalized to more dimensions. For example, the allowable injection conditions for an asymmetric slit system may be plotted in (the three-dimensional projection of) a five-dimensional space.

Phase-space analysis of particles passing through various force fields has received relatively little attention. Figure 6 shows the one-dimensional motion of a group of particles in a uniform-force field. Identical particles move along identical parabolas with their axes of symmetry coincident with the position axis, while varying initial conditions simply displace the curve along the position axis. An initially parallelogram-shaped distribution retains its straight sides. If we observe the passage of a group of particles through the boundary between a force-free region and a uniform-force region, however, as shown in Fig. 7, we find that some initially straight boundaries remain straight, while others do not. A simple geometric construction, however, shows how the shape transforms, and of course the area remains constant.

If particles are accelerated from a force-free region through a constant-force region and back into a force-free region, all particles gain the same energy, $\int F\,dx$, while the momentum spread is decreased, as shown in Fig. 8a. If the particles are not identical but have a distribution in mass, then the high-mass particles gain more momentum than the light ones, because p^2/m = constant.

If a constant force is applied for a fixed length of time instead of over a fixed distance, Fig. 8b, then all particles gain the same momentum independent of their initial momenta and independent of their mass, $\int F\,dt$. The momentum spread does not change, but the energy gained varies inversely with the mass.

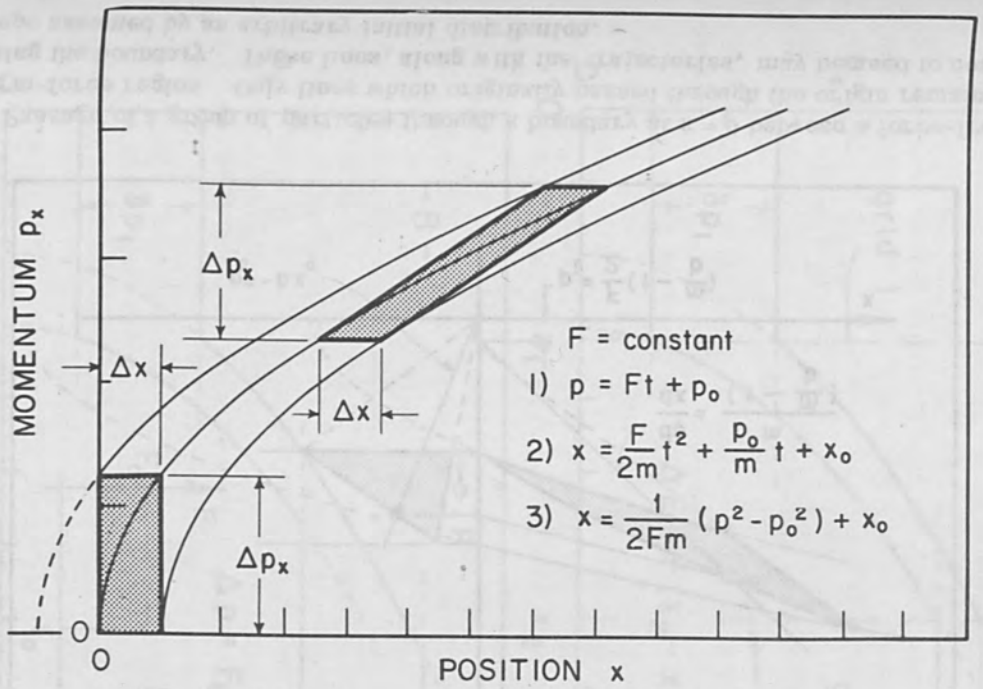

Figure 6. One-dimensional motion in a uniform-force field. Straight lines remain straight lines because of the linear dependence of x and p on the initial conditions, x_o and p_o.

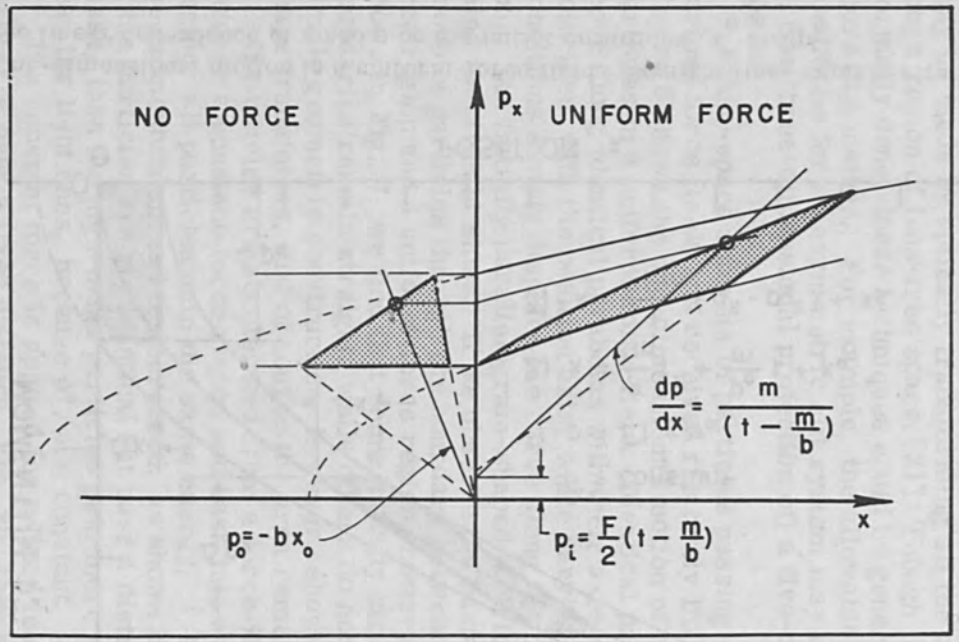

Figure 7. Passage of a group of particles through a boundary at x = 0 between a force-free region and a uniform-force region. Only lines which originally passed through the origin remain straight after crossing the boundary. These lines, along with the trajectories, may be used to compute the new shape assumed by an arbitrary initial distribution.

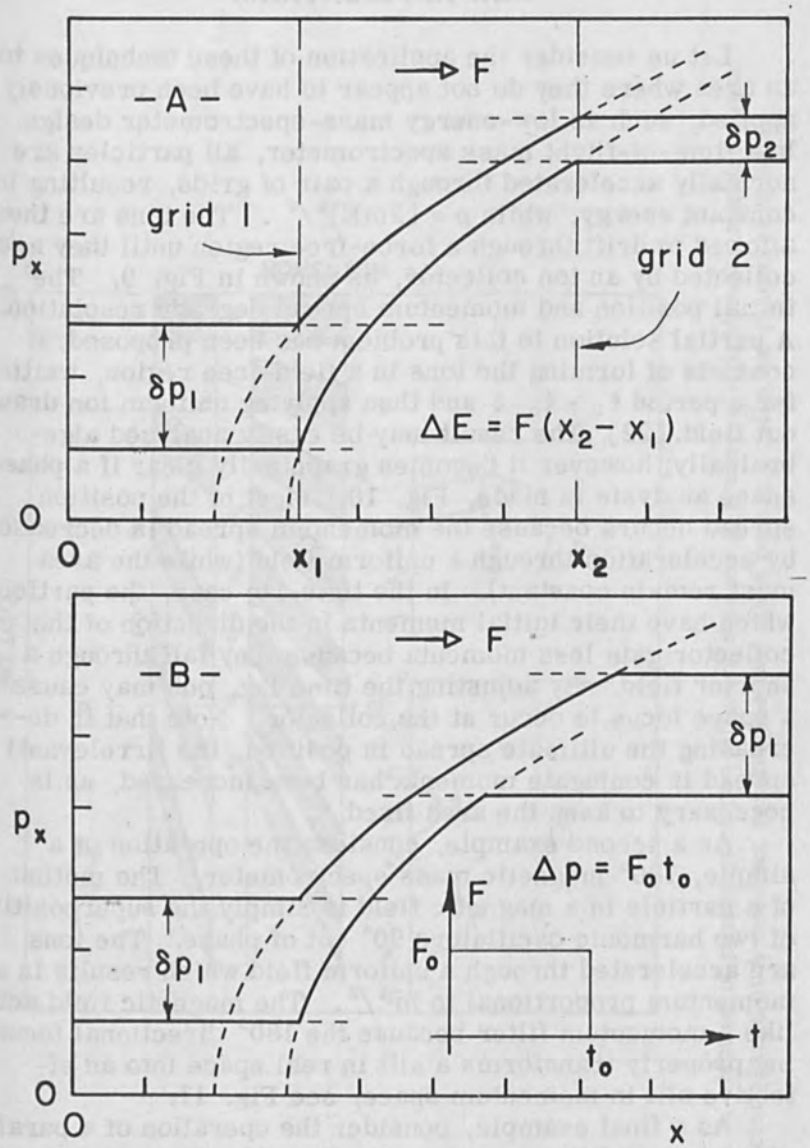

Figure 8. (a) Passage of particles through a **constant-force** region of limited extent. All particles gain the same energy dependent of mass and the initial conditions. (b) Constant force applied to a group of particles for a fixed time. All particles receive the same momentum impulse independent of mass and the initial conditions.

NEW APPLICATIONS

Let us consider the application of these techniques to an area where they do not appear to have been previously applied, such as low-energy mass-spectrometer design. In a time-of-flight mass spectrometer, all particles are normally accelerated through a pair of grids, resulting in constant energy, while $p = [2mE]^{1/2}$. The ions are then allowed to drift through a force-free region until they are collected by an ion collector, as shown in Fig. 9. The initial position and momentum spread degrade resolution. A partial solution to this problem has been proposed; it consists of forming the ions in a field-free region, waiting for a period $t_1 - t_o$, and then applying uniform ion draw-out field. [22] The result may be easily analyzed algebraically; however it becomes graphically clear if a phase-space analysis is made, Fig. 10. Most of the position spread occurs because the momentum spread is decreased by acceleration through a uniform field (while the area must remain constant). In the time-lag case, the particles which have their initial momenta in the direction of the collector gain less momenta because they fall through a shorter field. By adjusting the time lag, one may cause a space focus to occur at the collector. Note that in decreasing the ultimate spread in position, the (irrelevant) spread in conjugate momenta has been increased, as is necessary to keep the area fixed.

As a second example, consider the operation of a simple, 180° magnetic mass spectrometer. The motion of a particle in a magnetic field is simply the superposition of two harmonic oscillators 90° out of phase. The ions are accelerated through a uniform field which results in a momentum proportional to $m^{1/2}$. The magnetic field acts like a momentum filter because the 180° directional focusing property transforms a slit in real space into an effective slit in momentum space, see Fig. 11.

As a final example, consider the operation of a parallel-plane energy filter, as shown in Fig. 12. Here it is convenient to plot the position where the particles return to the $x = 0$ plane, as a function of the initial injection momenta, p_{xo} and p_{zo} (assuming $p_{yo} = 0$). The surfaces of

Figure 9. Motion of particles of two different masses in a time-of-flight mass spectrometer. A collector placed at A does not resolve the two mass peaks; a collector placed at B does.

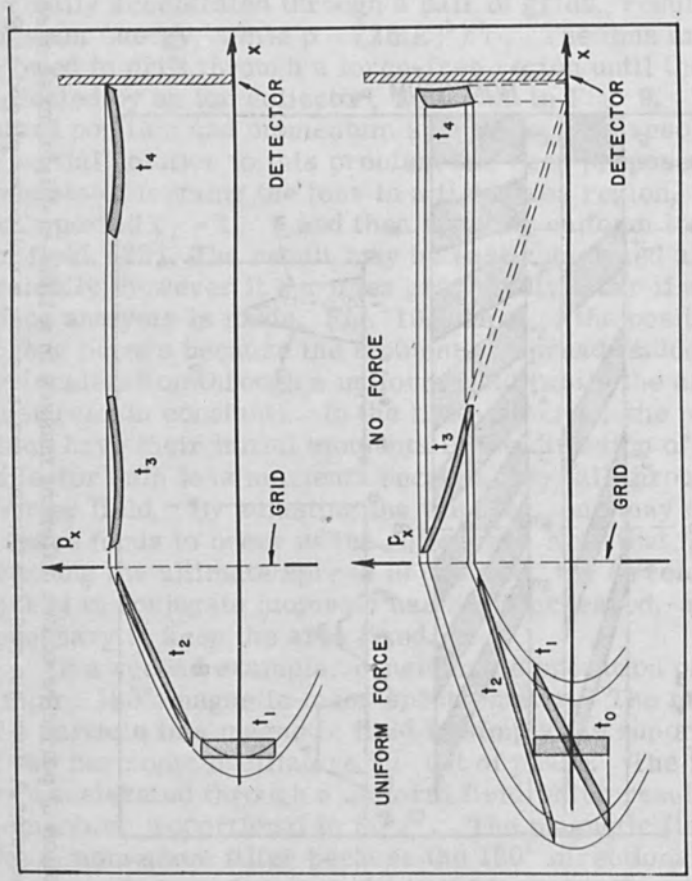

Figure 10. TOF mass spectrometer as originally conceived and with time-lag focusing. The time lag prevents the decrease in momentum spread and allows space focusing to occur.

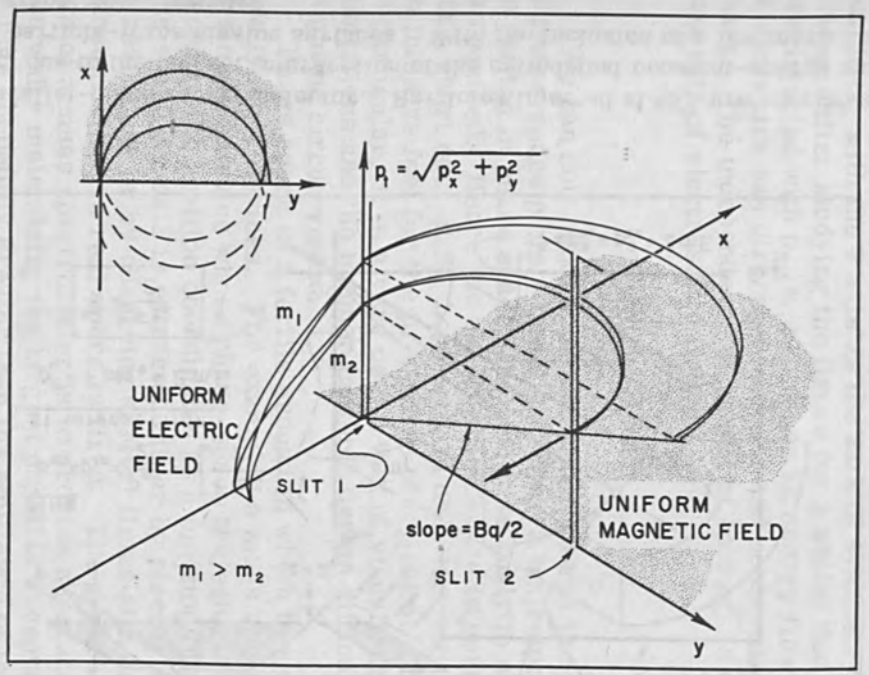

Figure 11. Small 180° magnetic mass spectrometer. Particles gain momentum proportional to $m^{1/2}$ falling through the electric field. The magnetic field acts as a momentum selector.

Figure 12. Parallel-plane energy selector. Particles injected at 45° are energy-selected with space focusing, due to the tangent intersection of the cylindrical constant-energy surfaces and the hyporbolic particle-transmission surfaces. With the inclusion of a few more lines the resolution may be graphically computed.

constant energy in this space are circular cylinders surrounding the z axis. The condition that a particle be returned to the $x = 0$ plane at some specified $z = z_o$, where we might place a slit, is that $p_{xo}p_{zo} = 1/2\ Fmz_o$. This equation describes a paraboloid whose intersection with any plane perpendicular to the z axis is a hyperbola, and whose intersection with any plane containing the z axis is a parabola, with the z axis as the axis of symmetry. It is evident (after studying the figure for a while) that if the ions are injected with $p_{xo} \simeq p_{zo}$, then an energy filter is obtained which has direction focusing and no dependence on mass. The independence of mass, of course, is a general property of electrostatic fields.

CONCLUSIONS

We can now make some statements about the usefulness of phase-space plots. Usually, before a trajectory can be plotted in phase space, the complete analytic solution is required. Hence the use of phase space is normally not a short cut. It is, however, an excellent way to gain an intuitive feel for the properties of a field or a device. In particular, it is a very useful way of visualizing basic limitations and the manner in which design difficulties might be circumvented.

Phase space is a fertile ground in which to search for new types of devices. For example, a mass spectrometer is simply a device whose phase-space trajectories separate in one of the position coordinates as a function of mass. The spectrum data is extracted either by placing apertures in real space or by observing arrival times at a detector whose position in real space is fixed. The general problem of a mass spectrometer is to provide adequate resolution while maintaining the largest possible acceptance volume, hopefully greater than the emittance of the source. The usual way to make a mass spectrometer (quadrupoles and monopoles are notable exceptions) is to generate ions with some particular function of momentum, position, and mass equal to a constant, and then run the particles through another field which has some different function constant. For example, a common time-of-flight spectrometer generates particles with uniform energy, p^2/m, and then

analyzes them by velocity, p/m. A magnetic spectrometer generates particles with uniform p^2/m, and then analyzes them according to p. Some magnetic spectrometers (Bainbridge type) generate particles with constant velocity, p/m, and then analyze them with constant p. A magnetic double-focusing instrument is more complicated; here the constant functions depend explicitly on position. Obviously, many other types could be made in this way; the number is unbounded. (For example, a force whose magnitude increases as t^n results in a group of particles with p^{n+2}/m^{n+1} equal to a constant.) Nor is it necessary to use this method (its main advantage is conceptual simplicity); one type of field is sufficient. Making phase-space plots would be a good way to search for new examples of such fields.

Note that though all the fields discussed in this paper have been trivial to analyze, it is quite feasible to analyze complicated motions. Any problem which can be analyzed algebraically (and many that cannot) can be studied in phase space. The problems are those of visualization, choice of appropriate projections, and time-consuming calculations. A particularly promising avenue of research is the use of computers to plot phase-space trajectories. In the worst case of a six-dimensional plot, a computer could easily generate three-dimensional projections, of which the normally-used three-dimensional real-space plots are a special case. In some examples it might be advantageous to add an additional dimension to represent density, thus allowing the study of non-uniform beams.

REFERENCES

1. R. C. Tolman, Principles of Statistical Mechanics, Oxford University Press (1938).
2. H. Goldstein, Classical Mechanics, Addison Wesley (1950).
3. C. Kittel, Elementary Statistical Physics, Wiley (1958).
4. L. D. Landau and E. M. Lifshitz, Statistical Physics, Pergamon Press (1958).
5. F. Reif, Fundamentals of Statistical & Thermal Physics, McGraw-Hill (1965).
6. J. R. Pierce, Theory and Design of Electron Beams, Van Nostrand (1954).

7. B. Lennert, Dynamics of Charged Particles, Interscience (1964).
8. P. A. Sturrock, Static and Dynamic Electron Optics, Cambridge University Press (1955).
9. M. S. Livingston and J. P. Blewett, Particle Accelerators, McGraw-Hill (1962).
10. J. J. Livingood, Principles of Cyclic Particle Accelerators, Van Nostrand (1961).
11. K. G. Steffan, High Energy Beam Optics, Interscience (1965).
12. C. Weber, Proc IEEE, 52, 996 (1964).
13. H. G. Herewald, K. Johnsen, and P. Lapostolle, CERN Symp. High Energy Accelerators P Ion Physics. Geneva: (1956), p. 179.
14. P. H. Rose et al., Nuc. Instr. & Methods 14, 79 (1961).
15. A. Galejs and P. H. Rose, Rev. Sci. Instr. 35, 644 (1964).
16. P. H. Rose et al., Rev. Sci. Instr. 35, 1283 (1964).
17. D. A. Baker, Am. J. Phys. 32, 347 (1964).
18. J. Rainwater, Am. J. Phys. 32, 626 (1964).
19. J. C. Helmer, Am. J. Phys. 34, 222 (1966).
20. R. Katz and B. Curnutte, Jr., Am. J. Phys. 32, 617 (1964).
21. K. Halbach, Am. J. Phys. 32, 90 (1964).
22. W. C. Wiley and I. H. McLaren, Rev. Sci. Instr. 26, 1150 (1955).

Calculation of Space Charge Effects in Pulsed Discharges

A. L. Ward

Harry Diamond Laboratories
Washington, D. C.

I. INTRODUCTION

Low-pressure glow discharges, either steady-state or pulsed, are commonly used as sources of ion and electron beams, especially for beams used in research.

The present paper describes a computer program which has been used to calculate the temporal behavior of electronic and ionic currents in a gas under space charge conditions. The formulation is summarized in section 2 and some of the more important published results are given in section 3. The fourth section presents new calculations of the temporal sequence of the collection of electrons and ions created in a gap by ionizing radiation. The last section presents a calculation of the current growth in a gas at low pressures and high voltages.

It is thought that some of the techniques used in this program to study electron avalanches and ion swarms might readily be adapted to the study of electron and ion beams.

II. SUMMARY OF FORMULATION

The computer program has been described fully; hence only a brief summary of the formulation is included here. The complete listing of the program, detailed flow charts, instructions for use and a bibliography of publications resulting from the program are given in a laboratory technical report [1].

The one-dimensional continuity equations governing the motion of electrons and ions in a gas are

$$\partial \rho_{\pm} / \partial t = \alpha j_{-} \pm \partial j_{\pm} / \partial x, \tag{1}$$

where x is the distance measured from the cathode, t is the time, α is Townsend's first ionization coefficient and the positive and negative subscripts refer to positive ions and electrons, respectively. The current densities $j_{\pm}$ are the product of the charge densities $\rho_{\pm}$ and the drift velocities $v_{\pm}$. In the present program the drift velocities are given by the product of the local electric field E and drift mobilities, where the latter may also be field dependent. An obvious extension of the program for electron and ion beam studies would be to calculate the particle velocities from "free fall" conditions, i. e., make them proportional to the square root of the local potential.

The one-dimensional Poisson's equation is used to account for space charge distortion.

$$\epsilon \, \partial E / \partial x = \rho_{-}(x, t) - \rho_{+}(x, t), \tag{2}$$

where ϵ is the permittivity of the gas and the field E is measured positively from the anode.

Townsend's first ionization coefficient α is defined as the number of electron-ion pairs formed by collisions of a single electron drifting 1 cm in the field direction. It is given by an empirical expression which includes the field-to-pressure ratio, E/p.

The boundary condition on the field is determined by a simple circuit constraint, where the applied voltage may be constant, have a step function, or a sinusoidal increment. The latter allows a ramp voltage to be applied.

The boundary condition for the electron current from the cathode is determined by the external radiation, and the positive ions and the discharge photons striking the cathode. Townsend's secondary coefficient γ_i gives the number produced by photons per primary ionizing (α) event.

The initial charge in the gap is given by input arrays of ion and electron densities, which may of course simulate the effect of external ionizing radiation.

III. REVIEW OF PUBLISHED RESULTS

The major accomplishment of the computer program has been to explain breakdown at high pressures and high overvoltages. Previously it had been generally accepted that breakdown in this regime was by the photoionization streamer process and that there was a transition region to the low-pressure and low-overvoltage region where the avalanche model was adequate. The avalanche model has now been shown to be adequate through the postulated transition region and has given accurate calculations of breakdown where the first light is observed in midgap[2]. It is indeed surprising that these one-dimensional calculations should give good results for these midgap breakdowns which are initiated by single electrons from the cathode.

Another result of the calculations that may be of interest to electron and ion beam physicists is the interaction of ionization, diffusion and space charge in electron avalanches and ion swarms. The computer program formulation neglects particle diffusion, but it has been shown[3] that the difference equations used introduce a spreading that is an almost perfect analog to particle diffusion. Further, it has been shown that when ionization and diffusion are present, the measured velocity of an electron avalanche will be increased or decreased, respectively, depending upon whether the avalanche is observed in space at successive times or observed in time at two or more spatial points[4]. The difference of the velocity is given by $2\alpha D$, where α is Townsend's ionization coefficient and D is the diffusion coefficient. Similarly, in the solid state, recombination and diffusion of carriers lead to mobility changes.

IV. COLLECTION OF ELECTRONS AND IONS

Let us consider the transient motion of electrons and ions, created by external irradiation of a gas, with an applied electric field. Analytic solutions, including space charge but neglecting diffusion, of certain aspects of this problem have appeared in two recent papers[5]. Both papers consider a uniform distribution of equal numbers of electrons and ions as an initial condition, and Young et al also consider a parabolic distribution, as resulting from

diffusion. Young et al calculate only the slow ion component of the current, while the analytic solution of Demetriades and Hill assumes that the ions are stationary during the electron collection time. However, Demetriades and Hill also presented computer solutions for the anode electron current and the cathode ion current for space charge conditions such that their analytic solution is invalid[5].

Calculations have been made with the present computer program to compare with the two cited papers. Generally, the agreement with both papers is quite good, the major difference being that the inclusion of diffusion in the present program removes discontinuities.

The first calculations utilize the conditions assumed by Demetriades and Hill, namely that the ion mobility is 0.023 of that of the electron and the total charge is such that if it were of one sign, the field would be zero at one electrode. Figure 1 shows the calculated electron and ion currents as a function of distance at various times for an initially uniform distribution of 10^8 electrons and ions per cm^3. There is qualitative agreement with the results of Demetriades and Hill but discontinuities in slope are replaced by rounded curves. Fig. 2 presents the calculated field as a function of distance at the same times. The anode electron current and the cathode ion current are plotted as a function of time in Fig. 3. Similar agreement with Demetriades and Hill is noted.

Young et al calculated a distinct qualitative difference between the transient ion currents resulting from assuming uniform initial distributions or parabolic initial distributions, the latter exhibiting a point of inflection in the plot of current versus time. The present computer calculation shows that space charge delays the collection of the electron pulse sufficiently to remove the inflection point from the total current. This is illustrated in Fig. 4, for the case of the NO^+ ion in helium at a pressure of 3 torr and an applied field of 10 V/cm. Therefore, the absence of the inflection point does not rule out the initial parabolic distribution. As stated above, Young et al did not consider the electronic component in their calculations.

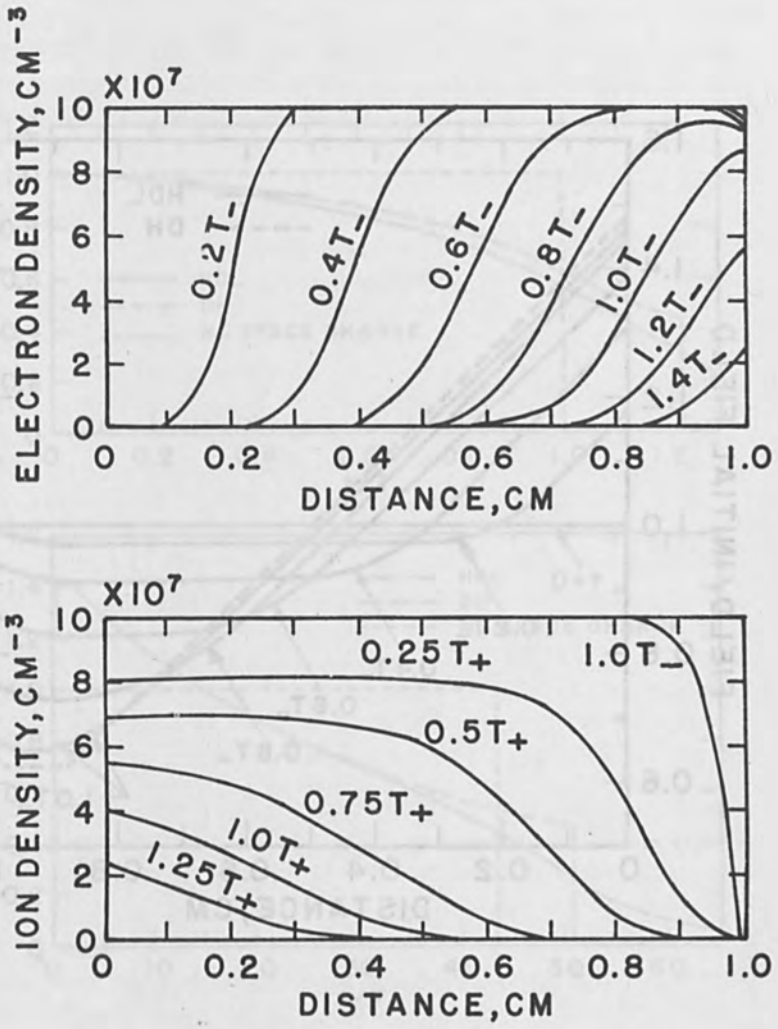

Figure 1. Electron and ion densities as a function of distance at various times, listed as fractions of the undistorted electron transit time, T_-, and ion transit time, T_+.

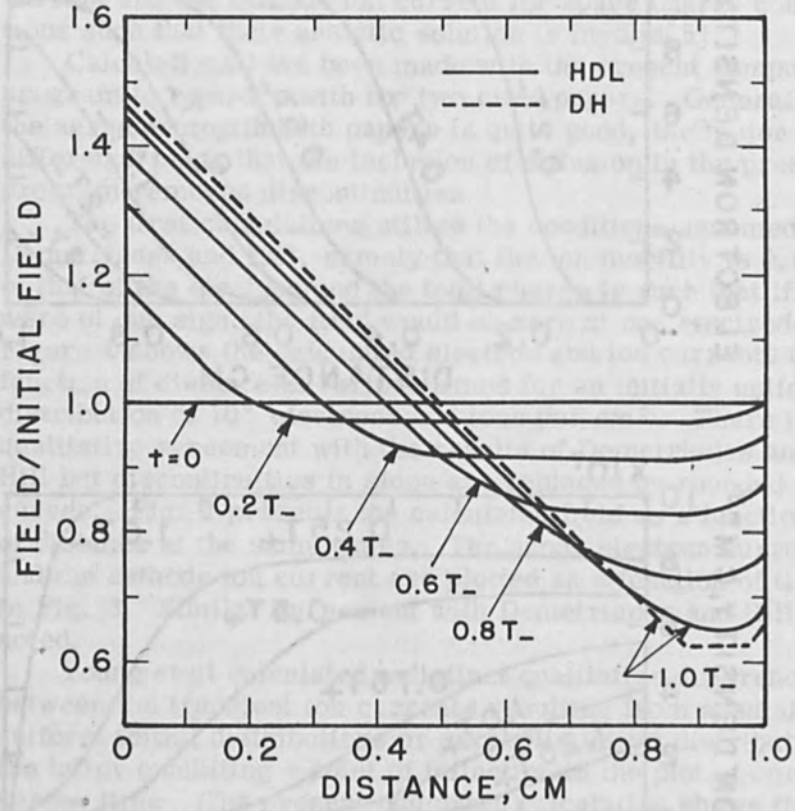

Figure 2. Electric field as a function of gap position for various times, plotted as the fraction of the initial undistorted field. The solid lines give the results for the Harry Diamond Laboratories computer program, while the dashed curve is from Demetriades

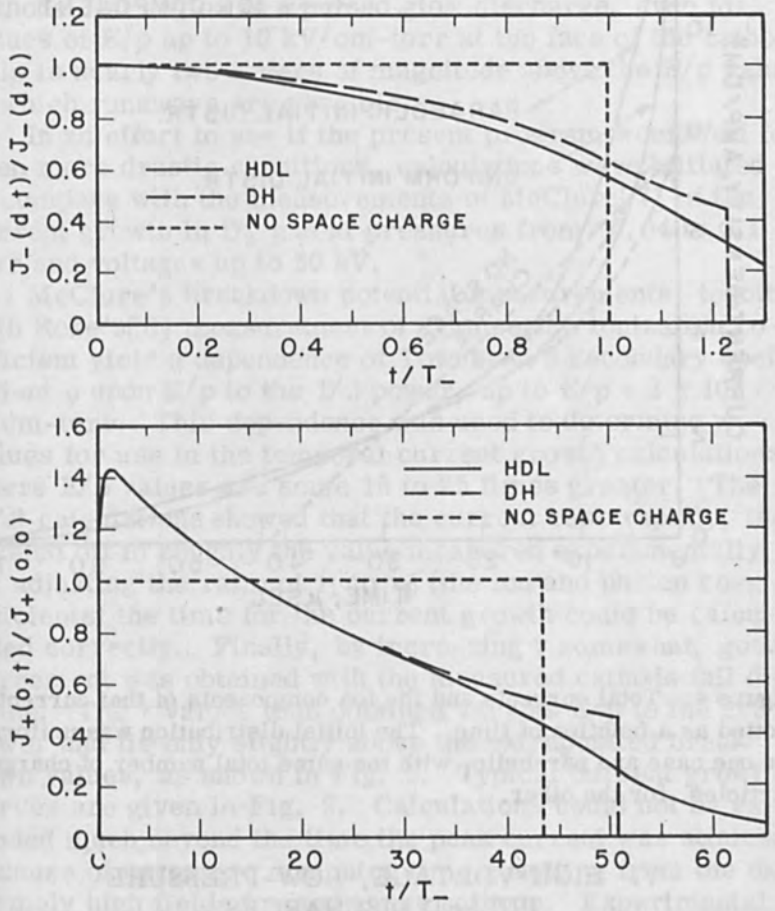

Figure 3. Electron current at the anode, $j_-(d,t)$, and the ion current at the cathode, $j_+(0,t)$, plotted as a function of time. The currents are plotted as ratios to their initial values and the time as multiples of the electron transit time, T_-.

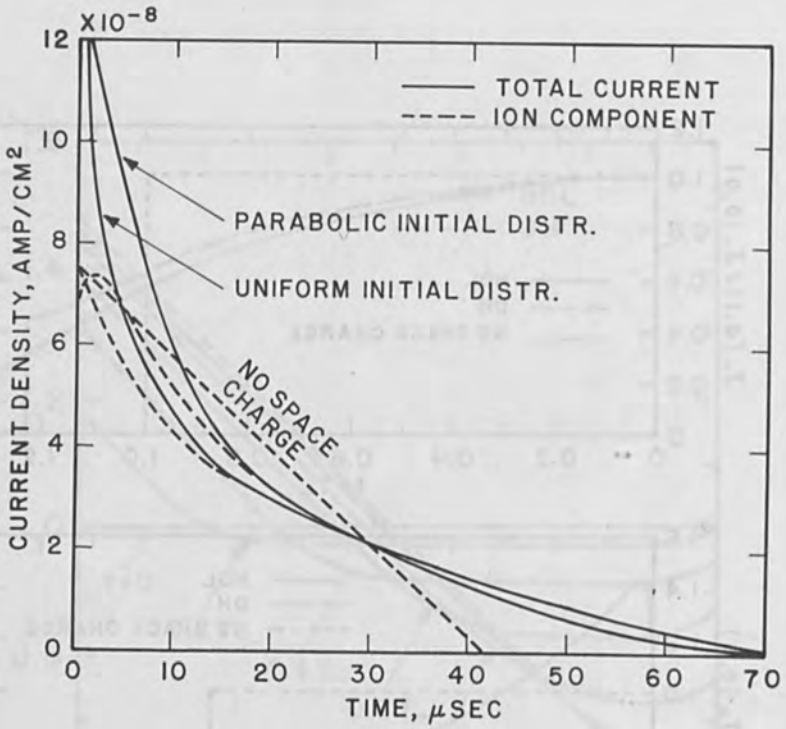

Figure 4. Total currents and the ion components of that current plotted as a function of time. The initial distribution was uniform for one case and parabolic, with the same total number of charged particles, for the other.

V. HIGH-VOLTAGE, LOW-PRESSURE PULSED DISCHARGES

The problem of determining those conditions of field and pressure where one may use either beam approximations or swarm approximations is an old one in glow discharges. Generally, experimental measurements have indicated that there is a very long transition region from the higher-pressure normal glow, where there are no runaway electrons,

to the low-pressure, highly abnormal discharge, where nearly all electrons are beam electrons. It has been shown [6] that the present swarm-model computer program gives satisfactory agreement with the measured formation of the cathode-fall region in a pulsed glow discharge, even for values of E/p up to 10 kV/cm-torr at the face of the cathode. This is nearly two orders of magnitude above the E/p value at which runaways are possible.

In an effort to see if the present program would fail for even more drastic conditions, calculations were initiated to compare with the measurements of McClure[7] of the current growth in D_2 gas at pressures from ~0.04 to 0.1 torr and voltages up to 50 kV.

McClure's breakdown potential measurements, together with Rose's[8] measurement of Townsend's ionization coefficient yield a dependence of Townsend's secondary coefficient γ upon E/p to the 1/3 power, up to $E/p = 2 \times 10^4$ V/cm-torr. This dependence was used to determine γ values for use in the temporal current growth calculations where E/p values are some 15 to 25 times greater. The first calculations showed that the current rose rapidly, then leveled off to roughly the value measured experimentally. By adjusting the ratio of γ_i to γ_p (the ion and photon coefficients) the time for the current growth could be calculated correctly. Finally, by increasing γ somewhat, good agreement was obtained with the measured cathode fall distance. The γ values thus obtained vary as E/p to the 2/3 power and lie only slightly above the extrapolated breakdown values, as shown in Fig. 5. Typical current growth curves are given in Fig. 6. Calculations could not be extended much beyond the time the peak current was attained, because of excessive computer time resulting from the extremely high fields formed at the cathode. Experimental measurements showed that it took from 20 to 200μ sec for a 20 percent delay in current.

The most critical test of the calculations is the variation of peak current with applied voltage and with pressure. These variations are plotted in Fig. 7 for constant values of γ. As shown above, γ should vary with the applied voltage, but the computer calculations are limited to a constant γ. However by using the variation of γ with E/p shown in Fig. 5, one may obtain the increase in peak

Figure 5. Plot of γ, Townsend's secondary ionization coefficient, plotted as a function of E/p. Each scale is logarithmic. Straight lines of slope of 1/2 and 2/3 have been drawn through data obtained from breakdown data and from cathode-fall distances, respectively.

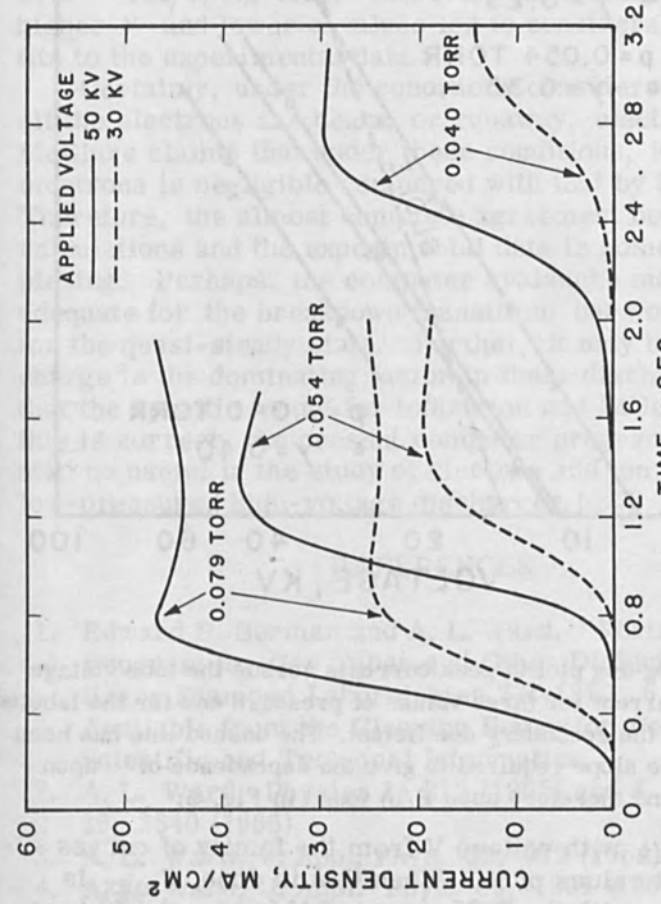

Figure 6. Temporal current growth for D_2 in 7.6-cm gap for three labeled pressures and for applied voltages of 50 and 30 kV. The circuit RC time constant was 1 microsecond for these calculations.

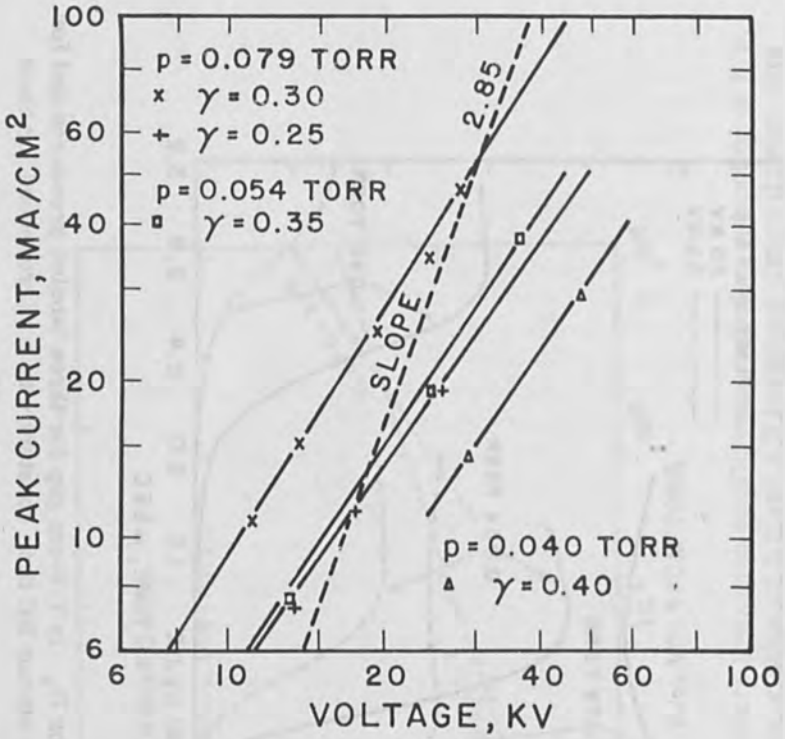

Figure 7. Log-log plot of peak currents versus the tube voltage at the peak current for three values of pressure and for the labeled values of , the secondary coefficient. The dashed line has been drawn with the slope required to give the dependence of upon the voltage (and therefore upon E/p) found in Fig. 5.

current J_{max} with voltage V from the family of curves for different values of γ. When this is done, J_{max} is found to vary with the 2.85 power of V for p = 0.079 torr and the 2.6 power for p = 0.054. These compare favorably with the measured value of 2.9. For a constant γ and tube voltage, the calculated variation of J_{max} with p is to the 3.1 power. For a γ that varies with the 2/3 power of V, the variation of J_{max} with p is the 1.8 power. These two values bracket the experimental value of 2.6.

McClure reported measured values of γ of about an order of magnitude greater than those used in these calculations. One can obtain the same breakdown voltages for higher γ values by appropriately reducing the values for α, which cannot be reliably measured for E/p values over ~ 150 V/cm-torr. However, all attempts to use higher γ and lower α values led to considerably poorer fits to the experimental data.

Certainly, under the conditions considered here nearly all the electrons are beam, or runaway, electrons. McClure claims that under these conditions, ionization by electrons is negligible compared with that by the ions. Therefore, the almost complete agreement between the calculations and the experimental data is somewhat perplexing. Perhaps, the computer avalanche model is adequate for the breakdown transition, but would not be for the quasi-steady state. Further, it may be that space charge is the dominating factor in these discharges, and that the specific model for ionization has little effect. If this is correct, the present computer program should still be useful in the study of electron and ion beams in low-pressure, high-voltage discharges.

REFERENCES

1. Edward R. Berman and A. L. Ward, "Fortran IV Program for Gas Tubes and Other Dielectrics," Harry Diamond Laboratories TR-1310, 5 Nov 1965. Available from the Clearing House for Federal Scientific and Technical Information.
2. A. L. Ward, Physics 1, 215 (1965) and J. Appl. Phys. 36, 2540 (1965).
3. A. L. Ward, J. Appl. Phys. 35, 469 (1964).
4. A. L. Ward, J. Appl. Phys. 36, 1291 (1965); Proceedings of the Seventh International Conference on Phenomena in Ionized Gases; to be published in 1966 by Gradevinska Knjiga Publishing House, Belgrade Jugoslavia.
5. Anthony Demetriades and Jack H. Hill, J. Appl. Phys. 36, 747 (1965). R. A. Young, C. R. Gate, R. L. Sharpless and C. M. Ablow, Phys. Rev. 138, A39 (1965).

6. M. Nahemow, N. Wainfan and A. L. Ward, Phys. Rev. 137A, 56 (1965).
7. G. W. McClure, Phys. Rev. 124, 969 (1961); 125, 3 (1962); 125, 1792 (1962).
8. D. J. Rose, Phys. Rev. 104, 273 (1956).

The Growth of Whisker-Like Projections at High Electric Fields in Vacuum

R. M. Oman*

Applied Science Division
Litton Systems, Inc.
Minneapolis, Minnesota

I. INTRODUCTION

Some of the recent work in the area of voltage breakdown has been concerned with the role of whiskers or whisker-like projections which appear to grow at the cathode electrode when this electrode is subjected to high electric fields. [1-4] These whisker like projections appear coincident with predischarge currents that preceed catastrophic breakdown characterized by the high-current, low-voltage arc accompanied with the emission of light.

The purpose of this paper is to describe an experiment wherein the growth of projections on single crystal and multicrystal tungsten ball cathodes was observed by a surface electron reflection or electron mirror technique. Because of the way the information in the reflected beam is presented, this method is extremely sensitive to the presence of sharp projections on the surface under examination.

The basic steps in the experiment consisted in the preparation of the electrode, insertion of the electrode into the apparatus where the application of electric fields and observation of the electrode could be performed in situ, and then alternatively applying an electric field and examining the electrode as an electron mirror.

*Present address: National Research Corporation, Cambridge, Mass.

II. EXPERIMENTAL APPARATUS AND CONDITIONS

A. Interpretation of the Electron Mirror Microscope Image

Before going into the discussion of the experimental apparatus, perhaps it is best to describe how the image observed at the screen of the electron mirror microscope depends on the sample under observation for the particular circumstances under consideration. A simple schematic of an electron mirror microscope is shown in Fig. 1.

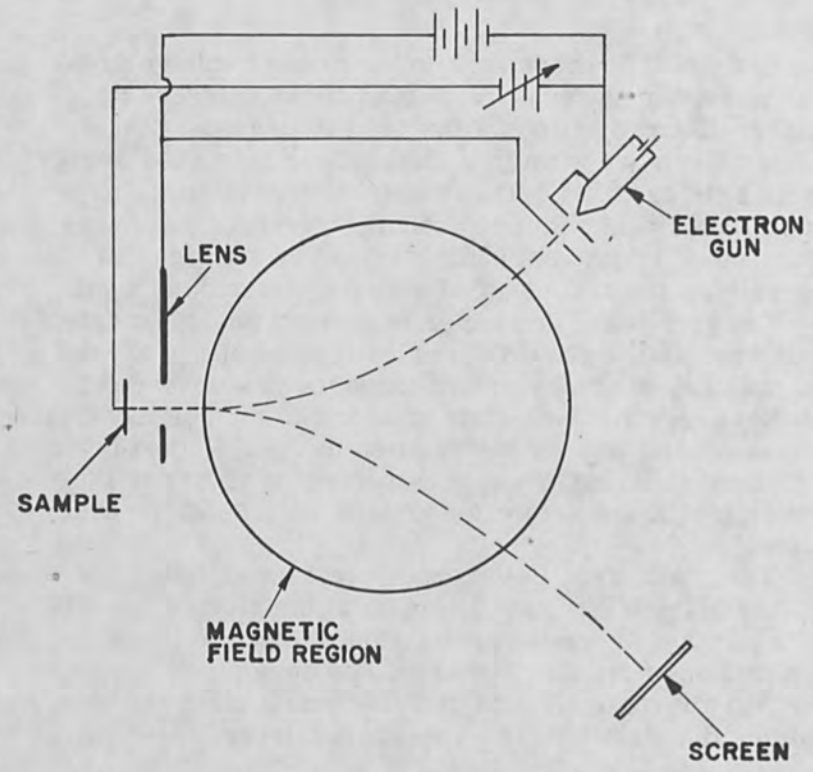

Figure 1. Schematic diagram of a simplified electron mirror microscope.

In electron mirror microscopy a beam of electrons, in vacuum of 10^{-5} Torr in this case, is directed onto a sample with the potentials adjusted so that the electrons are turned around just in front of the sample. After turning around, the electrons pass back out through the lens system and are displayed on a fluorescent screen. The sample voltage is variable from cathode potential to a few hundred volts negative. Depending on the average roughness of the sample, the mirror sample can be kept close enough to the cathode potential so that the electrons are mirrored very close (in some cases within a hundred angstroms) to the physical surface. The lens system serves to collimate and direct the beam normal to the sample. The magnetic field separates the incident and reflected beams so that the electron gun does not have to be in the center of the screen.

Since the electrons are reflected at equipotentials just outside the surface, the surface topology will influence the reflected beam. Potential differences across the sample which also influence the equipotentials and magnetic fields at the surface of the sample influence the beam, but in this discussion only the geometric effect will be considered. If the sample is very smooth, the electrons will be reflected from flat equipotentials giving a uniform intensity distribution at the screen. In Fig. 2 is shown the equipotentials outside of a sample with a cone shaped projection on it. The electron trajectories will be altered by the equipotentials resulting from this cone and will produce a dearth of electrons opposite the apex of the cone and an excess at the sides. The result at the screen is a dark spot surrounded by a bright ring. The photograph in Fig. 2 shows a surface with many projections on it. The size of the bright ring is not simply related to the size or shape of the projection since the electrons are refracted as they pass through the area where the electric field is non-uniform, reflected from an equipotential which depends on the potential of the sample with respect to the cathode and refracted again as they pass out of the vicinity of the disturbance. Thus in the case of a projection on the surface there is an additional "magnification" due entirely to the shape of the projection.

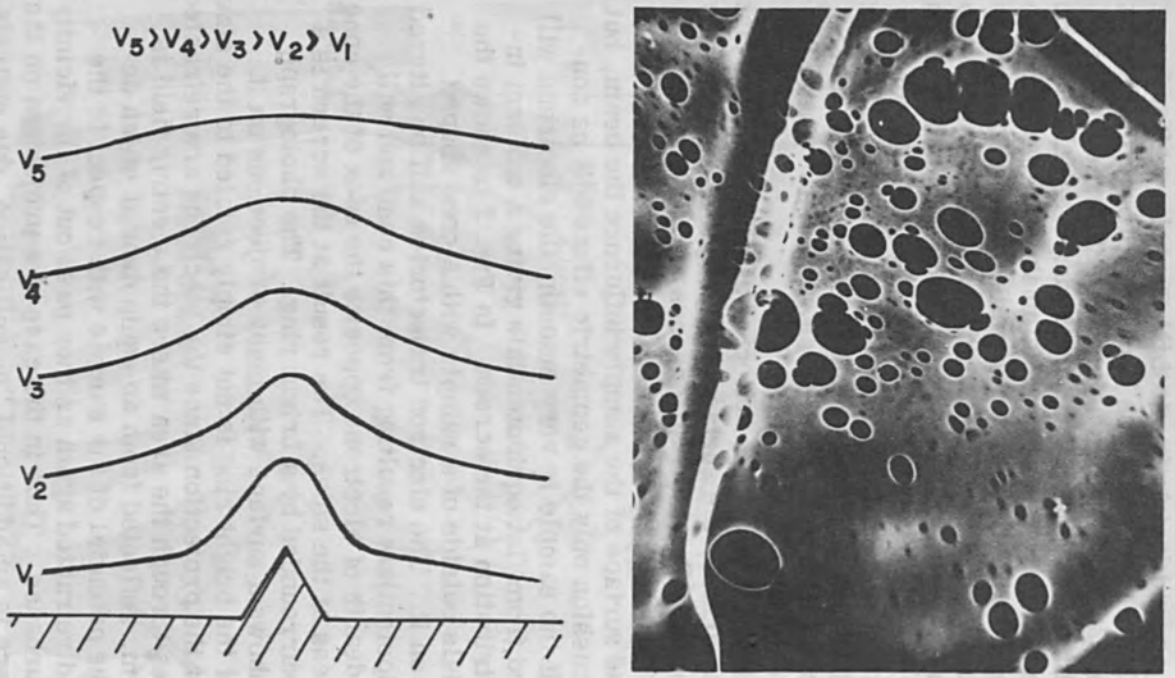

Figure 2. On the left is a diagram of the equipotentials outside of a sample with a cone shaped projection and on the right is an electron mirror micrograph of a sample on which there are many projections.

B. The Modified Electron Mirror Microscope

The basic apparatus has been described previously. [5] The microscope has been modified first so that an electric field can be applied to the sample and second so that the microscope can be used as a ball mirror instrument. Fig. 3 shows the final lens and sample electrode. The lens was modified to provide a pedestal so that the sample could be moved from the position shown in black to the position shown by the dashed outline where an electric field could be applied. In operation of the microscope as a ball mirror

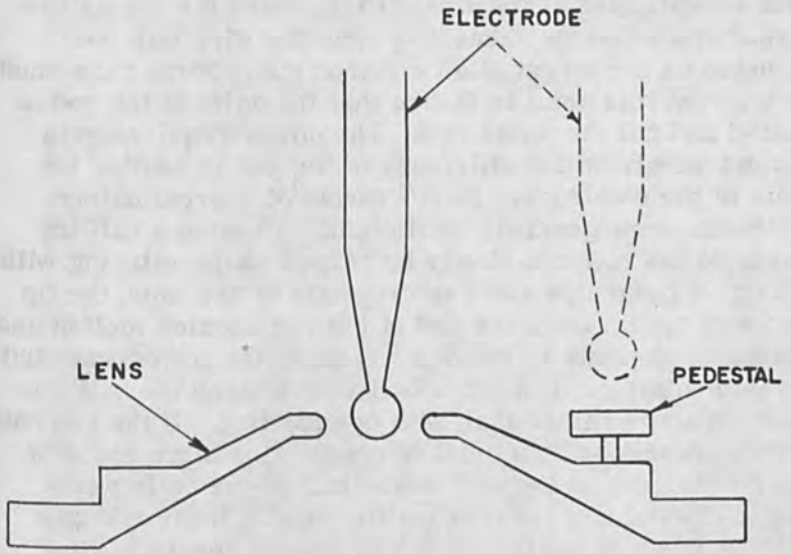

Figure 3. Schematic diagram of the lens and sample electrode arrangement showing the sample position for observation (solid) and sample position (dashed) for application of an electric field between the sample and the lens.

instrument it is necessary to have only one lens potential and the sample is placed inside of the lens. The magnification in this situation is determine solely by the geometry, that is, the radius of the ball and the ball to screen distance. [6]

C. Electrode Preparation

The single and multicrystal ball electrodes used in this experiment were prepared by melting the end of a tungsten rod in vacuum. [7] During the course of this experiment a very successful procedure for the production of ball electrodes of from 0.1 to 1.0 mm radius was evolved. A tungsten wire rod of approximately 0.1 mm diameter was mechanically ground to a point of the order of the dimensions of the crystallites in the wire. Of course, this size depended on the thermal history of the wire, but commercial grade tungsten wire worked quite well without special treatment to increase the crystallite size. In a separate vacuum system the wire was then mounted as the target of an electron gun. Some care must be taken at this point to insure that the point of the rod is heated and not the whole rod. The power requirements depend mostly on the efficiency of the gun in heating the point of the electrode. Power levels of approximately 100 watts were generally sufficient. To form a ball the power to the rod was slowly increased while watching with the aid of polaroids and a microscope to see when the tip began to melt. Once the end of the rod became molten and the ball had grown to the desired size, the power was shut off immediately. If a large ball was desired the ball was made in steps rather than with one melting. If the rod had been ground down to a point of roughly the dimensions of the crystallites in the rod, about half of the balls were single crystal and the rest multicrystal. If the rod was not sharpened a multicrystal ball always resulted. In multicrystal samples lines of crystallite boundaries like those in Fig. 2 were observed. The absence of these characteristic lines over the viewing area which was less than 10% of the surface area of the ball was taken as indicative of a single crystal ball. No attempts were made to determine the orientation of any of the balls. Of course the smoothness of the balls was far superior than anything obtained by the standard mechanical or chemical polishing techniques. A typical electron mirror micrograph of a vacuum melted single crystal tungsten ball is shown in Fig. 4. The geometric magnification of 3000X was de-

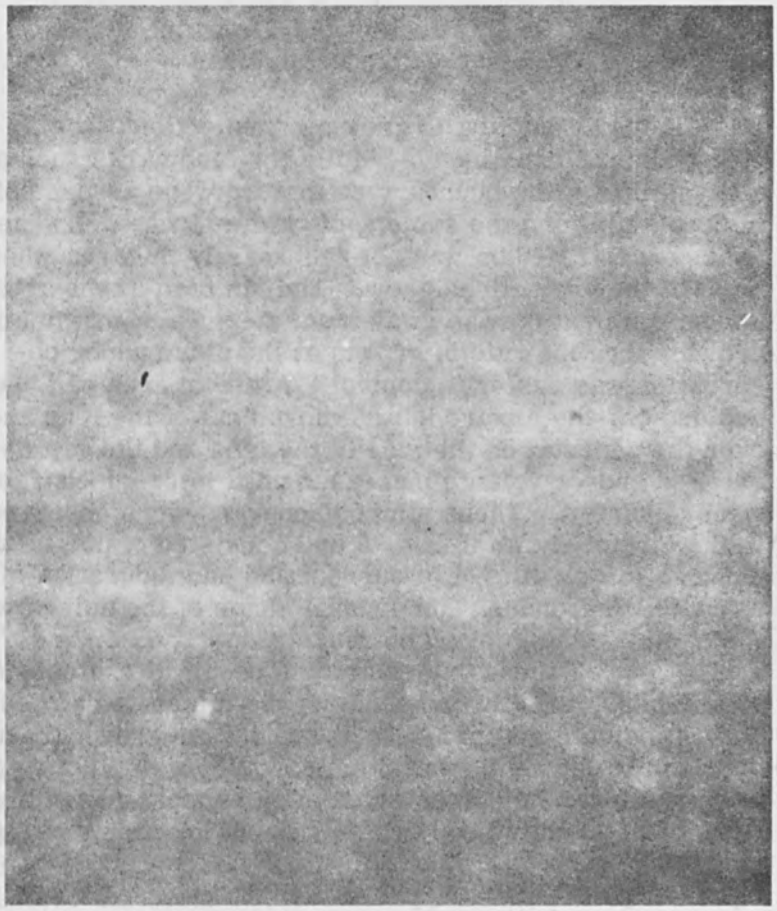

Figure 4. Electron mirror micrograph of a single crystal tungsten ball. Geometric magnification is 3000X.

termined by evaporating gold onto the ball through a mesh of known size and again observing the ball under the same conditions.

D. Observations of the Growth of Whisker-Like Projections

Before attempting to grow any projections, the electrode was examined carefully for landmarks such as a crystallite grain boundary so that we were assured of always examining the same spot on the electrode. The area concentrated on was not necessarily the area where most of the projections grew. And, in fact, if the area under examination was away from the area of maximum growth, then the rate of growth at the place under observation was easier to control. After an area had been decided on, the electrode was moved out of the lens and over the pedestal on the side of the lens and the gap decreased and/or voltage increased until microdischarges were observed. These microdischarges were observed in the circuit shown in Fig. 5 and consisted of pulses that were as low as 10^{-8} A of current and had a duration of a few milliseconds. The general shape of the pulses was the same as shown by Tomaschke, Alpert, Lee, and Lyman. [8] If these pulses are the result of explosions of whiskers, then the presence of the microdischarges should indicate that projections are indeed growing. In actual practice an area of the electrode was selected for examination and pictures taken after successive applications of the electric field while monitoring the discharge current.

III. RESULTS AND DISCUSSION

In Fig. 6 is shown a series of pictures taken after successive applications of an electric field of sufficient magnitude to produce the predischarge currents previously described. The gross fields were in the range of 10^5 to 10^6 V/cm. The predischarge currents in this case were of the order of 10 μ A and were maintained for a duration of 20 sec. It was rather difficult to place precise

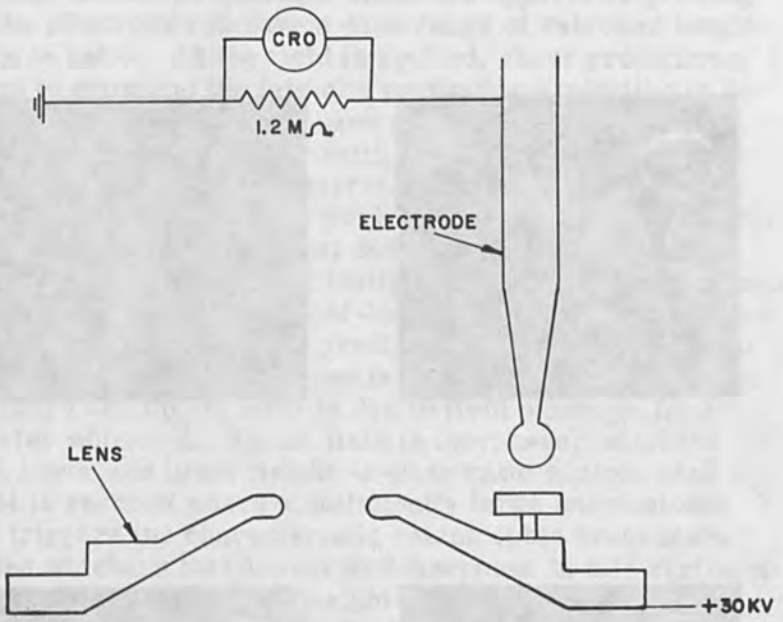

Figure 5. Schematic diagram of the circuit for observing micro-discharges in the high voltage circuit. The current pulses produced in the discharge gap could be observed as voltage pulses across the large series resistor.

values on the current because of the difficulty in maintaining a current at the desired level. The 10 μ A of current consisted of what appeared to be about A of dc current with another 5 μ A of random pulses of a few millisec duration. Before the application of high voltage this electrode was as shown in Fig. 4.

If the four photographs in Fig. 6 are examined carefully, several events appear to be taking place. A cursory examination indicates that some sort of projections are growing on the surface of the electrode. Looking further it can be seen that under the large dumbell shaped spot in the top left of the photographs a smaller spot appears (b) disappears (c) and reappears again at the same place (d). In (c) a spot has appeared which has disappeared again in (d). The smaller dumbell shaped spot which is in (b) and (c) has changed in (d).

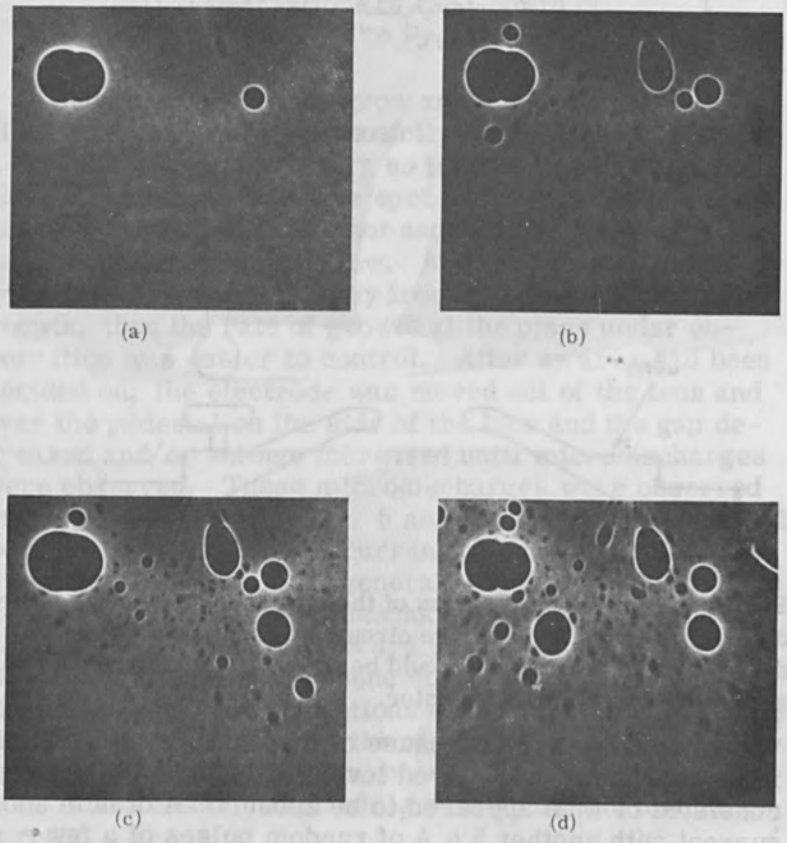

Figure 6. The photographs a, b, c, and d are numbers 2, 5, 7, and 14 in a series of pictures taken after repeated applications of the electric field necessary to produce 10 μA of predischarge current for a duration of 20 sec. Photograph a is after two such treatments, b after five, and so on. Geometric magnification is 3000X.

This observed behavior can be accounted for by assuming that the projections which are apparently growing on the electrode can have a wide range of values of height-to-base ratio. As the field is applied, these projections begin to grow and the fate of a particular projection is determined by its height-to-base ratio. The ones with a very large height-to-base ratio explode very quickly because the field emission current is so large as to cause excessive heating. Those projections with a smaller ratio last longer because the heat due to the field emission is more easily dissipated. Finally the very broad projections (those with a very low height-to-base ratio) almost never explode. Presumably the predischarge current observed on the oscilloscope as pulses is the explosion of very thin whiskers and the dc level is due to field emission from heavier whiskers. As the field is increased, whiskers with lower and lower height-to-base ratio explode until a point is reached where a sufficiently large one explodes and triggers the characteristic catastrophic breakdown. Those whiskers that appear and disappear in this series of pictures are those with a height-to-base ratio such that their lifetime is the order of minutes under these particular field conditions. This process could be called the "survival of the fattest".

Though it is very difficult to determine accurately from micrographs of this nature, there appear to be spots on this electrode where a projection appears, disappears (presumably explodes) and reappears again. This effect has been observed on numerous other tungsten ball electrodes.

IV. CONCLUSIONS

The growth of projections on the cathode of high-voltage vacuum electrodes has been investigated with an electron mirror technique which indicates that for the particular cathodes used projections do indeed grow in the electric field and are coincident with the presence of predischarge currents observed in the high voltage circuit. The observed results indicate that there are some projections which grow and disappear and others that grow to

a reasonably fixed size and thereafter remain essentially constant. The experimental evidence also suggests that there are sites where whiskers grow, explode, and begin to grow again.

The observed effects are accounted for by assuming whiskers or whisker-like projections with a wide range of height-to-base ratios.

ACKNOWLEDGEMENT

The author would like to thank Mr. Gerhard Voll for his help with the experimental work.

REFERENCES

1. D. Alpert, D. A. Lee, E. M. Lyman, and H. E. Tomaschke, J. Vac. Sci. and Tech. 1, 35 (1964).
2. R. P. Little and W. T. Whitney, J. Appl. Phys. 34, 2430 (1963).
3. R. P. Little and S. T. Smith, J. Appl. Phys. 36, 1502 (1965).
4. Leo Jedynak, J. Appl. Phys, 36, 2587 (1965).
5. L. Mayer, R. Rickett, and H. Stenemann, Proceedings of Fifth International Congress for Electron Microscopy (Academic Press, New York, 1962), p. D-10.
6. Details of the operation of a ball mirror microscope will be given in a later publication.
7. The basic idea for the preparation of the tungsten ball cathodes described in this paper was suggested to the author by Dr. H. F. Webster of the General Electric Research Laboratory, Schenectady, New York.
8. H. E. Tomaschke, D. Alpert, D. A. Lee, and E. M. Lyman, Proceedings of International Symposium on Insulation of High Voltages in Vacuum, 1964, p. 13.

Numerical Theoretical and Experimental Investigation of a High-Current Tele-Focus Electron Gun of Tetrode Type

E. B. Bas, G. Cremosnik, R. N. Thomas and H. B. Wiedmer

Department of Industrial Research (AfiF),
Swiss Federal Institute of Technology,
Zurich, Switzerland

Under the name telefocus electron gun we can define an electron gun which allows to focus the electron beam in a first real crossover outside the acceleration field far from the cathode by suitable choice of electrode geometry and potentials of the electrodes.

Steigerwald showed first [1] that telefocus characteristics can be achieved with a three-electrode electron gun. Since then such telefocus-guns have found a wide field of applications in practice and have also been systematically investigated by F. Braucks [2]. Of course in all these applications a hairpin cathode has been used, which limits strongly the maximum beam current and causes an axial astigmatism of the beam due to the assymmetry of the hairpin cathode, which is more or less pronounced according to the value of the beam current. This disadvantage has been partly eliminated by E. B. Bas and F. Gaydon [3] using a so called bolt-cathode after E. B. Bas [4] instead of the hairpin cathode. By the use of this bolt-cathode they have been able to simplify the Steigerwald's gun geometry, finding that the conical part of the Welnelt-cylinder around the cathode can be substituted by a plane

part without affecting the telefocus characteristics of the gun. Such an electron gun is in use in the commercial "Panoramix"-x-ray tube for dental diagnostics [5]. It allows, at a cathode diameter of 0.6 mm and an acceleration voltage of 50 kV, the focusing of a beam current of about 2.5 mA in a crossover of about 180 μ in diameter (half height width) at a distance of 170 mm from the cathode. But a substantial improvement of the beam current is handicapped by space charge, because in the given electrode geometry the strength of the electrical field in front of the cathode in this type of triode gun is very weak. To overcome this difficulty we started the study of a tetrode type of telefocus electron gun in 1960, which should be able to deliver very high currents. During this study we also had to overcome some technological design difficulties and improve further the bolt-cathodes. These investigations, continued during many years, form the contents of this report. It shall be mentioned that the tetrode system has also been studied by other authors [7] [8], who of course always applied hairpin cathodes which are not able to deliver the high beam currents we are looking for here.

2. GEOMETRY OF THE ELECTRON GUN FOR NUMERICAL-THEORETICAL INVESTIGATION

Figure 1 shows the electron gun geometry, with the main dimensions used for the theoretical investigations. The electron gun consists of: a planar cathode with circular emission area on potential zero; a Wehnelt-electrode on potential V_0, which is conically formed near the cathode according to Pierce [9]; a first anode containing two circular apertures on potential V_1; and an anode on potential V_a. In the theoretical investigation the distance between the cathode and the first aperture of the first anode Z_1 is used as variable parameter. Furthermore the effect of the variation of the potentials V_0 and V_1 is studied. In principle a tetrode type electron gun consist of a triode type electron gun and an immersion lens, which is built between the second aperture of the first anode and the main anode. However the potential fields

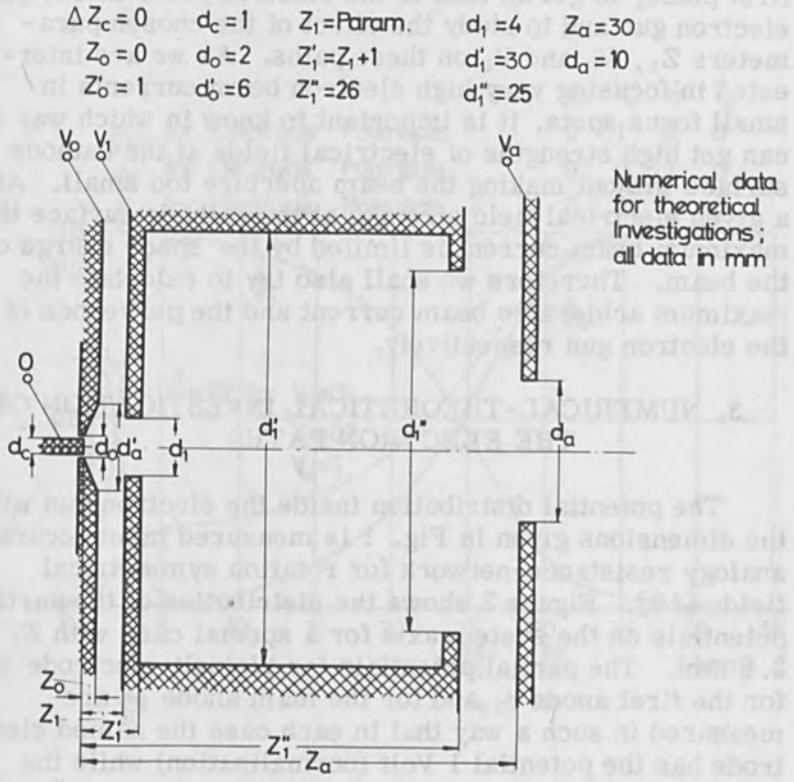

Figure 1. Electrode Geometry of the telefocus electron gun of tetrode type investigated in this paper. The dimensions given in the figure are used for theoretical investigations with only Z_1 as variable geometry parameter. (For the dimensions in experimental investigations see text.)

of these two lens systems penetrate each other, which makes it necessary to treat the whole acceleration field as a single immersion objective.

The purpose of the theoretical investigation is, in the first place, to get an idea of the electron paths inside the electron gun and to study the effect of the chosen parameters Z_1, V_0 and V_1 on these paths. As we are interested in focusing very high electron beam currents in small focus spots, it is important to know in which way we can get high strengths of electrical fields at the cathode surface without making the beam aperture too small. At a given electrical field strength at the cathode surface the maximum beam current is limited by the space charge of the beam. Therefore we shall also try to calculate the maximum achievable beam current and the perveance of the electron gun respectively.

3. NUMERICAL-THEORETICAL INVESTIGATION OF THE ELECTRON PATHS

The potential distribution inside the electron gun with the dimensions given in Fig. 1 is measured in an accurate analogy resistance-network for rotation symmetrical fields [10]. Figure 2 shows the distribution of the partial potentials on the system axis for a special case with Z_1 = 2.5 mm. The partial potentials for Welnelt-electrode ϕ_0, for the first anode ϕ_1 and for the main anode ϕ_a are measured in such a way that in each case the named electrode has the potential 1 Volt (normalisation) while the other electrodes are set at zero potential. By superposition of these partial potentials we can then get the resultant potential distribution along the system axis ϕ for any combination of electrode voltages V_1, V_0 and V_a. As an example the dashed curve in Fig. 2 represents the resultant potential distribution for V_0 = O, V_1 = 0.2 and V_a = 1 Volt. In the following we will always normalise the anode voltage to 1 Volt, as long as we are not dealing with the space charge effects. Since our electron path calculations are made non-relativistically, the scaling principles are valid, so the calculated electron paths remain the same for all other electrode voltages multiplied by a constant factor.

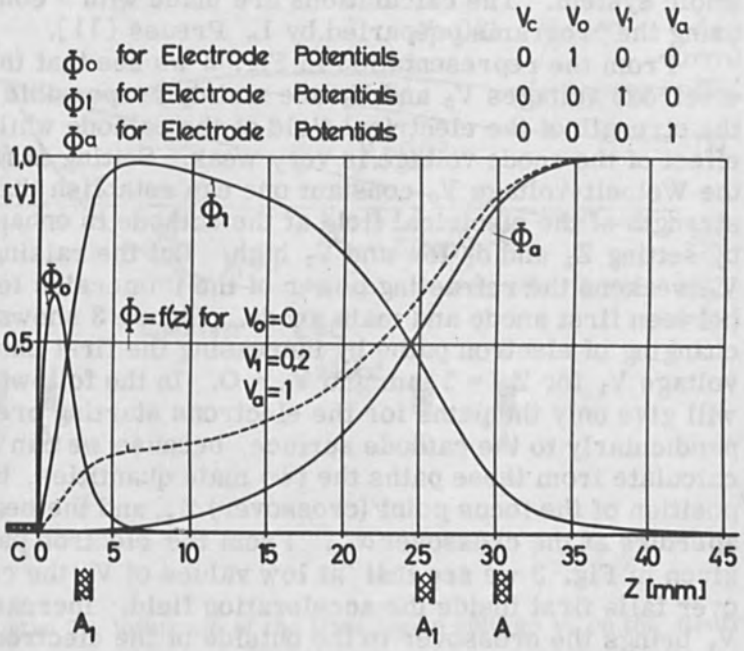

Figure 2. The normalised axial potential distributions ϕ_0, ϕ_1 and ϕ_a measured in an analogy-resistance network for the geometry dimensions given in Fig. 1, with $Z_1 = 2.5$ mm. The dashed curve gives the resulting potential distribution along the axis for the electrode voltages $V_0 = 0$, $V_1 = 0.2$ volt and $V_a = 1$ volt.

From the resulting potential distribution in Fig. 2 we see that the field of the triode immersion objective at the cathode and the field of the immersion lens between the first anode and the main anode are indeed penetrating each other so the separate treatment of the two parts can not be correct. We must calculate the electron paths through the whole system. The calculations are made with a computer using the programs preparied by L. Preuss [11].

From the representation in Fig. 2 we see that the electrode voltages V_0 and V_1 are mainly responsible for the strength of the electrical field at the cathode while the effect of the anode voltage is very weak. Setting at first the Welnelt-voltage V_0 constant one can establish that the strength of the electrical field at the cathode is enhanced by setting Z_1 and d_1 low and V_1 high. But the raising of V_1 weakens the refracting power of the immersion lens between first anode and main anode. Figure 3 shows the changing of electron paths by increasing the first anode voltage V_1 for $Z_1 = 3$ mm and $V_0 = O$. In the following we will give only the paths for the electrons starting pre-pandicularly to the cathode surface, because we can already calculate from these paths the two main quantities, the position of the focus point (crossover) Z_F and the beam aperture at the crossover α_F. From the electron paths given in Fig. 3 we see that at low values of V_1 the cross-over falls first inside the acceleration field. Increasing V_1 brings the crossover to the outside of the electron gun and at $V_1 = 0.2$ Volts it becomes already virtual. The whole focusing range for telefocus operation lies between $V_1 = 0.02$ and $V_1 \approx 0.18$ Volts. In Fig. 3 and in the following figures the axial position of the electrodes are marked below the diagrams. Figure 4 shows the electron paths for $V_0 = -0.01$ volt and $Z_1 = 2.5$ mm with V_1 as parameter. The character of the electron paths is not changed essentially, but the focusing range lies now between $V_1 = 0.13$ and $V_1 \approx 0.23$ volts. Additionally the beam profile in front of the cathode is a little more bundled. The effect of the negative Welnelt-voltage can be seen better if we plot the relevant quantities Z_F, α_F and field strength at the cathode E_c against the first anode voltage for two different Welnelt-voltages. This is done in Fig. 5

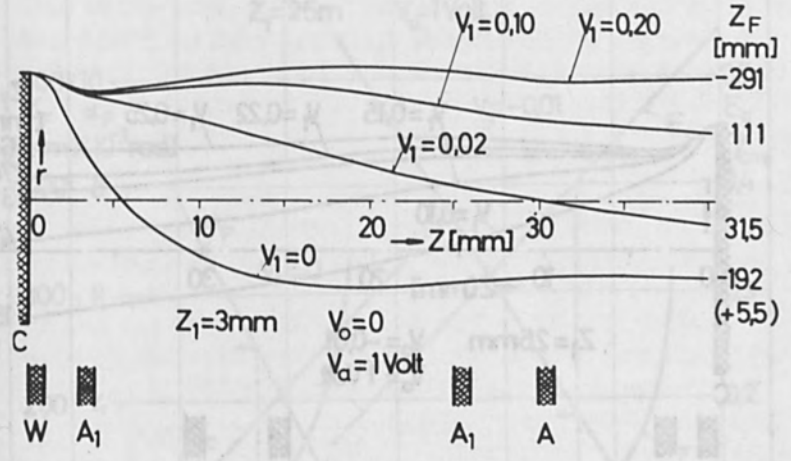

Figure 3. Influence of the first anode voltage V_1 on the electron paths at $V_o = 0$.

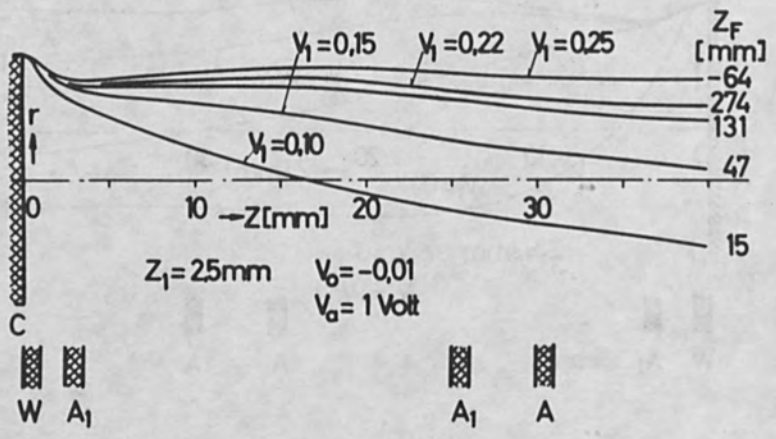

Figure 4 Electron paths at a negative Wehnelt-voltage with V_1 as parameter.

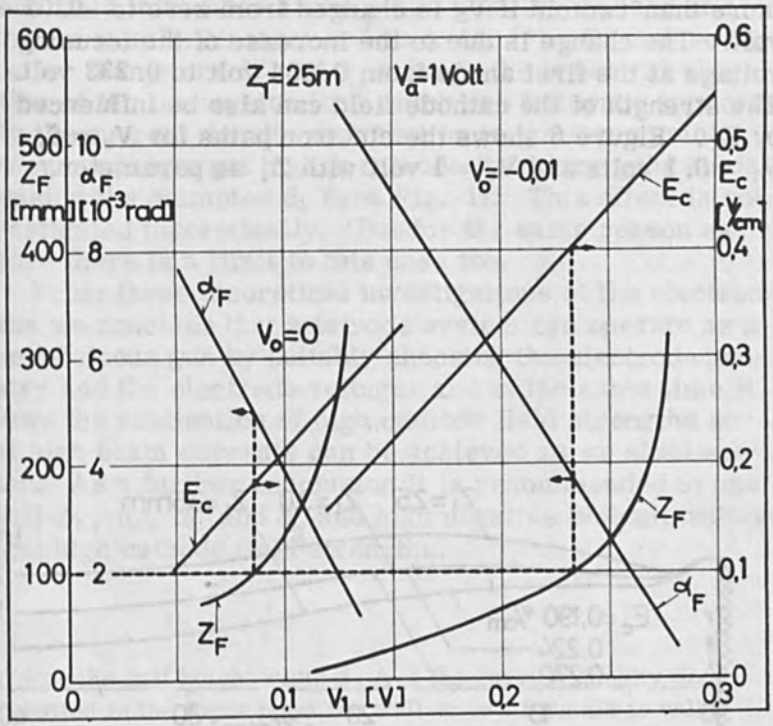

Figure 5. The relevant characteristic quantities Z_F, α_F and E_c as a function of V_1 with $V_o = 0$ and $V_o = -0.01$ volt. (V_a normalised to 1 volt)

Z_F = Distance focus-cathode

α_F = Angle of the edge path (for cathode diameter d_c = 1 mm) at the focus

E_c = Strength of the electrical field at the cathode surface.

for $Z_1 = 2.5$ mm. Looking in this diagram for E_c, α_F at a focus distance of for example $Z_F = 100$ mm we find $E_c = 0.185$ V/cm, $\alpha_F = 5 \times 10^{-3}$ rad at $V_0 = 0$ $E_c = 0.405$ V/cm; $\alpha_F = 3.8 \times 10^{-3}$ rad at $V_0 = -0.01$ volts. This means that although α_F is only a little influenced E_c rises to a value more than twofold if V_0 is changed from zero to -0.01 volt. The change is due to the increase of the focusing voltage at the first anode from 0.084 volt to 0.233 volt. The strength of the cathode field can also be influenced by Z_1. Figure 6 shows the electron paths for $V_0 = 0$, $V_1 = 0.1$ volts and $V_1 = 1$ volt with Z_1 as parameter.

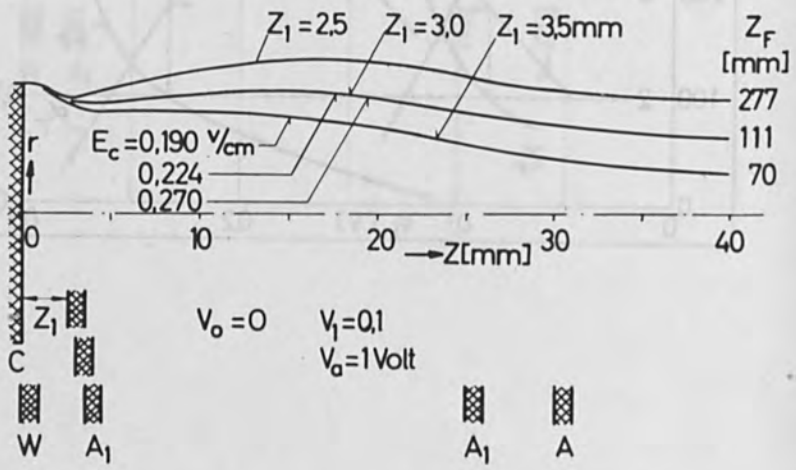

Figure 6. Influence of the geometry parameter Z_1 on the electron paths and cathode field strength.

Lowering Z_1 enhances the cathode field strength but at the same time moves the focus point fast away from the cathode. This can be compensated by increasing the refracting power of the anode field using smaller d_1'' and perhaps d_a values. This increase of the refractive power of the anode field influences also α_F in a positive manner and allows a smaller crossover diameter (*). Of course the smaller diameters d_1'' and d_a enlarge the spherical aberration of the immersion lens which can influence appreciably the current density distribution in the focus point. However one can get higher cathode field strengths by decreasing the diameter d_1 (see Fig. 1). This effect is not investigated theoretically. But for the same reason as before there is a limit in this case too.

From these theoretical investigations of the electron paths we conclude that a tetrode system can operate as a true telefocus gun by suitably choosing the electrode geometry and the electrode voltages and at the same time it allows the realisation of high cathode field strengths so that high beam currents can be achieved as we shall see later. As a further conclusion it is recommended to use small Z_1, d_1, d_1'' and d_a and high negative Welnelt-voltages to get high cathode field strengths.

(*) For the half height width $d_{1/2}$ of the current density distribution in the focus point the well-known formula is valid:

$$d_{1/2} = 1.66 \frac{\Gamma_c}{\alpha_F} \sqrt{\frac{V_T}{V_a}}$$

with V_T = the mean energy of the electrons leaving the cathode in volts, V_a = anode voltage. As this formula shows $d_{1/2}$ is inversely proportional to α_F. For example for V_T = 0.25v, V_a = 25 kv, $\alpha_F = 5 \times 10^{-3}$ and Γ_c = 0.5 mm we get $d_{1/2}$ = 0.5 mm.

4. THEORETICAL ESTIMATE OF THE PERVEANCE

To estimate the electron gun perveance, or the maximum attainable beam current respectively one has to determine the influence of the beam space charge on the potential distribution in the acceleration field. For this case it is necessary to introduce currents in the analogy resistance network into the network points which lie inside the area occupied by the electron beam. The exact solution of this problem is time consuming so we must make some simplifying assumptions. The first assumption is that the space charge flow has a laminar character; in other words the initial energy of the electrons at the cathode will be neglected. In consequence of this assumption the electron paths in Fig. 3, 4 and 6 represent the beam profile if their starting point is taken at the edge of the emission area of the cathode. By introducing a second assumption that the current density is constant over the entire emission area we can now calculate the current densities in each point of the beam by using the potential distribution from the static field for the determination of the electron velocity at each point as a first approximation. In every cross-section of the beam the current density is constant since we assumed the flow to be laminar and a constant current density at the cathode. The space charge density at every point of the beam is directly proportional to the current density at the cathode, so we have to calculate the space charge density distribution only for a single value of the cathode current density, for example for $j_c = 1\ A/cm^2$. However we can not use now the normalised distribution of the axial potential with $V_a = 1$ volt but we must consider the actual anode voltage.

We measured first the space charge field in an entire model of the electron gun with a network mesh-width equivalent to 0.5 mm of the actual dimension of the electron gun. (In this measurement all electrodes are held at zero potential and the network currents are introduced according to the space charge distribution). Afterwords an enlarged model is traced onto the network representing only a small area near the cathode using the boundary potentials which are determined in the first measurement. In this

way we are able to determine the potential distribution more exactly just in front of the cathode. Figure 7 shows as an example the distribution of the partial potential on the axis due to the beam space charge for an anode voltage of 25 kv and a cathode current density of 1 A/cm².

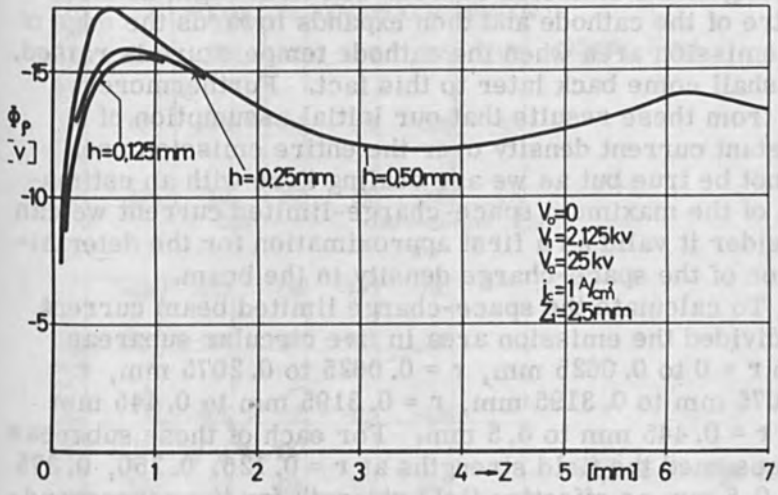

Figure 7. Distribution of the partial potential ϕ_p caused by the space-charge of the beam for $V_a = 25$ kv, $j_c = 1$ A/cm².

The diagram represents measurements for three different mesh-widths h. We see that the influence of the model dimension (respectively h) on the accuracy in determining

the negative field strength at the cathode due to space charge is very strong. Figure 8 shows the whole potential distribution in front of the cathode measured with a mesh-width, h = 0.125 mm. Figure 8a represents the static field and Fig. 8b the space charge field. We see from this figure that in both cases the strength of the field at the cathode surface is not independent of r. In the static field E_c is stronger at the edge of the emission area; on the contrary it is weaker at the edge in the field due only to the space charge. This means that the space-charge limiting of the emission current will first begin at the centre of the cathode and then expands towards the edge of the emission area when the cathode temperature is raised. We shall come back later to this fact. Furthermore we see from these results that our initial assumption of a constant current density over the entire emission area cannot be true but as we are dealing here with an estimation of the maximum space-charge-limited current we can consider it valid as a first approximation for the determination of the space-charge density in the beam.

To calculate the space-charge limited beam current we divided the emission area in five circular subareas with r = 0 to 0.0625 mm, r = 0.0625 to 0.2075 mm, r = 0.2075 mm to 0.3195 mm, r = 0.3195 mm to 0.445 mm and r = 0.445 mm to 0.5 mm. For each of these subareas we assumed the field strengths at r = 0.125, 0.250, 0.375 and 0.5 mm as effective field strength for the corresponding area. The space-charge limited beam current is defined in that way that in this stadium the resultant field strength in front of the corresponding subarea vanishes, this means:

$$E_c = (E_c)_{\text{static}} + (j_c)_{\max} (E_c)_{\text{space-charge}} = 0$$

with:

$(E_c)_{\text{static}}$ = static field strength without space-charge

$(E_c)_{\text{space-charge}}$ = space-charge field strength without electrode potentials for $j_c = 1\ \text{A/cm}^2$

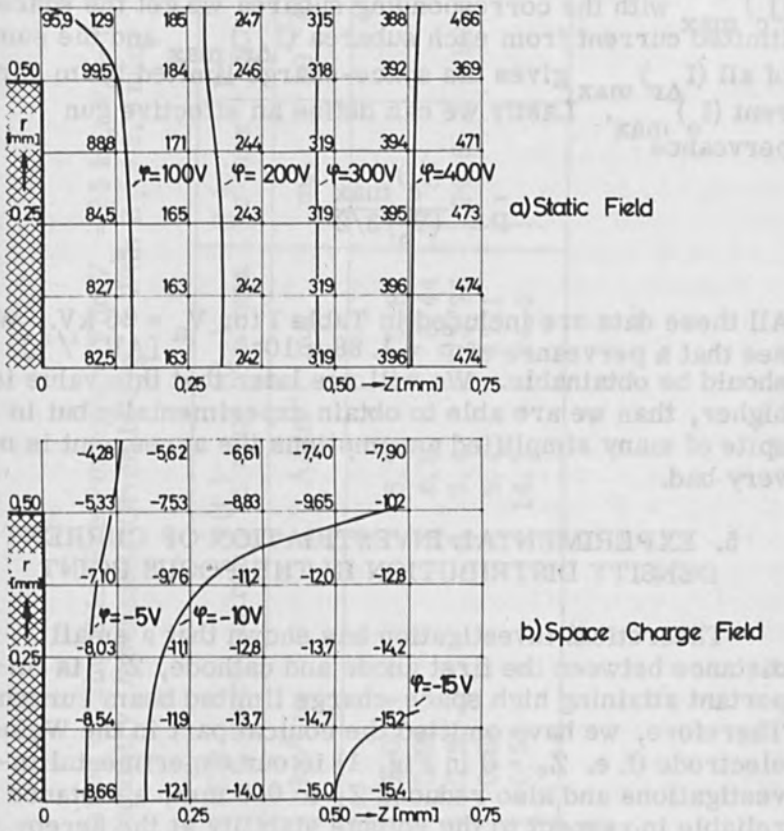

Figure 8. Potential distribution near the emission area of the cathode:
a) Static field for V_a = 25 kv, V_o = 0
b) Space-charge field for V_a = 25 kv, j_c = 1 A/cm^2
Geometry dimensions according to Fig. 1 and 7. Potentials in the resistance network points are given in volts.

The exact values of $(\bar{E}_c)_{static}$ and $(E_c)_{space\text{-}charge}$ are calculated from the numerical potential values given in Fig. 8 by cubic extrapolation to the cathode surface. These field strengths and the calculated $(j_c)_{max}$ for each subarea are tabulated in Table I. If we multiply each $(j_c)_{max}$ with the corresponding subarea we get the space limited current from each subarea $(I_{\Delta r})_{max}$ and the sum of all $(I_{\Delta r})_{max}$ gives the space-charge limited beam current $(I_e)_{max}$. Lastly we can define an effective gun perveance

$$\tilde{P} = \frac{(I_c)_{max}}{(V_a)^{3/2}}$$

All these data are included in Table I for $V_a = 25$ kV. We see that a perveance of $\tilde{P} = 1.88 \times 10^{-8}$ $[AV^{-3/2}]$ should be obtainable. We will see later that this value is higher, than we are able to obtain experimentally but in spite of many simplified assumptions the agreement is not very bad.

5. EXPERIMENTAL INVESTIGATION OF CURRENT DENSITY DISTRIBUTION IN THE FOCUS POINT

Theoretical investigation has shown that a small distance between the first anode and cathode, Z_1, is important attaining high space-charge limited beam currents. Therefore, we have omitted the conical part in the Welnelt-electrode (i. e. $Z_0 = 0$ in Fig. 1) in our experimental investigations and also reduced Z_1 to 0.5 mm, a distance just reliable in respect to the voltage stability at the hereby applied voltages (Total acceleration voltage 20 kv). By a given gun geometry and a prescribed focus plane to cathode distance the height of the first anode voltage is fixed as shown before. The tetrode system can be thought to consist of two parts: the immersion objective cathode lens given by the cathode field and the immersion lens given by the anode field as already mentioned. The cathode lens produces a virtual crossover behind the cathode which is then imaged by the immersion lens as a real crossover onto the focusing-

Table I. Estimation Of The Effective Perveance For $V_a = 25$ kv, $V_o = 0$
(For The Geometry Dimensions Given In Fig. 1 With $Z_1 = 2.5$ mm)

r	(E_c) static	(E_c) space-charge	(j_c) max	(I_r) max	(I_e) max	P_{EG}
mm	kv/cm	kv/cm	A/cm^2	mA	mA	$10^{-8} AV^{-3/2}$
0	6.7	1.00	6.7	0.82	74.6	1.88
0.125	6.7	0.99	6.8	8.44		
0.250	7.0	0.95	7.4	13.75		
0.375	7.5	0.83	9.1	27.1		
0.500	7.8	0.53	14.7	24.5		

plane. If we now enlarge the distance cathode to immersion lens (anode field) by fixed cathode to focusing-plane distance we have to weaken the refracting power of the immersion lens to keep the real crossover in focus on the focusing-plane. That means we have to increase the first anode voltage and in this way we get better conditions for a high space-charge limited beam current. We investigated this effect experimentally for a cathode to focusing-plane distance of $Z_F = 288$ mm. The current density distribution in the focusing-plane is determined by pulsed wobbling of the electron beam over a slot aperture of 40 μ width and registering the current through this aperture with an osciloscope (Scanning diagrams). This measuring method is discribed in detail in a previous paper [12]. In these experiments the distance between the first anode and the main anode is always kept constant; i. e. $Z_a - Z_1'' = 5$ mm. Furthermore the cathode temperature and the anode voltage of 20 kv are also kept constant in all measurements. For a fixed Z_a value we took through-focus scanning diagrams in function of V_1 to determine the exact focusing voltage $(V_1)_F$ and to get an idea about the beam profile. Although a determination of the half height width of the current density distribution in the focusing-plane by the measuring method used here is only acceptable for the exact focus with Gaussian distribution, we defined for all through-focus scanning diagrams the half height width in the same way. These "fictive" half height widths $d_{1/2}$ are shown in Fig. 9 as a function of V_1 for $Z_a = 50$ mm. We find from this diagram a focusing voltage $(V_1)_F = 1760$ V and a half height width in the focus of $d_{1/2}$ 0.5 mm. This half height width can be accepted as a real width of the current density distribution, then the scanning diagram in the exact focus has the Gaussian form as shown in the series of scanning diagrams represented in Fig. 10. We conclude from this result that the tetrode system is indeed able to focus high currents in a small spot at a great distance from the cathode and, secondly, that the focusing condition is very rensitive to variations of V_1. We shall see later that the $(V_1)_F$ also depends from the height of the beam current. Figure 9 also shows the emission current I_e (at constant cathode temperature !) in function of V_1.

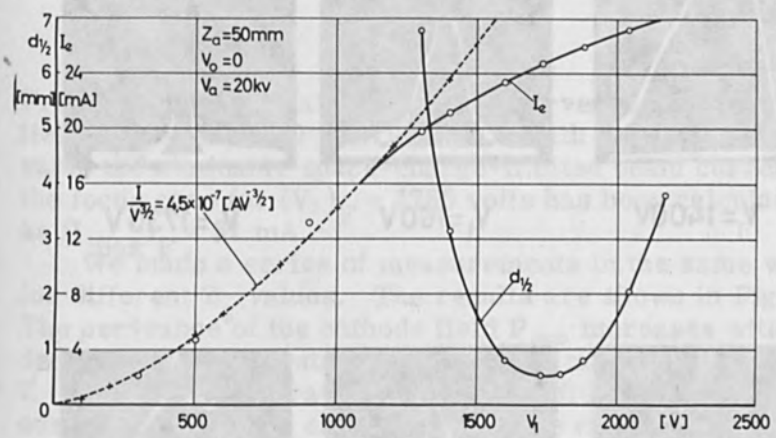

Figure 9. The "fictious" half height widths of the beam in the focus plane $d_{1/2}$ and the emission currents I_e as a function of the first anode voltage V_1 for Z_a = 50 mm, V_o = O, V_a = 20 kv and Z_F = 283 mm. The measurements are made with the following geometry parameter: (all in mm)

Z_c = O	Z_1' = 45	d_1 = 3
Z_o = 0	Z_a = Z_1' = 5	d_1' = 30
Z_1 = 0.5	d_a = 1	d'' = 25
Z_1 = 1.5	d_o^c = 1.5	d_a = 10

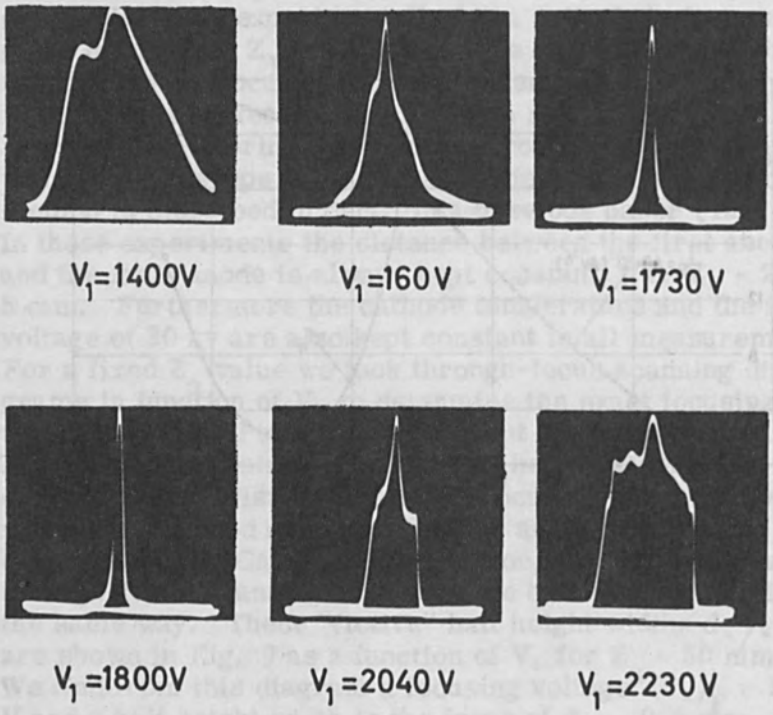

Figure 10. Scanning diagrams for various V_1 values for the measurements represented in Fig. 9.

We can see from this diagram that $(V_1)_F$ lies in the transition region between the space-charge-limited and temperature-limited regions. The strongly pronounced transition region indicates the slow progress of the space-charge limiting of emission current from the centre of the cathode to the edge of the emission area as mentioned above in the theoretical investigation. The first part of the I_e vs. V_1 curve can be approximated very well by the space-charge limited current equation

$$I = P\, V^{3/2}$$

From this approximation we find a perveance of the cathode field $P_{CF} = 4.5 \times 10^{-7}\ [AV^{-3/2}]$. With this perveance value the attainable space-charge-limited beam current in the focus case for $(V_1)_F = 1760$ volts has been calculated as $(I_{max})_F = 31$ mA.

We made a series of measurements in the same way for different Z_a values. The results are shown in Fig. 11. The perveance of the cathode field P_{CF} increases with decreasing anode distances Z_a. This means that at small Z_a values the penetration of the anode field into the cathode region becomes effective as can be expected. But the space-charge-limited beam current at focus $(I_{max})_F$ increases with increasing anode distance because the focusing first anode voltage $(V_1)_F$ increases linearly with Z_a as is indicated in Fig. 11. Therefore the overall perveance of the whole electron gun $(P_{EG})_F$ increases also with the increasing Z_a. In Fig. 11 the values of $(I_{max})_F$ and $(P_{EG})_F$ are converted to an effective anode voltage of 25 kv to be able to compare these results with the results from the theoretical investigation. We notice that in these results the values of $(V_1/V_a)_F$ as well as $(P_{EG})_F$ appear smaller than expected, although both Z_1 and Z_a had been changed in such a manner as to obtain an increase of both values.

The half height width of the current density distribution in the focus point remains constant, $d_{1/2} \approx 0.5$ mm, for all Z_a values. This is not suprising, because the virtual crossover lies far behind the cathode so the relatively small displacement of the immersion lens (anode field) becomes ineffective on the imaging of the virtual crossover into the

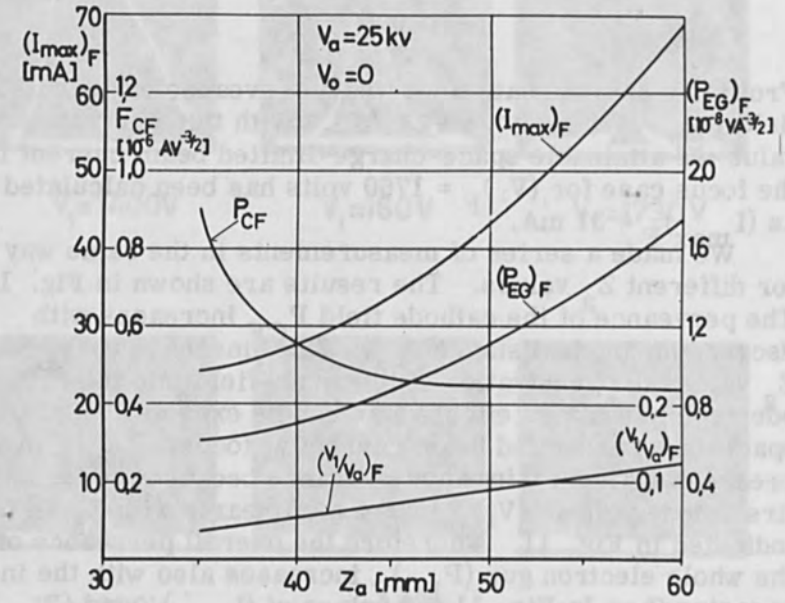

Figure 11. The perveance of the cathode field P_{CF} as a function of Z_a. The maximum space-charge limited emission currents for focus conditions $(I_{max})_F$ and the overall perveance of the electron gun $(P_{EG})_F$ calculated from P_{CF} for an anode voltage of 25 kv are also plotted. Other data as in Fig. 9.

real crossover in the focusing-plane. However it must be mentioned that for Z_a = 60 mm the scanning diagram deviates from the Gaussian distribution, which indicates an increasing influence of spherical aberrations of the anode field. The diameter of the beam in the anode region becomes too large.

In the experiments described above the desired high value of $(V_1)_F$ is obtained by enlarging Z_a, which makes it necessary to weaken the refractive power of the anode field so that V_1 has to be raised. But we can keep Z_a constant and decrease the diameter d_1' which makes the refractive power of the anode field stronger. To get the crossover image in the same focusing-plane, we must now increase again the first anode voltage V_1. In the experiments we are now going to describe we followed this way. We changed not only d_1' in these experiments, but we used different cathode diameters d_c and also we decreased the aperture diameter of the first anode d_1. The best data of the electron geometry we find from many experiments are listed in Table II. In Table II a new quantity ΔZ_c is introduced, which is not included in Fig. 1 so far. This quantity gives a small displacement of the emission surface against the position given in Fig. 1. Because in these experiments Z_o is set equal to zero as before (that means a plane Welnelt-electrode) the meaning of ΔZ_c with a negative sign is the displacement of the emission surface by the amount mentioned behind the front surface of the Welnelt-electrode. These displacements are given for cathode positions at room temperature. When the cathode is heated it expands by a certain amount as a function of the cathode temperature, for example for T_c = 3000°K and d_c = 1 mm this temperature-influenced displacement is about 0.3 mm; that means that for ΔZ_c = 0.3 mm the emission surface lies at this temperature at the same level as the front surface of the Welnelt-electrode. The focusing character is strongly influenced by ΔZ_c.

Table II. Examples For Empirically Found Optimum Dimensions Of The Tetrode Telefocus Electron Gun For High Beam Currents (All Dimensions In mm)

d_c	Z_c	d_o	Z_o	d_1	Z_1	d_1''	z_1''	d_a	Z_a
1	-0.3	1.5	0	2.0	0.6	14	25	10	34
1.5	-0.35	2.0	0	2.5	0.6	16	25	10	34
2	-0.35	2.5	0	3.0	0.6	18	25	10	34
	(1)	(2)		(3)	(4)	(5)	(6)	(7)	(8)

(1) optimalised
(2) smallest value for fool-proof operation of the cathode
(3) smallest value to eliminate current to the first anode
(4) a comprised smallest value to avoid electrical break down
(5) this dimension influences the focal length of the immersion lens
(6) given by overall dimensions of the gun
(7) kept constant, but large enough for the beam to pass unaffected
(8) given by overall dimensions of the gun

In the following investigations we measured the current density distribution in a focusing-plane at $Z_F = 410$ mm. The anode voltage was again set at 20 kv and the Welnelt-voltage is this time chosen as -500 volts, i. e. $V_o/V_1 = -0.025$. The measurements in function of the emission current were made with the geometry parameters given in Table II, i. e. the cathode temperature was varied. The same measuring method of current density distribution is applied as before. The narrowest scanning diagram is considered to belong to the exact focusing condition. Figure 12 shows the focusing voltages of the first anode $(V_1)_F$ thus determined as a function of the emission current. We see from this graph that very high beam currents can be focused at a distance of $Z_F = 410$ mm; in the case of

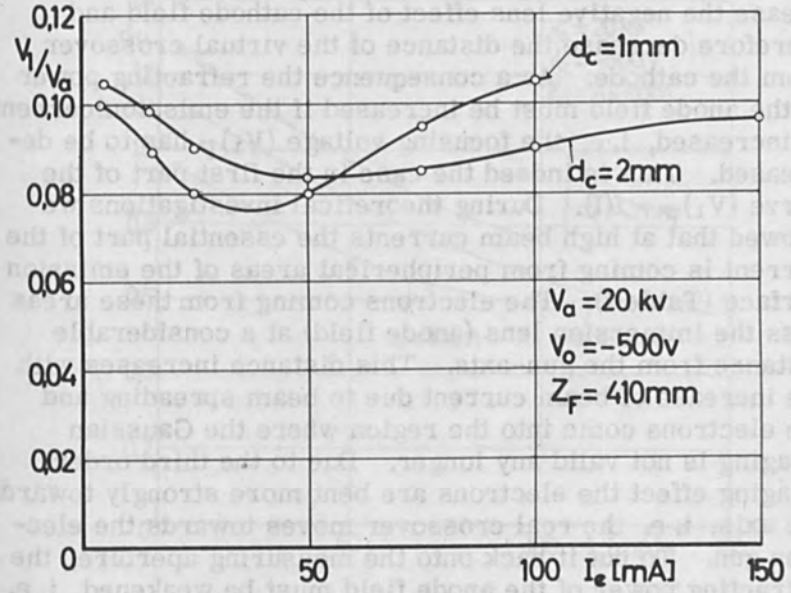

Figure 12. Focusing voltage of the first anode $(V_1)_F$ in function of the emission current I_e for Z_F = 410 mm and two cathode diameters d_e = 1 mm and d_e = 2 mm. Dimensions of the electrode geometry are given in Table II.

1 mm-cathodes about 100 mA and in the case of 2 mm-cathodes more than 150 mA. Furthermore we see that the focusing voltage $(V_1)_F$ is dependent from the emission current I_e. We cannot give a satisfactory interpretation for the form of this dependence $(V_1)_F = f(I_e)$ without considering the spherical aberration of the electron gun. The displacement of the emission surface with increasing temperature and the influence of the beam space-charge on the electron paths cause effects with the same sign, they increase the negative lens effect of the cathode field and therefore decrease the distance of the virtual crossover from the cathode. As a consequence the refracting power of the anode field must be increased if the emission current is increased, i. e. the focusing voltage $(V_1)_F$ has to be decreased. This is indeed the case in the first part of the curve $(V_1)_F = f(I)$. During theoretical investigations we showed that at high beam currents the essential part of the current is coming from peripherical areas of the emission surface (Table I). The electrons coming from these areas pass the immersion lens (anode field) at a considerable distance from the gun-axis. This distance increases with the increase of beam current due to beam spreading and the electrons come into the region where the Gaussian imaging is not valid any longer. Due to the third order imaging effect the electrons are bent more strongly towards the axis, i. e. the real crossover moves towards the electron gun. To put it back onto the measuring aperture, the refracting power of the anode field must be weakened, i. e. V_1 must be increased. This is the case for beam currents greater than about 50 mA. We see that the electron gun has strong spherical aberrations at very high beam currents, which also disturb the Gaussian form of the current density distribution in the crossover. Figure 13 shows the half height widths d_1/d_2 of the current density distribution in the focus point in function of I_e; again under the assumption of the Gaussian form of the scanning diagrams. The full curves refer to measurements from scanning the beam over the slot aperture. For the 2mm-cathode we took scanning diagrams also through a circular aperture of 0. 5 mm diameter. Although the diameter of this circular aperture has about the same diameter as the measured half height widths it is possible to evaluate such diagrams as will be

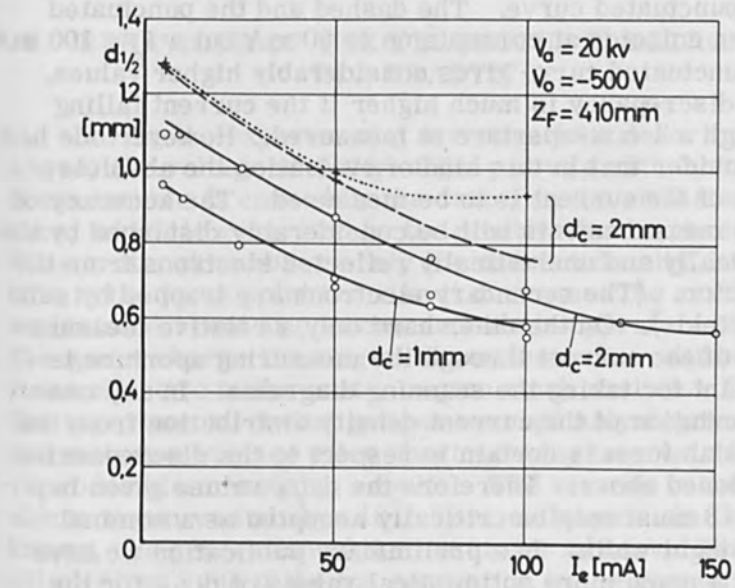

Figure 13. Half height widths of the scanning diagrams of current density distribution in the focus plane $d_{1/2}$ as function of the emission current I_e for Z_F = 410 mm and two cathode diameters d_c = 1mm and d_c = 2 mm. Dimensions of the electrode geometry are given in Table II. The full curve represents the measurements with a slot aperture (S = 40 μ), the dashed curve the measurements with a circular aperture of 0.5 mm diameter and the punctuated curve is calculated from the maximum beam current through the 0.5 mm - aperture assuming Gaussian distribution.

seen in another paper. This evaluation is also represented in Fig. 13. We can notice that the half height widths evaluated in this manner are a little higher than the values determined from the measurements with the slot aperture. We also calculated the half height widths from the maximum current through the 0.5 mm-aperture, assuming a Gaussian form of the current density distribution in the crossover. The results of these calculations are also given in Fig. 13 as a punctuated curve. The dashed and the punctuated curves coincide at currents up to 50 mA but a I_e = 100 mA the punctuated curve gives considerably higher values. This discrepancy is much higher if the current falling through a 1 mm-aperture is measured. However one has to consider that in this kind of evaluation the absolute value of the current is to be measured. The accuracy of these measurements will be considerably disturbed by the elastically and unelastically reflected electrons from the collector. (The secondary electrons are trapped by suitable fields). On the other hand only a relative measurement of the current through the measuring aperture is relevant for taking the scanning diagrams. In any case the deviation of the current density distribution from the Gaussian form is certain in respect to the discrepancies mentioned above. Therefore the $d_{1/2}$ values given in Fig. 13 must only be critically accepted as a nominal half height width. In a preliminary publication we have given a much more optimistical values of $d_{1/2}$ for the same reason. [13] In a later control measurement we found that, due to the spherical aberrations, a ring region with considerable current density appears besides the central current density maximum and rather far away from it. That means that a considerable part of the beam current was not contained in the central maximum which we had accepted as crossover. The deviations from the Gaussian form of the current density distribution in the focal plane is a consequence of the spherical aberrations of the electron gun, for which perhaps the potential distribution just in front of the emission area (including space-charge) is chiefly responsible. The anode field will also make a certain contribution.

The overall progress of the curve $d_{1/2} = f(I_e)$ in Fig. 13, i. e. the monotonous decrease of $d_{1/2}$ -values with

increasing I_e, can be interpreted in such a way that with increasing I_e the aperture of electron beam α_F increases also as a result of the space-charge field in front of the cathode. As is well known, "$\alpha_F \; d_1/_2$" is theoretically a system invariant for an aberration-free electron gun, therefore $d_1/_2$ must continuously decrease. The measurement of the angle distribution of the beam current confirm this interpretation.

6. BEHAVIOUR OF THE TELEFOCUS ELECTRON GUN IN A PRACTICE

During the experimental investigations described above, the voltage stability of the gun was satisfactory. Some trouble is caused by the crater in the emission surface, which is generated by the positive ion bombardement. This crater disturbs not only the current density distribution in the focus point but also it decreases the available emission current at constant cathode temperature because the space-charge limiting of the emission current begins to be effective in the crater region much earlier. During the experimental investigations we regularly regrinded the emission surface after short working intervals to get reproducible measuring results. The vacuum in the electron gun was always 10^{-5} Torr or lower. As is well known, the generation of the ion crater is unavoidable in all electron guns if the ion separation in the acceleration field according to E. B. Bas is not applied. [14] But the realisation of a telefocus tetrode gun with ion separation is a very difficult task. We tried to eliminate the positive ions coming from the field-free region of the electron beam into the electron gun by placing a positively charged aperture-electrode just after the main anode. In such an arrangement proposed by Field, Spangenberg and Holm [15] the positive potential barrier caused by the additional electrode should stop the movement of the positive ions towards the electron gun. But in our experiments we achieved now success in lowering the growing rate of the ion crater.

The satisfactory voltage stability of the electron gun vanished however, when we tried to use the new gun for

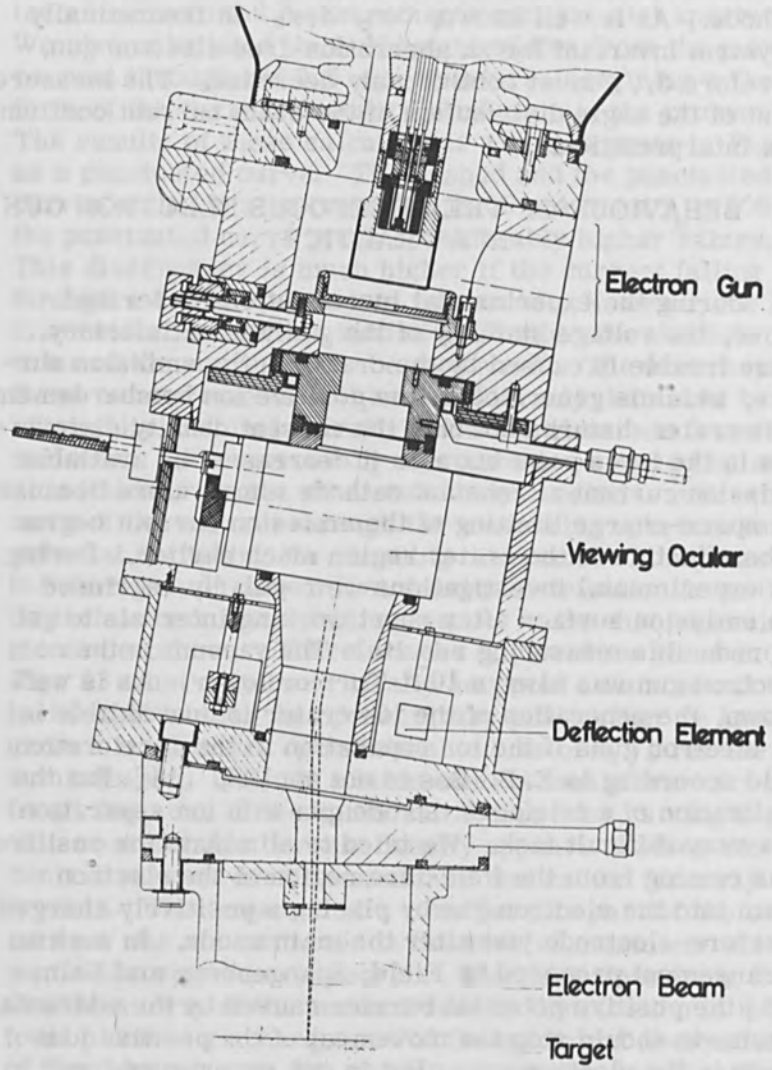

Figure 14. Design principles of the telefocus electron gun for welding experiments.

electron beam welding. As soon as the target began to melt in the welding point we got strong discharges in the gun. First when we bent the electron beam by an angle of 8 degrees at a distance of about 240 mm from the cathode, using a magnetic deflection field, and when we introduced an aperture 70 mm above the target so that metal vapour could not get into the electron gun, we were able to accomplish the electron beam welding without trouble. This arrangement of the electron gun in electron beam welding experiments is shown in Fig. 14. A course estimation of the deflection astigmatism of our deflection system according to W. Glaser [16] gives that the value of the axis of the eliptical distortion of a point beam focus must be $2a = 1.4$ mm and $2b = 0.2$ mm. This is a strong distortion of the focus. Unfortunately, the main axis 2 a falls in our experiments perpandicularly to the weld joint for design reasons. The width to depth ratio of the weld turned out to be unsatisfactory, as can be seen in the weld photograph in Fig. 15. By the elimination of deflection astigmatism using a stigmator or a corrected deflection field one could surely get better results. But this complicated electron beam system would reduce the big advantage of simplicity of the telefocus electron gun.

One important advantage of the tetrode telefocus gun should not be left unmentioned. The tetrode system allows a convenient pulsed operation, because only the low first anode voltage is to be pulsed; moreover it is not necessary to lower this voltage to the cathode voltage if a negative Welnelt-voltage is used.

The described telefocus gun must be of some interest for use in evaporation techniques. Such a tetrode telefocus gun has been used for evaporation by R. E. Thun already in 1960 [8]. But his experience was not satisfactory because he used a hairpin cathode and was able to obtain only a beam current of about 1 mA at 40 kv anode voltage. The simplicity of our high-current telefocus gun is especially of advantage if the gun is used in UHV-Systems. The construction of such a gun for evaporation purposes in UHV-region is planned in our laboratory.

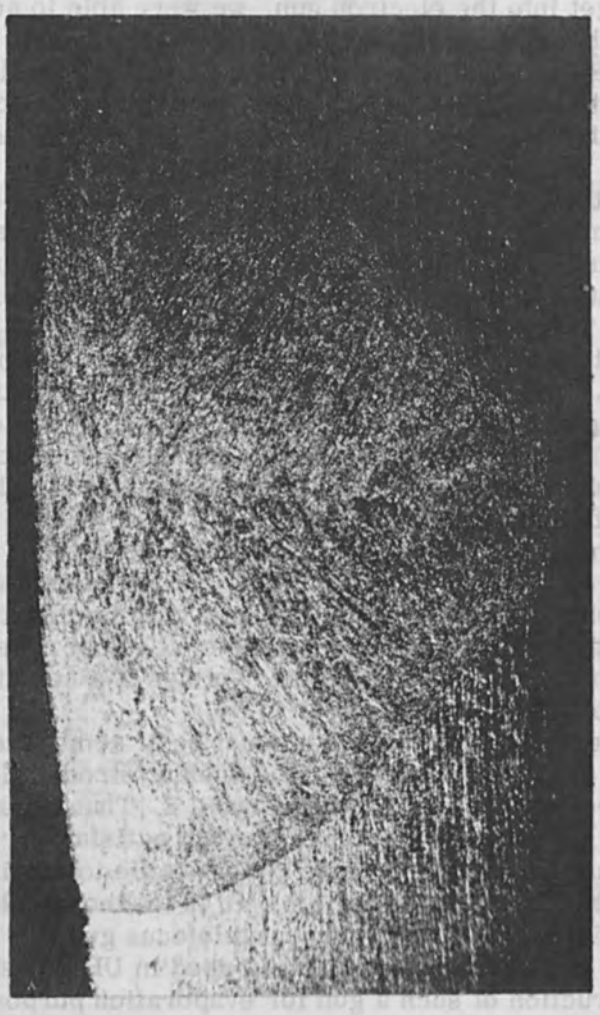

Figure 15. Result of a welding experiment with the telefocus electron gun with bent electron beam: Stainless stell 304, 5 mm thick, 20 kv, ca. 100 mA.

7. CONCLUSIONS

From the reviewed investigations we can conclude that a telefocus electron gun of tetrode type can be realised, which can focus high current beams at large distances from the cathode. At not too large distances (say Z_F = 150 to 250 mm) and not to high beam currents (say 50 mA at 20 kv) it is possible to achieve half height widths of the current density distribution in the focusing plane of only a few tenths of millimeters. At larger distances and higher beam currents the spherical aberrations begin to influence the focusing characteristics. Most critical in this connection is the potential distribution just in front of the cathode. An improvement of the results reported in this paper seems to be possible.

This work was supported partly by the Swiss Federal Research Commission and partly by the Firm Balzers AG für Hochvakuumtechnik und Dünne Schichten, Balzers (Principality of Lichtenstein) to whom our grateful thanks go for their generous help. The authors thank also Dr. L. Preuss and Mr. H. Merch for their help in theoretical calculations and Messrs. A. Meier and A. Jordi for the assistance at practical work. Not least our thanks go to Mr. J. B. Ansermoz for his assistance in translating this paper into English.

REFERENCES

1. K. H. Steigerwald, Optik 5, 469, (1949)
2. F. W. Braucks, Optik 15, 242, (1958)
3. E. B. Bas and F. Gaydou, Z. F. Angwdt. Phys. 11, 370, (1959)
4. E. B. Bas, Z. F. Angwdt. Phys. 7, 337, (1955)
5. E. B. Bas and F. Gaydou, Proc. First Intern. Conf. Vacuum Soc. and Tech. (Namure 1958) Pergamon Press; Vol. II, p 683
6. B. B. Wiedmer, Dipl. Arb. ETH, Zürich (1961)
7. F. W. Braucks, Optik 16, 304, (1959)
8. R. E. Thun, Proc. Second Symposum on Electron Beam Technology R. Bakish Ed (Boston 1960) p 70.
9. J. R. Pierce, J. Appl. Phys. 11, 548, (1940)

10. L. Preuss and E. B. Bas, ZAMP 17, 168 (1965).
11. L. Preuss, Zur Praxis der theoretischen Elektronenoptik; Diss. Nr. 3322, Eidg. Techn. Hochschule, Zurich (1963).
12. E. B. Bas and G. Cremosnik, Proc. First Intern. Conf. on Electron and Ion Beam Science and Technology (R. Bakish, Ed), John Wiley & Sons, N. Y. p. 109 (1965).
13. G. Cremosnik, R. N. Thomas and E. B. Bas, ZAMP 15, 320 (1964).
14. E. B. Bas, Optik 12, 377 (1955).
15. M. Field, K. Spangenberg, R. Holm, Electr. Comm. 24, 108 (1947).
16. W. Glaser, Z. f. Phys. 111, 357 (1938).

The Design of High Power Electron Beams for Welding

P. A. Einstein and R. Beadle

Vickers Research Establishment
Ascot, England

Evidence is not yet entirely convincing whether the desirable criterion in electron beam welding is power density (W/d^2) power per unit root spot diameter ($W/d^{1/2}$) or some intermediate function. [1] However, what is clear is that if deeper or faster welding is to be achieved effort must be directed towards high power density at greater powers. The present article considers the feasibility of doing this. Design predictions for an electron beam system of intermediate power (150 kV 10 kW) have been fairly well substantiated in the practical realization of this system in an electron beam welder. A design for a 200 kV - 140 kW system is outlined.

BEAM SYSTEM

The essential components of the beam system are, (a) the source of electrons, i. e. the electron gun, and (b) the focusing lens which concentrates the electrons on to a small region of the target. The gun may also produce some form of lens action (usually much weaker than the main lens, and not deliberate); this lens is associated with the anode aperture or may result from the configuration of the field in the cathode region when bias is applied to the Wehnelt shield electrode.

Limitations to the attainment of high power density at the target can arise in the gun or in the portion of

the beam beyond the main focusing lens. Limitations in the gun are the well known ones of emission i. e. the gun can be "space charge" or "temperature" limited. In the former case emission current drawn from the cathode is governed by the field in front of the cathode, in the latter by the cathode temperature. If the field is adequate to "strip" the required emission current from the cathode then temperature is the limitation and the value chosen is set by practical considerations of cathode material erosion and evaporation rates. Limitations in the beam system beyond the main lens can be considered to result from three main causes.

i. As a result of the spread in emission velocity and direction at the cathode of the emitted electrons, it is not possible to focus the electrons into a point and thereby achieve infinite power density. This is fundamental and well known, and has been discussed in many aspects and particularly in Langmuir's paper 1937 [2]. This is the "thermal velocity limitation".

ii. Mutual electron repulsion or space charge spreading is the second bar to the attainment of high power density - even if the thermal velocity spread effect were absent. Space charge spreading becomes very significant at the target at higher beam currents.

iii. The spherical aberration of the focusing lens, and to a much lesser extent the anode aperture lens, is the third factor which increases spot size and curtails spot power density. Though not a fundamental limitation, it cannot be avoided when using practical lenses of convenient design giving useful focal lengths.

These three limitations will be considered in more detail below. Under given conditions of operation one or other usually predominates. The overall spot size is here taken to be the result of the sum (arithmetic) of the three separate effects. * This gives the most pessimistic prediction.

*See Wells [3].

GUN

The basic requirements for the gun are fairly simple. A three electrode system is chosen to produce an initially cylindrical or diverging (conical) beam from a circular cathode. The shape of the cathode, Wehnelt electrode and anode to give such a beam profile can be established using well known design procedures laid down by Pierce [4] and Spangenberg [5] among others. The starting point for the calculations assumes a tolerable emission current density from the cathode (say 1 or 2 amp/cm^2) and this then fixes the cathode diameter to yield a required total current. Figure 1 shows the basic outline of this arrangement for a beam (a) initially parallel or (b) divergent, from the cathode. Thus the effect of the anode aperture lens whose focal length is approximately 4d (where d = anode cathode spacing) is to diverge the beam. The main lens images plane A onto the Target T at a throw distance z. It should be noted that z is not the focal length of the main lens nor is plane T an image of the cathode, but of plane A. Ideally the power density at T would be infinite.

LIMITATION BY THERMAL VELOCITIES AT THE TARGET

Figure 2 shows the conditions which exist at the spot minimum at the target when considering thermal velocity spread. A spot of finite minimum dimension $\delta_T = 2r_T$ only can be attained.

Applying the well known Langmuir relation giving the maximum current density at the image in terms of that at the source we have (Fig. 2)

$$\rho_T \text{ (at target)} = \rho_c \left\{\frac{V}{kT} + 1\right\} \sin^2 \gamma \qquad (1)$$

(V & kT in volts)

Hence

$$\frac{r_T}{r_c} = \sqrt{\frac{\rho_c}{\rho_T}} \approx \sqrt{\frac{kT}{V}} / \sin\gamma = \sqrt{\frac{kT}{V}} \frac{Z}{r_i}$$

or

$$\delta_T = 2\, r_T = \frac{2\, r_c}{r_i} \; Z \; \sqrt{\frac{kT}{V}} \qquad (2)$$

The same result can be obtained by an alternative approach as follows:

The mean semi-angular spread of emitted electrons at the cathode is $\alpha = \sqrt{kt/V}$ the electrons appear to emanate from a virtual cathode image (I) at a distance 2d to the left of the anode. The anode lens focal length as stated is approximately $f^1 = 4d$ giving a virtual cathode image (II) of height $(r_c{}^1)$ at 1.3d to the left of the anode with a semi-angular spread of $\alpha^1 = {}^3/_2\ \alpha$. The radius of the beam in the main lens is

$$r_i = u'p' = \frac{u'\, r_c}{4d} = \left(\frac{u + 4d}{4d}\right) r_c$$

We have (Fig. 2)

$$\delta_T = 2\,(v - Z)\,\gamma'' \qquad (3)$$

$$f = \frac{u'z}{u'+z} \qquad (4)$$

$$\gamma'' \quad \frac{\alpha u''}{v} = \frac{3}{2}\ \alpha\ \frac{u''}{v} \qquad (5)$$

$$v = u''f/(u'' - f) \qquad (6)$$

By rearranging these equations, it follows that: -

$$\delta_T = 2\alpha Z\ \frac{r_c}{r_i} = 2\sqrt{\frac{kT}{V}}\ Z\ \frac{r_c}{r_i} \qquad (7)$$

yielding the minimum spot as limited by thermal velocities in terms of throw distance.

LIMITATIONS BY SPACE CHARGE SPREADING AT THE TARGET

The effect of mutual repulsion of electrons in spreading of the beam minimum has often been considered [6]. The condition varies with increasing current from the ideal case at zero current (e. g. Fig. 1(a)) to that of Fig. 3 with large current content I where no electron crosses the system axis. The spot minimum diameter at the target ($2r_S$) is actually somewhat greater than the beam minimum. A convenient nomograph chart giving r_S for most practical conditions has been constructed by Holloway [7] based on the formula

$$r_S = 1/2\ \delta_S = 5.9 \times 10^{4}\ Z^{5/2} I^{5/4} V^{-15/8} r_i^{-3/2} \qquad (8)$$

SPHERICAL ABERRATION

Spherical aberration results in the marginal rays crossing the axis at a different position to the paraxial rays. This causes an ideal point image to be confused into a disc whose minimum diameter (located some way between marginal and paraxial crossing position of the rays (Fig. 4)) is given by

$$\delta_{S.\,A.\,min} = 2r_{S.\,A.\,min} = 1/2\ C_S \gamma^{3} \left(\frac{z^4}{f^4}\right) \text{[8-10]} \qquad (9)$$

where C_S is the spherical aberration constant of the lens
γ is the convergence angle of the electrons = ri/z
z the throw distance
f the focal length of the lens = $u^1 z/u^1 + z$ (Fig. 2)
and u^1 is "object distance" from plane A to lens. The spherical aberration constant in turn is given approximately by

$$c_S \simeq \frac{5f^3}{(S + D)^2} \quad [8] \qquad (10)$$

Where S and D are the lens pole piece separation and bore diameter respectively in the case of a magnetic lens.

Thus C_S can be minimized by making S + D large, the limit being set by the requirement for the lens focal length: $- f_{min.} = .5\ (S + D)$. This means that if short throw distances and thus short focal lengths are required then S + D must also be small.

Combining (9) and (10) and rearranging we obtain

$$\delta_{S.\,A.\,min} = 2.5\, r_i \frac{Z}{f(S+D)} = 2.5 r_i^3 \left\{\frac{u' + Z}{u'}\right\} \frac{1}{(S+D)} \tag{11}$$

Thus obtaining the spherical aberration in terms of r_i and z.

PRACTICAL BEAM DESIGN

The aim here is to minimize excessive contribution from any of the three above causes. Initially the lens design should be chosen such that S + D is as large as possible, but consistent with the requirement for the focal length

$$f = 0.5\ (S + D)$$

Thus in general the maximum value of S + D is of the order of the shortest throw distance.

Increasing r_i will decrease the space charge contribution but increase the spherical aberration contribution. These two should be equated at the longest throw distance to fix the optimum r_i. This now allows the determination of r_c from equation (2). Such that r_T does not vastly exceed r_S and $r_{S.\,A.}$ and at the same time be consistent with a reasonable value of cathode emission current density.

Attainable spot diameters and power densities have been calculated for a 150 kV system for a Pierce-type gun ($r_c = .15$ cm) for several anode-lens distances (u) and lens-target ("throw") distances (z). Variation of u has the effect of increasing the radius of the beam in the

lens (r_i) which reduces space charge spreading while increasing spherical aberration. The three effects (thermal, spherical and space charge) have been calculated separately and added to yield an overall spot size $\delta = \delta_T + \delta_s + \delta_{s.A.min}$ for several values of beam current. Figure 5 is a plot of these calculations. It is seen that for short throw distances z spot sizes are much smaller chiefly because space charge effect is small; by increasing u, that is r_i, the space charge can be reduced for the longer throw distances in the region of 25-50 cm at the expense of the spot size at the short throw distance. Of course u need not be increased physically to do this; the effect can be equally achieved by increasing the initial beam divergence by altering bias or shaping the cathode profile to lead to conditions as in Fig. 1(b). Likewise a weak auxiliary lens close to the anode would achieve the same effect and allow control of r_i.

In a working gun the equivalent u was confirmed from beam profile measurements to be around 40 cm with an r_i of .45 cm. Consequently spot size δ and power density = $4W/\pi\delta^2$ versus throw distance have been plotted for these values of u and r_i for 150 kV, 125 kV and 100 kV and beam currents of 70 mA and 30 mA (Fig. 6). Subsequent measurements using a cooled slit arrangement over which the beam was scanned revealed spot sizes in good agreement with these calculations. These experimental results are superimposed on Fig. 6 for comparison.

HIGH POWER BEAMS

It is seen that agreement with the measured values of spot size at 150 kV 70 mA, is good. Following this work, guns operating at 150-200 kV 700 mA have been examined theoretically. To achieve the high current emission the cathode size was considered increased by a factor of three giving a 10 times current increase for approximately the same specific cathode emission. Overall spot sizes and power densities were derived for throw distances up to 50 cms from the lens. Results have been plotted (Fig. 7) for beam currents of 300 and 700 mA and compared to those of the low power gun (30 mA, 70 mA). The chosen cathode radii are .45 and .15 cms and the beam radii in

the lens 1.35 and .45 cms respectively. S + D values are taken 16 cm and 8 cm. Power density can certainly be markedly increased at the higher currents particularly when also raising the voltage, or when working at short throw distances (below 20 cm). If power per unit spot width is the welding criterion then the improvement at the higher powers would be even more marked. On the other hand at long throw distances (around z = 50 cm) space charge spreading negates any gain due to increase in power, and power density falls very rapidly. As an example it should be possible to achieve a power density of 80 MW/cm^2 in a .05 cm diameter spot at 200 kV 700 mA 140 kW, or 60 MW/cm^2 in a .05 cm diameter spot at 150 kV 700 mA 100 kW at a throw distance of z = 20 cm. On the basis of linear dependence of weld depth on beam current the latter should lead to welds of some 25 cm depth in stainless steel at speeds of 0.5 cm/sec. Calculations are at present in hand to attempt to set down a more exact relationship between power, spot size, speed and weld depth on lines laid down by Hablanian [1].

PRACTICAL GUN DESIGN

In general, and certainly in the design examples quoted, the power density performance may be significantly improved by operating at higher values of specific cathode emission.

A study of Fig. 8 indicates that at pressures of 10^{-4} to 10^{-5} torr, the loss of cathode material by erosion occurs at about the same rate as that by evaporation when operating at a cathode temperature corresponding to some 5 amps/sq. cm. There is, therefore, little improvement in cathode life to be achieved by reduction of cathode loading below this figure. Above 5 amps/sq. cm. the evaporation loss increases rapidly with correspondingly short cathode lives. This is a particular problem with "hairpin" cathodes where fracture occurs when the reduction of diameter due to evaporation is about 12%.

Much increased cathode life may be obtained, under otherwise the same conditions, if the cathode is indirectly heated.

The low power (150 kV 10 kW) welding gun considered earlier is of the Pierce type and employs indirect heating of a relatively massive tantalum "button" cathode 3 mm dia. giving a conical beam. The button is supported on a shallow Ta cone and irradiated by an auxiliary back bombarding electron gun operating at some 5 kV 100 watts. The shallow Ta cone completely isolates the back-bombarding system from the main electron stream and prevents the leakage of these auxiliary electrons into the welding chamber, as well as providing a well alined and rigid support for the cathode button. The cathode button is surrounded by the Wehnelt control electrode (shield) having a 22° angle to the flat cathode face. This gives the desired beam angle from the cathode under operating bias conditions. The anode is located 5 cm from the button; this distance is about half that required to draw a space charge limited emission current of 70 mA from the cathode at 150 kV.* Conventional lateral anode shift is provided to allow beam tilt alinement. Figure 9 shows the gun in schematic form and Fig. 10 is a photograph of the gun. This photograph shows the anode sleeve in the raised position allowing access to the cathode electrodes. When this sleeve is lowered on to vacuum seals fitted at the top and bottom this closes the gun ready for pumping and normal operation.

ACKNOWLEDGMENT

We wish to thank Dr. C. F. Bareford, Managing Director of Vickers Research Establishment, for permission to publish this contribution.

*The cathode current loading may be increased (and the thermal radius decreased) at any given beam current by increasing the cathode temperature and the bias voltage on the control electrode. It is clear that the design parameters and operating conditions should be so chosen that space change does not become a significant limitation until the largest currents and longest throw distances are reached.

REFERENCES

1. Hablanian, M. H., 5th Symp. Electron Beam Techn. J. Morley, Ed., Boston, Massachusetts, 1963, p. 252.
2. Langmuir, D. B., Proc. IRE, p. 977, August 1937.
3. Wells, O. C., Introduction to Electron Beam Technology, edited R. Bakish (Wiley 1962), p. 354.
4. Pierce, J. R., Theory and Design of Electron Beams, van Nostrand, New York, 1954.
5. Spangenberg, K. R., Vacuum Tubes, McGraw-Hill, New York, 1948.
6. Thompson, B. J. and Headrick, L. B., Proc. IRE, p. 318, July 1940.
7. Hollway, D. L., Electronics, February 16, 1962.
8. Haine, M. E., The Electron Microscope, Spon London, 1961.
9. Liebman, G. and Grad, E. M., Proc. Phys. Soc. 64, p. 956, 1951.
10. Brown, G. and Nichols, G. K., Journ. of Mat. Sci. 1, 1966, p. 96.

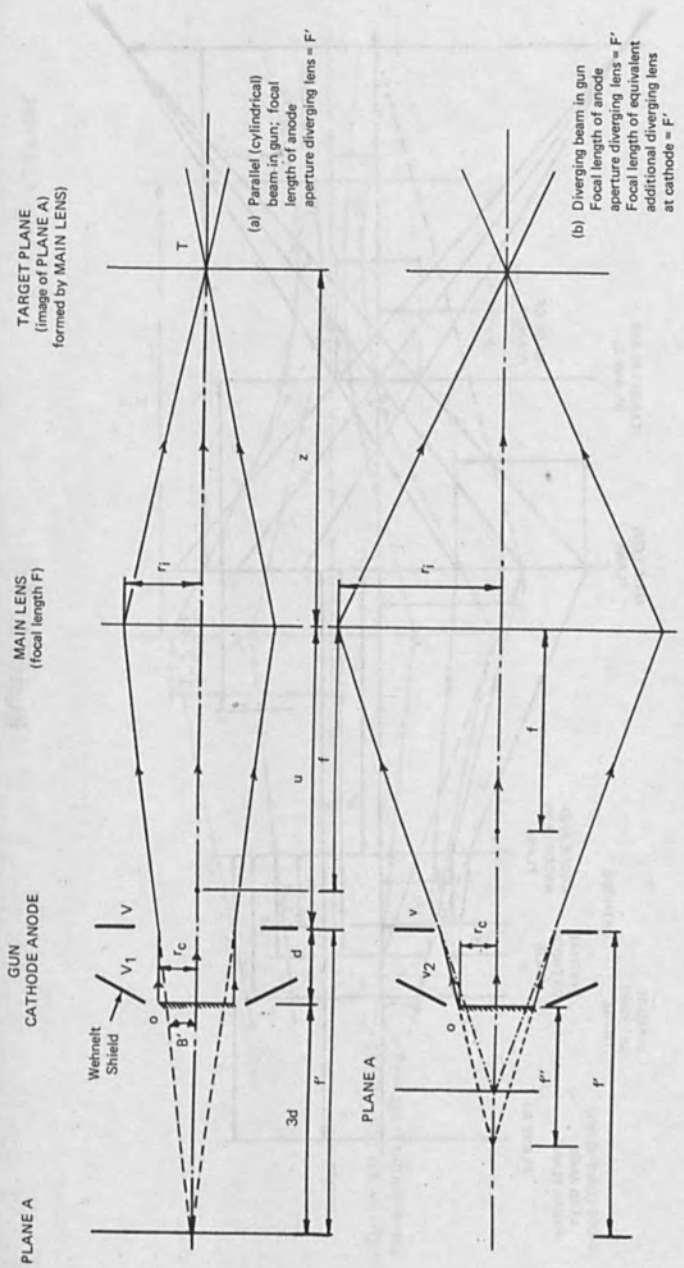
PLANE A
GUN
CATHODE ANODE
MAIN LENS
(focal length F)
TARGET PLANE
(image of PLANE A)
formed by MAIN LENS)
Wehnelt
Shield
V
V1
rc
o
B'
d
3d
f'
u
f
z
T
r1
(a) Parallel (cylindrical) beam in gun; focal length of anode aperture diverging lens = F'
PLANE A
V
V2
rc
o
f''
f'
r1
f
(b) Diverging beam in gun
Focal length of anode aperture diverging lens = F'
Focal length of equivalent additional diverging lens at cathode = F'
ELECTRON BEAM SYSTEMS (IDEAL)

Figure 1.

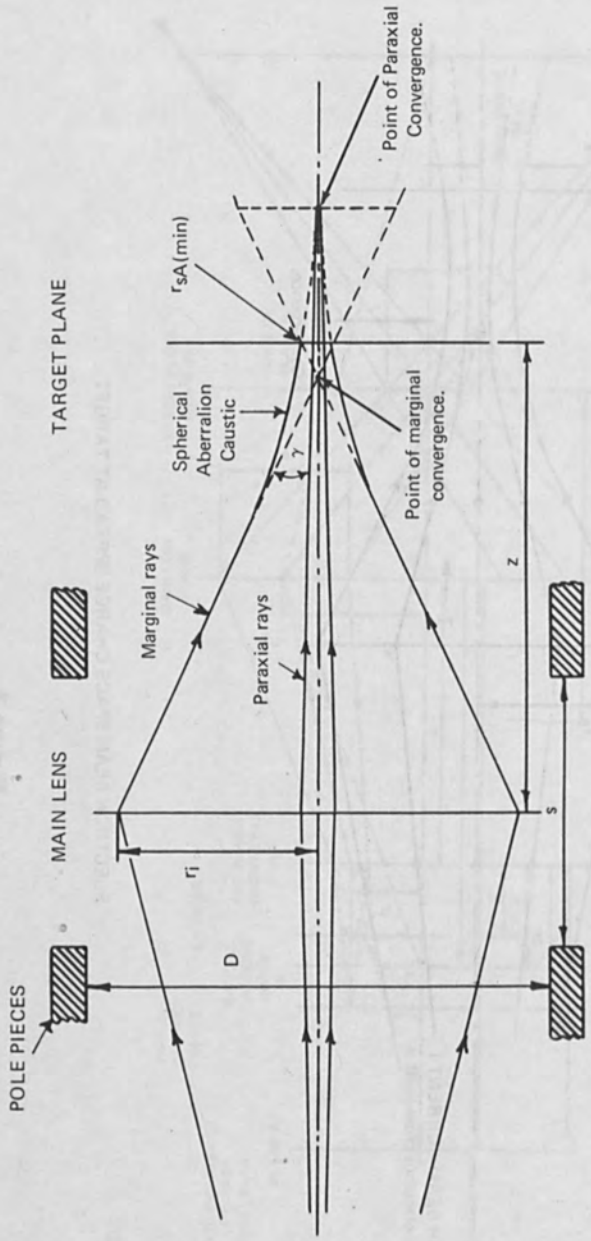

ELECTRON SPOT LIMITED BY LENS SPHERICAL ABERRATION

Figure 4.

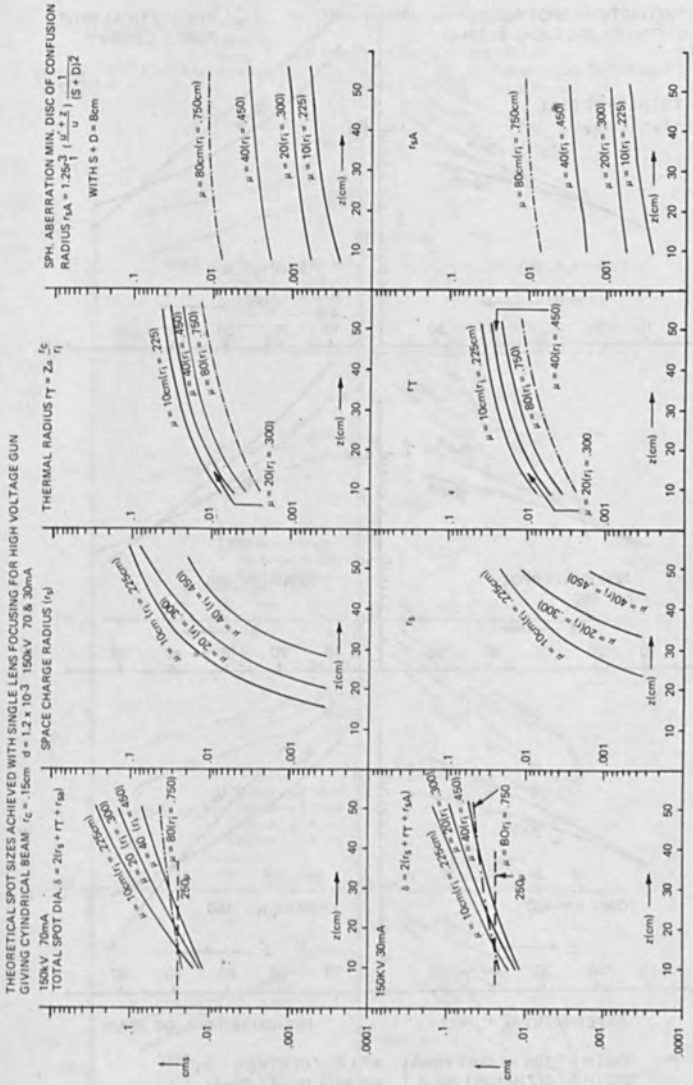
THEORETICAL SPOT SIZES ACHIEVED WITH SINGLE LENS FOCUSING FOR HIGH VOLTAGE GUN
GIVING CYINDRICAL BEAM r_c = .15cm d = 1.2 x 10^-3 150kV 70 & 30mA
150kV 70mA
TOTAL SPOT DIA. δ = 2(r_s + r_T + r_sA)
SPACE CHARGE RADIUS (r_s)
THERMAL RADIUS r_T = Z_a r_c/r_i
SPH. ABERRATION MIN. DISC OF CONFUSION
RADIUS r_sA = 1.25 r_i^3 (μ^2 z/u) 1/(S+D)^2
WITH S + D = 8cm
150kV 30mA
z(cm)
cms

Figure 5.

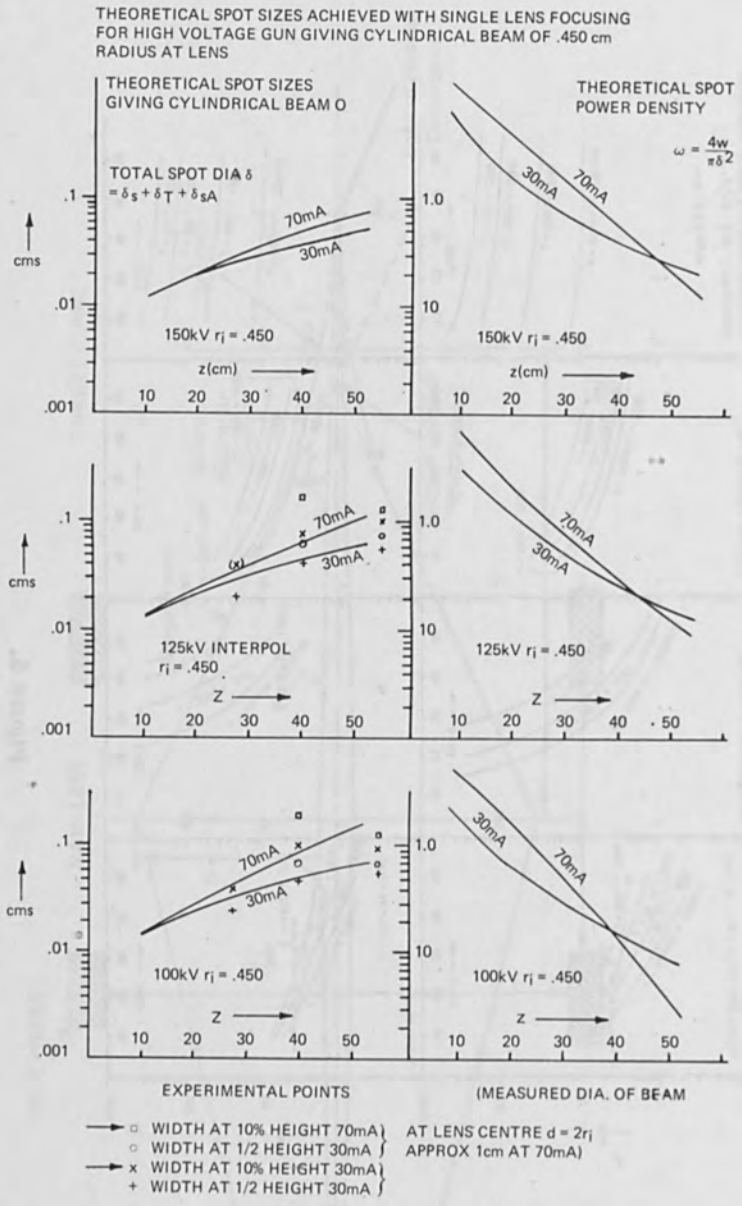
THEORETICAL SPOT SIZES ACHIEVED WITH SINGLE LENS FOCUSING FOR HIGH VOLTAGE GUN GIVING CYLINDRICAL BEAM OF .450 cm RADIUS AT LENS
THEORETICAL SPOT SIZES GIVING CYLINDRICAL BEAM O
TOTAL SPOT DIA δ = δS + δT + δSA
THEORETICAL SPOT POWER DENSITY
ω = 4w/πδ2
cms
.1
.01
.001
1.0
10
70mA
30mA
150kV ri = .450
z(cm)
10 20 30 40 50
125kV INTERPOL ri = .450
125kV ri = .450
100kV ri = .450
Z
EXPERIMENTAL POINTS
(MEASURED DIA. OF BEAM
WIDTH AT 10% HEIGHT 70mA
WIDTH AT 1/2 HEIGHT 30mA
WIDTH AT 10% HEIGHT 30mA
WIDTH AT 1/2 HEIGHT 30mA
AT LENS CENTRE d = 2ri
APPROX 1cm AT 70mA)

Figure 6.

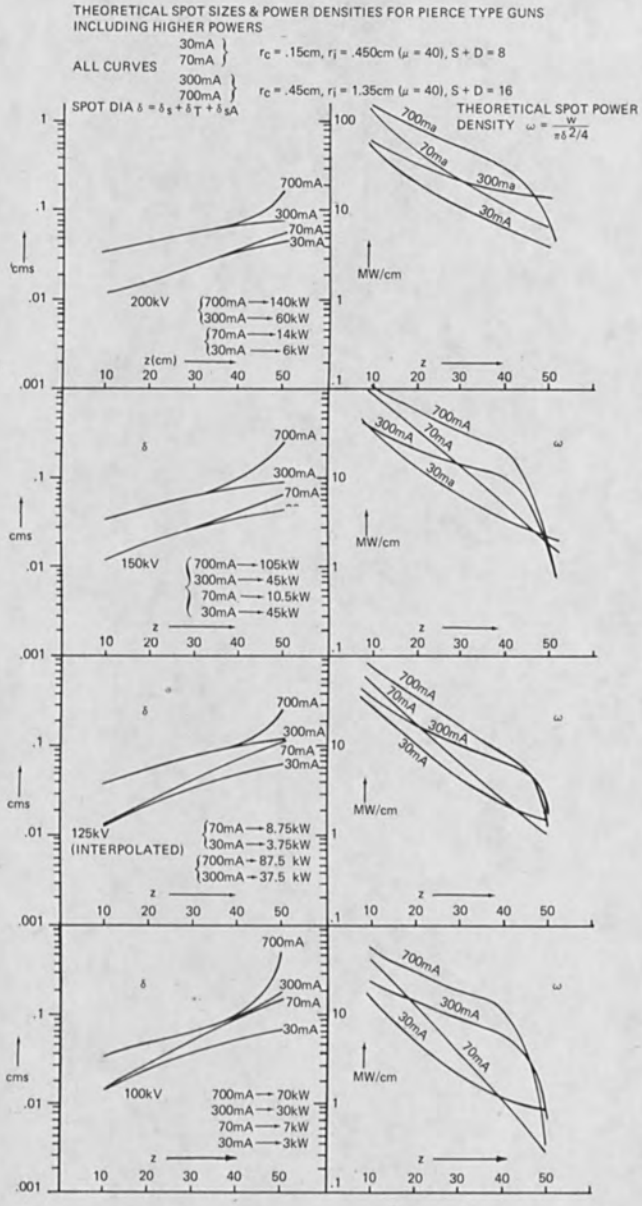
THEORETICAL SPOT SIZES & POWER DENSITIES FOR PIERCE TYPE GUNS
INCLUDING HIGHER POWERS
ALL CURVES
30mA
70mA
rc = .15cm, rj = .450cm (μ = 40), S + D = 8
300mA
700mA
rc = .45cm, rj = 1.35cm (μ = 40), S + D = 16
SPOT DIA δ = δS + δT + δSA
THEORETICAL SPOT POWER DENSITY ω = W/πδ²/4
cms
MW/cm
z(cm)
200kV
700mA → 140kW
300mA → 60kW
70mA → 14kW
30mA → 6kW
150kV
700mA → 105kW
300mA → 45kW
70mA → 10.5kW
30mA → 45kW
125kV
(INTERPOLATED)
70mA → 8.75kW
30mA → 3.75kW
700mA → 87.5 kW
300mA → 37.5 kW
100kV
700mA → 70kW
300mA → 30kW
70mA → 7kW
30mA → 3kW

Figure 7.

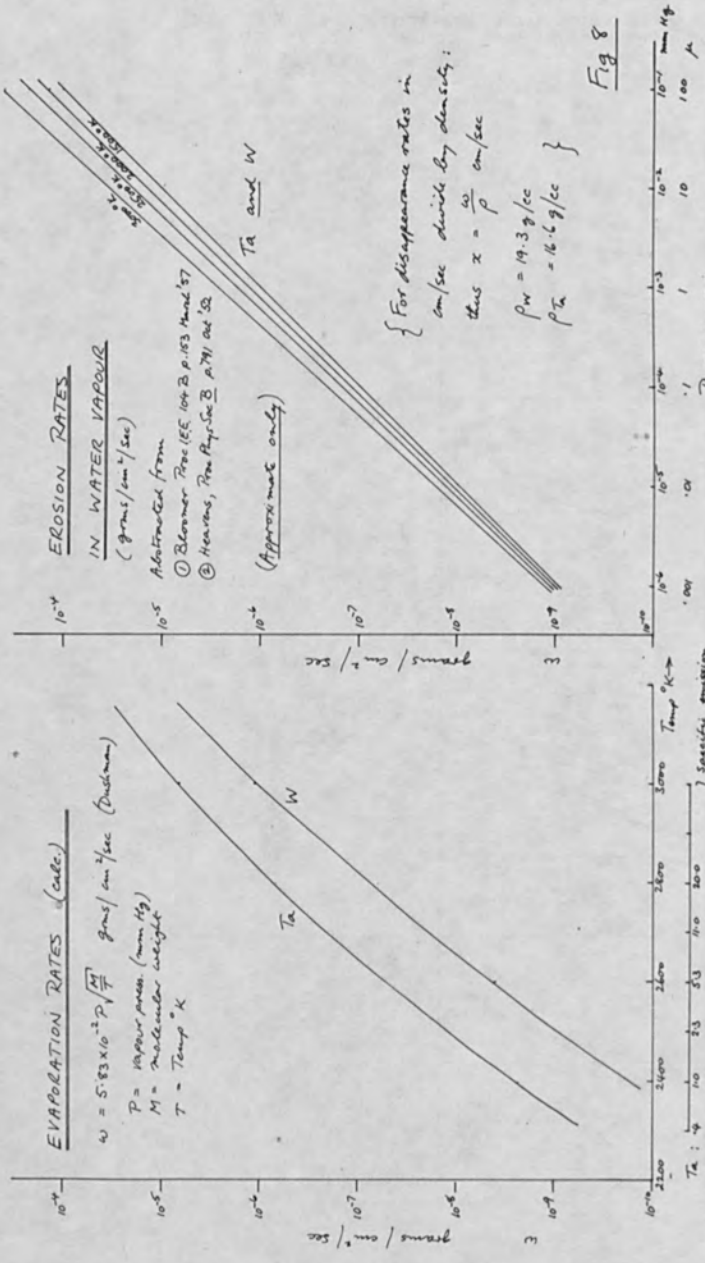
EVAPORATION RATES (calc.)
ω = 5.83×10⁻²P√(M/T) gms/cm²/sec (Dushman)
P = vapour press. (mm Hg)
M = Molecular weight
T = Temp °K
Ta
W
Ta : 4 10 23 53 100
W : 13 3 7 1.7 4 9
Temp °K
Specific emission A/cm²
EROSION RATES
IN WATER VAPOUR
(gms/cm²/sec)
Arbitrarily from
① Bloomer Proc IEE 104 B p.183 March '57
② Hearnd, Phil Physics B p.741 Oct '52
(Approximate only)
Ta and W
{ For disappearance rates in cm/sec divide by density; thus x = ω/ρ cm/sec
ρW = 19.3 g/cc
ρTa = 16.6 g/cc }
Fig 8
Pressure →
mm Hg
μ

Figure 8.

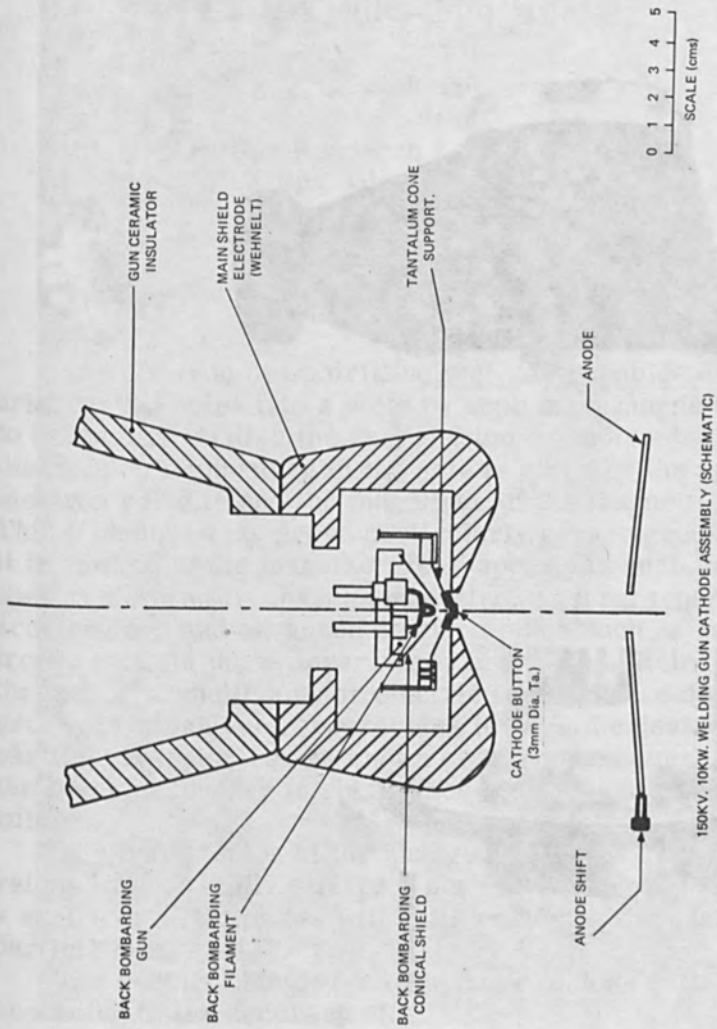
GUN CERAMIC INSULATOR
MAIN SHIELD ELECTRODE (WEHNELT)
TANTALUM CONE SUPPORT.
ANODE
0 1 2 3 4 5
SCALE (cms)
CATHODE BUTTON (3mm Dia. Ta.)
BACK BOMBARDING GUN
BACK BOMBARDING FILAMENT
BACK BOMBARDING CONICAL SHIELD
ANODE SHIFT
150KV. 10KW. WELDING GUN CATHODE ASSEMBLY (SCHEMATIC)

Figure 9.

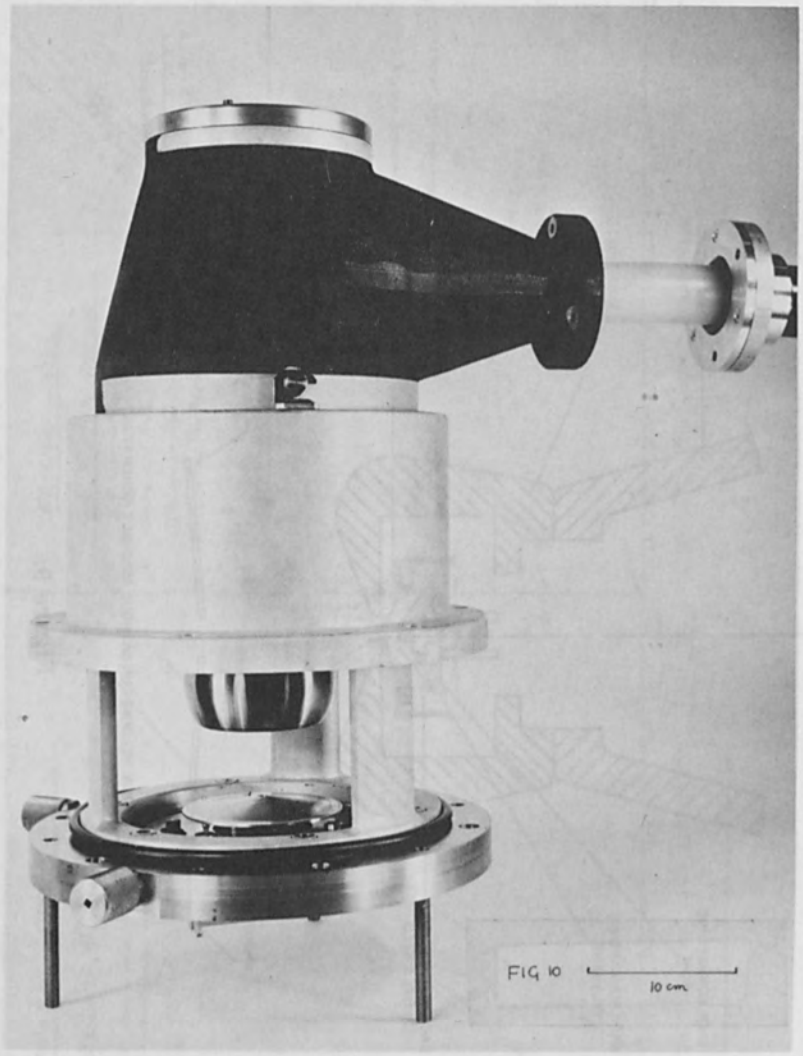

Figure 10.

Electron Beam Drilling of Curved Holes Into Solids

J. G. Siekman

Philips Research Laboratories
N. V. Philips' Gloeilampenfabrieken
Eindhoven, Netherlands

INTRODUCTION

The electron beam drilling technique enables us to drill curved holes into a solid by applying a magnetic field to that solid. Within the range of the experimental error the radius of curvature of the hole is given by the applied electron velocity and the magnitude of the magnetic field. This technique may prove particularly advantageous when it is applied to the manufacture of apparatus such as spectrometers for charged particles, several types of ion accelerator, and advanced electron tubes such as carcinotrons, etc. In these apparatuses charged particles pass through a magnetic and/or electric field. In the design problems which such apparatuses involve the desired particle trajectories are known or oftener assumed and the fields necessary to obtain those paths have to be calculated.

The trajectories of the charged particles have an envelope which usually strikes a series of diaphragms, i. e. a series of metal plates with slits enclosing the charged particle beams.

The results obtained will be more or less satisfactory according to the accuracy of:

1. the approximation method used for field and trajectory calculation.
2. the extent to which the calculated fields are realized, and

3. the mechanical machining and positioning of the diaphragms.

Afterwards corrections must be made and this is very time-consuming. In this electron beam drilling method the magnitude of the electron velocity and the magnitude and direction of the magnetic field selected must be appropriate to the problem. Now the hole or slits automatically envelope exactly the trajectories of the charged particles. This eliminates the need for time-consuming corrections. The method so far described is concerned with beams of charged particles in a magnetic field. In simple cases the method can be extended to electrical fields or to combined fields.

The Magnetic Field

The Lorentz force $\vec{f}$ on a charge q moving in vacuum with velocity $\vec{v}$, in a magnetic field $\vec{B}$ is

$$\vec{f} = q\ [\vec{v} \times \vec{B}\ ] . \qquad (1)$$

Newton's second law of motion in vector form is:

$$\vec{f} = m \cdot \frac{d^2\vec{r}}{dt^2} \qquad (2)$$

where m = mass of the charged particle
$\vec{r}$ = position vector locating the particle.

The force $\vec{f}$ affects only the direction not the magnitude of $\vec{v}$ as $\vec{f}$ is perpendicular to $\vec{v}$.
Substituting (1) for (2) and integrating yields the path-equation.
In our investigations electrons drill a hole in a region where the magnetic field B is considered to be homogeneous. Their velocity vector $\vec{v}$ lies in a plane perpendicular to the field $\vec{B}$. Therefore in vacuum the electrons would describe a circular path with radius of curvature ρ. This motion is given by

$$Bev = \frac{mv^2}{\rho} \qquad (3)$$

in which $m = \dfrac{m_o}{\sqrt{1-\dfrac{v^2}{c^2}}}$

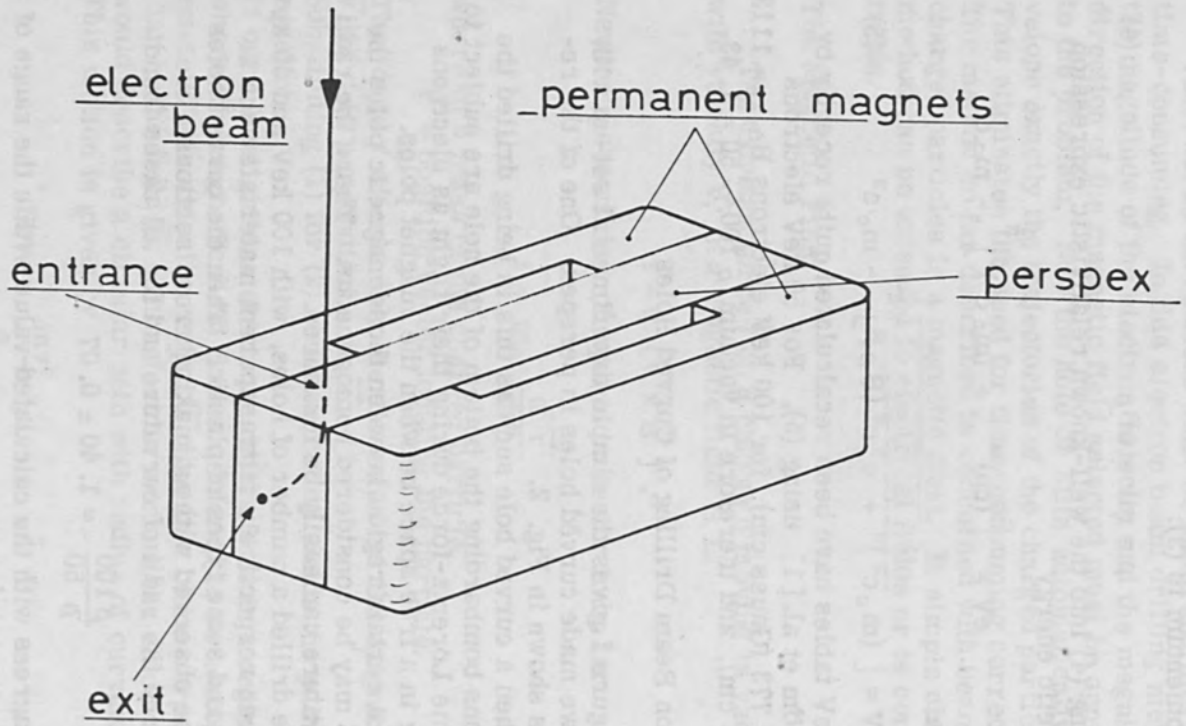

Figure 1. Experimental set-up for the drilling of curved holes.

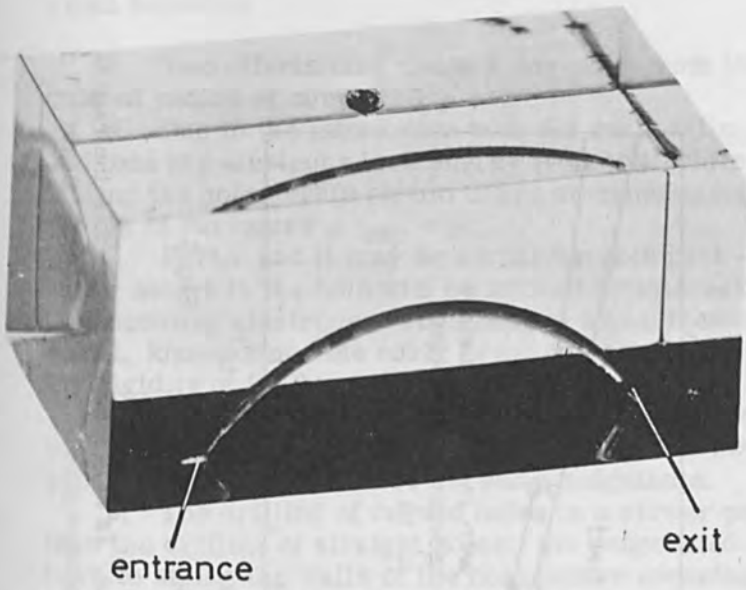

Fig.2

Figure 2. Curved hole drilled in perspex.
Radius of curvature 10.7 mm.
Beam parameters: V = 50 kV
pulse height: I_p = 1.1 mA
pulse length: τ_p = 4/us
repetition freq. ν_p = 5000 c/s

In another series of experiments we found that the entrance and exit of the electron beam did not depend on the material put between the magnets.

In this series of experiments we placed the magnets about 2 mm apart. The entrances of the beam were marked by scratches on the magnetic poles; the exit was found as a hole drilled in a copper plate mounted on the end of the pair of magnetic poles. The electron energy was 100 keV and $\rho \sim 5$ mm. The first experiment was done without filling the gap at all. The following experiments were done with a quartz plate, an aluminum plate, a copper plate and a nickel plate placed in the gap in that order.

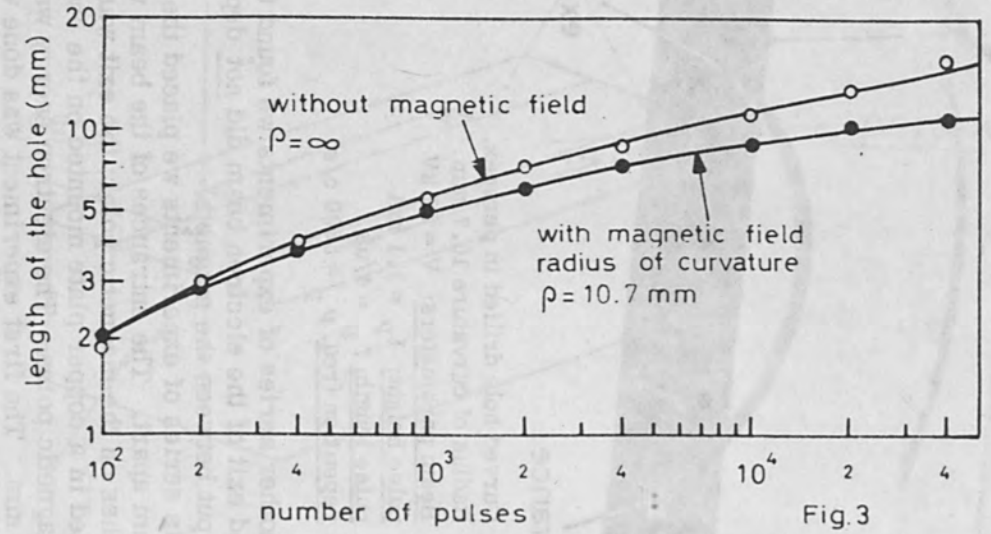

Figure 3. The hole length as a function of drilling time. In the case of a curved hole the rate of evaporation of atoms from the hole diminishes as the escape probability diminishes. Beam parameters: see Fig. 2.

Final Remarks

1. Two effects may cause a deviation from the calculated radius of curvature ρ :

a. Due to the interaction with the evaporating atoms and ions the electrons lose energy (velocity) while penetrating the hole. This should cause an experimental radius of curvature $\rho_{exp} < \rho$.

b. Part - and it may be a considerable part - of the vapor atoms in the hole will be ionized by interaction with the incoming electrons. Thus causes a gas-focussing effect, known since the early twenties [2] and increases the rigidity of the beam. Therefore $\rho_{exp} > \rho$.

As both effects act in an opposite way and no obvious deviation of ρ_{exp} from ρ could be found, one would expect both effects to be of the same magnitude.

2. The drilling of curved holes is a slower process than the drilling of straight holes: the evaporated atoms have to strike the walls of the hole before escaping. This straggling effect becomes more pronounced as the drilling proceeds, i. e. drilling gets slower and slower. Figure 3 gives the hole depth as a function of drilling time. This in turn has a strong influence on the temperature history of the work piece. Using the same electron beam parameters curved holes will therefore be somewhat wider than straight ones in most cases.

REFERENCES

1. S. Hagström, C. Nordling and K. Siegbahn: Alpha-beta- and gamma-ray spectroscopy, ed. K. Siegbahn, Amsterdam, 2nd ed. 1965, pp. 845-862. (1955 edition: T. Gerholm pp. 926-931).
2. J. B. Johnson: J. O. S. A. 6 (1922) pp. 701-712.
O. Scherzer: Z. Phys. 82 (1933) pp. 697-708.

ELECTRON BEAMS IN MELTING AND REFINING-BASIC

PREFACE

SECTION IIA

Electron Beam Refining-Basic

Calverley, Davis and Lever initiated the application of electron beams to floating zone refining in 1957. Since this technique has seen a steady growth and has been almost universally accepted as the basic approach for the growth and purification of refractory metal crystals. Its use has not been limited to the refractory metals alone and a score of metals, including ceramics, have also benefited from it.

A variety of refinements to the technique have been introduced with the years. Of particular interest appears the utilization of this technique in conjunction with externally imposed electric fields aimed at effecting an accelerated field assisted movement of the impurities in the molten zone. The limited work performed with field assisted refining is most encouraging and work with lager fields which could be much more consequential is presently in progress.

It can be said that besides enabling us to obtain materials of most consequential purity, the electron beam zone refining technique has enabled us to obtain crystals of the refractory metals and in turn to understand their flow characteristics which are of the greatest importance to our space age.

Though I have no idea as to the number of electron beam zone refiners operational today, it can be said without much exaggeration that virtually any government, industrial and university laboratory with interest in materials has one or more zone refiners at hand. While all of the work to

date has been directed here at preparation of single crystals and high purity materials for further studies there have been at least a couple of instances where single crystals of tungsten produced by this technique have been used for the production of wire of superior quality.

Considerable references are available and the list of publication given below is recommended to those seeking additional information on the subject.

(Editor)

REFERENCES

1. Proc. 1st Symp. Electron Beam Technology, J. Hetherington, (Ed), Boston, Mass., 1959.
2. Proc. Sym. on Electron Bombardment Floating Zone Melting, SERL, Baldock, England, 1959.
3. Proc. 2nd Symp. Electron Beam Techn., R. Bakish, (Ed), Boston, Mass., 1960.
4. Proc. 3rd Symp. Electron Beam Techn., R. Bakish, (Ed), Boston, Mass., 1961.
5. Proc. 4th Symp. Electron Beam Techn., R. Bakish, (Ed), Boston, Mass., 1962.
6. Proc. 5th Symp. Electron Beam Techn., J. Morley, (Ed), Boston, Mass., 1963.
7. Proc. 6th Symp. Electron Beam Techn., J. Morley, (Ed), Boston, Mass., 1964.
8. Proc. of a Symposium on Electron and Laser Beams, El Kareh, (Ed), University Park, Pa., 1965.
9. Introduction to Electron Beam Technology, R. Bakish, (Ed), J. Wiley & Sons, New York, 1962.
10. Proc. 1st International Conference on Electron and Ion Beams in Science and Technology, R. Bakish, (Ed), J. Wiley & Sons, New York, 1965.
11. Zone Melting, H. Schildknecht, Akademic Press, New York, 1966.
12. Zone Refining, W. Pfann, J. Wiley & Sons, 11nd Ed., 1966.

Some Experiences With a Point Focus Electron Beam Floating Zone Melting Device for Refractory Metals

E. B. Bas, H. Stevens

Swiss Federal Institute of Technology,
Department of Industrial Research
Zurich, Switzerland

1. INTRODUCTION

Since 1957, when Calverley, Devis and Lever[1] showed that refractory metals like Ta, Mo, Nb, etc. could be melted by heating with electron beams according to the floating zone method, which allows the formation of single crystals of these metals, this particular electron beam method has become increasingly widespread[2,3]. In the application of the electron beam method, an electron gun is generally used, whose circular cathode is arranged concentrically to the melting rod; we call this arrangement "ring focus arrangement" and can speak of "ring focus electron beam", to distinguish it from the point focus electron beam used in this particular work.

In the point focus method, the entire beam power is concentrated in one point, so to speak, of the rod circumference (Fig. 1a), whereas in the ring focus method, (Fig. 1b) the beam power is spread evenly along a line of the rod circumference. This brings us to the fundamental difference between the two methods: whereas in the ring focus method the even distribution of the heat input along the rod circumference leads to a rotation symmetrical temperature distribution in the melting zone, which can be a great advantage in obtaining single crystals, one must expect in the point focus method a strong assymmetry of the temperature distribution; it is true that this assymmetry

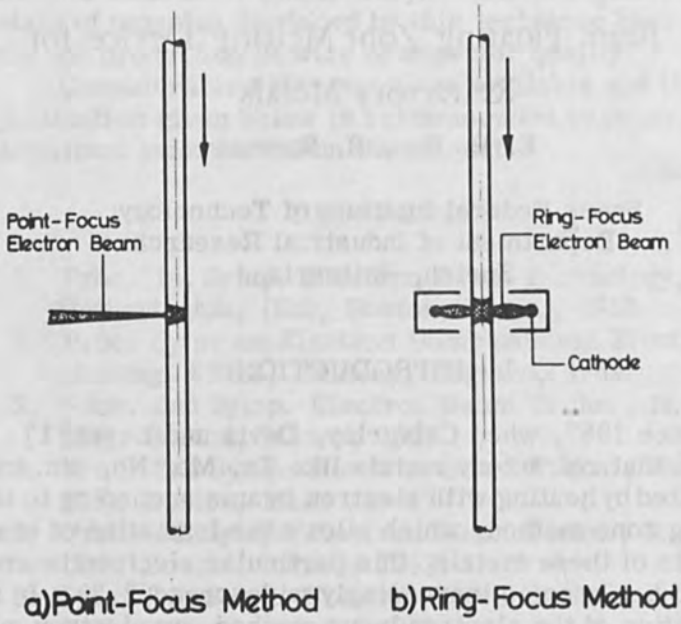

Fig. 1. Principle arrangement for floating-zone melting with electron beams:
a. point-focus method
b. ring-focus method

can be influenced by arranging several point focus electron beams simultaneously, by rapid wobbling of the beam and by rotating the melting rod, but the regularity of the ring focus method cannot be totally attained. There is another difference between the point focus and the ring focus method: in the first, the entire beam power is led into a small zone of the molten zone and therefore the beam penetrates rather deeply into it as in electron beam welding. The beam power will then be more effective in the vicinity of the rod axis inside the molten zone; the movements of molten metal inside the zone grow stronger. The aim of our investigation

is to grasp better all the particularities of the point focus method and to test the applicability of this method to zone refining and especially for the production of single crystals.

The point focus method has certain advantages over the ring focus method; the first of these advantages is that the electron gun can be placed far away from the melting zone; the molten zone is thus not contaminated by evaporated cathode material and eruptions of metallic vapours and particles from the molten zone do not influence the working stability of the electron gun. This is especially the case for the electron guns with ion separation which we used [4-7]. Samples giving off large quantities of gases can also be zone melted. Another advantage of the point focus method is that the heating power is not limited, so that the diameter of the rod to be melted is only limited by the zone stability, on which quantitative experimental data are however not yet available, except for a few theoretical investigations (8). Yet another advantage is that the melting can be done in ultra high vacuum as well as under increased pressure in a multi-chamber vacuum system by introducing the point focus electron beams through especially designed channels into the melting chamber.

2. DESIGN AND FUNCTION OF THE POINT FOCUS MELTING DEVICE WITH HORIZONTAL ROD MOVEMENT

We constructed for the first experiments a zone melting device with horizontal melting rod, using a single point focus beam for heating. This arrangement is shown schematically in Fig. 2. The rod to be melted (1) is fixed onto two massive copper holders (2) with molybdenum sheet springs, and these holders are held themselves in a copper tube (3) through which water circulates. The copper tube is flanged to two tubes of stainless steel (4) which lead out of the vacuum chamber, and allow the entry of cooling water, as well as the axial movement of the rod by the mechanism (5). The electron beam (6) is generated by a high power system which also allows the observation of the melting zone in the direction of the beam[7]; the beam is focussed onto the rod from above. The beam can also be

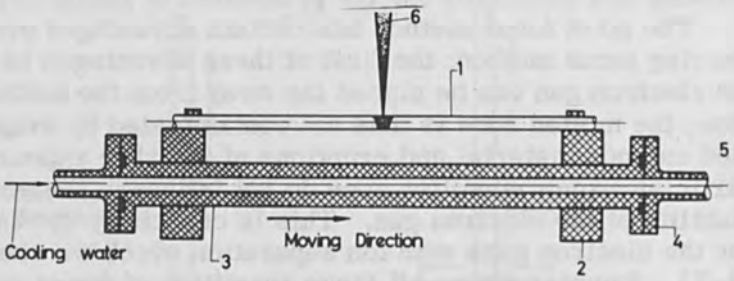

a) Principle Design of the Specimen Holding

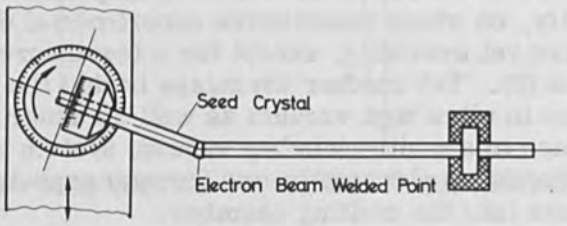

b) Goniometric Attachment for Seed Crystals

Fig. 2. Principle arrangement for floating-zone melting in horizontal position:
a. normal specimen holding with an axially oriented seed crystal
b. goniometric seed crystal attachment for growing single crystals of any desired crystallographic axis from a seed crystal of any given axial orientation.

wobbled perpendicularly to the rod axis. When growing single crystals with any desired orientation in the rod axis, a seed crystal with any given axial orientation, is introduced on one side into a goniometric holder and after adjustment using x-rays, welded to the rod to be melted. If the melting zone now starts from the inside of the seed

crystal, the orientation of the seed crystal grows into the rod to be melted with the desired crystal axis in the rod axis. This goniometric arrangement is shown in Fig. 2a, as seen in the direction of the electron beam. Fig. 3 shows the photograph of the same arrangement from the front.

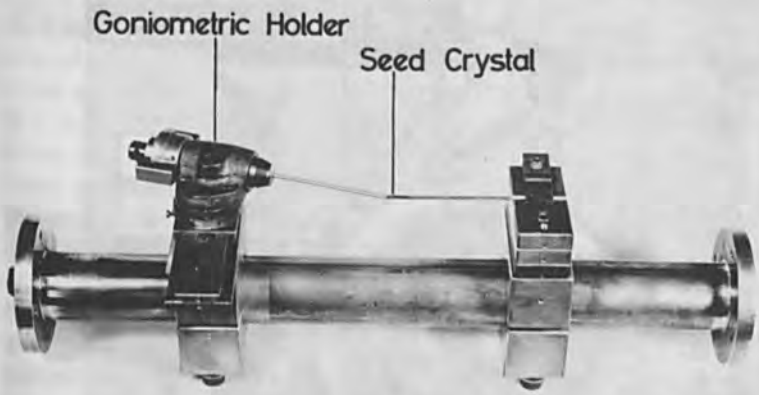

Fig. 3. View of the goniometric seed crystal holding.

Single crystals of all materials can thus easily be obtained with an accuracy in the desired axial orientation of about $\pm 0.5°$. Fig. 4 shows a general view of the zone melting device; the vacuum chamber is nearly spherical with an inner diameter of about 60 cm; it has double walls of stainless steel and can be cooled entirely with water. An oil diffusion pump (1500 l/s) allows the attainment of a high vacuum. The high power electron beam system (1) has been described in another paper[6, 7]. A single electron gun can yield a beam power of about 6 kW at an acceleration voltage of 22kV. The driving system for the rod transport is marked with (2). The rate of revolution of the motor of this system is kept electronically constant. (3) marks an electron trapping system which allows the accurate measurement and analysis of the residual gas pressure with an ionization gauge and a mass spectrometer (elimination of the electrons reflected from the molten zone).

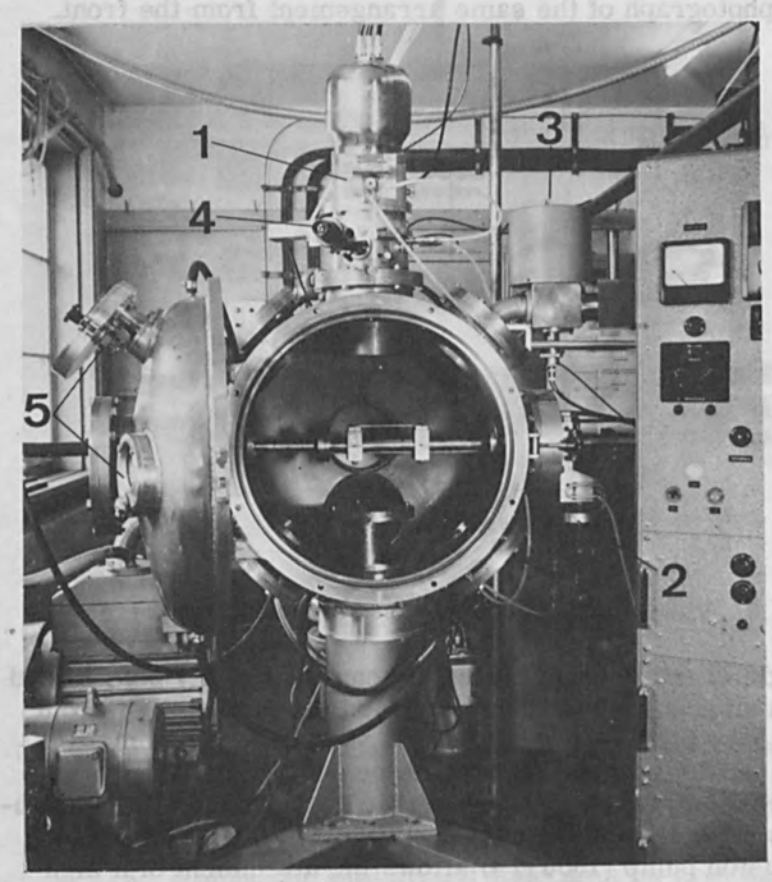

Fig. 4. Overall view of the zone melting device.

The melting arrangement with horizontal rod holding displays an important difference with the conventional vertical rod holding, in that gravity now causes the molten zone to "sag". Experience has shown however that this sagging is not very critical and that all metals melted so far (W, Ta, Mo, Nb and Zr) have caused no difficulties in zone melting; it must be said however, that until melting experiments have been conducted only up to a rod diameter of 5 mm with tungsten; experiments with larger diameters are planned. Fig. 5a shows a photograph of the melting zone as seen from the side during melting (W, rod diameter 3.5 mm, beam power 1350W); the sagging of the melting zone is clearly visible. Fig. 5b shows the principle of the zone passing through the sample. At the beginning, when the rod is being melted through, the zone sags in an approximate V-shape; when melting progresses, the solidification occurs at the level of the first zone sagging. Rods thus melted have a very regular rod diameter over the entire melted length of the rod, due to the beam power remaining rather constant. This can be seen in Fig. 6 where single crystals are shown. During the actual melting, however, a slight correction has to be applied to the beam power when the melting zone approaches the rod holder and heat conduction becomes more relevant compared with heat radiation. A programmed automatic control of the beam power is being developed.

Fig. 7 shows the melting zone as it is photographed through the observation ocular in the direction of the beam impact. The more strongly lit impact area can be seen in the centre. The penetration of the beam into the molten zone cannot be observed, however, because of strong overexposure; but if one turns off the cathode heating suddenly at this point, then the rapidly solidifying molten zone forms a crater, similar to that observed in electron beam welding. Fig. 8 shows a section through the melting zone with such a crater; we see the form of the melting zone in a tungsten rod of 3.5 mm diameter; the melting zone was not continued (first stage of melting). A slight sagging of the melting zone is visible; the length of the melting zone is about equal to the rod diameter.

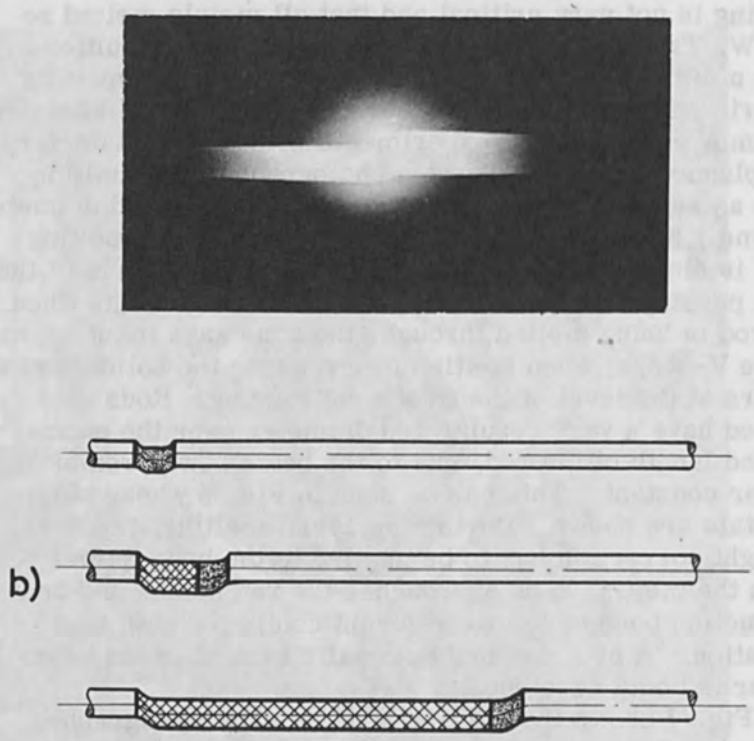

Fig. 5. Side view of the melting zone during melting.

3. SOME PROVISIONAL RESULTS OBTAINED WITH THE DESCRIBED DEVICE

Two important factors in vacuum zone melting are the beam power necessary for a given metal of given rod diameter and the material losses for each zone pass. As an example, Fig. 9 shows a graph of these two factors for a tungsten rod of 3.5 mm initial diameter for four passes.

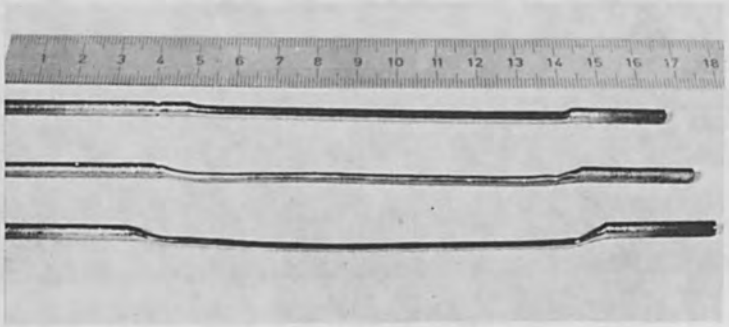

a) Tungsten after three passes

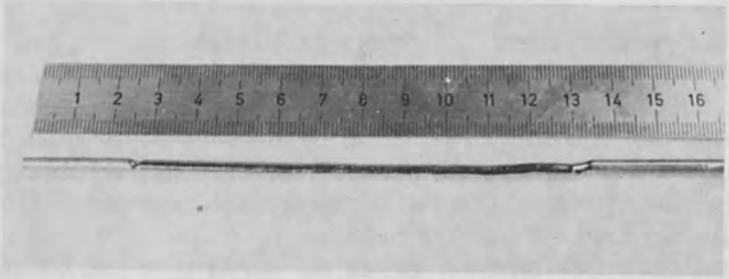

b)Tantalum after one pass

Fig. 6. Some horizontally zone refined samples:
a. tungsten after 1st, 2nd and 3rd pass
b. tantalum after 1st pass

The bombarding power is somewhat higher than the values given in literature for zone melting with ring cathodes[2]. The bombarding power depends of course more or less from the conditions of heat conduction at the clamped ends of the rod for short rod lengths. Whether the zone is more or less overheated (zone length and temperature distribution), can also influence the necessary bombarding power.

Fig. 7. View of the molten zone from the beam side, taken through the viewing ocular during melting.

In the measurement illustrated on Fig. 9, the diaphragm currents in the beam system were not measured, so that the power values are probably 5% too high. Fig. 9 illustrates the well-known fact that in the case of tungsten the material losses through evaporation are very important. After four passes, the rod diameter has decreased to half of its original value, although the zone rate of 5 mm/min is still comparatively high for the growing of good single crystals. In the case of niobium, which has a vapour pressure of about 10^{-3} Torr at melting point (against 4×10^{-2} Torr in the case of tungsten), conditions are rather more favourable, as can be seen in Fig. 10. The material losses, especially with tungsten, are very much higher than would be expected from a rough evaluation based on evaporating rate alone. Gas reactions with the residual gas atmosphere are surely responsible for a good deal of these losses. A provisional investigation of the partial pressure conditions, made with a mass spectrometer during melting, yielded the spectrograms shown on Fig. 11. The spectrogram shown in white lines refers to the residual gas composition before the start of the melting process, whereas the spectrogram shown in black lines was taken during the actual melting of a tungsten sample. Since these spectrograms are meant to give only a rough overall idea of the

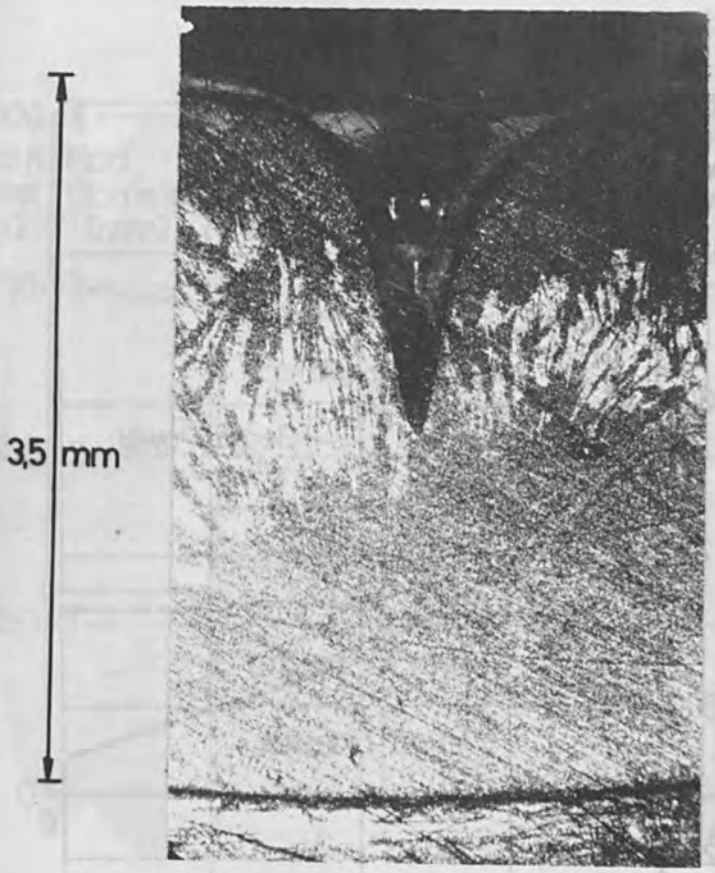

Fig. 8. Penetration of the electron beam into the molten zone; crater after rapid solidification.

gas conditions, only ion currents have been given in them and not converted into real partial pressure. The total pressure in the recipient before the start of the melting process was about 8×10^{-6} Torr and sank during operations to about 3×10^{-6} Torr. It should also be noted that a cooling trap, filled with liquid nitrogen, was installed in the immediate vicinity of the melting zone. It can be seen on Fig. 11 that the partial pressures of hydrogen and carbon

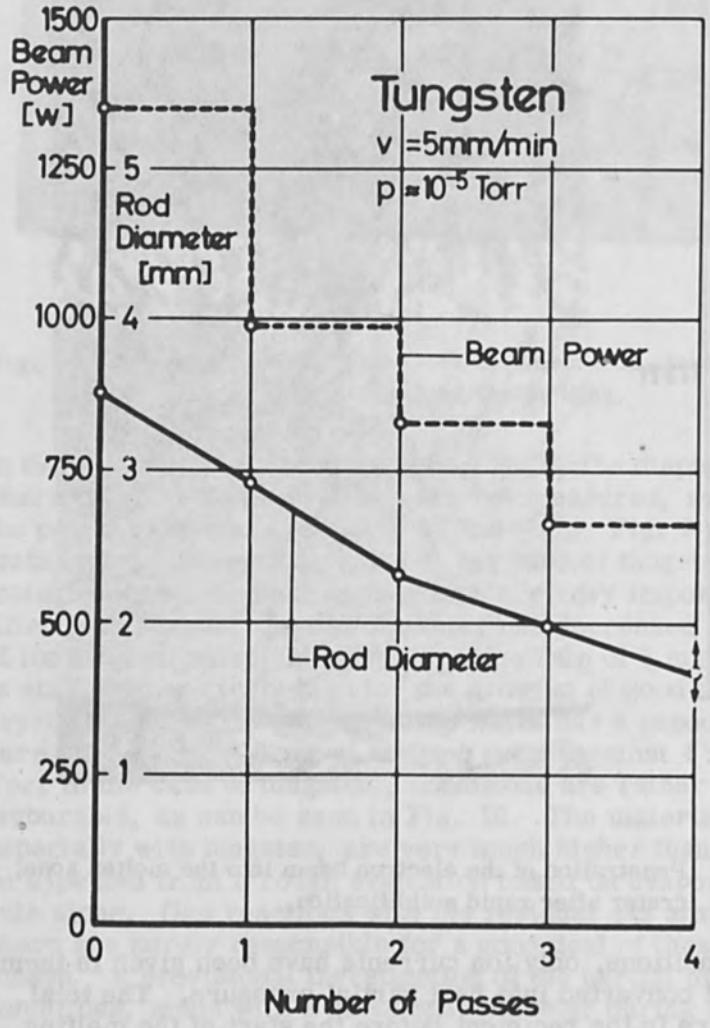

Fig. 9. Graph of the heating power and material losses for various passes when melting tungsten: pressure in the recipient about 10^{-5} Torr, zone translation rate 5 mm/min.

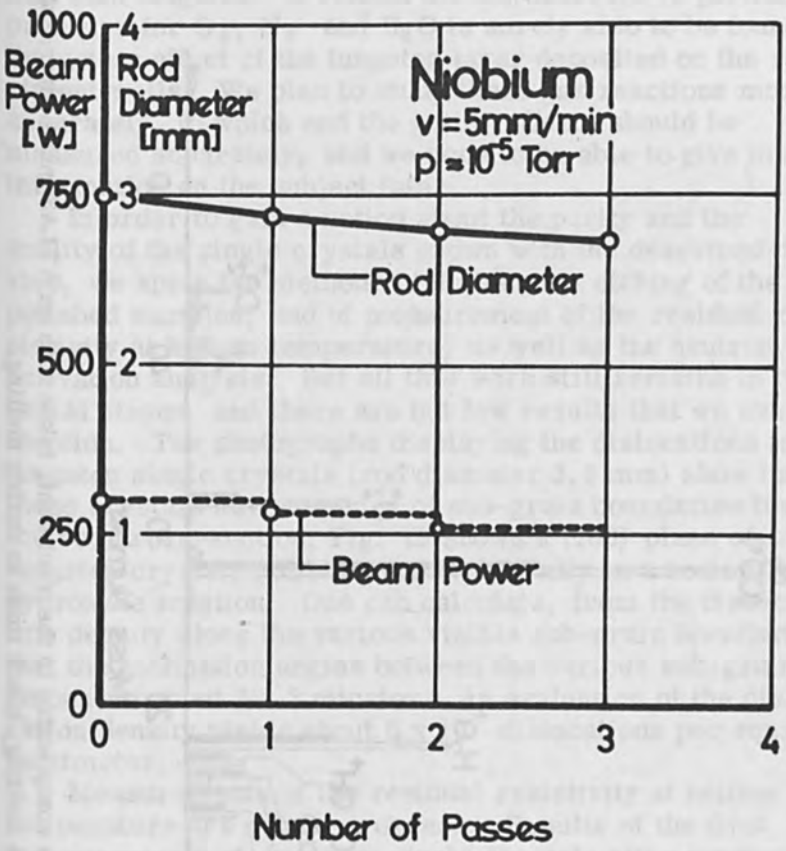

Fig. 10. Graph of the heating power and material losses for various passes when melting niobium: pressure in the recipient about 10^{-5}, zone translation rate 5 mm/min.

monoxide were the only ones to rise sharply. The partial pressure of water vapor sank quite considerably, which could lead to the conclusion that at least part of the hydrogen was formed in the reaction of H_2O with hot tungsten;

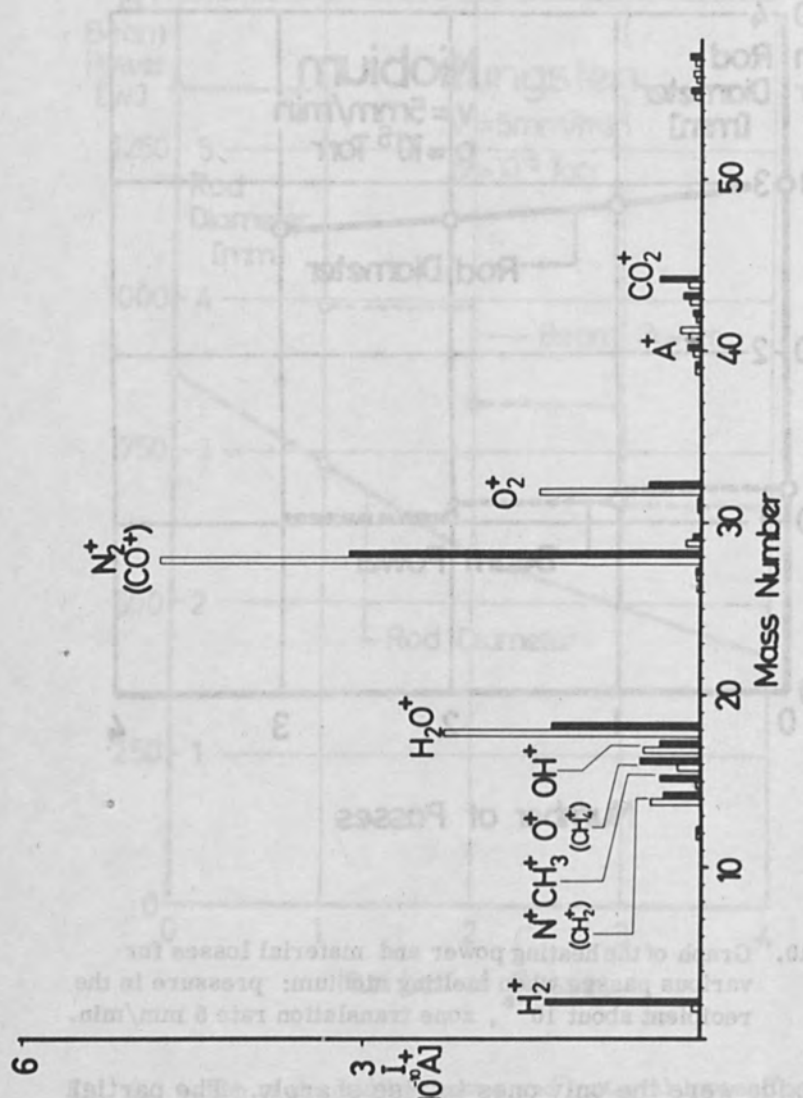

Fig. 11. Spectrograms of gas composition in the recipient, taken with an ATLAS mass filter: white lines refer to before melting, black lines to during melting.

the tungsten oxide formed evaporated immediately, since as one can see, the partial pressure of oxygen sank also rather sharply, a fact that seems to point to a strong reaction with tungsten. A reason for the decrease in partial pressure for O_2, N_2 and H_2O is surely also to be found in the getter effect of the tungsten layer deposited on the recipient walls. We plan to study these gas reactions more accurately, to which end the getter effects should be measured separately, and we hope to be able to give more information on the subject later.

In order to gain a notion about the purity and the quality of the single crystals grown with the described device, we apply the methods of dislocation etching of the polished samples, and of measurement of the residual resistivity at helium temperature, as well as the neutron activation analysis. But all this work still remains in its initial stages, and there are but few results that we can mention. The photographs displaying the dislocations in tungsten single crystals (rod diameter 3. 5 mm) show that these crystals have a series of sub-grain boundaries inside the rod cross-section; Fig. 12 shows a (100) plane of a tungsten crystal, polished electrolytically in a sodium hydroxyde solution. One can calculate, from the dislocation density along the various visible sub-grain boundaries that the inclination angles between the various sub-grains amount to about 1 - 3 minutes. An evaluation of the dislocation density yields about 5×10^7 dislocations per square centimeter.

Measurements of the residual resistivity at helium temperature are now in progress. Results of the first measurements of tungsten single crystals after several passes are shown in Fig. 13, from which one can see that our method allows to grow single crystals of at least the same degree of purity as ring focus method; we hope to obtain much better results still.

One interesting result must also be mentioned at this point; it is the result of the determination of the contents of W and Ta in zone refined niobium using neutron activation analysis and X-ray spectral analysis, although it should be stressed that it is a single measurement that should be valued as such. In this investigation, the initial

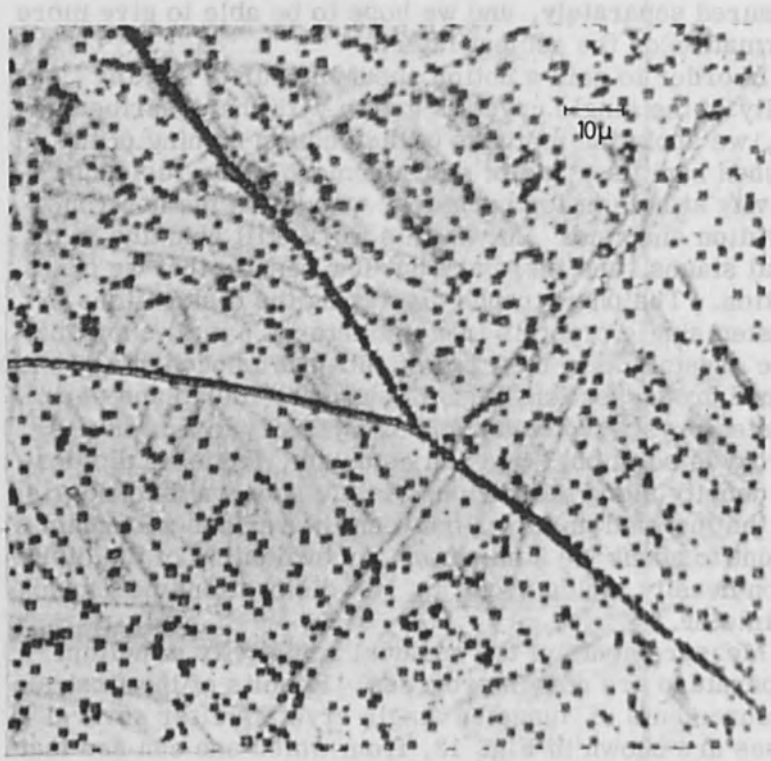

Fig. 12. Micrograph after electrolytical etching of a tungsten single crystal the ⟨100⟩ direction of which is in the rod axis, showing the dislocation and sub-grain boundaries. The inclination angle between sub-grains is about 1-3 minutes and the dislocation density about 5×10^7 dislocations per square centimeter.

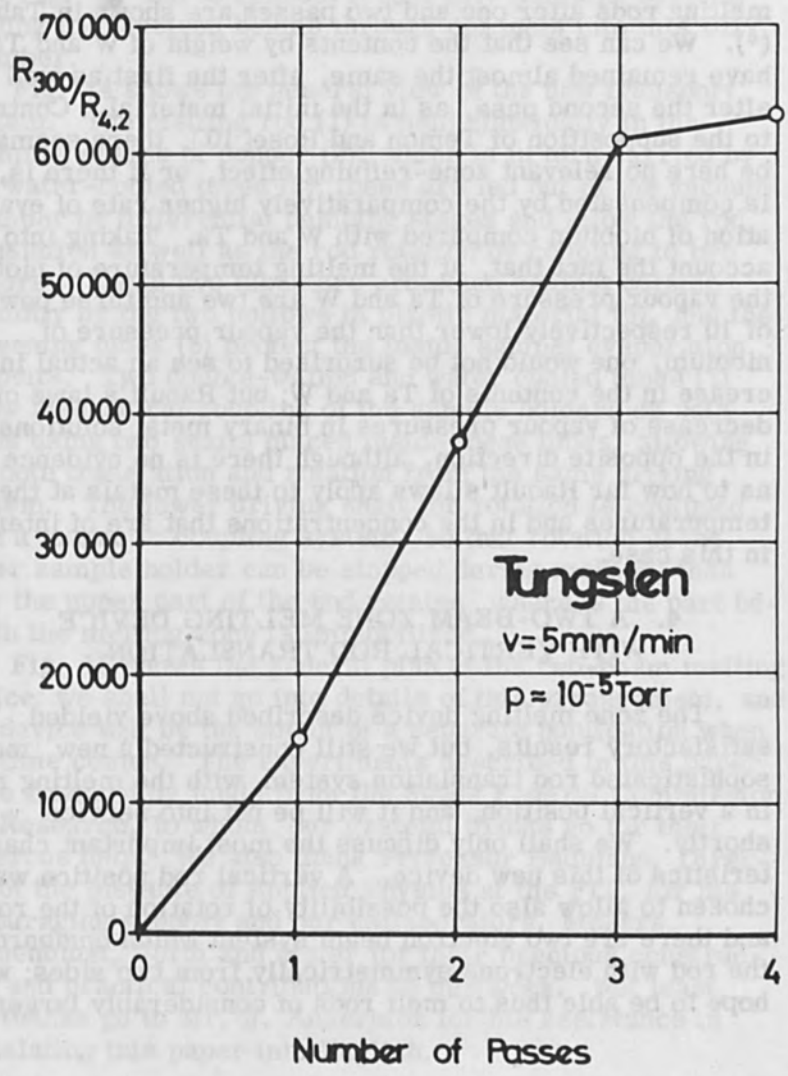

Fig. 13. Graph of average resistivity ratio for tungsten for four zone passes.

niobium used contained an important percentage of tungsten and tantalum, without our knowing it. The analytical results of the initial material and of the samples from the melting rods after one and two passes are shown in Table I (*). We can see that the contents by weight of W and Ta have remained almost the same, after the first as well as after the second pass, as in the initial material. Contrary to the supposition of Temon and Rose[10], there seems to be here no relevant zone-refining effect, or if there is, it is compensated by the comparatively higher rate of evaporation of niobium compared with W and Ta. Taking into account the fact that, at the melting temperature of niobium, the vapour pressure of Ta and W are two and three powers of 10 respectively lower than the vapour pressure of niobium, one would not be surprised to see an actual increase in the contents of Ta and W; but Raoult's laws of the decrease of vapour pressures in binary metal solutions work in the opposite direction, although there is no evidence yet as to how far Raoult's laws apply to these metals at the temperatures and in the concentrations that are of interest in this case.

4. A TWO-BEAM ZONE MELTING DEVICE WITH VERTICAL ROD TRANSLATION

The zone melting device described above yielded satisfactory results, but we still constructed a new, more sophisticated rod translation system with the melting rod in a vertical position, and it will be put into service shortly. We shall only discuss the most important characteristics of this new device. A vertical rod position was chosen to allow also the possibility of rotation of the rod, and there are two electron beam system which bombard the rod with electrons symmetrically from two sides; we hope to be able thus to melt rods of considerably larger

(*) The neutron activation analysis was conducted by Dr. A. Wittenbach (Federal Institute for Reactor Research, Würenlingen) and the X-ray spectral analysis by Dr. W. Rockenbauer (CIBA AG, Basel), and the authors wish to thank them at this point.

diameters and to grow crystals of better quality. It is planned for a later stage to install a second vacuum chamber around the melting rod, inside the large vacuum chamber (see Fig. 4), and to connect it to a UHV pumping system, leading the electron beams through channels into this UHV chamber.

Fig. 14 shows the general view of the new transport system. The melting rod (1) is held elastically in the clamping device of copper (2), which is in turn carried by two water-cooled tubes (3); these are led out of the vacuum chamber by differential pumping stages and allow the rod translation as well as the rod rotation by coupling to two motors. These two tubes are protected against outside humidity by the two bellows of plastic material (5), and the screening tubes (6) protect the inside against evaporation deposits. Two double-walled and water cooled tubes (7) allow mechanical coupling of the sample holders on both sides using two shafts placed inside these tubes, allowing for both translation and rotation from the same driving system. The lower driving shaft for rotation is equipped with a magnetic coupling system, so that rotation of the lower sample holder can be stopped during melting; then only the upper part of the rod rotates, whereas the part beneath the melting zone is immobilized.

Fig. 15 shows the general plan of the two-beam melting device; we shall not go into details of this arrangement, and the device will be the object of a separate publication when the time comes. The experiments described in this paper were financed by funds from the Swiss Federal Commission for Research, to whom our grateful thanks go for their generous help. We also thank Professor Baumann, Director of the Institute of Applied Physics at the FIT, for his encouraging support and our collaborators, Messrs. Bohnenblust, Jordi and Meier for their precious constructive and practical contributions to this work. Not least, our thanks go to Mr. J. Ansermoz for his assistance in translating this paper into English.

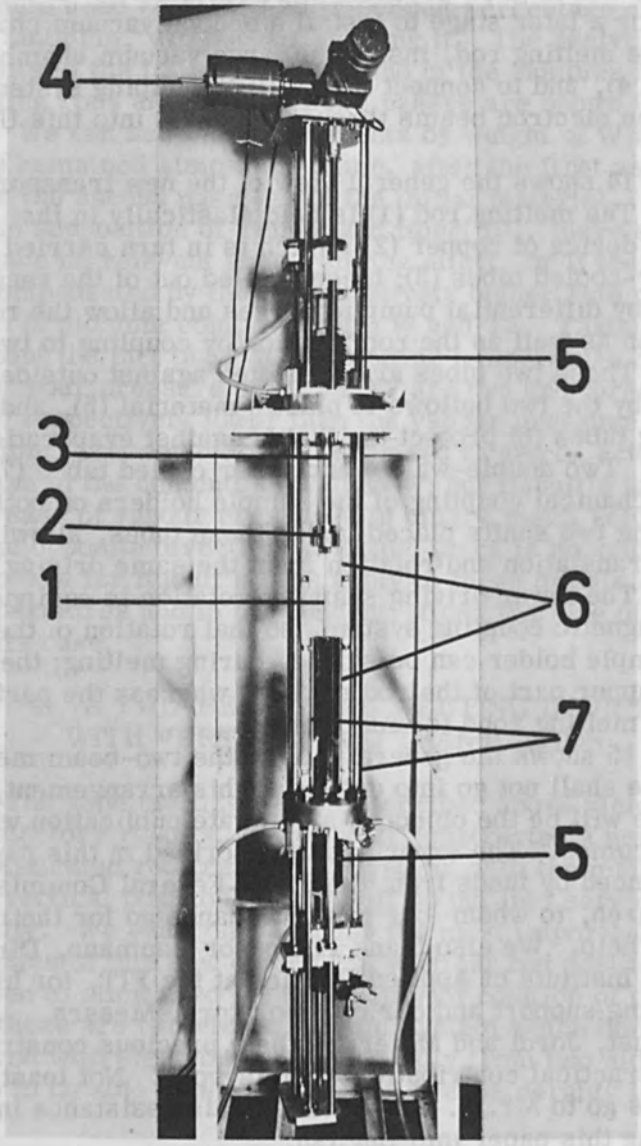

Fig. 14. Overall view of the new sample transport and rotation system for the floating zone melting device with vertical rod holding.

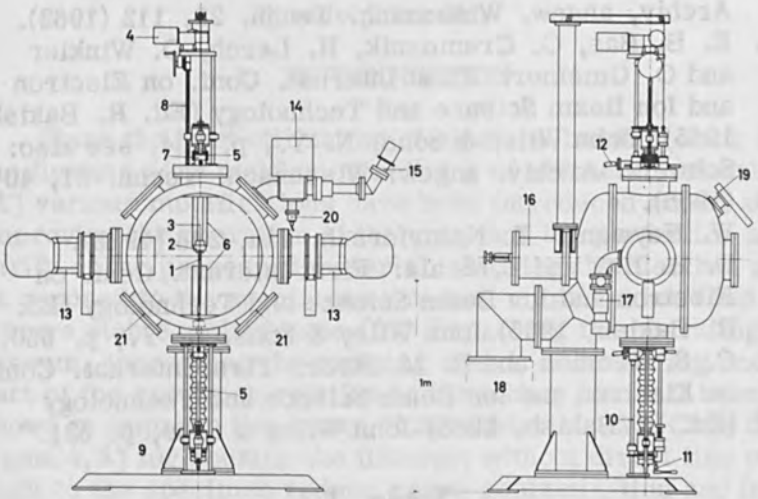

1	Sample	8	Driving Screw for Translation	15	Quadrupol Mass Spectrometer
2	Sample Clamp	9	Magnetic Coupling	16	Kryo Pump
3	Water Cooled Holder Tube	10	Rotation Drive	17	Auxiliary Pump for Electron Gun
4	Driving Motors	11	Fine Adjustment	18	Main Diffusion Pump (1500 l/s)
5	Screening	12	Differential Pumping	19	Viewport
6	Screening	13	Electron Beam Systems	20	Ionisation Gauge
7	Coupling system	14	Trap for Reflected Electrons	21	Flanges for UHV-Pumps

Fig. 15. General plan of the two-beam zone melting device.

REFERENCES

1. A. Calverley, M. Devis and R. F. Lever: J. Sci. Instrum. 34, 142 (1957).
2. A. Lawley (in "Introduction to Electron Beam Technology Ed. R. Bakish) p. 184, 1962, John Wiley & Sons, N. Y.
3. Proc. First Internat. Conf. on Electron Ion Beam Science and Technology (Ed. R. Bakish, 1965), John Wiley & Sons. N. Y.

4. E. B. Bas: US-Patent Nr. 2 835 837 (1954).
5. E. B. Bas: Optik 12, 377 (1955).
6. E. B. Bas, G. Cremosnik and H. Lerch: Transac. 8 Vacuum Sympos. and Second Internat. Congr. Vol. 2, p. 817, Pergamon Press., see also: Schweiz. Archiv, angew. Wissensch. Techn. 28, 112 (1962).
7. E. B. Bas, G. Cremosnik, H. Lerch, O. Winkler and O. Gmeiner: First Internat. Conf. on Electron and Ion Beam Science and Technology (Ed. R. Bakish, 1965), John Wiley & Sons, N. Y., p. 734, see also: Schweiz. Archiv. angew. Wissensch. Techn. 31, 40 (1965).
8. W. Heywang: Z. Naturforsch. 11a, 238 (1965).
9. D. R. Hay and E. Scala: First Internat. Conf. on Electron and Ion Beam Science and Technology (Ed. R. Bakish, 1965) John Wiley & Sons, N. Y., p. 550.
10. C. S. Tedmon and R. M. Rose: First Internat. Conf. on Electron and Ion Beam Science and Technology (Ed. R. Bakish, 1965) John Wiley & Sons, p. 521.

Table I

Contents of W and Ta in Niobium

	W [ppm]	Ta [ppm]	
Starting Material	880 800	21 000 17 000	Neutron Activ. X-Ray
After 1st Pass	860	20 000	Neutron Activ.
After 2nd Pass	920	21 000	Neutron Activ.

Fig. 16. (Table I): contents by weight of tungsten and tantalum in niobium.

Innovations in Electron - Beam Zone Refining of Molybdenum

H. L. Prekel, A. Lawley*

Franklin Institute Research Laboratories
Philadelphia, Pa.

1. INTRODUCTION

Since the first utilization of electron-beam heating for the floating zone melting or refining of refractory metals, [1] various modifications have been introduced aimed at improving the operation of the unit, and the perfection and purity of the processed material. Moving the electron gun as opposed to the specimen to reduce vibration has lead to a more stable molten zone. [2] Improving the operating vacuum, increasing the pumping speed, and rotating one part of the specimen relative to the other, have all been shown to improve the purity of the material. [3] Cage designs[4, 5] for housing the filament without direct line of sight to the specimen reduce cross-contamination and improve filament life, and a reduction of the zoning speed has been shown to decrease the in-grown dislocation density. [6]

The work presented here deals with two innovations in the floating zone preparation of molybdenum single crystals suitable for dislocation velocity studies. One describes the design and operation of a filament cage similar to that used by Brownsword and Farr[5] for Ni and Cu; this has substantially increased the stability of the unit and thereby the ease with which single crystals of very uniform diameter can be grown. The other deals with heat treatments of both the starting material and the zone-melted crystals whereby the dislocation density is reduced from ~6×10^7 cm^{-2} to ~2×10^5 cm^{-2}. This relatively low density is a prerequisite in material to be used for dislocation velocity studies since it is necessary that a) 'fresh' dislocations introduced into the sample by scratching the surface can be distinguished from the in-grown or 'aged' dislocations, and b) their movement is not impeded by the stress fields of other dislocations.

*Presently Drexel Institute, Philadelphia, Pa.

2. EXPERIMENTAL TECHNIQUES

2.1 Specimen Preparation

The single crystals used in this study were grown from 0.150" dia. arc-cast hot-swaged molybdenum rod (General Electric Lamp and Wire Division, Dover, Ohio). The purity of this material is discussed in Section 3.1. Cylindrical specimens ~0.5" in length were cut from the as-grown crystals with a diamond cut-off wheel. The dislocation structure was studied by optical microscopy, electron microscopy of high resolution replicas of etched surfaces, and transmission electron microscopy of thin foils. For the etching studies, flat observation planes were wet-ground on the cylindrical surface in an orientation known to give a one-to-one correspondence between etch-pits and dislocations.[7] Crystal orientations were determined by standard Laue back reflection techniques. Prior to dislocation etch-pitting (in a solution of 0.3 gm $K_3 Fe(CN)_6$ and 0.2 gm NaOH in 100 cc H_2O), the flats were hand polished on 600 grit paper and electro-polished in a bath of sulphuric acid in ethanol (1:6 by volume) to remove all surface damage due to the grinding operation. High resolution replicas were prepared from the etched surfaces by the method of Grube and Rouze.[8] A water soluble agent Victawet 35B is first evaporated onto the molybdenum surface followed by evaporation of silicon monoxide. In this way the replicas can be removed by immerision in distilled water without damage to the surface. Replicas were shadowed with tungsten oxide prior to examination in a Philips 100B electron microscope. Thin films for transmission electron microscopy were prepared via a sequence of slicing, jet-polishing and electropolishing operations.[9] A 20% nitric acid solution was found suitable for jet-polishing, and the sulphuric acid-ethanol bath used for final thinning to electron transparency.

2.2 Annealing Treatment

Annealing treatments were performed on zone-melted single crystals and starting material by induction heating in a dynamic atmosphere of dry hydrogen. The reason for

choosing this method in preference to others is dealt with in more detail in Section 3.3. The experimental arrangement is shown in Fig. 1. Zone-melted single crystals were placed inside a hollow molybdenum container and heated to 2000°C for 8 hours. Treatment of the as-received material was accomplished by freely suspending a 9" length of the 0.150" dia. molybdenum rod inside the quartz tube and moving the entire arrangment shown in Fig. 1 through the high frequency coil at a rate of 1" per hour. Since the coil was ~2" long this assured that every cross-section of the rod was at 2000°C for at least 1-1/2 hours. Hydrogen was introduced into the quartz tube after thorough flushing with argon and was burnt off at the exit end.

2.3 Zone-Refining in the Basic Unit

A short description is given of the conventional electron beam unit originally used, and two of its major drawbacks are discussed. The specimen is held stationary and at a potential of ~4000 volts. The circular tungsten filament is movable and held at ground potential. Focussing of the electron beam is accomplished by the usual method employing flat focussing plates above and below the plane of the filament. Temperature control of the molten zone is obtained by passing the beam current through a resistor and comparing the voltage drop with a reference voltage. The out of balance error signal is amplified and used to operate a control unit in the filament circuit. In this way any change in beam current- and thus zone temperature - is automatically corrected by an appropriate change in filament current - and thus electron emission. The main drawback to the unit lies in the fact that the filament can "see" the specimen so that cross-contamination is possible. This problem is especially troublesome in the case of molybdenum because of the high rate of evaporation during zone melting. The tungsten filament becomes coated with molybdenum at an appreciable rate and there is an associated continuous loss in emission current which must be compensated for by a continuous increase in filament current (≡ temperature). Finally, after about three zone passes, the filament current becomes so high that the filament burns through or the control unit becomes unstable. At the same time, the specimen becomes contaminated with tungsten from the hot filament.

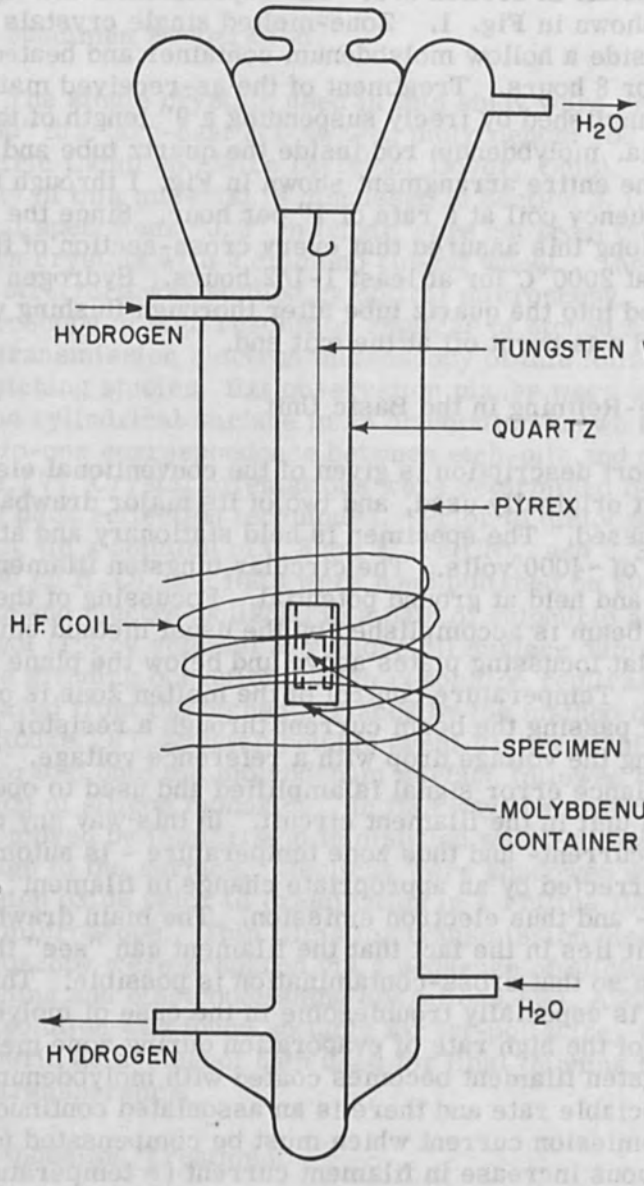

Fig. 1. Schematic representation of high frequency annealing facility.

2.4 Zone Refining with the Modified Filament Cage

To overcome these difficulties the filament arrangement was modified as shown in Fig. 2. The filament is housed in a stainless steel cage and is screened from the specimen by the inner tube. Since the electrons must now trace out a curved path to the specimen, cross-contamination is substantially reduced. The molten zone is observed through a 1/4" dia. hole in the cage wall in the position shown in Fig. 2. Originally the cage did not contain the grid shown in the figure and an accelerating voltage in excess of 9000V was required to melt molybdenum. This is due to the build up of a space charge in the vicinity of the filament; the space charge limits the beam current that can be obtained with a reasonable filament current. By introducing the grid and holding it at a positive potential of ~120 volts relative to the filament, a beam (emission) current adequate for melting molybdenum could be obtained at 8000 volts with about 10% less filament current. The following improvements have resulted from the use of this cage:

(i) Filament life is substantially prolonged. After as many as six zone passes no appreciable changes in the filament characteristics have been observed.

(ii) The stability of the unit has been improved resulting in single crystals up to 6" long with a very uniform diameter (0.130" ± 0.001") even when relatively large molten zones are used.

(iii) Centering of the specimen inside the filament is much less critical than with the "direct" arrangement.

(iv) Viewing of the molten zone is much easier since the bright filament is hidden from the eye.

3. EXPERIMENTAL OBSERVATIONS

3.1 Single Crystals Grown in the Conventional Unit

All crystals used in this study whether grown in the conventional unit or with the modified cage were given three zone passes at a zoning speed of 3 mm min^{-1} in a vacuum of ~5 x 10^{-6} mm Hg. The impurity levels listed in Table I are representative of the starting material and of crystals grown in the conventional unit. No analysis was performed

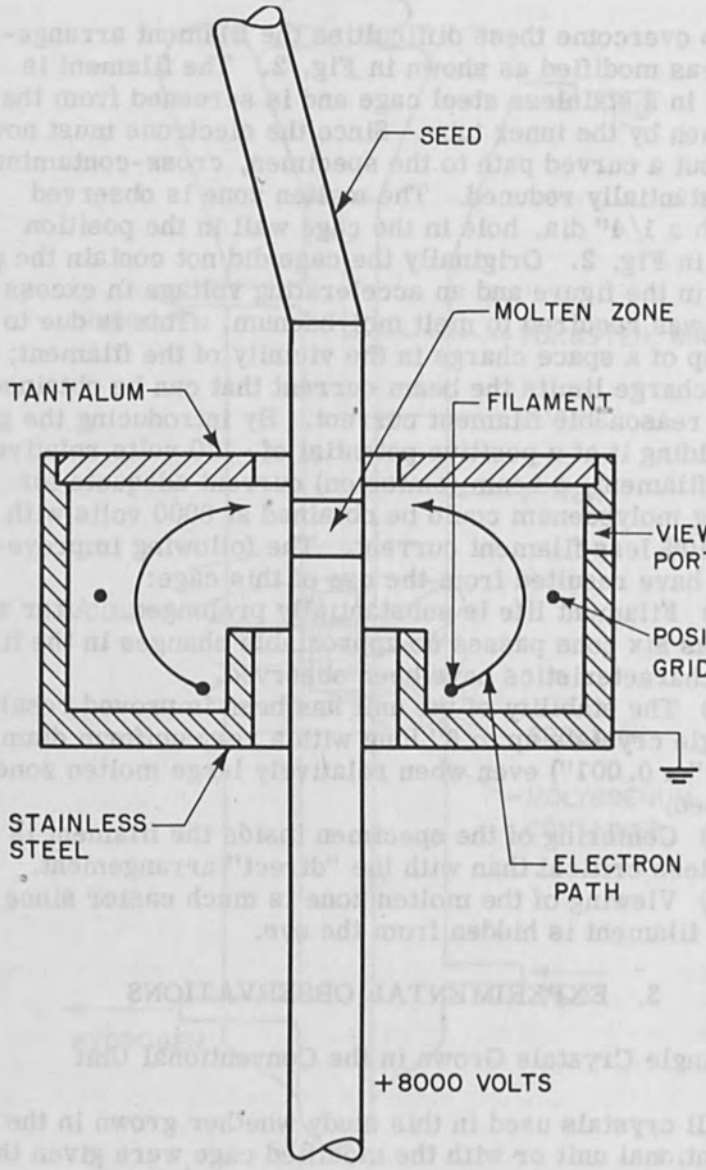

Fig. 2. Modified filament-specimen configuration for floating zone crystal growth.

to determine the amount of tungsten contamination. The results of Ferris et al[10] on electron beam melting of tantalum under similar conditions show that as much as 1000 ppm of tungsten may be picked up by the specimen after 3 zone passes.

TABLE I

Impurity Content of Zone Melted Molybdenum
(% by weight)

	C ±0.001	N ±0.001	O ±0.0005	H ±0.0001	others+
Starting material	0.004	0.002	0.006	<0.0001	~0.01
zone-melted (3 passes)	0.0013	<0.0001	<0.0001	<0.0001	~0.004

+ mainly Fe, Cu, Sn, Si

Purification of molybdenum comes about mainly by evaporation with apparently very little zone refining per se. Carbon is removed in the form of CO, CO_2 or CH_4 by combination with oxygen and hydrogen[3]. Since only small quantities of these gasses are present in the starting material removal of carbon is not very effective as can be seen in Table I. Typical dislocation arrangements are shown in Fig. 3. 3(a) is a transmission electron micrograph showing the high dislocation density associated with an inclusion. These inclusions are always observed in as-grown crystals of molybdenum and have been tentatively identified as Mo_2C.[11] The dislocations in the vicinity of these inclusions make up ~90% of the in-grown dislocation density and originate as a result of stresses set up in the molybdenum lattice by those particles as the metal solidifies behind the molten zone. Fig. 3(b) is an optical micrograph of an etched surface. The dislocation density obtained by etch-pit counts on similar micrographs is $\sim 6 \times 10^7\ cm^{-2}$. Subgrain boundary formation is only rarely observed. Note the

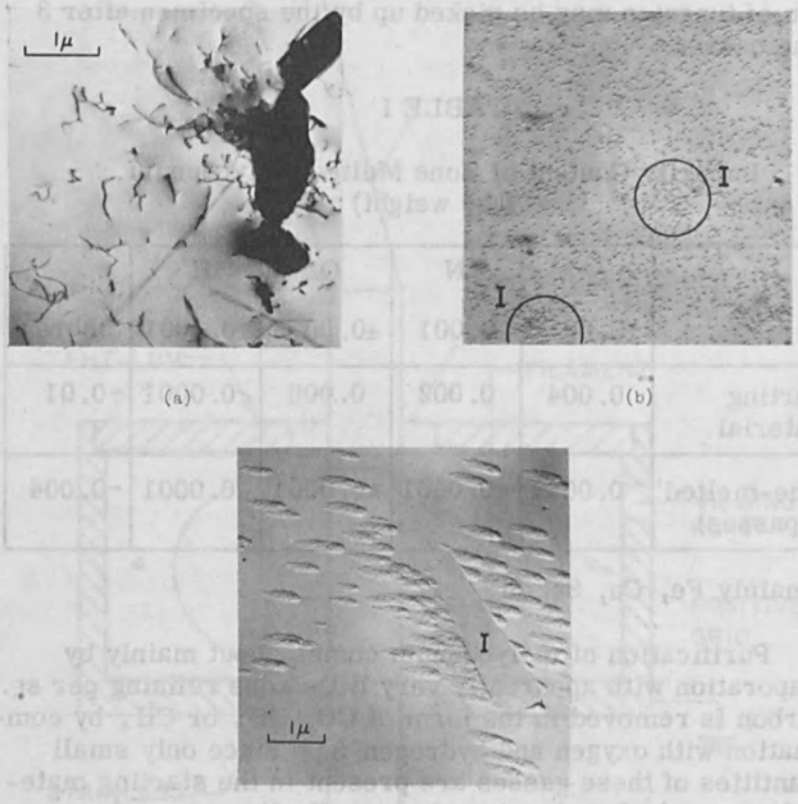

Fig. 3. Dislocation structure in molybdenum single crystals grown from arc-cast and hot swaged starting material.
a. Transmission electron micrograph
b. Optical micrograph of etched surface (X1000). Inclusions marked I.
c. Electron micrograph of SiO replica from similar surface. Inclusion marked I.

clustering of etch-pits in regions marked I where inclusions penetrate the surface. This effect is shown more clearly in Fig. 3(c) which is an electron micrograph of a replica from a similar etched surface. All the micrographs of etched surfaces in this paper pertain to {421} planes, this being the orientation for which a one to one correspondence between etch-pits and dislocations has been shown to exist.

3.2 Single Crystals Grown with the Modified Cage

Micrographs obtained from crystals grown in the modified unit are identical to those described in Section 3.1. It is therefore concluded that apart from a possible reduction in tungsten contamination no improvement in the purity or perfection of the crystals is obtained by this method. Nevertheless, all the crystals used in the following experiments were grown in the modified cage because of the obvious advantages described in Section 2.4.

3.3 Effect of Annealing As-Grown Crystals in Hydrogen

As-grown crystals were annealed at 2000°C for 8 hours in hydrogen as described in Section 2.2. The substantial decrease in dislocation density can be seen by comparing the optical micrograph of Fig. 4(a) with that of Fig. 3(b) which has the same magnification. The different pit sizes are due to different etching times. It has been shown previously[7] that the largest reduction in dislocation density occurs during the first two hours and is accompanied by the removal of the Mo_2C inclusions. The reduction in density is due to the formation of sub-boundaries and probably to the annihilation of dislocations of opposite sign. After 2 hours the overall dislocation density remains relatively constant but large dislocation-free areas are observed within the subgrains. A typical low magnification optical micrograph (Fig. 4b) is included to illustrate this effect. This structure was obtained after a 2-1/2 hour anneal. Note that some sub-boundaries are already well formed while others are still developing. The dislocation density obtained from etch-pit density counts (e.g. Fig. 4a) is $\sim 10^6\ cm^{-2}$. No inclusions have been observed

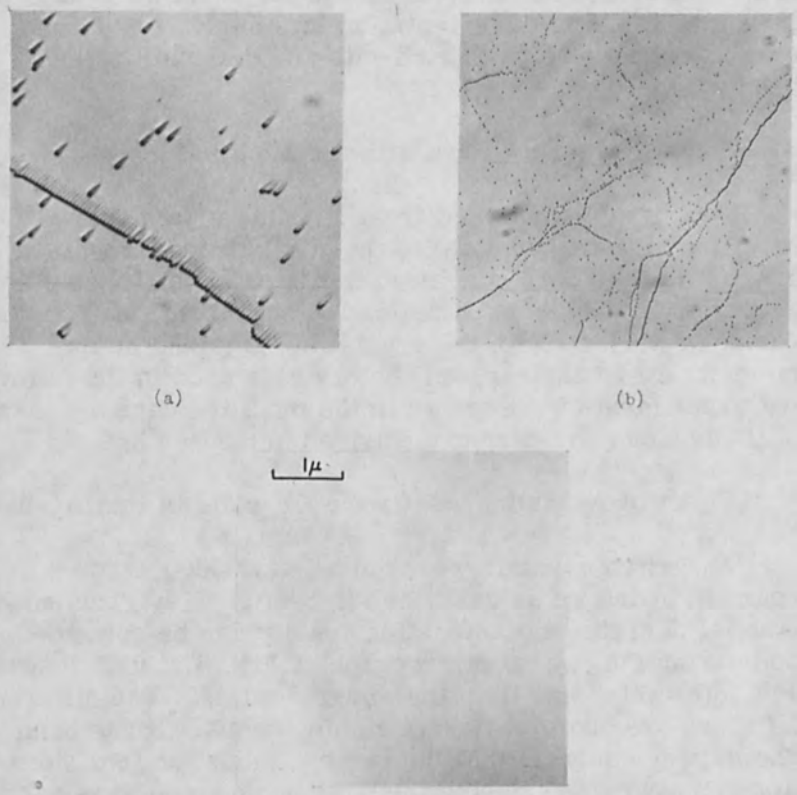

Fig. 4. Dislocation structure in hydrogen annealed single crystals.

a. Optical micrograph of etched surface (X1000) from specimen annealed 8 hours at 2000°C.
b. Low magnification (X275) optical micrograph of etched surface from specimen annealed 2-1/2 hours at 2000°C.
c. Transmission electron micrograph showing the absence of inclusions.

in electron transparent foils prepared from hydrogen annealed crystals. Typically, one dislocation is seen in about 100 square microns of foil which again gives a dislocation density of ~10^6 cm^{-2}. A typical dislocation and inclusion free area is shown in the transmission electron micrograph of Fig. 4(c).

3.4 Effect of Annealing the Starting Material in Hydrogen

It is clear that hydrogen annealing of zoned single crystals removes the carbide inclusions. Consequently it may be expected that annealing of the starting (rod) material in hydrogen (as described in Section 2.2) prior to zone melting will lead to a low carbon concentration, and an absence of inclusions in the zoned material. This proved to be the case. Typical results obtained from crystals grown from hydrogen treated stock are shown in Fig. 5. Fig. 5a is a typical optical surface micrograph showing a low in-grown dislocation density (~4.5×10^6 cm^{-2}) with no clustering as seen previously. This decrease in dislocation density by about an order of magnitude fits in well with the fact that ~90% of the dislocations present in crystals grown from untreated stock are associated with the Mo_2C inclusions. The transmission electron micrograph of Fig. 5b showing a single dislocation also shows the absence of the previously noted inclusions. The dark spots may be evidence of some residual finely dispersed precipitates.

3.5 Effect of Annealing Crystals Grown from Hydrogen Annealed Stock

Anticipating a further reduction in dislocation density by the processes mentioned in Section 3.3, crystals grown from hydrogen annealed starting material were again annealed at 2000°C for 8 hours in the induction unit. Hydrogen was again used in order to remove any residual carbon. Fig. 6 is an optical micrograph showing the further reduction in dislocation density by the formation of well developed sub-boundaries leaving large areas completely free of dislocations. The dislocation density found from micrographs similar to that of Fig. 6 is ~2×10^5 cm^{-2}.

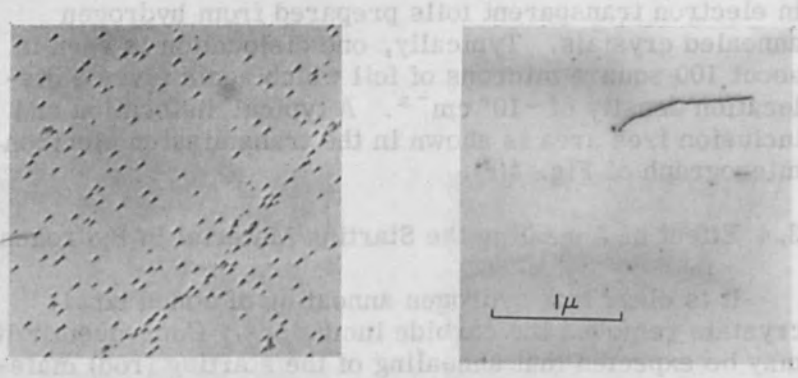

Fig. 5. Dislocation structure in single crystals grown from starting material which was hydrogen annealed before zone melting.
a. Optical micrograph of etched surface (X1000).
b. Transmission electron micrograph.

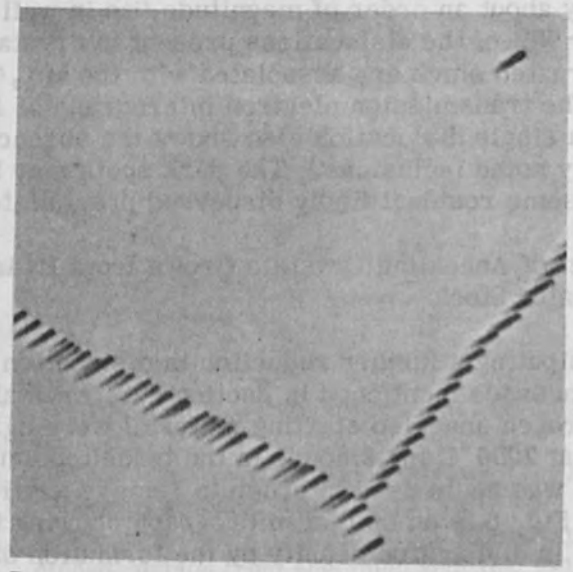

Fig. 6. Dislocation structure in hydrogen annealed single crystal grown from hydrogen annealed starting material. Optical micrograph of etched surface (X1000).

4. DISCUSSION

The presence of Mo_2C inclusions in crystals grown from "untreated" stock and their subsequent removal by hydrogen annealing deserves some comment. The markings shown in Fig. 7(a), which is an optical surface micrograph taken directly after zone refining are always observed on crystals grown from "untreated" material. These markings which Read[12] has identified as deposits of Mo_2C on the surface are not observed in crystals grown from starting material that has been annealed in hydrogen and thus arise by diffusion from the interior of the material during zone refining. The deposits are completely removed by electro-polishing to a depth of ~30μ. Although one would expect some of this impurity to escape from the surface and thus contribute to the carbon purification this effect appears to be small since no appreciable reduction in the inclusion density (e.g. Fig. 3(a)) is observed on increasing the number of zone passes. Thus carbon removal is due mainly to the process described in Section 3.1. That this combination of carbon with gases to form volatile compounds is likely supported by the fact that i) hydrogen annealing is extremely effective in removing the carbides and ii) carbon removal during zone melting is more effective[6] with sintered stock (which has a higher initial content of hydrogen and oxygen) than with arc-cast material. Calculations based on the number and size of inclusion such as that of Fig. 3(a) give a local concentration in these regions of 100-200 ppm carbon. Such local concentrations may well occur, although the starting material has only about 40 ppm carbon; and re-contamination has been shown not to occur. A high temperature gradient (~1000°C cm^{-1}) exists along the crystal during zone melting so that the final distribution of inclusions or impurities will be critically dependent on temperature fluctuations in the molten zone.

Annealing of molybdenum single crystals was at first performed in the electron beam unit with a multiple turn filament but was abandoned because of the excessive loss of material from the specimen by evaporation. The use of argon in the arrangement of Fig. 1 alleviated this problem but failed to remove the carbides although some diffusion to the surface was noted as shown in Fig. 7(b). Thus

(a) (b)

Fig. 7. a. Needle like deposits of Mo_2C on the surface of crystals grown from "untreated" starting material.
b. Smaller Mo_2C deposits on crystals annealed in argon.

hydrogen was chosen for its ability to remove the inclusions as well as substantially reducing evaporation.

5. SUMMARY

5.1 Floating Zone Melting with the Modified Cage

The effects of housing the filament in a cage such as that described can be summarized as follows: i) coating of the filament with material from the specimen is greatly reduced resulting in longer filament life, enhanced stability of operation of the unit and therefore production of single crystals with a more uniform diameter, ii) Contamination of the specimen with tungsten from the filament is avoided, iii) Viewing of the molten zone is easier since the hot filament is hidden from the eye, iv) Introduction of a positive grid in the cage effectively increases the beam current by reducing the space charge in the vicinity of the filament. Thus the filament can be operated at a lower temperature which further increases its life; v) Apart from avoiding tungsten contamination, no improvement in purity is noted in crystals grown in this fashion as compared to crystals grown in the conventional unit.

5.2 The Effect of Annealing Treatments in Hydrogen

i) Carbide inclusions are effectively removed from molybdenum single crystals by an anneal at 2000°C in hydrogen for 8 hours. This is accompanied by a reduction in dislocation density from ~6×10^7 cm^{-2} to ~10^6 cm^{-2}.

ii) No formation of carbides is evident in crystals grown from starting material which was hydrogen annealed before zone melting. This proves that re-contamination of the specimen with carbon from sources in the vacuum unit (back streaming oil vapours, vacuum grease) does not occur. Furthermore, crystals grown from hydrogen annealed stock have a dislocation density of ~4.5×10^6cm^{-2} as compared to ~6×10^7 cm^{-2} for crystals grown from untreated stock.

iii) A final anneal of 8 hours at 2000°C in hydrogen reduces this density (~4.5×10^6 cm^{-2}) by a further order of magnitude to ~2×10^5 cm^{-2}. Most of these dislocations are arranged in sub-boundaries leaving large areas completely free of dislocations. For convenience these results are presented in Table 2.

TABLE 2

Dislocation Structure in Molybdenum Single Crystals After Various Treatments

Material Condition	Dislocation Density (cm^{-2})	Remarks
As received + 3 zone passes -	$\sim 6 \times 10^7$	Few sub-boundaries, clustering of dislocations near inclusions
As received + 3 zone passes + H_2 anneal	$\sim 1 \times 10^6$	Pronounced sub-boundary formation, no inclusions
As received + H_2 anneal + 3 zone passes	$\sim 4.5 \times 10^6$	Moderate sub-boundary formation, no inclusions
As received + H_2 anneal + 3 zone passes + H_2 anneal	$\sim 2 \times 10^5$	Pronounced sub-boundary formation, large sub-grain areas without dislocations

ACKNOWLEDGMENT

This work was supported by the Office of Naval Research, Washington, D. C.

REFERENCES

1. Calverley, A., Davis, M., and Lever, R. F., J. Scient. Instr., 34 142 (1957).
2. Birbeck, F. E., and Calverley, A., J. Scient. Instr. 36, 460, (1959).
3. Murray, G. T., Weinig, S., and Drangel, I., MRC Research Rep., (1964).
4. Cole, M., Fisher, C. and Bucklow, I. A., J. Appl. Phys., 12, 577, (1961).

5. Brownsword, R., and Farr, J. P. G., J. Scient. Instr., 41, 350, (1964).
6. Adams, M. A. and Ianucci, A., WADC Tech. Rep. 59-441 pt. 2, (1960).
7. Prekel, H. L., and Lawley, A. (To be published).
8. Grube, W. L., and Rouze, S. R., Proc. ASTM, 52, 573, (1952).
9. Strutt, P. R., Rev. Scient. Instr. 32, 411, (1961).
10. Ferris, D. P., Rose, R. M., and Wulff, J., Trans. AIME, 224, 975 (1962).
11. Lawley, A., and Gaigher, H. L., Phil. Mag., 8, 1713, (1963).
12. Reid, C. N., Trans. AIME, 233, 834, (1965).

Improvements in the Floating-Zone Electron-Beam Technique for the Group V Refractory Metals

L. C. Skinner and R. M. Rose

Massachusetts Institute of Technology
Cambridge, Massachusetts

To improve the purity and perfection of single crystals of the Group V transition metals (V, Nb, Ta), elimination of specific sources of contamination and imperfection which are operative during the electron-beam floating-zone melting process has been attempted. To depress the level of interstitial contaminants, crystals are now regularly grown in ion-pumped vacua in the ranges of 10^{-9} - 10^{-10} torr, with a completely bakeable electron-beam floating-zone apparatus constructed for this purpose, which is described with various modifications.

Typical operating data and requirements are also presented, with some of the resulting electrical and mechanical properties. As a general rule, the benefits of ultra-high vacuum melting increase with the melting point, at least when commercial starting materials are used. The residual resistivity of Group V materials melted in ultra-high vacuum appears to be limited by non-gaseous impurities.

The influence of Ta as an impurity in Nb on the residual resistivity is discussed, and possible zone-refining effects for Ta and other elements considered; recent neutron activation analysis work on this subject is reviewed. An analysis of the residual gases in the vacuum system during the growth of a Nb crystal has been made to determine possible changes in interstitial concentrations. Tungsten contamination, another distinct possibility, is considered, and analyses of multi-pass material are presented for

crystals grown with direct and indirect electron guns, as a function of the number of passes. Techniques for the further depression of the residual resistivity of Group V single crystals are discussed.

I. INTRODUCTION

Single crystals of the refractory metals are useful in low-temperature studies of the solid state, provided that such crystals have low residual resistivities and high perfection. The Group V metals (V, Nb, Ta) are of particular interest, but electron beam melting by the floating zone technique, which works so well with the Group VI metals, is disappointing in this case. For instance, conventional high vacuum (10^{-5} -10^{-6} torr) electron beam floating zone melting of niobium yields single crystals where resistivity ratios, $\rho(300°K)/\rho(4.2°K)$, are typically about 100. Previous investigations in our laboratory[1] show that such single crystals, if grown at rates of about 4 mm/min., may have extremely high dislocation densities. Thus, although the electron beam floating zone technique can conveniently produce relatively large single crystals of closely controlled orientation, the crystals contain excessive quantities of impurities and imperfections. On the other hand, the residual resistivity (and therefore the overall level of impurity and imperfection) has been significantly improved by simply heating high-purity material near its melting point, in ultra-high (10^{-8} -10^{-9} torr) vacua; thus, the resistivity ratio of Nb can be raised to a few thousand[2, 3], and that of Ta to about ten thousand[4]. The question then arises: is the electron-beam floating-zone technique capable of equal or better results, and if not, why not? It was found that the dislocation density could be significantly lowered by using what were, for this technique, low growth rates, 1 mm/min. or less, preferably about 0.5 mm/min.[1]. However, the resistivity ratio remained low, a result of impurities which either are not removed or are actually introduced during crystal growth. We wish now to discuss the various possible sources of contamination, our recent efforts to identify and eliminate such sources, and the initial results of our efforts, which continue.

II. CONTAMINATION BY RESIDUAL GASES

Dissolved gases generally increase the residual resistivity sharply. DeSorbo[5] finds that dissolved oxygen increases the residual resistivity of Nb at the rate of 5.2 microhm-cm. per atomic pct.; Tedmon, Rose, and Wulff obtain about 7 microhm-cm. per atomic pct.[6]. A rough estimate for nitrogen from DeSorbo's data[5] yields about 7 microhm-cm. per atomic pct. It follows that during floating zone crystal growth of Nb in vacuum, equilibrium with residual gases is not attained, at least in the cooler single crystal below (or above) the molten zone. To demonstrate this, we can use the relation derived by Cost and Wert[7] from their data on the solubility of nitrogen in Nb:

Atomic pct. nitrogen =

$$6.2 \times 10^{-4} \sqrt{P_{N_2}} \exp\left(\frac{46,000}{RT}\right) \qquad (1)$$

where ρN_2 is measured in torr[7]. Now, consider the dissolution of nitrogen in the hot single crystal adjacent to the molten zone. For 1200°C at a pressure of 10^{-6} torr this formula gives about 4%, well in excess of the solubility limit (about 1%)[7]. Even at 1600°C, at 10^{-8} torr, pressure of N_2, the Nb should dissolve about .14% nitrogen, and the residual resistivity would be about 1 microhm-cm. and the resistivity ratio about 13, at most, (taking 13 microhm-cm. as the 300°K resistivity). The typical nitrogen content of Nb single crystals as grown at rates of 2-5 mm/min. with vacua in the middle or low 10^{-8} torr range is about 0.0006 atomic pct.[8,9]; the latter composition is in equilibrium with 4×10^{-8} torr of N_2 at about 2450°C, just below the melting point. Thus, recontamination by nitrogen of the cooling single crystal does not appear to be a problem under these conditions. Such a conclusion might also be reached from the simple observation that the residual resistivity of a Nb single crystal tends to drop further, on repeated zone passes, suggesting that gases are leaving the specimen on each pass. Table I presents typical data obtained in our laboratory.

TABLE I

Residual Resistivity as a Function of the Number of Zone Passes on Nb

Pass Number	$\rho_{4.2\,°K}$, $\mu\Omega$ - cm.
1	0.28
2	0.18
3	0.17
4	0.11

pressure: 5×10^{-6} mm. Hg.
zone speed: 10 mm/hr.

Because we wish, for the sake of crystal perfection, to use slower growth rates, we might inquire further into the kinetics of gas contamination of the crystal. We shall first assume that adsorption at the Nb surface is not the rate-determining step. This assumption is justified by the observations of Pasternack and Gibsin[10] for nitrogen adsorption by Nb; the surface is clean and the nitrogen diffuses in as fast as it arrives and sticks to the surface. Sticking probabilities at high temperatures appear to be in the range 0.01-0.1[10]. We therefore consider only the diffusion inward of the adsorbed gas. Rather than attempting an explicit solution for the diffusion equation, we refer to the work of Seraphim et al.[4] who used, for different circumstances, the solution to the cylindrical diffusion equation with constant diffusivity

$$C = C_{surface} + \frac{2(C_{initial} - C_{surface})}{2.405} \frac{J_o(\alpha_1 r)}{J_1(\alpha_1 r_o)} e^{\frac{-5.78Dt}{r_o^2}} \qquad (2)$$

where J_o and J_1 are zero and first order Bessel functions, and α_1 is fixed by the boundary conditions. The convenient feature of equation (2) is, as Seraphim et al. noted, the time constant[4]

$$\tau \equiv \frac{r_o^2}{5.78D} \qquad (2a)$$

which characterizes the relaxation of the concentration to its equilibrium value. If we use the low-temperature data of Powers and Doyle[11] for the diffusivity of nitrogen in Nb, the time constant for 3 mm. diameter Nb. rod at 2450°C (our contrived equilibrium temperature, above) is about 300 sec. The same thing can be done for oxygen. We can fit the data of Pemsler[12] on oxygen solubility in Nb to the relation

$$C(\text{at pct.}) = 2.5 \times 10^{-8} \exp\left\{\frac{50,000}{T}\right\} \sqrt{P_{O_2}} \qquad (3)$$

where P_{O_2} is again in torr. A partial pressure for O_2 of 10^{-8} torr and a typical final concentration of 100 ppm by weight of oxygen are in equilibrium according to equation (3) at about 2050°C; the time constant at 2050°C for oxygen diffusing into a 3 mm. rod is about 70 sec., if the diffusivity data of Powers and Doyle[11] are used. For nitrogen and oxygen, the time constants have reasonable orders of magnitude and, at least for oxygen, a smaller time constant implies a larger final concentration.

The many simplifying assumptions made in this approach are not the only weakness. Far more serious is the fact that the residual pressures of O_2 and N_2 during zone melting are usually not known and may not be comparable to the total pressure. Other possible sources may have been neglected. The magnitude of the time constant, however, is not very sensitive to the pressure in the above calculation for the circumstances discussed; typically, an error of ten in the pressure will change τ by less than 25%. Another error which may be quite large is our neglect of axial diffusion in the crystal due to axial thermal and composition gradients. Such effects may be favorable: oxygen, nitrogen, and other impurities may diffuse from the cooler material towards the hot zone (where concentration is lower) and then out of the crystal. At any rate, we wish to suggest that the above manipulations indicate that at zone speeds in the 2-5 mm/min. range, contamination is reduced because only at relatively high temperatures are the time

constants for the diffusion of interstitials small enough for equilibrium to be reached (~ 100 seconds) but at these temperatures, solubilities for interstitials are very low. If zone speeds and thermal gradients are lowered, longer relaxation times may alloy appreciable contamination; that is, equilibrium will obtain at lower temperatures where solubility is greater. It is therefore, conceivable that with relatively pure starting material we may be gaining higher perfection by reduced growth rates, but at the cost of higher gas content. One way to alleviate this problem is to grow crystals in significantly better vacua.

III. APPARATUS FOR CRYSTAL GROWTH IN ULTRA-HIGH VACUUM

(a) Description

To reduce the overall residual gas level during crystal growth ultra-high vacuum technique was used. An all-metal vacuum system, shown in Fig. 1, was constructed and was pumped by a combination titantium sputtering and sublimation arrangement. The system is mainly stainless steel with shear seals gasketed by OFHC copper. Roughing to the starting vacuum of the sputtering (ion) pump is done by sorption on chilled zeolite to avoid possible hydrocarbon contamination. Each of the sorption pumps is isolated from the roughing manifold by a stainless steel viton-gasketed valve, and the system is isolated from the roughing manifold by a bakeable all-metal valve. The ion pump is baked out by an internal heating element. The rest of the system may be baked out by either of two methods. One uses ovens, such as the one shown in Fig. 1, with the bell jar. The other method employs heating strips such as those used commercially to heat drums and tanks of liquids; the strips are tied or bolted onto the bell jar and base plate. Some insulation, either a sheet metal shroud or simply a wrapping of fiberglass blankets, should be provided. The upper limit to the chamber baking temperature is about 450° C. Although this arrangement can attain extremely low ultimate vacua, it was desirable for the sake of flexibility, ease of operation, and visibility, to use a glass bell jar with viton gasketing; this limited the baking temperature to the 150-200° C range.

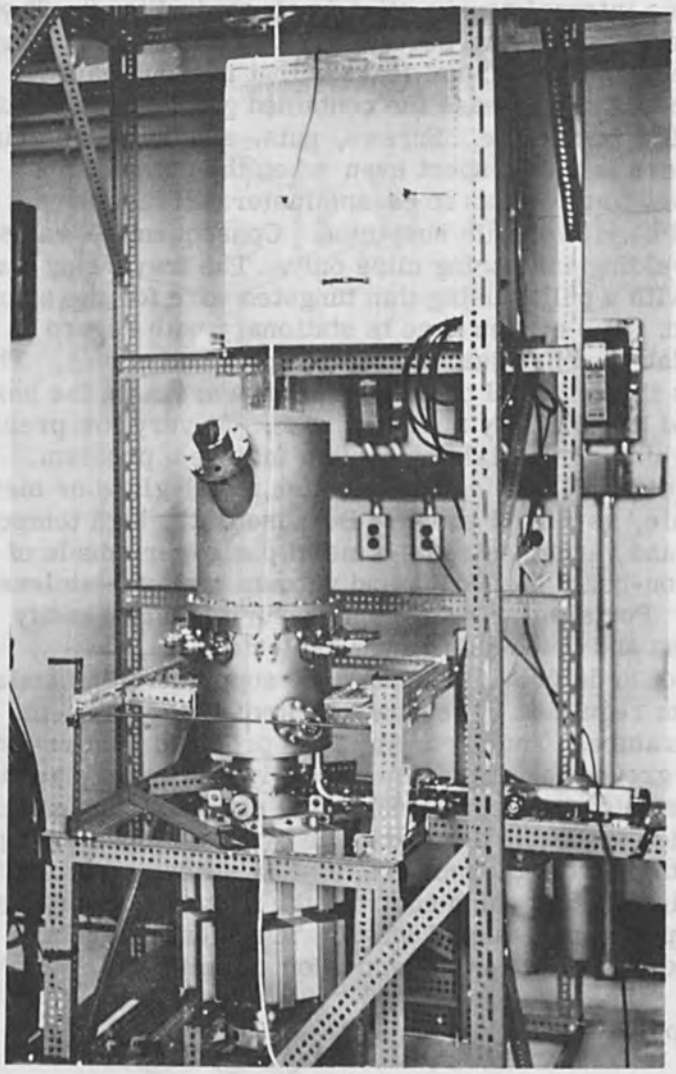

Figure 1. Ultra-high vacuum system used for crystal growth, with baking and control facilities removed. The titanium ion pump is underneath, and the sublimation chamber just below the ring of feedthroughs, isolated from the main chamber by an optical baffle. The roughing manifold is to the right rear, with the sorption tanks hanging down. A bakeout oven rests on the beam above and to the rear of the bell jar.

The internal construction is shown in Fig. 2. It was necessary to observe several general principles. One is that there be no "virtual leaks", that is, long narrow crevices which release the contained gas slowly due to the high flow impedance. Screws, nuts, and bolts are prime offenders in this respect even when the threads are modified to allow gas to escape faster; all fasteners should be viewed with suspicion. Consequently, we used spot welding and spring clips only. The traversing was done with a pulley using thin tungsten wire for the same reason. The molten zone is stationary with regard to the baseplate and bell jar; the entire specimen moves. This avoids the continual outgassing of new areas on the bell jar and baseplate by a moving zone. At very low pressures cold welding of metals on contact may be a problem. To avert this, all moving contacts are metal-glass or metal-ceramic, as Fig. 2 shows. Because of the high temperatures and vacua desired the metal parts were made of electron-beam melted Ta and vacuum melted stainless steel. For similar reasons high-purity, high density alumina and fused quartz were selected.

Power is provided by an 8 kV supply with the emission current regulated by feedback control of the filament temperature. The error signal is provided by a resistor in the ground leg of the power supply; the voltage across this resistor is proportional to the emission current and is nulled out at the desired value by a reference voltage. Deviations from the null are fed to a silicon controlled rectifier circuit which controls the filament power, acting to keep the error signal small. Transient pulses are limited by a choke in the emission circuit.

(b) Operation

The sorption pumps are chilled with liquid nitrogen and the system pressure reduced to about 5 microns. Power is applied to the ion pump and after it starts the sorption pumps are isolated from the main chamber. Titanium sublimation may be used to increase pumping speed at this point. The speed with which the system pumps down is very dependent on the length of time the system has been exposed to air. After a pressure below

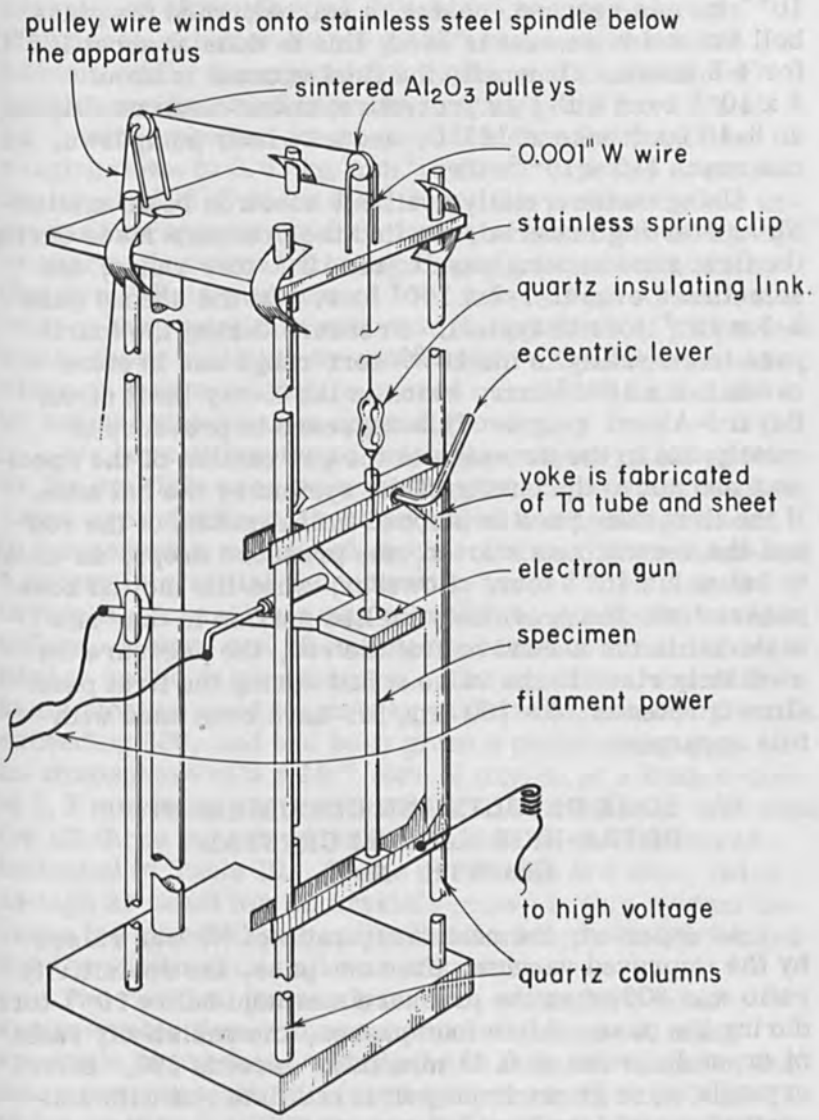

Figure 2. Electron gun and specimen holder. The specimen, at high voltage, moves through the gun. The yoke which holds the specimen rides on quartz rods and is pulled up by a tungsten wire. Three criteria influenced this design: virtual leaks must be minimized, the molten zone must be stationary, and there must be no metal-to-metal moving contacts.

10^{-6} torr is reached, baking is started; when the glass bell jar and viton seal is used, this is done at about 125°C for 4-6 hours. Generally the final vacuum is about 3×10^{-9} torr with this procedure; under clean conditions, an 8-10 hour bake at 125°C, and a 24 hour pumpdown, we can reach $1\text{-}3 \times 10^{-10}$ torr.

Using commercially available electron beam melted Nb as starting material, we find the pressure rises during the first zone melting pass to the 10^{-8} torr range, and sometimes even to $1\text{-}2 \times 10^{-7}$ torr. On the second pass $2\text{-}5 \times 10^{-9}$ torr is typical. Pressure during the fourth pass is generally in the 10^{-10} torr range and in some cases $1\text{-}2 \times 10^{-10}$ torr, which is the X-ray limit of our Bayard-Alpert gauge. This decrease in pressure is mostly due to the decrease in the gas content of the specimen and not to the baking of the system by the hot zone. If the first zone pass is stopped in the middle of the rod and the second pass started, the pressure drops, as usual, to below 5×10^{-9} torr. However, when the molten zone passes from the previously melted portion to the "raw" material in the second half of the rod, the pressure immediately rises to the value it had during the first pass. Growth rates of 10 - 100 mm/hr. have been used with this apparatus.

IV. SOME RESULTS AND DISCUSSION OF ULTRA-HIGH VACUUM CRYSTAL GROWTH: Nb

As expected, the resistivity ratio of Nb was raised by the improved vacuum; after one pass, the resisitivity ratio was 600 when the pressure was held below 10^{-8} torr during the pass. After four passes, the resistivity ratio of crystals grown at 0.42 mm/min. exceeds 800. Such crystals were grown from polycrystalline rod with concentrations of less than 100 ppm of No, O, and C.

The single crystal material is quite soft after the first pass. Cocks [13] has measured the yield stress in tension at a strain rate of 0.01 per minute of crystals grown at 0.85 mm/min. The resolved shear stress at yielding, on {110} <111> systems is slightly above 1 kg/mm^2, with some orientation sensitivity. By way of comparison, the

crystals of Mitchell et al. [9] which were grown with six passes at better than 5×10^{-6} torr are about 50% harder, while the crystals of Taylor and Christian [3] which were annealed near the melting point in vacua of 10^{-8} torr or better are somewhat softer, with values ranging down to 0.63 kg/mm^2. If our crystals are annealed at 1700°C at 1×10^{-5} torr, the yield stress is increased by approximately a factor of ten, up to 10 kg/mm^2 or more, thus demonstrating the influence of contamination by a "dirty" vacuum of 10^{-5} torr [13]. At any rate, neither the resistivity ratio nor the mechanical properties match those available by annealing in ultra-high vacuum, although they are much improved over these attainable by normal high vacuum crystal growing.

We have attempted to determine why crystals grown by the multiple pass zone melting technique in ultra-high vacua are inferior to those annealed in ultra-high vacua in the respects mentioned above. Primarily we suspected a higher interstitial concentration for the zone melted crystals. An analysis was made of the gas in the system before, during, and after three successive zone melting passes on the same specimen. The specimen was of the same niobium used to grow crystals with resistivity ratios exceeding 800, and had been given a preliminary pass in an atmosphere of 5×10^{-5} torr of oxygen at a zone speed of 2.3 mm/min. A zone speed of 0.85 mm/min. was used for all three passes which were made at the pressured indicated in Table III. These pressures are about twice as high as usual for Nb crystals grown in this system because the residual gas analyzer attachment was not baked and the sublimation unit was not used.

The residual gas analyzer was a standard mass spectrometer type with magnetic deflection. A mass spectrum is produced with peaks at integral values of the mass to charge ratio (m/e) ranging from 12 to 200 as shown in Fig. 3. With proper calibration, a fragmentation pattern can be obtained for each gas giving relative peak heights at values of (m/e) corresponding to multiply charged ions. Unfortunately, the high temperatures and intense electric field near the molten zone alter the fragmentation pattern considerably. In addition, peak heights

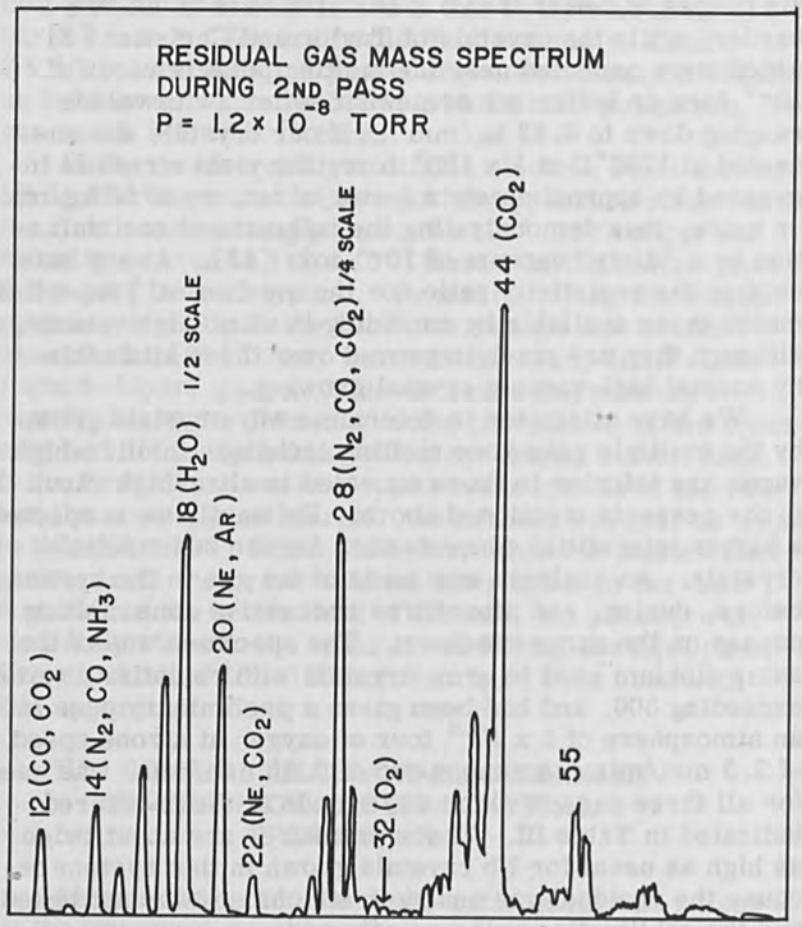

Figure 3. A typical residual gas spectrum. This particular example was made during the second pass and serves to indicate the complexity of the data. Beyond m/e 40, peaks overlap and spikes similar to those on the peaks near m/e 55 occur. The peaks are labelled in order of greatest contribution where more than one species contributes to a peak. This spectrum indicates only the atmospheric environment of the molten zone and is not characteristic of its outgassing characteristic which may be obtained only by detailed comparison with spectra made before and after a pass as explained in the text.

are not directly proportional to total pressure since the speed of the ion pump varies with the gas species and partial pressures. Thus we shall only be able to give a qualitative indication of the outgassing characteristics of the molten zone.

The major constituents of the residual gas are H_2O, N_2, CO, CO_2, H_2, and some organic compounds. Also present are He, Ne, and A, but we shall not be concerned with them since they are probably regurgitation products from the pump rather than from the molten zone. Only a negligible amount of O_2 is present. The major constituents contribute to peaks at m/e 12 (CO and CO_2), 14 (CO and N_2), 18 (H_2O base peak), 28 (N_2 base peak and CO base peak), and 44 (CO_2 base peak). Since both CO and N_2 have base peaks at m/e 28, it was necessary to observe the behavior of peaks at m/e 12 and 14 in order to determine their relative variation with respect to each other. The behavior of these peaks is shown in Table II which gives peak heights relative to the height of the peak at m/e 28 under various conditions.

The system was baked at 140°C for several hours and allowed to pump overnight to a pressure of 5.5×10^{-9} torr before the first pass was made. During the first pass, the pressure increased to 2×10^{-7} torr. The absence of oxygen implies that part of the peak at m/e 12 may be due to C which does not result from the ionization of CO or CO_2 and, in fact, the relative decrease of the CO_2 peak during the first pass indicates an excess of CO which implies again excessive carbon. It appears, however, that the outgassing of N_2 is mainly responsible for the increase in pressure of the two orders of magnitude during the first pass, since the peak at 14 and 28 both show a relative increase.

Some water is baked out of the system during the pass which accounts for an initial rise and an eventual decay of the relative partial pressure of H_2O.

Gettering by the Nb film on exposed surfaces is another factor which complicates the fragmentation pattern and has been ignored. During the second pass, the pressure rose to 1.2×10^{-8} torr. More water is baked out of the system though not so much as in the first pass.

Table II. Relative peak heights for peaks at (m/e) 12, 14, 18, 28, 44, based on height of peak at (m/e) 28 as a function of number of passes.

PASS NO. 1	P(torr)	12	14	18	28	44
Before	5.5×10^{-9}	0.1	0.02	1.3	1	0.6
During	2×10^{-7}	0.06	0.06	0.7	1	0.4
After	3×10^{-9}	0.12	0.025	1.5	1	0.6
Long After	2×10^{-9}	0.06	0.03	0.6	1	0.4
PASS NO. 2						
Before	3.7×10^{-9}	0.08	0.04	0.7	1	0.5
During	1.2×10^{-8}	0.055	0.07	0.5	1	0.4
After	2.7×10^{-9}	0.10	0.03	0.8	1	0.7
PASS NO. 3						
Before	3×10^{-9}	0.09	0.04	0.06	1	0.6
During	3.5×10^{-9}	0.12	0.04	0.6	1	0.7
After	1.2×10^{-9}	0.12	0.03	0.6	1	0.6

N_2 still appears to be the major out-gassing product of the molten zone, although the amount of carbon relative to oxygen appears to decrease. The behavior implies that an equilibrium state is being approached which depends on the ultimate pressure of the vacuum system. The rate of approach to this equilibrium state, however, must depend on the zone speed, recontamination effects, and the pumping speed of the system in the vicinity of the electron gun.

There is only a slight rise in pressure during the third pass and the stability of the peak at m/e 14 implies that the N_2 is not responsible. The slight rise in the relative partial pressure of the CO_2 peak (m/e 44) indicates that the C has been reduced sufficiently to allow the outgassing of CO_2 instead of CO or C as in previous passes. We can, however, conclude only that the approach to equilibrium is proceeding at a slower rate and not that we are actually on the verge of

achieving this state. At any rate, the major contaminants are C, O and N and at least the concentration of C and N is reduced with each of three successive passes. The reduction of the absolute rise in pressure for each successive pass would indicate also a reduction in the concentration of oxygen.

It is possible that the approach to a state of equilibrium by uniform annealing of a specimen unconstricted by a filament and focussing shields accounts for the difference in quality between our crystals and those produced by Taylor and Christian [3] and that only with a very large number of passes can this state be achieved using the zone-melting technique.

METALLIC IMPURITIES

Many impurities will not evaporate from the molten zone and remain in the specimen. One such, which is most difficult to remove, is tantalum in niobium. Previously, resistivity measurements were reported which suggested the possibility of zone-refining effects for this case [1]. A subsequent neutron activation study [14] has shown that zone refining is possible, as the segregation coefficient for Ta in Nb is about 1.4. However, due to the very low diffusion coefficient in the liquid (about 4×10^{-4} mm^2/sec) very little zone refining occurs, even at zone rates as low as 2.7 mm. per hour [14], for an unstirred zone. Consequently, Ta and probably other metallic impurities should be uniformly distributed in most cases, but stirred zones offer the possibility of further purification.

One possible source of metallic contamination is the electron gun itself; the hot filament, which may in many cases be bombarded heavily by positive ions might contribute tungsten to the molten zone. Mitchel et al [9] report that their six-pass material had a much higher (of the order of 1000 ppm) tungsten content than the starting material; Taylor and Christian [3] note that five-pass material had an unusually high yield point even after annealing and also point out this possibility. It has been our experience, however, that such contamination can occur only under unusual circumstances as when a filament melts

through in the presence of a molten zone. In such a case the tungsten content of niobium has been increased an order of magnitude. Under usual conditions, however, it appears that metal from the zone coats the filament. The filament is usually below the melting point of the specimen and tungsten has a vapor pressure at such temperatures about three orders of magnitude less than that of the metal film coating it. In order to investigate this possibility, however, two niobium crystals were grown under similar conditions but one with an intentionally optically shielded filament. Table III shows the results of chemical analysis for tungsten in the two specimens after one, two, three, and four passes.

Table III. Tungsten Content as a Function of the Number of Passes

Starting Material: 75 ppm

	Direct Gun	Indirect Gun
After 1 pass	68	62
2 passes	87	93
3 passes	79	71
4 passes	77	72

REFERENCES

1. C. S. Tedmon, Jr. and R. M. Rose, Proc. First Int. Conf. Electron and Ion Beam Science and Technology, R. Bakish, Editor, Wiley, p. 521, 1965
2. T. F. Stromberg and C. A. Swenson, Phys. Rev. Letters 9, 370 (1962).
3. G. Taylor and J. W. Christian, Acta Met. 13, 1216 (1965).
4. D. P. Seraphim, J. I. Budnick, and W. B. Ittner III, Trans. Met. Soc. AIME 218, 527 (1960).
5. W. DeSorbo, Phys. Rev. 132, 107 (1963).
6. C. S. Tedmon, Jr., R. M. Rose, and J. Wulff, Trans. Met. Soc. AIME 230, 1733 (1964).

7. J. R. Cost and C. A. Wert, Acta Met. 11, 231 (1963).
8. C. S. Tedmon, Jr., R. M. Rose, and J. Wulff, Metallurgy of Advanced Electronic Materials, G. F. Brock, Editor, Interscience, p. 35, 1963.
9. T. E. Mitchell, R. A. Foxall, and P. B. Hirsch, Phil. Mag. 8, 1895 (1963).
10. R. A. Pasternack and R. Gibson, Acta Met. 13, 1031 (1965).
11. R. W. Power and M. V. Doyle, J. App. Phys. 30, 514 (1959).
12. J. P. Pemsler, J. Electrochem. Soc. 108, 744 (1961).
13. F. H. Cocks, ScD. Thesis, Mass. Inst. of Tech., Cambridge, Mass., Aug. 1965; Dept. of Metallurgy.
14. F. H. Cocks, R. M. Rose, and J. Wulff, J. Less-Common Metals 10, 157 (1966).

Electron Beam Floating - Zone Refining of Niobium*

R. E. Reed

Solid State Division, Oak Ridge National Laboratory
Oak Ridge, Tennessee

INTRODUCTION

A great deal of interest has been shown in the properties of niobium. Such properties as high melting point, low vapor pressure, moderate density, good fabricability, low ductile-to-brittle transition temperature, and low thermal-neutron absorption cross section, make this metal attractive for high temperature and nuclear reactor applications. Some of these properties, particularly mechanical properties, depend markedly upon the purity of the metal. This investigation was initiated to evaluate the electron beam floating zone refining technique as a purification method for niobium.

Several investigators have utilized electron beam floating zone refining as a method for preparing pure niobium single crystals for mechanical testing. [1-7] The purity of these single crystals was evaluated using resistance ratios, hardness measurements, some chemical analyses, and the resolved shear stress for yielding. However, most investigators have generally used the electron beam floating zone technique as a convenient method to obtain pure single crystals of niobium and have not tried to identify the purification mechanisms that may be operating. This paper describes a study utilizing resistance ratios, extensive chemical analyses, and mechanical properties

*Research sponsored by the Research Materials Program for the U.S. Atomic Energy Commission under contract with the Union Carbide Corporation.

to assess the importance of various purification mechanisms in the electron beam floating zone refining of niobium.

EXPERIMENTAL PROCEDURE

A. Material Sources

The niobium used in this study came from two sources. One, a 1 1/8 in. diameter rod, 3 feet long was purchased from Wah Chang Corporation. This rod had been formed from an electron beam melted 3 inch diameter ingot (Heat No. 31831). The as-received rod was cold swaged down to 0.193 dia. rod for zone refining. Second, fifty pounds of niobium D3 granules from Lot No. 663 was purchased from DuPont Corporation. Arc melting with a tungsten tipped non-consumable electrode was used to drop cast the niobium granules into a 5/8 in. dia. water cooled copper mold about 6 in. long. Unfortunately, a tantalum starting peg was used to start the arc. Both tantalum and tungsten impurities were increased during this process. These small ingots were then cold swaged down to 0.193 inch diameter rod for zone refining. Table 1 gives the vendor's analysis and the ORNL analysis for each starting material.

B. Electron Beam Floating Zone Refining Equipment

Two different zone refining systems were used. The first which will be designated system LB was based on an electron beam floating zone module (Model No. 4-EBZ-6000) purchased from Material Research Corporation. The scanner consisted of a stationary specimen holder and an electron beam gun mounted on a traveling stage that moved the gun parallel to the vertical specimen rod axis. The position of the bottom specimen holder was adjustable from outside the vacuum chamber. The specimen chamber consisted of a glass bell jar and aluminum receiver section resting on a stainless steel base plate. Viton O-rings and gaskets were used in all the vacuum seals. A 4-inch oil diffusion pump with a water baffle and liquid nitrogen cold trap gave a pumping speed of about 150 liters/sec.

Table 1. Chemical Analysis of Niobium Starting Material in Weight ppm

Element	Wah Chang Ht 31831		DuPont Lot 663	
	Vendor Analysis	ORNL Analysis	Vendor Analysis	ORNL Analysis
Al	<20	1		1
B	<1	.01		.1
Ca		.2		5
Co	<10	.2		
Cr	<20	10	<30	4
Cu	<40	4		<.1
Fe	<50	5	80	7
Hf	<80	1		<.6
Mg	<20	3		3
Mn	<20	<.1		2
Mo	<20	2		
Ni	<20	2	<30	21
Pb	<20	1.3		1.2
Si	<20	10[4]		10[4]
Sn	<10	1.5		1.5
Ta	<500	3673	230	225(296)[1]
Ti	<40	.7	<50	.7
V	<20	.2		.03
W	245	2273	<50	54(73)[1]
Zr	<100	27		<.2
C	30	10[2]	<10	55[2]
O_2	110	110[2]	34	70[2]
N_2	35	60[2]	4	7[2]
H_2	4.4	4[2]		1[2]

[1] Analysis taken on material after arc melting to consolidate granules.
[2] Analysis taken from the unmelted handle of one pass rods.
[3] Average of Neutron Activation Data for one pass rods.
[4] The Si analysis on the spark source mass spectrometer was not taken as a true value since there were several glass components in the spark chamber which could act as sources of Si. It is probably much less than this number.

at the entrance to the specimen chamber. The base pressure obtained in the bell jar was usually 2×10^{-7} torr. The pressure during zoning ranged from $1\text{-}2 \times 10^{-6}$ torr for the first zoning pass to about $3\text{-}5 \times 10^{-7}$ torr after about the fourth pass. This was attributed to decreasing amount of outgassing from the specimen, scanner, and specimen chamber as the zone refining progressed.

The electron beam gun was a work accelerated type with an annular wire filament as the electron source. The gun design consisted of grounded tantalum focusing plates 8 mm apart, a plate aperture diameter of 14.5 mm, and a 23 mm diameter annular filament of 0.51 mm diameter tungsten wire. The high voltage supply had a voltage output variable to 5 KV and current to 400 ma. The emission current in the electron gun was maintained at a pre-set constant value by controlling the filament power.

The second system which will be designated system BB was a completely bakeable, high vacuum electron beam floating zone refiner based upon a scanner and power supply (Model EBZ-94) also purchased from Materials Research Corporation. The general features of the scanner were the same as that of system LB except that it was somewhat larger and was designed for low outgassing. The specimen chamber consisted of a 18 inch diameter water cooled stainless steel bell jar 20 inches high mated to a receiver section with a Wheeler flange using a copper wire crush gasket. All feed-through accessories were bakeable and flanged to the receiver using copper gaskets. A liquid nitrogen trapped, 10 inch stainless steel oil diffusion pump backed with a liquid nitrogen trapped 4 inch oil diffusion pump and a 425 liters/min. mechanical pump, delivered a pumping speed of 1750 liters/sec. at the entrance to the specimen chamber.

The specimen chamber was generally baked at 400° C for 16 hours prior to zoning a specimen. The base pressure in the chamber was generally about 5×10^{-9} torr. The pressure during zoning ranged from 2×10^{-7} to 5×10^{-8} torr during the first pass depending upon the starting material. At about the fourth pass the pressure was $6\text{-}8 \times 10^{-9}$ torr. It was noticed that after cooling down the specimen chamber after zoning the base pressure often got down to $1\text{-}2 \times 10^{-9}$ torr.

The electron beam gun design used in this unit was identical to that used in system LB.

C. Zoning Procedures

The swaged (4.8 mm diameter) niobium rod from both sources was electron beam floating zone refined at a zoning speed of 8-10 cm/hr. With the electron gun configuration described previously, the molten zone was about 3.5 mm long at a power level of 280 watts. The filament was kept at as low a temperature as possible to minimize W contamination. At a beam voltage of 4000V and a beam current of 70 ma the filament appeared much cooler than the molten zone. The Wah Chang material was zoned 1, 2, 4, 6, and 12 passes in system LB. This resulted in zoned single crystal lengths approximately 19 cm. long. In addition, 1 and 4 pass rods of the Wah Chang material was zoned in system BB. This resulted in zoned lengths of about 26 cm. Rods of the DuPont niobium were zoned 1 and 4 passes in both systems.

In addition, zone refined single crystal niobium rods were seeded so as to produce rod axis orientations at a single orientation near the center of the stereographic triangle where the Schmid factor on the $(\bar{1}01)$ [111] slip system has its maximum value of 0.5. These were zoned in system LB to produce 1, 2, 4, 6, and 12 pass single crystals from both material sources.

All rods were zoned from bottom to top and the rod was melted through at the end of the last pass.

D. Resistance Ratios

The as-zoned rods were first prepared for resistance ratio measurements along the zoned length. Lengths of 0.51 mm diameter platinum wire about 3 cm long were beaded on one end by melting it in a small gas torch flame. The beaded end of these wires were then spot welded to the zoned rod using a very light contact pressure. Copper wire current and voltage leads were then soft soldered to the platinum taps. The position of these taps are shown in Fig. 1 which is a schematic drawing of a typical as-zoned rod from system LB. Since niobium has a superconducting transition temperature of 9.2°C, the low temperature resistance measurements were made in a liquid

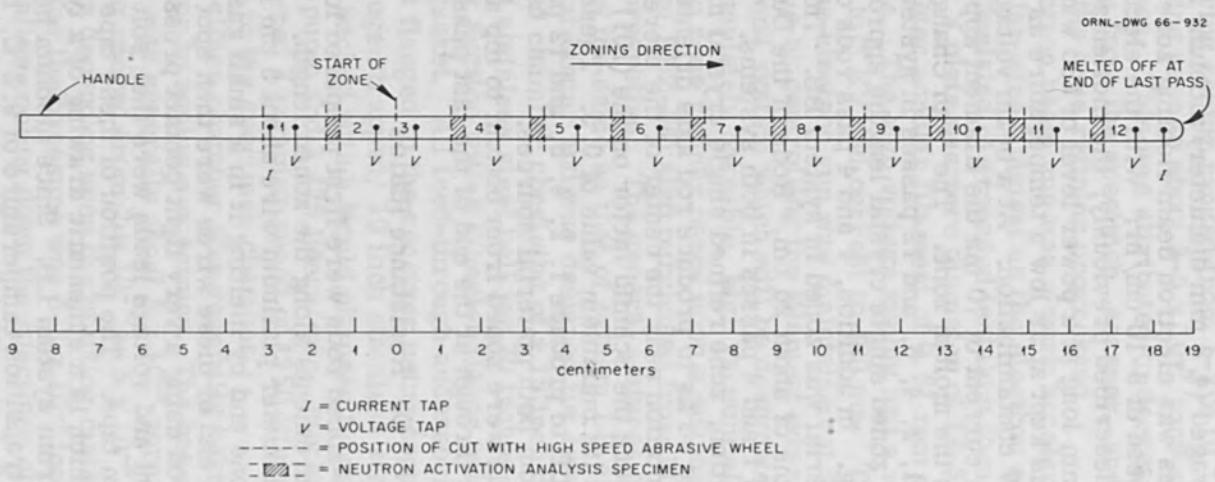

Figure 1. Schematic of a Typical Zone Refined Niobium Rod showing Sampling Procedure for Chemical Analysis. Note: Spark source mass spectrometric, Leco conductometric, and vacuum fusion analyses were made on the numbered sections as described in the text.

hydrogen bath (20.2°K). The high temperature resistance measurements were made in a mineral oil bath at room temperature (296°K). The resistance ratios were calculated as the resistance at room temperature divided by the resistance at liquid hydrogen temperature.

E. Chemical Analysis

After the resistance ratios were determined, the rod was next cut into sections as shown in Fig. 1. The cuts were made using a high speed abrasive cut-off wheel with water coolant. Small discs 3 mm long, 4.8 mm in diameter were cut from the center of each section which had a resistance ratio measurement. Each remaining section (numbered in sequence in Fig. 1) was beveled on the end toward the top of the rod where it had been melted off at the end of the last pass. All of the sections were then given a deep chemical polish in a solution of nitric acid (70%) and hydrofluoric acid (48%) mixed in the proportions of 3:2.

The discs were used for neutron activation analyses for Ta and W impurity. The other sections were first used to get spectrographic analyses for all metallic impurities using a spark source mass spectrometer (Associated Electrical Industries Model MS 7). These analyses were taken by striking an arc between adjoining sections taken from the rod. Thus mass spectrographic analyses were taken at essentially the same position as the neutron activation analyses. In fact, the W analysis as determined by neutron activation was used as an internal standard for the determination of the metallic impurities at each spark position along the zoned length. Next, each section was again chemically polished and approximately two-thirds of each section used for a carbon analysis and the other third for oxygen, nitrogen, and hydrogen analysis. Carbon content was measured by the Leco conductometric method. Oxygen, nitrogen, and hydrogen contents were determined using the vacuum fusion technique with a platinum bath at 2000°C.

F. Tensile Specimens

The seeded zone refined niobium single crystal rods that were used for tensile specimens were not sampled for chemical analysis. It was assumed that these rods would be similar in purity to those prepared in a duplicate procedure and analyzed. These rods were cut into 3.8 cm long sections using the abrasive wheel. The sections were then centerless ground to produce a gage section 1.9 cm long and 2.160 mm in diameter with a taper of less than 0.005 mm. After grinding, about 500 microns were removed from the diameter by chemical polishing in the $HF-HNO_3$ solution described previously. This was sufficient to eliminate all signs of cold work in the Laue backrefection patterns. Furthermore, the uniformity of orientation was checked by traversing the sample axially in the X-ray beam and no asterism or splitting of the Laue spots could be detected.

The perfection of some seeded one pass rods of Wah Chang niobium grown in system LB was studied using etch pitting, Berg-Barrett X-ray topographs, Borrmann anomalous X-ray topographs, [16] and double crystal X-ray spectrometry. The dislocation density of the as-zoned rods ranged from 10^4 - 10^6 cm^{-2}. The majority of the dislocations were in sub-boundaries. The misorientation of these sub-boundary walls were generally less than 180 seconds. The largest sub-boundary misorientation found was 8-10 minutes. This work will be reported in more detail in another paper. [8]

The tensile specimens were pulled in tension at room temperature at a strain rate of 1.8×10^{-4} sec^{-1}. A table model Instron tensile testing machine was used. The orientation of the tensile axis as a function of strain was determined for one pass Wah Chang niobium by taking back reflection Laue X-ray patterns every 5 or 10% tensile strain increment. Slip line observations were also made at each tensile strain increment.

RESULTS

A. Resistance Ratios

The resistance ratios of the DuPont and Wah Chang starting materials were 40 and 28 respectively. Table 1 shows that the Wah Chang material had 190 ppm more metallic impurities and 50 ppm more interstitial impurities than the DuPont material. This apparently was sufficient to cause the difference.

Resistance ratios plotted as a function of zoned length for 1, 2, 4, 6 and 12 pass Wah Chang material zone refined in system LB, are shown in Fig. 2. These data indicated that the finish end of the zoned length was slightly purer than the start end. The first pass resulted in the greatest resistance ratio change per pass. Subsequent passes had a continual decreasing effect upon the amount of increase in the resistance ratio.

The DuPont niobium was also zone refined in system LB for 1 and 4 passes. The resistance ratios measured along the zoned length for this material, compared to the 1 and 4 pass Wah Chang niobium are shown in Fig. 3. The DuPont niobium had much higher overall resistance ratios and also exhibited a greater variation in resistance ratio from the start to the finish of the zoned length. The finish end again had a higher ratio.

The vacuum existing in the specimen chamber during zone refining also had an effect upon the final resistance ratio. Figure 4 is a plot of resistance ratio versus zone length for Wah Chang niobium zone refined 1 and 4 passes in systems LB and BB. The high vacuum system obtained a larger increase in the resistance ratio per pass for the same material.

B. Chemical Analyses

1. Metallic Impurities

The major metallic impurities in both starting materials were Ta and W. Neutron activation analyses for Ta and W in the Wah Chang niobium zone refined in system LB gave the results tabulated in Table 2. For all rods tested, there was no significant variation of the tantalum

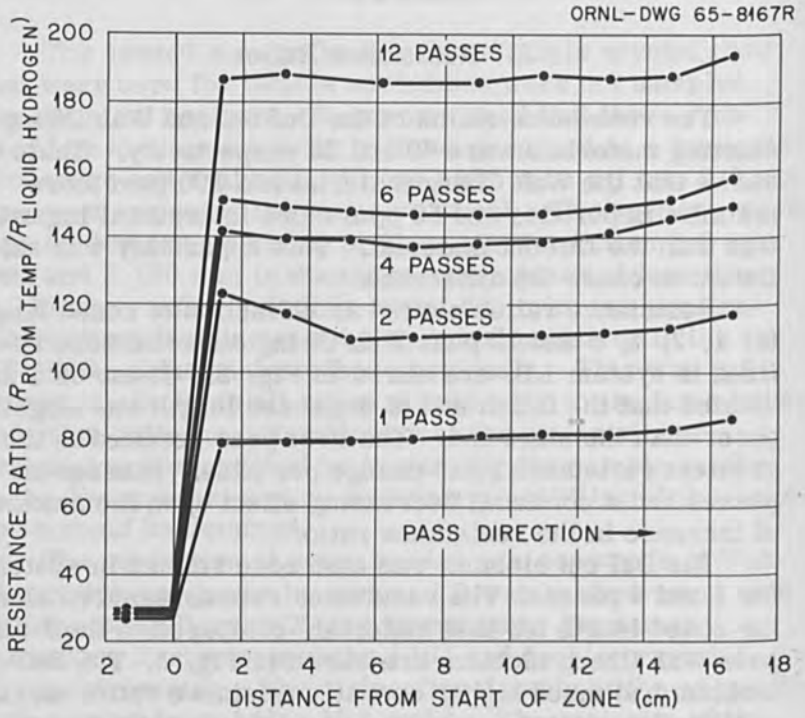

Figure 2. Resistance Ratio along a Niobium Single Crystal Rod as a Function of the Number of Floating Zone Passes. Source: Wah Chang Corp.; zone speed: 10 cm/hr; diameter: 4.8 mm (nominal); system: LB.

or tungsten content along the zone length. In addition, there was no difference in tantalum content as a function of number of passes. The arithmetic mean ($\bar{X}$) of the tantalum contents reported for all discs from the Wah Chang niobium was 367, 369, and 367 wt. ppm for 1, 6, and 12 pass rods respectively. However, there is some indication of a slight tungsten impurity increase as a function of number of passes possibly due to contamination from the electron gun tungsten filament. For this case, the arithmetic mean ($\bar{X}$) for tungsten content was 227, 229, and 242 wt. ppm for 1, 6, and 12 pass material respectively. Thus there was about a 6% increase in the amount

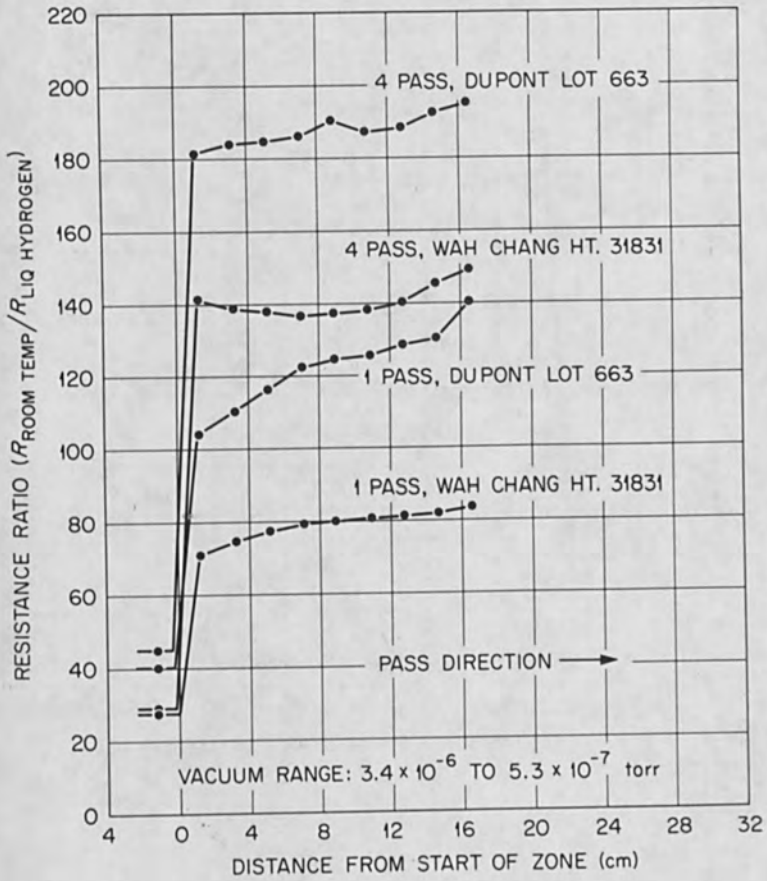

Figure 3. Resistance Ratio along a Niobium Single Crystal Rod as a Function of the Starting Material. Zone speed: 10 cm/hr; diameter: 4.8 mm (nominal); system: LB.

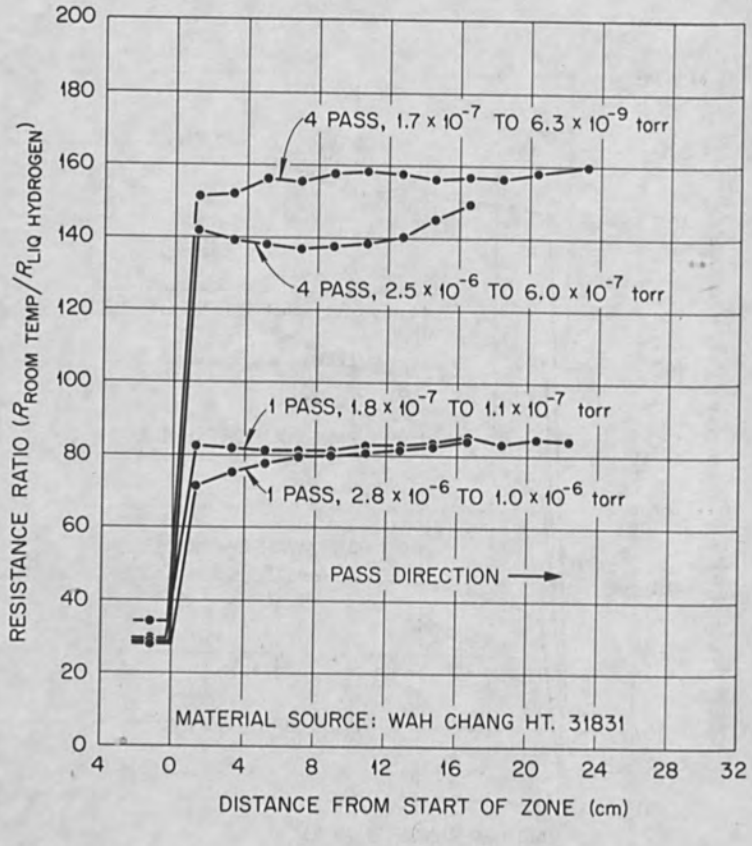

Figure 4. Resistance Ratio along a Niobium Single Crystal Rod as a Function of the Vacuum Level. Zone speed: 10 cm/hr; diameter: 4.8 mm (nominal).

Table 2. Neutron Activation Analyses for Ta and W in Wah Chang Niobium Zone Refined in System LB

	1 Pass		6 Pass		12 Pass	
Distance from start of zone (cm)	Ta (ppm)	W (ppm)	Ta (ppm)	W (ppm)	Ta (ppm)	W (ppm)
Handle	363	224	364	216	358	232
1.5	369	231	384	243	377	260
3.4	365	221	360	216	369	244
5.3	372	230	370	225	359	238
7.2	366	224	365	220	369	242
9.1	374	230	373	267	362	240
11.0	367	227	367	227	363	239
12.9	368	228	362	317	367	235
14.8	357	221	382	232	365	238
16.7	372	230	366	223	378	250
Mean ($\bar{X}$)	367	227	369	229	367	242
Std. Dev. (α)	4.7	3.7	7.7	15.1	6.5	7.7

of tungsten in the zoned refined rod after 12 passes. The same result was found for the Wah Chang niobium zoned in system BB. However, no significant W increase could be found between 1 and 4 pass material.

The neutron activation analyses for Ta and W in the DuPont niobium zone refined 1 and 4 passes in both systems also showed no significant variation along the zone length. There was no difference in Ta and W content as a function of number of passes (up to 4 passes). The results showed the DuPont niobium to have about 300 ppm Ta and 70 ppm W.

The only other metallic impurities above 2 ppm in the Wah Chang starting material were Cr, Cu, Fe, Mg, and Zr. The first pass reduced all of these metallic impurities except Zr to below 1 ppm. There was no significant trend along the zoned length to indicate a zone refining action. However, the data for the Zr impurity did indicate a movement of Zr with the zone direction. In addition,

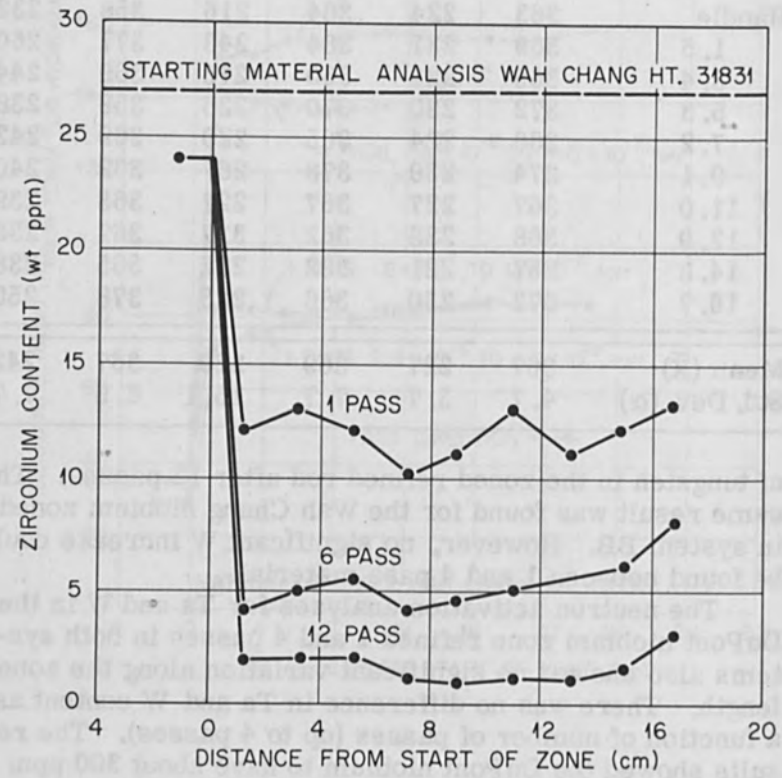

Figure 5. The Zirconium Content along a Niobium Single Crystal Rod as a Function of Number of Passes. Zone speed: 10 cm/hr; diameter: 4.8 mm (nominal). Note: This was data from a spark source mass spectrometer using the W 184 mass line as an internal standard.

each zoning pass lowered the overall Zr content of the niobium. Figure 5 is a plot of the Zr content along the zone length for 1, 6, and 12 pass Wah Chang niobium in system LB. This figure shows that after 12 passes the Zr content was reduced from 27 ppm to about 2 ppm with a slightly higher level of Zr at the finish end of the rod.

Other than Ta and W, the other metallic impurities above 2 ppm in the DuPont niobium were Ca, Cr, Fe, Mg, and Ni. After one pass of this material in system BB, all of these impurities were below 1 ppm. There was no significant trend along the zoned length for any of the metallic impurity analyses.

2. Interstitial Impurities

The vacuum fusion analyses for hydrogen in the Wah Chang niobium zoned in system LB showed no significant variation of hydrogen content either along the zoned length of individual rods or among zoned rods which were zone refined 1, 6, or 12 passes. The arithmetic mean ($\bar{X}$) for all analyses was 4.0 wt. ppm with a standard deviation of 1.1 wt. ppm.

The vacuum fusion results for oxygen and nitrogen contents in the Wah Chang niobium zone refined in system LB are best summarized in Figs. 6 and 7. Figure 6 is a plot of the oxygen content in wt. ppm as a function of distance along the rod for 1, 6, and 12 pass material. There was a marked drop of oxygen content from $\overline{X}$ = 116 wt. ppm in the handle to a level of $\overline{X}$ = 30 wt. ppm for the one pass rod. The arithmetic mean ($\bar{X}$) of the oxygen contents in the zoned region of the 6 and 12 pass rods were 25 and 24 wt. ppm respectively. There was such scatter in the results that no variation in oxygen content along the zone length could be found. In fact, some of the oxygen analyses were not used in calculating the arithmetic means since they were so far from the general trend of the curves. However, there was the indication that the first pass greatly reduced the oxygen content and subsequent zoning passes reduced this oxygen level only slightly.

The nitrogen content analyses are shown in Fig. 7. In this figure, the nitrogen content in wt. ppm is plotted versus distance along the zoned rod for 1, 6, and 12 pass

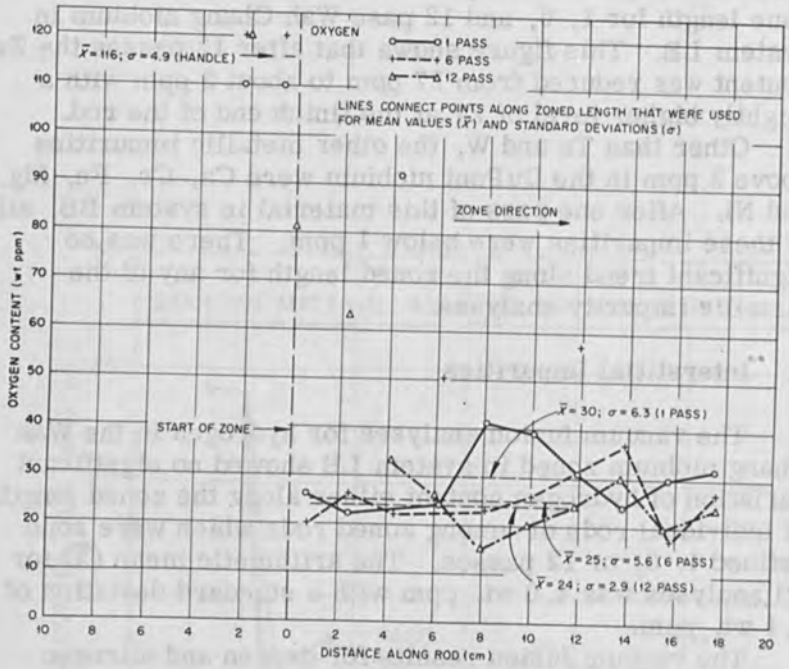

Figure 6. Oxygen Content along a Niobium Single Crystal Rod as a Function of the Number of Floating Zone Passes. Source: Wah Chang Corp.; zone speed: 10 cm/hr; diameter: 4.8 mm (nominal); system: LB.

material. This impurity behaved in a manner similar to that of oxygen. The first zoning pass decreased the nitrogen content from $\overline{X}$ = 61 wt. ppm in the handle to $\overline{X}$ = 24 wt. ppm. Increasing the number of passes to 6 and 12 decreased the nitrogen content to $\overline{X}$ = 9 and 5 wt. ppm respectively. In this case, increasing the number of passes decreased the nitrogen content quite clearly although the scatter still prevented assigning a significant variation of nitrogen along the zone length.

The carbon analyses made by the Leco conductometric method showed that for the Wah Chang niobium zone refined in system LB there was no significant variation of

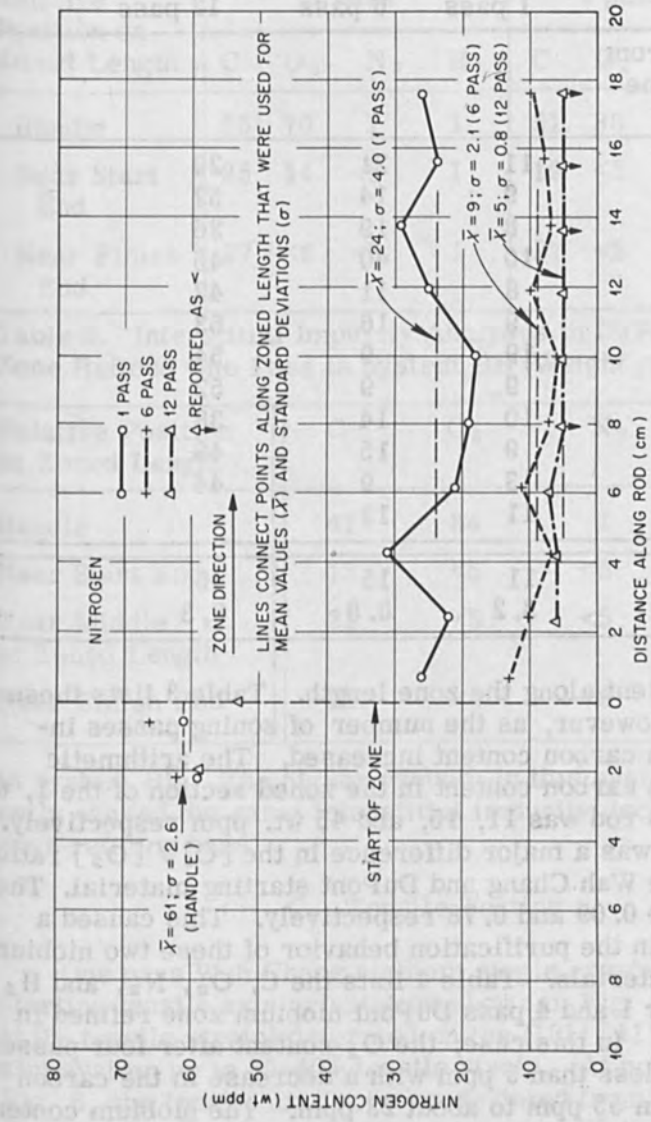

Figure 7. Niobium Content along a Niobium Single Crystal Rod as a Function of the Number of Floating Zone Passes. Source: Wah Chang Corp.; zone speed: 10 cm/hr; diameter: 4.8 mm (nominal); system: LB.

Table 3. Leco Conductometric Analyses for Carbon in Wah Chang Niobium Zone Refined in System LB (Weight ppm)

	1 pass	6 pass	12 pass
Distance from start of zone (cm)			
Handle	11	21	29
Handle	9	14	57
0.7	8	19	26
2.5	10	40	45
4.3	8	11	42
6.2	9	16	53
8.1	19	9	54
10.0	9	9	52
11.9	10	14	38
13.8	9	15	48
15.7	13	9	44
17.6	11	12	
Mean ($\bar{X}$)	11	15	45
Std. Dev. (α)	3.2	8.8	8.3

carbon content along the zone length. Table 3 lists these results. However, as the number of zoning passes increased the carbon content increased. The arithmetic mean of the carbon content in the zoned section of the 1, 6, and 12 pass rod was 11, 15, and 45 wt. ppm respectively.

There was a major difference in the $[C] / [O_2]$ ratios between the Wah Chang and DuPont starting material. These ratios were 0.09 and 0.78 respectively. This caused a difference in the purification behavior of these two niobium starting materials. Table 4 lists the C, O_2, N_2, and H_2 analysis for 1 and 4 pass DuPont niobium zone refined in system LB. In this case, the O_2 content after four passes dropped to less than 5 ppm with a decrease in the carbon content from 55 ppm to about 23 ppm. The niobium content also decreased to less than 5 ppm. Table 5 lists the C, O_2, N_2, H_2 analyses for the same material zoned one pass

Table 4. Interstitial Impurity Analyses in DuPont Niobium Zone Refined in System LB (Weight ppm)

Relative Position on Zoned Length	1 pass				4 pass			
	C	O_2	N_2	H_2	C	O_2	N_2	H_2
Handle	55	70	7	1	51	88	8	3
Near Start End	25	14	<5	1	19	<5	<5	<1
Near Finish End	27	<5	<5	1	27	<5	<5	2

Table 5. Interstitial Impurity Analyses in DuPont Niobium Zone Refined One Pass in System BB (Weight ppm)

Relative Position on Zoned Length	C	O_2	N_2	H_2
Handle	47	84	7	4
Near Start End	13	<5	<5	<1
Near Middle of Zoned Length	21	<5	<5	<1
Near Finish End	22	<5	<5	1

in system BB. The higher vacuum in this system apparently caused the same interstitial impurity decrease in one zone refining pass.

C. Tensile Testing

One pass Wah Chang niobium single crystals with a starting tensile axis orientation shown in Fig. 8 (position at 0% tensile strain) deformed on the $(\bar{1}01)$ [111] primary slip system up to 35-40% tensile strain. At point A on Fig. 8, the tensile axis rotation deviated from the predicted path after "overshooting" by some 8° the symmetry boundary where the conjugate slip system was expected to start operating. Also, at 35-40% tensile strain, slip lines

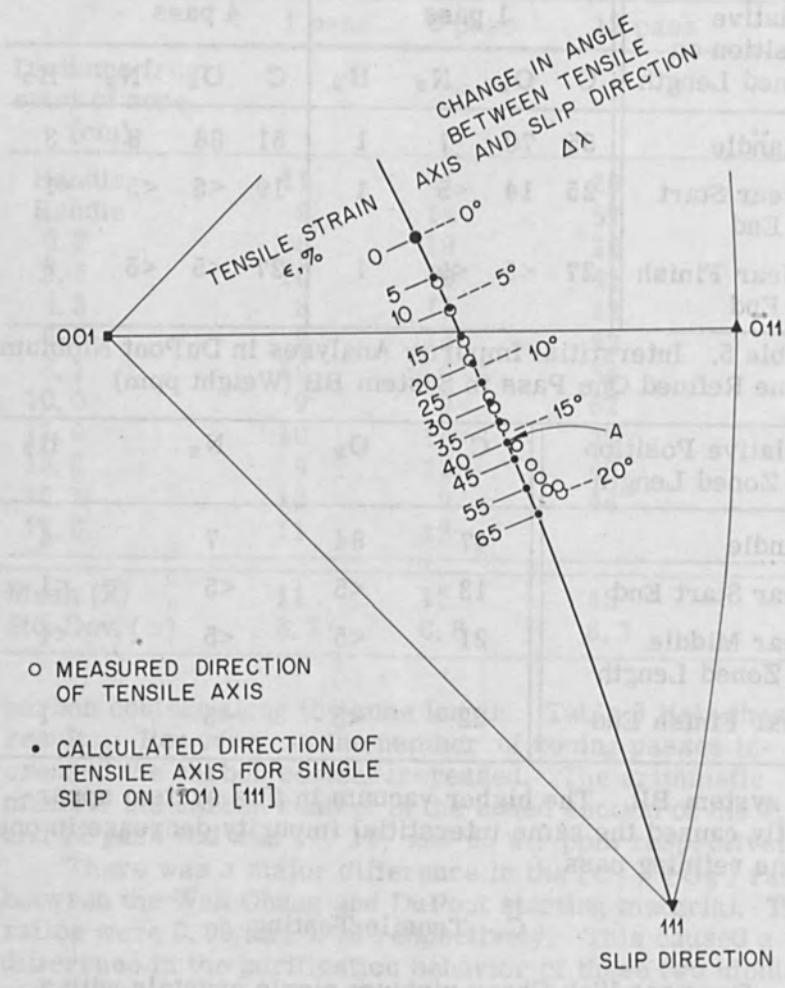

Figure 8. Rotation of the Tensile Axis Orientation as a Function of Tensile Strain for a Niobium Single Crystal. Source: Wah Chang Corp.; zone speed: 10 cm/hr; number of passes: 1; system: LB.

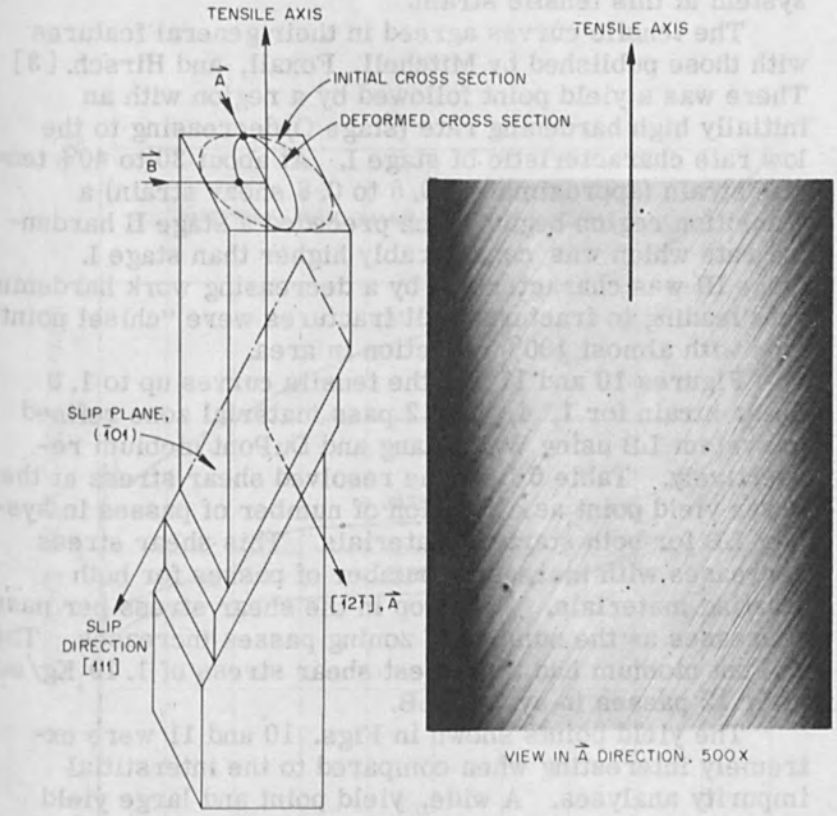

Slip Lines in Single Crystal Niobium After 30 % Extension

Figure 9. Slip Lines on a Niobium Single Crystal after 30% Tensile Strain. Source: Wah Chang Corp.; zone speed: 10 cm/hr; number of passes: 1; system: LB.

due to a second slip system began to appear on the specimen surface. Figure 9 is a photomicrograph of such a one pass Wah Chang niobium single crystal pulled to 30% tensile strain. There was no indication of slip on a second system at this tensile strain.

The tensile curves agreed in their general features with those published by Mitchell, Foxall, and Hirsch. [3] There was a yield point followed by a region with an initially high hardening rate (stage O) decreasing to the low rate characteristic of stage I. At about 30 to 40% tensile strain (approximately 0.6 to 0.8 shear strain) a transition region began which preceded a stage II hardening rate which was considerably higher than stage I. Stage III was characterized by a decreasing work hardening rate leading to fracture. All fractures were "chisel point" type with almost 100% reduction in area.

Figures 10 and 11 are the tensile curves up to 1.0 shear strain for 1, 4, and 12 pass material zone refined in system LB using Wah Chang and DuPont niobium respectively. Table 6 lists the resolved shear stress at the lower yield point as a function of number of passes in system LB for both starting materials. This shear stress decreases with increasing number of passes for both starting materials. The drop in the shear stress per pass decreases as the number of zoning passes increases. The DuPont niobium had the lowest shear stress of 1.19 Kg/mm^2 after 12 passes in system LB.

The yield points shown in Figs. 10 and 11 were extremely interesting when compared to the interstitial impurity analyses. A wide, yield point and large yield drop with an extensive stage O (from a stream strain of 0.05 to 0.35 in Fig. 10) was characteristic of the Wah Chang 1 pass niobium single crystals. The 12 pass Wah Chang niobium single crystal tensile curve exhibited a much sharper yield point and a smaller yield drop with a shorter stage O (Fig. 10). The chemical analyses were 11 ppm C, 30 ppm O_2, 24 ppm N_2 for the 1 pass niobium and 45 ppm C, 24 ppm O_2, 5 ppm N_2 for the 12 pass. This suggests that a sharp yield point and short stage O may be associated with the carbon impurity while the wide yield point and extensive stage O are due to oxygen and/or nitrogen.

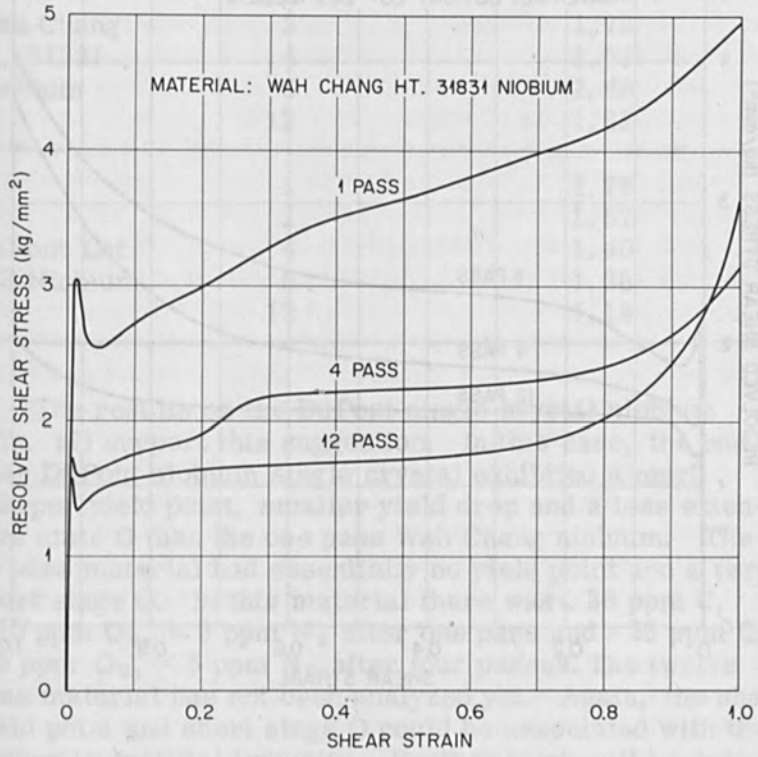

Figure 10. Resolved Shear Stress--Shear Strain Curves for the Tensile Deformation of Niobium Single Crystals as a Function of the Number of Floating Zone Passes. Source: Wah Chang Corp.; zone speed: 10 cm/hr; system: LB. Note: The curves are only plotted to a shear strain of 1.0.

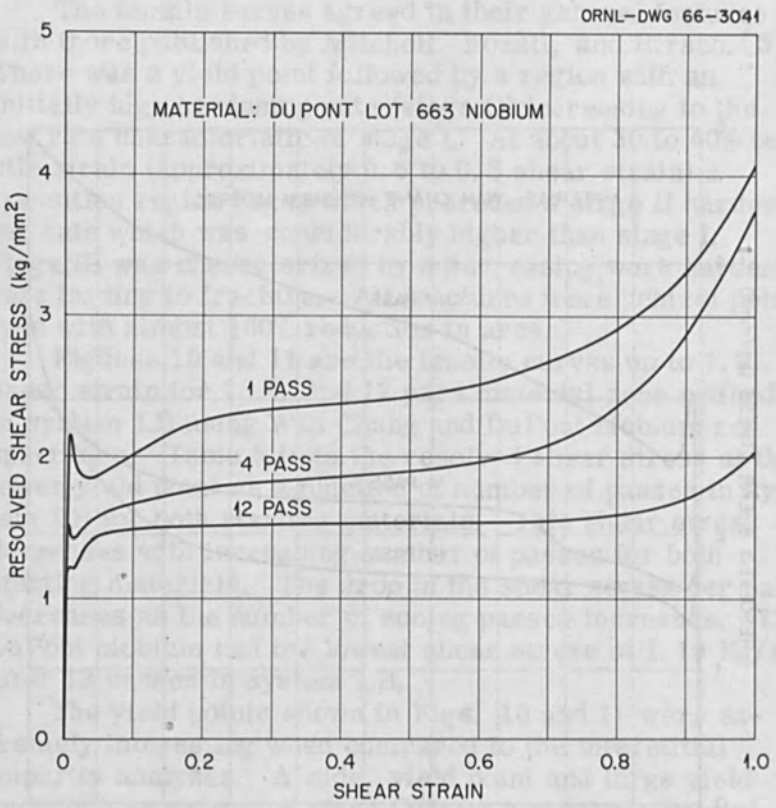

Figure 11. Resolved Shear Stress--Shear Strain Curves for the Tensile Deformation of Niobium Single Crystals as a Function of the Number of Floating Zone Passes. Source: DuPont Corp.; zone speed: 10 cm/hr; system: LB. Note: The curves are only plotted to a shear strain of 1.0.

Table 6. Resolved Shear Stress at the Lower Yield Point for Niobium Zone Refined in System LB

Starting Material	Number of Zone Refining Passes at 10 cm/hr	Resolved Shear Stress at Lower Yield Point in Kg/mm^2
Wah Chang Ht. 31831 Niobium	1	2.48
	2	1.96
	3	1.72
	4	1.57
	6	1.49
	12	1.32
DuPont Lot 663 Niobium	1	1.79
	2	1.57
	4	1.40
	6	1.28
	12	1.19

The results on the DuPont single crystal niobium (Fig. 11) support this suggestion. In this case, the one pass DuPont niobium single crystal exhibited a much sharper yield point, smaller yield drop and a less extensive state O than the one pass Wah Chang niobium. The 12 pass material had essentially no yield point and a very short stage O. In this material there was ~ 26 ppm C, ~ 10 ppm O_2, < 5 ppm N_2 after one pass and ~ 23 ppm C, < 5 ppm O_2, < 5 ppm N_2 after four passes. The twelve pass material has not been analyzed yet. Again, the sharp yield point and short stage O could be associated with the carbon interstitial impurity. Further work will be done on this point.

DISCUSSION

The present investigation generally agrees with the previously published results on the purification of niobium by electron beam floating zone refining. Votava, [1] after electron beam floating zone refining niobium from Murex Company at a zone velocity of 84 cm/hr in a maximum

vacuum of 3×10^{-6} torr, concluded that the purification largely takes place by vaporization of impurities with only a small zone refining effect. This was largely based on resistance ratios (R 273°K/R 77°K) taken on the zoned length. There was a slight indication that the finish end of the zone was purer than the start. The same trend was found in the present investigation. However, the reported resistance ratios (R 273°K/R 77°K) of Votava [1] (3.86, 5.05, 5.15, 5.10 for 0, 8, 16, and 27 passes respectively) indicated that the 27 pass material was more impure than the 16 pass rod. Since niobium metal was used throughout for the electron gun construction, this contamination must have been interstitial impurities.

A resolved lower yield shear stress of 2.6 Kg/mm^2 was reported by Votava for 3 pass (at 84 cm/hr) Murex niobium with a tensile axis orientation and tensile strain rate similar to the present investigation. A Vickers hardness number of 44-48 was also indicated. His gas analysis for this material was 0.2-1.5 ppm H_2, 12-17 ppm N_2, and 10-26 ppm O_2. No other analyses were given. This material compares with one pass Wah Chang niobium zone refined at 10 cm/hr in system LB. Here, the Vickers hardness number was 2.5 Kg/mm^2, and the gas analysis was 24 ppm N_2, 30 ppm O_2, and 4 ppm H_2.

The Murex niobium generally has a rather high carbon content (~ 10 ppm) [2, 9] and high Ta content (1200-3000 ppm) [3, 9] compared to the material sources used in this study. This could explain the difference between the flow stresses reported by Mitchell, Foxall, and Hirsch [3] and those given in Table 6. They reported values for the resolved shear stress at the lower yield point ranging from 3.5 to 1.8 Kg/mm^2 for 1 to 6 pass Murex niobium. This was obtained on material zoned in $<5 \times 10^{-6}$ torr vacuum at 30 cm/hr for all passes except the last one which was at 12 cm/hr. The tensile axis orientation was similar to that used in this study but the strain rate was lower (4.5×10^{-5} sec^{-1}). In addition, Mitchell, Foxall, and Hirsch [3] reported that after 6 passes the niobium picked up extensive Ta and W contamination from the electron gun while the O_2, N_2, and H_2 content decreased only slightly. No carbon analyses were reported.

It is unfortunate that the major metallic impurities that are generally found in niobium, namely Ta and W, are also the metallic impurities that cannot be removed from niobium by electron beam floating zone refining. The present investigation has shown that these two impurities did not vary along the zoned length and that Ta did not decrease with increasing number of passes. In addition, the W content increased slightly as the number of passes increased probably due to contamination from the tungsten filament in the electron gun. This occurred despite an effort to keep the tungsten filament considerably cooler than the molten zone in the niobium rod. The tantalum focusing plates evidently were not a source of tantalum contamination. It was noticed that the edges of the focusing plate aperture quickly became coated with niobium metal which possibly prevented the sputtering of Ta from this area by electron bombardment.

With the exception of the Zr impurity in the Wah Chang niobium and Ta and W as discussed above, all other metallic impurities were reduced to levels below 1 ppm in one zone refining pass at 10 cm/hr. In fact, the levels became so low that it was not surprising to find that no significant trend could be found in the spark source mass spectrometric data along the zone length. In the case of the Zr impurity in the Wah Chang niobium, the data (Fig. 5) suggested that the major mode of purification was still evaporation accompanied with a small zone refining effect which indicated that the impurity moved in the direction of the moving zone.

The data from the resistance ratio measurements (Figs. 2-4) indicated that a slightly purer metal generally existed at the finish end of the zoned length. Thus the small zone refining effect on the Zr impurity which would move the Zr to the finish end has little to do with the overall purification.

It is concluded that with the exception of Ta and W, the metallic impurities in niobium are removed mostly by evaporation to levels less than 1 ppm by the electron beam floating zone technique.

There was a good correlation between the resolved shear stress at the lower yield point and the resistance ratio of the niobium single crystals. The shear stress for yielding in

niobium is strongly influenced by the interstitial C, O_2, N_2, and H_2 impurity content. Therefore, it is reasonable to assume that the resistance ratio was also strongly influenced by the interstitial impurity content. The resistance ratios were generally constant with zoned length with a slightly higher ratio at the finish end (Figs. 2-4). This suggests that there was no significant trend in interstitial impurity content along the zoned length. The chemical analyses also indicated that this was probably so (Figs. 6-7, Tables 3-5).

However, the overall resistance ratio of a zoned length depended upon the purity of the starting material, the vacuum level during zoning, and the number of zone refining passes (Figs. 2-4). The overall impurity level of C, O_2, H_2, and N_2 also depended upon these variables (Figs. 6-7, Tables 3-5). The effect that these experimental variables have upon the purification mechanisms operating in the case of C, O_2, N_2, and H_2 impurities can be seen more clearly by relating them to more basic variables. These are as follows:

A. Time at a high temperature--This is directly related to number of passes and/or zoning velocities for a given electron gun design and beam power.

B. Partial pressures of C, O_2, N_2, and H_2 above the hot niobium metal--This is directly related to the total pressure in the specimen chamber during zoning. Also, it is related to the purity of the starting material if it is realized that outgassing from the niobium is a major part of the vacuum pumping load especially in the first few passes.

There are three probable purification mechanisms operating during the electron beam floating zone refining of niobium that account for the interstitial impurity level attained during the process. These mechanisms are:

1. The carbon monoxide and/or carbon dioxide reactions.

2. Attainment of equilibrium concentrations of O_2, N_2, and H_2 in the solid niobium adjacent to the molten zone.

3. Removal of O_2 from the solid niobium adjacent to the molten zone by the formation and volatilization of atomic oxygen and/or niobium suboxides.

The role of these purification mechanisms in the electron beam floating zone technique will be discussed separately.

1. The CO or CO_2 Reaction

The different $[C]/[O_2]$ ratios of the starting materials resulted in a difference in the final levels of the C and O_2 content in the zoned niobium. The results show that for a $[C]/[O_2]$ ratio of 0.78 the oxygen content decreased rapidly to below 5 ppm after 4 passes in system LB. For a ratio of 0.09 the oxygen content only dropped to 25 ppm after 6 passes in system LB. The possible mechanism acting here is the formation of CO or CO_2 gas in the molten zone which then escapes from the molten metal into the vacuum chamber. A low initial $[C]/[O_2]$ ratio in the metal would prevent much oxygen removal by this process. A high ratio would leave excess carbon. It appears that the proper ratio should be about $[C]/[O_2] = 0.5$. In addition, there is probably a carburization or decarburization effect occurring on the solid niobium rod depending upon the temperature and the partial pressures of CO and CO_2 existing in the vacuum system. This could account for the carbon pick up after 12 passes of the Wah Chang niobium in system LB. This effect would be kinetically slower than the reaction occurring in the molten zone because the rate controlling process is probably diffusion of the interstitials in the metal or surface adsorption-desorption at the surface.

There is some indication that the molten zone is protected from any interaction with gases in the vacuum environment. Allen [10] using the pendent-drop method to measure surface tensions of the refractory metals, found that wide variations in the vacuum from 10^{-4} to 10^{-7} torr as well as leak rate variations had no measurable effect on the surface tension determinations. Because of the sensitivity of the surface tension to interstitial impurities, he concluded that the vaporizing metal protected the surface from impingement of impurity gas molecules. Therefore, any pick up of interstitial impurity during zoning is probably due to the interaction of the solid niobium rod with the residual gases in the vacuum chamber. CO and CO_2 are common residual gases in oil diffusion pumped systems. [11]

Outgassing from the molten zone and heated solid niobium metal would also contribute CO and CO_2 residual gases.

2. Attainment of Equilibrium Concentrations of O_2, N_2, and H_2

Pasternak [12] has extensively studied the oxidation and nitridation of niobium in vacua in the 10^{-6} to 10^{-9} torr range. For the case of nitrogen, he proposed that absorption and desorption are the slowest steps in the overall sorption mechanism and thus determine the observed kinetics. The proposed reaction steps were:

$$\frac{1}{2} N_2 \text{ (gas)} + \Delta = N\Delta$$

$$\frac{N\Delta + \square = N\square + \Delta}{\frac{1}{2} N_2 \text{ (gas)} + \square = N\square}$$

The symbols Δ and $\square$ represent surface and interstitial sites respectively in the niobium. At equilibrium the following relationship holds:

$$C_e = \alpha P^{1/2} \exp\left[\Delta H_{soln}/RT\right]$$

where C_e = equilibrium concentration of nitrogen in niobium (atom %)
P = partial pressure of nitrogen in equilibrium with metal (torr)
ΔH_{soln} = heat of solution
α = entropy factor (torr$^{-1/2}$ · atom %)
R = gas constant
T = temperature

From the experimental kinetics of nitrogen pickup and outgassing and assuming the above reaction stops, Pasternak was able to obtain values of α and ΔH that agreed well with the values obtained under equilibrium conditions. These values were: $\alpha = 1.2 \times 10^{-5}$ torr $^{-1/2}$ · atom %; $\Delta H = 53,500$ calories.

The equation for the equilibrium concentration shows that a low partial pressure of nitrogen and a high temperature contribute to a low concentration of nitrogen in the metal. However, the kinetics for the attainment of this

equilibrium concentration is controlled by the adsorption and desorption of nitrogen at the metal surface. This indicates that the lowest nitrogen concentration will be attained by heating the niobium to a temperature near the melting point in a high vacuum for a time long enough to reach equilibrium and then cool the sample fast enough to prevent adsorption and desorption processes from maintaining an equilibrium concentration as the temperature decreases.

The slight continual increase in the resistant ratio as a function of zone length generally observed in this study (Figs. 2-4) can be explained by this process. The total pressure in the specimen chamber decreased as zoning progressed particularly on the first pass in system LB which was an unbakeable system (Fig. 3). Thus the partial pressure of N_2 and O_2 probably decreased as zoning progressed, resulting in lower equilibrium concentrations of oxygen and nitrogen. The vacuum fusion analyses for oxygen and nitrogen unfortunately exhibited too much scatter among sections along a zoned length to test this suggestion.

3. Formation and Volatilization of Atomic Oxygen and/or Niobium Suboxides

In the oxygen-niobium system, Pasternak [12] also found the same general sticking probabilities for oxygen on niobium below 1000° C as for nitrogen. However, at higher temperatures in addition to adsorption and desorption, two additional processes apparently occur which result in high "apparent sticking probabilities." The first reaction is the dissociation of the oxygen molecule on the hot surface followed by irreversible sorption of the oxygen atoms on a cold surface in the system. The second reaction is the formation of NbO at the hot niobium surface followed by the evaporation of the NbO molecule from the surface to a wall of the system.

Gebhardt, Fromm, and Jakob [13] also suggested that their results from degassing experiments on niobium could be explained by assuming that oxygen leaves the metal in the form of a volatile niobium suboxide such as NbO or NbO_2 at high temperatures.

Again it is apparent that a low partial pressure of oxygen in the system is very important. However, the

presence of the competing reactions in addition to the sorption process for the case of oxygen suggests a method of purification. This method would consist of heating niobium at very high temperatures in a good dynamic vacuum with low partial pressures of nitrogen and oxygen. This would reduce the equilibrium concentration (C_e) of both impurities to the lowest practical value. This should be done in a cold wall system such that the hot specimen can "see" the wall. Thus the competing reactions for oxygen would result in the deposition of oxygen atoms and NbO molecules irreversibly on the cold wall. Fast cooling from temperature would retain the low equilibrium concentration of N_2 and O_2.

Taylor and Christian [6] used essentially this treatment by resistance heating a 3 mm diameter zone refined niobium rod to ~ 2400°C in ~ 1×10^{-8} torr vacuum. This treatment improved the resistance ratio R 300°K/R 20°K of the as-zoned rod from ~100:1 to ~ 2000:1. Their value of resolved shear stress for yielding in compression at a strain rate of 6×10^{-4} sec^{-1} was 0.85 Kg/mm^2. Using the data of Cost and Wert [14] for the equilibrium solubility of nitrogen in niobium and extrapolating to high temperatures and low pressures, Taylor and Christian [6] explained the purification effect as due to the attainment of a low equilibrium concentration of oxygen and nitrogen. It is suggested here that some of the purification was due to the formation and volatilization of atomic oxygen and/or niobium suboxides with subsequent deposition on a cold surface in the system.

Wronski and Fourdeux [15] used a "flash annealing" technique which probably accomplished the same result on polycrystalline niobium sheet. They obtained a resistance ratio (R 295°K/R 77°K) equal to 5.68 and a resolved shear stress for yielding of ~ 2 Kg/mm^2. Their vacuum was 1×10^{-6} torr and the specimen was heated by resistance several cycles for a few seconds at a time to temperature near the melting point.

In the electron beam floating zone technique for the purification of niobium, all three of these mechanisms probably affect the interstitial impurity content of the zoned rod. The kinetics of these mechanisms, i. e. the CO, CO_2 gas reaction, the attainment of equilibrium

concentrations of impurities in the metal, and the formation and volatilization of atomic oxygen and/or niobium suboxides, depends upon such variables as time, temperature, and the partial pressure of the appropriate gas above the metal surface. Experimental factors that affect these variables are purity of starting material, quality of the vacuum environment, number of passes, zoning speed, electron gun design, and beam power.

SUMMARY

The results reported here on electron beam floating zone refined niobium indicated that very little purification was due to movement of impurities by the zone refining action. Instead, most metallic impurities were reduced by evaporation. Tantalum and tungsten were exceptions to this in that there was no significant reduction in the content of either impurity. In fact, tungsten showed a 6% increase at the end of 12 passes probably due to contamination from the electron gun tungsten filament. The $[C]/[O_2]$ ratio of the starting material was important and affected the final level of these two impurities. For one starting material, the carbon content increased during zone refining possibly due to a carburization reaction occurring among the residual gases in the vacuum environment. The initial low hydrogen content showed little significant change as a result of zone refining. Oxygen and nitrogen levels in the starting materials were greatly lowered by the first pass made during zone refining. Subsequent zoning passes had a smaller effect but the chemical analyses, resistance ratios, and tensile properties did indicate a decreasing oxygen and nitrogen content with increasing number of passes. This was attributed to a lower partial pressure of oxygen and nitrogen in the vacuum environment as zone refining proceeded. Adsorption and desorption of nitrogen at a heated, solid niobium surface was suggested to be the rate controlling mechanism for nitrogen purification during zone refining. The same held for oxygen except that the additional reactions of dissociation of the oxygen molecule and the formation of NbO on the hot niobium metal surface with subsequent vaporization of oxygen

atoms and NbO molecules to deposit on cold surfaces in the system also play an important role in the purification process.

REFERENCES

1. E. Votava, Phys. Sta. Sol. 5, 421-434 (1964).
2. E. Votava, J. Less-Common Metals, 9, 409-415 (1965).
3. T. E. Mitchell, R. A. Foxall, and R. B. Hirsch, Phil. Mag. 8, 1895-1920 (1963).
4. B. Harris, J. Inst. Met. 92, 89-92 (1963-64).
5. B. Harris, J. Less-Common Metals 7, 185-196 (1964).
6. G. Taylor and J. W. Christian, Acta Met. 13, 1216-1218 (1965).
7. J. W. Christian and B. C. Masters, Proc. Roy. Soc. (London) A, 281, 223-239 (1964).
8. R. E. Reed, H. D. Guberman, and T. O. Baldwin, to be published.
9. M. J. Leadbetter and B. B. Argent, J. Less-Common Metals, 3, 19-28 (1961).
10. B. C. Allen, Trans. AIME 227, 1175-1183 (1963).
11. H. Inouye, ORNL Report No. 3674, September, 1964.
12. R. A. Pasternak, Stanford Research Institute Report SRIA 132, November 1964.
13. E. Gebhardt, E. Fromm, and D. Jakob, Z. Metallk. 55, 432-444 (1964).
14. J. R. Cost and C. A. Wert, Acta Met. 11, 231-242 (1963).
15. A. Wronski and A. Fourdeux, J. Less-Common Metals, 7, 205-211 (1964).
16. F. W. Young, T. O. Baldwin, A. E. Merlini, and F. A. Sherrill, Advances in X-ray Analysis, Vol. 9, Plenum Press, New York, 1966.

On the Influence of Interstitial Impurities on the Recovery Behavior of Group Va Metals

E. Rexer, F. Schlät and A. Köthe

Institute for Metal Physics and Pure Metals
Dresden, E. Germany

1. INTRODUCTION

The application of electron-beam technology to the processing of refractory metals has allowed to produce these metals in a high-purity form. Especially the content of interstitial impurities which are known strongly to influence the physical properties of the group Va metals could be reduced. Advances achieved in the past years towards wider technical applications of these b. c. c. refractory metals were made possible to some extent by progress in their purification with respect to interstitial impurities.

Furthermore some problems can be reinvestigated now with samples of definite purity. One of these problems on which we shall report here is the recovery behavior of the group Va b. c. c. metals tantalum, niobium, and vanadium in the temperature range between room temperature and 700°K. In these metals, after deformation or irradiation, a marked recovery stage of the electrical resistivity can be found at temperatures about 420°K which is often termed "stage III" [1-5]. Until now, in the literature this stage has been ascribed to the annealing-out of intrinsic point defects. The activation energies, however, ascertained for this stage are in good agreement with the migration energies of interstitial impurity atoms. In Table 1 the migration energies of oxygen, nitrogen, and carbon in vanadium, niobium, and tantalum are listed.

Table 1. Migration energies (eV) of interstitial impurities in group Va metals [6]

	V	Nb	Ta
O	1.26	1.17	1.11
N	1.48	1.52	1.64
C	1.18	1.43	1.67

These values are very well known from measurements of the temperature and frequency dependence of the Snoek-damping [6]. As one can see, the migration energy of oxygen varies only slightly with the host metal. Because of the correspondence of the activation energies estimated from recovery measurements with the migration energies of interstitial impurities, Rosenfield [7] suggested that the resistivity recovery may well be caused by the migration of interstitial impurities.

This assumption is supported by the fact that in deformed metals in the same temperature range another process occurs which is definitely known to be caused by interstitial impurities, namely the effect of strain-aging. During strain-aging, interstitial impurity atoms diffuse to free dislocations pinning them. This dislocation pinning can be investigated by studying changes in certain physical properties, e. g. the yield-point return. A number of publications report on strain-aging effects due to oxygen in group Va metals using mechanical property measurements [8-13].

Furthermore, a rearrangement of interstitial impurity atoms can diminuish the electrical resistivity in a similar way as is expected for the annealing-out of intrinsic point defects. This was in fact already shown by Cottrell and Churchman [14] in 1949, Lücke and co-workers [15, 16], and more recently by Cuddy [17] with cold-worked iron containing carbon. Therefore, this work, parts of which have been published earlier [18-21], was undertaken to investigate the influence of interstitial oxygen and nitrogen on the recovery behavior of cold-worked tantalum, niobium, and vanadium in the temperature range between room temperature and 700°K.

2. EXPERIMENTAL

The investigations were performed on polycrystalline wires with diameters between 1 and 1, 5 mm made from electron-beam refined tantalum, niobium, and vanadium, and on electron-beam zone refined single crystals with diameters of about 5 mm.

The metallic contaminants of the test materials used are listed in Table 2.

Table 2. Concentration (wt. -ppm) of metallic contaminants of the test materials

	V	Nb	Ta
Mo	300	5	40
Nb	40		1100
Si	300	10	10
Ta	50	10000	
W	2	20	1400
Zr	200	40	-

The content of interstitial impurities could be varied by means of solid-state heat-treatment in vacuum and various gaseous atmospheres from below 10 ppm to about 1000 ppm (by weight) keeping it always below the limit of solubility given in the literature [22]. Only the nitrogen content of vanadium we were not able to reduce by heating in vacuum to less than 260 ppm, which corresponds to the as-received material. For the analysis of the interstitial impurity concentrations Snoek-peak measurements and the vacuum fusion method were applied.

The wires were used for internal friction and electrical resistivity measurements, the single crystals for the study of the dynamic elastic modulus.

For the internal friction measurements in the frequency range between 6 and 15 cps an inverted vacuum

torsion pendulum was used. The electrical resistivity was measured by a conventional potentiometric method at 273°K and 77°K. From the obtained values the additional residual resistivity as compared with a "pure" standard sample was calculated assuming that Matthiessen's rule is valid.

The changes of the dynamic Young's modulus were observed by means of a resonance method exciting transversal oscillations in the sample and measuring the period of the vibration which is inversely proportional to the square root of the modulus.

The wire samples were deformed by rolling at room temperature with diameter reductions between 35 and 50%. The single crystals were rolled at about 200°K with 4% diameter reduction.

The annealing of the wire samples was carried out in an oil-bath and above 500°K in vacuum (~ 5.10^{-8} mm Hg).

3. RESULTS

3.1 Resistivity Measurements

In Fig. 1 some typical isochronal annealing curves obtained with tantalum samples containing various amounts of oxygen and nitrogen are compiled. The additional specific resistivity is plotted versus annealing temperature. Temperature increments of 25°K and annealing times of 10 minutes were used. The curve at the bottom of the diagram was obtained with a degassed sample having an overall content of interstitial impurities of less than 5 ppm. This sample shows after 45% deformation a resistivity increase of $2,5 \times 10^{-2}\ \mu\Omega$cm. Only a part of this additional resistivity anneals out during a thermal treatment up to 650°K. The slight rise in the curve above 650°K is caused by a pick-up of a few ppm oxygen during vacuum annealing. Another tantalum wire containing 170 ppm oxygen shows under similar conditions a higher resistivity increase due to deformation and a pronounced resistivity drop during the recovery treatment leading to a value below that of the same sample prior to deformation. The latter fact is already an indication that this stage is not (or not only) caused by the annihilation of deformation-induced defects. Keeping the

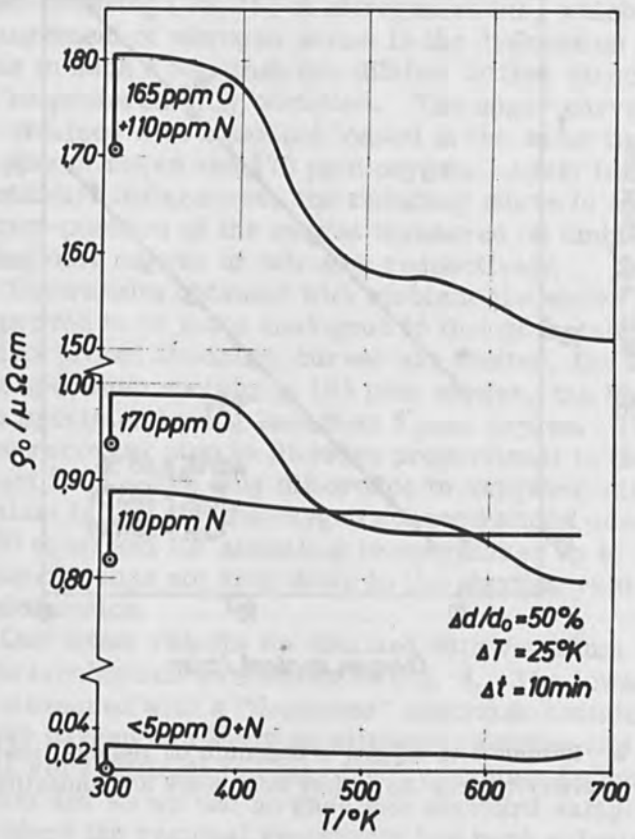

Figure 1. Isochronal recovery of the residual resistivity of cold-worked tantalum with different concentrations of interstitial impurities.

deformation constant the resistivity drop turns out to be proportional to the amount of dissolved oxygen. Figure 2 shows these results. The upper straight line shows the additional resistivity caused by oxygen in undeformed samples versus oxygen content, the lower straight line shows the resistivity decrease following a 45% deformation and a subsequent half-an-hour anneal at 503°K. About 13% of the additional resistivity of the undeformed samples anneal out. The observed proportionality between the vanishing resistivity part and the oxygen content indicates

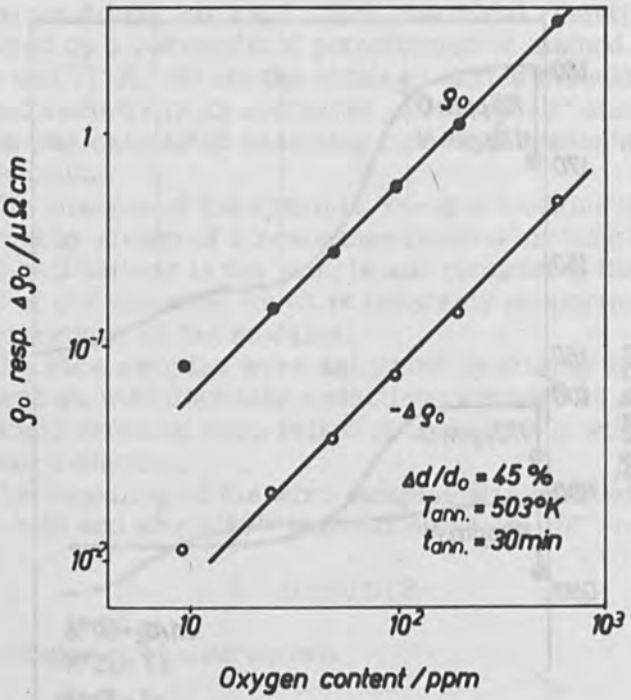

Figure 2. Influence of oxygen in tantalum on residual resistivity ρ_0 and resistivity drop $\Delta\rho_0$ after cold-work and annealing.

that the recovery stage may be caused by a rearrangement of interstitial oxygen atoms. This assumption is supported by the fact, that oxygen atoms become mobile just in the same temperature range in which resistivity recovery is observed, leading to the well known strain-aging effects.

If the group Va metals contain, instead of oxygen, another interstitial impurity with higher migration energy, the corresponding resistivity decrease should be shifted towards higher annealing temperatures. Figure 1 gives an example for a tantalum specimen containing 110 ppm nitrogen which shows a new stage occurring between 550°K and 670°K, the characteristics of which are qualitatively the same as those for the tantalum-oxygen system. A small stage centered at 450°K is probably caused by so-called

Snoek-ordering [23, 24] of nitrogen atoms, which is a rearrangement of nitrogen atoms in the dislocation stress fields in such a way that the dilated lattice directions will be preferentially occupied. The upper curve in Fig. 1 was obtained with a sample loaded at the same time with 110 ppm nitrogen and 170 ppm oxygen. Apart from small quantitative differences, the resulting curve is essentially a super-position of the curves measured on tantalum containing only oxygen or nitrogen respectively.

The results obtained with niobium are shown in Fig. 3 and proved to be quite analogous to that of tantalum. Again two isochronal annealing curves are plotted, the upper one for a specimen containing 195 ppm oxygen, the lower one for a specimen having less than 5 ppm oxygen. The height of the recovery step is likewise proportional to the oxygen content [19]. The only difference to oxygen-containing tantalum is that for the oxygen concentrations used (< 400 ppm) and for annealing temperatures up to 550°K the resistivity does not drop down to the starting value prior to deformation.

Our latest results we obtained with vanadium samples. Three isochronals are shown in Fig. 4. The lowest curve was measured with a "degassed" specimen containing about 70 ppm oxygen and 260 ppm nitrogen. Oxygen and nitrogen is very difficult to clean from vanadium by heating in vacuum and so we had no gas-free standard sample. Therefore the residual resistivity has been calculated by use of ideal resistivity values given by White and Woods [25].

However, keeping in mind the similarities between the three group Va metals, a similar behavior as observed on tantalum and niobium is expected for vanadium, too. Therefore we loaded one sample with additional oxygen and another with additional nitrogen (upper curves). The results show that the stage around 400°K is caused probably by migration of oxygen atoms, and the stage between 500°K and 600°K by migration of nitrogen atoms. The two stages around 350°K and 410°K can be explained by Snoek-ordering of oxygen and nitrogen respectively.

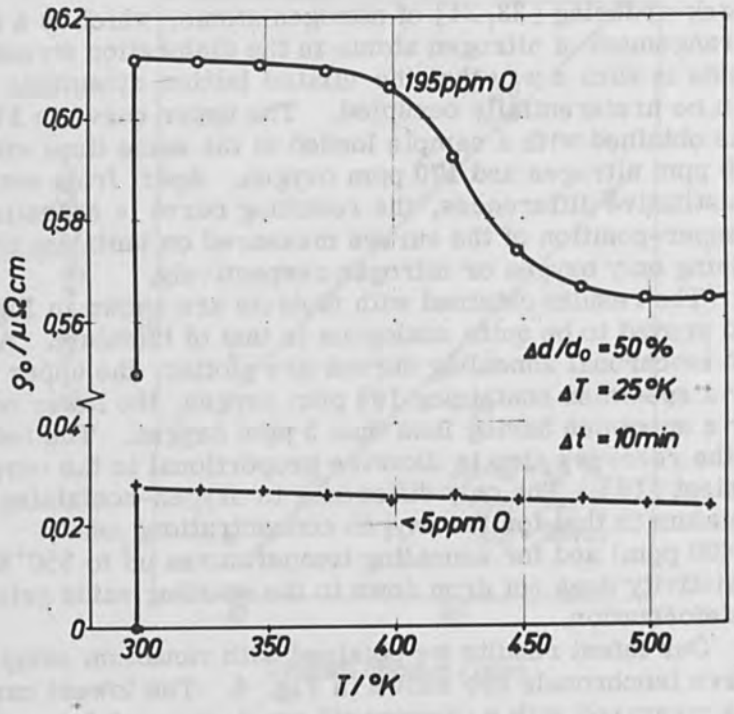

Figure 3. Isochronal recovery of the residual resistivity of cold-worked niobium with different oxygen content.

3.2 Internal Friction Measurements

Besides the resistivity measurements, internal friction investigations have been carried out on samples having the same history. Especially the change in Snoek-damping after deformation and subsequent annealing has been studied. Since the Snoek peaks are caused only by those interstitial atoms freely mobile in the lattice, their rearrangement will influence the Snoek-damping. In fact, in the systems studied til now, i. e. Ta-O, Nb-O, Ta-N, V-O, and V-N a decrease in the Snoek peak height has been observed. As an example, in Fig. 5 the results obtained with Ta-O are shown. The Snoek peak height (upper curve) and the Snoek peak decrease after a 45 percent deformation

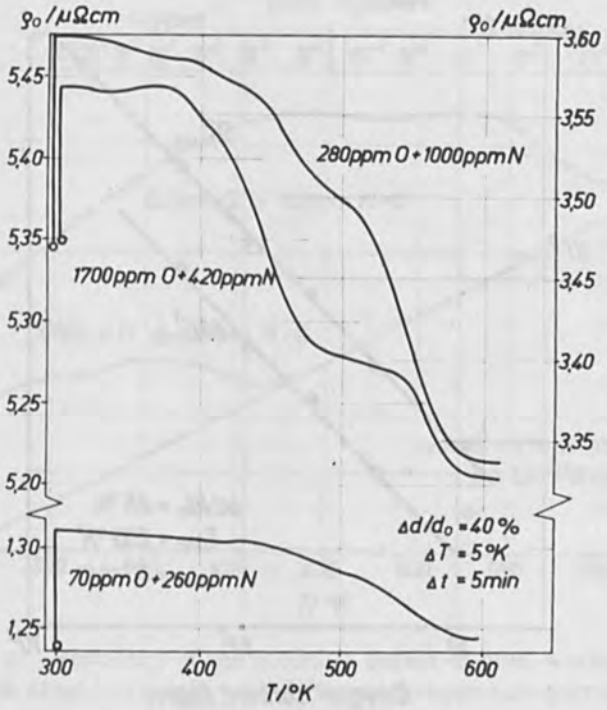

Figure 4. Isochronal recovery of the residual resistivity of cold-worked vanadium with different concentrations of interstitial impurities.

and a half-an-hour anneal at 503°K (lower curve) are plotted versus the oxygen content of the samples.

Within the limits of error, the decrease of the Snoek peak is proportional to the oxygen concentration and amounts to about 34% of the damping prior to deformation. This indicates that about one third of the oxygen atoms have been rearranged in such a way that they do no longer contribute to the Snoek relaxation.

The other systems mentioned before showed a similar behavior, merely the amount of the Snoek peak diminuition was somewhat less pronounced ranging for some systems to only a few percent of the initial value.

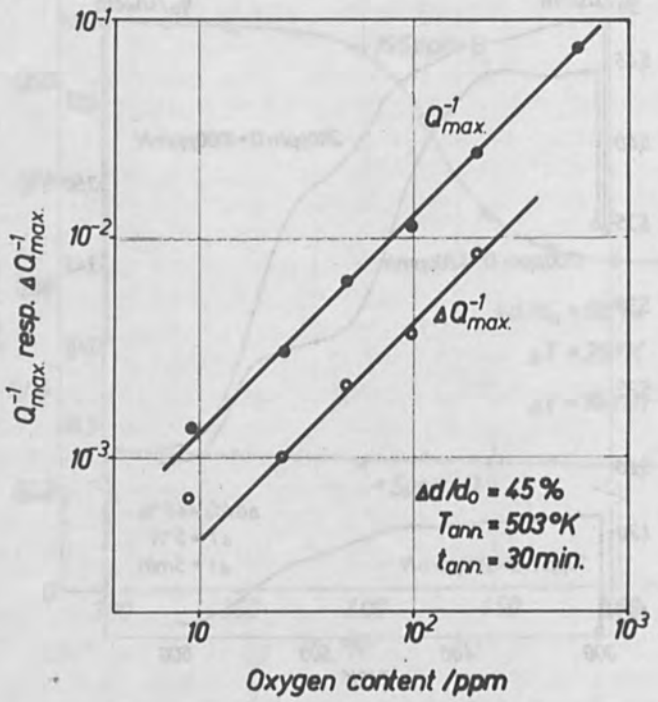

Figure 5. Height of the oxygen Snoek-peak Q^{-1}_{max} in undeformed tantalum and its decrease ΔQ^{-1}_{max} after cold-work and annealing.

3.3 Measurements of the Elastic Modulus

The recovery of the modulus defect of deformed single crystals has been observed using time-proportional heating with a rate of about 1°K/minute. Specimen axis and plane of oscillation were always approximately parallel to <100> -directions. Two heating cycles have been carried out, the first one to recover the deformed sample and the second one to study the temperature dependence of the modulus of the recovered sample.

Figure 6 gives two recovery curves obtained with tantalum crystals with different oxygen contents after a 4%

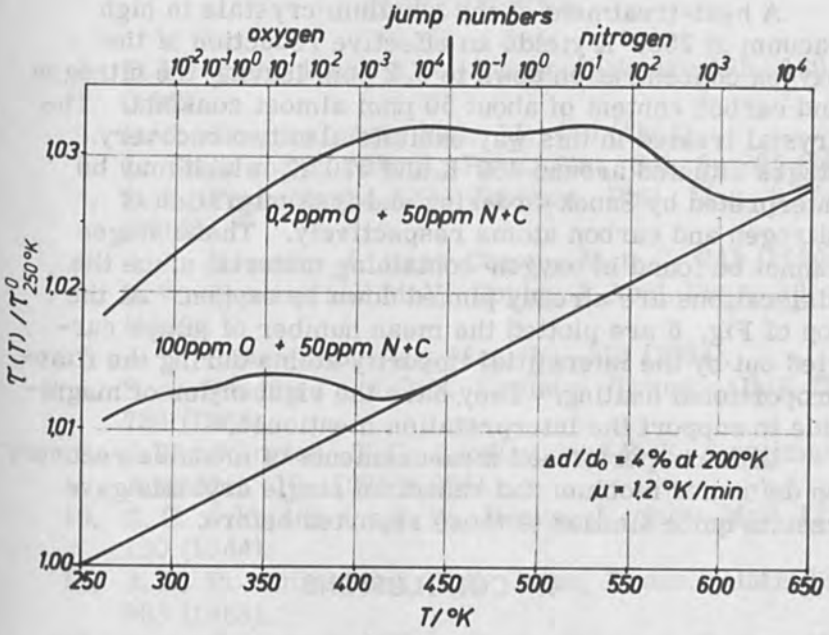

Figure 6. Recovery of the modulus defect of cold-worked tantalum single crystals with different oxygen concentrations

$$\left[\frac{\tau\ (T)}{\tau^{\,o}_{250\,^{o}K}}\right]^{2} = \frac{E^{o}_{250\,^{o}K}}{E(T)}$$

τ (T), E(T) = period of vibration respectively Young's modulus at temperature T

$\tau^{\,o}_{250\,^{o}K}$, $E^{o}_{250\,^{o}K}$ = period of vibration respectively Young's modulus of the deformed sample at 250°K after annealing

deformation at 200°K. The relative change of the period ($\tau \sim 10^{-3}$ sec) is plotted versus temperature. The sample containing 100 ppm oxygen shows a two-stage recovery process. The first stage at 300°K is believed to be due to Snoek-ordering of oxygen atoms, whilst the stage around 380°K can be ascribed to the free migration of oxygen atoms to dislocations.

A heat-treatment of the tantalum crystals in high vacuum at 2500°K yields an effective reduction of the oxygen concentration down to 0, 2 ppm leaving the nitrogen and carbon content of about 50 ppm almost constant. The crystal treated in this way exhibits also two recovery stages situated around 450°K and 570°K, which may be interpreted by Snoek-ordering and free migration of nitrogen and carbon atoms respectively. These stages cannot be found in oxygen-containing material since the dislocations are already pinned down by oxygen. At the top of Fig. 6 are plotted the mean number of jumps carried out by the interstitial impurity atoms during the time-proportional heating. They have the right order of magnitide to support the interpretation mentioned.

Hitherto performed measurements of modulus recovery on deformed niobium and vanadium single crystals gave results quite similar to those reported before.

4. CONCLUSIONS

It can be concluded that interstitial impurities in the cold-worked group Va metals give rise to a twofold recovery process, the first stage being caused by their Snoek-ordering which is a reorientation in the stress field of the dislocations, the second being due to their migration towards dislocations. In metals nearly free from interstitial impurities only very weak recovery has been found within the temperature range investigated. This indicates that, contrary to earlier interpretations [1-5], the recovery behavior of niobium and tantalum is strongly influenced by interstitial impurities, especially oxygen. In the investigated ranges of temperature, deformation, and sample purities no indication of the annealing-out of intrinsic point defects could be detected.

The fact that the so-called stage III has been observed also in neutron-irradiated niobium [1, 4] may be explained by trapping of interstitial oxygen atoms by vacancies. Such an interpretation has already been given for neutron-irradiated iron containing carbon [26].

REFERENCES

1. D. E. Peacock and A. A. Johnson, Nature 195, 169 (1962).
2. D. P. Gregory, Acta Met. 11, 455 (1963).
3. L. Stals and J. Nihoul, Phys. Stat. Sol. 8, 785 (1965).
4. D. E. Peacock and A. A. Johnson, Phil. Mag. 8, 563 (1963).
5. A. A. Johnson, J. Less-Comm. Met. 2, 241 (1960).
6. R. W. Powers and M. V. Doyle, J. Appl. Phys. 30, 514 (1959).
7. A. R. Rosenfield, Acta Met. 12, 119 (1964).
8. S. A. Bradford and O. N. Carlson, Trans. AIME 224, 738 (1962).
9. J. W. Edington, T. C. Lindley, and R. E. Smallman, Acta Met. 12, 1025 (1964).
10. Z. C. Szkopiak and L. W. Derry, J. Nucl. Mat. 13, 130 (1964).
11. A. R. Rosenfield and W. S. Owen, Trans. AIME 227, 603 (1963).
12. C. L. Formby and W. S. Owen, J. Less-Comm. Met. 9, 25 (1965).
13. P. L. Hendricks, J. Metals 15, 689 (1963).
14. A. H. Cottrell and A. T. Churchman, J. Iron Steel Inst. 162, 271 (1949).
15. W. Dahl and K. Lücke, Arch. Eisenhüttenwes. 25, 241 (1954).
16. W. Pitsch and K. Lücke, Arch. Eisenhüttenwes. 27, 45 (1956).
17. L. J. Cuddy, Phil. Mag. 12, 855 (1965).
18. F. Schlät and A. Köthe, Acta Met. 14, 425 (1966).
19. F. Schlät and A. Köthe in E. Rexer (Ed), Reinststoff-probleme, Bd. III, Akademie-Verlag Berlin, to be publ. 1966.
20. A. Köthe and F. Schlät in E. Rexer (Ed), Reinststoff-probleme, Bd. III, Akademie-Verlag Berlin, to be publ. 1966.
21. A. Köthe and F. Schlät, Frühjahrstagung der Deutschen Physikalischen Gesellschaft, Bad Pyrmont, 1966.
22. G. D. Rieck and D. L. Vogel in E. Benesovsky (Ed), Metalle für die Raumfahrt, Springer-Verlag Wien, New York, 1965, p. 636.

23. G. Schoek, Phys. Rev. 102, 1458 (1956).
24. G. Schoek and A. Seeger, Acta Met. 7, 469 (1959).
25. G. K. White and S. B. Woods, Phil. Trans. Roy. Soc., London A 251, 273 (1959).
26. F. E. Fujita and A. C. Damask, Acta Met. 12, 331 (1964).

ELECTRON BEAMS IN MELTING AND REFINING-INDUSTRIAL

Electron Beams in Melting and Refining
Industrial

Electron beam melting and refining of the refractory and reactive metals is firmly established as the preferred technique for the processing of these important materials. This industrial applications of electron beams in melting which recently passed its 10th anniversary has made a very substantial contribution to the processing of these materials, and in the cases of tantalum, columbium and their alloys it made the growth and industrial availability of these metals possible.

In the first decade only limited experimentation with the processing alloy steels in particular and ferrous metals in general, was conducted. Although from all information at hand the properties of the so processed materials were satisfactory, the economics of this processing prevented acceptance here.

Electron beam melting furnaces have grown almost a 100 times in capacity in the decade since their inception. The 25 KW and 60 KW furnaces are complemented in industrial operation with 250, 600 and 1700 KW installations. The drawing boards contain 3500 and 6000 KW installations ready for execution once the economic questions are clarified. It is in this matter of economics that the answer lays as to the acceptance of this technique for large tonnage ferrous metal production.

The papers in this section present the scaled up production status to day as seen on both sides of the iron curtain, they also discuss a variety of other industrial applications. The apparent property benefication on ferrous materials obtained by electron beam melting relative to alternate vacuum melting processing places this technique firmly in the steel processing techniques. The question is no longer whether the technique will at all be adopted to tonnage special steel production, the question is how large will its acceptance in the future be.

Before completing this brief introduction one should say that the work accellerated guns which pioneered electron beams in melting are just about extinct. The power today is applied by differentially pumped axial guns, by transverse guns and by radial electron beam heaters. Each and all of these approaches for power input have advantages and short-comings. The papers to follow discuss in some details the systems in operation, much additional information can be found in the references given below.

The technique of direct reduction electron beam installation has failed to develop as many, including this writer, expected. Perhaps difficulties in the selection of suitably reacting material and advances in alternate reduction techniques have been the reason. Perhaps the growth of this application in the future will tend to change the picture here.

Regardless of the outcome of the scope determining activities based on economic considerations, electron beams in melting and refining and a score of other industrial applications are firmly established today and continue to have an exciting growth potential.

(Editor)

REFERENCES

1. Proc. 1st Symp. Electron Beam Technology, J. Helherington, (Ed), Boston, 1959.
2. Proc. 2nd Symp. Electron Beam Technology, R. Bakish, (Ed), Boston, Mass, 1960.
3. Proc. 3rd Symp. Electron Beam Technology, R. Bakish, (Ed), Boston, Mass. 1961.
4. Proc. 4th Symp. Electron Beam Technology, R. Bakish, (Ed), Boston, Mass, 1962.
5. Proc. 5th Symp. Electron Beam Technology, J. Morley, (Ed), Boston, 1963.
6. Proc. 6th Symp. Electron Beam Technology, J. Morley, (Ed), Boston, 1964.
7. Introduction to Electron Beam Technology, R. Bakish, (Ed), J. Wiley & Sons, New York, 1962.
8. Proc. 1st International Conference on Electron and Ion Beams in Science and Technology, J. Wiley & Sons, New York, 1965.

Advances and the Future of Electron - Beam Processes

Hugh R. Smith, Jr. and Charles d'Ancona Hunt

Temescal Metallurgical Corporation
Berkeley, California 94710

The use of high voltage beams of electrons as heat sources has, until the past several years, been confined to rather specialized applications in which their use is justifiable, or in many cases necessary, on economic grounds. Although electron beam techniques hold great promise and the feasibility of their application to a wide variety of industrial processes can be readily demonstrated, their application has fallen far short of the potential that could be readily realized from a purely technological point of view. This is due to a combination of factors.

Firstly, applications of electron beam technology generally encompass a multiplicity of technical disciplines which may not be readily available in toto in an area of potential use. Thus better understood alternate processing methods are often favored in a competitive situation.

Secondly, many of the most promising and important uses of electron beam technology involve replacement or extensive renewal of existing capital equipment. The situation up to the present has been that decisions for appropriate expenditure have been mostly negative on the basis that electron beam processing was a largely unproven technology on an industrial scale. The information that follows in this presentation, as well as in subsequent papers, should help dispel the reluctance to accept the technology on a broad base.

Figure 1 is a tabulated presentation indicating the pertinent characteristics of a number of large electron beam installations, typifying both the variety and magnitude of the industrial equipment known to be in operation at this time. The chart is, of course, by no means comprehensive,

*This was the opening paper at the conference.

but does include some of the types of installations which hold forth the most promise for future exploitation.

There seems to be little doubt that the application of electron beam techniques to melting and casting will continue to grow. The experience gained on megawatt class furnaces in this country and in Russia over the last several years has provided the basic data from which to extrapolate to much larger installations. It has also been clearly shown that the larger the scale of operation, the fewer operational difficulties are encountered, and the better and more uniform is the product quality. Virtually all of the refractory metals tantalum and columbium produced today are presently routinely purified and consolidated by this technique.

Results obtained in both United States and Russian installations show the benefits to be gained by electron beam melting of steels in terms of resulting properties. Figure 2 shows the 1200 KW cold-hearth furnace in which much of the preliminary work on steel and cobalt and nickel base alloys has been done in this country. As a result of this experience, a much larger cold-hearth furnace has been designed to produce 15,000 tons of specialty steel ingots per year. Figure 3 is a schematic diagram of the furnace. It has 2000 KW of installed power; can cast either ingots or slabs; and its operating cost, not including amortization of capital, amounts to about $50 per ton of product.

One of the advantages of the cold-hearth type furnace shown is that all the purification and homogenization takes place on one pass through it. Thus the furnace can be thought of as a single-melt unit. The volatile impurities are removed in two stages, as shown. The first stage accomplishes the preliminary degassing and operates at a pressure of about 10^{-2} Torr, a pressure level at which the evolved gases can be pumped with great efficiency. It is separated from the second stage by a slag and pressure barrier which accumulates the major portion of the insoluble impurities which can be skimmed off at intervals. The second stage, operating at less than 10^{-3} Torr completes the homogenizing and purifying of the metal, which

is then poured in a continuous stream into the water-cooled casting mold. The hearth is constructed entirely of water-cooled copper, so that the molten metal is never in contact with contaminating refractory materials. The hearth concept, in addition to providing an extended surface area for the purification reactions, also permits the late addition of reactive alloy elements which are readily homogenized into the flowing stream of molten metal.

The subject of the promotion of surface reactions in the hearth furnace leads into another area of application of electron beam technology, which at present is still in its infancy. This is the reduction of metals either directly from beneficiated ores or from partially reduced material. In particular, both tantalum and columbium have been so reduced from their oxides, as well as being purified from the product of a preceding thermite reaction. In this latter case material containing 85% tantalum was run at very favorable economics on a production basis. As the furnaces are scaled up, and operating costs per unit weight processed go down, it will be economical to refine other metals by this method.

The casting of high melting point reactive metals into shapes has long been a problem. Some headway has been made on casting materials such as titanium with tilt-pour arc furnaces, but no general purpose technique is in wide use.

Figure 4 is a schematic of an electron beam heated tilt-pour furnace for accomplishing the casting of reactive metals. It can be seen from the diagram that the reactive material is only in contact with a skull of its own material, and therefore any reasonable degree of superheat of the pool may be utilized to assist in filling the mold. The casting can be made in investment, rammed graphite, or permanent molds. It can be seen that the electron gun assembly tilts right along with the crucible, thus keeping the material at temperature even while it is being poured. When the pour is completed, the beam trajectory can be relaxed to hot-top the riser and thus assist in obtaining directional solidification of the casting.

In addition to melting and casting operations, electron

beam techniques lend themselves efficiently to secondary operations such as surface conditioning, rolling, annealing, coating, and joining. Of particular interest at the present time are large air-to-air high-vacuum strip handling units which utilize electron beam heating for strip annealing and for the evaporative coating of a wide variety of materials. From the point of view of available high vacuum technology, such installations have been possible for a number of years. A 6-inch wide pilot model ran successfully in 1953. However on a large scale, such equipment would be uneconomic and impractical without the flexibility and efficiency provided by electron beam heating for the pre-treatment of the strip as well as for the vaporization of the coating material.

Figure 5 is a photograph of an installation for handling 24" wide material, from 0.0005 to 0.040 inch thick. Figure 6 is a schematic drawing indicating the various functional elements making up the line. This particular unit has been in operation for nearly two years. During that period a wide variety of strip material has been processed; and coatings of aluminum, stainless steel, chromium, ferrochrome, copper, nickel, tin, titanium, zinc, silicon dioxide, and aluminum oxide have been applied. In this line, the principle operating variables have been delineated, and solutions to the problems of their control have been worked out. The installed electron beam power of the line, 600 KW, is high enough that the operating data is directly applicable to fully commercial lines. One such line utilizing this basic electron beam technology to coat 48" wide black plate with aluminum at 2000 feet per minute is now going through checkout. It is very probable that construction will start in the near future on several other commercial lines.

Figure 7 shows a typical vapor source for evaporating several hundred pounds of material per hour. This source uses multiple guns. The electron beam from each of these is directed onto the surface of the vaporant to obtain an energy distribution which will provide a uniformly thick coating on the strip passing over the source. Uniformity of coating thickness is obtained by monitoring the vapor density between the source and strip at several positions

across the strip width. These signals are then fed back to the gun-power control loop, which regulates beam output to produce the required vapor density. The resulting product is also continuously or intermittently monitored, in terms of coating thickness, to provide a standardization check in the overall quality control procedure.

Similar sources are, of course, equally useful in coating non-metallic materials such as glass, paper and plastics. The classical methods of utilizing resistance heated sources for vaporization are steadily being phased out. The electron beam units require little maintenance, are not subject to crucible erosion, since the vast majority of material are evaporated from water-cooled crucibles, and lend themselves to automatic control.

In the coating of paper and plastics, the film that can be applied is limited in thickness to that amount which can be condensed on the substrate per pass without destructively overheating it. This limitation has not imposed a significant restriction in the application of these techniques; and a wide variety of decorative packaging, decorative trim, and electrical condenser stock are presently being produced. Coated items that are technologically more advanced, such as magnetic recording tape and vapor barrier packaging materials, are in the development stages.

The same operational advantages provided by high intensity electron beam heated vapor sources for the coating of strip accrue as well to the production of unsupported foils. The justification for application of this technique to production of thin foil lies in the range of products that can be produced in this way, as well as in the properties which can be incorporated in the deposited foil.

The problems of rolling very thin foil (that is foils of less than .001" in thickness)are well known. In contrast the buildup of foils by vapor deposition in this thickness range is strictly a matter of time and the rate of deposition of the vapor. The physical properties of deposited foils have been found to be dependent on the temperature of the substrate onto which they are deposited, the angle

of incidence of the vapor atoms or molecules, and the deposition rate.

It has been found, experimentally, that the deposition conditions under which suitable structures can be obtained vary widely with individual materials. However, almost any alloy or combination of materials can be produced, except for those in which one of the constituents has a very high re-evaporation rate at the substrate temperature at which suitable properties can be obtained with the other materials involved. Elements with such widely varying melting points as niobium, 2497 degrees C; and tin, 132 degrees C; have been successfully co-deposited to form a super-conducting alloy ribbon. Copper and zinc have been co-deposited to form brass foil. Stainless steel, titanium, zirconium, tantalum, columbium, molybdenum, copper, lead, zinc and aluminum foils have all been successfully made on an experimental basis. It is obvious that composite or layered films can also be deposited and layered combinations of dielectrics and conductors offer some interesting possibilities.

The economic justification for foil production by vapor deposition is dependent upon the cost of rolling a particular material to a given thickness. Thus it is more difficult to justify foil production by this process for a very easy material to roll, such as commercially-pure aluminum, than for difficult materials to roll such as stainless steel or high-strength aluminum alloys. In many cases, however, the improved quality of deposited foil, made possible by high purity, the wide variation in composition possible, the non-oriented structure, or superior physical properties, will justify the production by vapor deposition. No technological limitations for the deposition of foil have as yet shown up, although a great deal of empirical work has been required to ascertain the suitable operating parameters for each different material. Evaluation of the data generated indicates that to produce a ductile foil in a given system there is a minimum deposition rate required; and the substrate temperature must be at least 25% of the absolute melting point of the evaporant.

There are a number of fully integrated sheet and

plate mills in this country and Europe which are designed to take cast slab from a continuous casting machine and transfer it directly into the rolling mill. Unfortunately the surface imperfections in the as-cast slab require extensive conditioning before the slabs are in suitable shape for rolling. The imperfections are usually either cold-shuts, surface inclusions or tears. It can be shown theoretically that with a sufficient energy density an area on the surface of the slab can be remelted to any desired depth. Heat generation by means of a narrow rectangular beam of electrons is an ideal way of obtaining such an energy density on a strip of slab; and if the beam is translated relative to the slab, the entire surface can be successively remelted and conditioned for rolling. A number of slab samples of both steel and refractory metals have been experimentally so conditioned.

Figure 8 is a photograph of the beam traversing the slab and shows the extent of molten zone readily obtainable. The steel must be of a certain quality level to permit such processing since otherwise the gas content and other volatile impurities cause sufficient bubbling and eruption that a smooth surface on solidification is difficult to obtain.

The immediate objective for the application of this technique is to replace some of the inherently crude methods which are presently in use for conditioning the products from continuous casting machines or conventional slab production systems. Present methods include flame scarfing, arc scarfing, and grinding, all of which result in a significant loss of material as well as the necessity of further extensive finishing by hand. The cost of these procedures is one of the major production expenses in present installations. An appropriate electron beam conditioning unit could undoubtedly produce superior quality conditioned slab under carefully controlled conditions without appreciable loss of material.

The ultimate objective in utilizing this technique is more ambitious. Steel slabs would be cast semi-continuously in an electron beam furnace, and while still hot and under vacuum would be conditioned to remove

whatever cold shuts or hot tears might be present. The slab would then be removed from the vacuum system through a lock and be transferred directly to the rolling mill.

Still another advance of the technique is technically feasible. The possibility and advantages of rolling under high vacuum have been investigated quite extensively in Russia and to a lesser degree in the United States. Following electron beam conditioning it would be very efficient to process the slab on a high-vacuum rolling mill immediately following the conditioning step. The slab would still be hot and could be heated still further by another array of electron guns just prior to the mill. Under these conditions enormous reductions in thickness could be realized with relatively light mill equipment. The hot band would then be run out through a set of chilled vacuum seals, similar to those presently in use on strip processing lines, with an intermediate quench if necessary, in controlled atmosphere, prior to removal to air. While such a production installation may appear revolutionary at first glance, no great extrapolation of existing technology would be required. Both high vacuum and electron beam systems of the required magnitude and complexity are presently in operation.

Not all the advances in the application of electron beam techniques to processes require scale-up in size (as many of the following papers will show). In particular, certain joining, information recording, precision machining and electronic component manufacturing processes utilizing electron beams have necessitated very small and precise equipment. Because of the large amount of information presented by other papers on these general subjects, only a brief elaboration will be presented here.

Both electron beam welding and precision machining have come to be accepted as standard, though sophisticated industrial techniques. They are still relatively expensive operations, but their unique capabilities point to a steadily increasing use. An area which has received relatively little attention is the use of relatively broad electron beams of high power from multiple gun arrays to increase,

for example, rates of production of welded pipe and tubing, where the rates are presently limited by problems of arc cratering. This type of welding is not appropriate for applications involving critical heat-affected zones; but it is well suited to situations in which close-tolerance matching of joints is not practical, and mismatch of parts must be accommodated.

The flexibility and efficiency afforded by electron beam heating are the keys to the successful process operations described in this paper. The successful application of electron beam heating depends in turn on the various elements making up the electron bombardment system. It is necessary in industrial installations that the guns be trouble-free for extended periods of time, that the power supply to be appropriately regulated so that pressure excursions in the vacuum system do not cause interruptions of power, and that system controls be amenable to automation and programming.

There is a wide variety of electron gun systems in use; and several schools of though have developed concerning the optimum gun system. What finally seems to be evolving is a compromise of disciplines. By far the most widely used type of guns in this country and Russia are the linear type guns, known more generally as "transverse guns". These guns derive their name from the fact that both the electrostatic and electromagnetic focusing elements are essentially linear in character. These elements include the cathode emitter, the anodes, and the magnetic focusing structures.

Such a typical gun rated at 150 KW is shown in Fig. 9. A schematic of this gun follows in Fig. 10. Note that the cathode and anodes are simply rods which are supported by a rugged refractory metal structure. The cathode rod is spring loaded in its mounting clips so that it may be changed in a matter of seconds. In addition to the virtue of inherent simplicity of this type of gun, there seems to be no practical upper limit to the power output that can be obtained. This capability is in contrast to that obtained with guns with cylindrical symmetry and Pierce-type focusing, which are limited to approximately

100 KW of power per gun. Linear guns may also be conveniently paralleled or mounted in arrays.

Figure 11 is a schematic drawing of a typical installation of a linear gun in a melting and casting furnace. It has been found by experience that it is advantageous from the point of view of maintenance to isolate the gun as much as possible from the region in which the electron beam energy is being applied. In general, relatively large amounts of vapors are being generated in this region, and these vapors contain an appreciable percentage of ions. The erosion of the emitting cathode by ion bombardment has remained as the principle cause of gun failure, while other maintenance problems have been essentially eliminated. On continuously-operated equipment, such as a strip line or a melting furnace, both of which generate relatively high vapor densities, severe erosion of even very heavy rod-type filaments occurs in from 25 to 175 hours, depending upon the power output per unit length of emitter.

In production operations, such as the melting and casting of refractory metals, lock systems and spare guns permit complete gun exchange in minutes; and gun failure is no longer a major source of process interruption. However in other types of installations where gun exchange is not convenient cathode life is an important factor. In these systems, the power rating of the guns is held to a level which provides an emitter life greater than, for example, one week of round-the-clock operation. Intensive development work is now being done in the direction of providing emitter lifetimes of the order of a few months of continuous operation.

Electron beam power supply development has not proceeded nearly as rapidly nor with such variation of approach as gun system development. This fact is probably in part due to the condition that in laboratory scale work (arbitrarily defined here as that work at power levels less than 10 KW), the effect of electrical instability in the supply is much less important than in industrial scale installations. Thus power supplies utilizing only resistance or reactance limiting circuitry are considered

by many users of small equipment to be quite acceptable.

Experience has shown that in large industrial scale installations, stability is extremely important; and excessive excursions in power level are unacceptable. Tightly-clamped, constant-current power supplies have been almost exclusively used for the past few years in this country. Recently a constant-voltage power supply, with vacuum tube isolation of the electron guns has been developed. This new system has the advantage that large power supply units can drive any number of guns in parallel. Furthermore each gun can be individually controlled at any desired power level. A total of 4800 KW of power from this type of power supply has been put in operation. In one installation, 72 guns operate in parallel; and operating experience indicates the constant voltage supply will probably supersede the constant-current type in most future installations. Figure 12 shows a 600 KW constant-voltage power supply module and controls.

The constant-voltage supply, because of the vacuum-tube controlled output, lends itself admirably to various kinds of feed-back control loops. Signals such as target temperature, vapor density, evaporated film thickness, film deposition rate, degree of vapor ionization, and substrate strip velocity have all been used as inputs to the loops. On very large systems such controls contribute in a major way to the efficiency of operation by eliminating operator judgment. No known installation based on electron beam techniques is now as completely automated as various standard chemical and metallurgical processes. However the various elements required to achieve the same degree of control are essentially developed and ready for co-ordinated use in complex systems.

In view of the relatively advanced state of development of the basic technology of the generation and control of electron beams for industrial applications, as outlined in this and other papers, a brief prognosis of this field seems to be appropriate.

Approximately twelve years of concentrated efforts

on a world-wide basis have only lightly touched the full potential of the applications of electron beams. The basic technological capability now exists to accomplish an astonishing variety of industrial tasks that can be performed better with electron beam heating than by means of existing techniques. There seems to be little doubt that the spread of this new technology into industry will occur rapidly, limited only by the time required to prove out the economic advantages in each particular class of application.

The initial breakthrough in basic industry will probably occur in the replacement of electroplating lines for tin and zinc coated steel strip with vacuum vapor coating lines that use electron beams for heating of strip and evaporation sources.

Closely following will be the production of stainless steel and other specialty steels and superalloys in electron-beam-heated furnaces of the cold hearth type. It is believed that this type of system will rapidly find widespread use soon after the successful operation of the first commercial-scale furnace.

A host of applications in the semi-continuous coating of discrete objects are on the verge of industrial use, ranging in size from electronic micro-circuit elements to very large sheets of plate glass.

Electron beam joining techniques, both welding and brazing, are already important commercially today; but their future use will greatly overshadow their present status.

The development of a variety of potentially important new products will also occur, especially those involving multi-layer or multi-component coatings or free-standing structures, and those involving reactive constituents that are difficult or impossible to process economically with present-day techniques.

The fundamental physical and chemical features of high-vacuum environments, coupled with the exceptional versatility of electron beam heating techniques, provide a sound basis for the inevitable industrial changes described above.

TYPICAL EXISTING ELECTRON BEAM SYSTEMS

SYSTEM CHARACTERISTICS / APPLICATION	VACUUM TANK DIMENSIONS	PRODUCT DIMENSIONS	INSTALLED ELECTRICAL BEAM POWER	NUMBER OF ELECTRON GUNS	TYPE OF SYSTEM
COATING PROCESS DEVELOPMENT	8' DIA. x 4'	STRIP 12" WIDE x 24" O.D. COIL	160 KW	6	LARGE BENCH SCALE PILOT PLANT
COATING PROCESS & PRODUCT DEMONSTRATION	60' x 6' x 10'	CONTINUOUS STRIP 24" WIDE IN 4000 Lb. COILS	500 KW	12	PROTOTYPE PRODUCTION PILOT PLANT
SUPER ALLOY & REFRACTORY METAL DEVELOPMENT	10' x 6' x 6'	INGOTS UP TO 8" DIA. & 6' LONG	600 KW	4	SEMI-COMMERCIAL SCALE PILOT PLANT
SUPER ALLOY & REFRACTORY METAL PRODUCTION	25' x 12' x 6'	INGOTS UP TO 19 DIA. & 7' LONG	1,400 KW	8	COMMERCIAL SCALE PRODUCTION PLANT
COATED PRODUCT PRODUCTION	240' x 25' x 15'	PLATES 10' x 12'	3,600 KW	72 & 72 SPARES	FULL SCALE COMMERCIAL PRODUCTION PLANT
INGOT PRODUCTION SPECIAL STEELS	INFORMATION NOT AVAILABLE	ESTIMATED 30" DIA. x 10' LONG	1,700 KW	ESTIMATED 25	PRODUCTION PLANT

Figure 1.

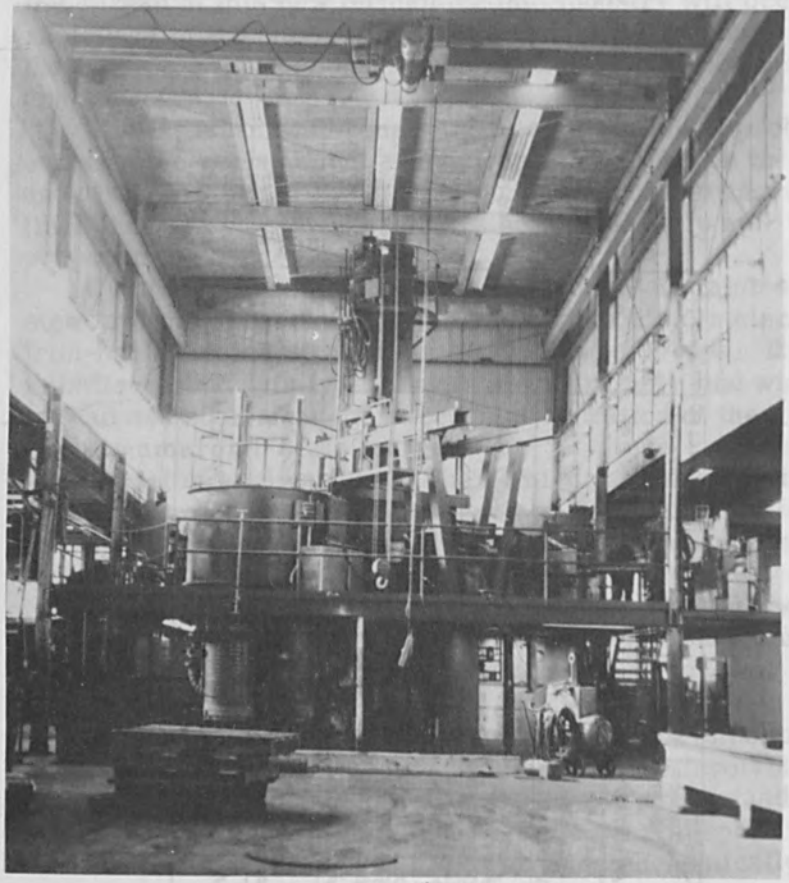

Figure 2.

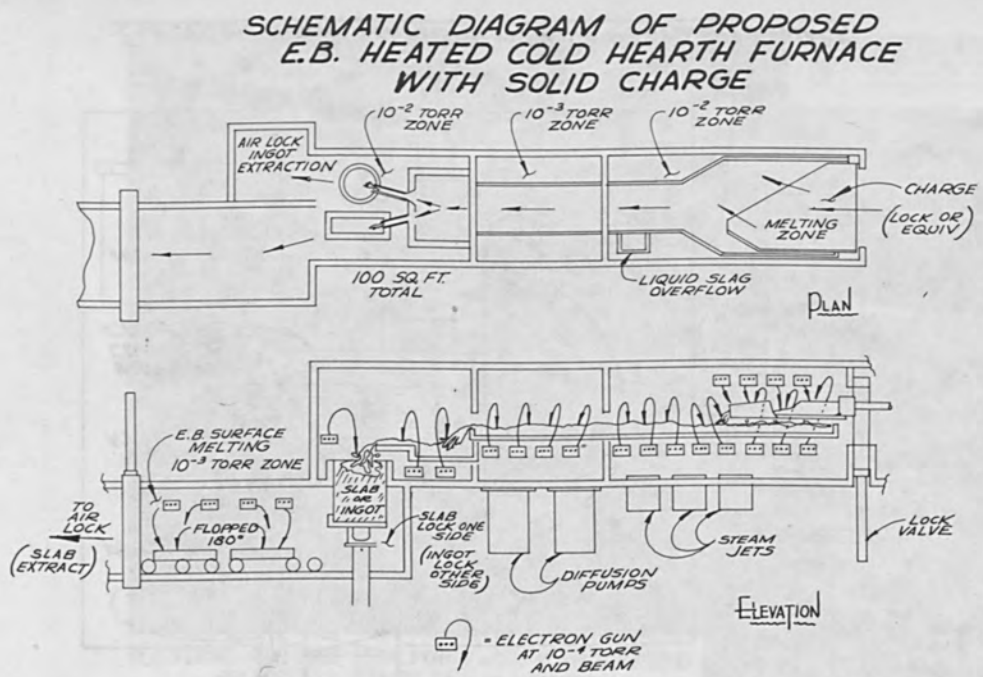
SCHEMATIC DIAGRAM OF PROPOSED
E.B. HEATED COLD HEARTH FURNACE
WITH SOLID CHARGE
10^{-2} TORR ZONE
10^{-3} TORR ZONE
10^{-2} TORR ZONE
AIR LOCK INGOT EXTRACTION
CHARGE
(LOCK OR EQUIV)
MELTING ZONE
100 SQ. FT. TOTAL
LIQUID SLAG OVERFLOW
PLAN
E.B. SURFACE MELTING
10^{-3} TORR ZONE
SLAB OR INGOT
TO AIR LOCK
SLAB (EXTRACT)
FLOPPED 180°
SLAB LOCK ONE SIDE
(INGOT LOCK OTHER SIDE)
STEAM JETS
LOCK VALVE
DIFFUSION PUMPS
ELEVATION
= ELECTRON GUN AT 10^{-4} TORR AND BEAM

Figure 3.

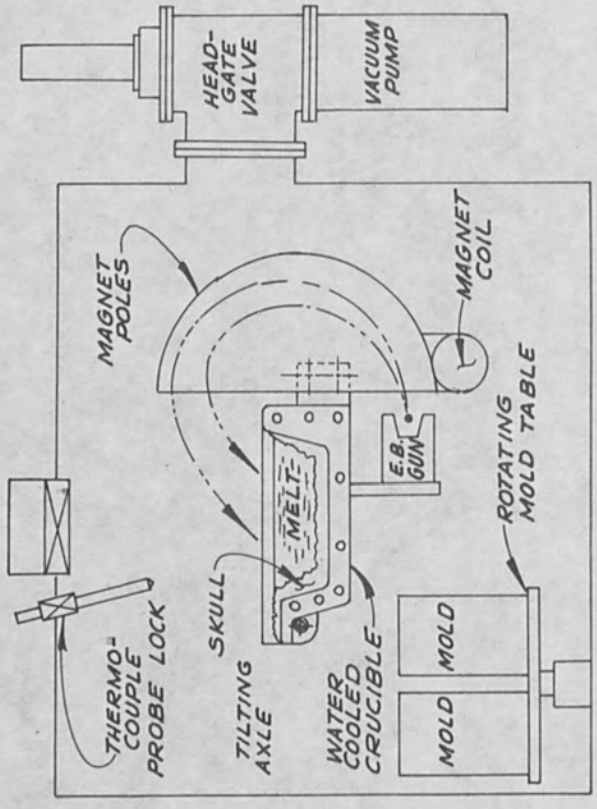

ELECTRON BEAM HEATED TILT-POUR CASTING FURNACE

Figure 4.

TEMESCAL
metallurgical corp
"CONTINUOUS STRIP LINE FOR VACUUM PROCESSING
OF METALS, PAPER AND PLASTIC".

Figure 5.

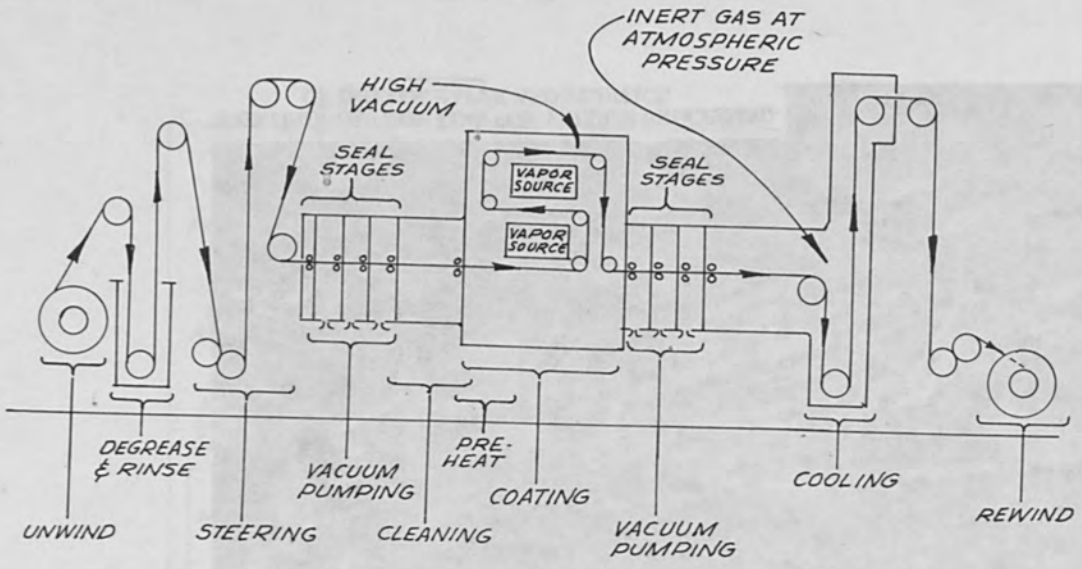

AIR-TO-AIR ELECTRON BEAM STRIP PROCESSING LINE

Figure 6.

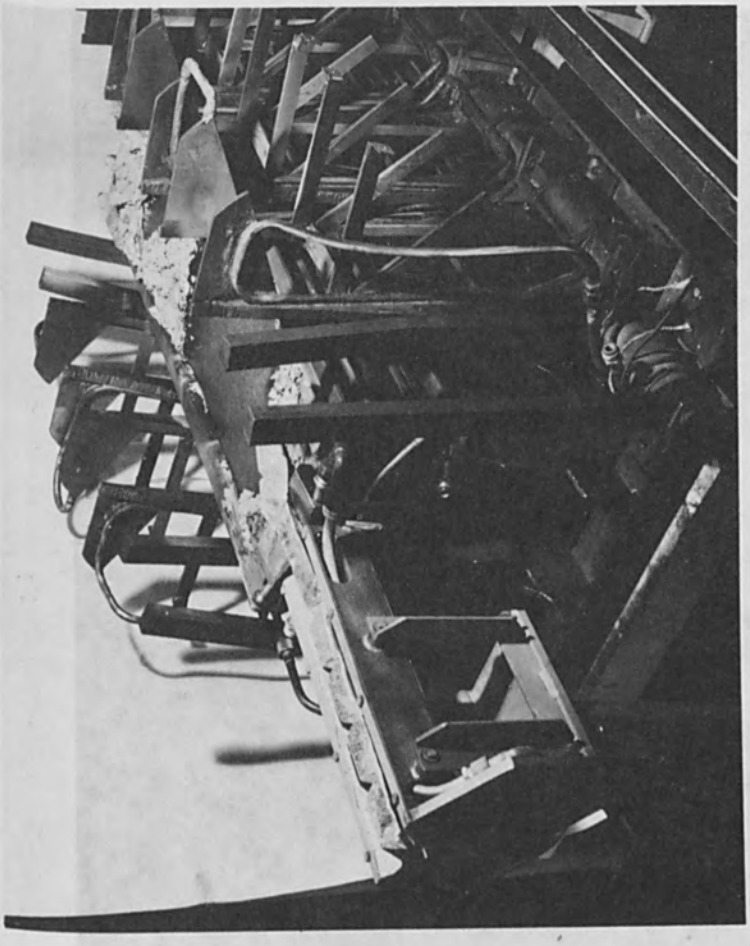

Figure 7.

Figure 8.

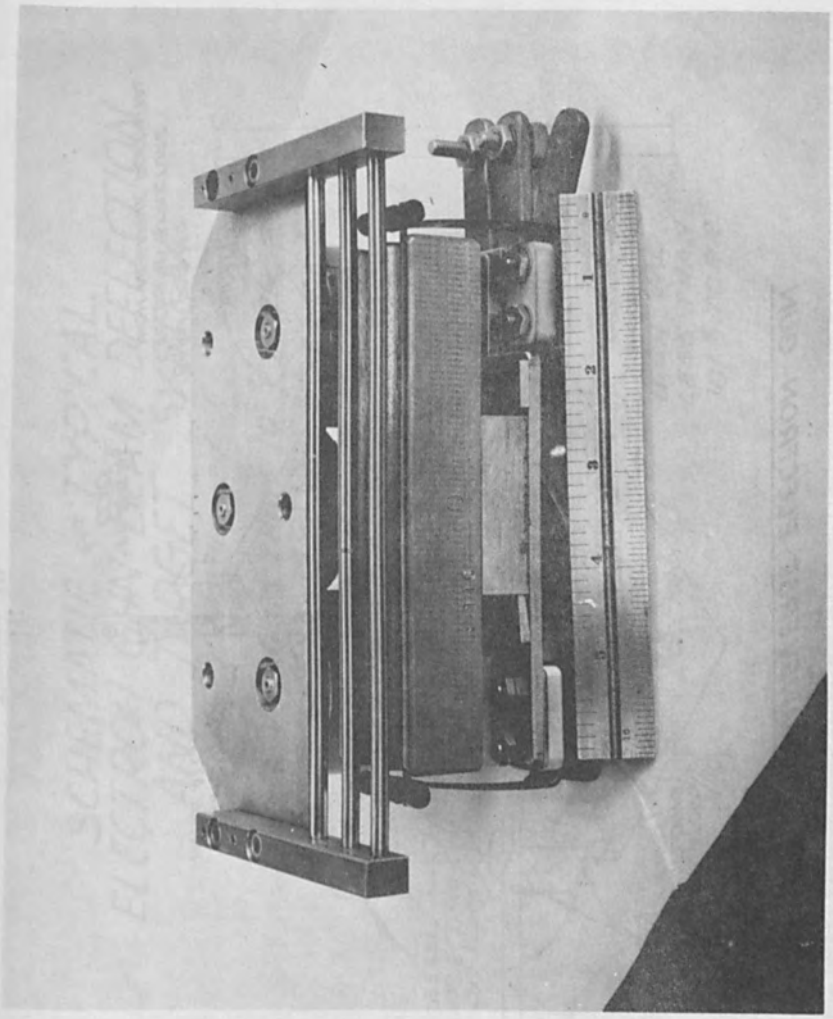

Figure 9.

TRANSVERSE ELECTRON GUN
ANODE
GROUND POTENTIAL
FILAMENT
BEAM FORMER
FOCUSING STRUCTURE
HIGH NEGATIVE POTENTIAL
FILAMENT
LEAD
INSULATOR
SHIELDING
CUPS
HIGH
VOLTAGE
INSULATOR
FILAMENT
SUPPORT SPRING
FILAMENT
INSULATOR

Figure 10.

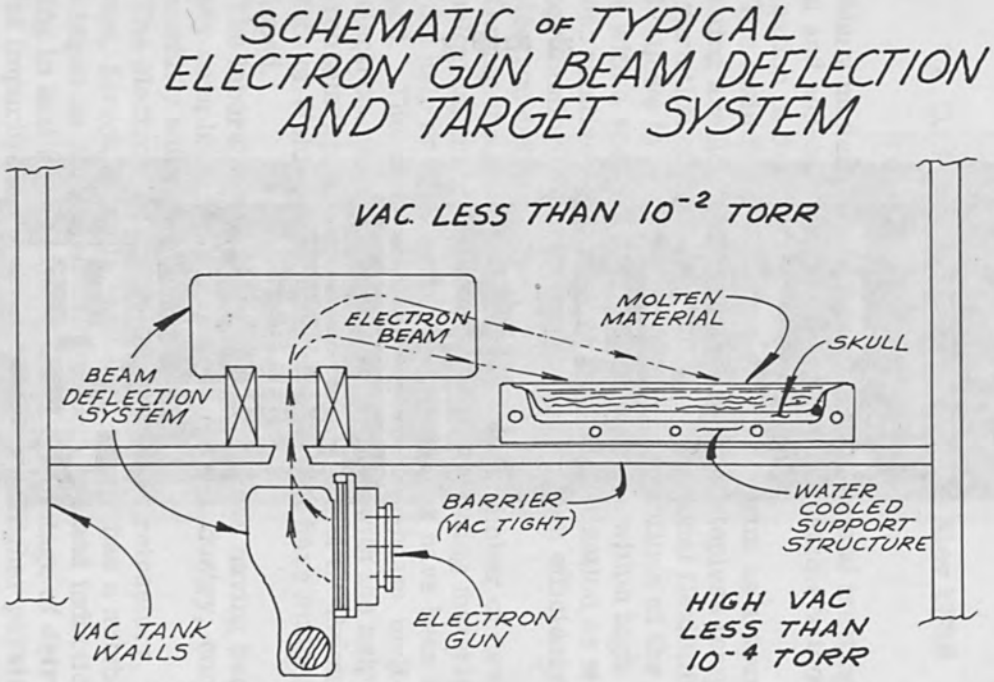
SCHEMATIC OF TYPICAL
ELECTRON GUN BEAM DEFLECTION
AND TARGET SYSTEM
VAC. LESS THAN 10^{-2} TORR
ELECTRON BEAM
MOLTEN MATERIAL
SKULL
BEAM DEFLECTION SYSTEM
BARRIER (VAC TIGHT)
WATER COOLED SUPPORT STRUCTURE
VAC TANK WALLS
ELECTRON GUN
HIGH VAC LESS THAN 10^{-4} TORR

Figure 11.

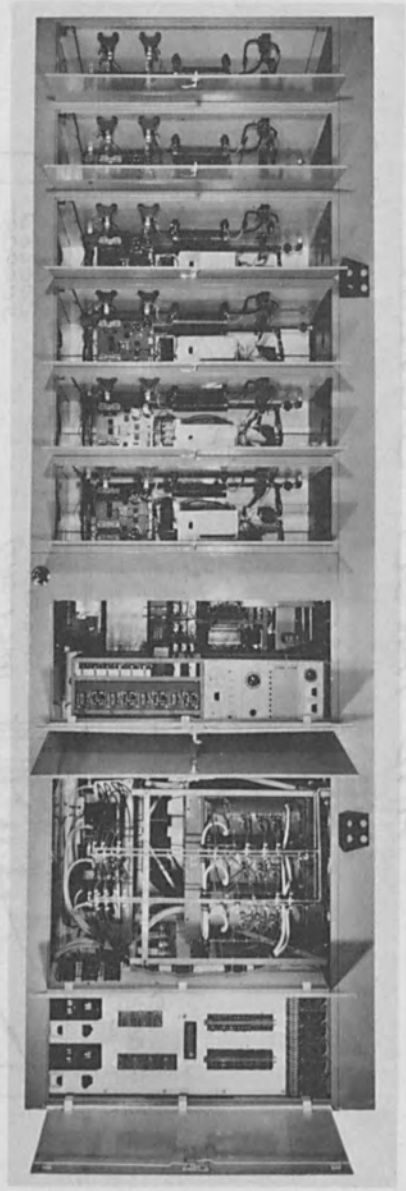

Figure 12.

Developements on Electron Beam Technology*

B. E. Paton

E. O. Paton Institute of Welding Kiev USSR

Many modern processes of producing and treating metal and non-metal materials are not possible without application of the electron-beam heating.

The main features of the electron-beam as a source of heating are as follows: possibility of stepless temperature variation of the body heated; exceptional flexibility which allows to produce various configurations of the heated zones with a specific heat power adjusted within high ranges; relative simplicity of the automatization as well as a programming of the heating process; high efficiency of the electron-beam heating.

During the last five or six years a number of new technological trends of producing and treating materials with the help of the electron-beam heating have been developed. The main ones are: electron-beam melting; electron-beam welding; evaporation with the help of electron guns; precise treatment. At the E. O. Paton Institute of Welding the first three trends have mainly been developed.

The laboratory phase of these methods having been already completed, they are used in the industry, competing successfully with other methods.

The electron-beam melting to refine refractory, nonferrous, ferrous metals, and their alloys has a number of advantages as compared with vacuum arc and induction melting in that the metals of lower percentage of detrimental impurities and, consequently, of higher physical properties are obtained.

*This was one of the plenary presentation at the opening session

When considering the electron-beam melting one cannot help noting that the most part of investigations was devoted to equipment development, especially, to that of electron optical systems (guns) and often without taking into consideration technological and metallurgical features of a vacuum refining.

For an effective refining by the electron-beam melting one should highly develop a surface of a liquid metal together with a thin overheated layer existing overall the surface. We believe that these conditions should be effected when melting is performed with radial electron-beam heaters, vertical feed of the remelted electrode and uniform distribution of energy in a crystallizer [1].

At the institute the electron-beam installations of 180 kW (16 kV voltage) and 600 kW (16 kV voltage) have been developed on the basis of the radial electron-beam heaters. Figure 1 shows a general view of 180 kW electron-beam installation. The installation is of a two-chamber design with a separate exhaustion. A radial electron-beam heater is located in the upper chamber; melting is performed in the lower one. A feed of the remelted metal and withdrawing of the ingot is performed by the upper and lower devices, respectively. Keeping of the level in the crystallizer, feeding of the remelted metal and withdrawing of the ingot are carried out automatically.

The installation of the design described, as well as these with axial systems and among them that of M. von Ardenne's design (MO-200) are in operation at metallurgical works which produce refractory, non-ferrous and ferrous metals and alloys.

Simultaneously with a production of pure niobium, tantalum, molybdenum, copper, nickel and their alloys a refining of structural steel is accomplished.

The result of refining of ball-bearing steel IIIX - 15 by electron beam melting is shown in the fatigue curves before and after refining in Figure 2.

The application of the electron-beam for welding is being further developed as new researches, device improvements, and new technique requirements are being accumulated.

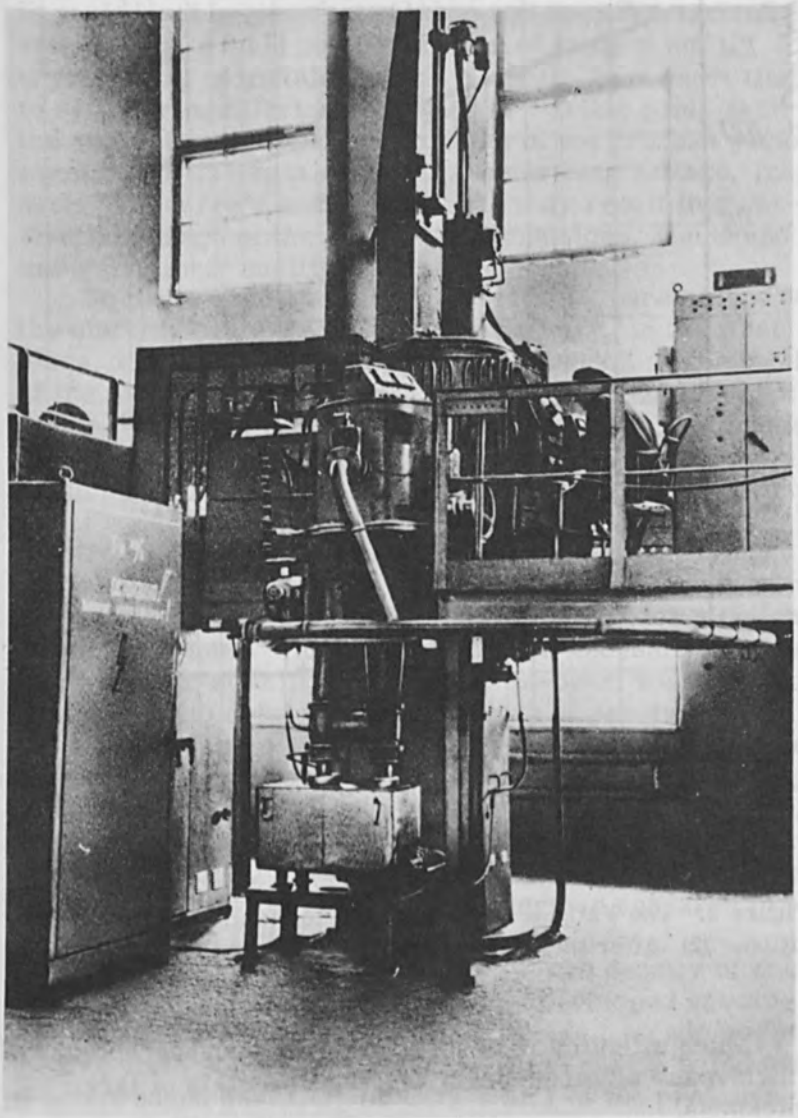

Figure 1. A General View of the Electron-Beam Installation for Melting of Metals.

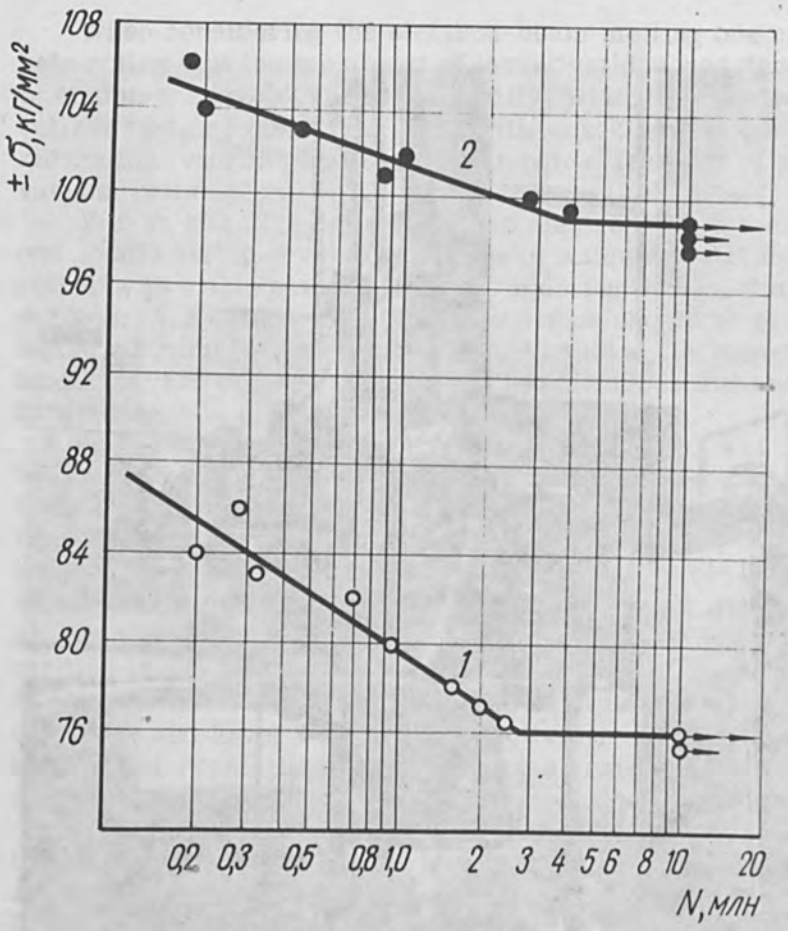

Figure 2. The Fatigue Curves of IIIX-15 Steel. (1) Initial Condition. (2) After the Electron-Beam Melting.

Much attention is devoted to devices and technology of single-pass electron-beam welding of metals of large thickness.

Single-pass welding of small products made of heat-proof steels with 15 mm thick weld edges and of large products with 10 mm and 35 mm thick weld edges is already put into production.

As the electron-beam welding of thick metal plates is performed by penetrated beam and is characterized by small sizes of weld pool, high rate of melting and crystallizing of metals and, as a result, by a short time to settle an equilibrium condition of welding pool, even the short time and small variations of the process parameters, such as-beam current, accelerating voltage, magnetic lens current and welding rate may result in a substantial change of the geometric dimensions, welds and in impairing their quality.

To secure the stability of the melting parameters with the electron beam welding it is necessary, in the first place, that the specific capacity of the beam on the product at the total constant capacity of the beam should be kept stable. This, in its turn, determines severe requirements as to the stability of the parameters of the electron optical systems of the welding electron gun and its power sources.

Figure 3 shows a relative change of the depth of electron-beam penetration at beam current variation (1), an accelerating voltage (2) and magnetic lens current (3) within the limit of ± 5% of optimal value for a typical low-voltage gun. This plot confirms a necessity of a sufficiently high stability of the electron-beam welding parameters to obtain a constant depth of penetration.

Though it was not too difficult to produce a stabilizer of the magnetic lens current for the low-voltage welding gun ($\underline{V}_{acceler.}$ 30 kV) with the stability of 10^{-4} (0.01%), but the sources of a stabilized accelerating voltage with the stability of 10^{-2} (1%), were developed and introduced into the industry only after a very serious research program had been fulfilled.

To obtain the electron-beams of high density of energy (10^8 W/cm^2 and higher) the Institute developed cascade electron guns combined with high voltage cascade power source units and assembled in the steel casing filled with a compressed gas (CO_2 or $CO_2 + SF_6$ at the pressure up to 7 atm.) (Fig. 4).

Electron-beams with energy up to 200 kilo-electron-volts and higher may be formed in these guns, whereas the isolators and cables used operate at the pressure not more than 10-12 kilovolts. The formation of the electron-

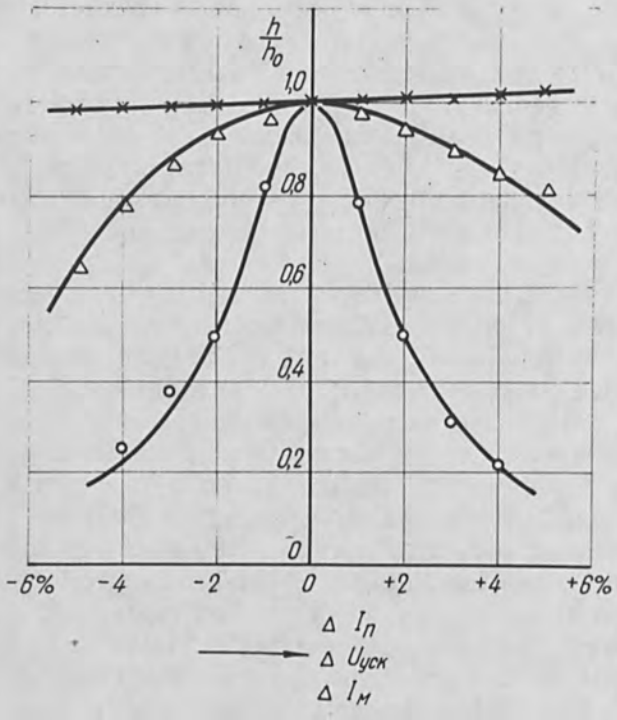

Figure 3. A Relative Variation of the Depth of Electron-Beam Penetration at the Beam Current Variation, Accelerating Voltage and Magnetic Lens Current (a Typical Low-Voltage Welding Gun).

beam is performed by means of three-electrode system (1) at the anode voltage of 10-12 kilovolts, and an acceleration of the beam electrons up to 200 keV and higher takes place in the acceleration tube (3) with flat electrodes and uniform electric field.

To reduce the electron-beam section electrostatic focusing (2) before the acceleration tube (pipe) and magnetic focusing after the acceleration tube (8) are used.

The correction of the beam position before entering the tube and the magnetic lens is performed by magnetic prisms (4). The cascades of the high voltage power

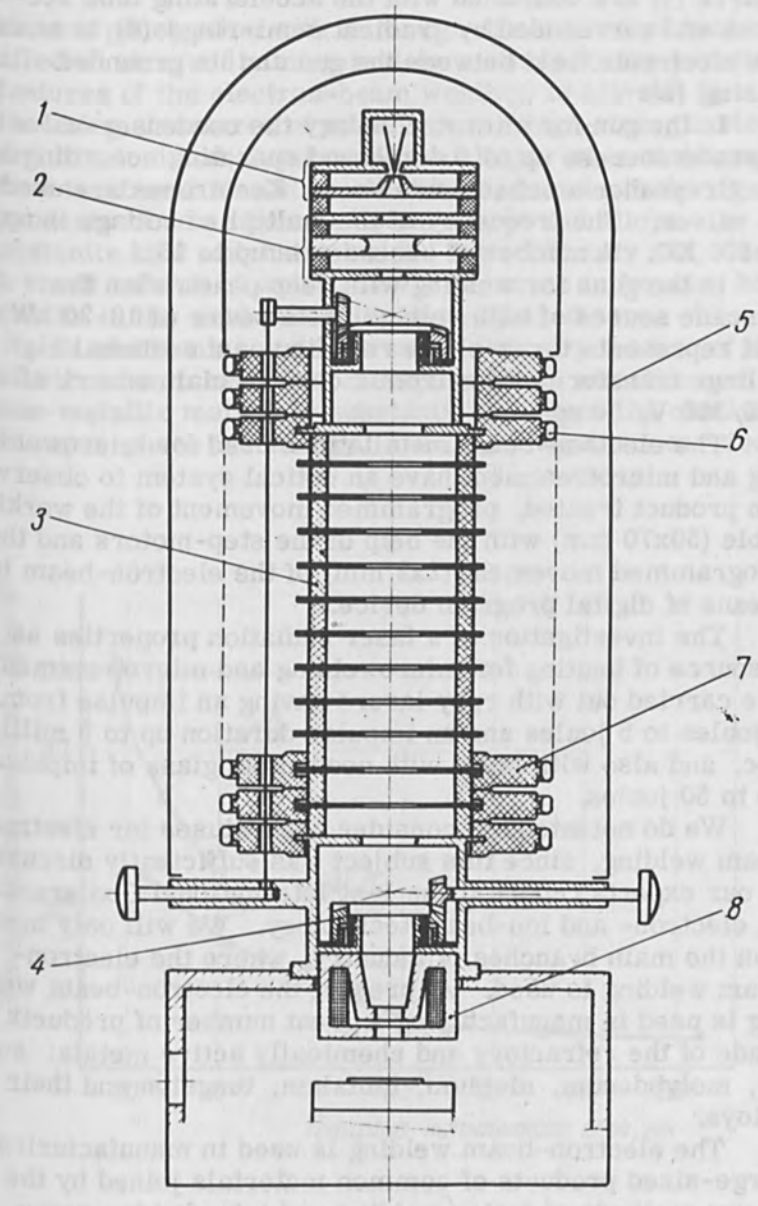

Figure 4. The Scheme of the Cascade Electron Gun.

source (7) are combined with the accelerating tube sections and surrounded by gradient semi-rings (6) to smooth the electronic field between the gun and its grounded casing (5).

In the gun for microtechnology the condenser-valve cascade sources up to 0.4 kWt and operating according to the Greynaher's scheme are used. Kenotrones are used as valves. The frequency of the multiplied voltage is up to 100 KC. A number of cascades is up to 15.

In the guns for welding with deep penetration the cascade source of high voltage has a power of 10-20 kW and represents three-phase rectifier on a sectional high voltage transformer fed from a commercial network of 220/380 V, 50 cps.

The electron-beam installations used for microwelding and microtreatment have an optical system to observe the product treated, programmed movement of the working table (50x70 mm) with the help of the step-motors and the programmed movement (2x2 mm) of the electron-beam by means of digital program device.

The investigation of a laser radiation properties as a source of heating for microwelding and microtreatment are carried out with ruby lasers having an impulse from 1 joules to 5 joules and an impulse duration up to 5 millisec. and also with laser with neodynium glass of impulses up to 50 joules.

We do not intend to consider apparatuses for electron-beam welding, since this subject was sufficiently discussed in our experts report at the 1-st International Conference on electron- and ion-beam technology. We will only mention the main branches of industry, where the electron-beam welding is used. At present the electron-beam welding is used in manufacturing a great number of products made of the refractory and chemically active metals: such as, molybdenum, niobium, tantalum, tungsten and their alloys.

The electron-beam welding is used in manufacturing large-sized products of common materials joined by the known methods of fusion welding and intended for some responsible service, when the welding is performed in hard-to-reach places (for example, at the bottom of deep and narrow edge preparation) or when only a deep and

narrow penetration with minimum dimensions of heat-affected zone and minimum deformations (being peculiar features of the electron-beam welding) is allowed in manufacturing structures of some types of high strength steels and titanium and aluminum-base alloys, when a subsequent heat treatment should be eliminated; in manufacturing products of some heat resistant steels and alloys of austenite kind which are welded with difficulty and, due to a small volume of weld, show a decrease in forming hot cracks in the weld and in its heat-affected zone.

In electronics and instrument industry the use of the electron beam heaters for evaporation of metallic and non-metallic materials substantially widens the chances of vapor-phase technology. The investigations carried

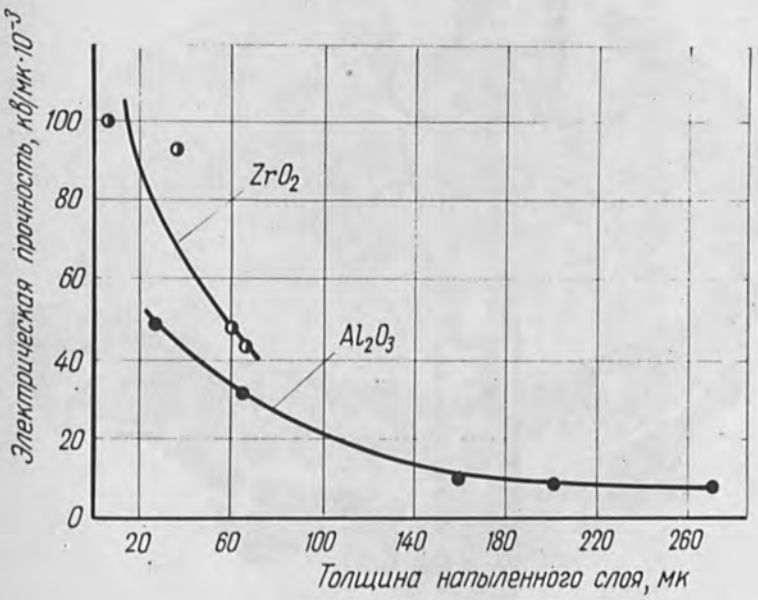

Figure 5. Electric Strength of Layers Depending on their thickness (Substratum Temperature at Spraying is 500°C).

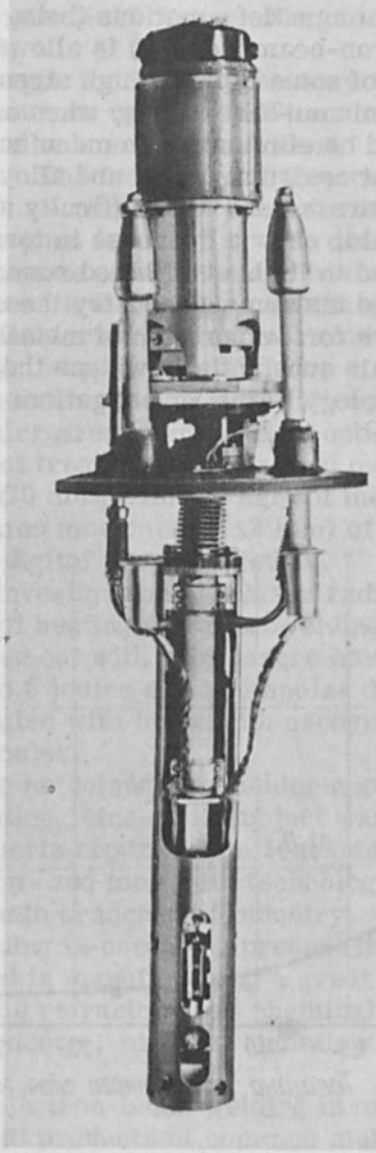

Figure 6. A General View of Single-Beam Evaporator.

out at the Institute aim at studying a condensation process of the vapor-phase of metallic and non-metallic materials, the factors determining condensate adhesion to a substrate and the physic-chemical properties of the condensates. The ratios between the electric strength and the film thickness of Al_2O_3 and ZrO_2 at substrate temperature of 500°C is given on the Fig. 5, illustrate the properties studied.

Technological developments are performed in two directions:

a. to make thin (0.1-50 microns) coatings with various physic-chemical properties on semifinished products (plate, sheet wire) or finished products;

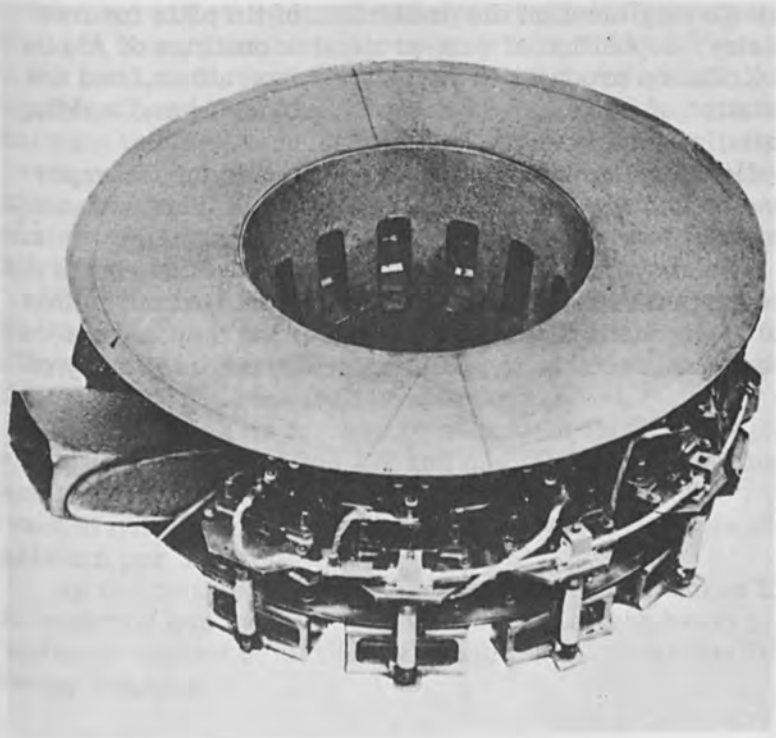

Figure 7. A General View of Multigun Evaporator.

b. to produce thick condensates (some millimeters) such as plates or bodies of rotation of various configurations.

In accordance with this some types of electron beam evaporators and respective installations have been developed. Figure 6 shows a general view of a single-beam evaporator of 18 kWt intended for producing thin layers on internal surface on bodies of rotation. Figure 7 gives a general view of multibeam evaporator of 200 kW (voltage 16 kV). A peculiar feature of the multibeam evaporators is that it is possible to simultaneously evaporate several materials. The above evaporator allows to perform a time-adjusted and simultaneous evaporation of four components.

As an example of already solved technological problems we may mention the production of tin plate for food industry; deposition of heat-protective coatings of Al_2O_3 and ZrO_2 on products of various configurations, and the formation of transition layers when soldering and welding dissimilar metals.

Developments connected with installations for vapor-phase technology tend to create continuous lines with a maximum level of automatization and programming.

The above examples taken from the electron-beam technology do not cover all the studies carried out in this field at the Institute; still we believe that they are sufficiently characteristic to illustrate the main tendency of our work.

A New 260 kW Electron Beam Production Melting Multiple Gun Furnace

W. Dietrich and H. Stephan

Heraeus Hochvakuum GmbH,
Hanau, Germany

The electron beam melting furnace described (Fig. 1) represents, in its final state, a 500 kW multiple gun unit in which the experience gained during the manufacture of 50 EB furnaces for research and production has been incorporated. It is equipped with four separately evacuated electron beam guns having a beam power of 150 kW each. In the final state, each gun is connected to a separate power supply unit and two diffusion pumps of 50 000 l/sec each maintain the high vacuum required during melting.

Upon engineering and designing this furnace, we have taken care to facilitate and simplify all operations connected with running production of ingots as well as for retain the versatile feature of this furnace type.

Its principal application is production melting of refractory metals, such as tantalum, niobium, and special alloys, and, furthermore, of nickel- and cobalt base alloys. Extended use for research is also considered.

At present, this furnace operates, in its first stage, with a beam power of 260 kW and one 50 000 l/sec diffusion pump. With this equipment, the furnace immediately reached quite high a production rate (nearly four tons of tantalum per month).

As far as this type is concerned, we also adhered to the multiple gun system - besides, the electron beam power required could not be attained with one gun only - for the following reasons:

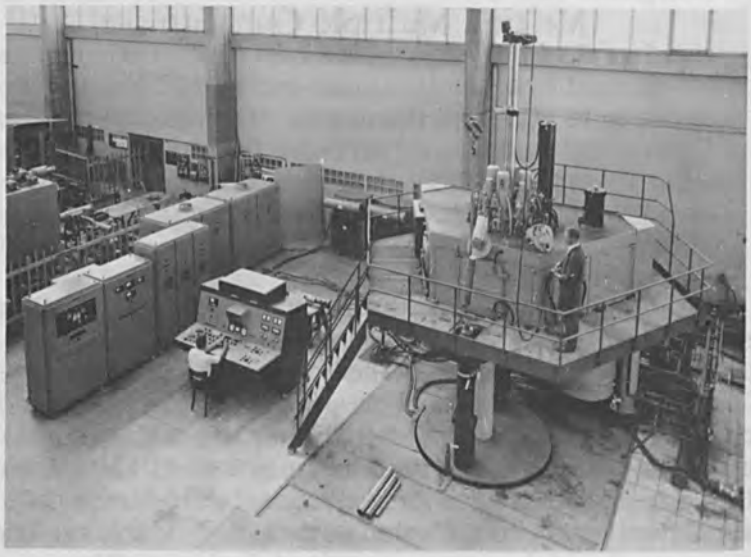

Figure 1. 260 kW Electron Beam Production Melting Furnace ESP 100/500

1. In our opinion, central-vertical feed stock is really important, particularly for remelting ingots of refractory metals with the diameter ratio 1:1.

2. Incidental arcing of a gun is only partially influencing the melting power. Therefore, higher continuity of the melting process can be reached.

3. While exchanging cathodes, melting can be continued by means of guns which remain in operation and run for this short period of time, with increased power. Although this incident normally occurs seldom, it is advantageous to eliminate its effect on the melting process.

4. The existence of the large deflection angle in the beam path of the multiple gun system seemed to us to be important, in order to eliminate back streaming ions, especially when melting refractory metals.

A few characteristics of this furnace are described as follows:

Gun System

Figure 2 shows the group of four electron beam guns. Each gun, together with its diffusion pump for separate pumping, represents a compact unit. A gate valve is installed in the beam guiding tube to separate the cathode room from the melting chamber in order to keep the cathodes under vacuum upon venting the furnace. Unaffected and for long time steadily working cathodes are the result. On the other hand, the cathode room can also be separately vented while the furnace is kept under vacuum. Inspection and exchange of cathodes is therefore possible, even during melting process.

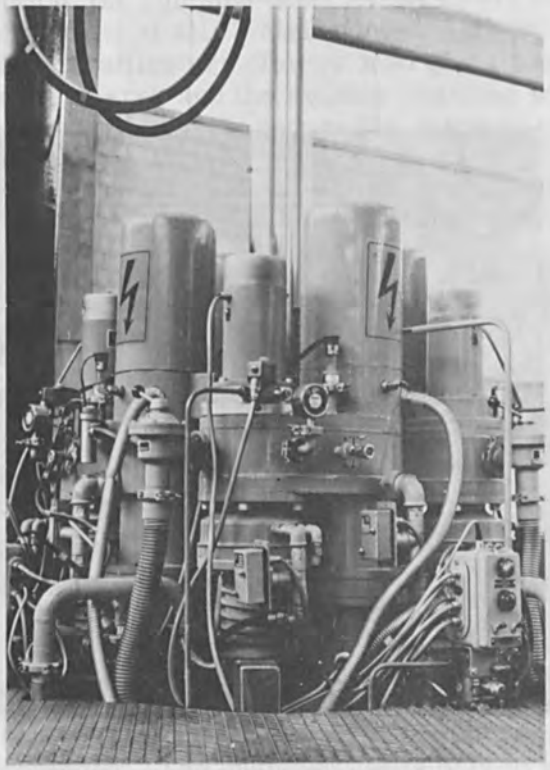

Figure 2. Group of 4 Electron Beam Guns of 150 kW each.

The electron beams, generated by indirectly heated block cathodes, are electromagnetically focussed to small spots and deflected to the melt. Each gun is equipped with two independent, perpendicular deflection systems for radial and tangential beam deflection. Adaption of power density to different pool and electrode sizes is perfected by either oscillating the beams radially or tangentially, or rotating them on the pool in circular or elliptical orbits.

Control of beam power and beam guiding of the four guns is mainly carried out simultaneously. Separate electrical adjustment is also possible. As the acceleration voltage of 20 kV, independent of variation of connection voltage and beam power, is automatically kept constant, the beam adjustment, performed at low power, remains valid for the entire power range.

Figure 3. Furnace Operation during Melting of 8" Steel-Ingot.

Observation of the Melting Process

At the monitor on the control desk (Fig. 3) the operator can watch the melting process alternatively from both sides by means of two TV cameras which are installed in such a way that their electron "eyes" look through stroboscopic windows into the furnace.

Pumping System

A common chamber houses the valves for the two diffusion pumps and the melting area. The diffusion pumps are arranged in the immediate proximity of the melting chamber. Due to a short pumping path and the large pump cross section, the pumping capacity of the diffusion pumps is hardly reduced at all. Water-cooled, anti-splash and anti-radiation baffles are dimensioned and arranged between the valve area and the melting chamber in such a way that they only slightly reduce the pumping capacity.

Crucible

The crucible unit in which the melting and casting process takes place, is introduced into the melting chamber from below.

Water inlet and water outlet are affected on atmospheric side. For cleaning or the exchange of a crucible insert, the crucible jacket with the insert can be lowered to the ground by means of a hydraulic system. Good access permits fast operation without any difficulty (Fig. 4). The pumping program is automated.

Charging System

The rotatable charging system with two ingot chambers is explained in Fig. 5.

Loading and unloading of ingots and electrodes can be done by one person without breaking the vacuum in the furnace chamber. The chamber needs only to be vented to atmosphere for cleaning of it or of crucible. Melted ingots may cool down slowly under vacuum or can be cooled more rapidly by forced inert gas cooling. Before interchanging

Figure 4. Cleaning of Crucible.

the two ingot retraction units, the crucible jacket and the valve below the crucible jacket are raised by means of a hydraulic system thus permitting ingot retraction units below the crucible to be turned aside easily. The pliable, metallastic sealing element between crucible jacket and chamber will thereby only slightly be deformed.

For loading the consumable electrodes with diameters larger than the crucible diameter, e. g. loading of bundled scrap and granule compacts, the electrode feeder rod is moved through the chamber in order to take over the bundled consumable electrode easily accessible. When applying this charging method (which is rarely done), the

chamber must be vented to atmosphere and the crucible lowered and turned aside.

Test melts have mainly been carried out with tantalum. A number of results are shown in the table, Fig. 6. It is interesting to see the fairly high melting speed despite the high gas contents of the starting material. Total power reductions by arcing of guns never happened, so that the expected continuity of the melting process could be attained.

The products of a one week furnace test are demonstrated in Fig. 7. Nearly one ton tantalum ingots with an excellent surface.

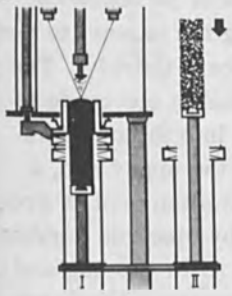

a

a)
During the current melt, the ingot previously melted and meanwhile cooled can be unloaded. Subsequently, the starting block and the new consumable electrode can be loaded into the ingot container, and the closed chamber can be evacuated with a fore pump.

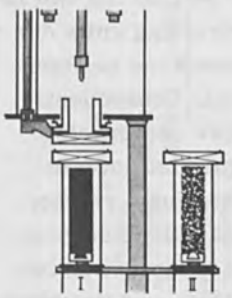

b

b)
Upon completion of the melt, the ingot is retracted into the container, and the valves on crucible and ingot container are closed under vacuum, so as to ensure a vacuum-tight seal. The room between the two valves is vented. By means of an oil hydraulic system passing through the tank,

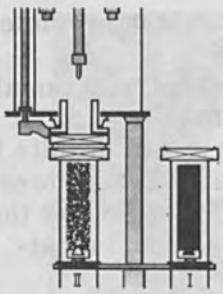

c

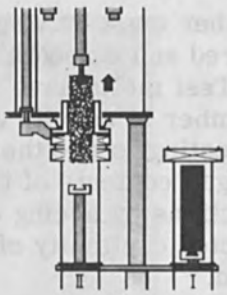

d

c) the crucible and valve are raised so that the two ingot retracting units can at the same time be interchanged. Subsequently, the valve and crucible are again let down to the other ingot retracting unit which has been moved to a position beneath them and the room between the two valves is evacuated.

d) The pressure in the tank which was increased by opening the valves, is reduced very quickly. The consumable electrode is moved into the crucible, and on the upper end, a small molten pool is produced by electron bombardment. After dipping and solidification of the stub, the consumable electrode is lifted and, at the same time, the starting block is moved into the crucible. The next melt can be started.

Figure 5. Unloading a Molten Ingot and Charging a Consumable Electrode.

Material	Ingot Diameter	Melting Speed	Total Beam Power	Average Pressure	Ingot Yield	Splattered and Evaporated Material Regained	Analysis			Brindell Hardness
	mm	kg/h	kW	Torr	% of material charged	% of material charged	H ppm	O ppm	N ppm	kg/mm²
Pressed Bars from Scrap 80x80 mm							50	11300	125	
1. melt	100	25-30	180-200	$4\text{-}8\cdot10^{-4}$			3	1200	100	
2. melt	100	120-150	220-240	$5\text{-}8\cdot10^{-5}$	76	17	1-2	182	90	75 - 80
Pressed Bars from Powder 80x80 mm							146	2500	258	
1. melt	100	35-45	180-200	$3\text{-}5\cdot10^{-4}$	80	12	5	200	70	
2. melt	100	130-150	220-240	$5\text{-}8\cdot10^{-5}$	80	12	1-2	115	43	70 - 75
Pressed Bars from Powder 80x80 mm							50	800	180	
1. melt	100	60-70	180-200	$2\text{-}5\cdot10^{-4}$			2	150	50	
2. melt	100	130-150	220-240	$5\text{-}8\cdot10^{-5}$	85	8	1-2	100	22	70 - 75

Figure 9. Results of Tantalum Melting in an EBM-Furnace with 260 KW Melting Power and 50000 l/sec Pumping Capacity

Figure 7. Tantalum Ingots of 2" and 4", produced within one week.

Problems Encountered When Melting Steel with the 1,700 kW Multichamber Electron Beam Furnace

M. von Ardenne, S. Schiller, P. Lenk
Research Institute Manfred von Ardenne Dresden,
H. Fiedler, G. Scharf VEB Edelstahlwerk Freital,
H. Schonberg VEB LEW Hennigsdorf, East Germany

INTRODUCTION

Metallurgical advantages obtained when melting reactive and refractory metals by means of an electron beam has caused the extensive application of this method in the metal producing industry.

Various types of electron beam furnaces in the power range from 60 kW to 300 kW are in use and operate very efficiently [1-11].

Electron beam melting has not yet gained the same headway in ferrous-metallurgy. One of the reasons for the hesitating introduction of this method is that in this field vacuum arc furnace of mature design were available when development of electron beam melting technology began, and that with the vacuum arc furnace materials could be produced which were able to meet many demands [12, 13].

Opinions whether electron beam melting can keep pace with vacuum arc furnace processing in the field of ferrous-metallurgy can be expected only when comparable equipment is available with respect to furnace power and degree of accomplishment.

With electron beam melting it is a simple matter to independently vary the parameters which are relevant for the melting process. This involves melting rate (kg/min) and consequent depth of the pool, and the temperature distribution across the melt. Favorable outgassing conditions of the gases evolved from the metal with electron beam melting due to the low partial pressure at the melting

site are an added advantage. Compared to the vacuum arc furnace, the same vacuum conditions are established across the entire length of the ingot.

Consequently, the selection of essential melting parameters as desired permits the exercise of control to a considerably greater extent in electron beam melting, as is possible with the vacuum arc furnace [14].

In the process of developing our electron beam melting equipment special attention has been given to its use in ferrous-metallurgy [15-17]. After respective metallurgical examination and study of a 60 kW plant (Forschungsinstitut Manfred von Ardenne) a furnace with a beam power of 200 kW was installed and has been in use for production purposes since 1961 at VEB Edelstahlwerk Freital. The results that could be obtained with this multichamber electron beam furnace, together with the mentioned properties of the electron beam melting method, have led to the decision to design a multichamber furnace at our Institute operating with a beam power of 1,700 kW. This plant enables the melting of steel ingots of 800 mm max. diameter and a max. unit output weight of 12 tons [18]. This plant also operates at VEB Edelstahlwerk Freital, and will be further detailed on the following pages.

2. CONSTRUCTION OF THE PLANT

It has been our aim to construct an electron beam furnace which could be used preferably for the melting of steel.

In this connection it must be considered that the metal vapor can assume values around 1 Torr, also directly above the melt. Gases evolved during the melting process can produce total pressures ranging from 10^{-3} to 10^{-2} Torr. To provide for functional dependability of the electron gun assembly its direct subjection to vapor had to be avoided and a separate evacuating system for the electron gun assembly had to be arranged for. These demands are fully met by our multichamber single beam system which we have been using for some time. Employing only one electron beam also permits the deflection of the beam according to a specific time cycle programme without difficulty. This allows an extensive variation of the tem-

perature distribution across the melt and of the melting speed.

As is the case with our smaller plants, the electron beam is here also introduced into the melting chamber from above. The melt stock consists of cast billets which are fed in laterally [3]. On Fig. 1 the principle arrangement is shown. A magnetic lens serves to vary the diameter of the electron beam across 80 to 200 mm. A magnetic cross deflection system is provided to distribute the energy on the feed stock and the melt.

Molten material drips into the pool from above, and provision is made that sufficient energy is directed also on the pool under the feed stock by suitably spacing the deflection system, the feed stock, the melt and by appropriate adjustment for the feed stock melting face.

The melting pool is located in a watercooled copper crucible having a withdrawable bottom. At present ingots with a maximum diameter of 800 mm could be obtained, however, plant construction provides for ingot diameters of 1,000 mm max.

In Fig. 2 the plant is schematically illustrated.

As feed stock, billets are used with a diameter of 280 mm, and a length of 2,000 mm. They have a weight of about 1 ton. Feed stock enters the plant from two sides, which permits charging one side through a lock, while the other melts. For re-charging about 20 minutes are required.

An ingot pulling arrangement is incorporated below the furnace, which can handle ingots up to a length of 3,000 mm. With an ingot diameter of 800 mm this results in an output weight of about 11 tons.

For evacuating the melting chamber four oil diffusion pumps are provided, each having a pumping speed of 30,000 litres per second. An accessory rough pumping set is included. Later the installation of four pumps, each with a pumping speed of 80,000 litres per second, is intended.

A picture of the multichamber electron beam furnace EMO 1700 at the Vacuum-Steelworks Freital is shown in Fig. 3.

For the direct operation of the furnace two operators are needed, with one controlling the melting process while

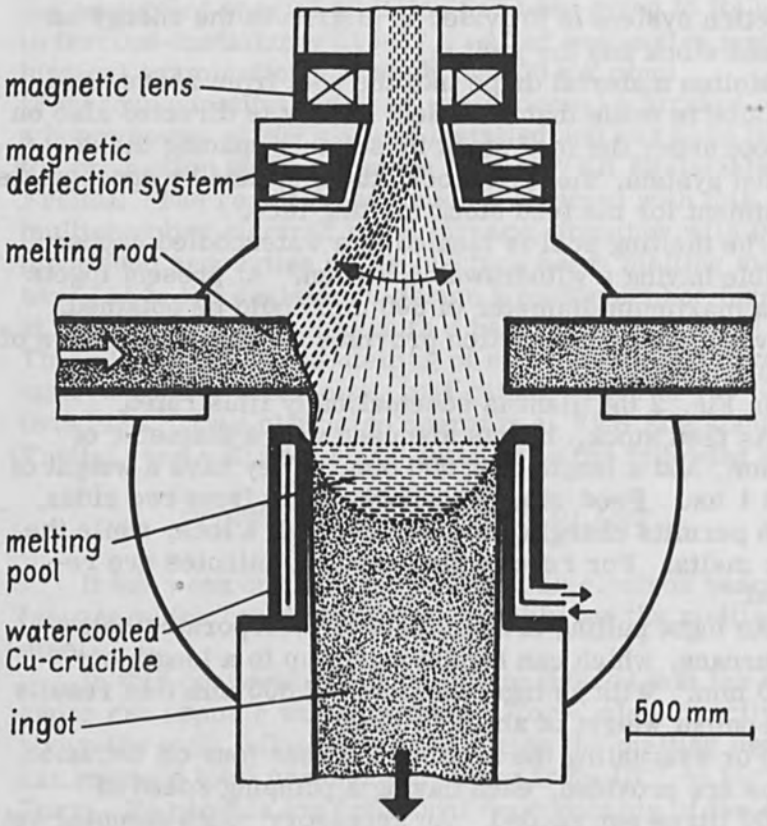

Figure 1. Melting Geometry of the EMO 1700 Equipment

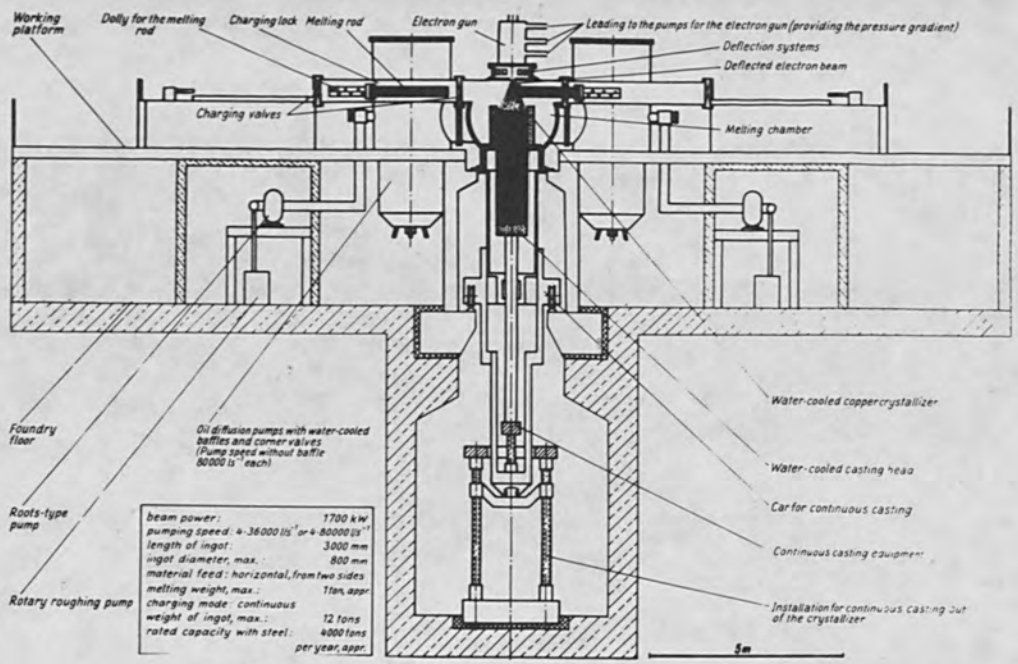

Figure 2. Vertical cross-section of the 1700 kW-Electron beam multi-chamber furnace of VEB LEW/GDR

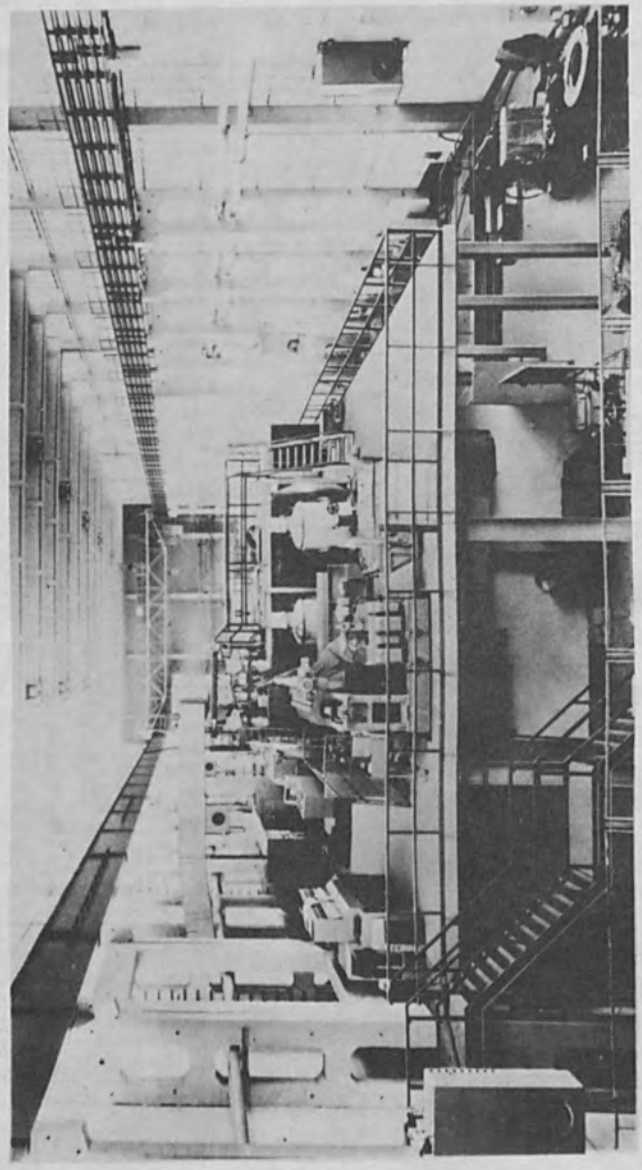

Figure 3. View of the vacuum steel works' hall at VEB Edelstahlwerk Freital. Multi-chamber single-beam furnace in the foreground operates with a beam power of 1700 kW and has been manufactured by VEB LEW/GDR

the other cares for the uninterrupted re-charging of the plant with feed stock. A stroboscopic arrangement is provided for the visual observation of the melting process [19]. Despite the large pool surface, viewing by means of this device is not noticeably obstructed even when operating with a prolonged melting period of 10 hours, for example.

3. PHYSICAL ASPECTS

With 200 kW equipment, we use accelerating voltages (U_B) of 27 kV, max. Under condition of retaining the single-beam multichamber system, the marked increase of the beam power could practically be realized only by also increasing the accelerating voltage (U_B). It is well known that the accelerating voltage cannot be raised indefinitely, but that it is subject to practical limitations resulting from the deterioration of the high-voltage strength of the gun assembly and of the high-voltage rectifier. With our plant assembly this voltage can have a maximum level of about 40 kV. Figure 4 shows the voltage-current characteristic of the electron gun. From the diagram it can be seen that an electron current of 43 A is necessary for a power of 1,700 kW, which is equivalent to a perveance value of about $5,3 \cdot 10^{-6}$ A $V^{-3/2}$.

Rectification of the high-voltage required for the electron gun is handled by thyratrons arranged in three-phase bridge circuitry. A high-voltage control is provided which permits the adjustment in 10 steps from 8 kV on.

Because high-voltage breakdowns cannot be avoided in practical operation, a brief interruption of the high-voltage supply is effected by blocking the thyratrons through a medium frequency transmitter.

Generally, a rate of 10 to 30 breakdowns per hour can be expected. With every breakdown the beam is interrupted for a period of about 3 seconds, which in the case of 20 breakdowns per hours, results in an average power drop of about 2%.

Two magnetic lens arrangements are utilized to guide the beam through the system of pressure stages. To keep losses to a minimum, massive molybdenum rings are

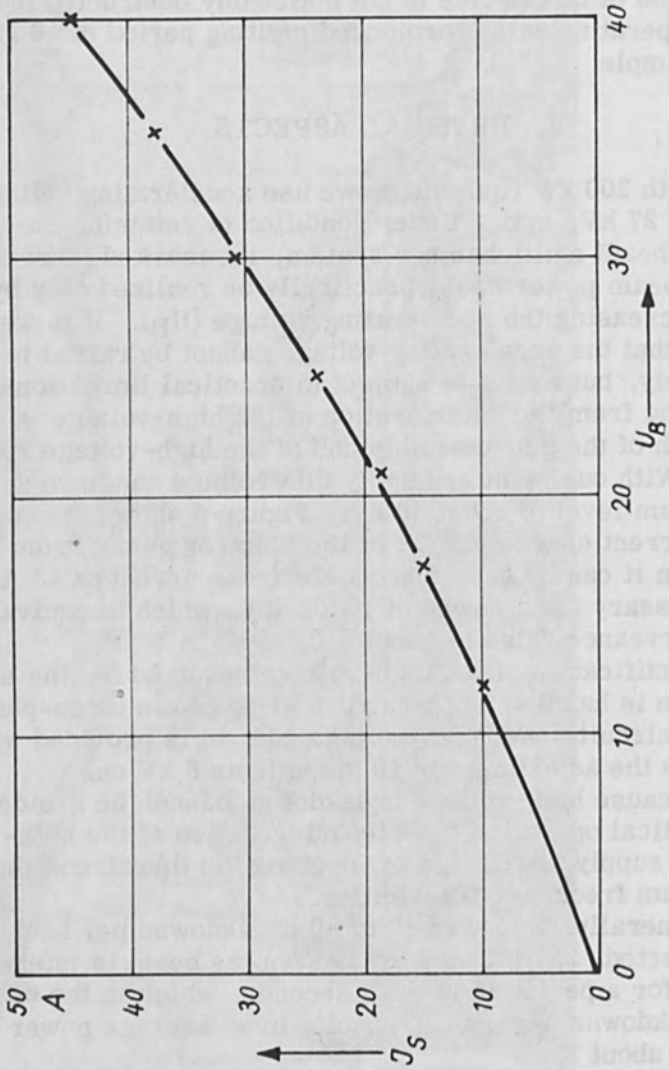

Figure 4. Current-Voltage Characteristic of the Electron Gun of EMO 1700 Equipment.

provided in the beam trajectory. Their inner diameter is about equal to the employed flow impedances. An undesirable beam trajectory will cause the molybdenum rings to heat up to glow temperature, which is observable through the viewing system and permits the operator to correct the beam trajectory. Flow impedance assemblies include watercooled copper tubing.

To assure rapid operational readiness of the electron gun assembly, it is separated from the other equipment by a suitable valve when the melting chamber undergoes ventilation.

To maintain the pressure gradient between the melting chamber and the gun assembly compartment three oil diffusion pumps are used, each having a pumping speed of 2, 000 litres per second. One of the pump units serves to evacuate the gun assembly compartment, while the other two are applied at an intermediate chamber interposed between gun assembly compartment and the melting chamber. Separation is effected by means of flow impedances designed in length and diameter to attain a pressure ratio of 100 between the two chambers, and still pass the beam with little loss.

Suction socket, magnetic lens assemblies and length of flow impedance structures necessitate a beam trajectory of 1 metre from the point of generation to the entry into the melting chamber. Without exploitation of space charge compensation by means of ions generated by the beam itself, this distance would cause beam spread to such an extent that with the practically required flow impedance diameters no guiding could possibly be achieved, despite the use of the magnetic lens arrangement.

This problem of beam spread by space charge has already been encountered with our 200 kW electron beam furnace using an accelerating voltage (U_B) of 27 kV and a beam current (J_S) of 7, 5 A.

Partial compensation of the space charge is effected by the ionization of the metal atoms emerging from the melt, but melt stock and melting parameters influence the degree of compensation.

With our 200 kW electron beam assembly, however, we overcame this undesirable effect by introducing argon through a valve into a chamber interposed between the

melting chamber and the gun assembly compartment. We used a pressure of about $3 \cdot 10^{-4}$ Torr for the argon gas, and could in this manner effectively compensate the space charge spread largely independent of the melting parameters [20].

When using our 1,700 kW plant, experience showed no additional advantages when introducing a gas. Probably caused by the considerable metal evaporation due to the high current intensity of the beam, notable scattering of the electron beam could be observed at the produced plasma or at the vapor itself. This is particularly the case when the melt is excessively overheated.

This scattering effect becomes less with increasing accelerating voltage, which is a familiar fact and the main reason why the generation of a focused electron beam in the power range of 1,700 kW requires accelerating voltages of about 40 kV. Further power increase of the electron gun assembly seems at present possibly only through a rise of the accelerating voltage, if the multi-chamber system is retained.

Electron beam power is utilized for the heating of the melt and for melting. The power component necessary for heating the melt is essentially influenced by the diameter of the crucible and the temperature desired for the melting pool. Approximate values of power P_o, as a function of the crucible diameter d_k, are shown in Fig. 5. That power is required to keep steel at melting temperature up to the rim of the crucible.

Generally, at a crucible diameter $d_k = 400$ mm, an electron gun assembly will be required capable of furnishing a power $P = 800$ to 1,000 kW. Using a crucible with a diameter of $d_k = 800$ melting proceeds usually at a power of $P = 1,100$ to 1,500 kW. At a beam power of $P = 1,200$ kW and a crucible diameter of $d_k = 800$ mm consequently about 700 kW are available for overheating the melt and for melting, as shown in Fig. 5. This power can be distributed according to metallurgical requirements. If the total power difference $P - P_o$ would be concentrated, for example, on melting only, this could yield a melting rate of $n \approx 30$ kg/min if a power $P \approx 1,200$ kW is used. It is, however, advisable to melt more slowly, for metallurgical reasons. Overheating of the melting pool is necessary to obtain an

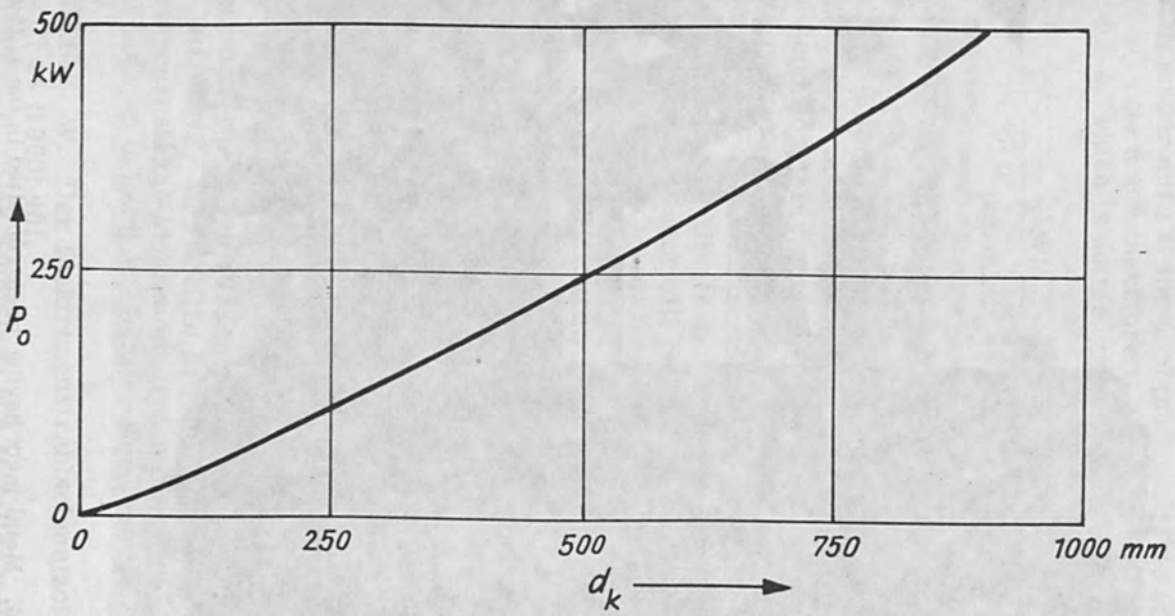

Figure 5. Approximate data for the minimum beam power P_o to keep molten pool at desired temperature with reference to diameter d_k of the watercooled Cu-crucible (steel, watched at d_k = 230 mm, 380 mm, 800 mm).

Figure 6. Metal ingot having been remelted in the 1,700 kW multichamber electron beam furnace of VEB LEW/GDR.
P = 1200 kW e = 1.5 kWh kg^{-1} G = 8000 kp

ingot with a satisfactory surface, and also to favorably influence the physico-chemical reactions. Thus, the specified temperature at the pool principally determines the melting rate n and therefore the specific energy requirement e, which is defined by

$$e = \frac{P_{(kW)}}{60\ n_{(kg.\ min)}} \qquad (kWh/kg)\ .$$

In conjunction with the programme controlled deflection, i. e. by variation of the melting rate n, these physico-chemical reaction processes can be widely varied and optimized. In practical operation, experience has shown that the specific energy must be $e > 1$ kWh/kg to attain adequate refining effects. In Fig. 6a metal ingot is shown which has been remelted with $e = 1,5$ kWh/kg at a power of about 1, 200 kW. The illustration demonstrates that the surface of the metal ingot will be able to meet any demands made by subsequent hot working.

Metallurgical results will be dealt with in a subsequent paper.

REFERENCES

1. H. R. SMITH, Ch. D'A. HUNT, Ch. W. HANKS, An Electron Bombardment Furnace for the Production of Vacuum-Metals, 5. Vac. Symp. Trans., Pergamon Press, New York, 164, 1958.
2. CANDIDUS, E. S.; SIMONS, I. C.; An Electron Bombardment Furnace for the Production of Vacuum-melted Metals, Fifth Nat. Symp. Vacuum Technology Transact. New York 1958 p. 86.
3. v. ARDENNE, M.; SCHILLER, S.; Ein 45 kW-Elektronenstrahl-Mehrkammerofen für das Schmelzen und Giessen beliebiger Metalle, Kernenergie 3 (1960) 507.
4. SCHEIBE, W.; Der Elektronenstrablschmelzofen, Metall 14 (1960) 401.
5. GRUBER, H.; Das Schmelzen von Metallen mit Elektronenstrahlen, Z. Metallkunde 52 (1961) 291.

6. GRUBER, H.; STEPHAN, H.; DIETRICH, W.; LESSER, R.; Electron Beam Melting with Multiple Guns, 8. Vac. Symp. Trans., Vol. 2, Pergamon Press, New York, 722, 1962.
7. v. ARDENNE, M.; Tabellen zur angewandten Physik. Dtsch. Verl. d. Wiss. Berlin, 1962, Bd. 1, S. 319 ff.
8. SPERNER, F.; ERBEN, E.; Das Schmelzen von Metallen mit Elektronenstrahlen, Z. Metallkunde 55 (1964) 1885.
9. M. v. ARDENNE; Some New Contributions in the Field of Electron Beam-, Ion Beam- and Plasma-Beam-Technology, in R. Bakish; "First International Conference on Electron and Ion Beam Science and Technology", 1965, Wiley, New York, S. 370-405.
10. v. ARDENNE, M.; SCHILLER, S.; Fortschritte in der Vakuum-metallurgie, III. Internat. Vakuumcongres Stuttgart, 1965.
11. SCHILLER, S.; FORSTER, H.; LENK, P.; SCHMIDT, K.; ALTMANN, W.; Ein neuer 60 kW-Elektronenstrahl-Mehrkammerofen, Elektrie, 20 (1966), 2, S. 60-63.
12. GRUBER, H.; Consumable Electrode Vacuum Arc. Melting, Electrical Furnace Steel 15 (1957) 110.
13. KRALL, F.; OGIERMANN, G.; Vakuum-Lichtbogenofen, Elektrowärme 19 (1961) 226.
14. FIELDER, H.; SCHARF, G.; Vergleichende Betrachtungen der Umschmelzbedingungen beim Vakuumlichtbogenofen und Elektronenstrahl-Mehrkammerofen; Vortrag auf dem III. Internat. Vakuumkongres 1965 in Stuttgart.
15. v. ARDENNE, M.; SCHILLER, S.; KUNTSCHER, W.; THIEL, H.; MEYER, L.; Hockvakuumschmelzen von Stahl im 60 kW-Elektronenstrahl-Mehrkammerofen, Neue Hütte 6 (1961) 198.
16. THIEL, H.; MASCHLER, H.; FORSTER, H.; Reinheitsgrad und Umlaufbiegefestigkeit eines Wälzlagerstahles nach dem Umschmelzen im Vakuumlichtbogenofen und im Elektronenstrahl-Mehrkammerofen, Neue Hütte 8 (1963) 313.
17. FIELDER, H.; Neue Wege bei der Erzeugung von Edelstählen, Neue Hütte 9 (1964) 129.

18. v. ARDENNE, M.; SCHILLER, S.; JÄGER, G.; LENK, P.; SCHÖNBERG, H.; STEIN, P.; SCHMIDT, K.; BARSIKOW, G.; Ein Elektronenstrahl-Mehrkammerofen mit einer Leistung von 1700 kW; Vortr. auf der 11. Internat. Tagung der Elektrotechniker, Nov. 1965 in Berlin.
19. WESTMEYER, H.; SCHILLER, S.; GODENSCHWEG, M.; Eine Beobachtungseinrichtung für Hochvakuum-Elektronenstrahl-Schmelzöfen, Vakuumtechnik 12 (1963) H. 1, S. 17-19.
20. DAS-Nr. 1 176 771 Patent "Fokussierhilfe bei Elektronenstrahl-Schmelzöfen und Verfahren zu ihrer Ausführung."

ELECTRON BEAM WELDING

ELECTRON BEAM
WELDING

SECTION III

Electron Beam Welding

The papers presented in this section are a good representation of the type of work being conducted today in the field. They discuss not only the accepted types of equipment which is utilized, but also some of the recent approaches used leading to modification of this technique.

There have been many problems associated with electron beam welding but X-Ray radiation has not been one of them. The reason being the fact that this type of corpuscular radiation has been around for a considerable while, therefore even though dangerous we do thoroughly know how to protect ourselves. It can even be said that for most practical purposes this responsibility is even outside our hands; it falls under the occupational health and related State and Federal Agencies. Just as a reminder of our state of understanding you are advised to review Reininger's paper. Its subject matter actually is related to much of the material in this volume.

Mueleman's text here discusses the mechanism and penetration aspects of electron beam welding, a most important subject which deserves continuous attention. Stohr, after a survey which could well be referred to as a brief promenade with electron beams through "nuclear power land", gives us a good impression of the state of affairs in this technology in France, one of the pioneering countries here. Foti takes us through a comparable excursion in Hungary's developments in electron beam welding. Koch's and Joerg's papers show us but two examples of the wide scope of automation approaches being adopted at ever increasing rates to electron beam welding. Meier's and James's papers next presented the new so called mid

vacuum electron beam mode complementing the now established high vacuum and non vacuum electron beam welding modes. These two papers are notable by the similarity of thought as expressed by the two main electron beam equipment producers in the United States. Olshansky, Miller and Gerken and Groves take us through actual electron beam welding studies and share their accomplishments there, and Miller gives us some thoughts on lasers as complementary to electron beams. It is indeed a pity that the reader could not have been presented with the transcript of the most interesting discussion on welding defects which took place at the meeting. One of the notable facts advanced, namely the recognition of existance of defects, truly spoke of maturity being achieved by the industry. The last paper in this section present results of continued effort with alternate corpuscular beams, closely related to the electron beam and another corpuscular beam which has industrial possibilities.

Much has been done to date with electron beams and the writer suggest the newcomer consult the following references for work performed to date [1-11]. For those not so inclined I am summarizing the highlights and essential features of the process for his benefits:

1. Electron beam welding is a powerful joining technique.
2. Electron beam welding operates within the confines of physical metallurgy and thermodynamics.
3. Electron beam welding is a low heat input process.
4. It permits the highest depth to width ratio from any of the known joining processes though this is not necessarily the best solution for all joining problems.
5. Electron beams are an economical processing tool and should not be considered only as a high cost advanced Research and Development tool. Note the evidence at hand today is considerable.
6. Electron beam welding has come of age at its 10th anniversary because of recognition that the process has certain problem areas, and because the manufactures of equipment and its users have taken a constructive attitude aimed to overcome the problems here.

7. Today there are three modes of electron beam welding: a) the pioneering mode operational at 10^{-4} Torr and below, b) the inert atmosphere electron beam welding operational at 1 atm. and c) the recently announced intermediate vacuum mode operationat at 10^{-1} Torr.
8. The electron beam welding process and equipment to perform the same need badly specifications.
9. As a party who has been involved in electron beam welding since 1959, the growth, accomplishments and developments here have been truly exciting and have in many ways surpassed the fondest expectations.
10. Electron beam welding in the future will be used both on earth and outer space.

REFERENCES

1. Proc. 1st Symp. Electron Beam Technology, J. Hetherington, (Ed), Boston, 1959.
2. Proc. Symp. Electron Bombardment Floating Zone Melting, Serl, Baldock, England, 1959.
3. Proc. 2nd Symp. Electron Beam Techn., R. Bakish, (Ed), Boston, Mass., 1960.
4. Proc. 3rd Symp. Electron Beam Techn., R. Bakish, (Ed), Boston, Mass., 1961.
5. Proc. 4th Symp. Electron Beam Techn., R. Bakish, (Ed), Boston, Mass., 1962.
6. Proc. 5th Symp. Electron Beam Techn., J. Morley, (Ed), Boston, Mass., 1963.
7. Proc. of a Symposium on Electron and Laser Beams, El Kareh, (Ed.), University Park, Pa. 1965.
8. Introduction to Electron Beam Technology, R. Bakish, (Ed), J. Wiley & Sons, New York, 1964.
9. Proc. 6th Symp. Electron Beam Techn., J. Morley, (Ed), Boston, Mass., 1962.
10. Handbook of Electron Beam Welding, R. Bakish and S. S. White, J. Wiley & Sons, New York, 1964.
11. Proc. 1st International Conference on Electron and Ion Beams in Science and Technology, R. Bakish, (Ed), J. Wiley & Sons, New York, 1965.

ELECTRON BEAM WELDING

PREFACE

Measurement of X-Radiation on Electron Beam Devices

W. G. Reininger

Aerospace Division
Westinghouse Electric Corp.
Defense and Space Center

1. GENERATION OF X-RAYS

Electrons have a negative charge of $e=1.59 \times 10^{-19}$ coulombs. In an electrostatic field they are attracted to the positive side of the field (target) and they fall through this field to the plate with an accelerated motion. The equations for this motion are:

$$Ve = \frac{mv^2}{2} \quad \text{(kinetic energy of the electron)} \tag{1}$$

where V = the potential difference between field boundaries
e = the negative charge of the electron
m = the mass of the electron
v = the velocity of the electron at the time of input

Because of the high velocities involved one has to use the Einstein equation for the mass.

$$m = \frac{m_o}{\sqrt{1 - \frac{v^2}{c^2}}} \tag{2}$$

where $m_o = 9.11 \times 10^{-28}$ grams (rest mass of the electron)
$c = 2.998 \times 10^{10}$ cm/sec (light velocity in vacuum)

These high velocity electrons are normally decelerated during their interception by matter.

a. This deceleration can be in two ways. They hit the orbital electrons of the absorbing matter and either lift these spinning electrons from their K, L, M, N shells to higher energy shells or they remove them all the way (ionization). Other free electrons fall into the vacant places of the K, L, M, N shell, and start to spin around the nucleus. During this fall into the inner shells, the electron is attracted by the positively charged nucleus, is accelerated, and increases its kinetic energy. This kinetic energy is liberated at the instant of stopping as electromagnetic radiation. This way the so called "Characteristic Radiation" is produced.

b. The high speed electrons are decelerated by intersection with the electrostatic field inside the atoms of the anode material. This process is a random one. Electrons can give up their full kinetic energy in one process, or they can lose their energy in several steps. Each kinetic energy loss is transformed into a Photon ($h\nu$) of electromagnetic radiation.

This random process produces a whole spectrum of wave lengths (λ) starting with the shortest (λ min) in which an electron has lost its full kinetic energy in one single step, to longer and longer wavelengths. This spectrum is called the "Bremspectrum" (deceleration spectrum).

The transformation of the kinetic energy into a radiation quantum (Photon $h\nu$) energy is shown in

$$E = \frac{mv^2}{2} = h\nu \tag{3}$$

where

h 6.63×10^{-27} erg sec (Plauk's constant)
ν the frequency of the produced electromagnetic radiation.

Combining equation (1) and (3) gives

$$Ve = h\nu \tag{4}$$

This means: An electron being accelerated in an electrostatic field V which is lucky enough to give up its whole kinetic energy in one step produces an electromagnetic radiation quantum with the frequency ν.

The wave length

$$\lambda = \frac{c}{\nu} \quad \text{or} \quad \nu = \frac{c}{\lambda} \tag{5}$$

where c is the light velocity again.

Replacing v of equation (4) makes

$$V_e = \frac{hc}{\lambda} \quad \text{or} \quad \lambda = \frac{hc}{Ve} \tag{6}$$

replacing for h, c and e their values, measuring V in kV and λ in Å (Angstroms);

$$\lambda = \frac{12.35}{kV} \quad \text{in Å (Hunt and Duane)} \tag{7}$$

λ of equation (7) is the shortest possible wavelength which can be obtained from electrons which were accelerated by a field of kV kilovolts; all multiple collision events produce longer wavelengths. Figure 1 shows the intensity versus wavelength distribution of X-rays which were produced by decelerating accelerated electrons (Bremsstrahlung ≡ deceleration-radiation).

Superimposed on this spectrum are the high intensity characteristic K_α, K_β and L_α, L_β radiations which are produced by shell electrons of the atoms of the target material, as soon as λ_{min} of the Bremsspectrum becomes shorter than the characteristic wavelength.

2. HARDNESS OF X-RAYS

X-radiation with a short wavelength has a better penetration into and through matter, than radiation with longer wavelengths. X-rays produced by a high accelerating voltage have therefore better penetration or "hardness". The thickness of matter which reduces the intensity of x-radiation to one half of the incoming beam is called the half-value layer, HVL. The tenth-value layer (TVL) reduces the incoming intensity to one tenth of its value.

The attenuation for monochromatic x-radiation is an exponential function of the thickness.

$$I = I_o e^{-\mu t} \tag{9}$$

where I_o = incident intensity
e = base of natural logarithm
μ = absorption coefficient
t = thickness of the absorber (filter, shield)
I = intensity of radiation penetrating the shield.

The absorption coefficient μ is dependent on the atomic number of the filter material ($\sim Z^4$) and it is dependent of the wavelength of the radiation ($\sim \lambda^3$). High atomic number materials like Cu, Pb, W, have better attenuating power than those with lower atomic numbers (like Fe, Al). It is easier to shield soft or long wavelength x-rays than short wavelength or hard ones.

There are attentuation tables for different elements and λ in the Handbook of Chemistry and Physics. (Careful! The tables show the mass absorption coefficients μ).

The National Bureau of Standards handbook 76 has the Braestrup attenuation curves for x-rays of 50 kV to 3000kV, in lead and in concrete.

3. X-RAY DOSE UNITS

The dose unit for x-rays is one Roentgen (1r). It is the radiation which produces in 0.001293 gram of air, ionization of both signs which can transport one Electrostatic Unit (ESU) in both directions.

There are newer units which are derived from the r, like the rem = Roentgen Equivalent Man. It is used for different radiations (α, β, γ) with different biological effect to man. Then there is the rad, a unit of absorbed dose. One rad is 100 ergs/gm. Finally, the rep, or Roentgen Equivalent Physical. For the purposes of this article the r unit is sufficient. 0.001 r = one milliroentgen = 1 mr.

The dose rate is expressed in r/min or r/hr or mr/hr etc.

To give an example: A deep therapy x-ray tube (W-target) running on 200 kV and 2 m A with a 1 mm Cu filter produces on the average 20 r/min at 20 cm distance from the W-target.

An electron beam of one amp which is accelerated by 100 kV should produce 10,000 r per minute at 50 cm distance. These are deadly doses as shown in the next paragraph.

4. TOLERANCE DOSE

The presently-established tolerance dose is 5 r accumulated per year; 0.1 r per week (for 50 work weeks per year); or 2.5 mr per hour (for a 40 hour week).

Biologically, most radiation damage is done during the process of cell division, when the new cell is mutated in its genes. Therefore radiographs of pregnant women should be avoided and children and youngsters up to 18 years should not receive any occupational radiation.

The maximum integrated dose which an adult of N years of age is allowed to receive from his occupation is $D = 5\ (N-18)$. This is for a full body irradiation, the gonads or the eyes. Feet and hands can receive doses 3 to 5 times higher.

5. MEASUREMENT OF THE DOSE

In general doses can be measured by:

1. Chemical process and color changes in appropriate salts.
2. Ionization chambers.
3. Geiger Muller Counters.
4. Crystal Counters.
5. Photographic emulsion

1. Chemical and color changes occur only after relatively large doses have irradiated the salt. This method was used around the beginning of the century to determine doses which were given to medical patients. The sensitivity is too low to measure tolerance doses.

2. The ionization chamber is a very small air capacitor which is charged up to about 100 to 200 volts. X-radiation passing through the sensitive volume of such a capacitor ionizes the air molecules. The electrons go to the anode of the capacitor and the +ions to the cathode. The electrostatic charge in this capacitor will eventually be discharged,

according to the intensity of the radiation. The amount of discharge is proportional to the dose which is accumulated by the volume of the chamber.

A battery can be connected to the chamber and a nanoammeter in the circuit can measure the ionization current. This instrument shows a dose rate (mr/min etc.). The air volume of these chambers has to be very large in order to be sensitive enough to measure tolerance doses.

The ionization chamber as described above is often built in the shape of a pencil and can be worn in the shirt pocket. This chamber is charged up to 100 or 200 volts in the morning and worn during work. In the evening this chamber is connected to an electrometer capable of measuring the loss of charge. This electrometer is directly calibrated in mr and the dose accumulated during the day can be determined. These chambers are generally built to measure 0 to 200 mr.

Another pencil type monitor has the electrometer with a calibrated microscope built in. This monitor pencil is charged up in the morning and it can be read during the day without disturbing the charge.

All ionization chambers depend on the highest quality electrical insulation (10^{18} ohm-cm) between + and - electrode. Humidity on the surface of the insulators can make these instruments unusable. For each reading control runs without radiation have to be made to determine errors due to humidity.

A pulsed high voltage supply for electron beam acceleration will produce very short bursts of ionization in the chamber. Before these high numbers of ions can reach the collecting electrodes, many recombinations will have occurred and the discharge will be smaller than it should. This might give a false safe reading.

3. Geiger Mueller Counters consist of a tubular outer electrode and a very fine wire as inner electrode. A high electrostatic field is applied between the electrodes, and special gasses are admitted at certain pressures, to the structure.

A single photon ($h\gamma$) of x-radiation produces one or more ions. Because of the high field strength these ions will produce ion avalanches, which are discharged over a high ohmic resistor and which can be heard as a click in

headphones or which can be displayed on a meter after suitable electronic processing.

These instruments are very well suited to measure low dose rates such as would produce the tolerance dose.

Several precautions have to be taken in using G-M counters.

a. If soft radiation is expected, the walls of the probe have to be of adequately thin material.

b. Certain high voltage supplies used to generate the electron beam produce high frequency electrostatic or magnetic fields. These fields sometimes interfere with the electronics so that the instrument reads incorrectly or not at all.

c. Batteries should be checked frequently.

d. Calibration should be checked frequently.

e. Background radiation (cosmic radiation) should be checked at each location.

f. Some of the high voltage beam generators pulse the beams with high intensities over periods so short that the inertia of the indicating instrument cannot follow.

4. Crystal Counters have a large organic crystal mounted in front of a photomultiplier. This crystal can be made sensitive to x-rays, so that each passing photon produces one small light burst in it. The photomultiplier produces a signal similar to the one from the Geiger-Mueller Tube. The precautions have to be the same as the ones in the previous paragraph.

5. Photographic emulsions were used for dosage measurements since the beginning of the century. Films read the accumulated dose which the film saw during the exposure time.

The sensitivity of a film is dependent upon so many variables, that a reading should only be done by a skilled person. For example:

a. The sensitivity to x-rays is different for films of different manufacturers.

b. Different film types of one manufacturer have different x-ray sensitivities.

c. The sensitivity of the same brand can change in different production batches.

d. Developing time changes the sensitivity.

e. Developing temperature changes the sensitivity.

f. Age of developer changes the sensitivity.

g. The sensitivity changes with the hardness of the x-rays. Most film types have their highest sensitivity around 50 kV; below and above it, the sensitivity is lower. At some film types this sensitivity ratio can be as high as 20:1!

Films which have been calibrated for kV, developer and which are developed under controlled conditions can be used to measure doses with about 20% error.

Films packaged in 1-1/4 x 1-5/8 envelopes can be worn as badges by personnel working in radiation-hazardous environment. There are often two films per package, one highly sensitive and one of low sensitivity. This is in case the received dose blackened the highly sensitive film so much that no reading could be made.

There are several companies offering to develop the films monthly and report the results.

Large size films (up to 14 x 17 inches) can be used to monitor large areas for cracks or holes in the shielding of large housings. Sometimes the whole exterior of an electron beam equipment has to be covered with film. An exposure of several hours can show radiation leaks which are above the tolerance dose. From these approximate leakage dose rates, the necessary additional shielding can be computed or determined. Leakage doses found by film should be verified with Geiger or crystal counters and with ionization chambers, and vice versa.

6. SHIELDING

Electron beams as they are used for melting, welding and other technological work produces at the place of impact dose rates of 10^4 to 10^7 per hour. Shielding is necessary to reduce these high dose rates, which would give a person a lethal dose within minutes. Since the tolerance dose is 2.5×10^{-3} r per hour, the shielding has to have a thickness of seven to ten tenth-value layers (TVL).

Fortunately, melting ovens have to have heavy layers of refractory material which in many cases will be sufficient to reduce the generated radiation to values below tolerance dose. However, voltages over 80 kV or thin confining structures (as in electron microscopes and others) should be measured for safe radiation levels. The Braestrup curves mentioned in paragraph 2 or the tables of the Handbook of Chemistry and Physics are handy to determine any additional shielding.

Windows for direct observation of the processing should be measured in every case. The use of lead glass or mirrors is recommended. Caution: the lead equivalent of lead glass is only a fraction of the glass thickness!

From the standpoint of radiation safety all electron beam devices working above 30 kV should be monitored for radiation leaks under full load at least once.

Even once surveyed, machines can become unsafe; if the electron beam changes its direction or distribution, x-rays can be generated at different geometrical locations. Personnel working near should wear monitoring ionization chambers or film badges and semi-annual general measurements should be made.

RESUME

In the previous paragraphs it was shown that very high x-ray doses are produced inside of all electron beam devices working over 30 kV and 10 mA. Many methods can be used to establish the radiation leakage dose rate. Adequate shielding and monitoring of the personnel has to be done in places where the leakage is near the tolerance dose.

Physical Aspects of Electron Beam Penetration in Metals

M. Meulemans

Centre d'Etudes de l'Energie Nucléaire
Mol, Belgium

INTRODUCTION

The penetration obtained by high power density bombardment with electrons has many and complex physical aspects. The difficulty of backing up the statements on this mechanism by experiments led several authors to more or less valid formulations. We thought it a worthy contribution to use the more common means at our disposition viz. direct observation, metallography and operating parameters chosen after a series of orientation tests. Concerning the physical aspects, the process at the atomic scale is an energy transfer with the interaction of collision between particles.

The Experimental Aspect

Means

The experiments are carried out by means of a 3 kW electron gun with a maximum acceleration voltage of 150 kV. This gun is equipped with an optical system for the observation of the electron impact. The target material consists of joining pieces of copper and stainless steel (18/8). In most tests, the electron beam is pulsed, the period being 0.36 ms and the pulse duration of 0.15 ms. By well choosing these parameters, a minimum heating of the target occurred leading to a very fast "freezing" of

the liquid parts in the electron beam when the latter is switched off. The metallographic examination thus shows the morphology of the electron impact immediately before the switching off. Furthermore, the preferential chemical attack of the bimetal clearly displays the transport of material along the electron path.

Experiment I

a. Operating conditions: welding of a 1mm copper sheet superposed on a 2mm stainless steel sheet. 130 kV, 5μA, pulsed beam, welding speed: 10mm/s.

b. Observations: (Figure 1)

The steel is transported towards the electron impact around the electron beam.

The melting zone in the lower sheet shows linear traces of insoluble material. The concavity of these lines is downwards corresponding to the subsidence of the liquid lateral parts after the passage of the beam.

The latent melting heat of the last upward motion of the steel starts melting the lateral copper parts (upper part of the metallography).

The fast cooling of the melt causes cracks indicating the existence of tensile stress in the direction of the electron path. The melt is brittle due to the numerous intermetallic compounds between iron, copper, chromium and nickel.

The inclusions of the original metal are no longer found in the melting bath.

The copper and the steel sheets are held together by a bond 0.15mm width. One may therefore assert that the channel for the passage of the electrons has a smaller diameter.

Since the above bond has been out in the liquid state and since it did not subside by gravity, one may conclude that it has been retained by surface tensions.

Experiment II

a. Operating conditions: a stainless steel test piece, 10mm dia., clad by a 1mm thick copper tube. A hole of

Figure 1.

2mm dia. is bored at the point of impact. The piece does not move during the test. 130 kV, 5 mA, pulsed, duration of the beam: 5 seconds.

b. Observations: (Figure 2)

The projections from the channel hitting the walls of the initial hole are absorbed by the liquid spherical cap covering the channel (Figure 2a).

Shortly before the switching-off of the beam several superposed bubbles which are separated by liquid films have to be crossed by the electron beam. This multiple perforation is shown by oval melting baths at the narrow areas of the channel (Figure 2b).

Along the whole path one notices a melting zone with slight grain coarsening.

Figure 2c is a 500x photograph of an explosion inside one of the cavities. The explosion occurred exactly at the solidification of the liquid metal. There are good reasons to suppose that this explosion is caused by gas present in the base metal. The cooling is such that cracks appear at the limit of the austenite grain boundaries.

Figure 2d is a photograph taken at low incidents light and gives an idea of the shape of the cavities formed.

One may therefore say that the electron beam penetration is highly influenced by the surface tensions as well as by the initial amount of gas included in the base material.

An equally important part is played by the upper liquid cap which holds a high temperature plasma; this cap ruptures due to overpressure.

Experiment III

a. Operating conditions: Welding of a plug into a stainless steel tube 130 kV, 2 ma, pulsed, circumferential speed 10 mm/s.

b. Observations: (Figure 3)

Every symmetrical line on both sides of the electron beam corresponds to a beam pulse.

Each pulse is accompanied by the rupture of the liquid film covering the weld.

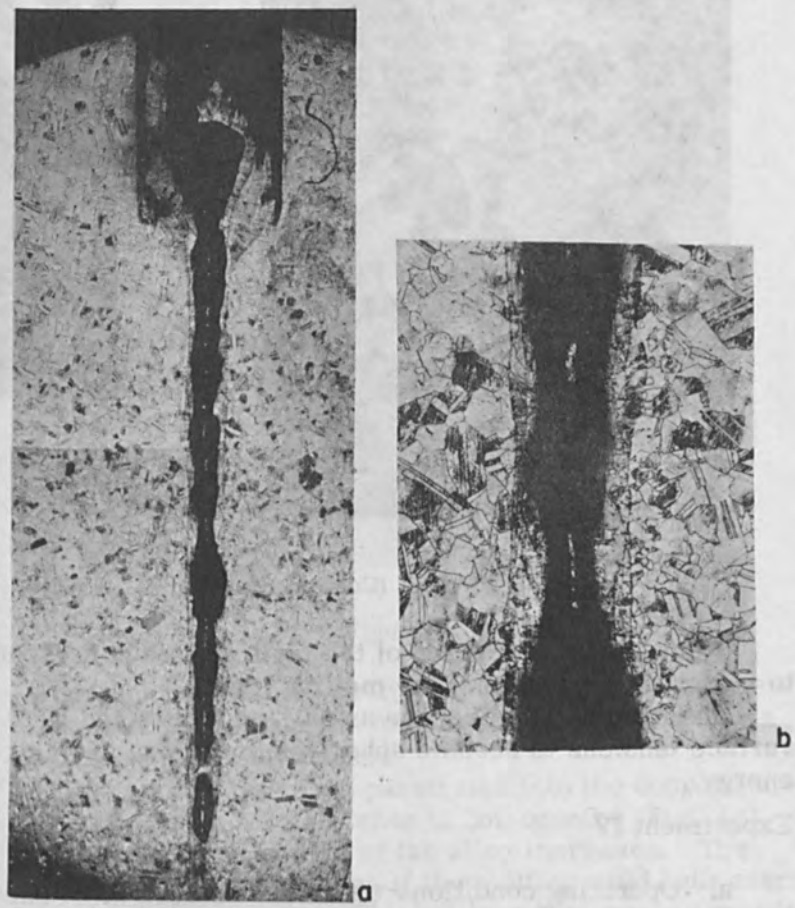

Figure 2.

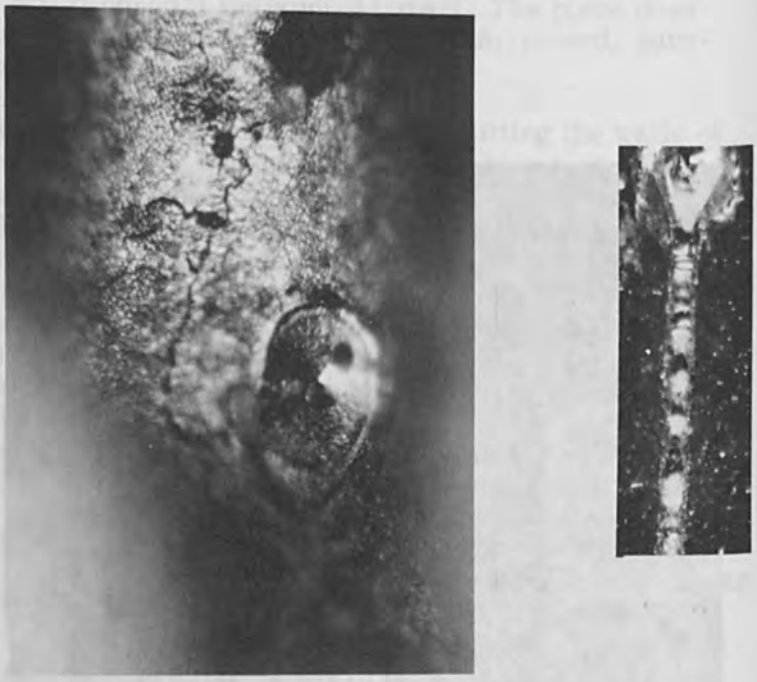

Figure 2. (Continued)

The widening at the top of the melting bath corresponds to a greater curvature of the melting lines.

The melting lines behave as any liquid affected by surface tensions to become spherical (minimum surface energy).

Experiment IV

a. Operating conditions: a 2mm stainless steel sheet superposed on a 1mm copper sheet. 130 KV; 2, 3, 4, 5 mA continuously; welding speed: 10/mm/s.

b. Observations: (Figure 4)

The stainless steel subsides on the copper (Fig. 4a). The copper acts as a coolant except the central part where the specific power of the beam is very high. An electron refocusing occurs when the beam penetrates into the copper (Fig. 4b). The difference between the melting baths of different chemical composition shows, even for

Figure 3.

a continuous electron energy input, the discontinuous nature of the phenomena affecting the liquid materials which move in the channel.

The more the beam penetrates into the copper, the more the alloy formed tends to homogenize (Fig. 4c).

The copper content of the alloy increases. The melted copper behaves as if the melting weld bath exerts a hydrostatic pressure which drives the copper towards the interval between the two pieces. The initial grains of the starting copper recrystallize in the melting line according to their initial axes. By the rupture of the plasma at the bottom in the vacuum, the liquid walls are carried away (Fig. 4d).

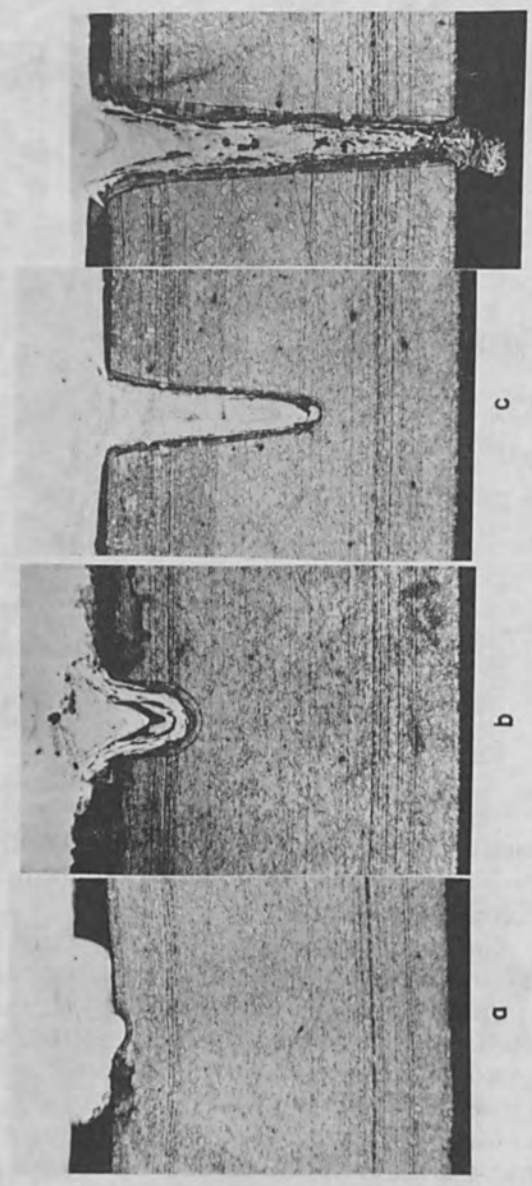

Figure 4.

Experiment V

a. Operating conditions: A 10mm dia. stainless steel cylinder clad with 1mm copper 130 kV; 3mA; pulsed; clockwise circumferential speed: 10mm/s.

b. Observations: (Figure 5)

Discontinuities in the chemical composition of the formed alloy.

S-shaped melting baths each corresponding to an electron beam perforation.

Antirotative electron beam deviation during the first impacts.

When the metal becomes hot, the beam starts deviating towards the zones where the circumferential speed is low.

When the beam becomes perpendicular to the surface, an important deflection occurs (left part of the metallograph) which affects the weld.

Figure 5.

The same process then starts again (lower left part of the photograph).

These phenomena do not occur for test pieces with larger diameter, since the difference in circumferential speed is smaller.

The electron beam behaves as if it follows the least resistant path through the areas where the metal temperature is highest.

Experiment VI

a. Operating conditions: Two 8mm thick aluminum plugs on two aluminum vessels. The first one is preheated to ±300°C, the second one is at room temperature. The welding parameters were 130 kV, 15 mA, pulsed. The former maintained for 7 seconds in the electron beam, while the latter is kept till the appearance of a large projection of oxide i. e. that the electrons penetrate the vessel containing air at overpressure.

b. Observations (Figure 6)

The preheated test piece (Fig. 6a) cannot be perforated although the energy is far higher than for a similar cold operation (Fig. 6b).

While the beam is maintained on the preheated test piece, a large spherical cap appears whose periphery is visible on the macrograph. When the beam is switched off, the cap subsides.

In order to obtain the maximum electron beam penetration a high thermal gradient is necessary or at least the lateral parts should remain solid.

Physical Aspects of the Process

Collisions between Particles

In the theory of gas kinetics, the mean free path of a particle with radius σ_1 moving among particles with radius σ_2 is defined as the mean distance covered between collisions; a collision occurring when the distance between the centres $\sigma_{12} = \sigma_1 + \sigma_2$ [1].

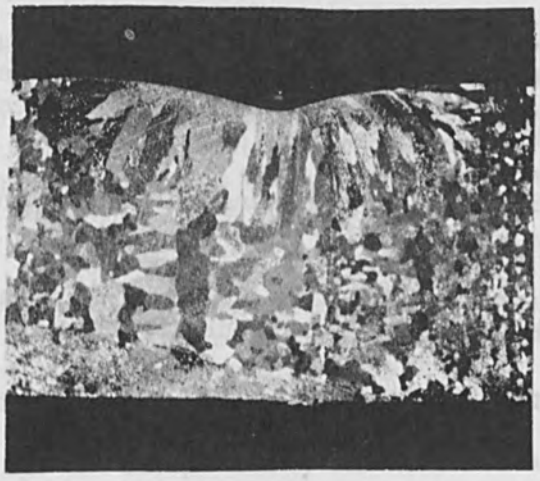

a

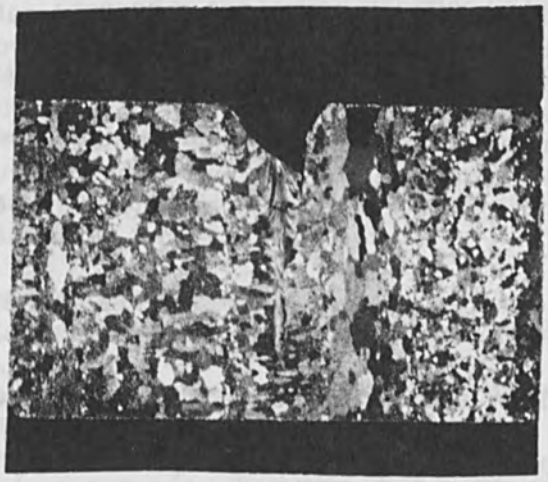

b

Figure 6.

$$\lambda_1 = \frac{1}{\tau_1 n_2 \sigma_{12}^2 \left(1 + \frac{C_2^2}{C_1^2}\right)^{1/2}} \qquad \text{where}$$

λ_1 is the mean free path of a type 1 particle among type 2 particles; n_2 is the number of type 2 particles per volume unit. C_1 and C_2 are the mean square speeds resp. of the type 1 and type 2 particle.

Collisions Between a Molecule and Molecules of the Same Type

In this case $C_1 = C_2$, $2\sigma_1 = 2\sigma_2 = \sigma$ (σ is the diameter of the molecule) and formula (1) becomes

$$\lambda = \frac{1}{\sqrt{2}\pi n \sigma^2}$$

Collisions Between an Electron and Molecules

At 20°C the mean square speed of a molecule is equivalent to that of an electron which is accelerated by a potential difference of only 335 thousandths of a volt. This voltage is very small as compared to the acceleration voltage of an electron gun.

The radius of the electron (10^{-13} cm) being negligible as compared to the radius of the molecules (10^{-8} cm); $\sigma_{12} = \sigma_2 = \sigma/2$ and formula (1) becomes

$$\lambda = \frac{4}{\pi n \sigma^2} .$$

The mean free path of the electron among the molecules is therefore $4\sqrt{2}$ times that of the molecules.

The Mean Free Path is a Function of Temperature

The speed of the molecules varies according to the Maxwell [2] distribution law

one finds $\lambda = \frac{KT}{\sqrt{2}\pi\sigma^2 p}$

where K: the Boltzman constant
T: the absolute Kelvin temperature
p: the pressure in mm Hg

The temperature of the plasma above the electron impact is very high. One may therefore suppose that the mean free path of the electrons is longer than that resulting from the formulas which take into account but the pressure of the vacuum chamber at room temperature.

Energy Loss of an Electron Colliding with a Molecule

Applying the momentum and the conservation of energy equations to the case of a collision between an electron with given speed and mass m and an initially immobile molecule with mass M $Ep = Eo(4m/M)\cos^2\theta$

where Ep: the energy lost by the electrons during the collision
Eo: the energy of the electron before the collision
θ: the deviation angle after the collision with regard to the initial direction of the electron

This energy loss is very small: an electron loses one hundred thousandth of its initial energy when colliding with a Hg atom.

The Real Nature of the Forces Acting Between the Particles [3]

Between neutral molecules:

At long distance: the Van der Walls interaction forces, generally attractive.

At short distance: the quantum type forces, generally repulsive and very strong.

Between an electron and a molecule

At long distance: the interaction potential is a so-called induced dipole mechanism: the electron builds up a field which polarizes the molecule and the molecule then builds up a potential. This field is attractive.

At short distance: the quantum type forces which are repulsive and vary rapidly.

Between an electron and an ion (between electric charges).

At long distance: the Coulomb interaction potential which is attractive or repulsive according to the sign of the electric charges present.

At short distance: the quantum type forces which are repulsive and vary rapidly.

Collisions Between Electrons and Ions in Metal [4]

The electrons lose some of their energy in gases; similarly, the free electrons affected by an external force lose a considerable part of their energy when colliding with the ions which are periodically distributed at the nodes of the crystal grid.

The mean free path of an electron in a vacuum of 10^{-6} mm Hg is of the order of 70 meter, in a metal at room temperature it is some 400 Angströms.

An electric field gives an acceleration in the direction of the field to the "initially disordered movement of the free electron" followed by collisions. The amplitude of the ion vibration increases. If the electric field is maintained there is equilibrium between the acceleration of the electrons and its subsequent collision. The temperature of the metal increases: this is the Joule effect. The same process occurs in the case of welding by electron bombardment. The external force, however, is here an enormous electron concentration of potential energy (negative charge) and of kinetic energy, the speeds of the electrons are directed along the electron path according to a Maxwell speed distribution.)

Loss of Cohesion of a Metal by Electron Impact

The sublimation heat i. e. the energy which is necessary to dissociate a molecule into free atoms is a good measure of the cohesion of a metal [5]. A crystal may be considered as an aggregate of atomic oscillators. The range and the direction of the amplitude of these oscillations change. The mean of these fluctuations is proportional to KT° (K: the Boltzman constant; T°: the absolute temperature). For instance, a molecule-gram

of a metal has an energy accumulation at a given time. This can be expressed in electron-volts per mole, in thermochemical units, or in kilocalories per mole. If the metal immediately thereafter, receives an additional energy (eV) equivalent to its sublimation heat, the metal will break up into free atoms without going through the liquid phase. Sublimation has occurred.

Electron guns allow the concentration of energy in a small volume element of the metal, this energy actually being higher than the sublimation heat of the volume element considered. Some phenomena counteract this "instantaneous dissolution of the electrical energy"; they are the negative charges at the electron impact; the heat carried off by the free atoms, and the thermal conductivity of the underlying metal.

Order of Magnitude of the Electron Penetration into a Solid Metal [6]

The penetration x_{max} calculated according to the Whiddington law is expressed as $x_{max} = a\,(A/z\rho)V^2$

where a: a constant
A: the atomic weight
Z: the atom number
ρ: the mass density
V: the acceleration voltage of the electrons before the penetration into the metal.

x_{max} is the path of the electrons at the end of which the most probable speed is zero.

This penetration x_{max} is of the order of 30 microns in iron at a voltage of 100 kV. The fact that the electrons pass through metal of several centimeter thickness without loss of energy indicates that an important alteration of the mass density occurred; the electrons cross thus the gaseous phase of the metal.

The Forces of Surface Tensions and Penetration in the Target Material

At the electron impact one supposes an electron density sufficient to sublime a small volume element of the target material. A cavity forms whose inner surfaces will melt very quickly. Indeed, the melting results from

1. the latent condensation heat of the sublimed atoms;
2. the electron impact of the electrons deflected from their path by a plasma whose temperature and pressure increase;
3. the radiation of the plasma

Due to the presence of this liquid phase, the plasma may be locked in a liquid bubble by the action of the capillary forces. The liquid surfaces tend to adopt a state of minimum energy. Each liquid particle near the surface is drawn towards the interior of the liquid by the attractive force of its neighbors. In this way, there remains only the number of particles necessary to form the surface. A very thin liquid spherical cap is formed through which the electrons can pass easily. Then the electrons pass through the plasma; some are deflected, but most of them hit the underlying solid material. Furthermore, the phenomena connected with an increase of the temperature occur: surface diffusion, volume diffusion, increase of the pressure of the gases which are included in the base material, periodic rupture of the liquid spherical cap which causes the projection of spheroid particles into the vacuum chamber.

The spherical cap plays an important part. Due to its surface tension, it maintains the pressure of the plasma and it also acts, according to Helmut Schwarz [6], as a thermal screen.

The thickness of this spherical cap is stabilized by the following mechanism: at the one hand, at the electron impact, some material is carried away by evaporation; on the other hand, some material is added from below by the sublimed atoms. Furthermore, when the thickness increases, a greater part of the electron energy is dissipated for the benefit of a more intense evaporation.

When the spherical cap ruptures, a small amount of the incoming energy is sufficient for the instantaneous sublimation of an already very hot material.

This liquid plasma bubble is held by the solid lateral walls of the target material. When all the target material is melted further penetration is impossible since at this moment the surface tension affects the whole liquid which takes a spherical shape or since the plasma bubble reached such a volume that Archimedes trust will position it at the surface of the liquid where it ruptures periodically. Electron impact on indium displays this phenomenon. The electron penetration into the material should be connected with three important parameters:

a high electron density at the impact
a temperature gradient such that the plasma bubble is held by solid walls.
the capillary forces which allow the formation of a liquid spherical upper cap maintaining the high temperature of the plasma.

The "electron guns are able to emit a specific power of 10^9 watts/cm^2" [7].

The electron guns with a specific power of 10^5 watts/cm^2 do not display the above-mentioned mechanism.

In the first case, the gradient distribution is, in the material, perpendicular to the electron path; in the second case, it is approximately radial, the electron impact being the origin.

Viscosity

Liquid metals have a certain viscosity which is shown by the internal friction during alterations of shape. According to the general theory of the friction of fluids, the alteration of shape of fluids gives rise to tensions similar to those in elastic bodies, however, differing in the aspect that they are not proportional to the alterations of shape but to the speeds of these alterations [8]. Now the speeds of these alterations of shape of the liquid metal membrane are of the order of a millisecond [6] and on the other hand, the viscosity of liquids decreases with the

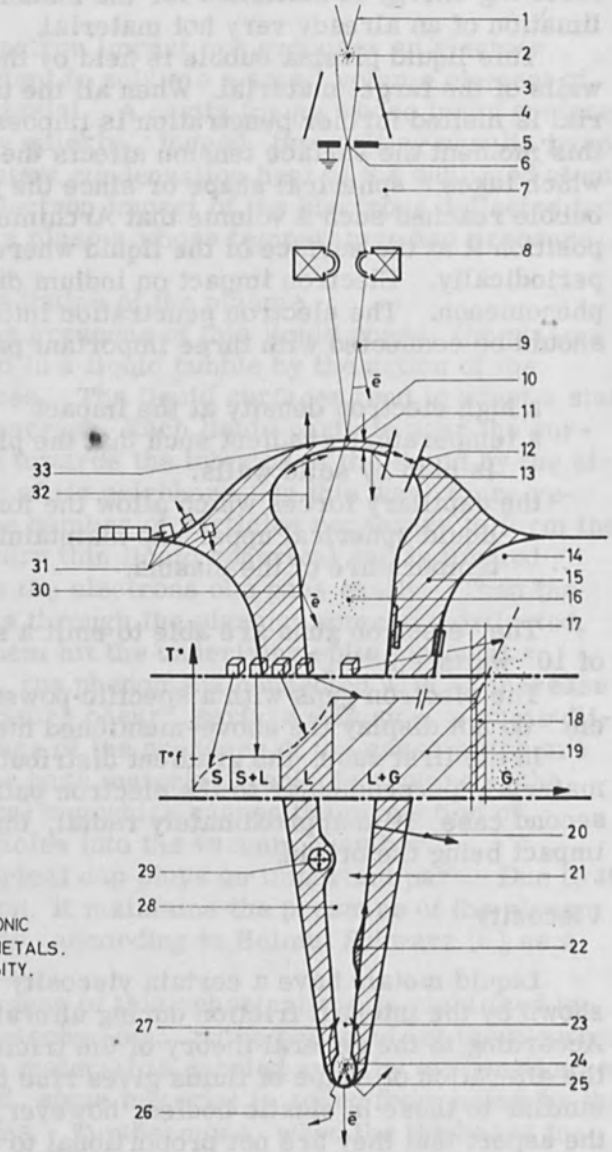

SCHEMA OF ELECTRONIC PENETRATION IN METALS. HIGH POWER DENSITY.

Figure 7.

temperature. One may thus assume that the relaxation times of the tensions are of the same order of magnitude.

Diagram of the Mechanism of Electron Penetration into a Metal

High Power Density (10^9 watts/cm^2)

Figure 7 shows the various phases of the electron penetration at a given moment of the welding. The aspect can be altered continuously by the parameters mentioned below. The figure represents the classical diagram of an electron gun with high acceleration tensions. The following items are numbered on the diagram of the weld.

The direct heating filament 1 establishes in 2 the thermionic electron chamber which in fact, forms the cathodic point. The curvatures 3 of the equipotentials of the electrons in the focus 6.

The vacuum 7 is of the order of 10^{-5} mm Hg and has no electric field. The curvature of the magnetic flux lines in the air-gap of the coil 8 converges the electrons in the focus 10 where the highest electron power density exists. The probability of an electron-molecule collision 9 is very small since the mean free path of the electrons is approximately six times larger than that of the molecules [1]. The liquid spherical cap 11 is very thin, and thus transparent for the electron beam; it maintains the plasma 16 at a critical pressure of $p = 4\ C/R$ [8].

where C: the surface tension coefficient of the liquid metal at the given temperature (dyn/cm)

R: the curvature radius of the spherical cap (cm)

The plasma pressure is higher if the curvature radius is smaller. A cross-section in 12 shows the surface tensions by means of arrows.

The inner surface 13 of this membrane acts as a thermal screen [6].

In 14 one finds the solid metal, in 15 the liquid metal and in 16 the plasma consisting of the primary electrons, the secondary electrons, the electrons deflected by the

membrane, the walls and the plasma, the evaporated and ionized atoms, and the gases initially included in the base metal. By the periodic rupture of the cap, numerous spheroid particles are entering the vacuum chamber.

The transport of matter by surface diffusion and by capillary movement is shown diagrammatically in 17. The energies playing a part in the surface diffusion are smaller than those of volume diffusion; the resistance to displacement in viscous media is proportional to the deflection speed and not, as in the elementic theory, to the deflection itself.

The temperature diagram vs. amount of heat of a metal, is given in 18 and 19. This diagram is very schematic. It does not take into account the allotropic transformations eventually occurring in the solid phase, nor the real values of the specific heats. It gives information on the thermodynamic state of the volume elements along a cross-section through the weld, at a given time of the welding. However, it indicates that a small energy alteration results in the transformation to the gaseous phase of an amount of already very hot metal. This continuous process 18 of instantaneous alteration of density, in connection with the tendency of the channel to be closed by the forces of capillary tension are the most important factors of the welding by high density electron bombardment.

It also shows that the very hot metal vapors condense on cooler liquid walls where they lose their high latent sublimation and evaporation 19 heats and also that, after the switching-off of the electron beam, the liquid phase heat dissipates by direct conduction, thereby widening the melting bath.

The arrow in 20 is a schematic representation of the temperature gradient which is almost perpendicular to the electron path and the arrow in 21 the departure of reevaporated atoms, the liquid walls being in constant interaction with the plasma. The reaction force of the departure of the atoms is added to the force of the impact of the particles forming the plasma. At the impact, expansion of the gases included in the metal carries macroparticles 22 of the underlying metal to the inner walls.

The energy of the electrons in 23 loses the energy which is necessary to maintain the opening of the channel. The hottest area is found in 24; here also the electron dispersion in the plasma is greatest due to the presence of important negative charges. The electron paths in the solid 26 are determined by probability functions [9].

The area 27 is the origin of the formation of the spherical cap. When the membrane 11 ruptures and the beam fully repenetrates into the channel, some matter will form an obstructing bridge between the lateral walls above 24. The minimum energy of the liquid surfaces enclose the plasma at 24 in a small liquid sphere. The electron beam crosses the obstructing liquid by dissipating in the latter as amount of energy which reduces its thickness till transparency. The pressure of the plasma increases and the formed membrane is thrusted upwards.

Some tests in which the electron beam is directed towards the bottom of a small pit machined in the metal clearly show an upwards movement - sometimes together with an oscillating movement - of the liquid membrane up to the surface. At a given moment, several bubbles may exist in the liquid column; this would explain the melt discontinuities in some weld.

Along the electron path 28 there probably exist two electric field gradients: one perpendicular to this path, another parallel.

The gas bubbles included in the liquid lateral walls expand due to the pressure and they explode in the channel 29.

The elastic and inelastic collisions of the primary electrons and the liquid lateral walls are shown schematically in 30. The collisions electron ions of the liquid phase of the channel give rise to quantum forces of repulsive nature and with rapid variation. Since the angle of incidence of de-collision is small and since the frequency and the amplitude of ions oscillation are important, one may think that there is a minimum of energy transfer between electron and ion.

The foil (e. g. oxide) dissolves in the liquid or it evaporates when the oxide is more volatile than the base metal 31. The addition of matter resulting from the electron impact in 25 is shown in 32.

The evaporation, in the vacuum chamber, of the upper part of the cap is shown diagrammatically. The thickness of the latter is stabilized by a carrying off and an addition of matter. When it increases, a greater part of the beam energy dissipates for the benefit of a more intense evaporation in the vacuum chamber.

Low Power Density

For welding by low power density electron bombardment i. e. with specific power of the order of 10^5 watt/cm^2 [7], the mechanism of the weld formation is completely different.

In this case, there is no instantaneous alteration of the density of the target metal; the thermal conductivity is preponderant. During the welding, the temperature of the metal surface ranges from its melting temperature of the metal surface at the given pressure.

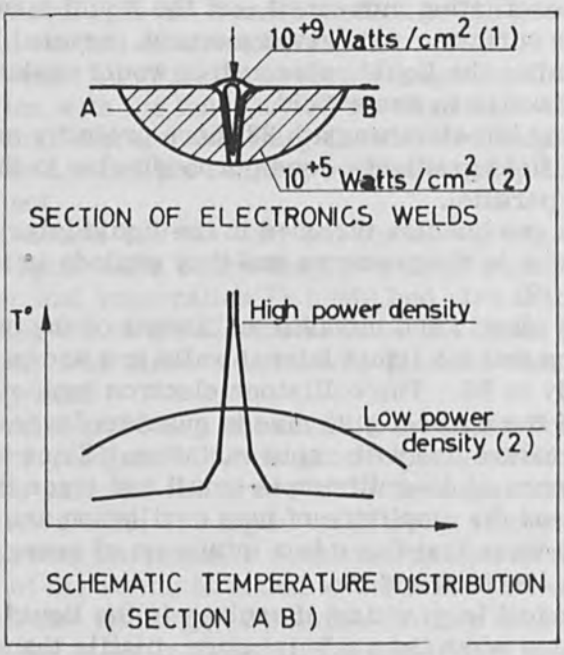

Figure 8.

The isotherms are distributed regularly and concentrically in the underlying metal, the origin being the electron impact.

Figure 8 shows a schematic temperature distribution along a cross-section in two welds. This diagram also gives a rough indication of the thermally influenced areas in both cases.

CONCLUSIONS

The electron penetration is entirely governed by the impact power density. In the extreme case, i. e. even higher power densities, the plasma pressure exceeds the critical pressure of the liquid spherical cap which does not appear anymore: due to the carrying off of matter by sublimation, evaporation and projections the beam effects an actual milling.

REFERENCES

1. F. L. Arnot, "Collision Processes in Gases" Methuen and Co. Ltd. (1957).
2. R. Champeix, "Physiques et Technique des Tubes Electroniques" Tome I, Dunod (1958).
3. J. L. Delacroix, "Introduction à la Théorie des Gas Ionisés" Dunod (1959).
4. W. Boas, "An Introduction to the Physics of Metals and Alloys" Melbourne University Press (1947).
5. Frederick Seitz, "Théorie Moderne des Solides" Masson et Cie (1964).
6. Helmut Schwarz, "Mechanism of High-Power-Density Electron Beam Penetration in Metal" J. Appl. Phys., Vol. 35, No. 7, July 1964.
7. A. B. El-Kareh, "An Electron-Beam Machine", RCA Review, Vol. XXIV, March 1963, No. 1.
8. L. Prandtl, "Guide à Travers la Mécanique des Fluides" Dunod (1952).
9. M. Green, "A Monte Carlo Calculation of Spatial Distribution of Characteristics X-ray Production in a Solid Target", Proc. Phys. Soc., 1963, Vol. 82.

A Survey of Some Applications of Electron Beam Welding in the Field of Atomic Energy

J. A. Stohr

Chief of Technology Services
French Atomic Energy Commission
Saclay, France

INTRODUCTION

First tests of Electron Beam Welding of fuel elements were made in 1956 and this method has been applied to the second set of fuel elements canned with Aluminum for the EL_3 reactor, then for the welding of fuel plate elements canned with Zirconium. This method has been extended to high pressure reactors of the gas-graphite range.

As to structures, this welding method was also applied to the vessel of the homogeneous Plutonium reactor "PROSERPINE", to some structures of the EL_4 reactor and more recently to the "OSIRIS" reactor vessel.

General Considerations

After a study of Electron Beam Welding, and a few tests in the voltage range of 100-120kV, the French Atomic Energy Commission took up this work with lower voltages.

The acceleration voltages used are between 30-60kV. These voltages enable one to get a high specific power of W/S and consequently a deep welding penetration. The penetration depth for a given material depends only on specific power W/S and welding speed V_s.

This range of voltages permits to obtain a small width of molten zone and consequently a higher ratio of welding depth/welding width.

It is interesting to remember that excellent welds have been performed with voltages between 15-20kV. However, in the case of this voltage range one encounters difficulties in gun construction which disappear practically in the range of 30-60kV.

Generally speaking, the choice of parameters W/S and ^{V}s was made in order to obtain the lowest JOULE value per length unit of welding seam. For an equal penetration depth this condition permits to obtain a weld with a small melted zone, as well as a small heat affected zone.

Application on Fuel Elements

With Electron Beam Welding, numerous forms of assemblies can be obtained. Figure 1 shows several forms frequently used for the making of fuel elements and of assemblies of fuel plate elements.

According to the purpose in mind we are using several welding methods producing different forms of melted zones. Generally speaking, the first weld is always followed by smoothing if the appearance of the welded seam is rough. This smoothing is not absolutely necessary for the welding quality but makes easier the tightness control by helium sweating (pressure of 35 kg/cm^2 followed by detection by Mass Spectrograph) by reducing the background noise.

Fuel Elements of Alloyed Uranium for the EL_3 Reactor at Saclay

At both ends of this fuel element the Uranium tube is closed by Electron Beam Welding Uranium pellets; the tube surface shows square grooves in order to avoid the ratcheting effect.

The Uranium tube is put into an extruded Aluminum can and the end cap is welded (Weld No. 1, Fig. 1). By putting the fuel element under pressure (400 kg/cm^2 at 400°C), the can is pressed into the grooves.

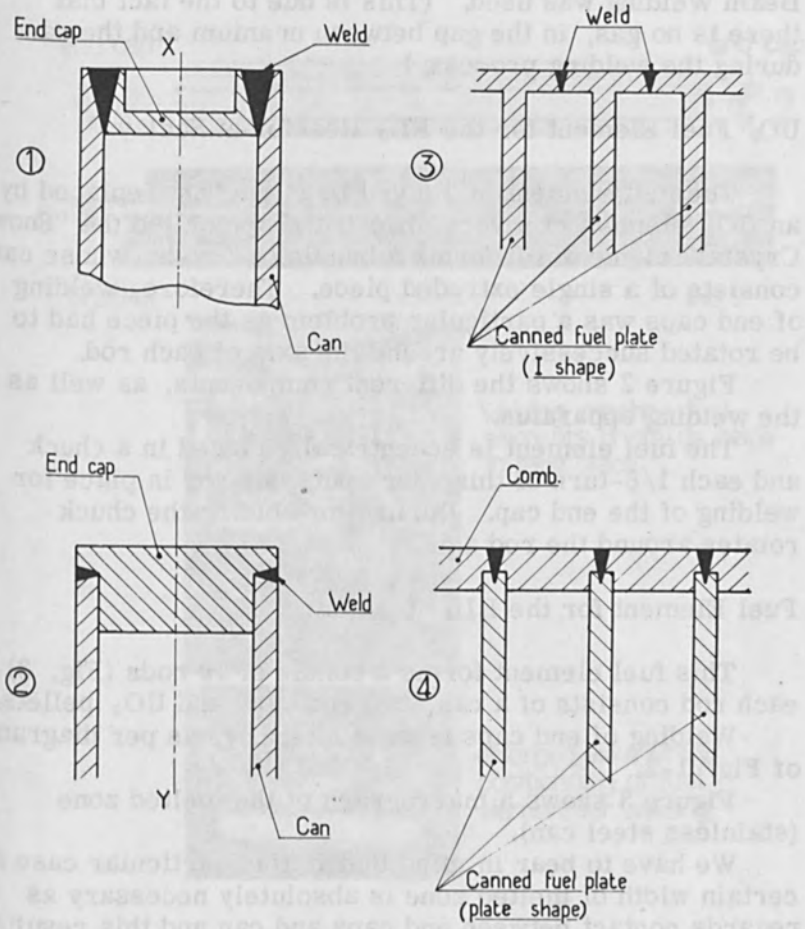

Figure 1. Some examples of welds used in fuel elements fabrication

In 1957-1958, this method was applied to the second set of fuel elements for the EL_3 reactor; the first set was welded by Argon-arc, which produced rejects up to 20%. For the second set, all scrap was avoided as Electron Beam Welding was used. (This is due to the fact that there is no gas, in the gap between uranium and the can during the welding process.)

UO_2 Fuel Element for the EL_3 Reactor at Saclay

The fuel element of alloyed Uranium was replaced by an UO_2 element of a very different shape called the "Snow Crystal" element. It forms a bundle of 8 rods, whose can consists of a single extruded piece. Therefore, welding of end caps was a particular problem as the piece had to be rotated successively around the axis of each rod.

Figure 2 shows the different components, as well as the welding apparatus.

The fuel element is eccentrically placed in a chuck and each 1/8-turn of this chuck puts one rod in place for welding of the end cap. During the welding the chuck rotates around the rod axis.

Fuel Element for the EL_4 Reactor

This fuel element forms a bundle of 19 rods (Fig. 3); each rod consists of a can, two end caps and UO_2 pellets.

Welding of end caps is done laterally, as per diagram of Fig. 1-2.

Figure 3 shows a macrograph of the melted zone (stainless steel can).

We have to bear in mind that in this particular case a certain width of melted zone is absolutely necessary as regards contact between end caps and can and this results in a relatively large heat affected zone.

An apparatus identical with that used for "Snow Crystal" elements permits welding of 48 rods in one cycle.

This cycle is wholly automatic; after machine loading, all operations, such as air evacuation, barrel rotation, and welding of rods are done in sequence without interruption.

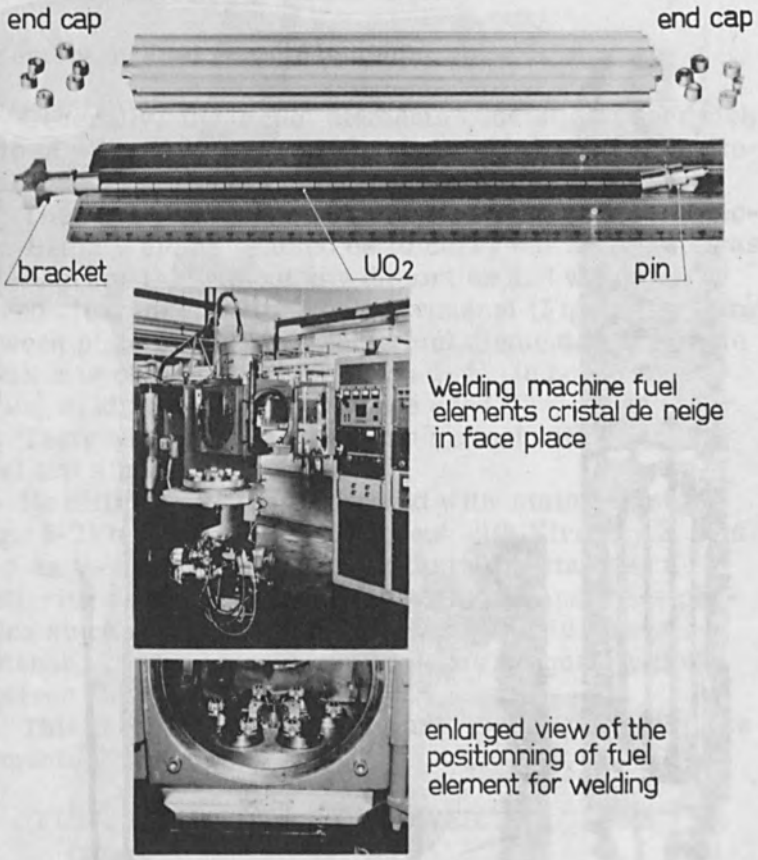

Figure 2. Fuel element "Cristal de Neige" for EL3 reactor Aluminium can obtained directly by extrusion fuel = UO_2 sintered pellets

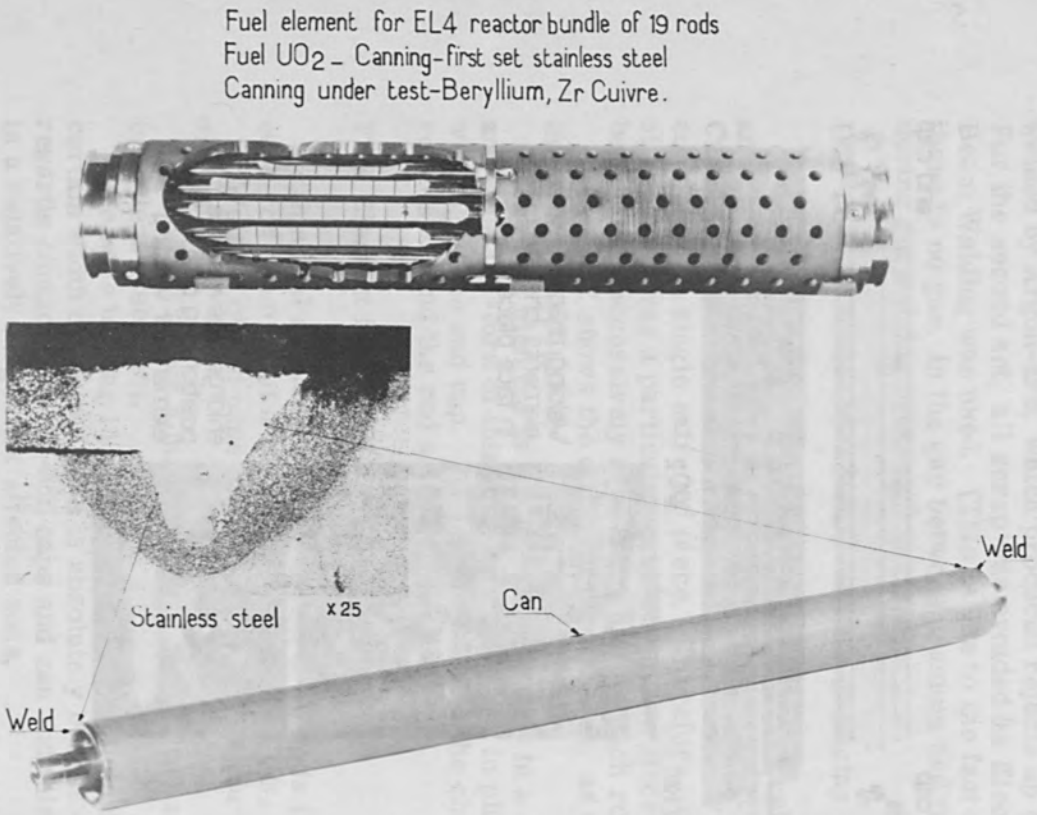

Figure 3. Fuel element for EL4 reactor bundle of 19 rods Fuel UO_2 — Canning-first set stainless steel Canning under test-Beryllium, Zr Cuivre.

Figure 4 shows a micrograph of the melted zone of a can and a Beryllium end cap. In this case the welding parameters have been chosen to obtain the smallest quantity of Joules per unit of welding seam unit, in order to affect the parent metal structure as little as possible. The quality obtained is remarkable.

Assembly of Fuel Plate Elements

Generally, these fuel elements consist of a sandwich plate of alloyed fuel covered on both sides with can material.

These "sandwich" plates are welded together. Electron Beam Welding enabled us to carry out assemblies as per diagram 1-3 without any distortion and with the required clearance for the cooling channel (Fig. 5) (spacing between plates) along the whole fuel element. The same result was obtained with diagram 1-4. In both cases during welding no mandrels were used.

Tests were made with plates canned with stainless steel and also with Zircaloy 2.

No difficulty was encountered with stainless steel (Fig. 5-2) but things were different with Zircaloy 2. As soon as the full depth of penetration was attained, a sputtering of fine metal particles started and these particles stuck to the plates. In order to avoid this phenomenon, it was necessary to defocus adequately the Electron Beam (Fig. 5-3).

This method was used for various types of fuel plate elements.

FUEL ELEMENTS FOR POWER REACTORS

These fuel elements consisting of an Uranium alloy canned with a Mg-Zr alloy (0, 4-9, 6% Zr) are of two major designs:

a tube of U-Mo alloy (Mo - 1%, length 60cm) cooled externally (Fig. 6)

The can is closed at both ends by an end cap of Mg alloy;

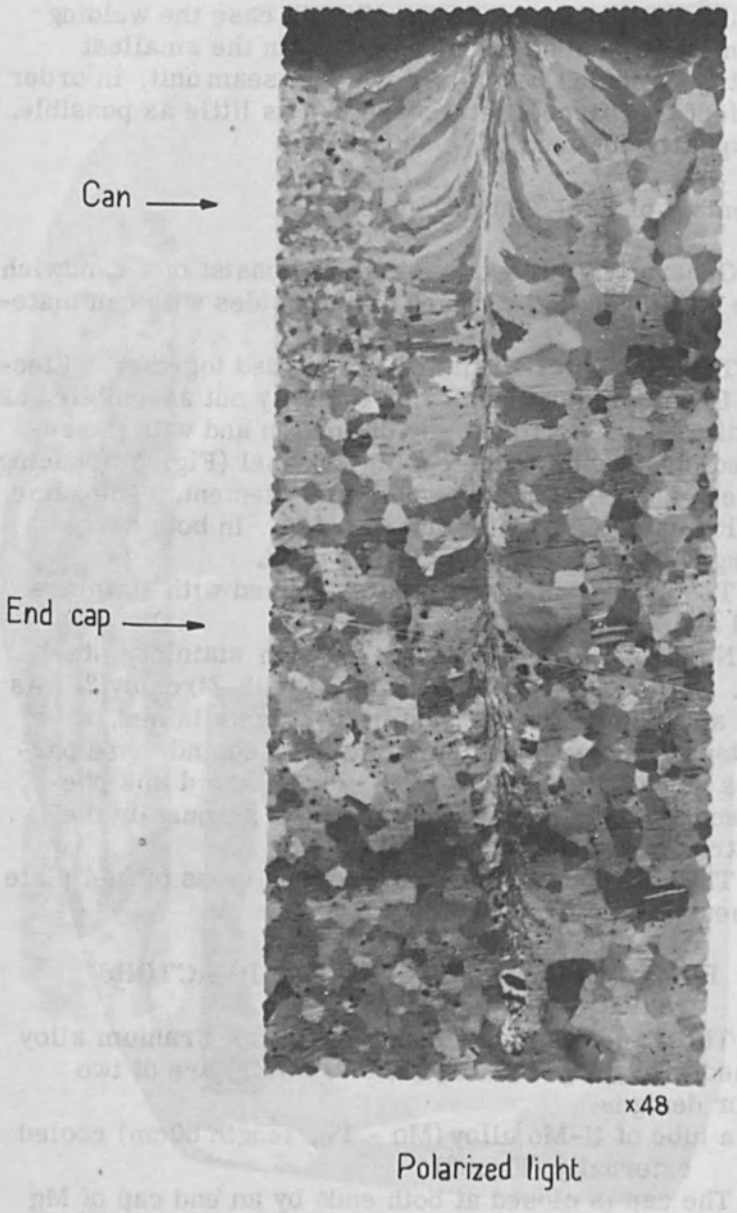

Figure 4. Micrograph of a weld between a can and an end cap (Beryllium) (EL4 fuel element)

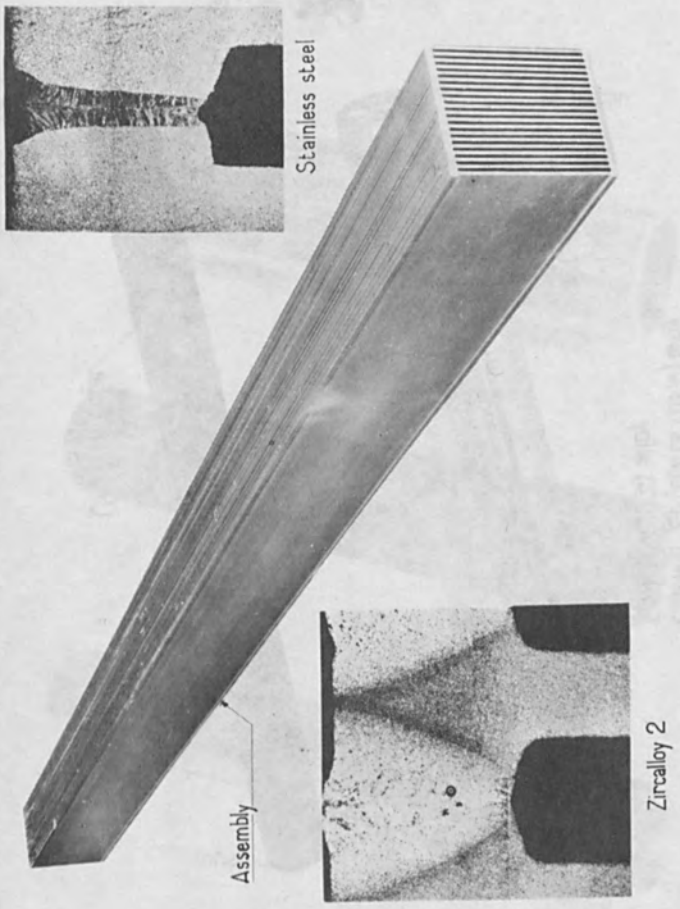

Figure 5. Plate Fuel Element Assembly

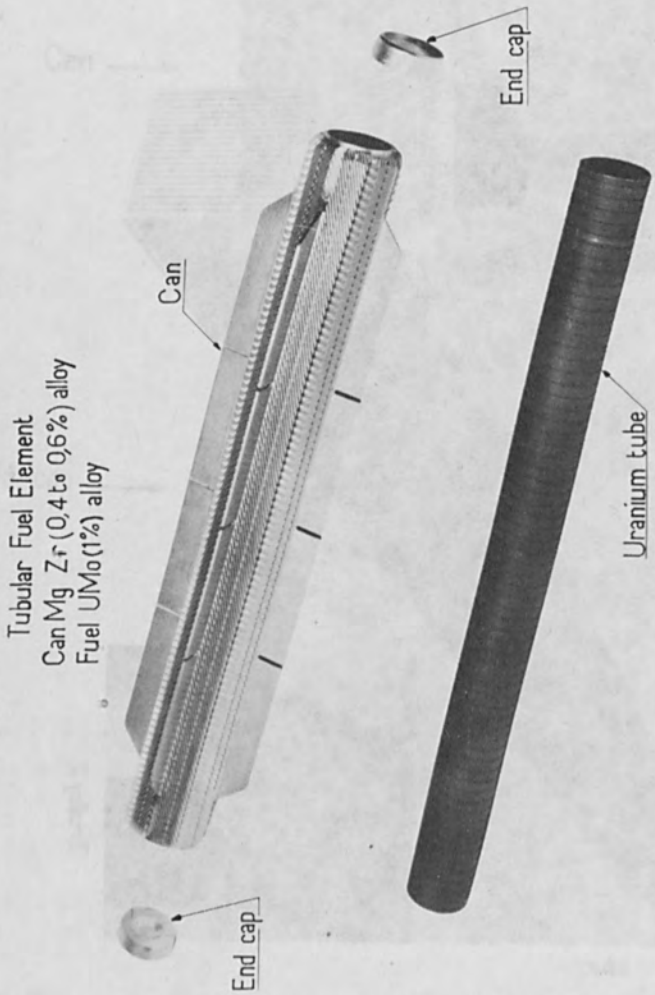

Figure 6. Tubular Fuel Element Can Mg Zr (0,4 to 0,6%) alloy Fuel UMo(1%) alloy

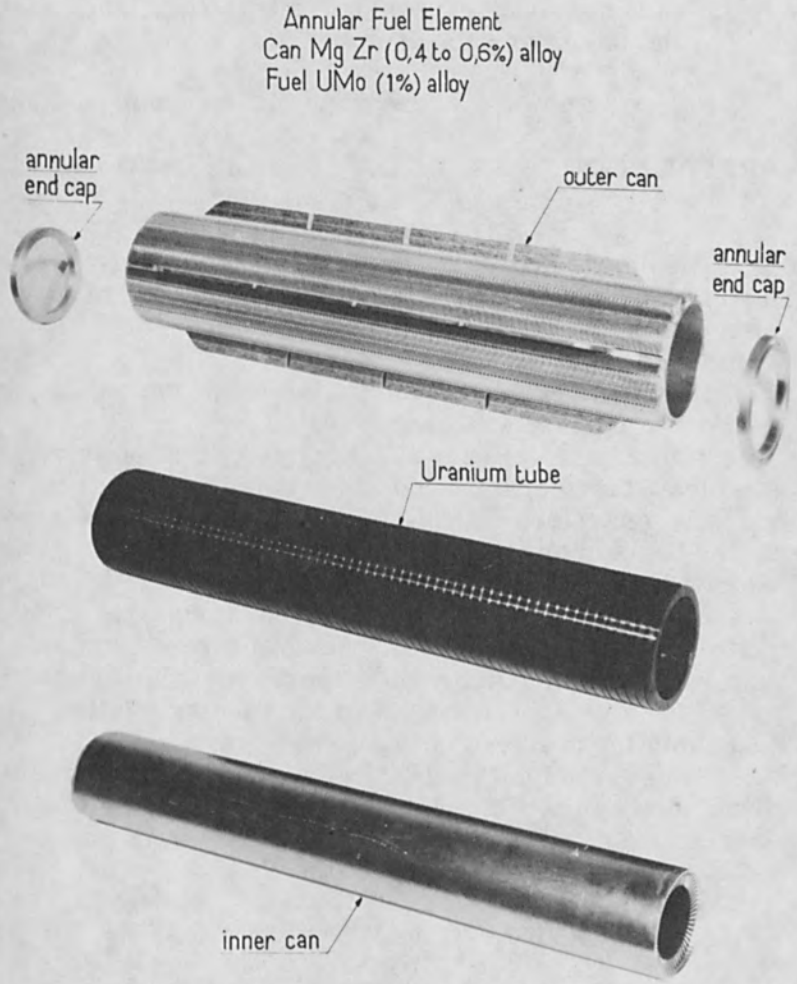

Figure 7. Annular Fuel Element Can Mg Zr (0,4 to 0,6%) alloy
Fuel UMo (1%) alloy

a tube of SICRAL alloy (U, Si, Cr, Al), (inner diamater 77, outer diameter 95mm) canned internally and externally (Fig. 7) and closed at both ends by an end cap welded to both cans, the inner and the outer cap.

Figure 8 shows a macrograph of this double welding.

PREPARATION OF BILLET ASSEMBLIES AND PLATE COMPONENT ASSEMBLIES

The object is always to effect a bond between two metals, either between fuel and can in the case of fuel elements or between two sleeves in the case of structural elements.

Diffusion becomes much easier if the gap existing between components is air evacuated.

With Electron Beam Welding this operation is very simple and furthermore the welds obtained are mechanically very strong. This is very important, inasmuch as the parts are submitted to substantial stresses during extrusion or rolling.

Figure 9 shows an apparatus used for preparation of plate component assemblies. Several plates clamped in a vise are welded in a single vacuum cycle.

The same approach is used for welding a billet assembly for coextrusion.

Some fuel elements obtained directly by coextrusion from such a billet (outer can Zr_2 - fuel U Zr alloy - inner can Zr_2) were tested satisfactorily in the EL_3 reactor at very high burn-up rates.

APPLICATION TO REACTOR COMPONENTS

The PROSERPINE Reactor Vessel

The method was applied for the first time to the vessel of the PROSERPINE reactor (Fig. 10). The vessel consists of a flange and a cylinder made of rolled sheet of 1mm of thickness, a pressed bottom and a tube of 12mm ID x 14mm OD.

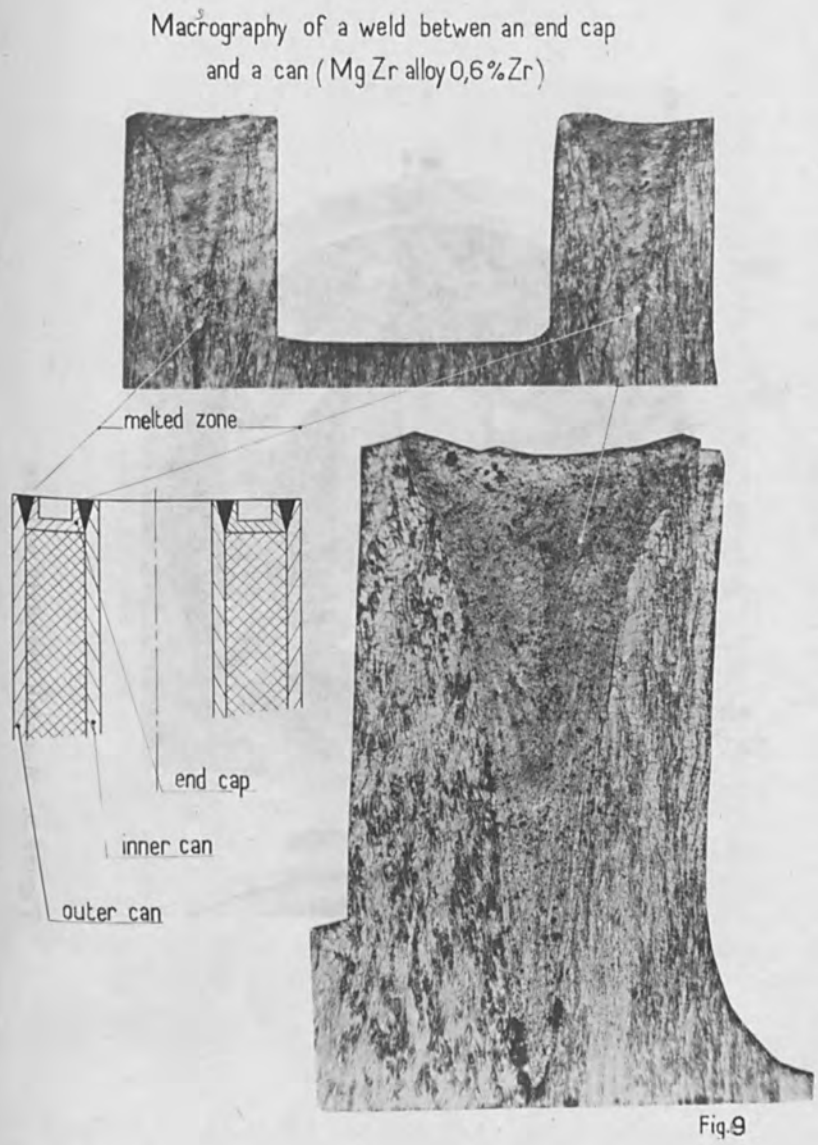

Figure 8. Macrograph of a weld between an end cap and a can (MgZr alloy .006% Zr)

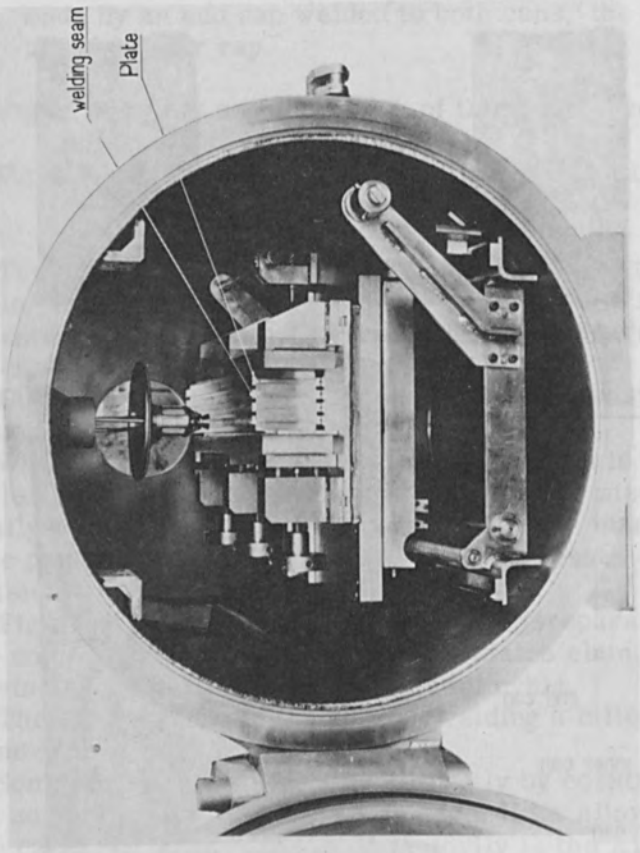

Figure 9. Machine for plate welding

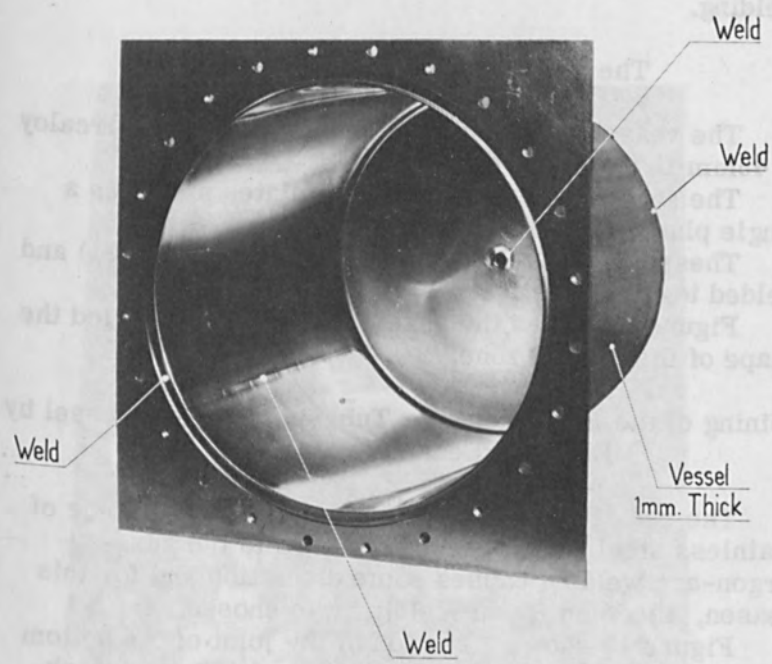

Figure 10. Zirconium vessel of the homogeneous reactor (Pu) Proserpine

Welding operations were the following:
longitudinal welding of the cylinder
circumferential welding of the tube to the bottom
circumferential welding of the bottom to the cylinder
circumferential welding of this assembly to the flange.

All the work was carried out by Electron Beam Welding.

The Vessel of the OSIRIS Reactor

The vessel was fabricated from 8 plates of Zircaloy of 45mm thickness.

The square butt welding of two plates produces a single plate of 710 x 1200mm.

These plates are mounted on a fixture (Fig. 11) and welded together.

Figure 12 shows the assembly after welding and the shape of the melted zone.

Joining of the EL_4 Pressure Tube and Reactor Vessel by Electron Beam Welding

The end of the pressure tube consists of a piece of stainless steel. This piece is welded to the vessel. Argon-arc welding causes some distortion and for this reason, Electron Beam Welding was chosen.

Figure 13 shows a section of the joint of the bottom of the vessel (a stainless steel sheet of 45mm of thickness) and the sleeve (a stainless steel tube of 30mm of thickness).

Joining of Zircaloy 2 - Zircaloy 2 of the EL_4 Pressure Tube

For the joining of the Zircaloy 2 tube with stainless steel pipes for the outlet of gas, the Zircaloy 2 tube at each end had to be provided with a part of greater thickness, called a sleeve. As it was impossible to produce these thicker parts by drawing, they were joined by

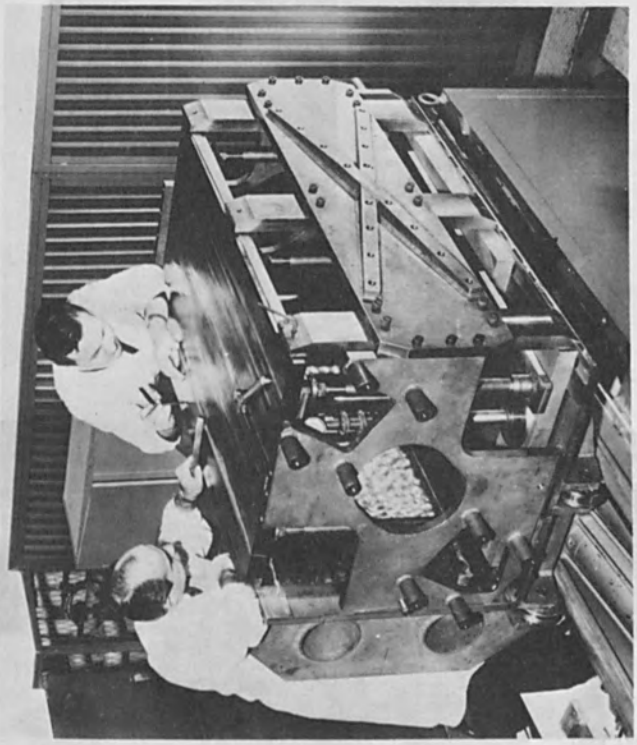

Figure 11. Preparation of the assembly for welding Osiris vessel

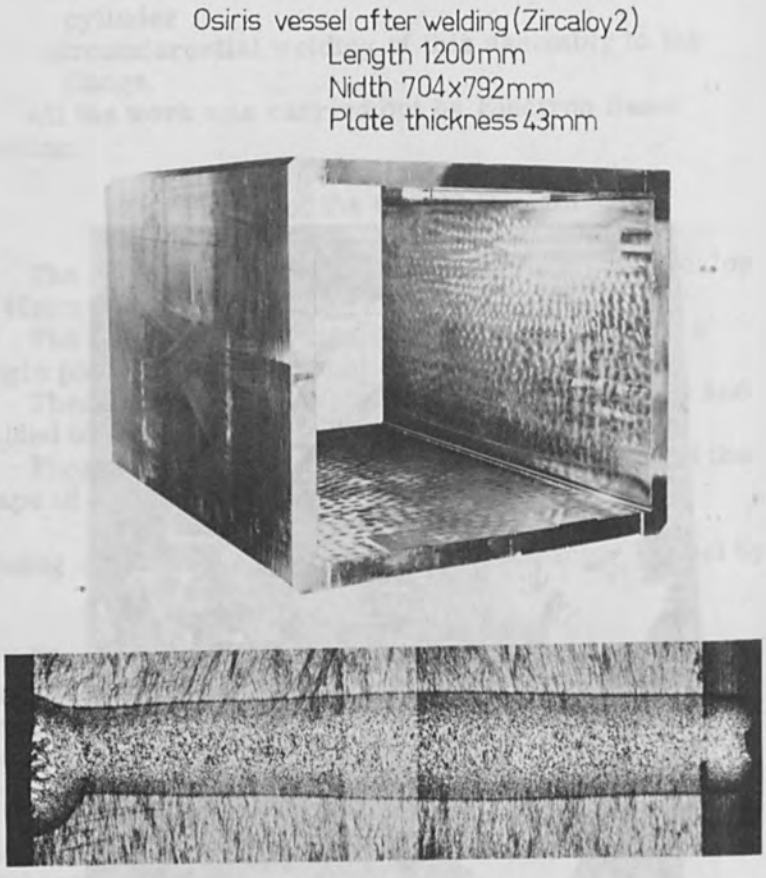

Figure 12. Osiris vessel after welding (Zircaloy 2) Length 1200mm Width 792mm Height 704mm Plate Thickness 43mm

Figure 13. EL4 pressure tube (stainless steel) weld of a pressure tube on the end plate of the vessel

Electron Beam Welding. The as drawn tube (length - 5m; thickness 3. 2mm) was Electron Beam Welded to the end parts (thickness 4. 5mm, Fig. 14) on the apparatus shown by Fig. 15 and only the part to be welded was placed into the vacuum chamber; air tightness was insured by rotary seals. This is one of the very few uses of a fixed position gun; otherwise the fixed gun concept has not been used because of its lack of flexibility.

Proposed Applications of Electron Beam Welding on Vessels for Heavy Water Moderated Reactors

Among heavy water moderated types of reactors, one was considered for Electron Beam Welding which comprised a vessel closed at both ends by flat circular plates of about 8mm diameter and 160mm thickness. Openings, of about 145mm in diameter run through these flat end plates.

Each end plate is delivered in two semi-circular parts and welding has to be carried out on site with the apparatus of Fig. 16.

This apparatus consists of a vessel to be evacuated (10^{-2} mm of Hg) by a mechanical pump. The gun chamber is evacuated by a special diffusion pump of circular shape. Its foreline discharges directly into the vessel in order to use the same mechanical pump.

Two rails, fastened to the plate to be welded, allow the displacement of a carriage, supporting the gun chamber and the diffusion pump, along the welding seam.

In spite of the fact that with the power of existing guns one can make single pass welds in stainless steel up to 160mm thickness, tests proved however that it is better to make welds of half the thickness on both sides of the stainless steel plates.

Our experience with Argon-arc Welding of the EL_4 pressure tubes proved that in spite of all precautions, it was difficult to avoid some distortion, even when using special piecepart designs and specially designed Argon-arc torches, to produce a melted zone similar to EB welds.

Figure 17 shows the welding application and the apparatus to be used for these welds. It was necessary to develop water cooled electron beam guns of high power and small size.

Figure 14. Part of a pressure tube for EL4 reactor Tube Zircaloy 2 - length 4,6 meter - diameter 113mm - thickness 3,2mm End part Zircaloy 2 thickness 4,5mm

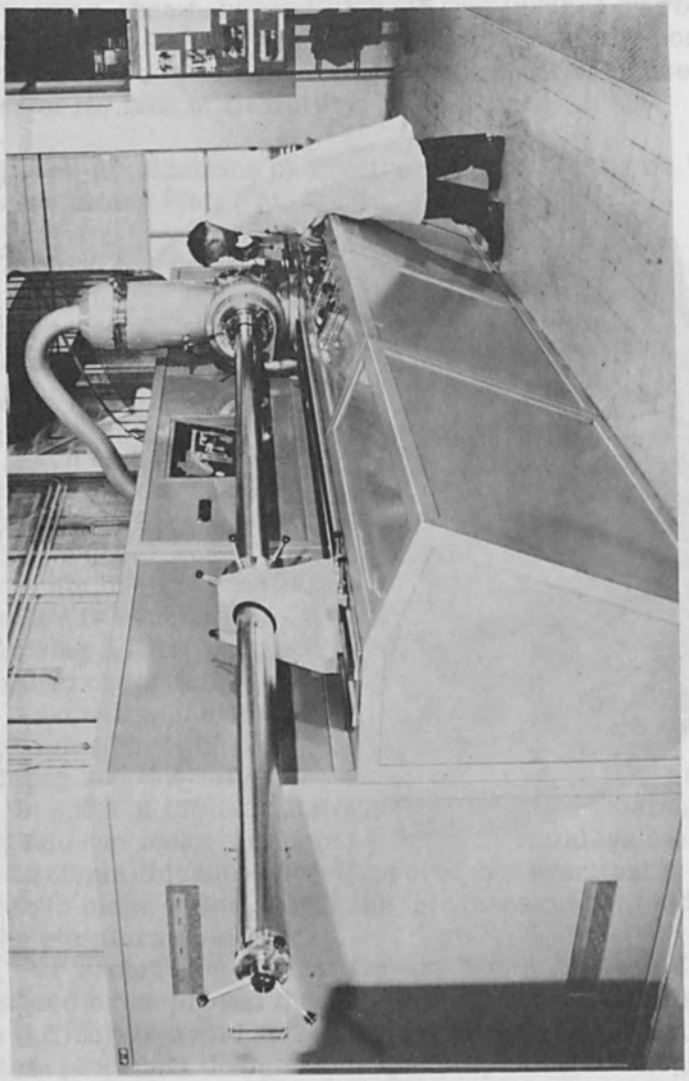

Figure 15. Welding machine used for EL4 pressure tube

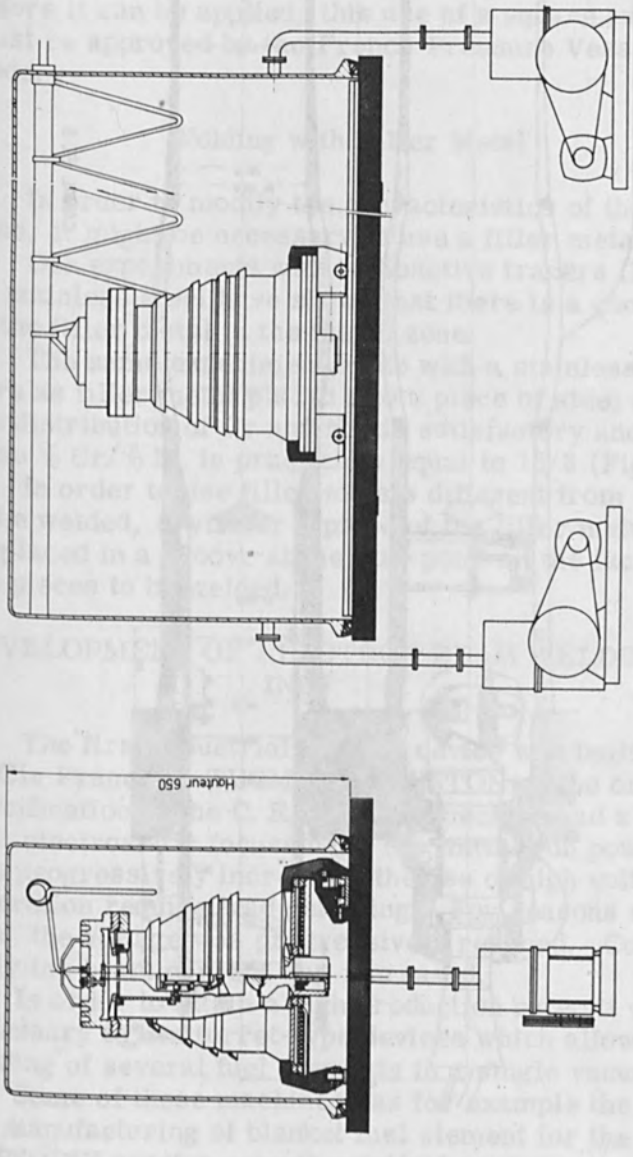

Figure 16.

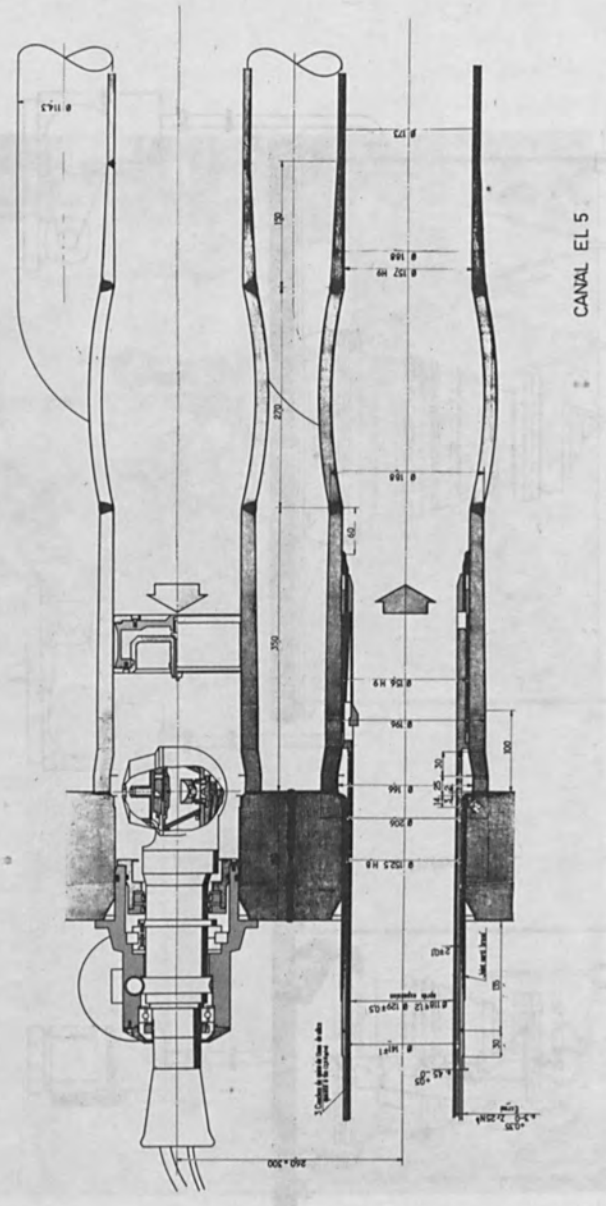

Figure 17.

One encounters the same difficulties for the passage of control rods. A new method is under investigation. Figure 18 shows the solution we recommend; however, before it can be applied, this use of a square butt joint must be approved by the French Pressure Vessel Boiler Code.

Welding with Filler Metal

In order to modify the characteristics of the fusion zone, it might be necessary to use a filler metal.

Our experiments with radioactive tracers (Fig. 19) on stainless steel have shown that there is a good mixing of the filler metal in the fusion zone.

The same experiment made with a stainless steel wire as filler metal placed into a piece of steel shows that the distribution of Cr and Ni, is satisfactory and that the ratio % Cr/% Ni is practically equal to 18/8 (Fig. 20).

In order to use filler metals different from the metals to be welded, a wire or a piece of the filler metal should be placed in a groove at the mid-point on the face of one of the pieces to be welded.

DEVELOPMENT OF ELECTRON BEAM WELDING MACHINES

The first industrial welding device was built in 1956 by Cie Francaise THOMSON-HOUSTON on the order and specification of the C. E. A. This machine had a fixed gun with electrostatic focussing. The initial gun power of 1KW was progressively increased; the use of high voltage acceleration require lead shielding. For reasons of protection, the voltage was progressively reduced. Correspondingly the beam current was increased.

In order to attain a high production rate, it was necessary to use turret-type devices which allowed the welding of several fuel elements in a single vacuum cycle.

Some of these machines, as for example the one used for manufacturing of blanket fuel element for the RAPSODIE reactor permit manifold operations.

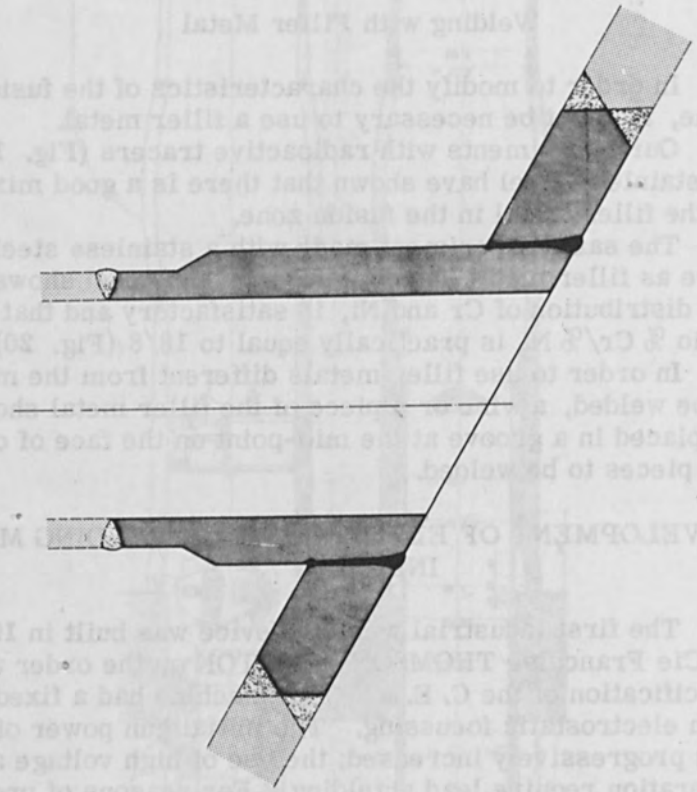

Figure 18.

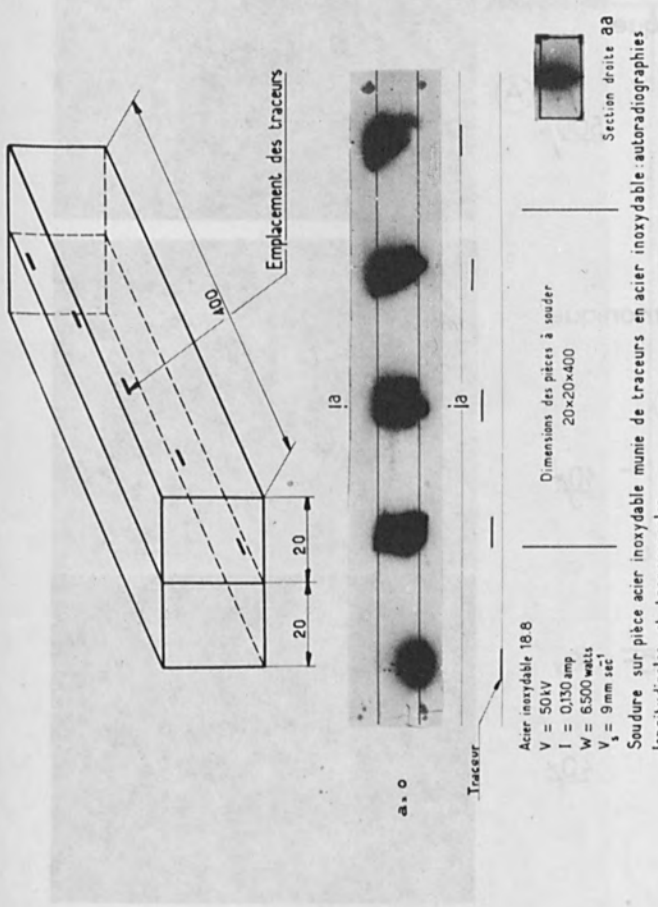
Emplacement des traceurs
100
20
20
a
a
a . o
Traceur
Acier inoxydable 18.8
V = 50 kV
I = 0,130 amp
W = 6.500 watts
V = 9 mm sec⁻¹
Dimensions des pièces à souder
20×20×400
Section droite aa
Soudure sur pièce acier inoxydable munie de traceurs en acier inoxydable : autoradiographies
longitudinales et transversales

Figure 19.

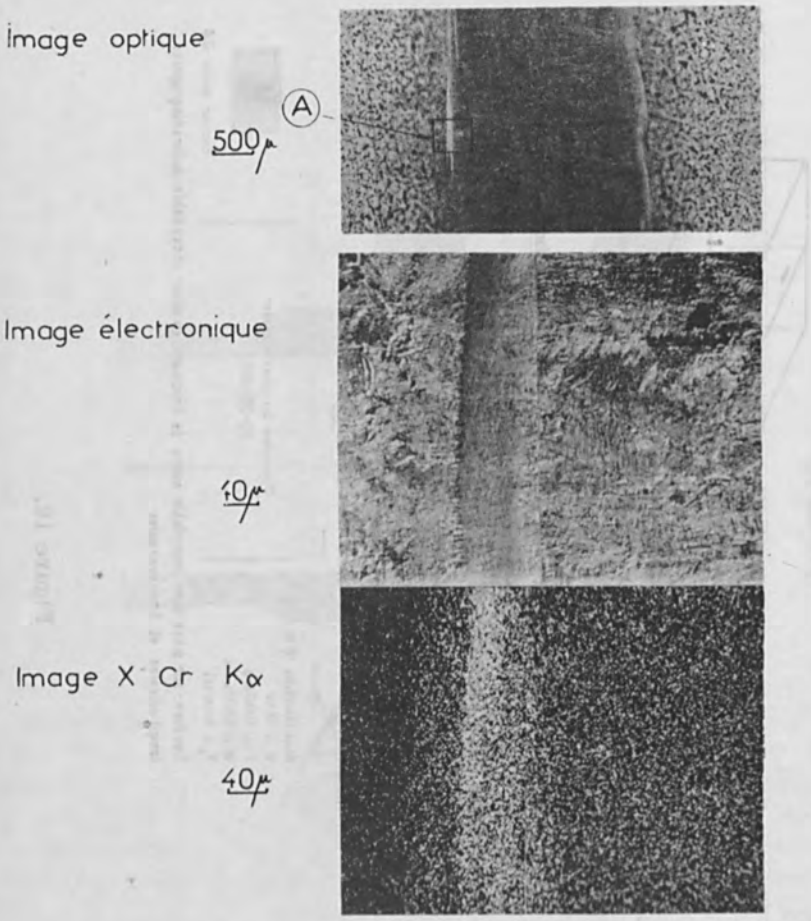

Figure 20. (Part 1 of 3)

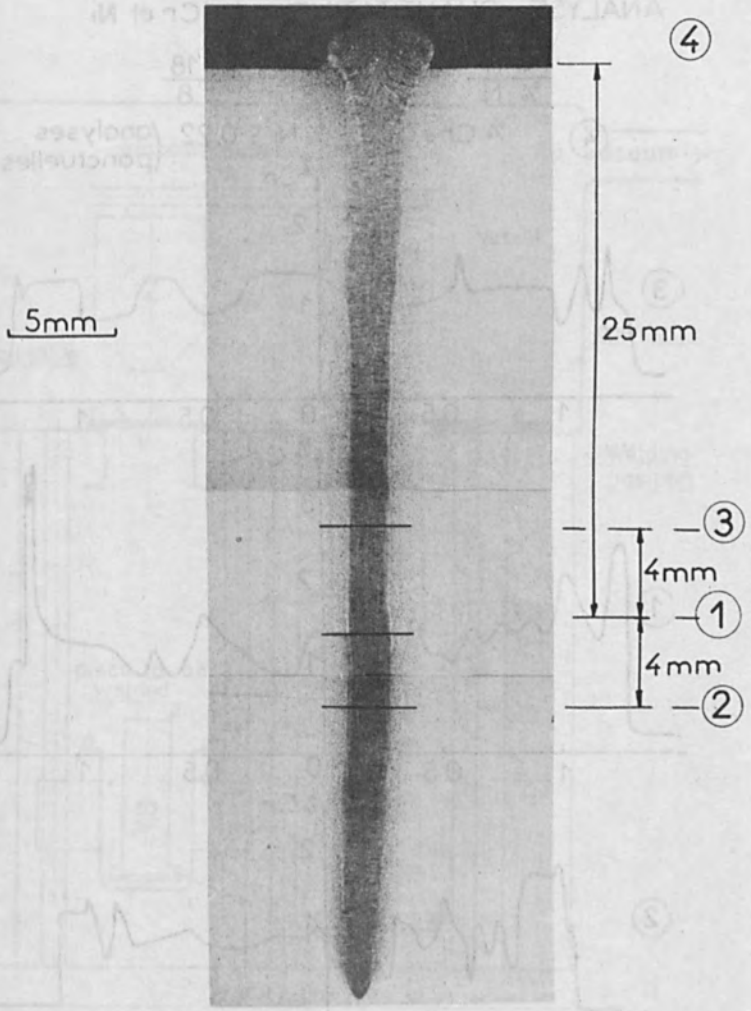

Figure 20. (Part 2 of 3)

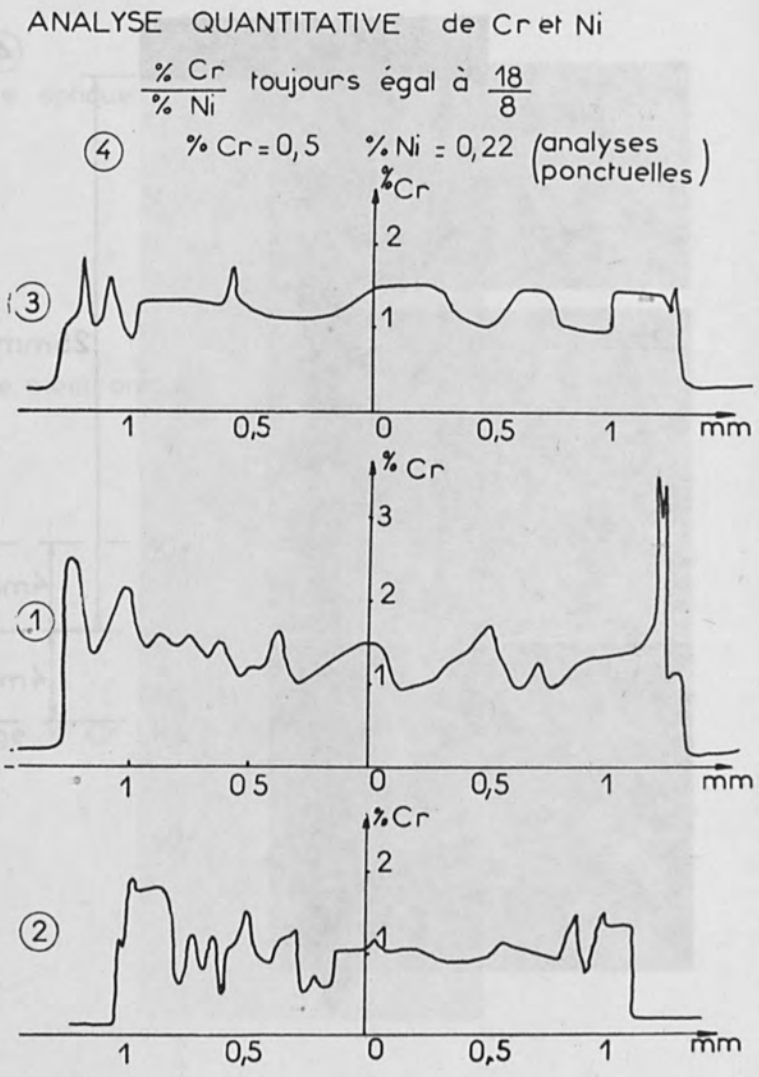

Figure 20. (Part 3 of 3)

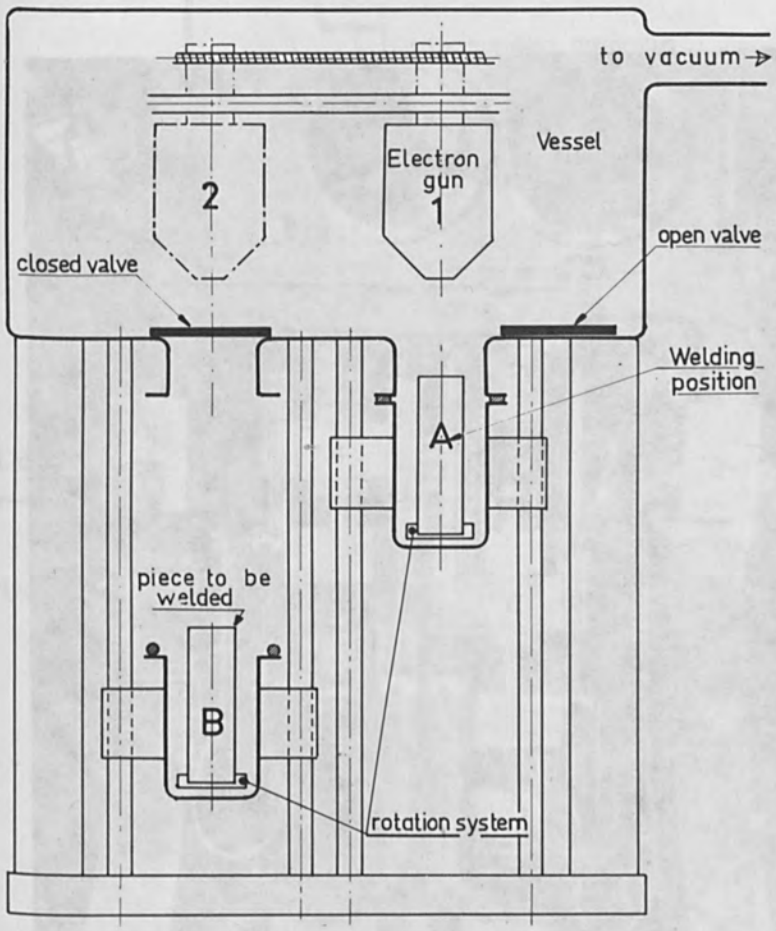

Figure 21. Schematic diagram of the Sciaky machine

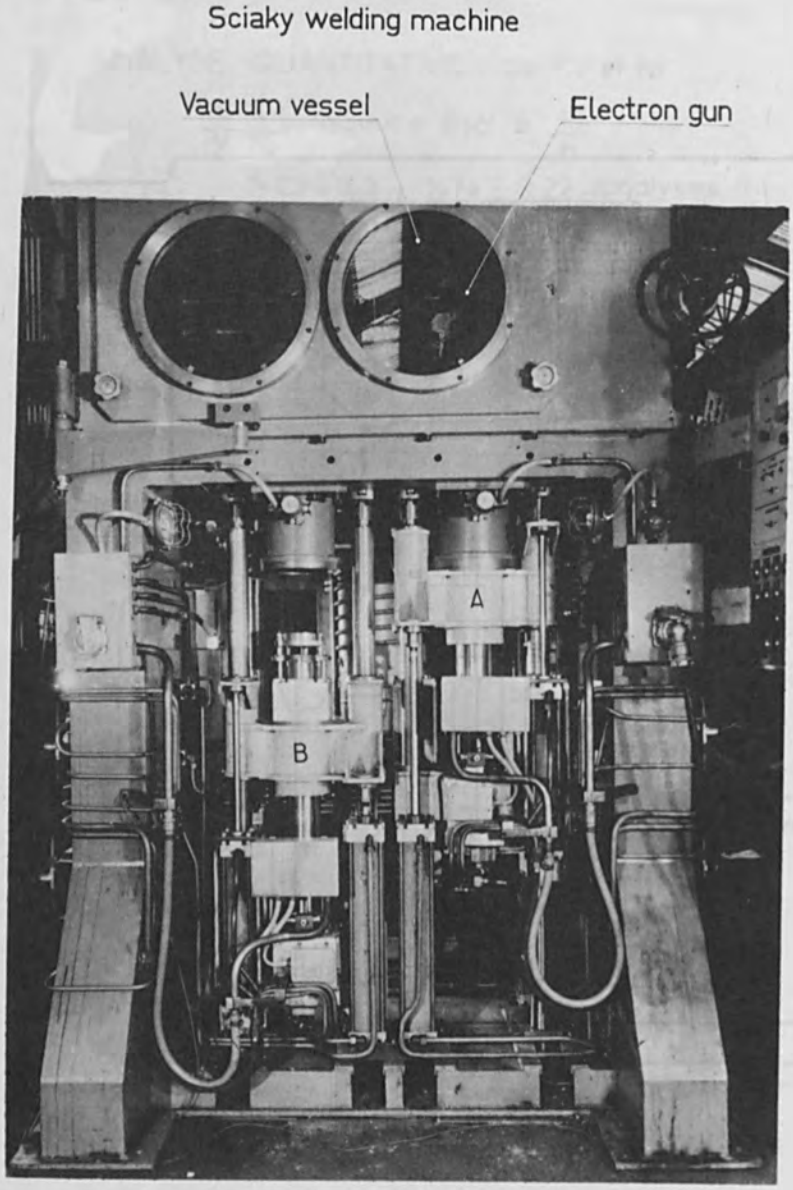

Figure 22. Sciaky welding machine

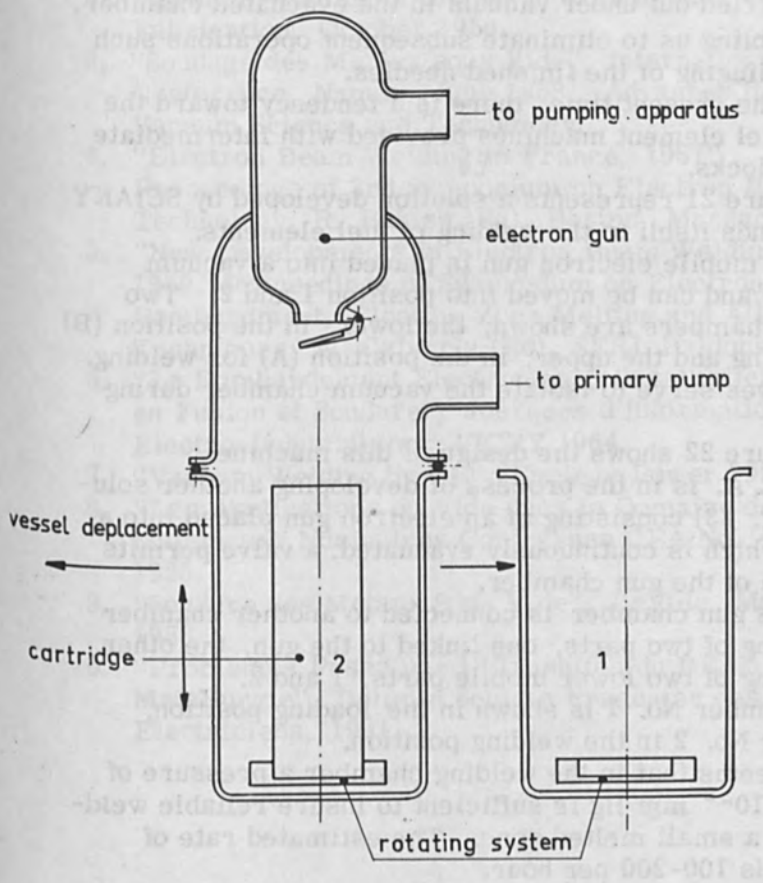

Figure 23. Schematic diagram of the new design for a welding machine (fuel elements welding)

In the case of the device used for RAPSODIE, all operations, such as introduction of uranium, distillation of sodium, putting into place of end caps, and welding were carried out under vacuum in the evacuated chamber, thus enabling us to eliminate subsequent operations such as centrifuging of the finished needles.

At the present time, there is a tendency toward the use of fuel element machines provided with intermediate vacuum locks.

Figure 21 represents a solution developed by SCIAKY which lends itself to the welding of fuel elements.

The mobile electron gun is placed into a vacuum chamber and can be moved into position 1 and 2. Two mobile chambers are shown, the lower, in the position (B) for loading and the upper, in the position (A) for welding. Two valves serve to isolate the vacuum chamber during opening.

Figure 22 shows the design of this machine.

C. E. A. is in the process of developing another solution (Fig. 23) consisting of an electron gun placed into a vessel which is continuously evacuated; a valve permits isolation of the gun chamber.

This gun chamber is connected to another chamber consisting of two parts, one linked to the gun, the other consisting of two lower mobile parts, 1 and 2.

Chamber No. 1 is shown in the loading position, chamber No. 2 in the welding position.

It seems that in the welding chamber a pressure of 10^{-1} to 10^{-2} mm Hg is sufficient to insure reliable welding with a small melted zone. The estimated rate of welding is 100-200 per hour.

As shown on Figs. 16 and 17, welding problems of reactor vessels, pressure tubes and, generally speaking, of big-sized components might be solved by constant gun pumping and welding under high pressures in the welding chamber.

REFERENCES

1. "Electronic Welding of Metals", Fuel Elements Conference, Paris, 1957.
2. "Vacuum Welding of Metals", Welding and Metals Fabrication, October 1958.
3. "Soudage des Metaux sous Vide", International Conference, Namur, June 1958. Advances in Vacuum Science and Technology.
4. "Electron Beam Welding in France, 1961" Proceedings of 3rd Symposium on Electron Beam Technology, R. Bakish (Ed). Boston, Massachusetts.
5. "New Developments in Electron Beam Welding", 1959, Proceedings of Symposium on Electron Bombardment, Floating Zone Melting and Allied EB Techniques, A. Calverly (Ed), SERL Baldock HERTS.
6. "Le Bombardement Electronique, Ses Applications en Fusion et Soudure", Journees d'Information Electro-Industrielles, VICHY 1964.
7. "Vacuum Welding by EB", Nuclear Power 1958.
8. "Les Applications du Vide dans le Domaine des Materiaux" Nucleaires Conference CEA No. 44, 1958.
9. "Soudure des Metaux Sous Vide", LeVide, May-June 1958.
10. "Problemes Poses par l'Utilisation du BE en Metallurgie", Bulletin Societe Francaise des Electriciens, 1961.

Developement , Design and Applications of an Electron Beam Welding Machine for the Instrument Industry

E. Fóti

Central Research Institute for Physics
Budapest, Hungary

Though research work in the field of electron beam welding has been started in our Institute with the aim of solving some nuclear fuel element canning problems on a pilot plant scale, needs emerged in a rather early stage of this program made us to start with developing an equipment for the instrument industry too, designed for production scale applications.

In this branch of industrial production the inherent advantages of electron beam welding can be extensively exploited for production welding of high quality components. Special points of interest here in this industry are: welding of minute parts, mostly composite parts of intricated shapes without any serious deterioration or thermal damage; welding of dissimilar materials; joining parts of very different thickness; production of special situation welds and also frequently production of vacuum tight weld seams and some others.

Development of our industrial machine designated as Type ESH-21 took place in three steps but cannot by far be regarded as finished though two pieces of it are already in use and a slightly modified version gone into industrial production.

First some preliminary experiments were carried out on a small experimental machine [1] to define the basic data of an appropriate specification. These experiments proved that the necessary beam power is not more than two kilowatts (or even much less when welding of small parts is meant only) and that choosing an accelerating voltage of 25 kV would be a rational compromise keeping

in mind weld quality (fine focusing) requirements, cost factors and easy introduction of this technology into industrial production equally. With these main data the laboratory version could be designed and built (Fig. 1).

Designing and building this laboratory version gave a possibility to try and prove some points of the design concept and the basic units of the final version and also for welding several production runs with actual components of industrial firms [2]. Apart from these the laboratory machine proved very useful in experimental techniques since it offers a very convenient way of solving a lot of

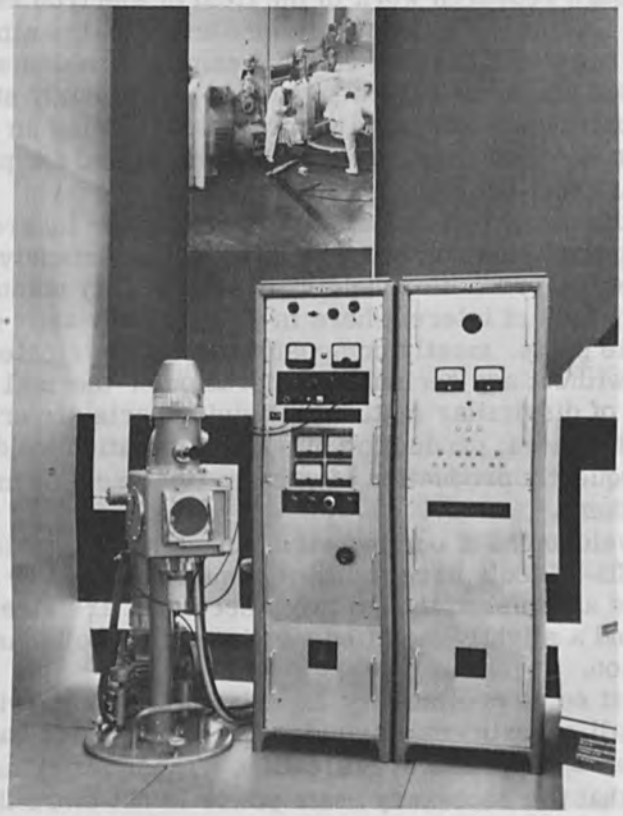

Figure 1. The laboratory version of the electron beam welding machine Type ESH-21.

welding problems in building experimental apparatuses in nuclear research and in general laboratory practice. These works served the experimental basis for the design of our present final version called ESH-21 (Fig. 2).

Since there are only these few machines in use as yet in our country when drafting up the design we had to strive to work out a system as versatile as possible to allow technological studies highly necessary in the present state of this art here.

This machine does naturally not contain too many new features - though it is hoped that some details of the con-

Figure 2. The 2 kW, 25 kV electron beam welding machine Type ESH-21, developed for use in the instrument industry.

struction might be of general interest among people working in this field either technologists or designers.

The electron gun - rightly regarded as the most important part of a machine - is of the well known simple plane-triode system with a slight modification of the control electrode geometry only. Although use of this kind of gun is most customary in small power electron beam devices like cathode ray tubes and electron microscopes, up to a limit current as high as about 120-150 milliamps its application can be justified on account of some of its advantages, first of all its great transconductance, simple geometry and easy control, especially pulsing.

The cathode holding structure allows the use of different types of directly and indirectly heated cathodes, e. g. hair pin, spiral and plate cathodes and a so called bolt-cathode, something like that developed by Bas [3].

The gun housing made of polished stainless steel permits a careful adjustment of the optical system by sliding the cathode-bias cup suspension structure in a plane vertical to the optical axis and by tilting it on a spherical surface whose centre lies in the anode hole. This seems to be of great importance since misalignments not only spoil the focusing properties of the gun and affect harmfully its current efficiency but distort current density distribution in the beam too, what may lead to nonsymmetrical workpiece heating. Even slight misalignments which do not cause visually observable changes in focusing or measurable change in current efficiency can be traced by measuring current density distribution along the diameter of the unfocused beam (Fig. 3).

In designing the focusing lens system two main specific features of the electron gun had to be taken into account, i. e. the varying of the place of the crossover along the axis and of the space angle distribution of the electron stream with changing beam current and bias voltage respectively, and also the changing workpiece distance.

Having investigated a series of possible solutions, application of a twin lens system proved to be expedient. This system consists of two completely uniform magnetic lenses (Fig. 4), which differ slightly in their stray fields only because of their relative positions. The lens design have been based on Liebman's charts [4]. The internal

pole diameter is 40 mm and the ratio of gap length to internal pole diameter is 1. The lenses are hermetically sealed and placed within the vacuum atmosphere sank well down into the work chamber to get close to the workpieces. Their maximal excitation is 3000 ampereturns.

This lens system offers a great versatility in focusing. There are four possible modes of operation regarding the relative excitations of the two lenses. From among these only two modes are practically exploited.

In the first case lens 1. is not excited and the second lens is effective only. This lens gives now a rather large

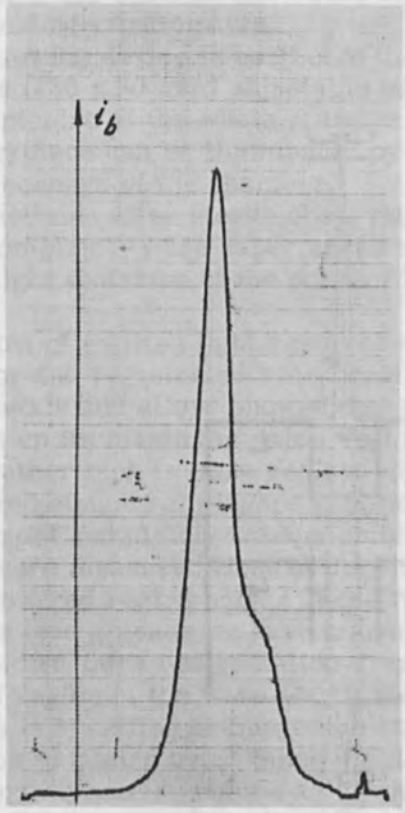

Figure 3. Distortion of current density distribution in an unfocused beam on account of slight misalignment of gun column.

demagnification M = 0, 2 - 0, 4 depending on workpiece height. This mode of operation is employed with small beam currents. When working with high currents the beam solid angle becomes also larger. In this case the first lens is excited so that the crossover fall into its focus point. Then it gives a parallel beam which is focused by the second lens onto the workpiece. In this case the dial settings of the helipots which control output voltages of excitation power supplies can be calibrated in beam current and workpiece height for proper excitation of the first and second lens respectively.

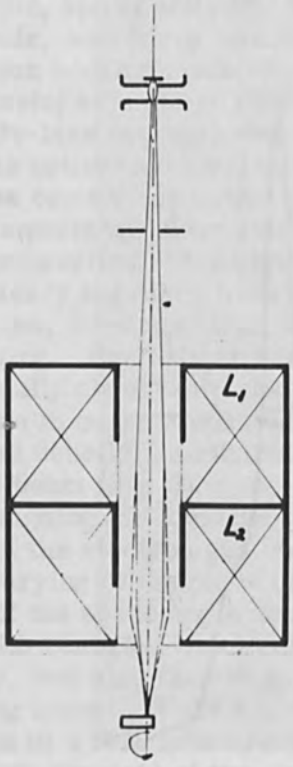

Figure 4. The electron optical arrangement.

With the appropriate choice of geometrical dimensions of the whole electron optical system it is ensured that the smallest possible spot achievable is limited practically by the aberations of the system alone. The smallest spot diameter is about 0, 15 mm when working with small beam currents say up to 10 milliamps and about 0, 3 mm for high currents.

There is a monocular optical viewing microscope built into the electron gun body (Fig. 5). This gives a ten times magnification and provides a 20 mm field of view at the workpiece. With the help of an optical cross incorporated the operator can line up the workpiece with the centre of the beam while the beam is off. This aid is especially useful when welding minute parts.

Another viewing device is built onto the chamber door. This is a large (130 x 80 mm) adjustable panorama optics which gives a picture of the whole chamber at 3x magnification. The workpiece can be illuminated by bulbs placed in the top inside corners of the chamber.

Since sometimes after steady observation of the weld process eye complaints were experienced we had to investigate the light emission of the point of impact of the beam.

The spectra of emitted light resolved by a mirror-monochromator and registrated while welding several kinds of technical metals and alloys showed that although light intensity takes up its maximum value well inside the visible region, it is rather rich in infra red and ultraviolet alike. Since optical and structural glasses generally absorb ultraviolet light almost completely transmissibilities of the glasses used were measured first in the visible and so called near infra red region only. These measurements proved that the lead glasses we have transmit about 80 per cent of the incident infra red radiation even close to the near infra red region of the wave length between 0, 78 - 2, 0 microns which is specified in Hungarian standards as the most dangerous to human eye. Since the dazzling effect of the brilliant spot appearing before a dark background had also to be cared for, we had to place filters in the optical viewing microscope and under the panorama optics too and build up the large work chamber windows from three layers of different transparency glasses. For sake of

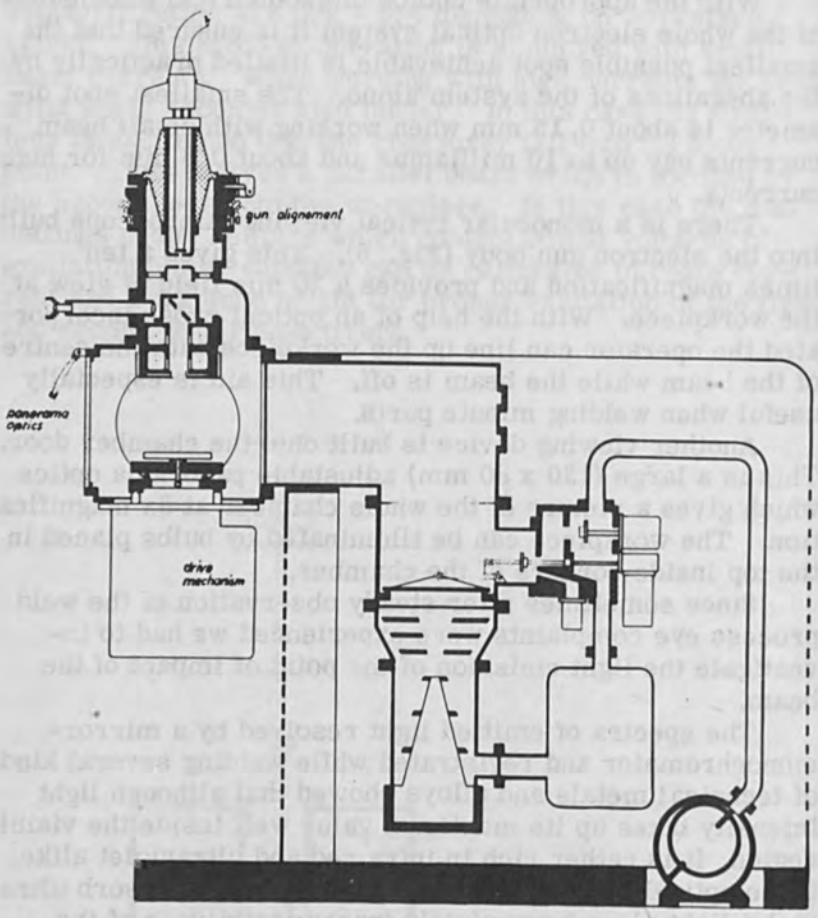

Figure 5. Principal scheme of the machine.

safety light filters used by electric arc welders are applied when steady visual observation of the process is necessary, until we manage to clear up completely health hazards involved and make perhaps a better choice.

Radiation hazards on account of X-ray generation had also been attended to. We were not able even with the most rigorous measurements to detect an X-ray intensity greater than two times the background level anywhere

around the machine when working with a beam power 50 per cent greater than the nominal.

This relatively high degree of safety has been ensured by careful construction of the almost full size access door and windows to prevent X-ray leakage and by choosing a rather large 30 mm chamber wall thickness.

The work chamber is a welded mild steel cube with the inside dimensions 350 x 350 x 350 mm. All the openings on it have the same geometry and dimensions for easy change of planned accessories.

The vacuum system is of a rather conventional arrangement. It consists of a rotary mechanical fore-pump with gas ballast, a backing pressure container, a high speed fractionating oil-diffusion pump and a water cooled baffle in series. This compact unit has a pumping speed of about 1000 1. s^{-1} at 10^{-4} torr pressure and is capable to maintain an operating vacuum (1-5) x 10^{-5} torr in the work chamber. The valves are electromechanically actuated. The complete pumping and valving system is controlled by a six position controlling switch placed on the left hand console. With a group of interlocks a practically foolproof system is provided the mess instruments not included for ease of inspection. A separate safety instrument is built in to ensure that the high vacuum measuring head, cathode heating and accelerating voltage should not be switched on before achieving a safe vacuum level while pumping down. This is all the more important since the door of the work chamber and the upper part of the electron gun are closed down mechanically by the outside atmospheric pressure only. Pump-down time between chamber loads to operating vacuum level is generally shorter than four minutes. The precision standard drive mechanism (Fig. 6) is bolted up to the bottom opening of the chamber. It consists of a d. c. servo motor, a gear box giving transmission ratios 1:17, 1:17 x 5, 1:17 x 15 and 1:17 x 15 x 5, adjusting and drive shafts and a worktable. The worktable is motor driven in the longitudinal (x) direction and can be adjusted manually both in the x and y directions by a rack and pinion system. The table travels on linear ball bushings in hardened steel beds. Table travel is 120 mm in both directions. The entire drive system is designed to minimize backlash. The table

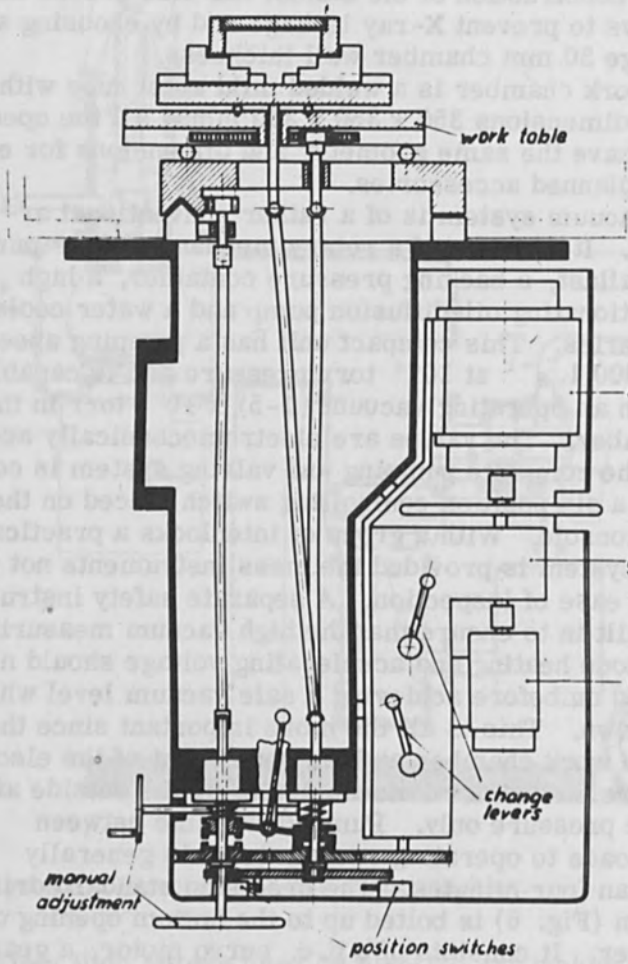

Figure 6. Scheme of the standard drive mechanism.

which can be water cooled accepts different kinds of chucks and jigs for convenient fitting of workpieces (Figs. 7a and 7b).

The speed of the drive motor is electronically stabilized so that speed deviation is smaller than 0, 5 per cent and is electronically controlled over a range in excess of 1:20. Building in a gear-box was necessary to ensure a welding speed range between 0, 1 - 1, 5 m. min^{-1} with a workpiece diameter of 1 mm and 100 mm alike.

The block scheme of the electronic speed control and stabilization system is shown on Fig. 8.

Concerning the stabilization of the whole system the concept of working point stabilization has been accepted, that is all the supplies and controls defining operation and weld parameters have been stabilized and form in themselves closed stabilization circles like speed stabilization.

The only specific feature worthy to mention is the stabilization of the high voltage power supply. This is an analogue system applying an operational amplifier and

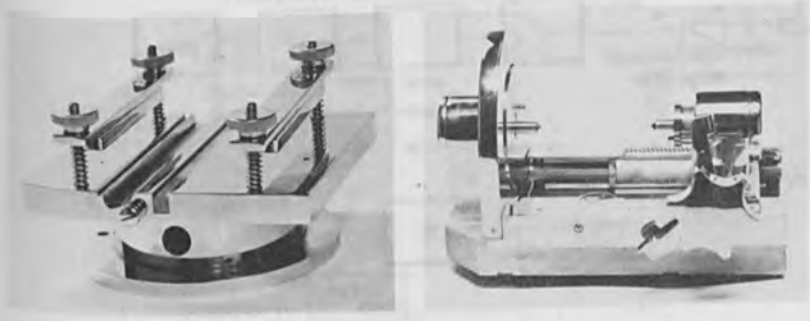

Figure 7. Two exchangeable jigs.

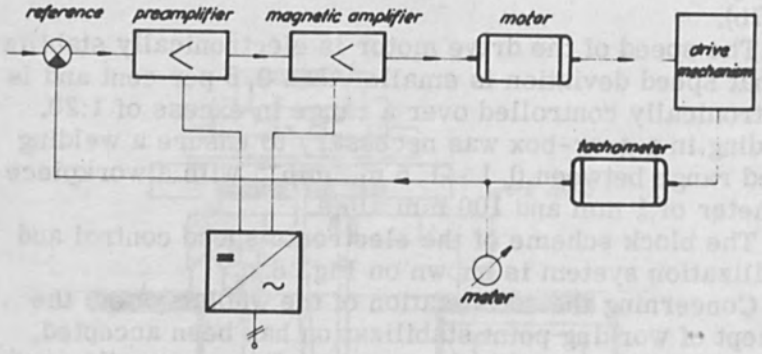

Figure 8. Block-scheme of speed control.

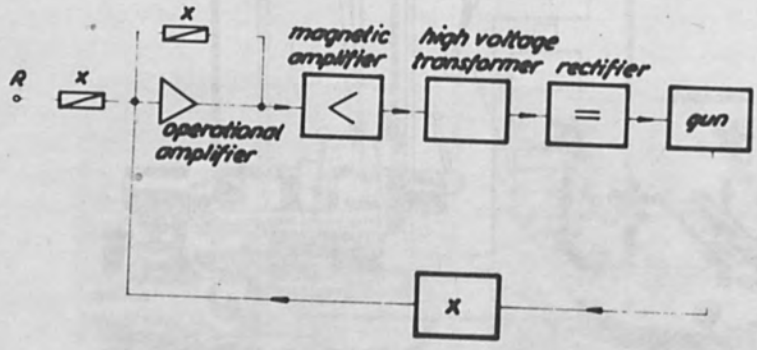

Figure 9. Block-scheme of high voltage control and stabilization.

magnetic power amplifiers together (Fig. 9 and 10). The self saturation magnetic amplifiers ensure easy control of high power levels and the operational amplifier a good possibility of forming exact error signal. With the proper choice of the X impedances different transfer functions can be realized almost at will. This is very useful both for the suppression of disturbances while welding and for achieving a good reproducibility of adjustment.

By this term, reproducibility of adjustment we mean the uniformity of power pulses what a workpiece receives during its complete weld period repeated several times when the setting is changed and re-set in between.

The analysis based on a linearized model of the system and certain experimental evidences prove that this is influenced first by the transients of the electronics then by mechanical instabilities and by the stability of the supplies in the third order only. The mechanical instabilities originating mainly from the non-uniform thermal expansion of the parts of the gun and cathode structure have been most marked when using bolt cathodes which require a somewhat higher heating power.

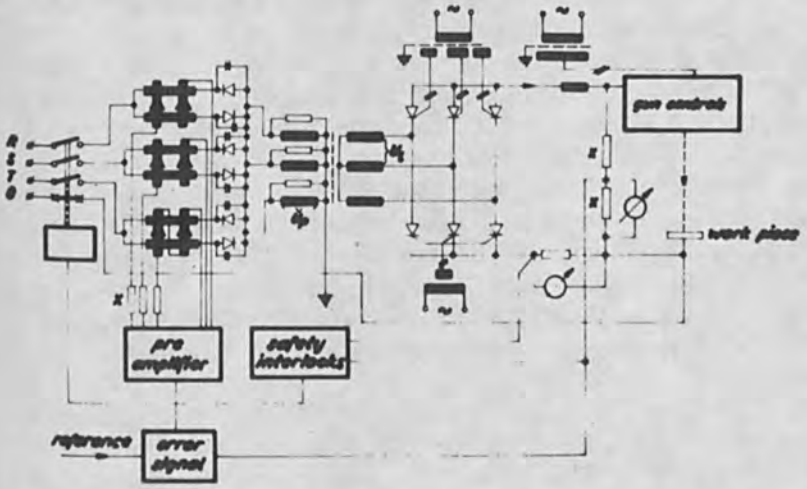

Figure 10. Simplified diagram of high voltage control and stabilization.

Interlocks ensure that when the machine is switched on the constant cut off bias voltage appears on the bias cup. This is switched over to the variable pre-set bias voltage for the weld period by a relay photo electronically actuated through an electronic timer started by a foot lever having the weld parameters been pre-set. This timer is a high precision RC clock which allows setting any periods between 1 - 200 sec. with the greatest deviation smaller than 0, 5 per cent.

Continuous and pulsed operation can be preselected by a selector switch. The square negative pulses are superimposed onto the bias voltage. Pulse width has a constant value 80 μsec, repetition frequency infinitely variable between 1 and 10 kHz. Thanks to the great transconductance of the electron gun, the relatively low voltage well formed pulses (the pulse generator is grounded on the accelerating high potential) are transferred without any serious deformation.

Many a times we have experienced crater building at weld seam endings due to the sudden cessation of beam current. This is a rather undesirable effect since it not only spoils weld seam uniformity but also lessens its strength and when welding vacuum tight seams might result in air leaks especially in thin walled structures.

Switching off beam current i. e. giving out the constant cut-off voltage happens in our machine therefore through a damping impedance, which ensures a gradual fall of beam current and elimination of crater building. According to our experiences insertion of an RC member with a time constant of say one sec seems quite satisfactory for this purpose. The form of long current pulses can be seen on Fig. 11 where the effect of switch-off damping is clearly demonstrated. When on the contrary a sudden stop of welding is required, the damping member can be disconnected with a switch.

The whole machine is built up in three main units: the central mechanical unit consists of the work chamber, the drive mechanism, the vacuum pumps and the electron gun, the left-hand cupboard contains all the low voltage supplies and control organs except the timing clock and the right-hand cupboard in turn contains the high voltage supplies and control organs with the timing device. The main

Figure 11. Form of long current pulses of different durations.

operating and welding parameters can be directly read on the instruments placed on the front plates of the cupboards. Those of them which are on a high potential (on the right) have been placed inside the cupboard behind a plexi-glass window and well illuminated for clear observation.

All the switches and controls are placed within easy reach of the operator when seated. The welding operation itself can be started with a foot lever placed in front of the operator on the machine base. Of course the machine is equipped with a lot of usual aids and devices to help high quality production welding, not mentioned here.

To illustrate what kinds of works have successfully been conducted on this machine during the first few months of its use some examples are shown on Figs. 12-18.

The pressure sensing membranes used in hydraulic instruments (Fig. 12) are now production welded with our machine. They are made of beryllium bronze and assembled with three weld seams. First the bolts are welded into the membrane plates then the two plates joined on their periphery. The membrane plates have a thickness of 0, 1 mm and the bolts have a diameter of 3 mm where welded. The overall diameter of the membrane is 31 mm, and the diameter of the working region 28 mm so there is only a 1, 5 mm distance between the outer weld seam and the working region. The main point is therefore that the membrane must not become annealed. The welds must be vacuum tight since there is a pinhole in the shorter bolt and the membrane senses the difference between outside

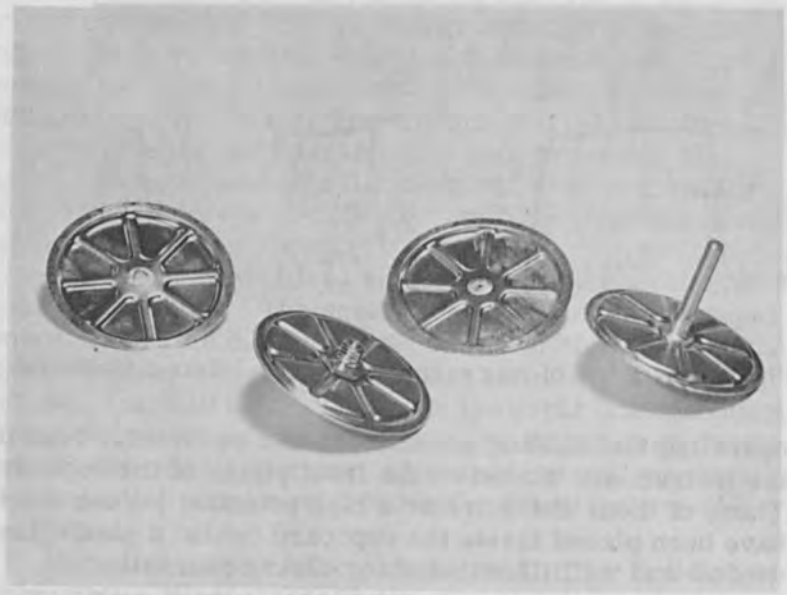

Figure 12. Pressure sensing membrane and its components.

and inside pressure. Weld parameters are the following: 25 kV, 7, 5 mA, when welding the shorter bolt; 25 kV, 7 mA, when the longer bolt is welded and 25 kV, 6 mA, when the two plates are joined, speeds are 1, 2 and 1, 7 m. s^{-1} respectively. Micro hardness tests revealed that the width of the heat affected zone is not greater than one mm around the outer and smaller than 0, 5 mm around the inner weld seams. Vacuum tightness is proved by leak tests. No change could be detected in the elastic properties of membranes properly welded. Having completed the first few hundred pieces reject rate decreased to a negligible minimum.

In Fig. 13 the anode-screen holding structure of a high power electron tube can be seen as welded with electron beam (b) and for the sake of comparison, the same part welded with argon arc (a) too. This part consists of an enlighted central tube made of nickel with a wall thick-

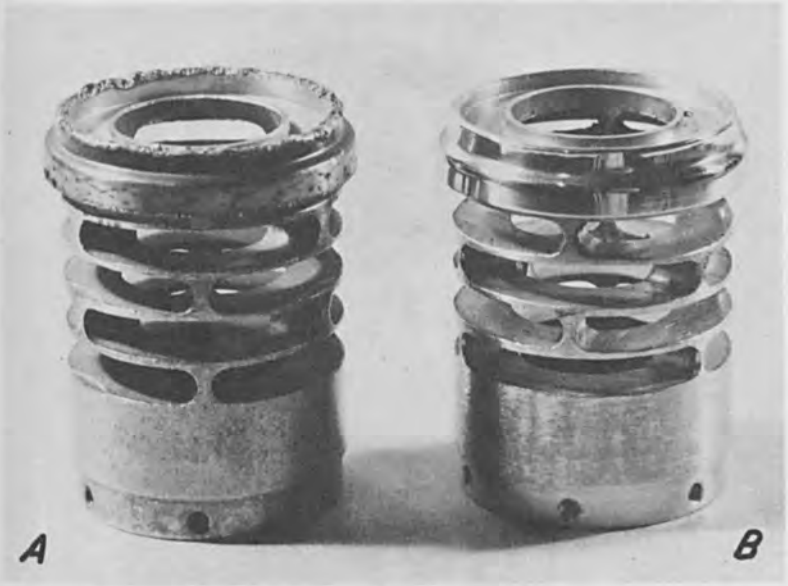

Figure 13. Anode-screen holding structure of a high power electron tube as welded by argon arc (a) and by electron beam (b).

ness of five mm and a small collar pressed from 0, 5 mm thick molybdenum plate. Diameter of the weld seam: 40 mm. Apart from this rather great difference in thickness there are also great differences between the thermal properties of the two materials (all the important thermal properties differ round by a factor two). The accelerating voltage was 25 kV, beam current 20 mA and the speed 0, 6 m. min^{-1}. Several runs of this part have been welded up to now practically with no rejects at all.

When welding the transistors shown on Fig. 14, a vacuum tight closure had to be ensured without overheating the semi-conductor material itself. The steel cans have a diameter of 5 mm. This task could be solved without any serious difficulties. Long time leak tests carried out on a number of pieces could not reveal any increase of the inside pressure in the cans. Temperature measurements showed that the temperature of the semiconducting element did not exceed 60°C.

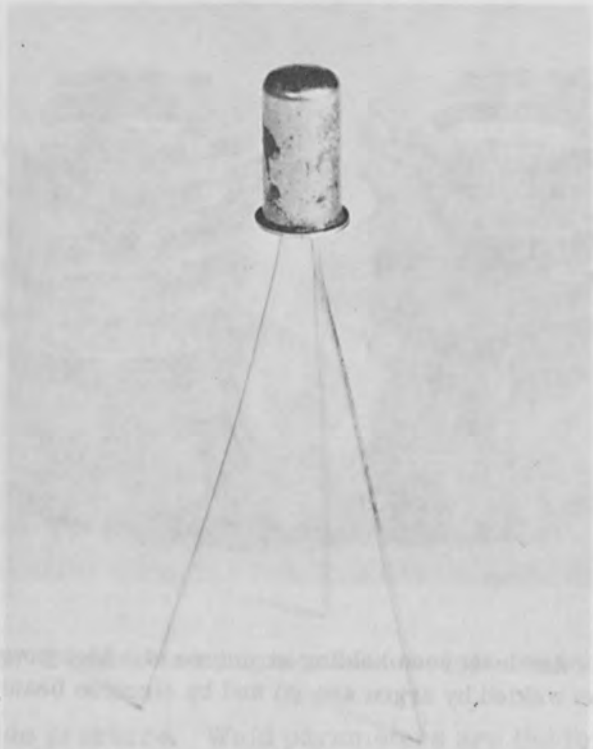

Figure 14. Small power transistor closed by electron beam welding.

Welding experiments and production welding of small batches of several ultra high vacuum component parts (see two of them on Figs. 15 and 16), showed a very high degree of reliability in the production of ultra high vacuum equipment. Weld parameters in welding both parts were: 25 kV, 20 mA, speeds 0, 8 and 0, 6 (valve) m. min^{-1}.

The measuring feed-through shown in Fig. 17 is a composite metal-ceramic part, it is used in gas-chromatograph detectors. The central ceramic piece containing the two wires is brazed into a thin FeNiCo tube and this had to be welded into the stainless steel ring which seals

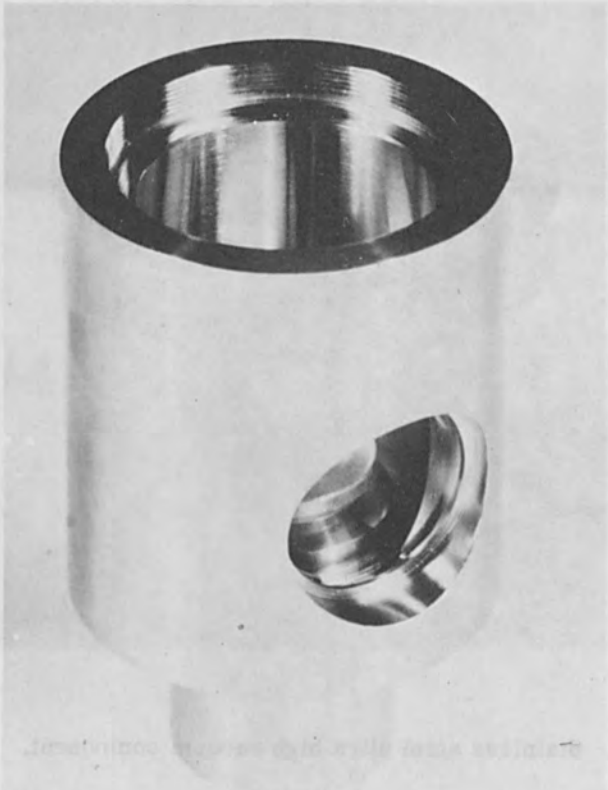

Figure 15. Ultra high vacuum valve welded in the bottom of the central bore.

high vacuum. The main point was here to produce a vacuum tight weld seam with the minimal power input possible to avoid cracking of the ceramics. With the weld parameters 25 kV, 2 mA and a weld time of 12 sec, which means a heat input 143, 5 cal resulting an overall temperature raise of the piece less than 200°C, sound welds were produced.

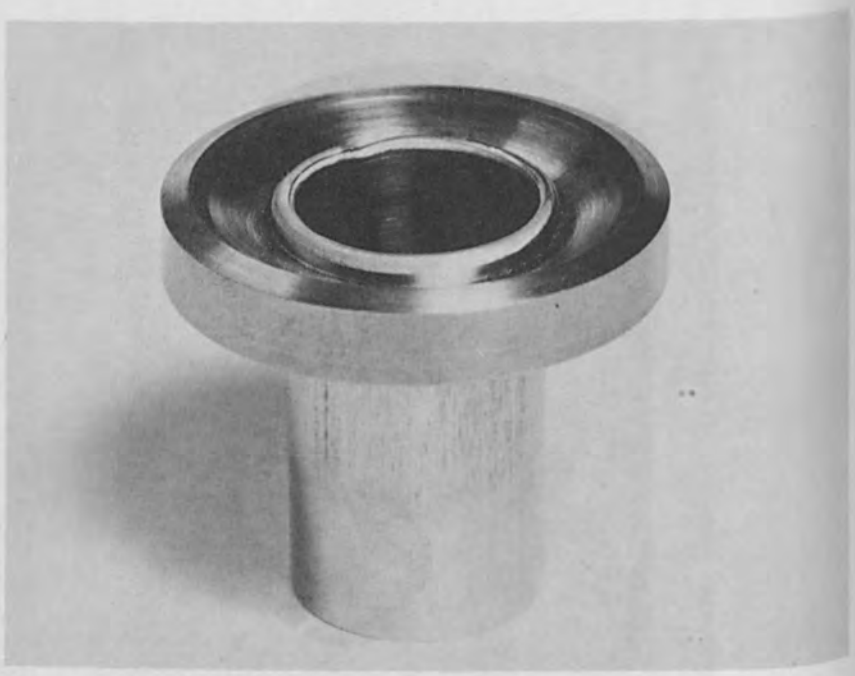

Figure 16. Stainless steel ultra high vacuum component.

Bounding of stators of small electric motors composed of 30 - 63 plates (Fig. 18) with four shallow weld seams (20 kV, 8 mA, 0,6 m. min^{-1}) have been also completed with excellent results.

Naturally quite a lot of other components have been welded in small numbers, such as artificial heart valves, small fluor furnaces, cryostat parts, high power transistor cans, soil pressure measuring cells, thermo elements, etc. All these works and experiments proved that electron beam welding has a wide field of applications in instrument industry and that they are mostly economical. They also proved that our machine can be used for these advantageously.

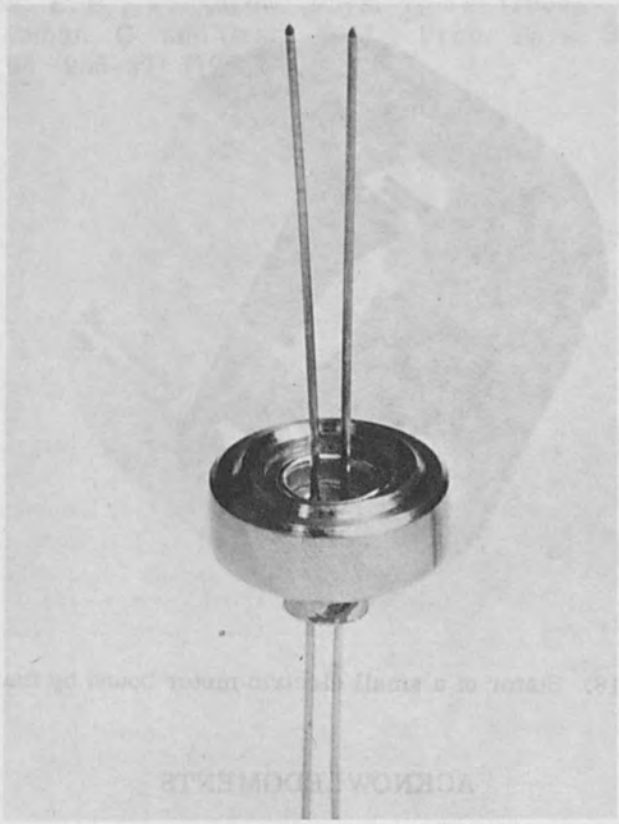

Figure 17. A ceramic-metal feed-through for a gas cromatograph.

We hope that these promising initial results achieved in the application of electron beam welding in instruments industry will help us spread in our national industry not only the use of this technology but other electron beam technologies too now under developed in our laboratories.

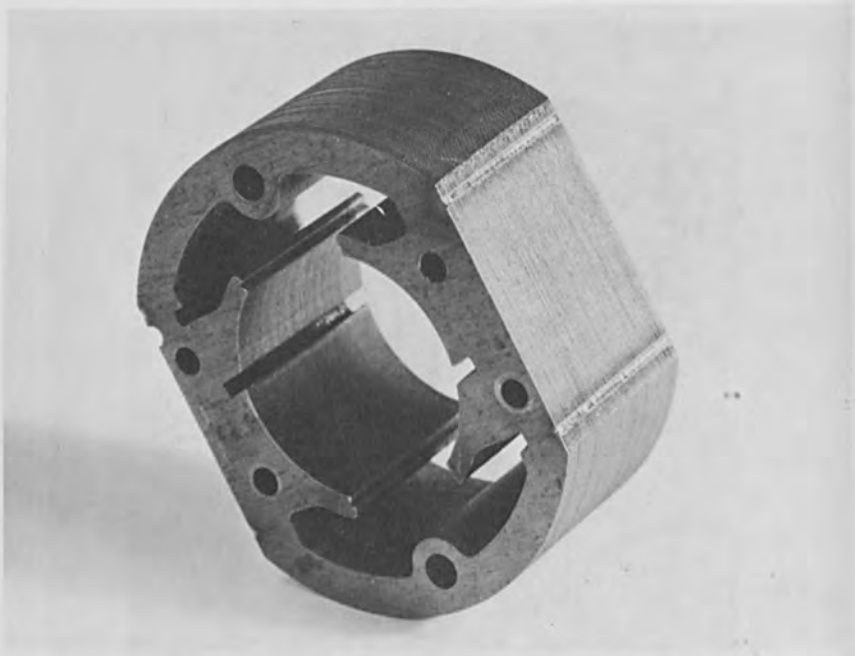

Figure 18. Stator of a small electric motor bound by four weld seams.

ACKNOWLEDGMENTS

The author is gratefully indebted to many of his colleagues for their valuable assistance. Thanks are due to Messrs. L. Bollok, Gy. Kovács, P. Pellionisz and E. Zobor who made a great part of design work and also to Dr. Mary Kántor and Messrs. T. Szücs, Gy. Vágó for their help in carrying out the experiments reported.

REFERENCES

1. Fóti, E., "Problems Concerning Vacuum Electron Beam Welding", Proc. of the Symp. on Electron and Vacuum Physics, Hungary 1962. pp. 475-482.
2. Fóti, E., "Electron Beam Welding Experiments in the Central Research Institute for Physics", Gépgyártástechnológia, 4 (6) 261-65 (1964) (in Hungarian).

3. Bas, E. B., Z. Angew. Phys. 7, 377 (1955).
4. Liebman, G. and Grad, E. M., Proc. Phys. Soc. B. 64, 956-971 (1951).

Production and Unusual Applications for Electron Beam Welding

Mel. M. Schwartz, Research Specialist
Advanced Manufacturing Technology
Martin Company, Baltimore, Md. 21203

Electron beam techniques are an adaptation of electron bombardment heating as originally described by Crookes in 1870. This technique of using a generalized heat source has been refined recently so that the electron stream of bombarding electrons is concentrated into a small area.

There are two distinct types of electron beam welding equipment being marketed commercially. The first incorporates an electron emission and focusing system with welding voltages up to 60,000 volts (the maximum voltage that can be used without hazard of x-ray radiation). The second is similar to an electron microscope in design and complexity and has welding voltages as high as 150,000 volts. Consequently, all parts of the equipment must be carefully constructed and insulated to avoid primary and secondary x-ray radiation. It is possible to draw an analogy to this process by the passing of a white-hot wire through a solid block of ice. Consider now the passing of an electron beam through a solid material. Parameters influencing energy density having been properly adjusted for a specific condition, it is possible to move the work piece at a given velocity under the electron beam. The results are surprising, for it is found that in addition to a remarkable weld geometry, extremely rapid table speeds may be used to accomplish them. It is also found that, as a result of very rapid heating and cooling rates, fine grain sizes are produced with extremely small heat-affected zones. (See Fig. 1.) In general, it may be shown that electron beams produce narrow, sound, fine grained welds

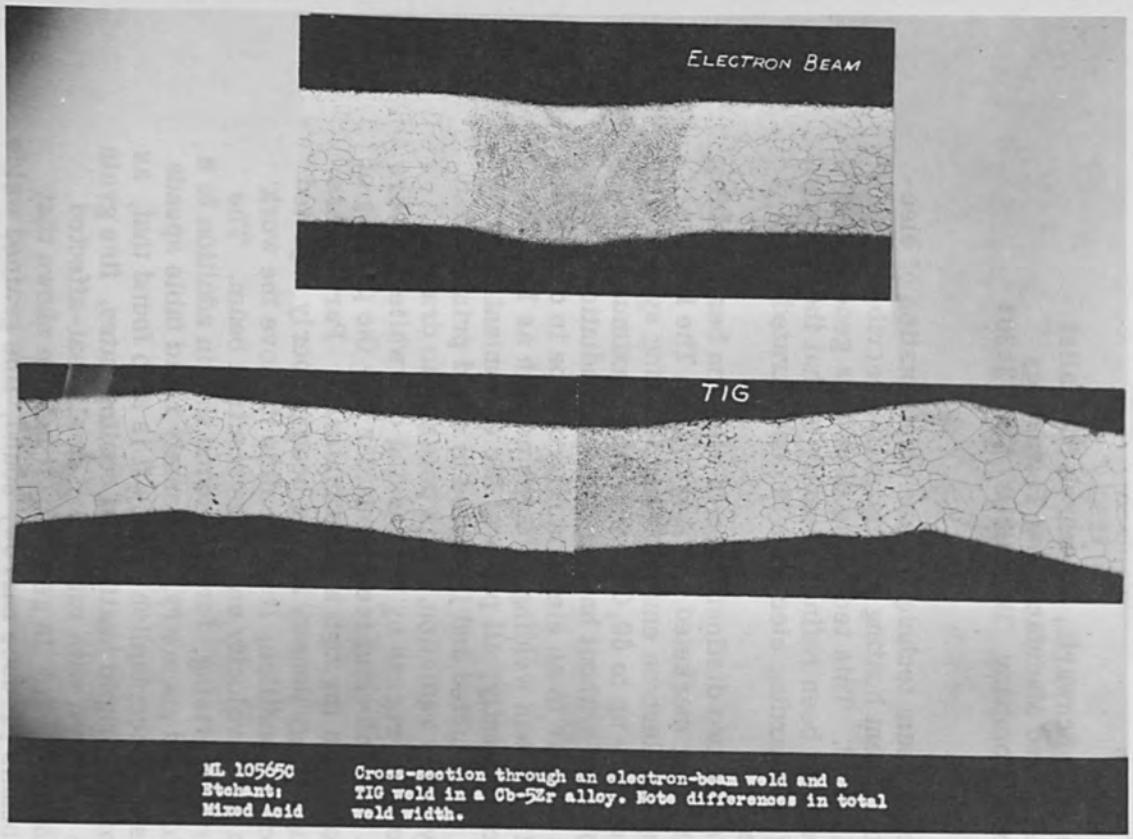

Figure 1. A small weld and very small heat affected zone in D-14 columbium alloy by electron beam welding in upper photo as compared with the increased weld and heat affected zone by TIG welding in lower photo.

at very high speeds. A further implication may now be appreciated. The high welding speeds and energy densities provide conditions which drastically reduce the distortion and shrinkage usually associated with normal techniques of materials joining.

As may be seen, a limited heat-affected zone is adjacent to the weld. The rapid heating and cooling rates have restricted recrystallization and grain growth of the weld joint and heat affected zone to a small grain size compared to other welding techniques. (See Fig. 2.) The ability to produce reliably strong joints in materials by electron beam is just about as important as the ability to make the materials in the first place. One of the first applications of electron beam welding at Martin was to nuclear components. Here, the requirements were leak tightness, corrosion resistance, and strength--in that order. (See Fig. 3.) In many ways, the electron beam welding technique is very versatile. Nevertheless, the basic metallurgy cannot be changed by any technique. Any metal can be welded to any other, but the phase diagram of the two will dictate what phases are present in the weld. If brittle intermetallic phases occur in the system chosen, the weld may be brittle. Assuming a favorable combination of metals is to be welded, what advantages does electron beam welding bring to the job? In addition to purity, there is the fact that a large amount of heat can be concentrated in a very small area. This means the fused zone which forms the weld bead can be deep and narrow--with a depth-to-width ratio of from 4 to as high as 25, compared to about 1 for other fusion welding techniques. With much less molten metal to give off heat during cooling, there is less distortion of the weldment and, more important, the microstructure of the parent metal adjacent to the fusion zone is much less affected. And this "heat-affected zone" is very often the place where welds fail.

Another, more subtle advantage to the process is that the amount of heating can be varied smoothly by varying the voltage; this means pre-heating and post-heating are easily accomplished and spatter is seldom a problem.

Since the advent of commercially-available electron beam equipment, many other interesting applications have evolved. Electron beams can effectively weld material

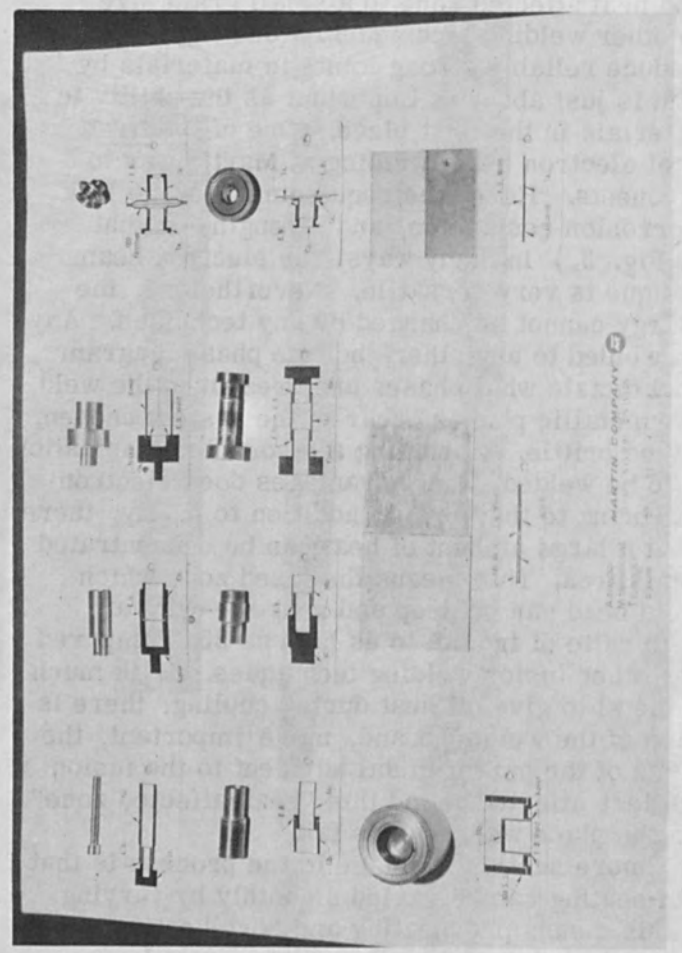

Figure 2. Electron beam welds in refractory metal components for nuclear applications. Many joints are .002" thick.

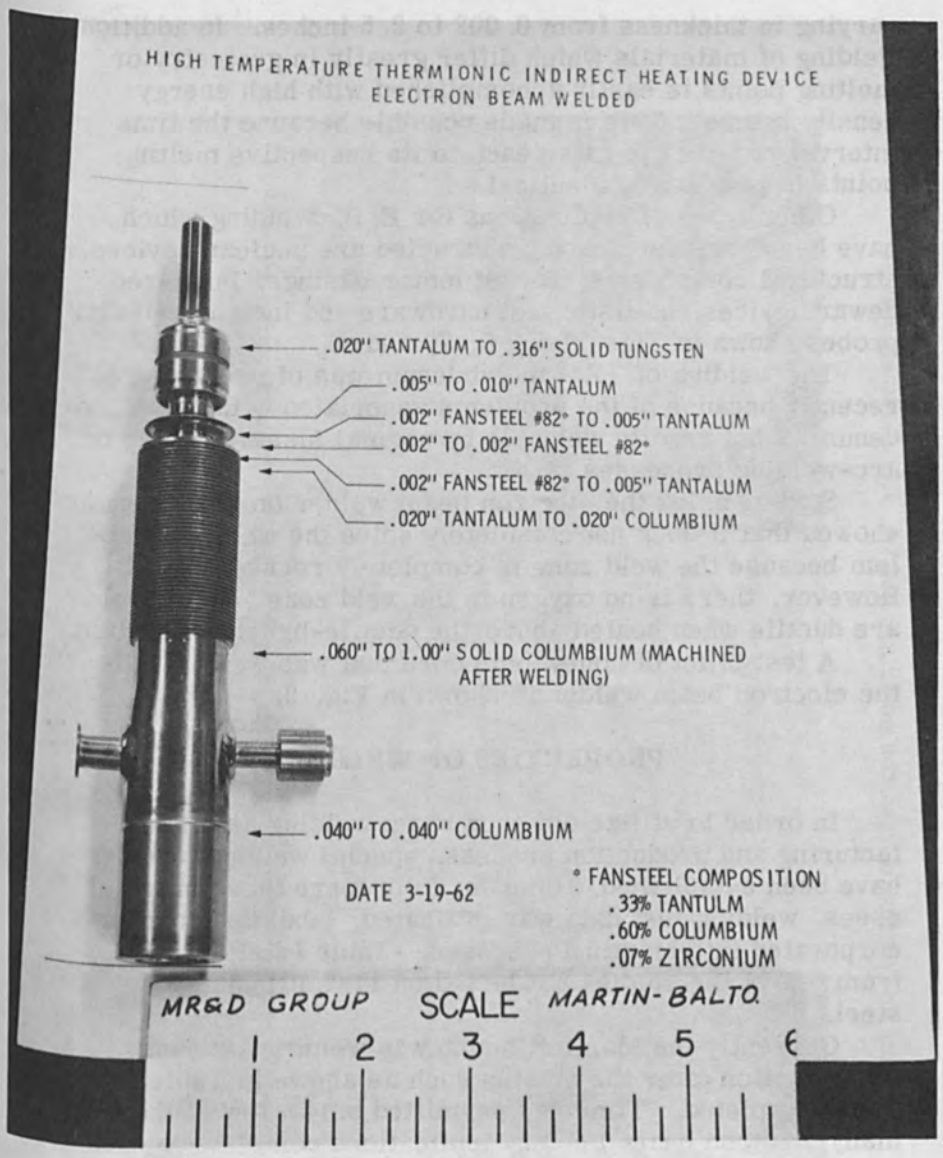

Figure 3. Similar and dissimilar electron beam welds produce a thermionic generator.

varying in thickness from 0.002 to 2.5 inches. In addition, welding of materials which differ greatly in geometry or melting points is easily accomplished with high energy density beams. This is made possible because the time interval required to raise each to its respective melting points is practically identical.

Other types of applications for E. B. Welding which have been engineered and constructed are nuclear devices, structural components, rocket motor casings, infra-red dewar devices, ballistic test hardware and instrumentation probes shown in Figs. 4, 5, 6, 7, and 8.

The welding of TZM molybdenum was of main interest recently because of the problems associated with it. Molybdenum is not readily weldable by normal fusion-welding or arc-welding processes.

Studies using the electron beam welder on molybdenum showed that it does not completely solve the welding problem because the weld zone is completely recrystallized. However, there is no oxygen in the weld zone and the welds are ductile when heated above the ductile-brittle transition.

A test billet of honeycomb core that was welded with the electron beam welder is shown in Fig. 9.

PROPERTIES OF WELDS

In order to utilize electron beam welding as a manufacturing and production process, special welding processes have been established. In order to prepare these processes, welding test data was evaluated, tabulated, and incorporated into Martin Processes. Table I lists figures from one of the studies conducted on 17-7 PH annealed steel.

Currently the Martin Company is welding air vanes in production after the studies such as shown in Table I were completed. Time has permitted only a few of the many electron beam welding applications completed and in progress currently. Some heretofore were planned and attempted by other joining techniques and failed or were costly to fabricate however, with the advent of E. B. Welding and the knowledge gained by the tool designer, the materials engineer, the structures specialist and manufacturing technician of electron beams and their potential;

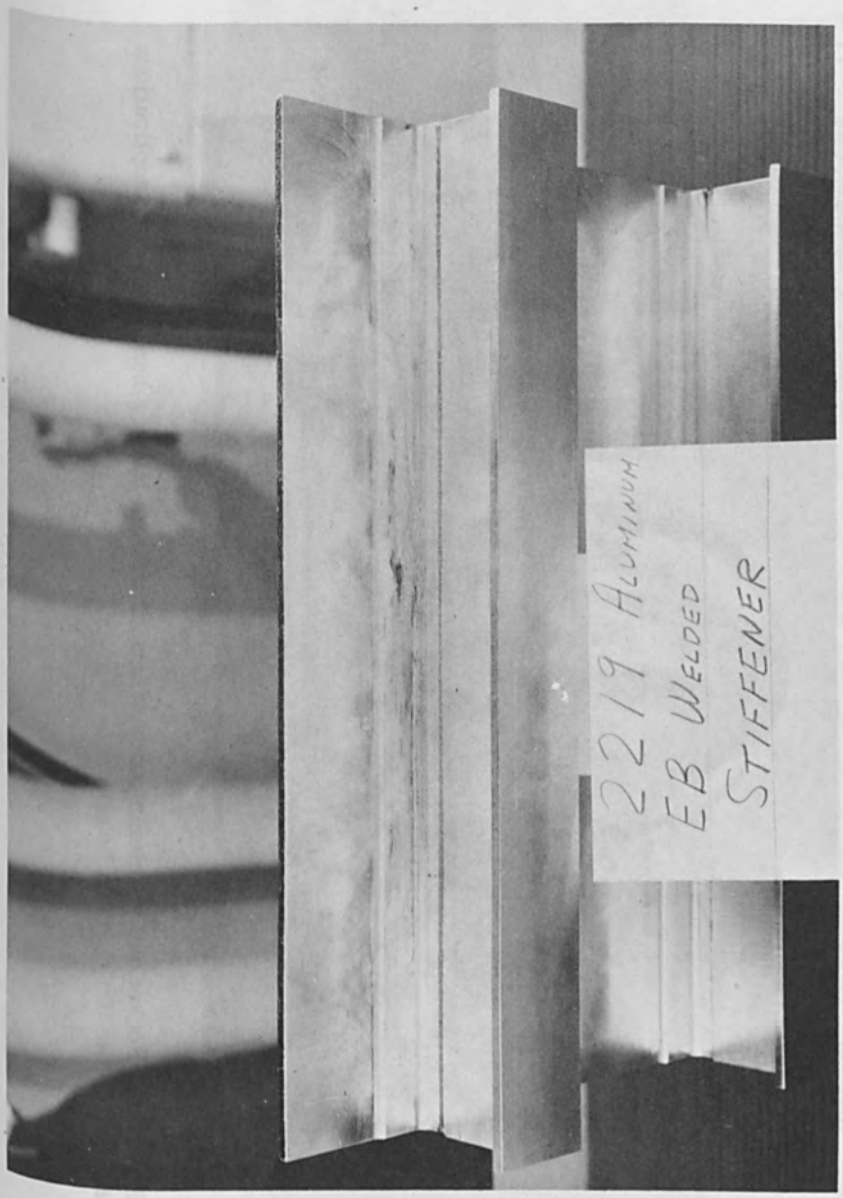

Figure 4. Potential application of electron beam welding for aerospace structure.

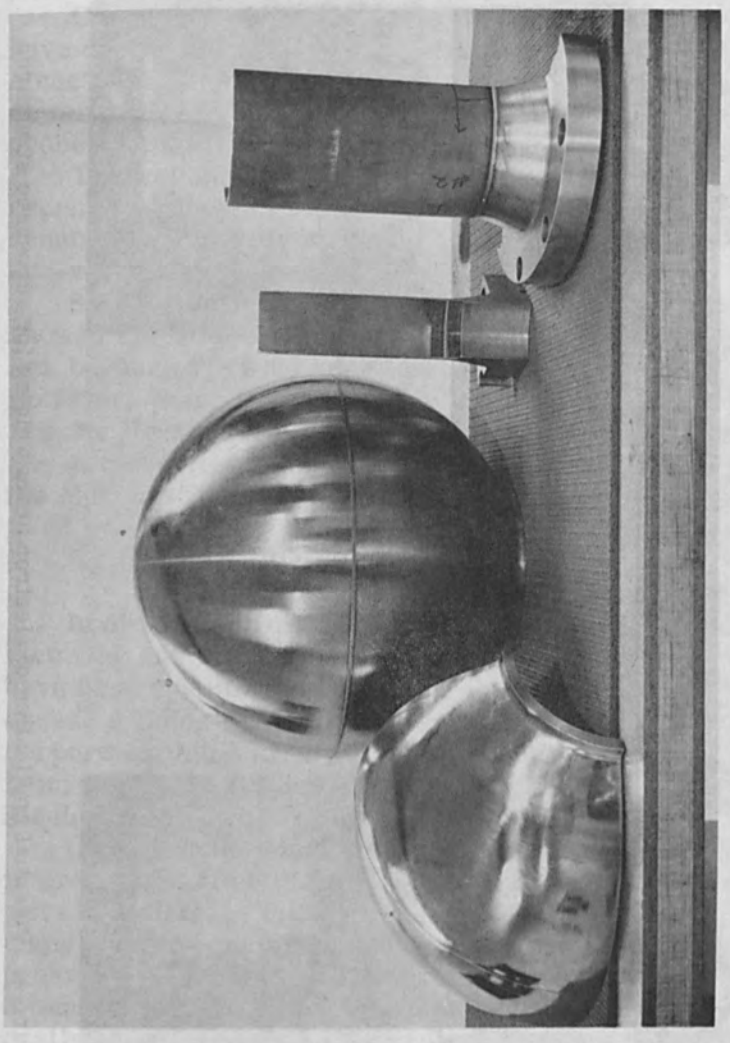

Figure 5. Rocket and vernier motor casings as well as tube-to-header nuclear applications show promise for electron beam use.

Figure 6. The tubular section in the center of the photo is a silver ring electron beam welded to a steel tube. The copper disc to the left of the tube and the brass rod to the right were the tools used to hold the infra-red tubular container.

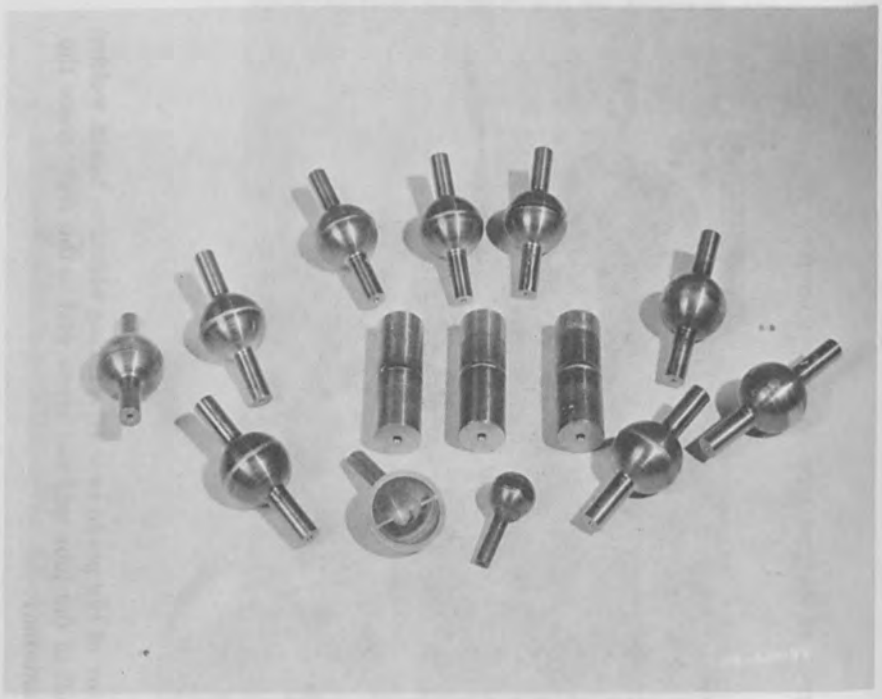

Figure 7. The small 17-7 PH and A-110AT titanium spheres were electron beam welded with a disc shown in lower central portion of the photo completely enclosed. Complete penetration through the disc was required in order to evaluate the ballistic tests subsequently performed. This is an excellent example of the use of electron beam to weld a blind joint completely hidden during welding.

this new joining media has come of age. Since these aforementioned engineers have become accustomed to literally "working in a vacuum", they have no trouble designing, analyzing, fabricating, testing and evaluating E. B. welds.

Figure 8. An unusual application of electron beam welding to intricate wind tunnel test model assemblies of tantalum.

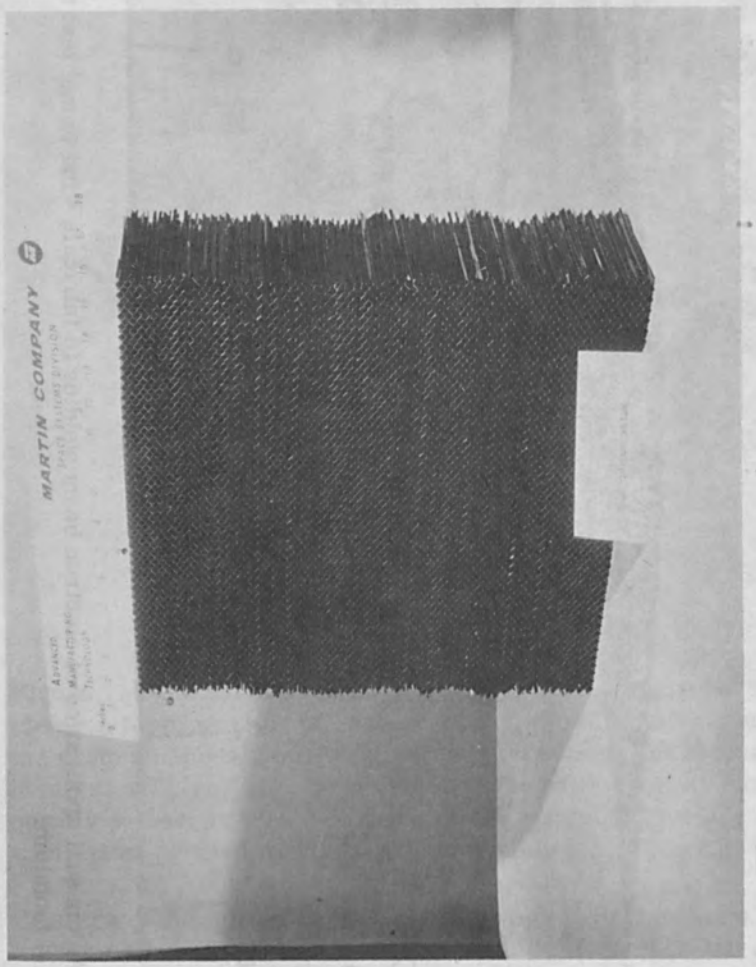

Figure 9. Electron beam welded TZM molybdenum honeycomb .002" foil into 14" x 14" billet.

Table I

Effect of Gap on Strength of Electron Beam Welds

17-7 PH Annealed		0.020" Thick
Parent Metal Strength		125000 psi
Gap	001"	123300 psi
	002"	115800
	003"	116100
	004"	111000
	005"	103200
	006"	81850

The Application of Electron Beam Welding Techniques to the Manufacturer of Computer Parts

E. Joerg

IBM Deutschland, Manufacturing Research
Sindelfingen, Germany

Melting of metals by an electron beam of high energy focussed on a minute area predestinates the electron beam welding process for the production of some of the many precision parts used on computer systems by butt, overlapped, tee, and spot welding.

This is a pictoral case study of a production electron beam welding task aimed at the production of computer parts. The welding parameters obtained in the manufacturing research laboratory were incorporated in an automatic welder built by Heraeus . The quality of spot or butt welded assemblies is dependent on the components to be connected, the electron beam machine, and the welding fixture.

The item produced is the hammer assembly (Fig. 1) for the 2203 IBM high speed printer. Two leaf springs (nickel chromium steel Sandvik 11 R 51), about 0. 02 x 0. 09 in. cross section, are positioned in the slots of both the hammer (2. 5% silicon iron) and the socket (0. 15% carbon steel) by means of a precision fixture as the sequence indicates. The material joining is made by small, deep, and through spot welds at the very ends of the springs. Though actual welding was performed at a voltage of 100 kV and a current of 2. 8 mA, a welding time of 1. 2 sec, and a deflection of 0. 032 in. at a frequency of 50 oscillations per second is applied.

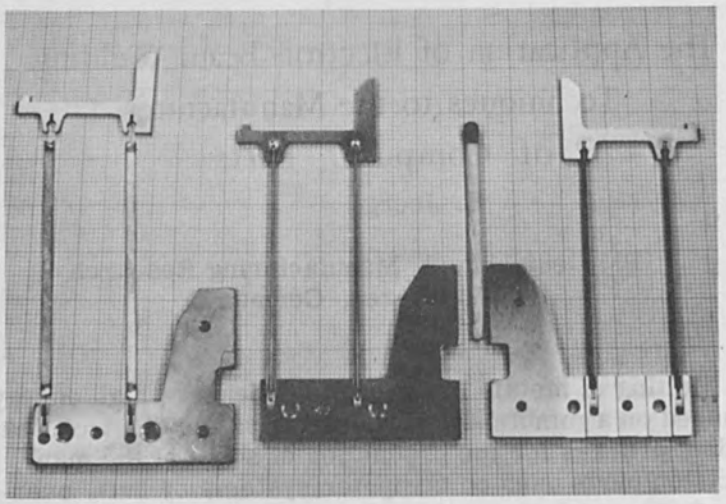

Figure 1. Socket, 2 leaf springs, hammer. Top view (center) and bottom view (right) of hammer assembly.

Figure 2. Electron beam spot weld of hammer and leaf spring (top view).

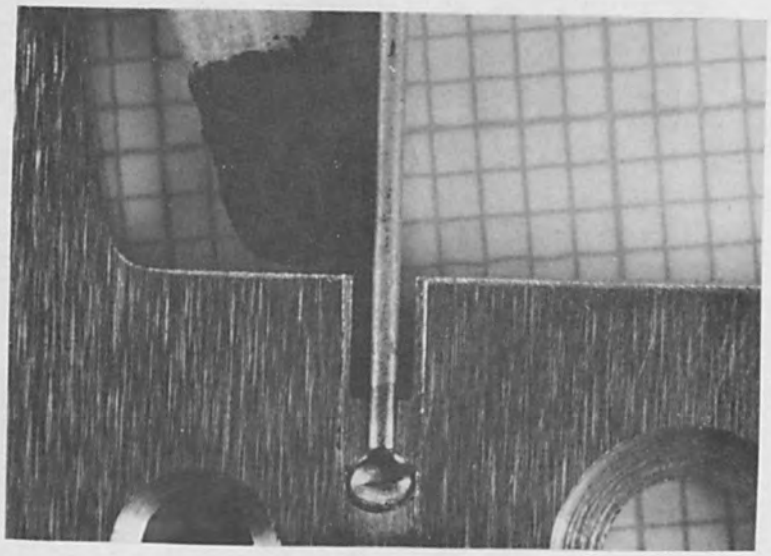

Figure 3. Electron beam spot weld of socket and leaf spring (top view).

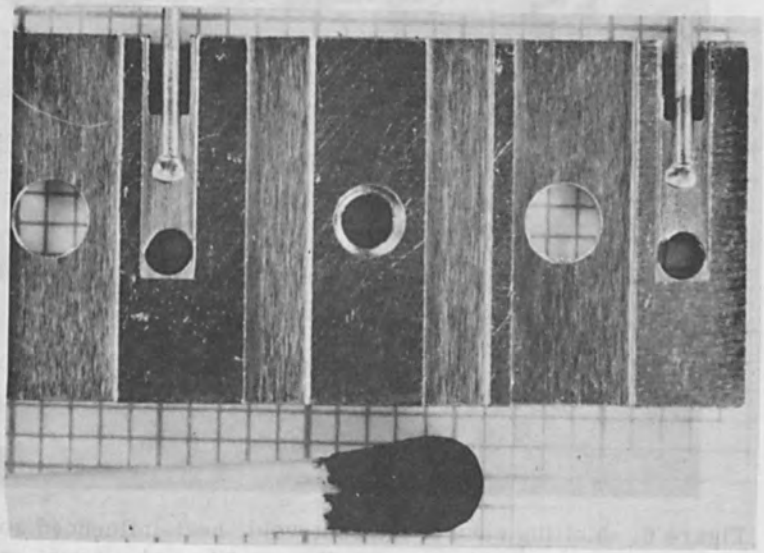

Figure 4. Small weld pimples on bottom side of socket indicate perfect through welding.

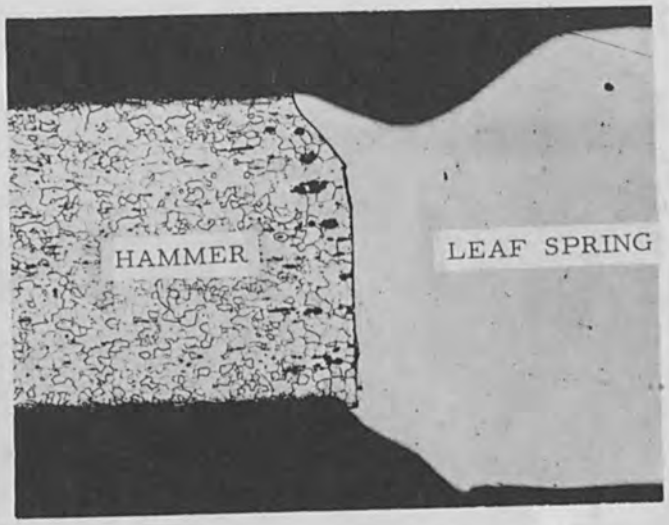

Figure 5. Cross section through spot weld of hammer and leaf spring (magnification 30 x).

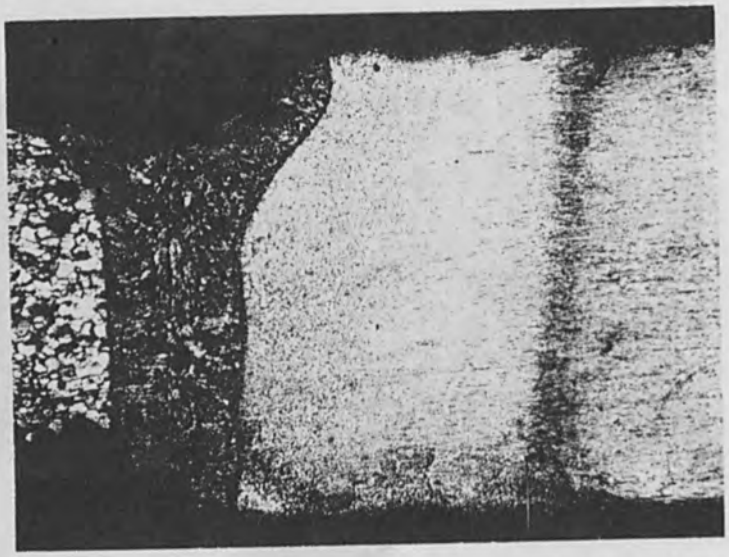

Figure 6. Melting zone of the spot weld, heat-influenced zones of the leaf spring (coarse grain, fine grain), and original spring material. (Microsection surface etched to show stainless steel spring structure, magnification 30 x).

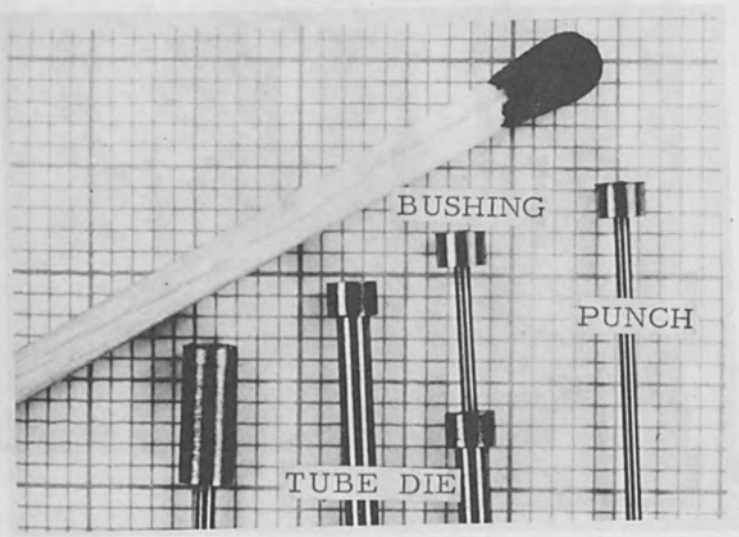

Figure 7. Bushings spotwelded to various slender punches and tube dies.

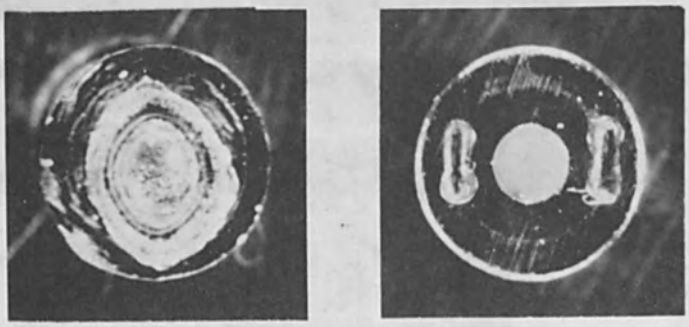

Figure 8. Left: Spot weld on a circular path.
Right: 2 spot welds on a straight path.

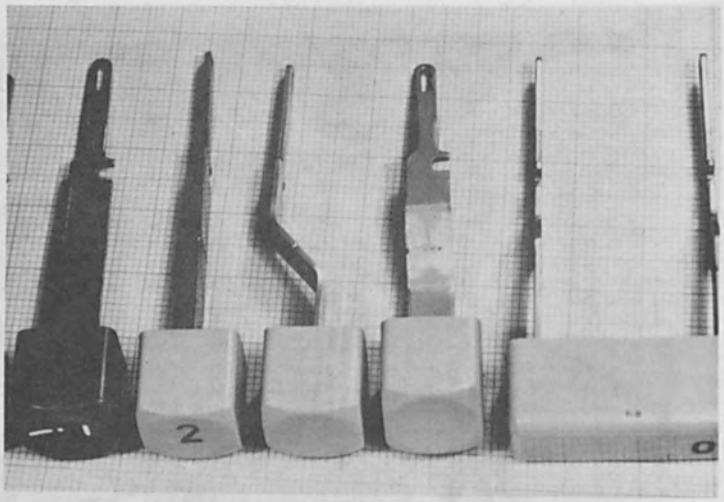

Figure 9. Electron beam welded key stems for special key boards.

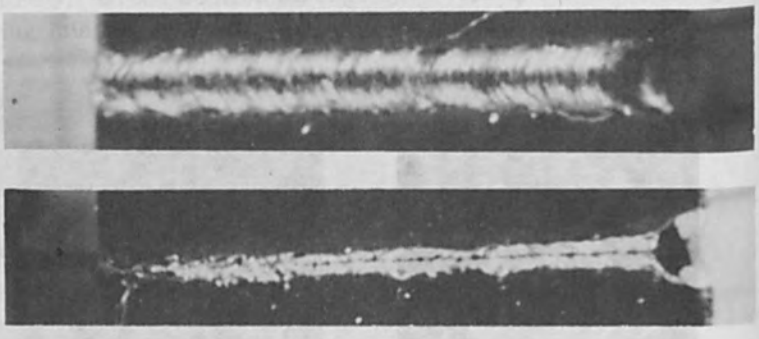

Figure 10. Butt weld of key stems, top and bottom. (magnification 13 x).

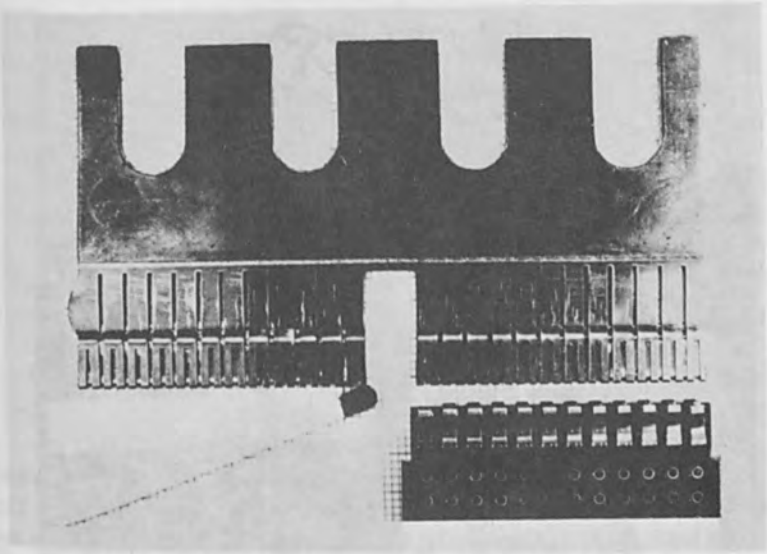

Figure 11. Soldering electrode seam welded by electron beam and a small card to be soldered.

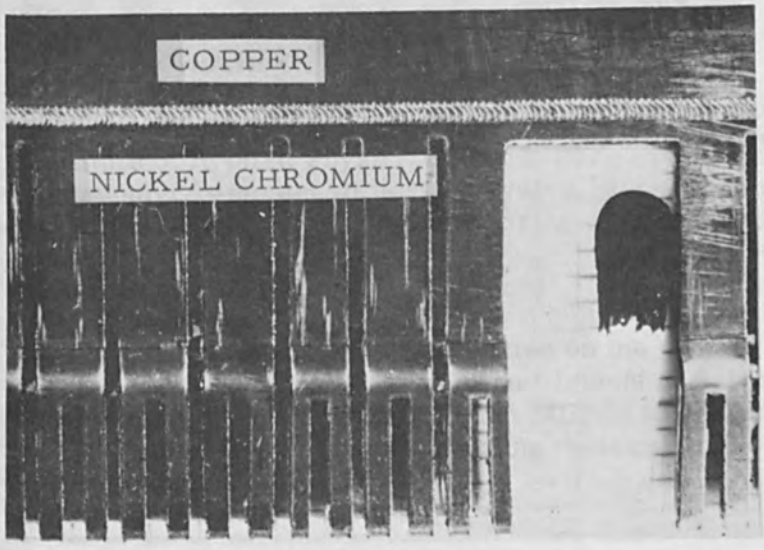

Figure 12. Electron beam seam weld made by oscillating the beam at 50 cycles per second perpendicular to the welding seam.

Figure 13. Front view of production electron beam welder Heraeus ESW 900/3.

Automatic Electron - Beam Welding of Tubes

Fritz Koch

Central Welding Institute
Halle (Saale) East Germany

1. INTRODUCTION

In the "Central Welding Institute" in East Germany there was developed the ZIS 456 electron-beam welding unit which, on the one hand, is used for welding trials on the most different materials, with directions of motion being possible in three axes of coordinates, and which, on the other hand, through the use of a specially designed jig provides for automatic circumferential tube welding. It is the latter problem that will be discussed in the present paper.

2. CONSTRUCTION OF THE UNIT

The unit consists of a beam generator developed by the "Institute of Applied Physics of Extra-Pure Substances", a power supply, pump set with corner valve, work chamber with welding jig, and control and measuring instrumentation.

2.1 Beam Generating System

The beam generating system operates on the remote focus principle. As cathode, a tungsten filament of 0.1 mm thickness and 1 mm width is used. The cathode is heated directly. There are no special deflecting devices for the electron beam.

2.2 Power Supply

A transformer of the type used in apparatus for X-ray diffraction is used as a high-voltage source, the maximum voltage being 120 kilovolts at a current of 40 milliamperes.

2.3 Pump Set

The pump set comprises a rotary-valve, Root's and oil-diffusion pump. The double-stage rotary-valve pump has a pumping rate of 150 cubic meters per hour, whereas that of Root's pump is 1,800 cubic meters per hour. The high vacuum is generated by an oil-diffusion pump having a pumping rate of the order of 5,000 liters per second. A power-driven corner valve clears the pumping way for the high vacuum. In order to prevent oil from being expelled from the oil-diffusion pump, an oil-vapor barrier has been

Figure 1. Rotary-valve and Root's pump of the ZIS 456 electron-beam welding unit.

provided between the corner valve and oil-diffusion pump. A forepump protecting valve is arranged between Root's pump and the rotary-valve pump so that on disconnection of the pumps oil may not enter the suction line. The line connecting the rotary-valve pump and Root's pump has a nominal diameter of 65 mm. Between Root's pump and the corner valve 300-mm diam. lines are arranged. Figure 1 shows the rotary-valve pump with attached forepump protecting valve as well as Root's pump and part of the oil-diffusion pump. In the foreground there is a transformer transforming the operating voltage of Root' pump to 42 volts.

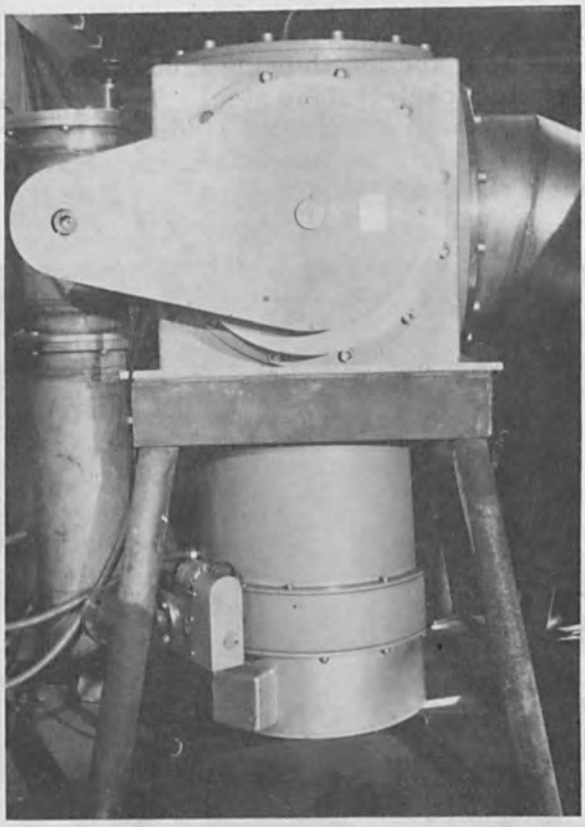

Figure 2. Oil-diffusion pump with corner valve of the ZIS 456 electron-beam welding unit.

For changing the pumping path before the corner valve, a straight-way valve has been provided. For generating the high vacuum, the oil-diffusion pump is located directly in the pumping path. A power-driven straight-way valve provides for opening or closing this pumping path. Figure 2 shows the oil-diffusion pump and the power-driven corner valve. The straight-way valve is arranged at the lower left of the oil-diffusion pump. The said straight-way valve located ahead of the corner valve is shown on the upper left of Fig. 2.

2.4 Work Chamber

The work chamber is of cylindrical shape. It has a diameter of 800 mm, the length being 1,600 mm. It is made of austenitic nickel-chrome steel. There are 4 windows for observing the course of welding. The drive mechanisms for the tubes and the magazine are arranged on the outside of the work table. Figure 3 shows the drive unit for tube feeding.

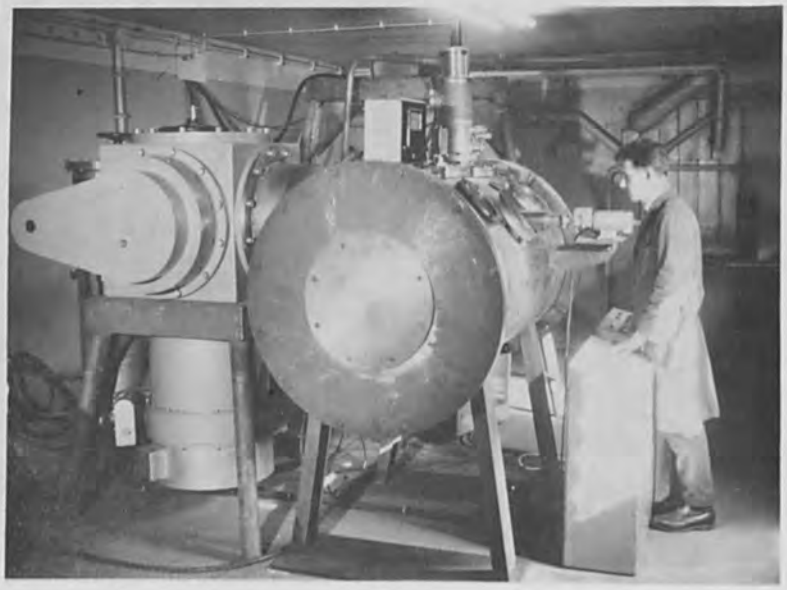

Figure 3. Receiver of the ZIS 456 electron-beam welding unit.

2. 5 Welding Jig

The welding jig has been so designed and constructed that 40 tubes may be held and welded. So that the deflection of the tubes will not exceed a maximum degree, these are arranged at distances of 200 mm in 4 layers. For the receiving and transporting of the tubes, use is made of ball bearings. These are arranged at the circumference of the disks in accordance with the spacing. By a drive unit located outside of the receiver the magazine may be indexed step by step. So that the tubes during this indexing will not fall out upon reaching a critical angle, a clip which is open at its top has been placed about each disk to keep the tubes in position (Fig. 4).

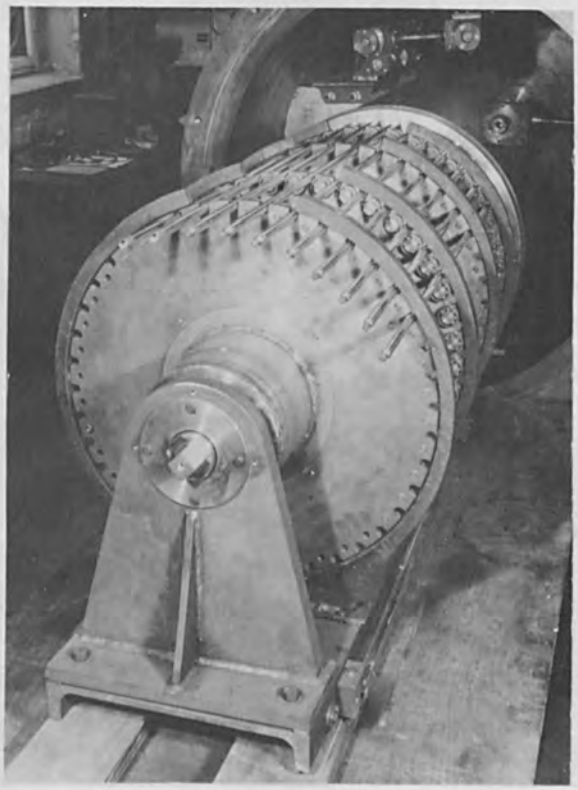

Figure 4. Magazine.

At one end of the jig there is an adjustable stop that may be adjusted in accordance with the weld's distance from the end of the tube. The magazine drive moving the individual tubes under the beam system is shown in Fig. 5.

The driving motor is provided with an eccentric disk. Through a connecting rod a pawl is driven which engages a ratchet connected with the welding jig free from play, moving that ratchet by one step each. The drive of the geared motor will make one full revolution for each and every step. Disconnection is through a limit switch. In order that the jig due to its weight will not continue moving forward, the receiver was additionally equipped with an index wheel with forty notches for slowing down. The gear wheel required to this end is rigidly connected with the shaft of the jig. A pin with a ball bearing, which through a spring is urged into the gear wheel, insures exact adjustment of each tube in the welding position.

The drive of the tubes for welding is through the motor (shown in Fig. 3) at the circumference of the receiver. It is by the shaft introduced vacuum-tight into the receiver

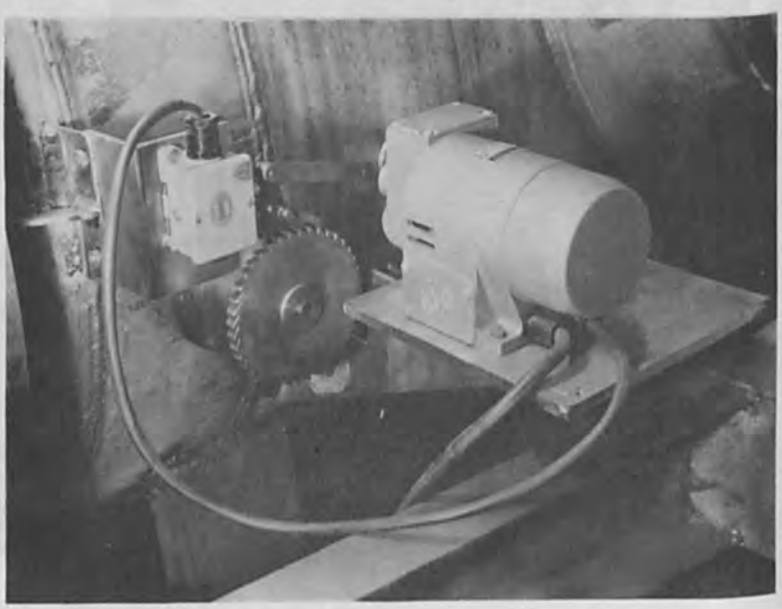

Figure 5. Magazine drive.

that, through 3 bevel gear systems, the driving rolls rotating the tube are driven. By tilting the rolls the tube is moved all the way to the said stop so that the point of welding will come to lie below the gun (Fig. 6).

For placing the tubes in position it is necessary for the jig to be moved out of the chamber. The base plate carries ball bearings on which the entire jig may be moved in and out. Laterally arranged ball bearings insure an always correct position of the jig in the chamber.

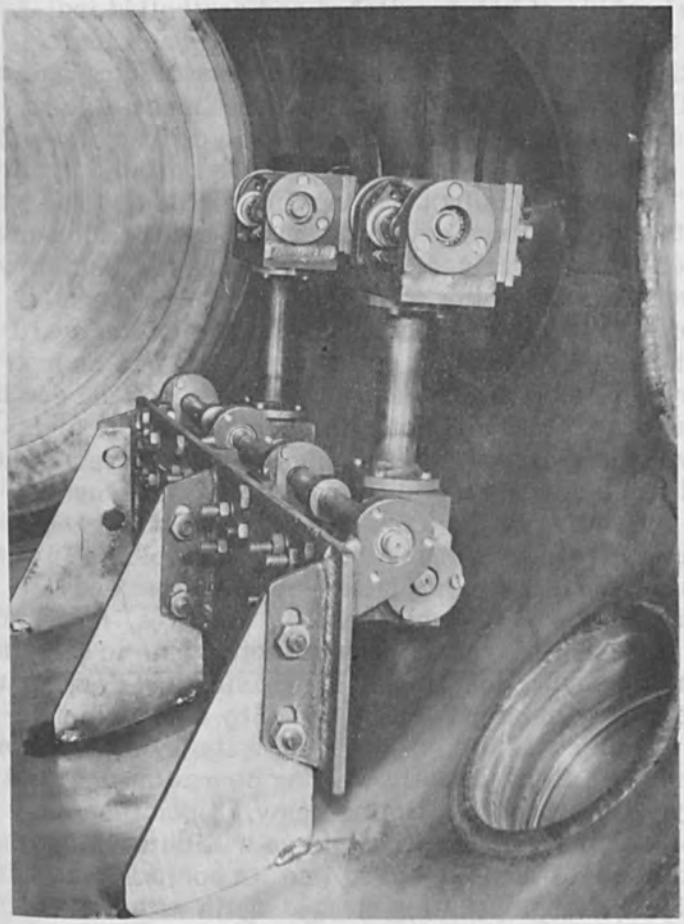

Figure 6. Tube transport.

2.6 Controlling the Course of Welding

The circuitry for controlling the electron-beam welding unit does not only provide for the fully automatic welding of tubes, but may of course also be used for controlling other welding assignments. This universal applicability is due to the possibility of alternatively switching to "AUTOMATIC" or "SINGLE STEPS". In the "SINGLE STEPS" position the tube and magazine drives, the high voltage, high-voltage control, beam focusing, and weld time are capable of being switched and controlled individually and independent of each other. When changing over to the "AUTOMATIC" position these switching operations will be interlocked so that it will be impossible to inadvertently interfere with the automatic course of welding.

The automatic operation of welding is initiated by the "START" button. It is by pressing this button that the gun heater, the focusing system, tube drive, and the tube-feed timing relay are energized. The tube drive mechanism will be in operation during the entire period. In the event of failure of the tube drive mechanism the high voltage will be switched off immediately so that the beam will be prevented from penetrating the stationary tube. At the end of the pre-set feed time the motor for controlling the high voltage will be switched in. The high voltage is set to the required value during one tube revolution. This insures uniform preheating of the tube. Then the weld is executed. Following the execution of the weld the high voltage is again zeroed slowly. It is by this latter measure that end craters in the weld are to be avoided. In cases, however, where it is essential that the heat-affected zone in the tube be extremely small, the gradual increasing and decreasing of the welding voltage may be replaced by a sudden energization and disconnection of the high-voltage unit. Before the beginning of the automatic welding operation the weld time may be set through a timing relay. Upon the completion of welding, the magazine drive will be switched in. The next tube will then be moved into its position under the gun and the welding operation started again with the advance of the tube. The welding operation is stopped by a timer after passage through the machine of all tubes. Figure 7 is a diagrammatic representation of an automatic welding cycle.

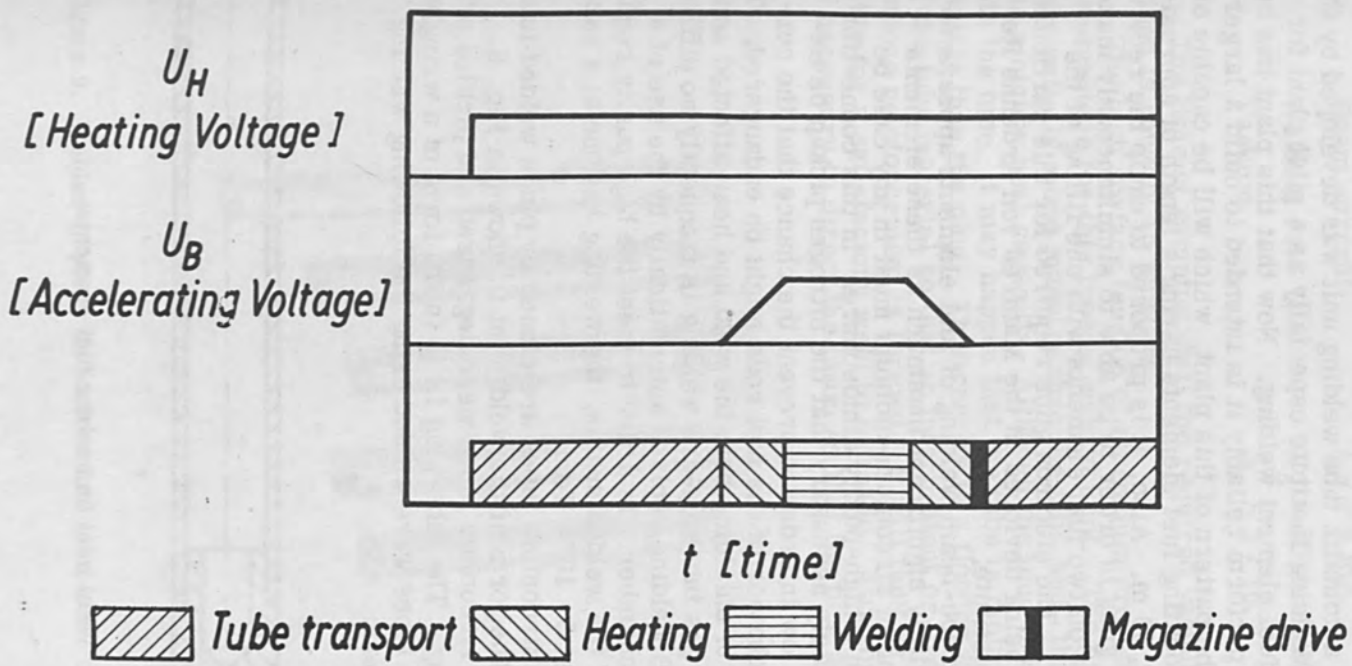

Figure 7. Automatic course of a weld cycle.

3. THE WELDING OF REACTOR FUEL ELEMENTS

The automatic tube welding unit was developed by the Central Welding Institute especially as a pilot plant for nuclear fuel element welding. Now that this plant has been found to perform reliably it is intended to build a larger unit on the pattern of this plant, which will be capable of accommodating fuel elements having a length of approximately 2.50 m. Also, it is proposed to equip the receiver with two guns in order to be able to simultaneously make the welds on two fuel elements with one filling of the chamber. The electron guns required for this particular unit are being devloped in the Manfred von Ardenne Research Institute.

Electron-beam welding of fuel elements appears to be especially significant inasmuch as these elements consisting of zirconium-niobium must in any case be welded in a high-purity atmosphere. In this connection it is absolutely necessary that the nitrogen pickup be extremely low in order to prevent the chance that the corrosion behavior of the fuel rods might be endangered. The problem of shielding both the weld and heat-affected zone, which in gas tungsten-arc welding is frequently so difficult, is, in EB welding, solved automatically by the use of a vacuum chamber. In order to meet the high purity requirements of the welded seams, the welding is done at a vacuum of at least $5 \cdot 10^{-5}$ Torr.

The zirconium tubes are closed by plugs welded into the tubes. The form of the weld joint is shown in Fig. 8.

The zirconium tubes were degreased and pickled prior to welding. The tube-plug fit is in the form of a wringing fit. The tubes were welded using the following welding parameters:

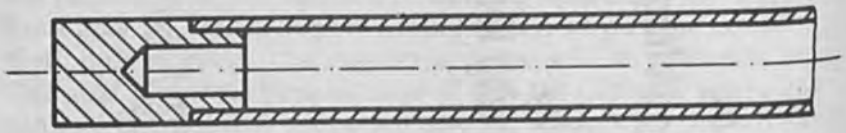

Figure 8. Weld joint on nuclear fuel elements.

Accelerating voltage	$U_B = 45$ kV
Beam current	$I_S = 4$ mA
Welding rate	$V_S = 30$ cm/min
Vacuum	$p_V = 5 \cdot 10^{-5}$ Torr

The time of pumping until the required vacuum is obtained is roughly 15 minutes.

The high surface tension of zirconium proved to be a disadvantage for this type of welded joint. The plug is substantially more massive than the tube and, therefore, has a higher heat capacity. Although the plug is pressed into the tube, it may happen that the tube is melted more rapidly than the plug. This results in a flowing together of the tube material so that an intermittent or even continuous reinforcement is formed. It will then be impossible for a satisfactory weld to be made. To avoid this it is necessary to direct the beam so that the plug will be

Figure 9. Welded-in plugs on nuclear fuel elements.

heated more strongly than the tube. In this connection it has been observed that excessive beam focusing is detrimental. If the focal spot is held larger, more material will be melted and weld formation will also be more uniform. In addition to the focal spot diameter, the width of the weld is also dependent upon the weld rate. Figure 9 shows some welded joints. If the welding parameters are chosen correctly, then there will not be any weld and root reinforcements. If the input power it too high (right-hand fuel rod in Fig. 9), the weld will 'collapse'.

Figure 10 shows a weld-joint macrosection. Because of the relatively large focal spot diameter the heat-affected zone is quite large.

For comparison purposes Fig. 11 shows a gas tungsten-arc welded joint. A comparison shows that with the gas tungsten-arc process the heat-affected zone is much wider and coarse grains may be found throughout the plug.

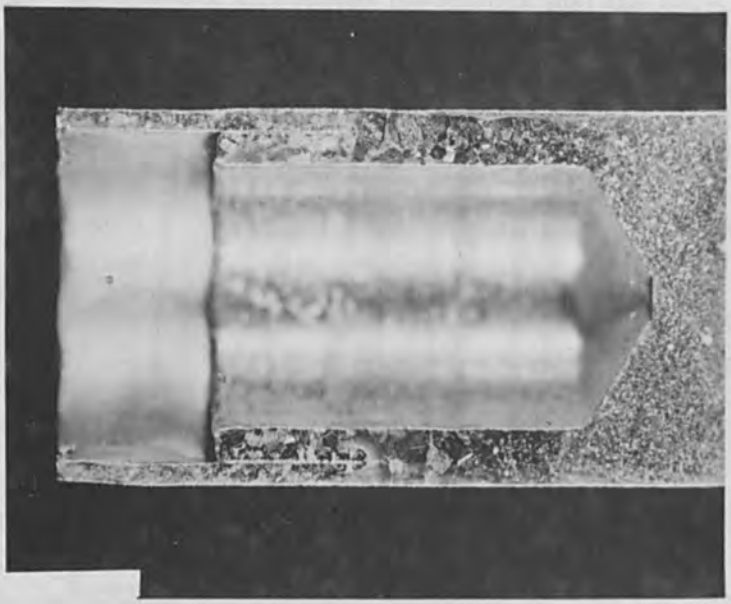

Figure 10. Macrosection of an electron-beam weld in a nuclear fuel element.

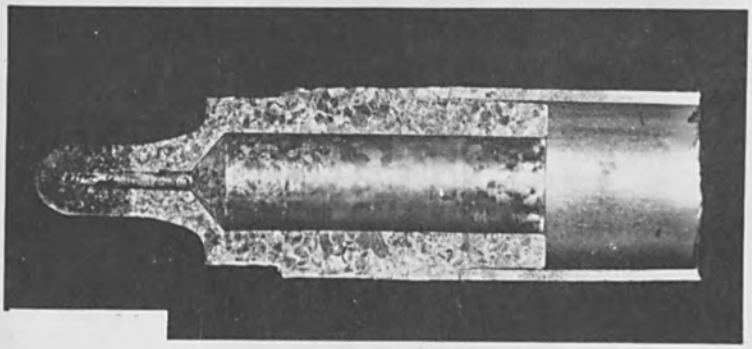

Figure 11. Macrosection of an inert-gas tungsten-arc weld in a nuclear fuel element.

4. SUMMARY

By means of the EB unit developed by the Central Welding Institute it is possible to make, by fully automatic electron-beam welding, circumferential welds on forty tubes with one filling of the receiver. This unit lends itself particularly well to the sealing of nuclear fuel elements since high requirements are placed here on the quality of welds - no weld or root reinforcement, absolute weld density and high resistance to corrosion.

Evaluation of Electron Beam Welds in Thick Materials

M. T. Groves and J. M. Gerken

TRW Equipment Laboratories,
Cleveland, Ohio 44117

1. INTRODUCTION

The objective of this investigation was to determine the mechanical properties and economics of electron beam welded thick sections of structural materials. Although considerable data has been published in the literature on the properties of electron beam welds in thin sections, relatively little has been published for thick sections. A literature review showed that electron beam welds in sections under 0.5 inch were generally sound and had properties comparable to parent metal. For thickness over 0.5 inch, a number of investigators reported the occurrence of defects such as porosity and/or cold shuts in a variety of materials.

This program consisted of making welds in a number of structural materials and evaluating these welds for quality, mechanical properties and metallurgical structure. A cost comparison was made between the electron beam welding process and conventional arc welding process. In addition, a questionnaire was sent to users of electron beam welding equipment to assess the extent to which this process is being used in industry and the considerations that have prompted manufacturers to use it.

II. MATERIALS AND EXPERIMENTAL PROCEDURE

The materials and thicknesses investigated are listed in Table I. These materials were obtained in pieces ap-

Table I. Program Materials

Material	Thickness (in.)
Ti-6Al-4V	1.0, 1.5, 1.75
Rene' 41*	0.5, 1.0, 1.5, 1.75
18 NiCoMo Maraging Steel	0.5, 1.0, 1.5, 1.75
HP 9 Ni-4 Co Steel**	0.5, 1.0, 1.5, 1.75

*General Electric Company Alloy
**Republic Steel Corporation Alloy

proximately 3 in. x 13 in. Chemical analysis of each material were normal for each alloy.

Welding was performed on either a 7.5 kW electron beam welder rated at a maximum beam current of 300 milliamperes and an accelerating voltage of 25 kilovolts, or a 30 kW welder rated at a maximum beam current of 500 milliamperes and an accelerating voltage of 60 kilovolts.

Single pass welds were made in 1.0 inch plate of each material while two pass welds were made in the 1.5 and 1.75 inch plate. A number of repair welds, mismatch welds, and welds at a chamber pressure of 1×10^{-3} mm Hg, rather than the normal 1×10^{-4} mm Hg, were made in each material. Figure 1 shows the joint alignment used for the mismatch study.

Mechanical property evaluation consisted of longitudinal all weld metal tensile tests, transverse tensile tests and notch bend fracture toughness tests. Stress rupture tests were performed on Ti-6Al-4V and Rene' 41 weldments. The tensile and stress rupture tests were prepared from various levels of the thickness of the weldments. Pre-cracked notch bend specimens used to evaluate the fracture toughness properties of the weldments were prepared such that the notch was placed in either the fusion zone or the heat affected zone. The machined notch was in the plane of the plate surface.

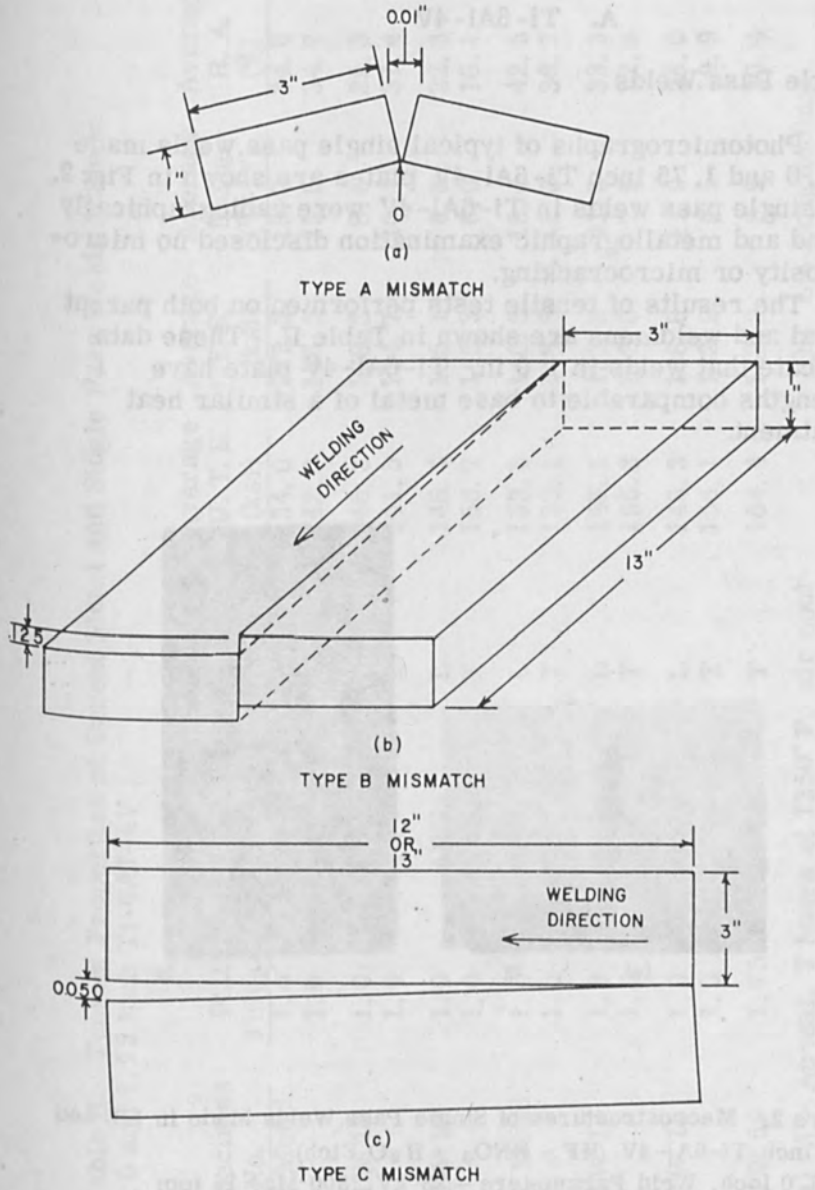

Figure 1. Joint Alignment Used for Mismatch Study.

III. RESULTS AND DISCUSSION

A. Ti-6Al-4V

Single Pass Welds

Photomicrographs of typical single pass welds made in 1.0 and 1.75 inch Ti-6Al-4V plates are shown in Fig. 2. All single pass welds in Ti-6Al-4V were radiographically sound and metallographic examination disclosed no microporosity or microcracking.

The results of tensile tests performed on both parent metal and weldmens are shown in Table II. These data indicate that welds in 1.0 in. Ti-6Al-4V plate have strengths comparable to base metal of a similar heat treatment.

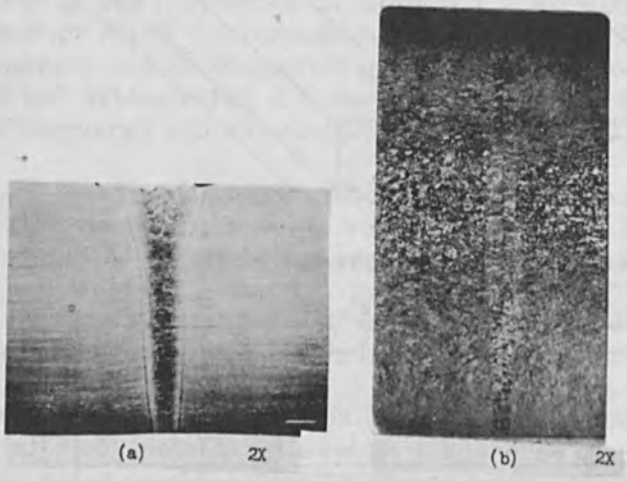

Figure 2. Macrostructures of Single Pass Welds Made in 1.0 and 1.75 Inch Ti-6Al-4V ($HF + HNO_3 + H_2O$ Etch)
(a) 1.0 Inch, Weld Parameters - 23 kV, 300 Ma, 15 ipm
(b) 1.75 Inch, Weld Parameters - 55 kV, 360 Ma, 40 ipm

Table II. Tensile Properties of Parent Metal and Single Pass Welds Made in 1.0 and 1.75 Inch Ti-6A1-4V

Specimen No.	Plate Thickness	Process Cycle[a]	Test Direction[b]	Average U. T. S. (ksi)	Average Y. S. (ksi)	Average Elong. (%-1")	Average R. A. (%)
Parent Metal	1.0	Sa	L	134.0	127.3	18.0	34.6
	1.0	Sa	T	142.0	136.5	13.5	34.7
Weld TW 17	1.0	AW	L	145.3	128.3	8.6	29.3
	1.0	AW	T	141.5	134.7	10.4	37.4
Weld TW 16	1.0	AWSa	L	146.4	135.1	6.8	22.3
	1.0	AWSa	T	156.7	145.3	6.0	16.1
Parent Metal	1.0	Sa	L	153.3	140.5	18.0	42.5
	1.0	Sa	T	159.1	148.5	18.0	36.7
Weld TW 14	1.0	SaW	L	146.1	133.3	21.8	33.3
	1.0	SaW	T	155.3	142.0	7.5	22.9
Weld TW 15	1.0	SaWa	L	148.3	138.8	11.9	26.0
	1.0	SaWa	T	156.1	143.9	6.5	19.9
Weld TW 59	1.75	SWSa	T	154.4	142.2	8.9	20.4

(a) A - Anneal, 2 hours at 1350° F, air cool
W - Weld
S - Solution treat, 4 hours at 1750° F, water quench
a - Age, 4 hours at 1000° F, air cool

(b) L - Longitudinal
T - Transverse

For example the transverse strength of weld TW 17 which was made in annealed plate and tested in the as welded condition was comparable to annealed parent metal strength. The remainder of the welds in 1.0 in. material were either post weld heat treated (welds TW 15 and TW 16) or were made in aged plates and tested as welded (weld TW 14). These welds had transverse strengths comparable to solution treated and aged parent metal. Longitudinal weld metal tensile strength was consistently lower than transverse tensile strength. This may be an effect of weld dendrite orientation with respect to loading direction. The strength of the weld made in 1.75 inch Ti-6Al-4V was comparable to that of weldments in 1 inch plate for specimens taken near the top or bottom surface. Specimens prepared from the center of the 1.75 inch weldment, however, had lower strengths. This behavior is attributed to the inability to quench the center portion of the thick 1.75 inch Ti-6Al-4V plate rapidly enough.

The results of the notch bend fracture toughness tests performed on parent metal and single pass welds in Ti-6Al-4V are shown in Table III. Values of K_{IC}, the fracture toughness parameter, obtained for solution treated and aged parent metal were 51.5 and 70.7 ksi $\sqrt{in.}$ for the two directions of testing. Values of K_{IC} obtained for the heat-affected zones of the weldments were either within this range or higher.

The results of stress rupture tests from the welds in 1 inch Ti-6Al-4V plate are summarized in Table IV. The values shown are necessary to cause failure after 100 and 1000 hours at 850°F. These data indicate that the stress rupture properties of electron beam welds in 1 inch Ti-6Al-4V are comparable to unwelded plate.

A comparison was made between the mechanical properties of the electron beam welds in 1 inch annealed Ti-6Al-4V and published data for MIG welds [1] in this material. This indicated that base metal tensile properties are obtainable in welds made by either process; however, the electron beam welding process produces welds with much less porosity than the MIG process.

Table III. Results of Notch Bend Tests Performed on Parent Metal and Single Pass Welds in 1.0 and 1.75 Inch Ti-6Al-4V

Specimen No.	Plate Thickness (in.)	Process Cycle(a)	Specimen Type or Notch Location	Average Calculated Fracture Toughness (ksi $\sqrt{in.}$)
Parent Metal	1.0	Sa	L	51.5
	1.0	Sa	T	70.7
Weld TW 14	1.0	SaW	FZ	68.0
	1.0	SaW	HAZ	64.8
Weld TW 15	1.0	SaWa	FZ	63.0
	1.0	SaWa	HAZ	76.3
Weld TW 16	1.0	AWSa	FZ	83.0
	1.0	AWSa	HAZ	64.4
Weld TW 17	1.0	AW	FZ	81.9
	1.0	AW	HAZ	78.1
Weld TW 59	1.75	SWSa	FZ	75.0
	1.75	SWSa	HAZ	67.0

(a) A - Anneal, 2 hours at 1350°F, air cool
W - Weld
S - Solution treat, 1 hour at 1750°F, water quench
a - Age, 4 hours at 1000°F, air cool

(b) L - Longitudinal
T - Transverse
FZ - Fusion Zone
HAZ - Heat affected zone

Two Pass Welds

The first group of two pass welds in Ti-6Al-4V made on the 7.5 kW welder were found to contain cold shuts at the tip of the fusion zone of the second pass. Figure 3(a) shows the overall contour of a typical weld in 1.75 inch plate while Fig. 3(b) shows an enlarged view of the cold shut occurring at the tip of the fusion zone of the second

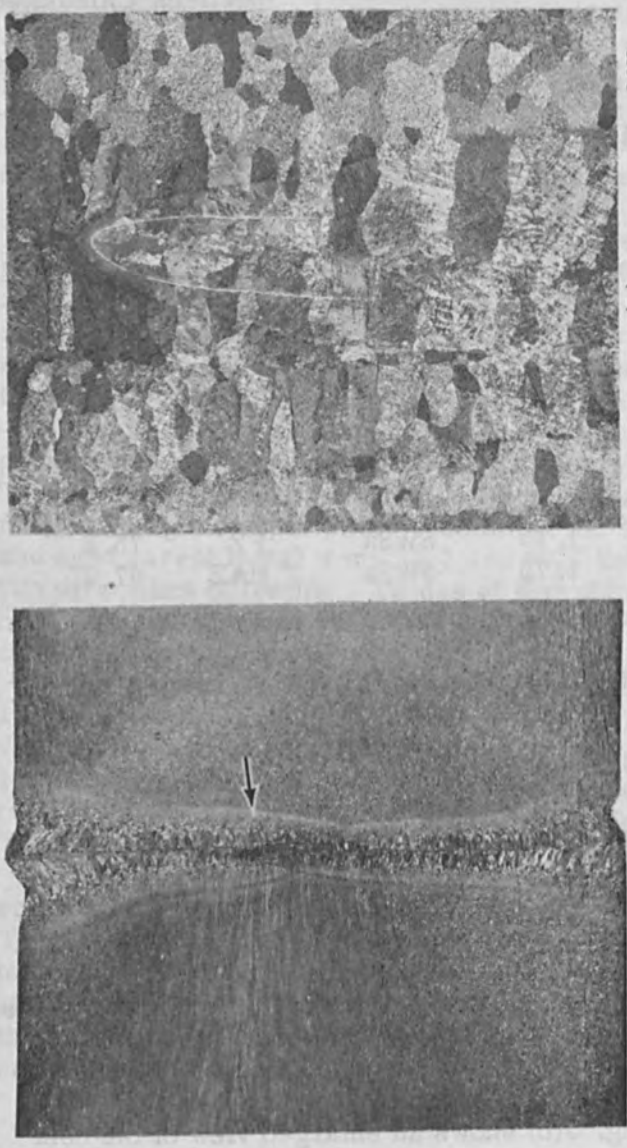

Figure 3. (a) Photomacrograph of Two Pass Weld Made in 1.75 Inch Ti-6Al-4V. (b) Cold Shut Occurring at Tip of Fusion Zone of Second Pass ($HF + HNO_3 + H_2O$ Etch). Weld Parameters - 22 kV, 300 mA, 25 ipm, Both Passes.

Table IV. Stress to Cause Failure in 100 and 1000 Hours for Parent Metal and Single Pass Welds in 1 Inch Ti-6Al-4V at 850°F*

Specimen No.	Process Cycle(a)	Rupture Stress (ksi) 100 Hours	1000 Hours
Parent Metal	Sa	79	62
Weld TW 14	SaW	78	59
Weld TW 16	AWSa	77	63
Weld TW 17	AW	73	56

(a) S - Solution treat, 1 hour at 1750°F, water quench
a - Age, 4 hours at 1000°F, air cool
W - Weld
A - Anneal, 2 hours at 1350°F, air cool

*Data abstracted from graphs

pass. Further welding was done on the 30 kW electron beam welder in an attempt to eliminate the cold shut. An example of the overall macrostructure of a weld made on the 30 kW welder is shown in Fig. 4(a). In this particular case, cold shuts were not found at the tip of the second pass, Fig. 4(b); however, cold shuts did occur along the side of the fusion zone, Fig. 4(c). Other welds made on the 30 kW welder contained cold shuts at the tip of the fusion zone of the second pass or at locations similar to that shown in Fig. 4(c). The results of additional bead-on-plate welds made on the 7.5 kW welder indicated that the occurrence of the cold shut could be eliminated or minimized if a slightly defocused beam and wide fusion zone were used to make the second pass. The wide fusion zone was characterized by a blunt tip at the bottom of penetration. This type of weld, as illustrated in Fig. 5(a) and 5(b), did not contain cold shuts. Welds that were made using the wide fusion zone technique generally exhibited mechanical properties equivalent to those of single pass welds. For example, a two pass weld made in 1.5 inch Ti-6Al-4V and solution treated and aged after welding had a transverse yield strength of 141.0 ksi. K_{IC} for the

Figure 4. (a) Macrostructure of Two Pass Weld in 1.5 Inch Ti-6Al-4V. Made on 30 kW Electron Beam Welder. (b) Tip of Fusion Zone of Second Pass Showing Absence of Cold Shut. (c) Cold Shut Occurring Along Walls of Fusion Zone ($HF + HNO_3 + H_2O$ Etch). Weld Parameters – 50 kV, 320 mA, 65 ipm

Figure 5. Photomacrograph of Two Pass Weld in Ti-6Al-4V Made Using a Defocused Beam. (b) Tip of Fusion Zone of Second Pass Showing Absence of Cold Shut ($HF + HNO_3 + H_2O$ Etch) Weld Parameters - 22 kV, 290 mA, 13 ipm, Both Passes.

heat-affected zone and fusion zone of this weldment averaged 80.3 and 75.4 ksi $\sqrt{in.}$, respectively.

In examining two pass welds to determine the presence of defects it was found that radiographic inspection would generally not reveal the existance of a cold shut. The reason for this is that many of the cold shuts are not voids but areas where the weld metal is in contact with the surrounding metal, but is not bonded to it. Ultrasonic testing may be a better method of non-destructive detection of the cold shuts.

B. René 41

Single Pass Welds

Single pass welds were made in 1 inch René 41 plates using several pre- and post-weld heat treatments. These included welding plates which were in the solution annealed condition and then aging directly or re-solution treating and aging after welding. Plates were also welded in the solution treated and aged condition and then either tested as welded or aged directly after welding. The sequence of welding a solution treated and aged plate followed by direct aging produced severe strain age cracking, which is common to conventional arc welds in René 41. A weld produced using this sequence is shown in Fig. 6(a). The gross cracking occurred when the weldment was aged. The remainder of the heat treating produced weldments which were radiographically sound and free from surface cracking as determined by dye penetrant inspection. The heat affected zones of all weldments contained a few microcracks as illustrated in Fig. 6(b).

The results of tensile tests performed on the René 41 weldments are shown in Table V. The sequence of solution anneal, weld, solution anneal then age (weld RW 13) produced the highest average transverse yield and ultimate weld strengths. These values were slightly lower than those for solution annealed and aged parent metal. The lowest transverse weld tensile properties resulted from welding plates in the solution annealed and aged condition and testing them as welded. Longitudinal all weld metal test results were not consistent so trends could not be definitely established.

(a) 2X

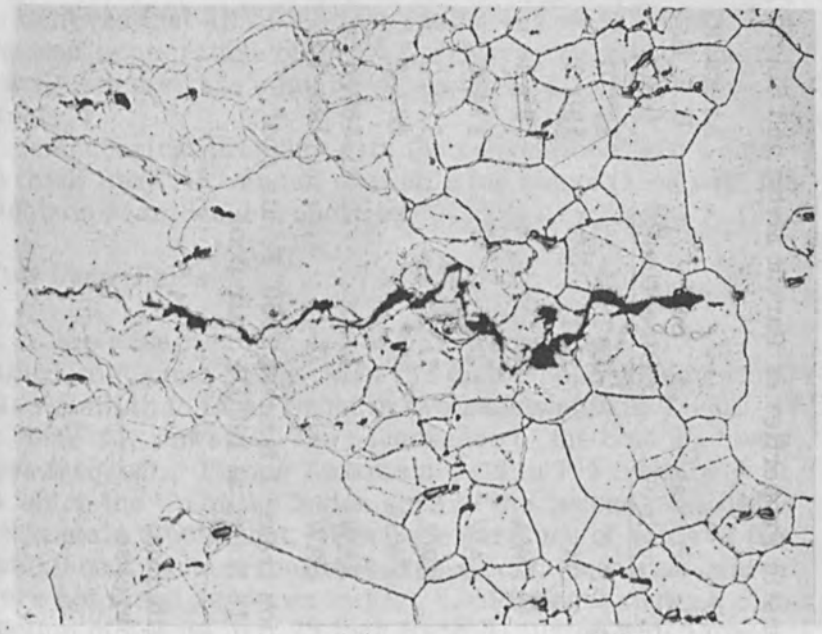

(b) 100X

Figure 6. (a) Photomacrograph of a Weld Made in Aged Rene' 41 and Aged After Welding. (b) Typical Microcrack Occurring in Heat Affected Zones of Welds Made in 1 Inch Rene' 41 ($HF + H_2SO_4 + HNO_3 + H_2O$ Etch). Weld Parameters - 22 kV, 290 mA, 13 ipm

Table V. Tensile Properties of Parent Metal and Single Pass Welds in 1 Inch Rene' 41

Specimen No.	Process Cycle[a]	Test Direction[b]	Average U. T. S. (ksi)	Average Y. S. (ksi)	Average Elong. (%-1")	Average R. A. (%)
Parent Metal	S	L, T	177.0	125.1	34.5	34.4
	SA	L, T	190.2	148.5	15.5	14.9
Weld RW 31	SWA	L	195.1	155.9	19.3	21.3
Weld RW 12	SAW	T	174.0	141.5	8.1	9.7
Weld RW 13	SWSA	L	110.0	-	9.0	8.6
	SWSA	T	183.2	146.5	9.7	9.5
Weld RW 14	SAW	L	167.6	-	21.9	25.8
	SAW	T	148.7	118.6	6.8	28.8

(a) S - Solution treat, 1 hour at 1950° F, air cool
A - Age, 16 hours at 1400° F, air cool
W - Weld

(b) L - Longitudinal
T - Transverse

A good comparison between parent metal and weld fracture toughness values could not be made because the parent metal specimens and some of the weldment specimens violated the criteria [2] that the σ_{nom}/σ_{ys} must be lower than 1.2 for a valid fracture toughness test. This is considered to indicate that yielding preceded fracture. In addition, a number of specimens from the weldments fractured during the precracking operation.

The results of the stress rupture tests performed on parent metal and 1 inch René 41 weldments are summarized in Table VI which show the stress to cause rupture at 100 and 400 hours at 1600° F. The stress rupture properties of the weldments were all lower than those for parent metal. There is little difference in the values obtained from the three different processing sequences. It is believed that all of the test specimens were overaged at the test temperature of 1600° F. Overaging would tend to equalize the stress rupture strengths of all of the weldments.

Mechanical property data for conventional arc welds in thick René 41 was not available for comparison with the electron beam weld properties.

Two Pass Welds

Two pass welds in 1.5 and 1.75 inch René 41 contained cold shuts at the tip of the fusion zone of the second pass similar to those found in two pass welds in Ti-6Al-4V. In René 41, however, the occurrence of the cold shut was less frequent. Figure 7 shows a weld in 1.5 inch René 41 in which the tip of the fusion zone of the second pass did not contain a cold shut. Fracture surfaces of some of the notch bend fracture toughness tests contained areas which were not fused as shown in Fig. 8. Figure 9 shows a cross section of a weld in 1.75 inch René 41 plates which exhibited a cold shut at the tip of the fusion zone.

The two pass welds in René 41 had a greater propensity for strain age cracking than the single pass welds. One weldment which was made in solution annealed plates and which was aged after welding cracked upon heat treatment. This is believed to be the result of higher residual stresses in the two pass weldment. One two pass weld was

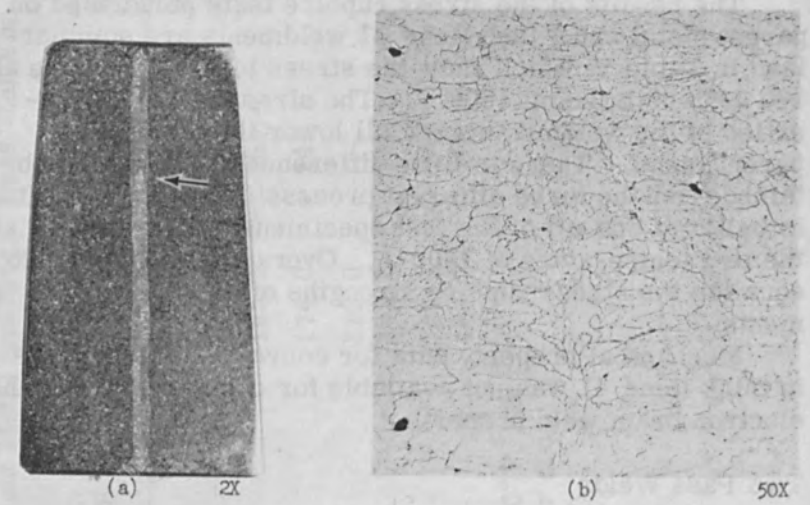

Figure 7. (a) Macrostructure of Weld RW 33 Made in 1.5 Inch Thick Rene 41. (b) Tip of Fusion Zone of Second Pass ($HF + H_2SO_4 + HNO_3 + H_2O$ Etch). Weld Parameters - 50 kV, 320 mA, 50 ipm, Both Passes.

Table VI. Stress to Cause Failure in 100 and 400 Hours for Parent Metal and Single Pass Welds in 1 Inch Rene' 41 at 1600° F*

Specimen No.	Process Cycle(a)	Rupture Stress (ksi) 100 Hours	400 Hours
Parent Metal	SA	27.0	19.0
Weld RW 12	SWA	24.0	16.0
Weld RW 13	SWSA	25.5	18.0
Weld RW 14	SAWA	25.5	18.5

(a) S - Solution treat, 1 hour at 1950° F, air cool
A - Age, 16 hours at 1400° F, air cool
W - Weld

*Data extrapolated from graphs

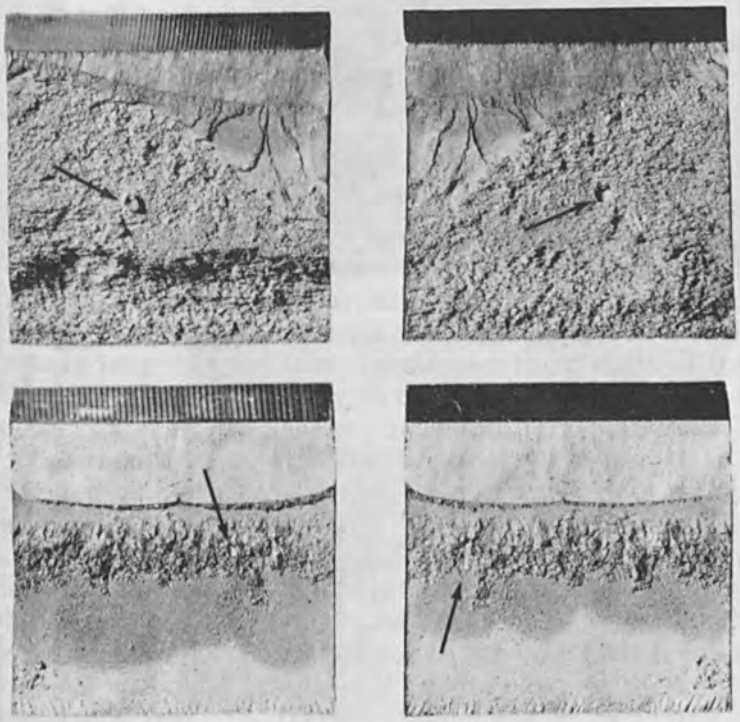

Figure 8. Fracture Surfaces of Notch Bend Fracture Toughness Specimens from Weld RW 33 Showing Small Areas of Cold Shuts.

Figure 9. (a) Macrostructure of Weld RW 26 Made in 1.75 Inch Thick René 41. (b) Tip of Fusion Zone of Second Pass. (c) Porosity in First Pass ($HF + H_2SO_4 + HNO_3 + H_2O$ Etch). Weld Parameters - 50 kV, 320 mA, 45 ipm, Both Passes.

made using an Inconel shim as filler material on the basis that the lower strength solid solutioned strengthened Inconel would decrease the strain age cracking tendency. This weld cracked, however, upon heat treatment.

C. 18 NiCoMo Steel

Single Pass Welds

Initial attempts to make single pass electron beam welds in 1 inch 18 NiCoMo maraging steel on the 7.5 kW electron beam welder resulted in cold shuts at the root of the fusion zone. An example of one of these welds is shown in Fig. 10. It should be noted that this section contains not one but several overlapping cold shuts indicating a pulsing or oscillating nature of the electron beam. Subsequent welds were made on the 30 kW electron beam welder using greater beam energy density. These welds were free of cold shuts in the fusion as illustrated in Fig. 11. A narrower fusion zone with parallel sides was obtained by using the higher beam energy density and higher welding speeds.

The results of tensile tests performed on the welds in maraging steel are shown in Table VII. Comparison of welds MW 15, MW 16 and MW 28 shows that the comparable transverse tensile strengths were obtained by the various post weld heat treatments and that they were approximately the same as obtained for parent metal. In weld MW 28, however, the longitudinal weld metal strength was considerably less than the transverse tensile strength of the weldment. This may be due to the different orientation of loading with respect to the weld dendrite orientation.

The results of notch bend fracture toughness tests performed on parent metal and the maraging steel weldments are shown in Table VIII. Fracture toughness K_{IC}, of the plate ranged between 88.6 to 113.5 ksi$\sqrt{\text{in.}}$ depending on whether the specimen was oriented parallel or perpendicular to the long dimension of the plate. The fracture toughness of the heat affected zones for both heat treated conditions was comparable to the higher parent metal values. However, the fracture toughness of the fusion zones was considerably less than that of the heat affected zone

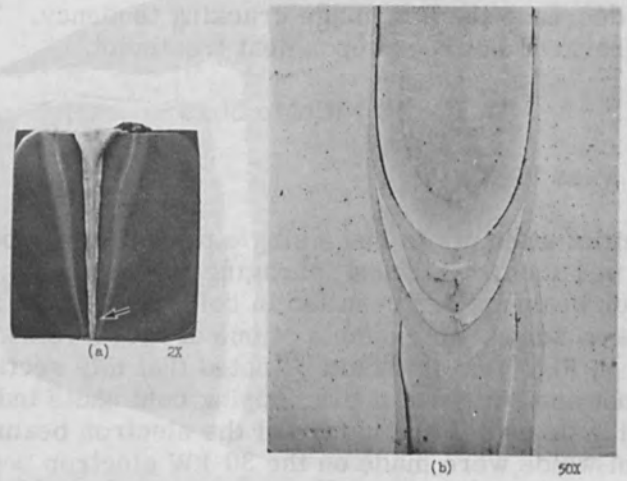

Figure 10. (a) Macrostructure of Single Pass Weld Made in 1 Inch Thick 18 NiCoMo Maraging Steel. (b) Cold Shuts at Root of Joint ($HCl + HNO_3 + CuCl_2 + H_2O$ Etch). Weld Parameters - 22 kV, 290 mA, 13 ipm.

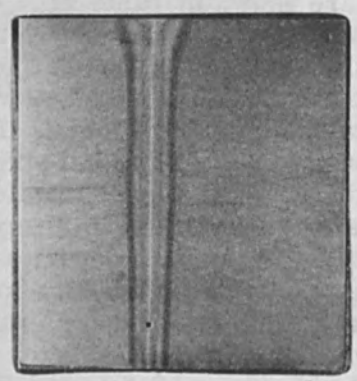

Figure 11. Macrostructure of Single Pass Weld Made in 1 Inch Thick 18 NiCoMo Maraging Steel. ($HCl + HNO_3 + CuCl_2 + H_2O$ Etch). Weld Parameters - 50 kV, 320 mA, 50 ipm.

Table VII. Tensile Properties of Parent Metal and Single Pass Welds in 1 Inch 18 NiCoMo Maraging Steel

Specimen No.	Process Cycle[a]	Test Direction[b]	Average U. T. S. (ksi)	Average Y. S. (ksi)	Average Elong. (%-1")	Average R. A. (%)
Parent Metal	SA	L, T	258.8	251.0	12.1	51.9
Weld MW 15	SWSA	T	257.2	254.9	6.3	35.3
Weld MW 16	SAWA	T	263.3	259.4	4.0	24.8
Weld MW 28	SAWA	T	252.0	247.9	4.0	26.6
Weld MW 28	SAWA	L	212.5	207.2	2.3	21.9

(a) S - Solution treat, 1 hour at 1500° F, air cool
A - Age, 3 hours at 900° F, air cool
W - Weld

(b) L - Longitudinal
T - Transverse

Table VIII. Results of Notch Bend Tests Performed on Parent Metal and Single Pass Welds in 1 Inch 18 NiCoMo Maraging Steel

Specimen No.	Process Cycle (a)	Specimen Type or Notch Location (b)	Average Calculated Fracture Toughness (ksi $\sqrt{in.}$)
Parent Metal	SA	L	113.5
	SA	T	88.6
Weld MW 15	SWSA	FZ	79.1
	SWSA	HAZ	119.1
Weld MW 16	SAWA	FZ	65.2
	SAWA	HAZ	102.2
Weld MW 28	SAWA	FZ	79.2
	SAWA	HAZ	118.1

(a) S - Solution treat, 1 hour at 1500° F, air cool
A - Age, 3 hours at 900° F, air cool

(b) L - Longitudinal
T - Transverse
FZ - Fusion zone
HAZ - Heat affected zone

for both heat treated conditions and somewhat less than the lowest value obtained for plate. This is believed to be caused by alloy segregation typical of cast structures.

The mechanical properties of the electron beam welds in 18 NiCoMo maraging steel were compared with published mechanical properties of MIG and TIG welds [3-6] in this material. The comparison indicated that electron beam welds are capable of developing slightly higher tensile properties than TIG or MIG welds. It is pointed out, however, that there is a possibility of obtaining defects in electron beam welds in maraging steel, such as cold shuts at the root, which are very difficult to detect non-destructively.

Two Pass Welds

Defect free two pass welds could not be made in 18 NiCoMo maraging steel. Welds made using low beam power and slow welding speeds resulted in cold shuts at the tip of the fusion zone of the fusion zone of the second pass similar to the initial two pass welds in Ti-6Al-4V. Welds made using higher beam energy and higher welding speeds resulted in cracks or shrinkage voids near the tip of the second pass. An example of this condition is shown in Fig. 12. The cracks or shrinkage voids were continuous throughout the length of the weldment. Cracking is probably a result of the restraint imposed on the weld after the first pass has been completed.

D. HP-9Ni-4Co Steel

Single Pass Welds

Single pass welds in 1 inch HP-9Ni-4Co steel contained cold shuts at the root of the fusion zone. Initially,

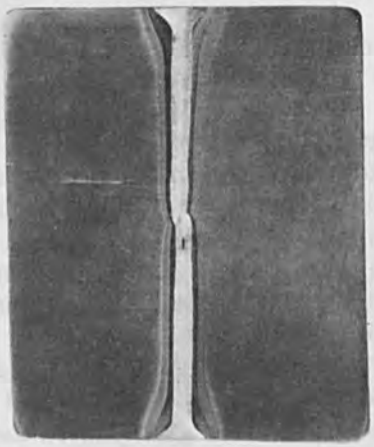

Figure 12. Photomacrograph of Two Pass Weld in 18NiCoMo Showing Void in Fusion Zone of Second Pass ($HCl + HNO_3 + CuCl_2 + H_2O$ Etch). Weld Parameters - 50 kV, 320 mA, 65 ipm.

dye penetrant tests indicated the presence of cracks or cold shuts at the bottom of the joint. Therefore, the root of the joint was ground out (approximately 1/16 inch) until no further dye penetrant indications were obtained. However, metallographic examination revealed that the cold shuts extended further into the weldment as shown in Fig. 13. Even at 100X magnification the cold shut appears as a faint line, Fig. 13(c). Figure 13(b) shows that the cold shut does not necessarily extend to the bottom surface of the weldment but can be contained within it.

In sound areas of these weldments, tensile and fracture toughness properties were comparable to parent metal. Test specimens containing cold shuts exhibited mechanical properties which were much lower than parent metal properties as would be expected.

Two Pass Welds

Many two pass welds were made in 1.5 and 1.75 inch HP-9Ni-4Co steel, however, none of these were free of defects. In general, low welding speeds resulted in cold shuts at the tip of the fusion zone of the second pass, and high welding speeds resulted in gross porosity.

E. Mismatch, Repair, High Pressure and Non-Vacuum Welds

It was generally found that the mechanical properties of mismatch welds were equivalent to those of single pass welds without mismatch, provided the resulting mismatch welds did not contain severe undercutting, porosity or root cold shuts. The detrimental effect of mismatch or undercutting could readily be determined by visual examination of the weld surfaces and radiography. All types of mismatch increased the possibility of obtaining cold shuts at the root of single pass welds. The amount of mismatch that could be tolerated depended upon the material and the weld parameters.

Repair welding with partial penetration electron beam weld passes resulted in cold shuts at the tip of the fusion zone of the repair pass similar to that found in two pass electron beam welds. A cold shut which occurred at the

Figure 13. (a) Photomacrograph of a Single Pass Weld in 1 Inch Thick HP 9Ni-4Co Steel. (b) and (c) Cold Shuts at Root of Joint (2% Nital Etch). Weld Parameters - 23.5 kV, 300 mA, 7.5 ipm.

Figure 14. (a) Macrostructure of a Repair Weld in 1 Inch 18 NiCoMo Maraging Steel. (b) Cold Shut at Tip of Fusion Zone of Repair Weld Pass ($HCl + HNO_3 + CuCl_2 + H_2O$ Etch). Weld Parameters - Initial Pass - 50 kV, 320 mA, 40 ipm. First Repair Pass - 50 kV, 320 mA, 80 ipm. Second Repair Pass - 22 kV, 223 mA, 9 ipm.

tip of the fusion zone in a repair weld in 1 inch maraging steel is shown in Fig. 14. The broad fusion zone technique using a defocussed beam minimized the formation of cold shuts and was successful in eliminating cold shuts in repair welds in Ti-6Al-4V. When the same technique was used to repair weld René 41, the repaired weldments cracked upon heat treatment.

Welds could be made in all materials at a chamber pressure of 1×10^{-3} mm Hg rather than the normal vacuum of less than 1×10^{-4} mm Hg. There appeared to be a slight reduction in fracture toughness properties in the fusion zone of welds made in Ti-6Al-4V and René 41, but not in maraging steel or HP-9Ni-Co steel.

A number of non-vacuum electron beam welds were attempted by an outside source in each of the program materials. However, no welds suitable for mechanical testing were obtained. All of the weldments contained a large amount of cracks and/or porosity similar to that shown in Fig. 15. It was concluded that non-vacuum electron beam welding is not suitable for welding thick materials at the present state of development.

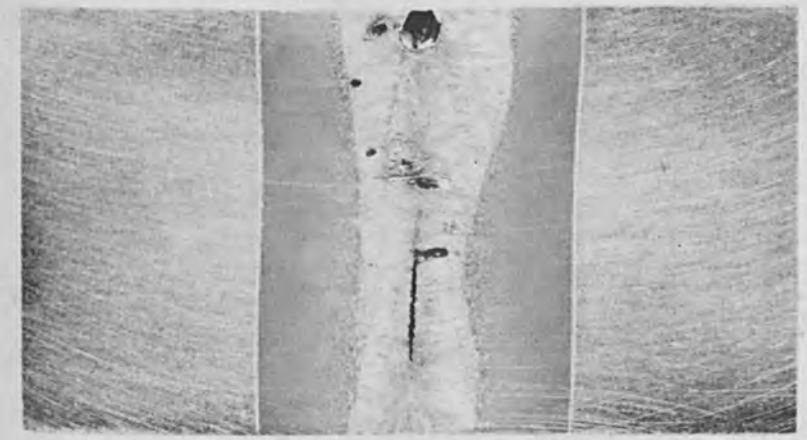

Figure 15. Macrostructure of Non-Vacuum Electron Beam Weld Made in 1/2 Inch HP 9Ni-4Co Steel (2% Nital Etch). Weld Paramaters - 175 kV, 70 mA, 20 ipm.

F. Process Engineering Study

The results of a survey of users of electron beam welding showed that this process was employed for joining nearly all structural metals in thicknesses ranging from 0.001 inch to over 2 inches. However, the survey showed that approximately 78 percent of the welding was done on thicknesses of 0.25 inch or less. Many replies mentioned characteristic problems such as cold shuts, porosity, spatter loss and undercutting which must be overcome or allowed for in production. The major reasons given for using electron beam rather than other welding methods in production were improved mechanical properties, reduced distortion and the only applicable method for joining specific assemblies.

A cost analysis study was performed on the welding of two domed heads on a 24 inch diameter 36 inch long cylinder in 1/4 inch and 1 inch thicknesses. The analysis was performed for Ti-6Al-4V, maraging steel and HP-9-4-25 steel.

Electron - Beam Welding at Various Pressures

J. W. Meier

Hamilton Standard
Windsor Locks, Connecticut

INTRODUCTION

Electron beam welding has become firmly established as a very useful, versatile joining process; its basic capabilities and characteristics have been investigated and publicized. Today, a large portion of the technical effort relative to this process is aimed at adapting it to high-speed production operations. In this regard the requirement for a vacuum environment, particularly at the workpiece, is of considerable significance and, therefore, worthy of detailed consideration.

MODES OF OPERATION

Since electrons are of very small mass they are deflected upon impact with bodies of greater mass; for example, gas molecules. As a result an electron beam passing through a gas at atmospheric pressure very quickly becomes diffuse and its effectiveness as an intense heat source is lost. For this reason and since high voltages are involved, electron beams usually are generated, formed, and controlled in regions of very low pressure, usually in a vacuum environment of 10^{-4} mmHg or lower.

Until recently almost all electron beam welding was accomplished with the workpiece also in a high-vacuum environment. However, during the past few years technological breakthroughs have resulted in a capability for electron beam welding with the workpiece in a protective gas at atmospheric pressure. In addition experimental

work has shown that very satisfactory welding often can be accomplished at intermediate vacuum levels of about 100 to 400 microns. Thus, there appear to be three welding modes - high vacuum, intermediate vacuum, and atmospheric pressure. Each has its advantages and disadvantages.

As stated above most electron beam welding to date has been accomplished with the workpiece in a vacuum environment of 10^{-4} to 10^{-5} mmHg or 0.1 to 0.01 microns. In this environment it is possible to obtain the most precise, highest quality welds. Electron scattering is not encountered and, thus, an extremely fine, high-power-density beam can be produced and maintained over relatively long distances. In a high vacuum extremely deep, narrow fusion zones can be obtained minimizing energy input; a long working distance, that is, the distance from the machine structure to the point of welding, can be used. Obviously, such an environment produces welds with minimum chemical contamination because the concentration of foreign atoms is extremely low.

The major disadvantage associated with high-vacuum electron beam welding lies in the requirement for a work chamber large enough to enclose the workpiece, including any workpiece motion, and incorporating structures and seals which have extremely low leak rates. Furthermore, surfaces, materials, and designs must be such as to minimize outgassing. In order to provide reasonable chamber pumpdown times, it is necessary to incorporate relatively large mechanical and diffusion pumps. These add to the cost and the complexity of the system. In spite of these disadvantages, high-vacuum electron beam welding has proved to be a practical and economical production process providing construction and design possibilities not available when other joining techniques are used. It can be considered the most flexible and versatile electron beam welding mode.

When the workpiece is enclosed in an environment of intermediate vacuum level, that is, 100 to 400 microns, some beam spread occurs because of electron-molecule collisions, particularly as working distances are increased. However, this spreading of the beam is relatively small. Figure 1 is a photograph of a beam passing through sixteen

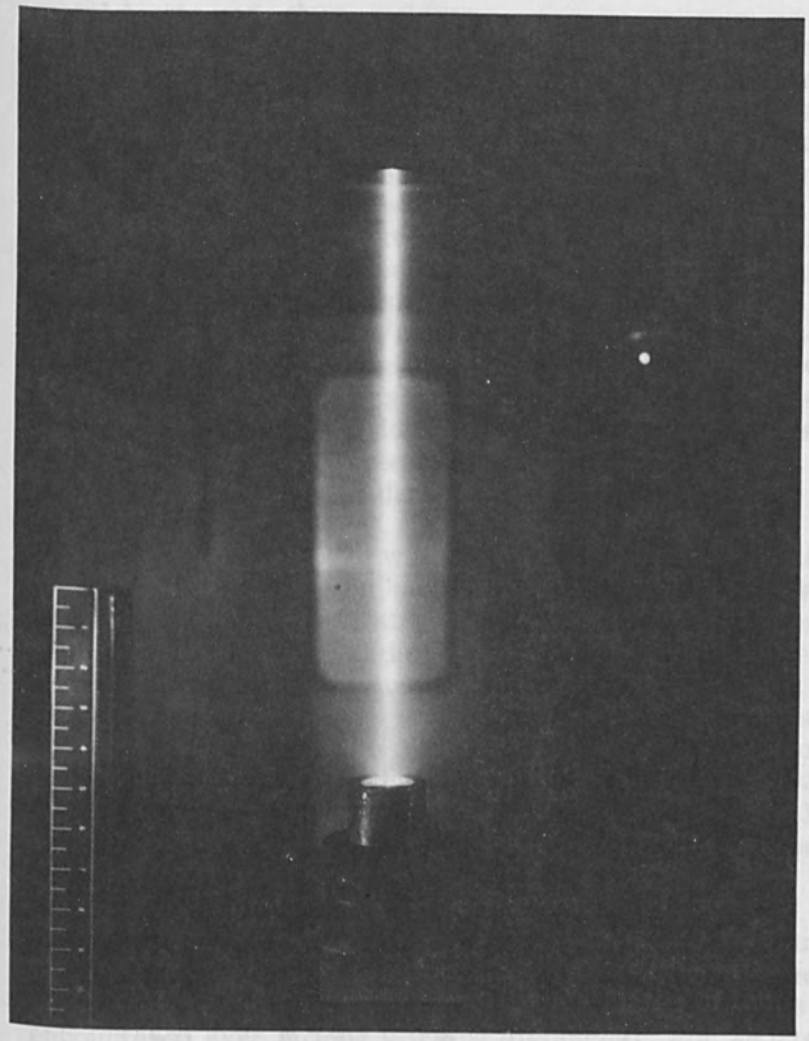

Figure 1. Electron Beam in Partial Vacuum.

Figure 2. Schematic of Experimental Partial Vacuum Welder

inches of air at 300 microns pressure and shows some fringe effect. But even, at this pressure and this distance, beam power densities still remain high enough to produce metal fusion and, thus, welding.

The characteristics of electron beams of the welding variety have been investigated to a limited extent at intermediate vacuum levels. Figure 2 is a schematic diagram of the equipment involved in these experiments. Basically, it consists of the modification of a standard high-vacuum electron beam welder in which a diffusion pumping port with an orifice just below it have been inserted in the electron optical column. As can be seen, in the upper portion of the electron column, the pressure is maintained at normal high-vacuum levels while in the lower portion, that containing the optical viewing system, magnetic lens, and deflection coil, higher pressures exist. This modification was simple to make and does not necessarily reflect the optimum design for an intermediate vacuum welding machine. The following data were obtained using this equipment.

Figure 3 is a plot of weld penetration versus operating pressure at two different working distances. It must be noted that the working distances indicated do not include about fifteen inches of higher pressure beam path in the lower portion of the electron optical column. As might be expected, penetration falls off at higher pressure levels and the point at which this occurs is somewhat lower for a longer working distance than for a shorter one. However, it is of interest that for the shorter working distance full penetration could be maintained up to a pressure of over twenty microns. Figure 4 presents similar data in a somewhat different way. In this case, penetration is plotted against working distance but at different operating pressures. This again shows that until pressures exceed about twenty microns very little effect on penetration is encountered even at long working distances. For shorter working distances pressures in the 100 to 300 micron range still produce significant depth-of-weld penetration.

Figure 5 shows the effect of pressure on the shape of the fusion zone. From these photographs it can be seen that extremely deep, narrow fusion zones, or the so-called "deep weld" effect, can be obtained up to pressures greater

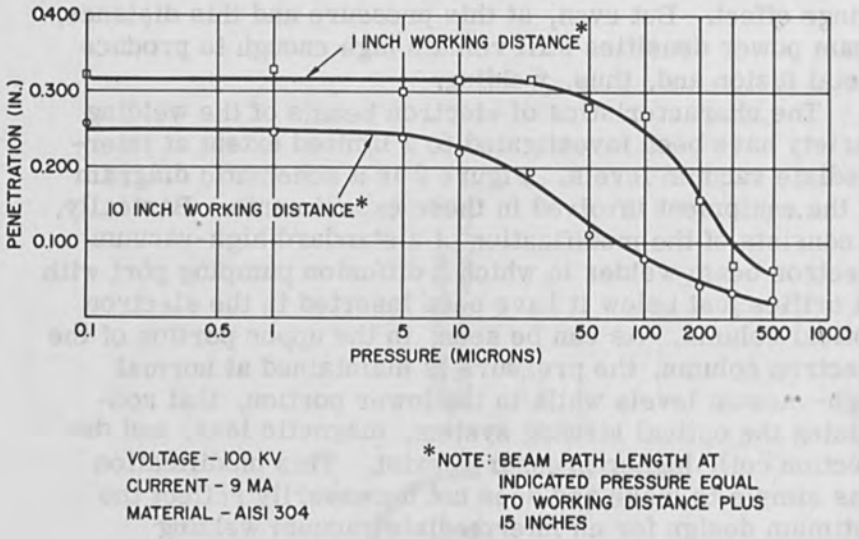

Figure 3. Effect of Pressure on Weld Penetration.

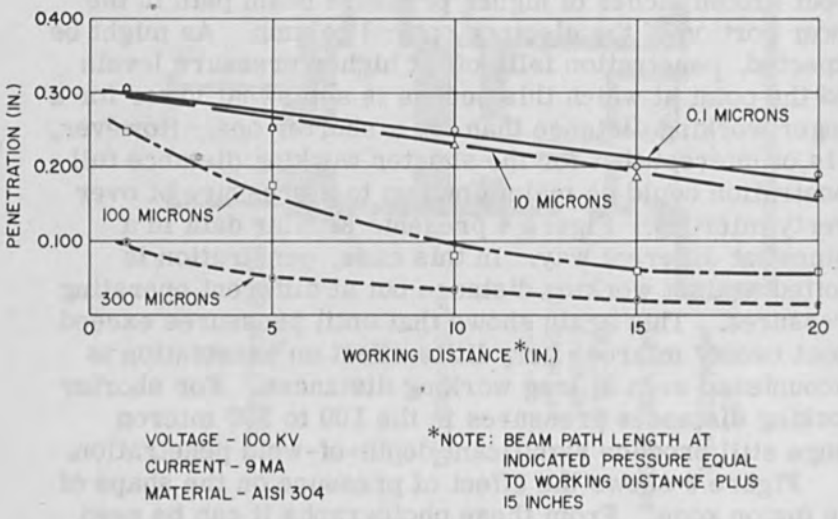

Figure 4. Effect of Working Distance on Weld Penetration at Various Pressures.

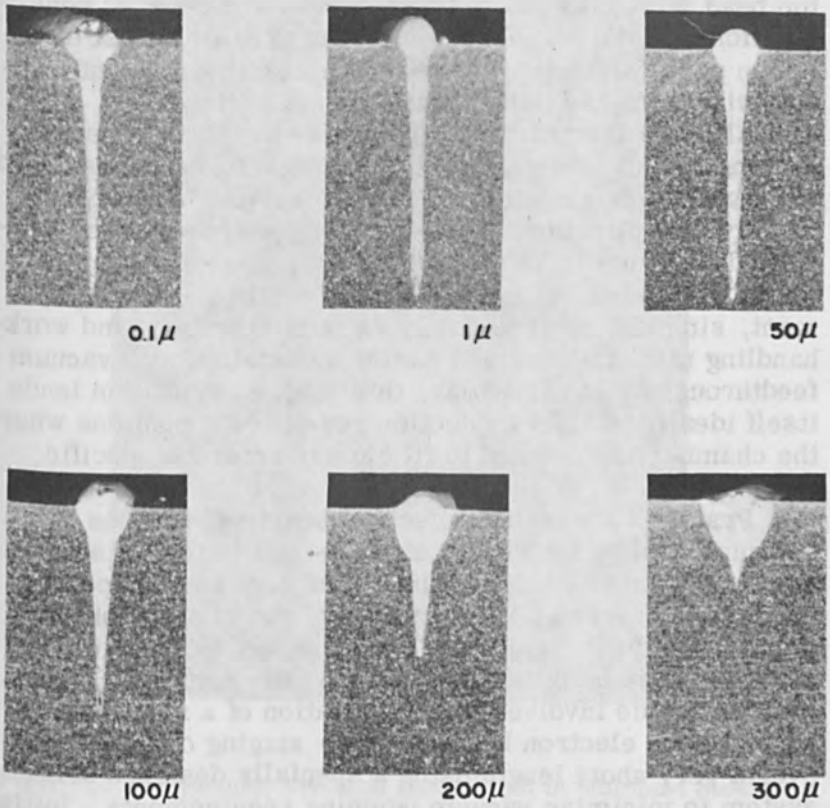

Figure 5. Effect of Pressure on Shape of Fusion Zone.

than 200 microns at the operating conditions involved. In fact, very little effect of pressure can be seen up to fifty microns. However, above this pressure the width of the top bead increases due to beam spread and depth of penetration is reduced. At 300 microns pressure most of the fusion penetration appears to be the result of thermal conductivity from the initial beam impact surface.

Although the ultimate capabilities of electron beam welding cannot be obtained at these higher pressures, weld characteristics remain perfectly acceptable for a wide variety of applications. The advantages of using the intermediate vacuum level are significant. They include much faster pumpdown, simpler and less costly vacuum equipment, simpler and less costly vacuum chambers and work-handling mechanisms, and easier automation with vacuum feedthroughs. In particular, this mode of operation lends itself ideally to high-production repetitive operations where the chamber is designed to fit closely around a specific part.

Practical nonvacuum electron beam welding has been accomplished by the design of equipment which permits an electron beam to escape from the vacuum environment in which it is formed into a region of gas at atmospheric pressure without significant loss of power. Thus, the workpiece can be positioned outside the vacuum enclosure. This technique involves the combination of a relatively high-voltage electron beam with the staging of the vacuum over a very short length using a specially designed orifice system to minimize vacuum pumping requirements. Initial nonvacuum electron beam work was done with relatively low powered machines limiting penetration capability to about one-eighth inch. However, today, with improved electron optics and orifice systems and with output powers of about 12 kW, it is possible to produce deep welds in many materials to depths exceeding three-quarter inch and at relatively high speeds. Figure 6 shows such a weld in type 302 stainless steel. It can be seen that, although this weld is wider than those encountered with vacuum and intermediate vacuum welding, it still is relatively deep and narrow as compared with other fusion welding techniques. Obviously, electron scatter is much greater at atmospheric pressure than at lower pressures. This can be seen in

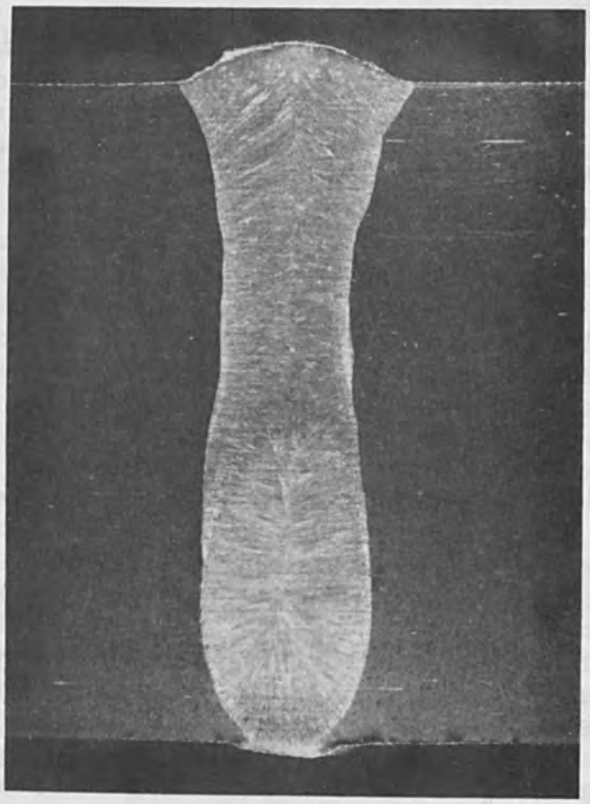

Figure 6. Nonvacuum Electron Beam Weld in Stainless Steel.

Fig. 7 which shows that penetration falls off very rapidly with working distance and, thus, in order to produce welds with significant depth, it is necessary that the workpiece be in close proximity to the final pressure staging orifice. This is the major disadvantage of the nonvacuum process in that it imposes a limitation on the shape of the workpiece. The contour of the workpiece must be reasonably smooth so that the beam impingement can be within one inch of the machine structure and at a relatively constant distance. Also, in general, wider fusion zones are produced by this technique with lower depth-to-width ratios. Chemical purity is controlled by the extent of inert gas

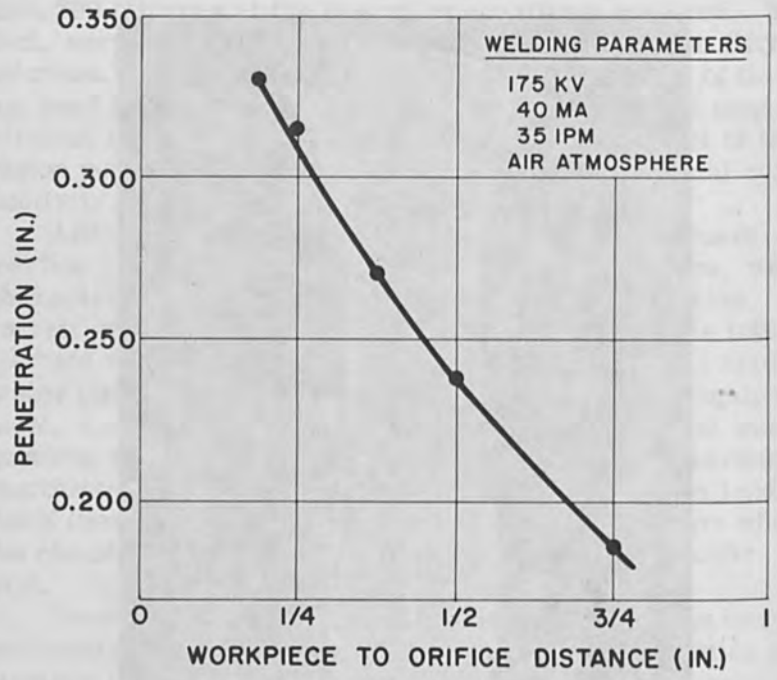

Figure 7. Effect of Working Distance on Weld Penetration.

shielding in the vicinity of the weld. Obviously, nonvacuum electron beam welding has the very significant advantage of not placing a limitation upon the size of the workpiece being welded. Furthermore, it simplifies high-speed work-handling and high-production application for parts of certain geometry.

WELD PROPERTIES

It has been clearly demonstrated that high-vacuum electron beam welding produces welds with superior mechanical properties. In many materials these properties approach or equal those of the base material; for example, this is true of heat-treated high-strength alloy steels. In solution-treated and aged materials, tensile properties

70 to 95% of base metal can be obtained, depending upon the thermal treatment following welding. Excellent properties also can be obtained in high-temperature alloys and refractory metals. Limited fatigue testing indicates that the endurance properties of high-vacuum electron beam welds are quite remarkable, often approaching those of the wrought base material. In general, the soundness of welds is extremely good and cracking tendencies are minimized.

As might be expected, electron beam welds made at intermediate vacuum levels also exhibit excellent mechanical properties. Table I lists the tensile properties of butt welds made in annealed AISI 304 stainless steel, rimmed AISI 1010 low-carbon steel, 6061-T4 aluminum alloy, and 6 Al 4V titanium alloy. It can be seen that in three of the four materials failure occurred in the base metal, while in the fourth - the aluminum alloy - failure occurred at the edge of the weld, but at strengths exceeding the established minimum for this alloy in the solution-treated condition. Furthermore, porosity in gas producing materials such as rimmed steels appears to be minimized. With regard to chemical contamination, it can quite readily be shown that the concentration of foreign atoms at a vacuum level of 100 to 200 microns is about the same as that found in inert shielding gases. Thus, with most materials chemical contamination will not be a problem at these vacuum levels.

In many materials outstanding mechanical properties can be realized in weldments made by the nonvacuum technique. For examples, Tables II, III, and IV present data on nonvacuum electron beam welded AISI 4340 chrome-nickel-molybdenum low-alloy steel showing that in this material excellent weld properties can be obtained. Similar data have been obtained with other materials such as stainless steel, high-temperature alloys, and refractory alloys. Table V lists typical materials that have been successfully welded at the parameters shown.

Table I. Mechanical Properties of Partial Vacuum Electron Beam Welds

	UTS (PSI)	YS (PSI)	Elongation (% in 2")	Fracture Location
Stainless Steel AISI 304 - Annealed 1/4 inch - Butt Weld				
Weld 1	89,000	31,800	74	base metal
Weld 2	86,100	33,700	66	base metal
Base Metal - Nominal	85,000	30,000	62	-
Rimmed Steel - AISI 1010 3/16 inch - Butt Weld				
Weld 1	49,000	38,700	24	base metal
Weld 2	48,400	37,700	25	base metal
Aluminum - 6061 (welded in T4 - no postweld treatment) 1/4 inch - Butt Weld				
Weld 1	34,400	31,000	5	edge of weld
Weld 2	35,500	28,000	5	edge of weld
Base Metal - Minimum (T4)	30,000	16,000	18	-
Titanium 6A1 - 4V - Annealed 1/4 inch - Butt Weld				
Weld 1	137,500	-	9	base metal
Weld 2	131,250	129,000	10	base metal
Base Metal - Minimum	135,000	130,000	15	-

Note: All welds made at pressure of 200 microns.

Table II. Room Temperature Tensile Properties of AISI 4340 Base Metal and Non-Vacuum Electron Beam Weldments

Specimen Thickness, In.	Heat Treat Condition [a]	Ultimate Tensile Strength, psi	Yield Strength at 0.2% Offset, psi	Elongation in 2 In., %	Location of Failure [b]
Base Metal					
0.400	AT	222,000	209,000	9	...
0.400	AT	222,000	211,000	11	...
0.400	AT	219,000	208,000	9	...
Weldments					
0.400	ATWT	192,500	186,800	5	HAZ
0.400	ATWT	191,000	185,000	5	HAZ
0.400	ATWT	191,000	184,500	6	HAZ
0.400	ATWNAT	220,000	210,000	11	BM
0.400	ATWNAT	218,000	207,000	11	BM
0.400	ATWNAT	216,000	203,000	11	BM
0.400	ATWNAT	222,000	204,000	11	BM

[a] A - austenitized at 1525°F for 1 hr, oil quenched; T - tempered at 775°F for 2 hr, air cooled;
W - nonvacuum electron beam welded; N - normalized at 1650°F for 1 hr, air cooled.

[b] BM- base metal; HAZ - heat affected zone.

Table III. Room Temperature Bend Properties of AISI 4340 Base Metal and Nonvacuum Electron Beam Weldments

Specimen Thickness, In.	Heat Treat Condition [a]	Bend Radius [b]	Bend Span In.	Angle or Bend, deg	Location of Failure [c]
Base Metal					
0.400	AT	2t	3	19	...
0.400	AT	2t	3	19	...
0.400	AT	2t	3	19	...
Weldments					
0.400	ATWT	2t	3	13	HAZ
0.400	ATWT	2t	3	12	HAZ
0.400	ATWT	2t	3	14	HAZ
0.400	ATWNAT	2t	3	21	FZ
0.400	ATWNAT	2t	3	19	FZ
0.400	ATWNAT	2t	3	18	FZ
0.400	ATWNAT	2t	3	9	FZ

[a] A - austenitized at 1525° F for 1 hr; oil quenched; T - tempered at 775° F for 2 hr, air cooled;
W - nonvacuum electron beam welded; N - normalized at 1650° F for 1 hr, air cooled.

[b] t - thickness of specimen.

[c] FZ - fusion zone; HAZ - heat affected zone.

Table IV. Room Temperature Charpy V-Notch Impact Properties

Base Metal, ft-lb	Nonvacuum Electron Beam Weldment, ft-lb
14	10
14	9
14	19
16	15
—	11
14. 5 avg.	8
	11
	14
	15
	15
	—
	12. 7 avg.

APPLICATIONS

As mentioned earlier, electron beam welding is finding wide and general acceptance in industry and many interesting applications have been developed. Perhaps one of the most interesting involves the fabrication of gears. Completely finished gears or gear components can be assembled by electron beam welding without subsequent finishing operations. Figure 8 shows a double helical aircraft engine gear assembled from two pieces which had been cut, hardened, and ground separately prior to being welded. This technique eliminated the necessity of a large gap for grinding wheel clearance. At present, cluster gears requiring high levels of accuracy often are joined together with splines, locknuts, or bolt flanges in order to avoid the necessity for providing space for grinding wheel clearance. Such a complex assembly can be simplified greatly

Table V. Typical Nonvacuum Electron Beam Welding Parameters

Base Metal	Thickness In.	Voltage kV	Current mA	Weld Speed ipm	Work Distance In.	Atmosphere
SAE 1010 Steel	0.010	150	2.5	145	1/4	Air
AISI 4340 Steel	0.250	175	40	60	1/2	3He-1A
AISI 4340 Steel	0.430	175	40	15	3/16	4He-1A
AISI 304 Stainless Steel	0.120	175	60	480	3/8	He
AISI 304 Stainless Steel	0.400	170	35	10	1/4	Air
AISI 304 Stainless Steel	0.750	175	70	10	3/8	Air
17-7 PH Stainless Steel	0.100	175	25	108	1/4	Air
2219 Alimunum	0.500	175	70	125	1/8	He
2219 Aluminum	0.750	175	70	27	1/8	He
3003 Aluminum	0.010	175	15	3500	1/4	He
Rene 41 Superalloy	0.275	175	40	15	1	4He-1A
Udimet 500 to A-286	0.200	175	40	50	1/2	Air
Inconel X	0.125	150	25	18	3/16	Air
TZM Molybdenum	0.187	175	40	15	1/2	He
Copper	0.008	150	8	145	1/4	Air

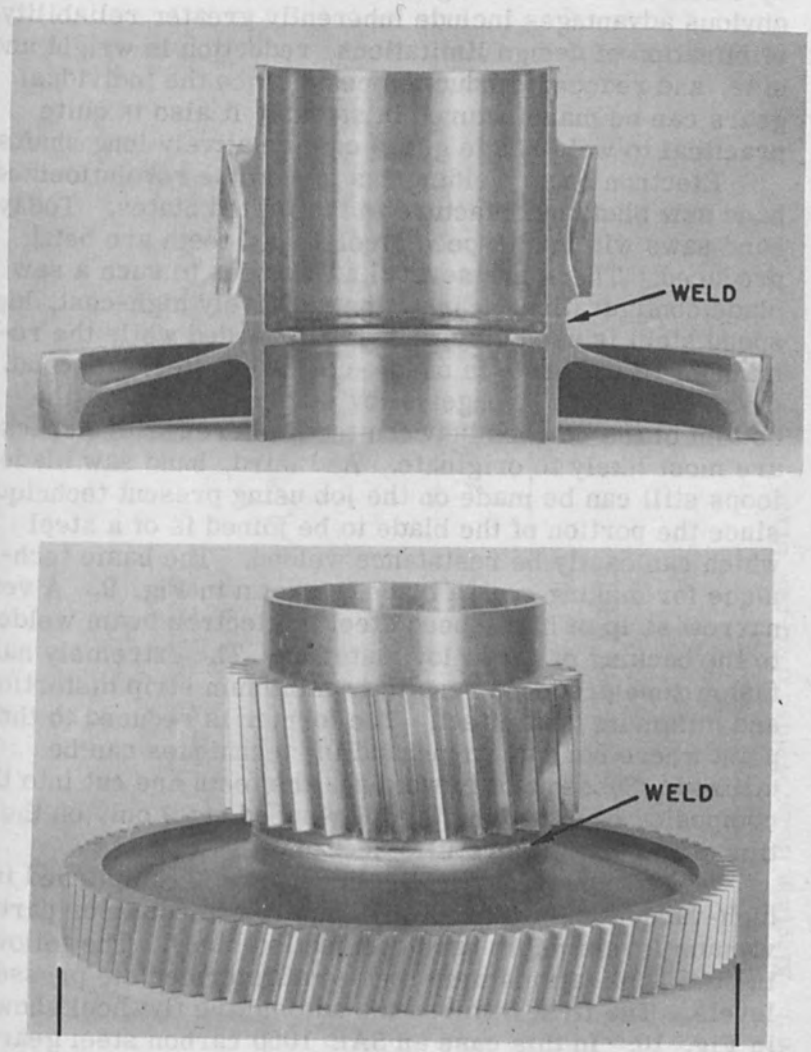

Figure 8. Electron Beam Welded Aircraft Gear.

by electron beam welding the components together. The obvious advantages include inherently greater reliability, elimination of design limitations, reduction in weight and size, and reduced production costs since the individual gears can be manufactured in stacks. It also is quite practical to weld single gears onto relatively long shafts.

Electron beam welding has in a sense revolutionized band saw blade manufacture in the United States. Today, band saws with high-speed steel-tipped teeth are being produced. There are several advantages to such a saw blade configuration. First, the relatively high-cost, high-speed steel is used only where it is needed while the remainder of the blade is of low-cost alloy steel. Second, the more ductile stronger alloy steel is present at the bottom of the notches between teeth where flexure cracks are most likely to originate. And third, band saw blade loops still can be made on the job using present techniques since the portion of the blade to be joined is of a steel which can easily be resistance welded. The basic technique for making such a blade is shown in Fig. 9. A very narrow strip of high-speed steel is electron beam welded to the backing of low-alloy material. The extremely narrow fusion zone produced results in minimum strip distortion and minimum heat effect. The former is reduced to the point where normal strip-handling techniques can be utilized. Subsequent to welding, the teeth are cut into the composite strip leaving the high-speed steel only on the tips of the teeth where it is needed.

The two previous applications were accomplished in a high-vacuum environment although intermediate or partial vacuum levels might have been satisfactory. The following two applications were welded at intermediate pressure levels. The first involves the automotive flywheel shown in Fig. 10. In this case an SAE 1050 carbon steel gear was welded to a rimmed SAE 1010 steel sheet metal disc or hub. Excellent welds were obtained at a welding speed of 300 ipm. Using a specially designed but very simple single spindle machine, these parts can be welded one at a time at a rate of three per minute. In other words loading, pumpdown, welding, and unloading all can be accomplished in about 15 seconds. Thus, practical high-production rates can be realized.

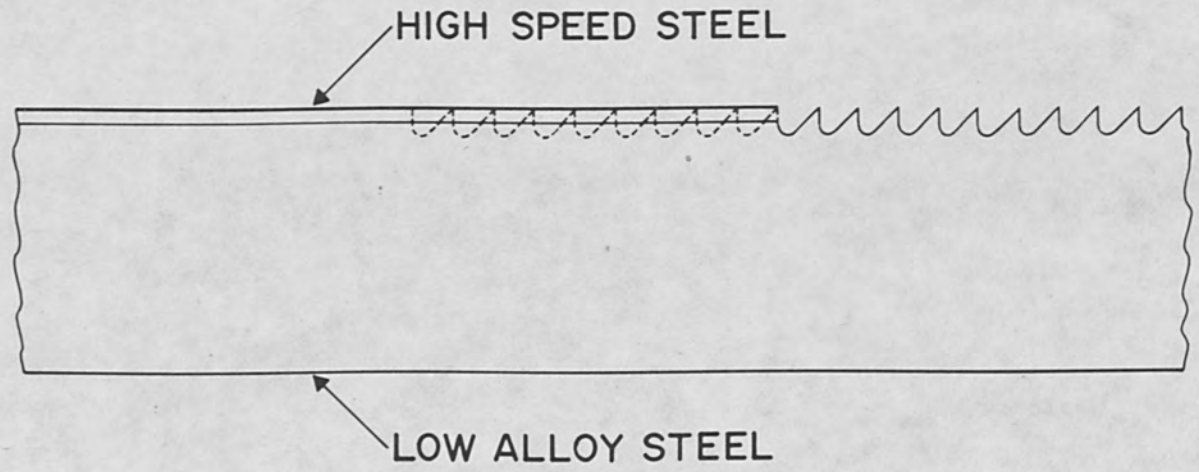

Figure 9. Electron Beam Welded Band Saw Blade.

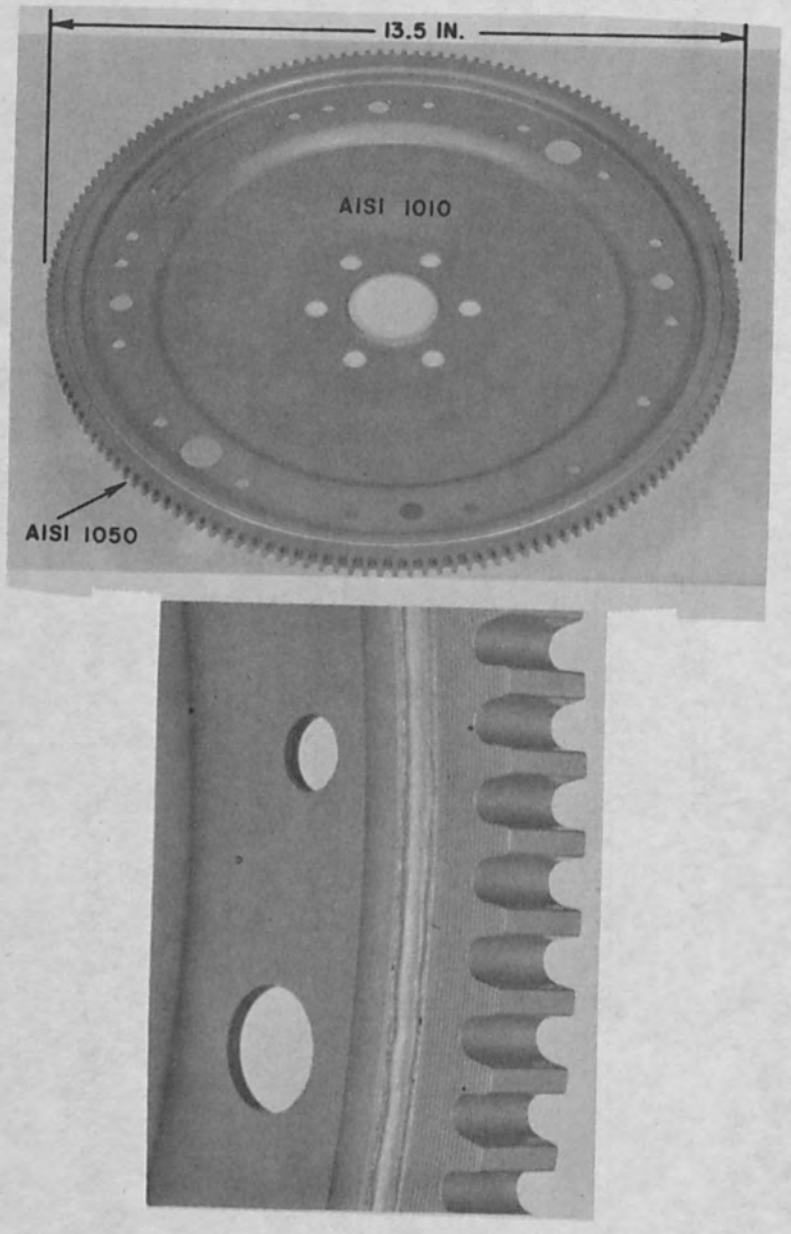

Figure 10. Automotive Flywheel.

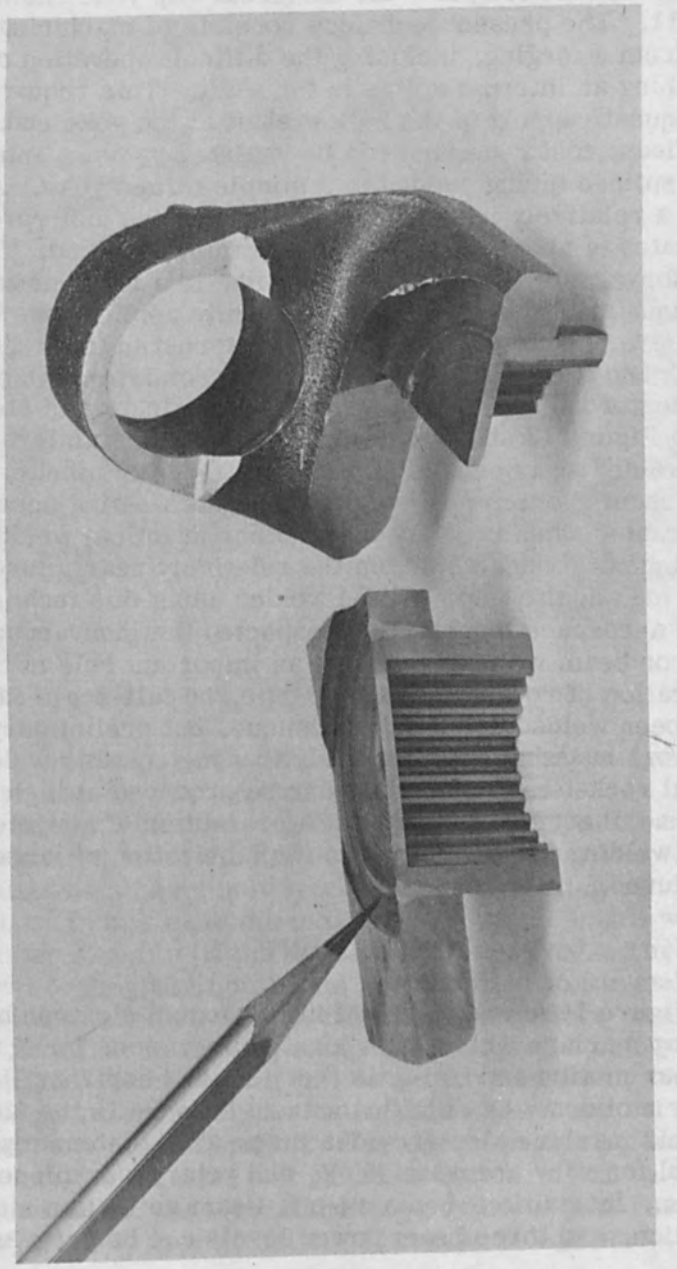

Figure 11. Automotive Slip Yoke.

A second intermediate vacuum application consists of another automotive part, the universal slip yoke shown in Fig. 11. The present technique consists of machining this part from a forging, including the difficult operation of broaching an internal spline in the shaft. This requires subsequent capping of the hollow shaft at the yoke end. Significant cost reduction can be realized by using internally splined tubing welded to a simple forged yoke. Again, using a relatively inexpensive single-purpose unit, production rates of about four per minute can be realized.

Nonvacuum electron beam welding is a much newer technique and, therefore, fewer specific applications have been developed to date. However, interest in this technique is high and its production potential is promising. One outstanding broad application lies in the fabrication of steel pipe. Figure 12 shows one-eighth-inch wall stainless steel pipe welded at a speed of about thirty feet per minute. Weld beam geometry is excellent and the welding speed remarkable when compared with other practical welding techniques. Undoubtedly, in the relatively near future much high quality pipe will be welded using this technique. In the aerospace industry it is expected that nonvacuum electron beam welding will play an important role in the fabrication of rocket cases. To date, no full-scale cases have been welded using this technique, but preliminary test work has shown conclusively that high quality welds in typical rocket case materials can be produced at high speeds. Figure 13 is an artist's conception of how electron beam welding can be applied to the fabrication of large structures.

EQUIPMENT

Figure 14 shows a typical high-vacuum electron beam welding machine which incorporates provisions for X and Y linear motion and two-axis (vertical and horizontal) rotary motions. Of significance and interest is the fact that this machine also provides three-axis contour tape control for very accurate X, Y, and rotary workpiece motion. In addition, beam on-off, beam deflection mode selection, and three beam power levels can be programmed.

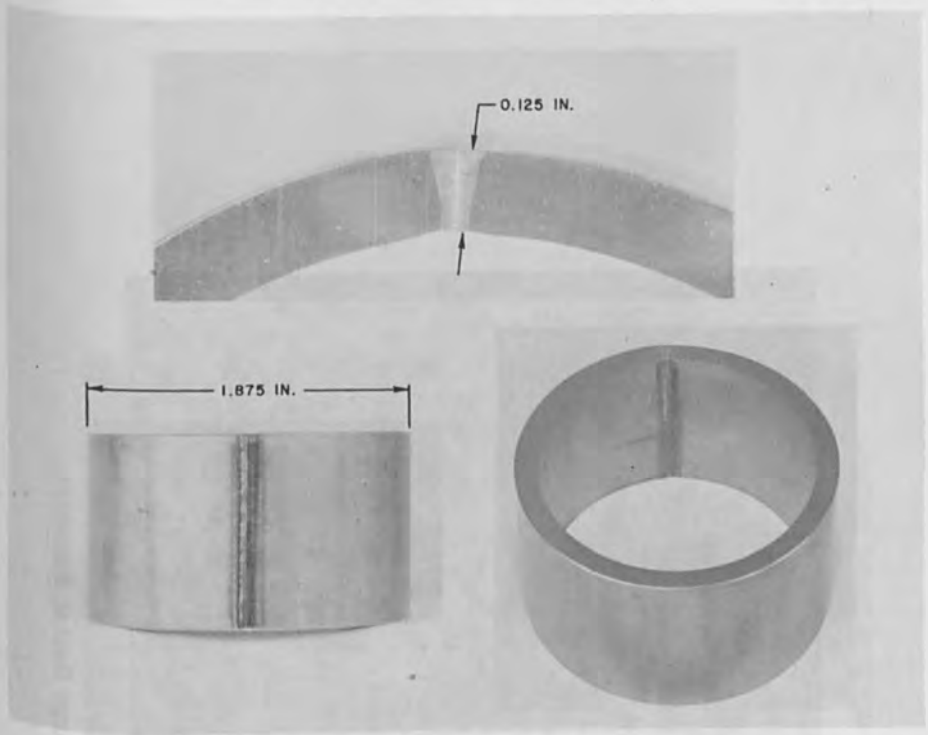

Figure 12. Nonvacuum Electron Beam Welded Pipe.

Such a welding system is an extremely versatile, reliable, and repeatable production tool.

Figure 15 is a sketch of a production-type intermediate or partial vacuum electron beam welding machine. It consists of a basic unit to which special tooling can be attached. In this case the tooling includes the small work chamber sized to fit the specific part involved. Three typical tooling configurations are shown, two for making relatively large circular welds using workpiece rotation and the third for making small circular welds using beam deflection. Such tooling can be quickly and easily changed. With this machine the operating parameters are set and locked at a control station. The operator merely loads the part into the machine and pushes a button, closes a door, or perhaps moves the fixture into position. The rest of the cycle is fully automatic. This type of equipment

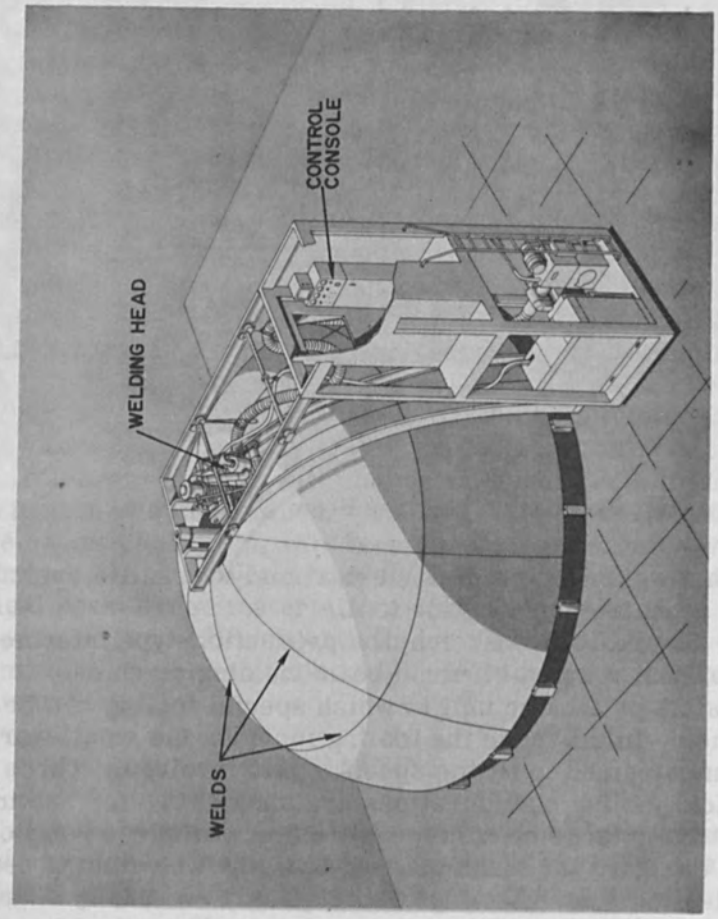

Figure 13. Welding a Large Rocket Structure.

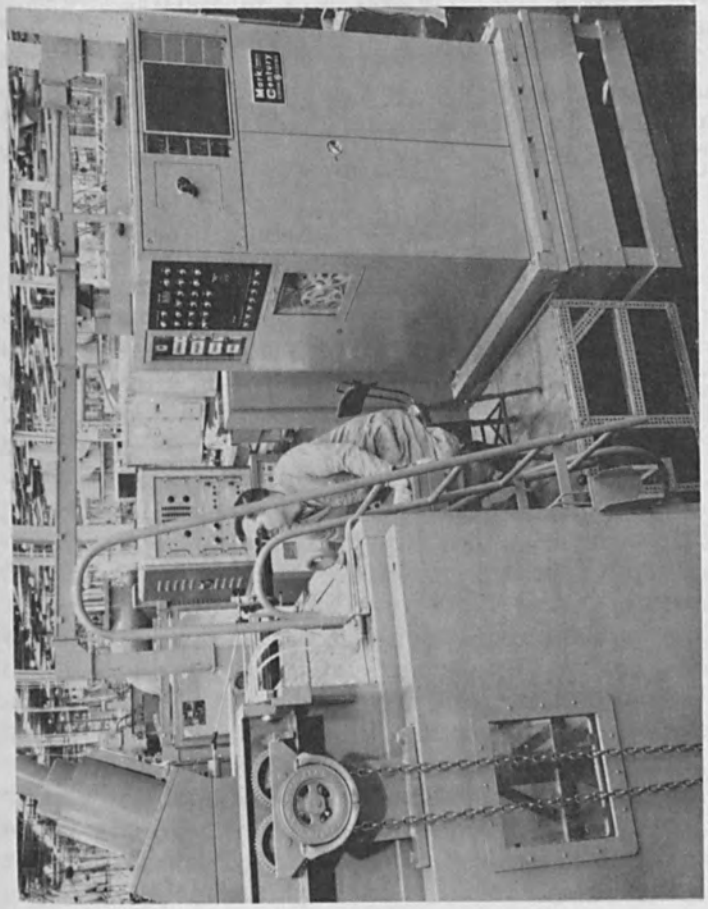

Figure 14. Tape Controlled Electron Beam Welder.

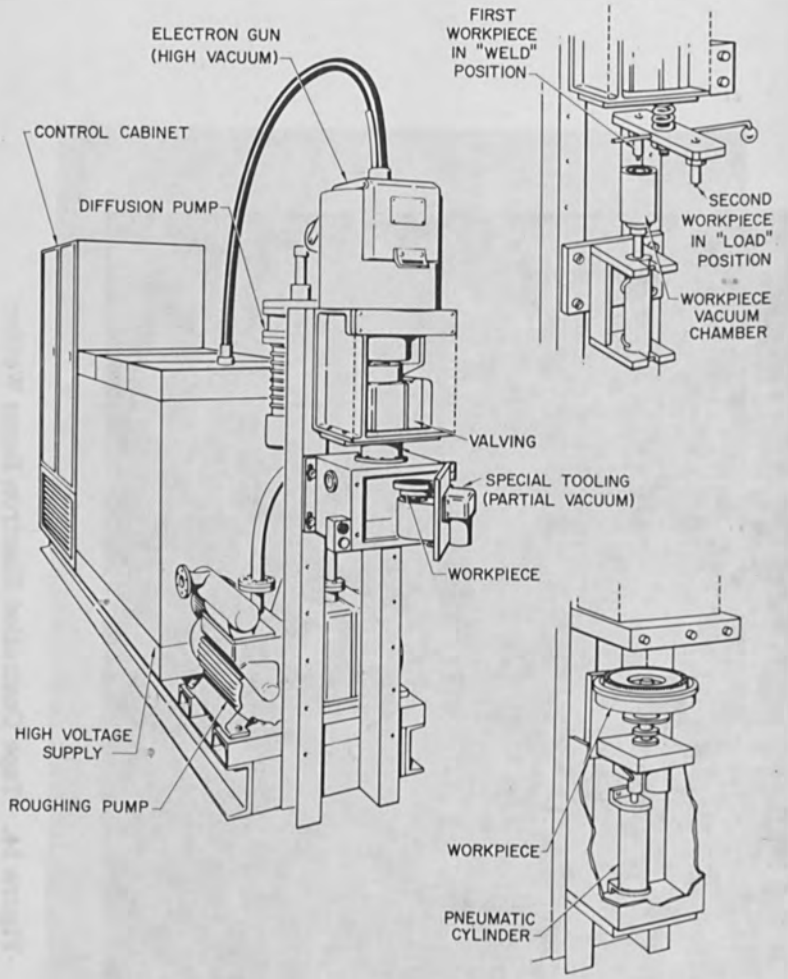

Figure 15. Production Partial Vacuum Electron Beam Welder.

undoubtedly will find widespread industrial use for high production.

Fugure 16 is a photograph of a nonvacuum electron beam welding machine. This, of course, does not include any work chamber and as can be seen there is a relatively clear space beneath the machine structure which provides ample room for workpiece handling mechanisms. For example, this machine can readily be integrated into a typical tube mill.

Thus, it can be seen that a variety of electron beam welding and tooling is available to meet most production needs. Obviously, the equipment and tooling must be carefully selected so that full advantage can be taken of the many capabilities of electron beam welding in production operations.

CONCLUSIONS

In summary, electron beam welding presents significant advantages over other joining techniques. It is a rapid, precise, controllable process which produces exceptionally high quality welds while minimizing distortion and other effects on the workpiece. Usually, the most precise, highest quality welds can be obtained with the workpiece in a vacuum of about 0. 1 microns. At this pressure deepest, narrowest fusion zones are produced; chemical purity is extremely high; and large working distances can be used. However, for many applications an intermediate vacuum level of 100 to 300 microns is satisfactory. This permits more rapid pumpdown, simplifies vacuum feedthroughs, and usually reduces vacuum equipment costs. It is particularly well suited for single-purpose high-production machinery. Nonvacuum welding, while producing wider fusion zones and restricting working distances, does have the advantage that the workpiece need not be enclosed in a vacuum chamber. Thus, it is more readily adapted to large structures and to high-speed continuous processing.

Electron beam welding is finding wide acceptance in industry. It no longer is restricted to laboratory and relatively exotic uses, but is proving to be an economic

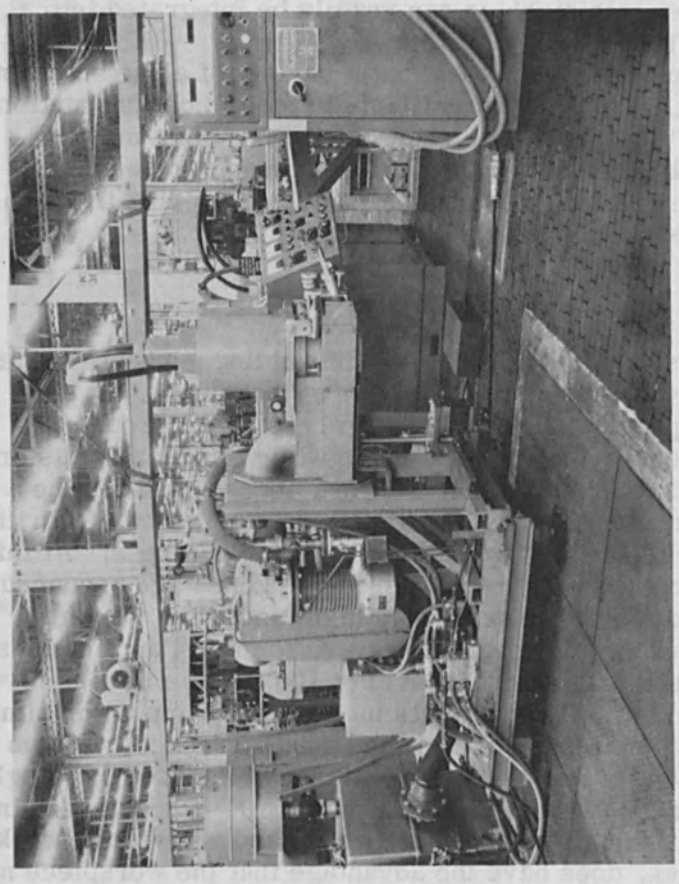

Figure 16. Nonvacuum Electron Beam Welder.

joining process for many ordinary run-of-the-mill applications. However, as with any other process, equipment must be carefully selected and tooled in order to realize the full potential of electron beam welding.

Electron - Beam Welding of Ceramics

N. A. Olshansky, V. M. Mesharekov

Moscow Power Engineering Institute
USSR

Ceramics based on oxides, carbides, borides, etc. are of considerable interest as engineering materials. Many of these materials have high melting points, are chemically resistant at high temperatures, they are heat resistant and have good dielectric properties. A distinguished feature of oxide based ceramics is their resistance to oxidizing atmospheres. One of the most common ceramics based on aluminum oxide is inert with respect to air, water vapor, carbonic oxide, nitrogen and vacuum up to 2,000°K.

Wide application of ceramic materials in various fields of engineering requires the development of reliable methods of joining ceramic articles. At present a number of methods are used for joining ceramics, namely, mechanical joining, pasting and brazing.

The existing methods of joining have some disadvantages. Thus, for example, a mechanical joint does not provide the tightness of butted details, pasting does not ensure the capacity of the joint for work at high temperatures, brazing does not secure the work of the joint at temperatures over 1,300-1,500°K. The presence of solder in co-ordinated metal ceramic brazing seams results in arising additional mechanical stresses which decrease the reliability of the articles.

Development of the methods of joining ceramics by fusion welding will make it possible to avoid the many drawbacks of presently utilized methods.

If successful in welding one may get such a material in a joint which does not differ from the base material in its properties. It should be possible to join ceramic parts of different wall thicknesses, those of complex configurations and also various ceramic materials.

Electron-beam welding is the most likely method of joining ceramic materials. Some research work has been carried out by us in this field.

To study the electrical processes which take place on electron-beam welding of ceramic materials, we carried out experiments to clarify phenomena observed when bombarding ceramics by electrons.

Peculiarities of electron-beam welding ceramics consists in introducing a dielectric unit into the electric circuit. In this case the flow of electrons getting onto the surface of a ceramic article cannot be grounded across the article, as ceramics are perfect dielectrics. Visually, the presence of ceramics in a welding electric circuit results in the defocusing of the beam. While the diameter of a focused beam on welding a grounded metal part is about 1 mm, its minimum diameter on welding a ceramic plate is about 10-15 mm, the form of the spot differing sharply from that one on welding metals. In this case the spot migrates spontaneously along the surface of ceramics. When bombarding ceramics by electrons, the temperature of the article was observed to rise very slowly in spite of a considerable power of the beam - (850-1, 000 watts). A considerable heating up of the electron gun flange took place as well. These phenomena take place due to the interaction of electrons with the charge accumulated on the surface of the plate. The results of experiments on welding ceramics carried out in a Faraday trap with the help of special probes showed that a charge of a considerable value was formed on the surface of the ceramics on bombarding it with the electrons of the beam. On moving away from the place of collision of electrons with the surface the potential decreases in value and there is practically no potential at the distance of 25-30 mm from the centre of the plate. Potential distribution on the probes depending upon the angle of rotation is shown in Fig. 1. In this figure one can see that potential reaches

its maximum value on the probe nearest to the surface of the plate (curve I) when probes are placed in positions close to vertical ones.

In these experiments a stream of electrons moving to the trap walls was observed. Since the potential difference between the surface of ceramics and the trap walls is great, the electrons may have large energies. This explains the intensive heating up of the trap walls and the tantalum diaphragm.

The process of welding "cold" ceramics may be represented in the following way (Fig. 2b). As dielectric properties of ceramics are very good practically there is no current (e_1). It may also be assumed that there are no electrons (e_4) due to fact that a ceramic has practically no free electrons. Thus, the main part in

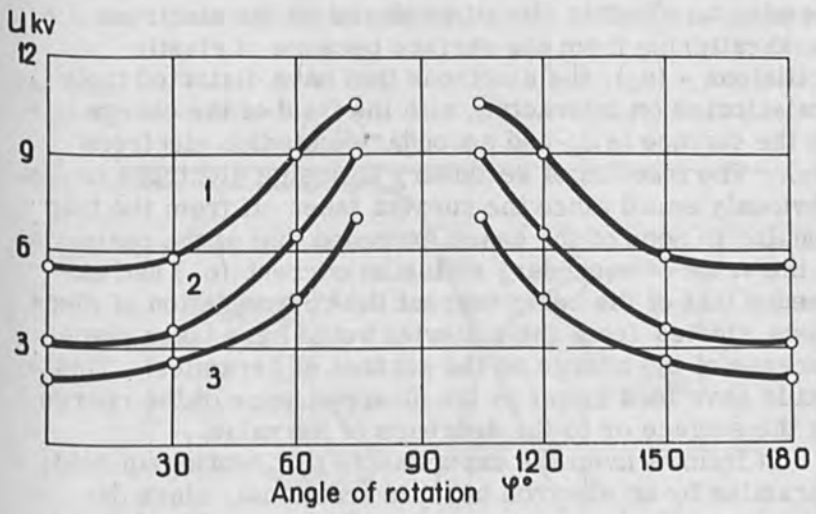

Figure 1. Potential distribution on sounds depending on the angle of rotation; e_1 - conduction electrons, e_2 - secondary electrons, e_3 - electrons scattered due to bumping collisions, e_4 - thermal electrons, e_5 - electrons reflected by the space charge field.

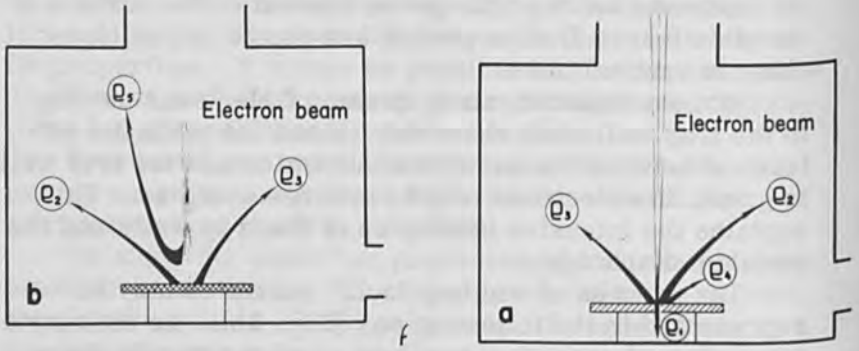

Figure 2. Electron transport paths, (a) on welding metals (b) on welding ceramics.

forming an electric circuit is played by the electrons backscattering from the surface because of elastic collisions - (e_3), the electrons that have distorted their trajectories on interacting with the field of the charge on the surface (e_5), and secondary emission electrons (e_2). The fraction of secondary emission electrons is obviously small since the current taken off from the trap housing in none of the cases exceeded that of the beam. If the value of secondary emission current (e_2) had exceeded that of the beam current the compensation of electrons ejected from the material would have taken place because of the charge on the surface of ceramics. This would have lead either to the disappearance of the charge on the surface or to the decrease of its value.

It follows from the experiments that heating up cold ceramics by an electron beam is irrational, since defocusing of the beam takes place and a considerable part of the electrons do not reach the surface of ceramics because of the reflection of the electrons under the influence of the field of the charge.

The process of electron-beam welding ceramics can only go on normally according to the scheme of welding metals. This makes it necessary to create conditions for taking off the charge from the surface of ceramics. One

of the ways to prevent the accumulation of charge on the surface of ceramics is to heat it up to such a temperature that the current equal to that of the beam could flow through ceramics.

The determination of the necessary preheating temperature at which the normal procedure of electron-beam welding takes place was done according to the scheme given in Fig. 3. Experimental results are given in Fig. 3. From the diagrams it follows that current starts flowing through ceramics at the temperature of about 800°K. In spite of the fact that at this temperature the resistance of ceramics is still high and is of the order of 10^7 ohm/cm current does start flowing between the upper and the lower surfaces of ceramics under the influence of a considerable difference of potentials (of the order of 10-15 kV).

The value of this current is about 1.5 mA. Further, rise in current takes place much more intensively due to a more intensive rise in temperature, since the energy of

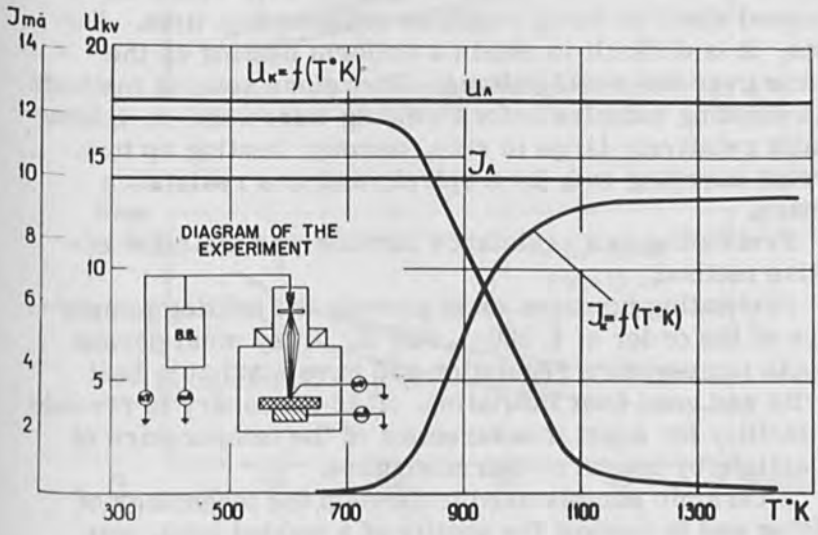

Figure 3. The influence of temperature upon potential distribution on the surface of ceramics, (a) experiment scheme, U_b, I_b - voltage and current of the beam, U_c, I_c - voltage and current through ceramics.

the beam spent on preheating ceramics is used more fully. As soon as the current in ceramics reaches in value that of the beam current the charge on the surface of ceramics disappears and the process of welding ceramics becomes analogous to that of welding metals.

Thus, from the standpoint of electrical processes, to effect the welding of dielectrics with an electron beam it is necessary to preheat articles to take off the charge which prevents the normal procedure of the welding process. As it will be shown below, preheating is necessary to prevent ceramics from cracking.

Experiments on welding small parts with wall thickness up to 1 mm have shown that good results may be obtained and high quality of welded joint may be got using preheating with a defocussed beam.

Attempts to effect welding articles relatively large in size and having wall thickness over 1 mm by using the same technology were not successful. This may be explained by the fact that preheating an article with a defocussed electron beam requires considerable time. Besides, it is difficult to obtain a uniform heating up the article over the whole volume. Therefore several methods of preheating samples before welding were used on welding details relatively large in size, namely, heating up by a current carrying rod, by a spiral, and in a resistance furnace.

Preheating in a resistance furnace was the most effective method.

Preheating furnaces must provide the heating temperature of the order of 1, 800-1, 900°K. They must permit smooth temperature regulation and have maximum heat inertia and good heat insulation. It is necessary to provide the facility for exact measurement of the temperature of the article by means of thermocouples.

A ceramic sample used to develop the technology of welding and to control the quality of a welded joint, was a cylinder made of ceramics containing 95% of alumina. Its outer diameter was 14 mm, its wall thickness - 2. 5 mm, and it was 15 mm long. Further, welded samples were tested for bending strength and the influence of thermal cycle on vacuum tightness and thermal resistance were studied. Macro- and microstructural studies as well as

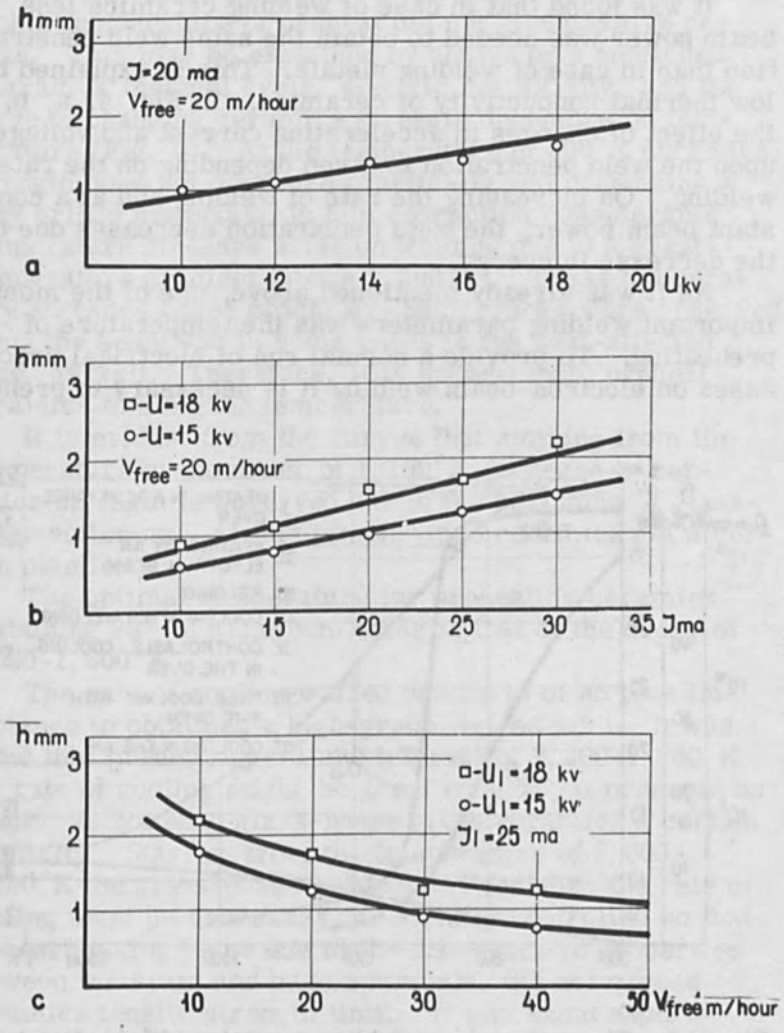

Figure 4. Ceramics weld penetration depending upon:
(a) accelerating current; (b) beam current; (c) welding speed.

X-ray analyses were made and microhardness of different zones of the joint was measured.

It was found that in case of welding ceramics less beam power was needed to obtain the same weld penetration than in case of welding metals. This is explained by low thermal conductivity of ceramics. In Fig. 4, a, b, c, the effect of changes in accelerating current and voltage upon the weld penetration is given depending on the rate of welding. On increasing the rate of welding and at a constant beam power, the weld penetration decreases due to the decrease in energy.

As it was already mentioned above, one of the most important welding parameters was the temperature of preheating. To provide a normal run of electrical processes on electron-beam welding it is necessary to preheat

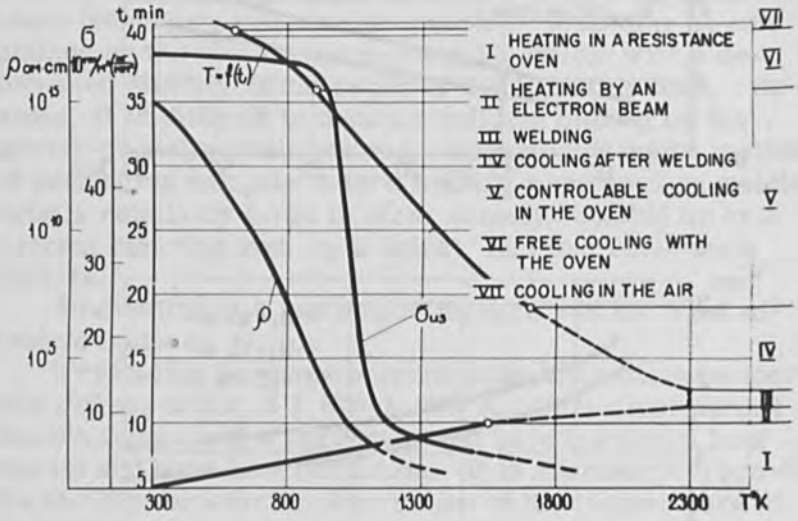

Figure 5. Thermal cycle of welding ceramics 95% Al_2O_3

I. heating in the furnace
II. heating by an electric beam
III. welding
IV. cooling after welding
V. controlled cooling in the furnace
VI. free cooling with the furnace
VII. air cooling.

ceramics up to the temperature of the order of 900°K. However, attempts to get a welded seam without cracks at such a temperature of preheat did not give positive results. This may be explained by analyzing a combined diagram of thermal cycle, electric resisitivity, and the curve of changing ceramics strength depending on temperature (Fig. 5). At the temperature of 900°K ceramics strength does not decrease practically and it remains a very brittle material. In this connection considerable temperature stresses arise on welding due to a great temperature gradient (above 1, 300°K). These temperature stresses cause cracking. Such cracks were observed along the seam and in some cases in the heat-affected zone, as well. Therefore, it is necessary to preheat ceramics to a higher temperature.

It is evident from the curves that starting from the temperature of the order of 1, 100°K decrease in ceramics strength is observed due to the beginning of glass-phase softening. At this temperature ceramics get a certain plasticity.

The optimal temperature for preheating ceramics containing 95% of aluminum oxide is that of the order of 1, 550-1, 600°K.

The rate of cooling welded details is of no less importance in obtaining a high-grade welded joint. It was found that in the temperature interval of 2, 200-1, 700°K the rate of cooling might be great enough. It presents no danger as softened glass-phase gives ceramics a certain plasticity. Starting from the temperature of 1, 600-1, 700°K the glass-phase hardens. Therefore the rate of cooling must be decreased and strictly controlled so that stresses taking place due to the difference in properties between the seam and base materials, did not exceed ceramics tensile strength limit. It was found experimentally that in this temperature interval the rate of cooling had to be about 50° k/min. At temperatures lower than 1, 000°K the rate of cooling may be increased.

Recommended rates of cooling obtained on welding ceramics with aluminum oxide content of 95%, are given in Table I.

Table I.

Temperature Interval, °K	Rate of Cooling
2,250 - 1,700	100° K/min.
1,700 - 1,000	50° K/min.
1,000 - 300	100° K/min.

Petrographic investigations of joints showed that welding resulted in good weldability of base and melted materials. A macrosection of ceramics welded joint is given in Fig. 6a. It is seen in the photograph that a welded seam material formed as a result of melting ceramics, is compact and has no pores and cracks. The seam has a pronounced crystal structure (Fig. 6 b, c). As one can see in the macrograph grains have considerable sizes (Fig. 6d). Parameters for welding samples with different wall thicknesses are given in Table II.

Table II.

Wall Thickness mm	Preheating temperature, °K	U kV	I mA	V m/hr
0.8	1,600	15	12	20
1.5	1,600	15	20	20
3.5	1,600	20	35	20

As a result of experiments made with ceramics having different contents of alumina, it was found that the preheating temperature increased with the increase in alumina content.

The preheating temperature of pure oxides may approach that of roasting which is 0.8-0.9 of melting temperature.

In this connection preheating temperature value is determined by the appearance of a certain ceramics plasticity which in its turn, depends upon the quantity of glass-phase and upon the temperature when the latter

Figure 6. Petrographical studies; (a) macrostructure of welded joint x14, (b) surface of welded seam x340, (c) microstructure of welded seam upper part x85, (d) lower part of welded seam x360.

begins to soften. The preheating temperatures of different types of ceramics can be determined from following expression:

$$T_{pr} = T_{sb} + (350 - 450)^\circ K$$

where

T_{pr} = preheating temperature of welding

T_{sb} = the temperature of glass-phase softening beginning that corresponds to the decrease in ceramics strength.

Thus, for example, on welding alundum with alumina contents of 75% the preheating temperature was about 1, 400-1, 450°K. On welding ceramics with aluminum oxide contents of the order of 95% the preheating temperature was about 1, 550°K for the temperature of glass-phase softening beginning is about 1, 000°K. On welding ceramics having practically no impurities the preheating temperature was chosen to be equal to 1, 850°K, proceeding from the fact that these ceramics acquire plasticity at a temperature of about 1, 500°K.

The choice of the preheating temperature, proceeding from the analysis of strength-versus-temperature diagram, made it possible to get a high-grade welded joint.

To evaluate the properties of the joints obtained tests were made for mechanical strength on bending, for vacuum-tightness, and thermal stability.

Mechanical Strength

Mechanical-strength tests were made on a testing machine. Two butt-welded cylinders were taken as a sample. A sample having a total length of 30 mm was put on two supports and was broken down by the force applied in the middle of it. Test results are presented in Fig. 7.

One of the principal indices of ceramics joint quality is its thermal stability that is the number of temperature changes that it endures without losing its vacuum-tightness.

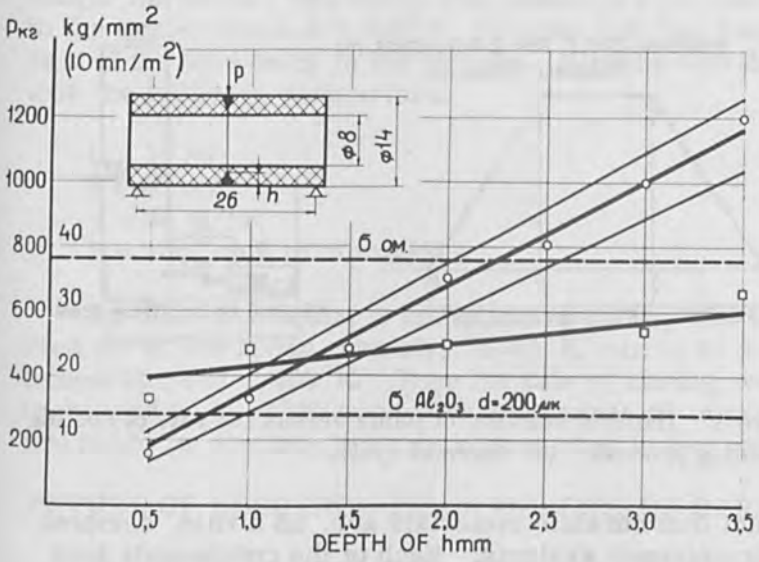

Figure 7. Welded joint strengths at bending test (a) test scheme.

The samples were tested for vacuum-tightness by heating them in a furnace up to the temperature of 1,100°K. After 3-5 minutes' heating at this temperature the samples were cooled in the air. Tests for vacuum-tightness were made after each cycle of heating by means of a helium leak detector. The results of thermal stability tests are given in Fig. 8 versus the rate of cooling after welding in a critical temperature interval. At cooling rate up to 90°K/min and greater it is possible to obtain vacuum-tight articles. Their thermal stability, however, is extremely low due to micro-cracking in the process of cooling after welding. Obviously, the cracks open during thermal stability tests and this is the reason of failure in vacuum-tightness. On welding articles working under conditions of rapid temperature changes one should cool them at a speed not more than 50°K/min.

On the electron-beam welding of ceramic materials processes taking place during melting and crystallization of the molten bath play an important role. This is due to

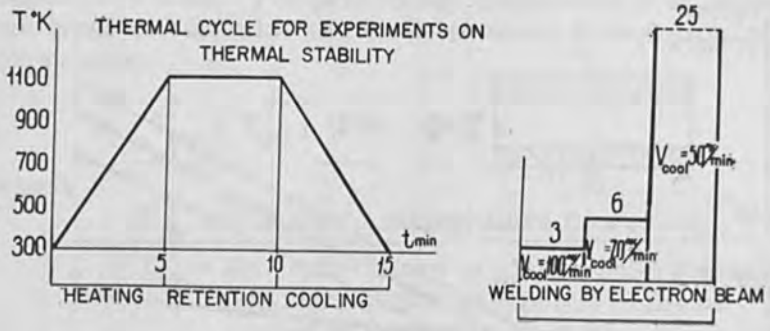

Figure 8. Thermal stability of joints versus the rate of cooling in welding process. (a) thermal cycle.

the fact that ceramic materials are, as a rule, complex multicomponent systems. Each of the components may have a great influence on the welded joint formation when molten bath material hardens.

Ceramic structure is greatly influenced by impurities. This influence tells on the sizes and forms of corundum grains and on formation of new phases. Since the process takes place in vacuum, evaporation of components having low vaporization temperature, is possible. Petrographic analysis of seams showed that they consisted of big crystals of α corundum, there was no glass-phase in the seam while the base material had some amount of glass phase.

The results of testing welded ceramic samples show that joints of ceramic materials having high strength and thermal stability may be obtained by means of electron-beam welding. The technology of welding ceramic materials by an electron beam was also used in manufacturing articles. One of the articles had to work in an aggressive medium at a high temperature and its butt had to have good dielectric properties and be vacuum-tight. The article is a tube 380 mm long, 12 mm in diameter, and its wall thickness is 3 mm. The tube was welded to a massive bell 60 mm long, 48 mm in diameter, with a

wall 4 mm thick. The detail was heated in a furnace up to the temperature of 1,700°K, only the bell itself and a part of the tube being in the furnace. Welding was done with the following parameters:

U = 18 kV.
J = 25 mA.
V = 20 m/hr.
P = 10^{-4} mm of mercury.

As the construction is complicated cooling was carried out at low speed, namely, 15-20°K/min up to the temperature of 1,200°K. Then the rate of cooling was increased up to 50° K/min. The appearance of an article welded by an electron beam is represented in Fig. 9a.

FUTURE OF ELECTRON-BEAM WELDING OF CERAMICS

The study of welded joints shows that electron-beam welding ceramic materials is a highly probable method. It may successfully be used in industry. First of all it may be used for joining ceramic parts operating at high temperature in different aggressive media.

The method of electron-beam welding ceramics may be applied where high dielectric properties are required from the joint.

It is known from the technology of ceramic articles production that it is very difficult to produce articles having great length and small wall thickness (tubes). It is due to the fact that a great reheat shrinkage (up to 20%) takes place during roasting. This causes deformation and wastes because of cracking. Another difficulty in manufacturing long articles is to obtain exact dimensions as the value of deformation greatly depends on the quantity of impurities. Application of electron-beam welding will make it possible to produce long welded articles from relatively short parts, whose manufacture is developed well enough. Successful tests were made in welding alundum tubes of about 300 mm long.

Only the butt zone was heated while the ends of the article were practically cold. As a result of welding a

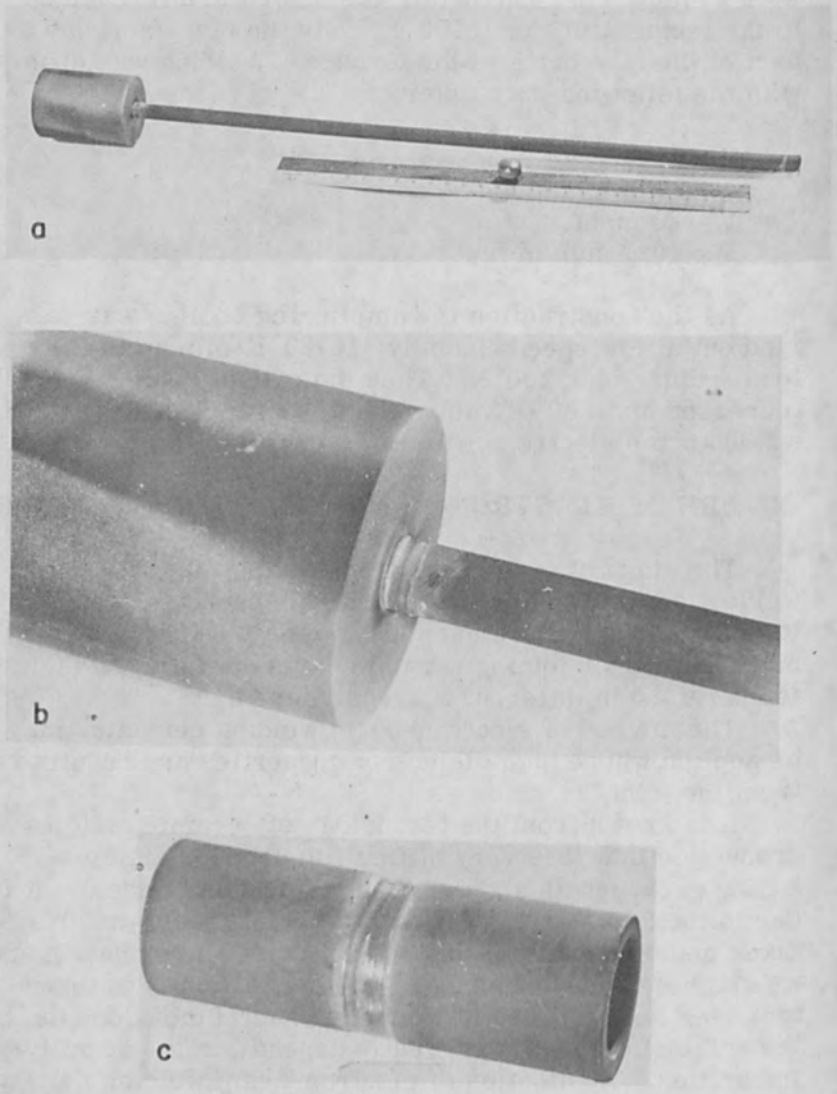

Figure 9. Samples of welding ceramics by an electron beam. (a) welding ceramics with 95% Al_2O_3 content, (b) welding ceramics with 99% Al_2O_3 content, (c) welding ceramics of different types (95% Al_2O_3 content).

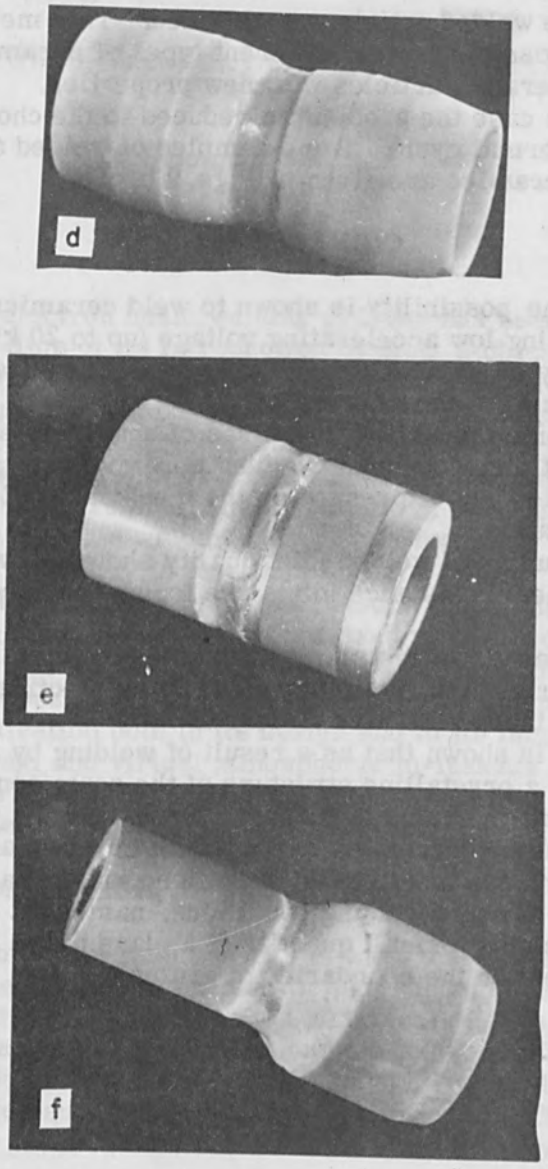

Figure 9. (Continued). (d) welding ceramics of different types (95% and 99% Al_2O_3), (e) electron-beam welded article appearance, (f) welded article appearance

high-grade welded article was obtained. This method makes it possible to weld different types of ceramics and to obtain ceramic articles with new properties.

In this case the problem is reduced to the choice of optimal thermal cycle. Some samples of welded articles made of ceramics are given in Figs. 9 b, c, d.

CONCLUSIONS

1. The possibility is shown to weld ceramics by melting using low accelerating voltage (up to 20 kV). Technology of welding a series of ceramic grades based on aluminum oxide is developed.

2. Some theoretical premises of characteristic features of electron-beam welding ceramics are given and a supposition was expressed on the mechanism of welded joint formation.

3. Studies of welded joint quality show that vacuum-tight and heat resistance joints are formed as a result of welding.

The results of tests for mechanical strength show that the strength of the joint welded by an electron beam is 90-95% that of the base material.

4. It is shown that as a result of welding by an electron beam a crystalline structure of the seam consisting of α-corundum grains is formed. On welding, a two-phase structure ceramics α-corundum crystals are formed in the seam. In most cases there is no glass phase. However, at some welding conditions, namely at a short time of welding a small quantity of a glass phase is probably present on the boundaries of grains.

Medium Vacuum Electron Beam Welding

J. L. Solomon* and H. A. James*

INTRODUCTION

The electron beam welding process has been regarded from the time of its introduction by J. A. Stohr in 1957 to the present time generally as a process which requires and uses a high vacuum environment in order to operate and to produce the welding results which are recognized to be characteristic of this process. Thus, in high vacuum electron beam welding, the magnitude of the pressure present within the welding chamber is less than 1×10^{-3} Torr and generally is less than 1×10^{-4} Torr. To obtain and maintain this low level of pressure (i. e., high vacuum) a vacuum pumping system is required which incorporates diffusion type as well as mechanical type vacuum pumps and which possesses in general a rather substantial degree of sophistication both in its design and in its fabrication so that the real and virtual atmospheric in-leakage of the system is limited to a value consistent with that deemed acceptable in a high vacuum process.

First Considerations

The metallurgical benefits of the exceptionally pure environment which is present in high vacuum electron beam welding are well known. And, historically, it is important to note that this attribute was one of those specifically cited by Stohr in November 1957 when he made the first public disclosure of his new welding process. The benefits of the low level of contamination afforded by high vacuum

*SCIAKY BROS., INC. -Chicago, Ill.

electron beam welding are still of primary importance today with regard to the welding of those materials such as molybdenum, tantalum, etc. which are easily oxidizable or whose weldments exhibit significantly degraded mechanical properties as a result of the presence of only a few parts per million (ppm) of contaminants in the welding atmosphere. However, it has long been recognized that the high degree of atmospheric purity obtainable with high vacuum electron beam welding is neither necessary nor beneficial for many metals and welding applications.

Now, it is necessary that the electron beam be produced and accelerated in a high vacuum pressure environment in order to obtain optimum performance of the electron gun and to generate an electron beam of optimum properties. The source of electrons in an electron gun is a heated metal filament, which is operated at a temperature on the order of 2000°C. The electrons emitted by this filament are energized by an accelerating potential which is applied between the filament (actually, the cathode electrode) and the anode of the gun. This accelerating voltage may be from 10,000 to 60,000 volts in some electron guns. These gun elements are physically separated by a relatively small distance. This interelectrode spacing and its geometry, together with the accelerating voltage applied to the elements, determines the power, power density and the focal geometry of the electron beam. There is always some amount of gas in this interelectrode space, whatever the degree of vacuum may be. If this gas population is too great, then electrical discharges of the high potential may occur across the interelectrode space and thereby affect the gun's production of the electron beam. Thus, for this reason and also in order that the beam power dispersion and dissiptation be minimal, and also to maximize the filament life, it has been found necessary and desirable to provide for the electron gun an operating pressure environment on the order of 1×10^{-4} Torr, or less.

Thus, the obvious step is to provide two pressure environments, one pressure environment for the generation of the electron beam, and a second pressure environment for the use of the electron beam.

The Selection of Welding Chamber Pressure

What then should be the pressure environment surrounding the piecepart to be welded? The answer to this question is dictated by the following two objectives:

1. The weld size and geometry should be similar to that obtained at high vacuum conditions.
2. The weld joint properties should be suitable for the desired service and design level of the weldment.

The first and most obvious idea would be to choose atmospheric pressure as the environment for welding, and thereby eliminate the spatial servitude that is imposed by the need for a welding chamber. This idea has been applied with some success and some limitations. It was found necessary to use extremely high accelerating potentials in the gun chambers, voltages on the order of 100,000 to 200,000 volts, in order to enable the electron beam to transit the atmospheric pressure gun-to-work distance and still arrive at the work with power and power density adequate to do some useful work. At the same time, since the point of impact of the beam was now outside the vacuum, the high energy X-rays produced at this point were not confined. And, finally, due to scattering of electrons by the atmosphere, the dissipation and dispersion of the beam was such that these welds were substantially wider than those produced under 1×10^{-4} Torr pressure conditions, and the power required at the gun in order to penetrate the same depth of material was also greater by a factor of three to five times, approximately.

What welding environment pressure then, if not atmospheric, should be used? The resolution of this question may be found by reference to the experience of arc welding where the effects of atmospheric purity and weld contamination are known. Years of arc welding experience have shown that the contaminant level in commercial quality inert gas (which usually is about 500 parts per million) is adequately low for most welding applications, and indeed that contaminant levels substantially greater than 500 ppm can be experienced in many applications with no detrimental effects upon the weld joint properties.

Now, the pressure exerted by the gases of the ambient atmosphere at sea level and 0°C is given, in various

units, as: one (1) standard atmosphere; 14.7 psia; 29.2 in. Hg; 760 mm Hg; or 760 Torr. The pressure level customarily used for high vacuum electron beam welding is 1×10^{4} Torr, or less. If all the gas species present in a 1×10^{-4} Torr environment are arbitrarily called contaminants, then, relative to the conditions at one atmosphere, the contamination level at 1×10^{-4} Torr is 0.132 ppm. Similarly, the contamination level at 1×10^{-3} Torr would be 1.32 ppm; at 1×10^{-2} Torr, 13.2 ppm; at 1×10^{-1} Torr, 132 ppm; etc. This contamination of the vacuum environment is due to the residual ambient atmosphere and hence it is composed of nitrogen, oxygen, and water vapor in essentially the same proportion as they are present in the ambient atmosphere.

The contamination of inert gases, such as commercially available argon and helium, is principally oxygen and nitrogen, the remainder being oil and water vapor. Two quality levels of inert gases are customarily available: 99.95% pure (500 ppm impurities); and 99.995% pure (50 ppm impurities). Considering then the vacuum level at which an equivalent impurity level obtains, it can be said that electron beam welding at a pressure level of 3.8×10^{-1} Torr provides an impurity level similar to that experienced in arc welding using commercial quality inert gas, i.e., 500 ppm impurity and 3.8×10^{-2} Torr provides the same impurity level as when using the best quality inert gas, i.e., 50 ppm impurities. Thus, by comparison to arc welding practice, the pressure level for medium vacuum electron beam welding has been evaluated and deduced to fall within a range of values whose upper limit may be taken as 3.8×10^{-1} Torr, generally, but this limit may be lowered to 3.8×10^{-2} Torr in cases where weld metal purity equivalent to best arc welding practice is required.

However, other considerations in addition to weld metal purity may influence the selection of the pressure for medium vacuum electron beam welding. Recall now that the other aforestated basic objective is to produce welds at medium vacuum that are similar in size and geometry to those produced under high vacuum conditions. It is apparent that this objective in effect instructs one to choose not only a welding chamber pressure but also such initial beam power and power density characteristics as

may be necessary in order to provide a power and power density at the workpiece which are similar to those obtained under high vacuum conditions.

An electron beam in passing through a gas is affected in two ways by the gas density, and both these effects are due to scattering of the electrons of the beam due to collisions between the beam electrons and the gas molecules. The two effects are loss of power and lower of power density, and of these two effects the loss of power density is by far the more important effect.

The magnitude of these effects depends upon the number and kinds of collisions that the electrons undergo in their passage through the gas. The number of collisions depends upon the length of the beam path in the gas and upon the length of the mean free path of an electron in the gas. The mean free path, in turn, depends upon the scattering cross-section of the gas molecules; and the scattering cross-section of the gas molecule depends upon the type of gas and the velocity of the electron. It has been found that from a few hundred electron volts up to about one-hundred thousand electron volts that the scattering cross-section varies inversely as the square of the electron velocity or, that is, inversely as the electron beam voltage. The mean free path is also a function of the particle density, that is, the pressure of the given gas at a given temperature. A plot of the mean free path of low voltage electrons as a function of gas pressure is given in Fig. 1 for air.

For convenience, electron scattering may be classified into three categories: single, plural, and multiple. In multiple scattering every electron experiences such a multiplicity of deflections that the total effect may be summed in accordance with the Theory of Errors, thereby leading to a Gaussian distribution. Plural scattering and its effects are less well definable since here each electron is deflected more than once on the average, yet not often enough to allow the application of the Theory of Errors and thereby to permit assessment of the effect of these deflections.

In addition, some electrons will be scattered completely out of the beam; however, the number of electrons experiencing this type of scattering will be relatively few. Furthermore, at the pressures and voltage herein of

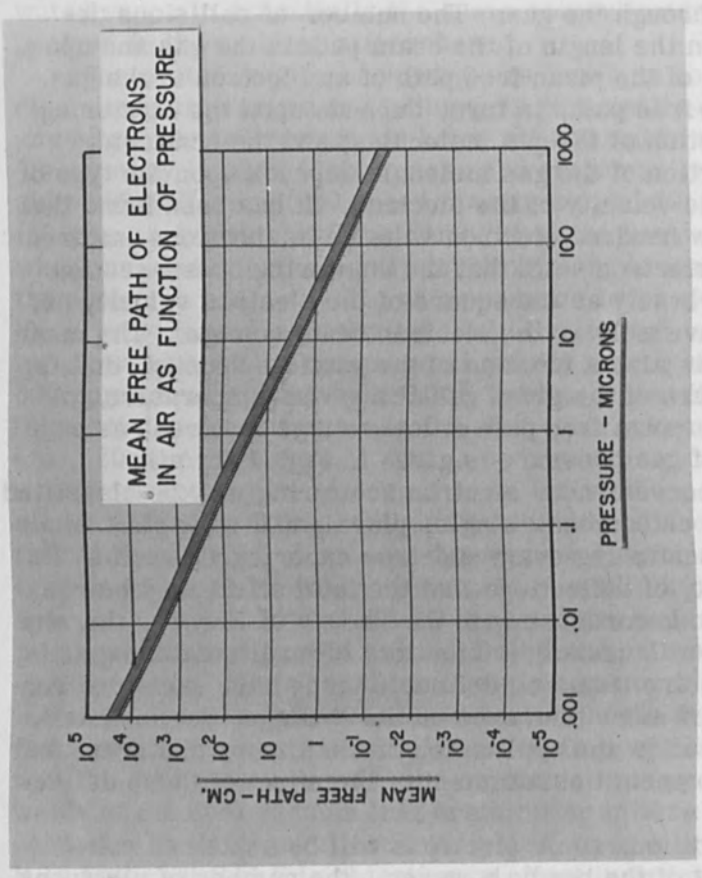

Figure 1. Mean Free Path of Electrons in Air as a Function of Pressure.

interest, the energy lost due to ionization was found to be negligible; the chief effect of scattering under the conditions herein of interest is to gradually increase the beam diameter (and thus the beam area) and thereby correspondingly to decrease the beam power density.

Accordingly, it is important to minimize dispersion of the electron beam by reducing the pressure to some reasonable level. It is interesting to note that at 760 Torr the mean free path of a gas molecule is on the order of five millionths of a centimeter, but at a pressure of 1×10^{-3} Torr, the mean free path is 5 centimeters, or 1 million times greater; and at 1×10^{-1} Torr, the mean free path of a molecule of gas is 10 thousand times greater than at one atmosphere. The effect of pressure on the mean free path and quantity of gas molecules is shown for air in Fig. 2. As the beam dispersion is directly proportional to the density of the gas, and as weld penetration is inversely related to the beam size, it can be seen that the beam dispersion will decrease as the pressure decreased, with the result that weld penetration will increase. It can be concluded, therefore, that at some intermediate pressure below atmosphere pressure, the melting efficiency of the beam can be approximately the same as that obtained under conditions of high vacuum, or at least adequate to produce welds that are characteristic of the process.

Experimental Medium Vacuum Welding

Therefore, the work of concern here is first to produce an electron beam within a high vacuum chamber and then to bring it into another chamber held at some moderately low pressure. This concept is shown schematically in Fig. 3. At some point in the system, the beam must pass through a transition zone from the high vacuum environment of the gun chamber to the medium vacuum environment of the work chamber. As the electrons move to the point of egress, the beam encounters first, extremely rarified gas at 1×10^{-4} Torr, and then later denser gas at a pressure of 1×10^{-1} Torr. The requirements and techniques for producing, accelerating and concentrating the electrons within the vacuum are known factors, as Dr. Stohr pointed out nearly ten (10) years ago. These known factors lend

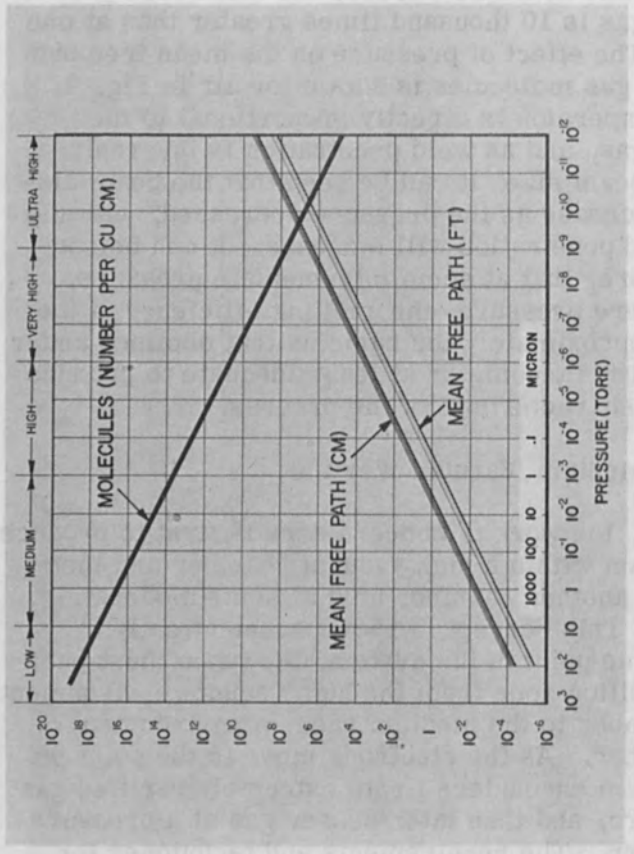

Figure 2. Effect of Pressure on Mean Free Path and Density of Air Molecules.

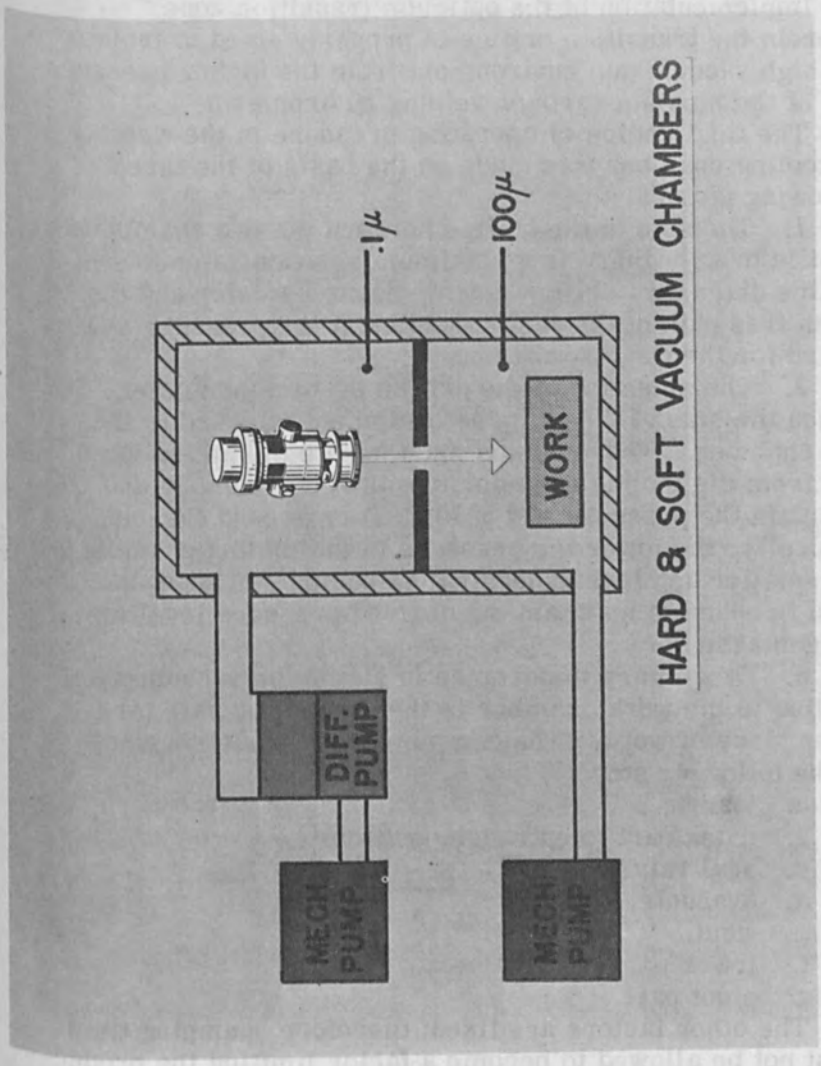

Figure 3. Schematic Illustration of Medium Vacuum Welding Equipment.

themselves to theoretical and empirical analyses of voltage requirements and the contingencies of electron optics. One new factor has been introduced; this is the design and implementation of the optimum transition zone, wherein the transition orifice is properly sized to isolate the high vacuum gun environment from the higher pressure gas of the medium vacuum welding environment.

The final choice of operating pressure in the welding or tooling chamber was made on the basis of the three following factors:

1. The size of the orifice between the two chambers. That is to say, there is an optimum relationship between orifice diameter, orifice length, beam diameter and the mean free path of the gas molecules at the pressure selected for the welding chamber.

2. The selection of the orifice system then determines the size of the pumping equipment attached to the gun chamber. These pumps must handle the migration of gas from the tooling chamber into the gun chamber and maintain the pressure of 1×10^{-4} Torr around the gun. Naturally, the lower the pressure in the tooling chamber, the smaller and less expensive the pumps that must be used in order to maintain the desired pressure level in the gun chamber.

3. Of primary importance in sizing the vacuum pumps applied to the work chamber is the production rate for a given piece of work. The complete work cycle consists of the following steps:

   a. load,
   b. index part to entrance position,
   c. seal valve to part,
   d. evacuate,
   e. weld,
   f. lower part from valve,
   g. eject part.

The other factors are fixed; therefore, pumping time must not be allowed to become a factor limiting the production rate.

Experiments have shown that the beam configuration that produces the preferred weld geometry is not appreciably altered by pressures as high as 5×10^{-2} Torr. Figure 4 shows welds that have been produced at high

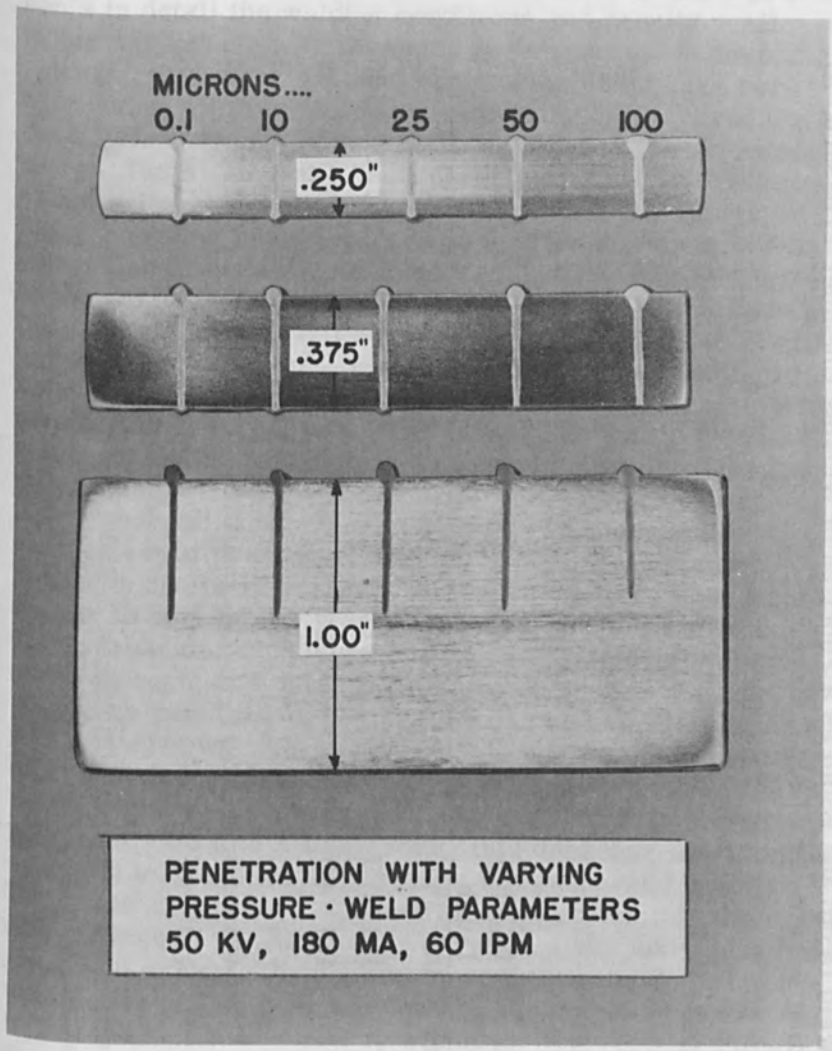

Figure 4. Transverse Cross-section of Medium Vacuum Electron Beam Weld Specimen showing effect of several pressure levels upon weld penetration depth.

Table 1. Weld Depth and Width as a Function of Welding Chamber Pressure, All Other Welding Parameters Held Constant

E_B = 50 kV I_B = 100mA $\dot{S}$ = 60 in/min

h_{GW} = 2.0 in. I_F = 5.6A Material: 304 Stainless Steel

Pressure	D Weld Depth		Weld Width* at Top Surface	at Nailhead Base	W** at 0.5D	D/W		D x W	
(milli Torr)	(in)	(%)	(in)	(in)	(in)	(-)	(%)	(in^2)	(%)
.1	.468	100	.046	.026	.026	18.0	100	.0122	100
10	.456	97	.052	.028	.026	17.5	97	.0119	98
25	.456	97	.062	.026	.026	17.5	97	.0119	98
50	.444	95	.070	.028	.026	17.1	95	.0115	94
100	.414	89	.082	.028	.026	16.0	89	.0108	88

*Weld Width in all three part thickness: .250", .375", and 1"
**Weld Width in only 1" thick material

vacuum, 1×10^{-4} Torr and at four values of medium vacuum: 10, 25, 50 and 100×10^{-3} Torr. Table 1 presents in detail the welding conditions and results. All welds were made with the same power and the same focal setting. The same depth of penetration could have been obtained at all pressures if desired simply by increasing the applied power. Although the depth could be re-established, the width of the "nail head" would still be relatively great at the higher pressures, as this is a function of elastic angular beam scatter, as well as the loss of beam power due to inelastic scattering. Looking then in Fig. 4 at the partial penetration welds made in the 1" thick stainless steel block, it will be observed that penetration depth is reasonably constant, within 5%, from high vacuum up through the weld made at 50×10^{-3} Torr. The penetration depth, however, decreased by 11% at 100×10^{-3} Torr weld which indicates that some of the beam power is beginning to be dissipated in the increased population of the gas. Although welding experiments have been successfully carried out at pressure levels up to 1 Torr, the most judicious choice of pressure in the welding chamber would appear to be 1×10^{-1} Torr, based on an optimum balance of the preceding considerations. The configuration of an electron beam at 1×10^{-1} Torr can be seen in Fig. 5.

Some variation in penetration can be expected in the process even when all the welds are made at high vacuum. However, it is significant that the change in penetration is in the expected direction, i. e., decreasing with increasing pressure. Up to 5×10^{-2} Torr, this decrease is within the expected tolerance of the system; however, at 1×10^{-1} Torr, the 11% change in penetration indicates that the curve of the graph of penetration vs. pressure has taken a radical change in slope. It can also be noted than the "nail head" or the size of the top of the weld at the top surface has also increased at 1×10^{-1} Torr, although, the width of the stem of the weld measured below the "nail head" is approximately the same (.026") throughout the pressure range reported in Table 1. This is also true of welds made at higher pressures up to 1 Torr, which has been the limit of the tests.

For these reasons then, 5×10^{-2} Torr is the pressure level which meets all the tests of practicability and economy.

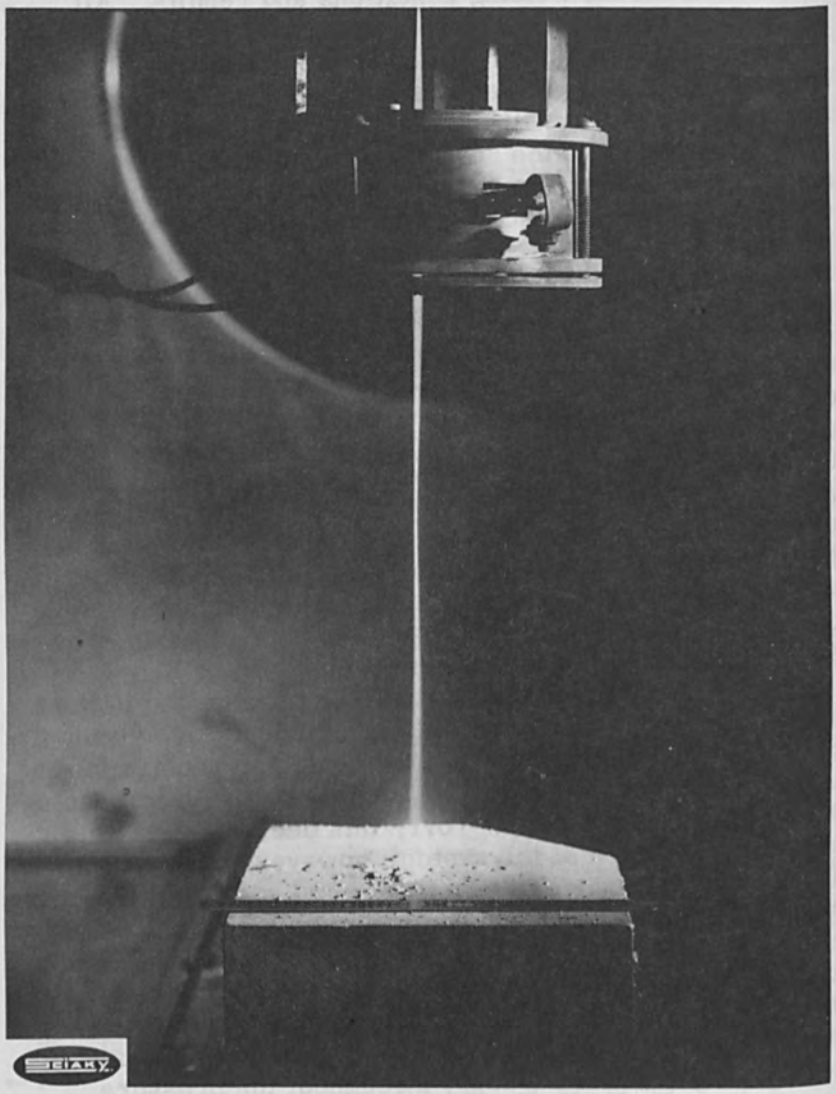

Figure 5. The Electron Beam at a Pressure of 1×10^{-1} Torr.

Certainly, the mode of welding at medium vacuum will be used throughout the range of 1×10^{-3} to 1 Torr--depending upon the demands of the product being welded.

Welds having 100% penetration are seen to be less sensitive to the effects of various pressure levels. For example, the same welding parameters that were used to produce the partial penetration welds in the 1" material were also used to produce 100% penetration welds in both .250" and .375" thick materials under the same variations in pressure level. The results of this work can be seen in Fig. 4 and in Table 1.

While the foregoing may seem reminiscent of electron beam welding at atmospheric pressure, a comparison of the magnitude of pressure differential between the gun and the exit nozzle, at atmospheric pressure, must be considered. When considering the use of an electron beam in atmosphere, a high voltage (180kV) beam is going from an environment of 1×10^{-4} Torr to an environment of approximately 760 Torr; whereas, in the case of welding in medium vacuum, we are discussing a low voltage (60kV) electron beam developed at a pressure of 1×10^{-4} Torr going into a second chamber to weld at approximately 1×10^{-1} Torr. The first case (electron beam in air) represents a pressure ratio of 7.6 million times; the second case represents a pressure ratio of only 7.6 thousand times.

In view of the discussion above, it might be thought that any gas at all would cause beam scatter and enlargement. This is not necessarily true--neglecting the gun for the moment, it must be remembered that the electron beam itself never exists in total vacuum while welding, even when the system is totally enclosed within a vacuum chamber at 1×10^{-4} Torr; for when the melting begins, vapor is discharged from the molten metal at reasonable high velocity, which increases the pressure locally at the point of the beam impingement to some high unknown value.

It is known that in both a theoretical sense and in a practical sense, characteristically narrow and deep electron beam welds are produced (by proper equipment) at all pressures lower than 1×10^{-4} Torr, and that narrow welds are not usually produced at 760 Torr (ambient atmospheric pressure). Thus, the pressure limits estab-

lished by existing data are: 1×10^{-4} Torr is adequate, and 760 Torr is inadequate.

The experimental equipment employed to make the welds in Fig. 4 is itself shown in Fig. 6. Essentially, this equipment consists of a small vacuum chamber contained within a larger vacuum chamber. The chambers are fixed in their relation to each other. The pressure in each may be varied independently. The electron beam gun is contained within the inner chamber and is maintained at all times at a pressure not exceeding 1×10^{-4} Torr. The material to be welded is placed in the outer chamber whose pressure level can be adjusted to any value desired. The work is fixtured to a moving platen, which moves beneath the electron beam issuing from the gas chamber; thus, providing the relative motion for controlled welding speed.

Applied Medium Vacuum Welding

To attain a high vacuum, e. g., 1×10^{-4} Torr, requires the pumping of both the volume and the surface area of the vacuum chamber and its contents. The volume is pumped by the mechanical roughing pump and the surface area of the chamber, the tooling, and of the piecepart can be thought of as being pumped by the diffusion pump (see Fig. 7). Basically, however, the important consideration is the time required to evacuate the chamber to the high vacuum level.

Fortunately, it is almost axiomatic that pieceparts which are produced in large quantities are also reasonably small in size. It is uneconomical to open and close the chamber and to pump down the chamber for each individual piecepart. Therefore, the first attempts to adapt the electron beam welding process to commercial use was by the batch-loading of a large number of small parts in multiple fixtures into the vacuum chamber where they were then sequentially welded by manipulating each part by some form of remote positioning device to produce the desired weld path. This might mean either a simple or complex form of programming to move the beam from piece to piece and to trace the weld path. When one considers that the individual pieceparts must be independently fixtured, it is obvious that a batch of 100 parts might require

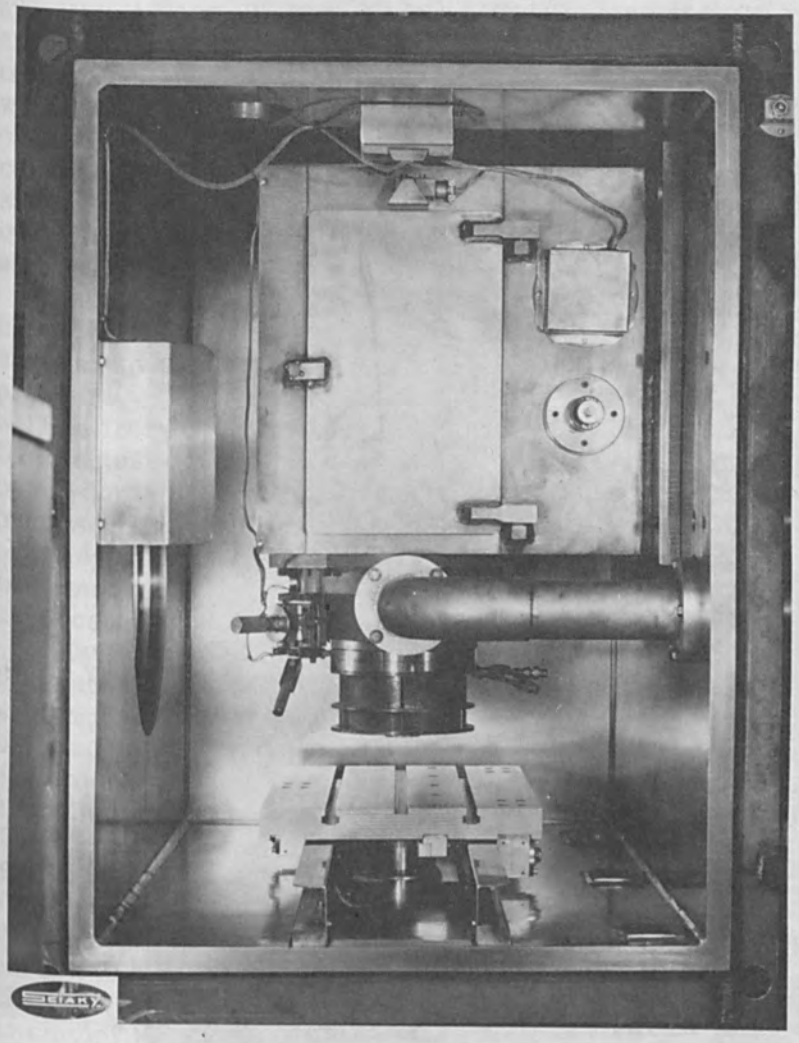

Figure 6. An Experimental Machine for Medium Vacuum Electron Beam Welding.

Figure 7. The Regime of Vacuum.

100 fixtures of great dimensional accuracy. Remote manipulation of a piecepart, either simple or complicated, locked up within a vacuum chamber is a difficult procedure, and at times, a frustrating problem. The electron beam is extremely small; therefore, alignment of the beam to the weld joint is extremely critical. Optical alignment of each of the 100 parts in the batch load is time consuming and cannot be called a high production technique. What is saved in vacuum pump-down time is lost in the multiplicity of problems involved in remote manipulation and remote alignment.

Currently, general purpose or batch-loaded electron beam welding vacuum chambers must be pumped to a vacuum level of 1×10^{-4} Torr, starting from atmospheric pressure. The required time for this pumping operation will be from five minutes for a small chamber, to 15 to 20 minutes for an extremely large chamber. During this pump-down time the equipment is, for all practical welding purposes, inactive. It must be remembered that this pumping time is expended each and every time the chamber is opened and closed to take the entry of a single or batch of pieceparts.

Having now examined the problems of cost and production rate associated with general purpose electron beam welding machines, the elements of an electron beam welding machine will now be examined to see how the cost of equipment may be reduced while, at the same time, increasing the production rate of small size production parts. The design of the electron beam gun cannot be changed appreciably; however, something can be done about the other elements of the system. As a beginning, the size of the vacuum chamber can be reduced so as to be just large enough to house the electron beam gun. With a small chamber surrounding the electron beam gun, it is possible to employ an extremely small vacuum pumping system that will be capable of producing a suitably high vacuum of 1×10^{-4} Torr in the gun region only; this vacuum system will consist of a small mechanical roughing pump (or backing pump) and a small diffusion pump.

Consider now the welding of one piecepart at a time: this piecepart can have its own little vacuum chamber (a simple vacuum cavity in the tooling) which is just large enough to clear the piecepart with an absolute minimum of

excess volume. Further, this small cavity shall be evacuated to a pressure level in the medium vacuum range of 1×10^{-2} to 1 Torr--the particular values depending upon the application and the considerations previously discussed. Conveniently, this pressure level can be reached using only mechanical pumps which, because of the small size of the cavity, can be of small size also. Standard roughing pumps can be used to evacuate a given size of cavity in a fraction of a second, or combination roughing and blower pumps can be used to evacuate large volumes in the same time. The use of only mechanical pumps provides other non-obvious advantages: e. g., no expensive and time-consuming valve sequencing is required, as would be the case in combination roughing and diffusion pump systems.

In the system just described, the pieceparts are loaded into the "nest" or fixture one at a time, in atmosphere, and automatically sequenced through the machine. It is true that this concept limits the size and types of parts that can be welded, and the type of joints that can be used; however, machines using this system concept have been designed to handle a variety of pieceparts: e. g.,

1. 36" of linear weld at a production rate of about 120 pph;
2. annular welds varying from 1" to 3" in diameter, on the same piecepart, at 120 pph;
3. spot welds made at 1,000 pph;
4. small annular welds at 750 pph;
5. large castings weighing 75 pounds welded at 10 pph, etc.

This type equipment falls into the category of the special purpose welder, as opposed to the general purpose welder. The basic machine is standard, as shown in Fig. 8, having always the same elements of gun, gun vacuum system, high voltage power supply sized to fit the intermediate job, and the necessary instrumentation and electrical interlocks. The tooling on the other hand is designed and built to fit a specific piecepart, or group of very similar pieceparts.

Although quickly interchangeable tooling can be added to this type of equipment, the machine is primarily

Figure 8. A Production Machine for Medium Vacuum Electron Beam Welding.

intended for that segment of industry that can justify the assignment of a specific machine solely to the mass-production of a specific piecepart during the design life of that product. The standard portion of the machine may be adapted and made use of with a new set of tooling for a model change.

CONCLUSION

It is apparent that the concept of welding at higher pressures than 1×10^{-4} Torr can be more economically implemented at the medium vacuum level, rather than attempting to weld at full atmospheric pressure. Welding at atmospheric pressure, which at first look appeared desirable, has its own field of application but, in general, suffers from increased weld size, X-ray generation, lower weld quality, and generally higher cost. Welding at medium vacuum extends the process to the commercial application field by providing lower equipment cost, higher production rates, simplicity of tooling, and weld quality and characteristics which are competitive with hard vacuum electron beam welds.

(Ed.) The reference to X-ray generation in connection with welding in atmospheric pressure above is of no consequence. All electron beam welding machines exceeding 22 kV generates X-rays. No industrial enterprise today permits usage of X-ray emitting facilities without protection and whether a machine generates little or more X-rays is irrelevant to its use without harm to its users. To this writer the above reference reminds only of the futile argumentation as part of low vs high voltage electron beam welding controversy in the early sixties.

Applications of Electron Beam Generated in Gas Discharges

J.W. Davis, E.A. Pinsley and A.P. Walch

United Aircraft Research Laboratories
East Hartford, Connecticut

INTRODUCTION

Certain classes of cold cathode gas discharges can be used to generate high energy (>1 kev) electron beams at intermediate ambient pressure levels. Two types of discharges appear particularly suitable for electron beam heating applications: 1) the abnormal glow discharge - in which the ambient pressure is adjusted to a level such that the cathode fall distance is small compared to cathode dimensions, and 2) the hollow cathode abnormal glow discharge - in which the cathode fall distance is adjusted to a value comparable to the dimensions of the cathode. In each type of discharge efficient electron beam heating at a workpiece can be attained because a large fraction of the applied voltage drop occurs in the vicinity of the cathode. An objective of this work was to develop cathode configurations which provide localized heating over extended focal lines and curves at sufficiently high efficiencies such that the majority of the discharge power appears at the workpiece. The discharges considered operate at relatively high ambient pressures (10^{-3} to 1 torr) and high electron energies. Accordingly, the workpiece need not constitute the anode since it can accept ions from the discharge, which combined with the emission of electrons from the workpiece surface (either due to secondary emission, or in some cases, thermionic emission), is sufficient to close the circuit by conduction through the weak ambient plasma to a remotely located anode.

These factors suggest that a high-voltage cold-cathode discharge of extended geometry can be an extremely flexible and versatile tool in performing a number of materials processing and joining applications. The present investigation was undertaken to evaluate the more promising types of discharges in terms of their operating characteristics, efficiency, focusing, and control. Particular attention has been paid to welding complete seams, diffusion bonding, crystal growing by the floating zone technique, and vacuum brazing.

GENERATION OF ELECTRON BEAMS IN GAS DISCHARGES

The structure and potential distribution of the region adjacent to the cathode of a low pressure glow discharge are shown schematically in Fig. 1. Essential features of such discharges have been investigated extensively; detailed reviews are given in Refs. 1, 2 and 3.

As current increases the discharge passes from the normal to the abnormal glow regime. The abnormal glow is characterized by emission over the entire cathode surface and a positive slope to the voltage-current curve. Electrons are released from the cathode by a variety of nonthermionic processes including positive ion bombardment, photoemission, and emission resulting from the impact of fast neutrals and metastables. These electrons are emitted at low energy from the cathode and are accelerated in a narrow "cathode fall" region, d_c, through a potential difference, V_c, which is very nearly equal to the applied voltage. It has been observed [4] that nearly all of the electrons entering the negative glow in a strong (i.e. high voltage) abnormal flow discharge do so at energy eV_c, and that the lateral extent of the negative glow region, L_g, is approximately equal to the range of electrons at energy eV_c in a gas of equal pressure and composition. Hence the beam-like character of the electrons emanating from the cathode can be exploited in electrostatically focused devices provided that working distances and cathode dimensions are small compared to L_g and large compared to d_c. Under such circumstances equipotential surfaces lie parallel to the cathode and electrons emitted from the cathode closely follow straight line trajectories normal to the

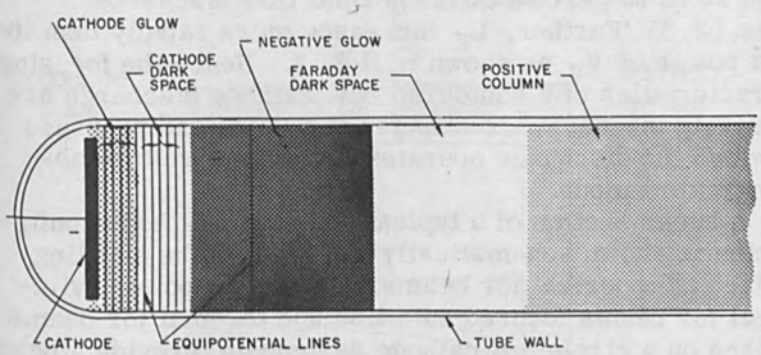

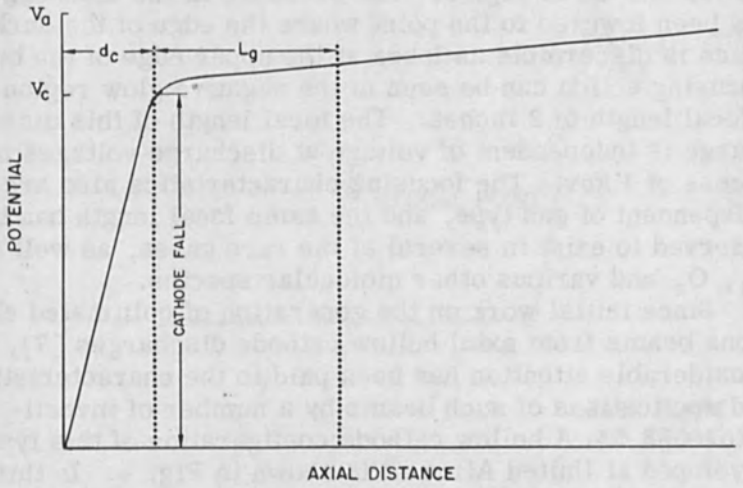

Figure 1. Structure and Potential Distribution of a Glow Discharge.

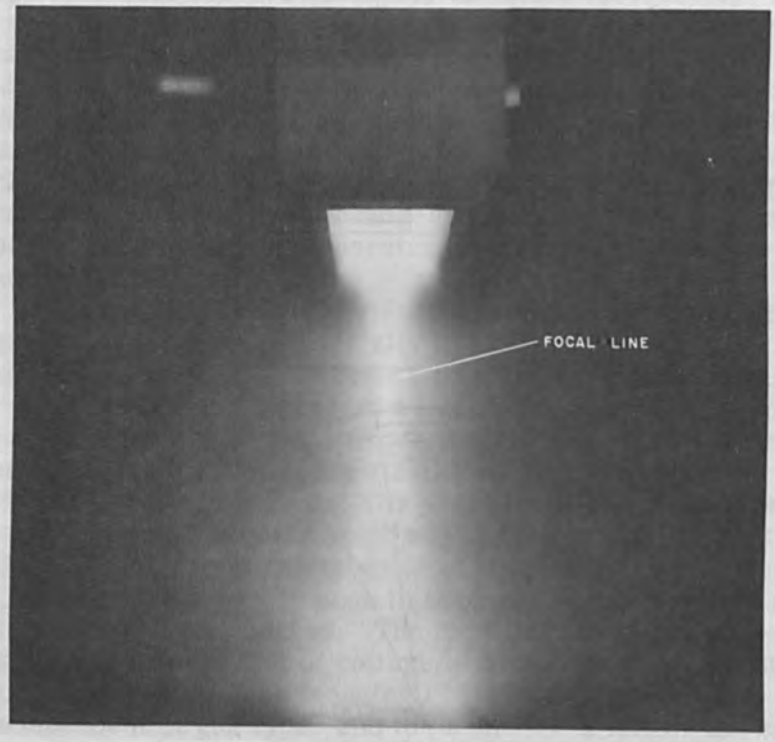

Figure 3. Linear Contoured Cathode with Electron Beam Focusing to a Line in Negative Glow Region.

major problems with this type of cathode are associated with the sensitivity of its voltage-current characteristic to changes in ambient pressure and its susceptibility to spurious arcing and transition to an arc-like mode of operation. The former problem has been solved by the development of an independent magnetic field current control (Fig. 4) which can be used to provide constant power input to a workpiece under conditions of changing ambient pressure. The problem of transition to an arc mode is now the major limitation of this type of hollow cathode.

It has been found that the high-voltage hollow cathode processes can be applied to the generation of beams of

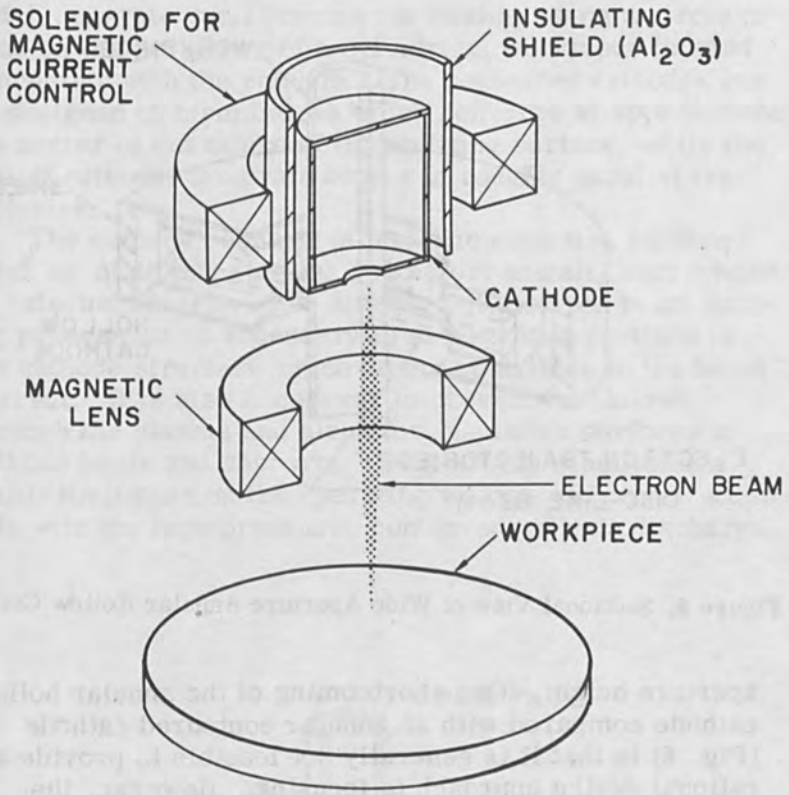

Figure 4. Axial-Beam Hollow Cathode with Magnetic Current Control.

more complex geometry and that spatially symmetric emission can be obtained over a wide range of ambient pressures and power levels. A particularly promising configuration for many applications is the annular hollow cathode shown schematically in Fig. 5. This cathode is generally toroidal in shape with an aperture around the inner periphery. As in the case of the axial hollow cathode, electron acceleration occurs in a region in the vicinity of the aperture over dimensions comparable to the

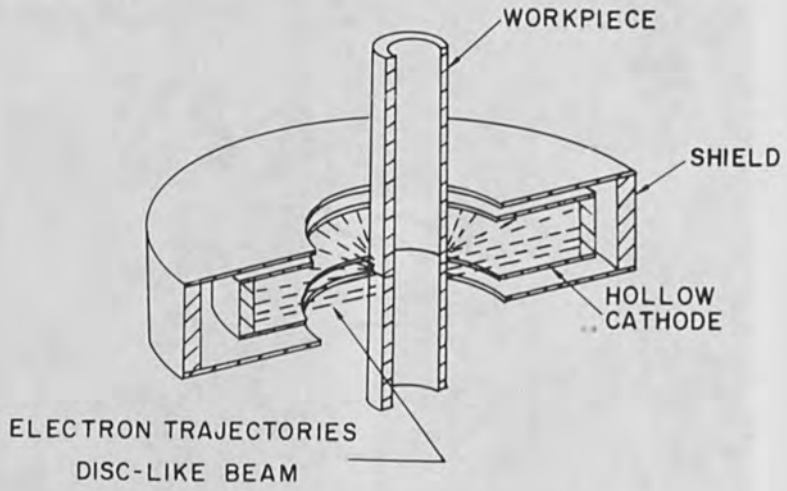

Figure 5. Sectional View of Wide Aperture Annular Hollow Cathode.

aperture height. One shortcoming of the annular hollow cathode compared with an annular contoured cathode (Fig. 6) is that it is generally not feasible to provide a rational design approach to focusing. However, the beam emitted by the hollow cathode is in the shape of a disc with a relatively long depth of field. With the beam directed radially inward the power density does increase with radius.

CATHODE DEVELOPMENT

Hollow and contoured cathodes have been tested to date in three different configurations. These configurations comprise (1) axial geometries (Figs. 7 and 8) which generate pencilform or conical, axially-symmetric beams to produce spot heating on a workpiece, (2) linear (or two dimensional) geometries (Figs. 9 and 10) which generate beams of constant cross section over the length of the cathode for heating along a line or zone on a planar

workpiece, and (3) annular geometries (Figs. 5 and 6) which generate radial beams for heating along a circle or zone on the periphery of a cylindrical workpiece located concentric with the cathode. The contoured cathodes can be designed to form beams which converge at approximately the center of curvature of the emitting surface, while the hollow cathodes generate beams of roughly parallel trajectories.

The cathodes consist of metallic emission surfaces (such as stainless steel or refractory metals) surrounded by external shields. For an efficient electron beam heating process, it is necessary to shield those portions of the cathode structure which do not contribute to the beam current. It is also necessary to prevent breakdown through the plasma and along the insulating surfaces at cathode leads and supports. Such arcing constitutes a major limitation on the operating voltage and power attainable with the high pressure, contoured cathode discharge.

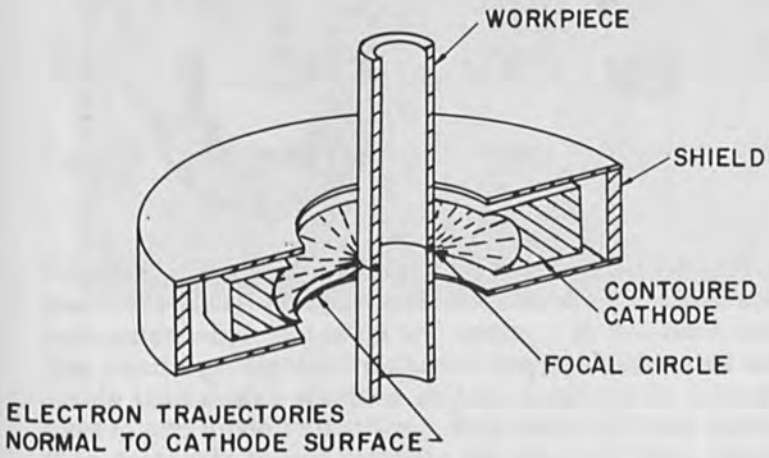

Figure 6. Sectional View of Annular Contoured Cathode.

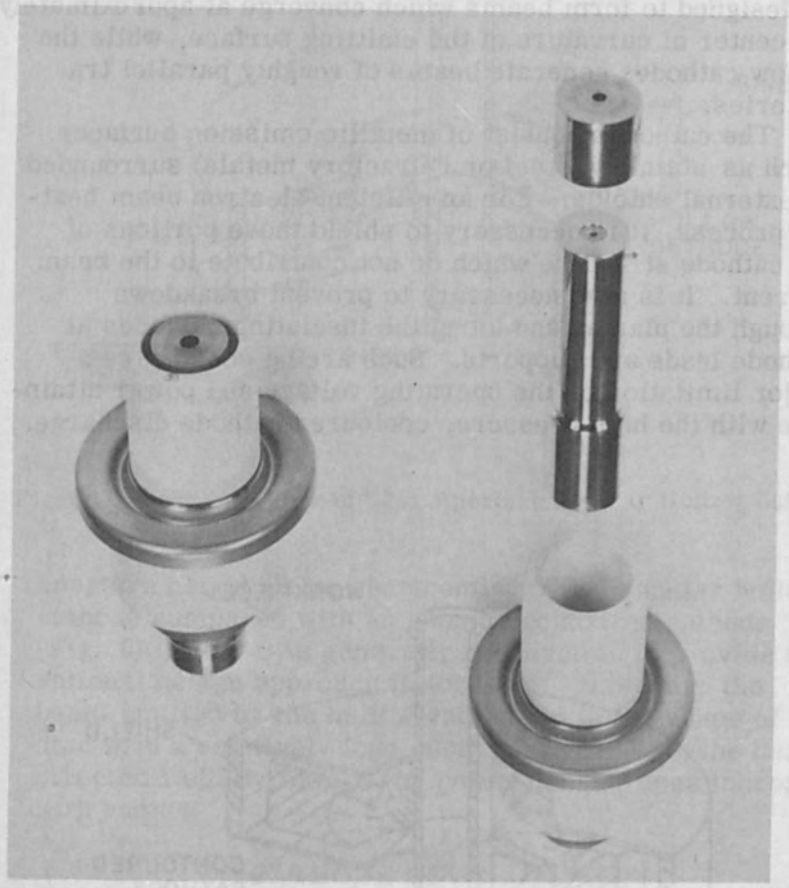

Figure 7. Axial-Beam Hollow Cathodes; 1-in. dia.

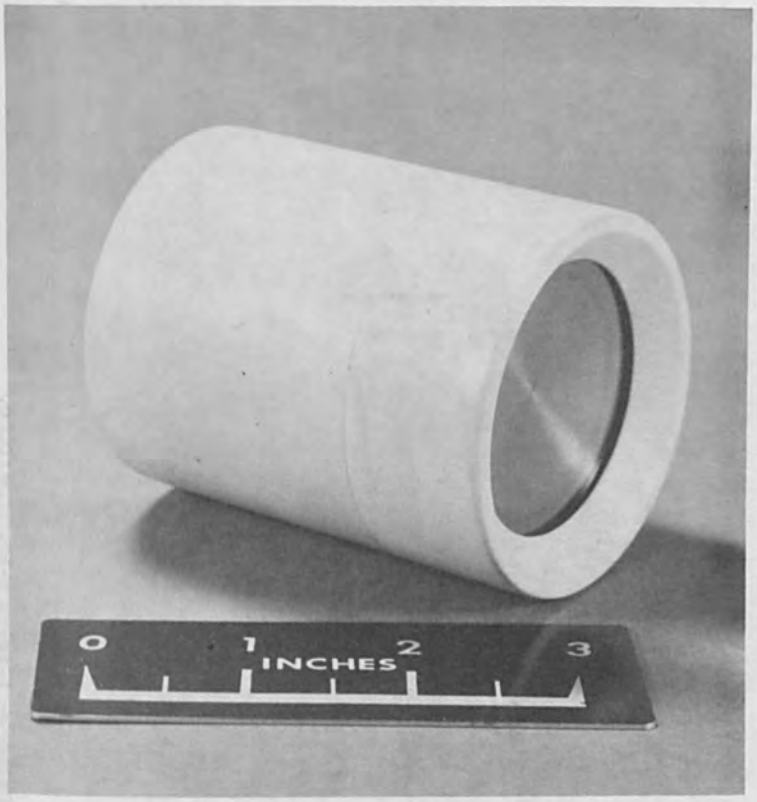

Figure 8. Axial-Beam Contoured Cathode; 2-in. Focal Length.

Shielding the cathode surface with an insulating ceramic at distances small compared to the cathode fall can suppress both extraneous emission and arcing. It has been found that insulator-shielded cathodes operate somewhat more stably than metal-shielded cathodes and resist a tendency toward arc mode transition. However, in many instances, it is desirable to use metallic shields with their attendant simplicity in fabrication and reduction in cost rather than dielectric shields. Ceramic shields generally have been used with the axial and some linear cathodes while metal shields have generally been used with annular cathodes.

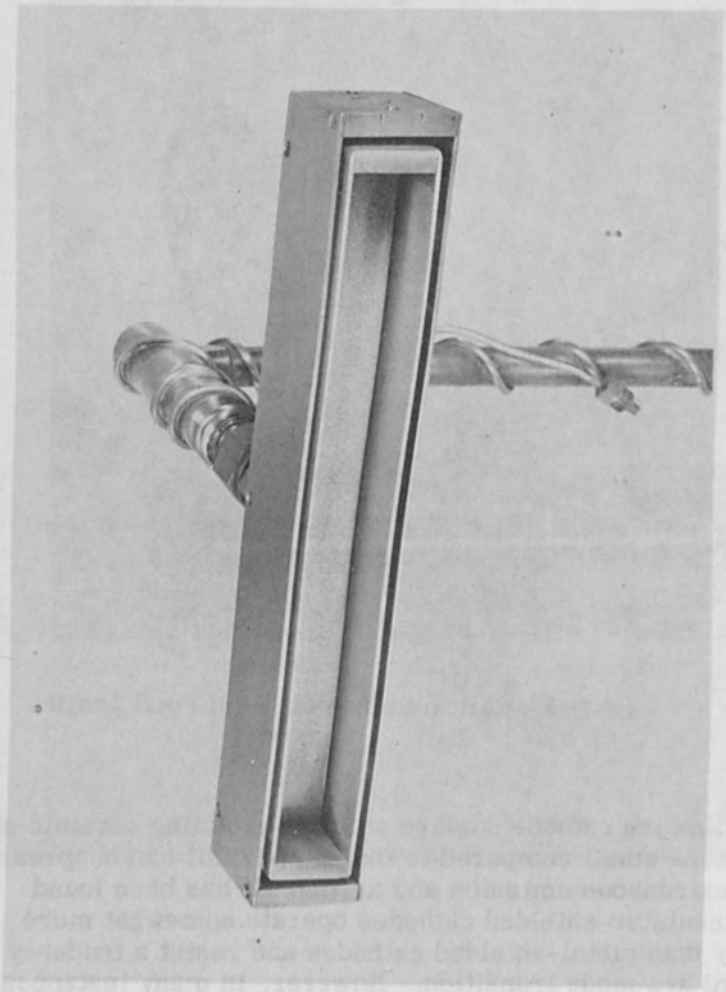

Figure 9. Linear Hollow Cathode; 1-in. x 9-in. Aperture.

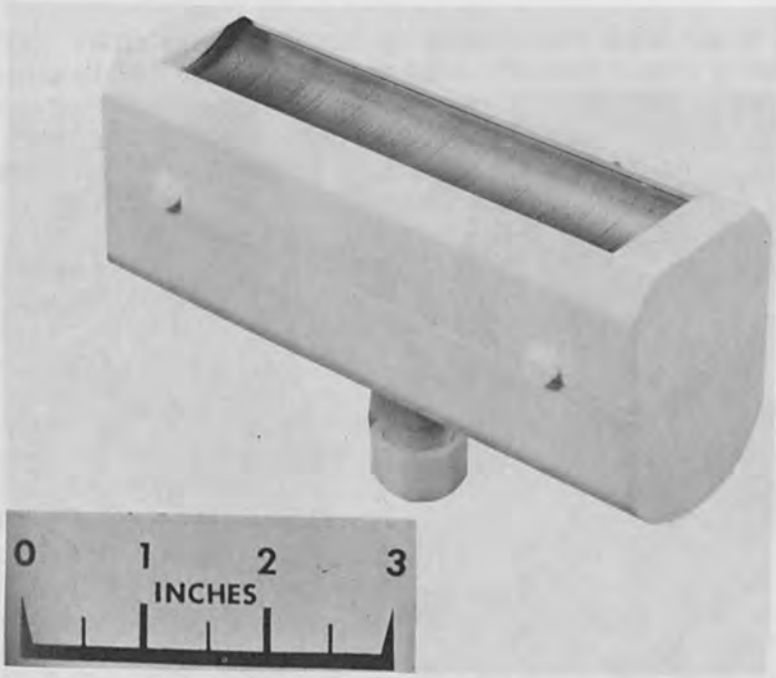

Figure 10. Linear Contoured Cathode; 1.5-in. Focal Length.

Hollow Cathodes

Axial beam hollow cathodes have been operated in several gas environments at pressures of the order of 1 to 100 microns. The pressure range of operation for a given cathode in a given environment has been found to vary approximately inversely with cathode size. Gas type has a strong effect on operating pressure range; with helium the discharge operates at about a factor of ten higher in pressure than with argon or nitrogen. Beam power efficiencies in excess of 90 percent have been obtained with shielded configurations. As shown in Figs. 4 and 7 this configuration incorporates a cylindrical insulating shield surrounding the cathode to suppress extraneous electron emission from the external cathode surfaces. Operation has been achieved at accelerating potentials greater than 100 kV and beam power levels greater than

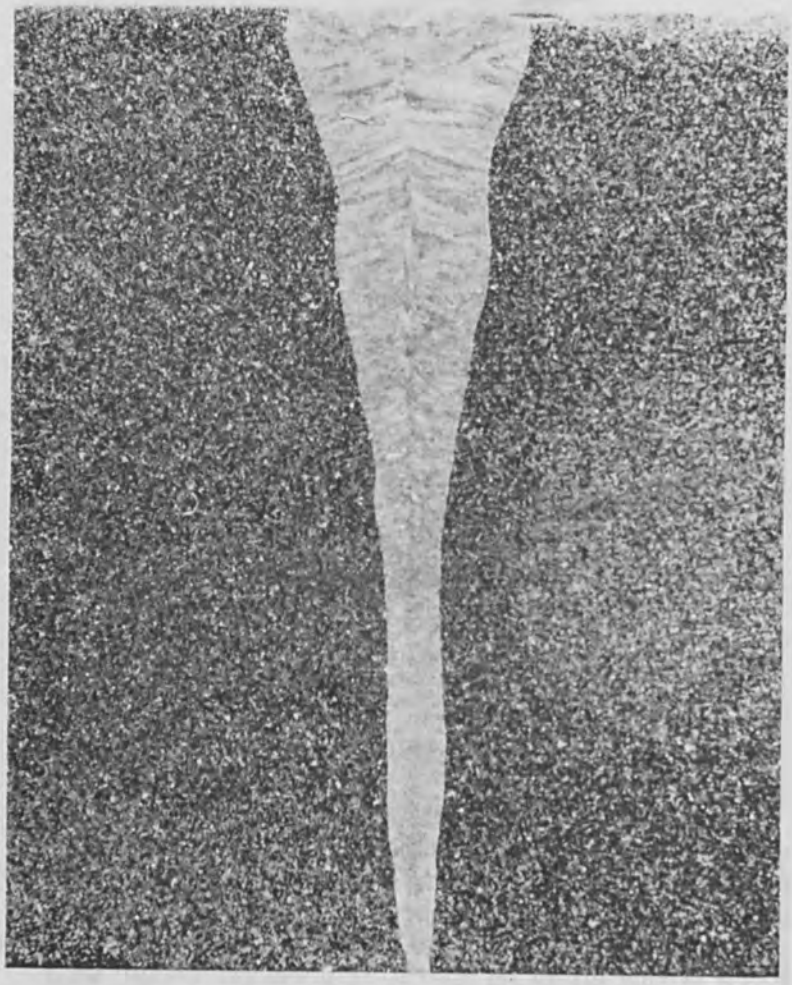

Figure 11. Deep Penetration Weld in 3/4 in. SS Plate Made by Axial Beam Hollow Cathode; 3 kW, 20 in./min.

7kW. With external focusing, beam power densities of the order of 10^6 watts/in.^{2} have been obtained making possible deep penetration welds of the type shown in Fig. 11.

The sensitivity of the axial hollow cathode to operating pressure, as shown in Fig. 12, leads to variations in discharge current during welding as a result of outgassing and evaporation of the workpiece. To provide a means for rapid and automatic compensation for these variations, a magnetic current control was developed. The control consists of a coaxial solenoid which surrounds the hollow cathode as shown in Fig. 4. An increase in the magnetic field generated by this coil provides improved trapping of high energy electrons in the interior of the cathode. The resulting increase in ionizations and excitations leads to an increase in beam current at constant voltage (Fig. 13), an effect similar to an increase in pressure. The variation is seen to be nearly linear with field strength making it feasible to provide a simple feedback circuit for automatically maintaining a constant current and power setting. Since the control solenoid is located remote from the active discharge, it is not subject to bombardment heating and sputtering. Furthermore changes in the current control field cause no undesirable changes in beam focusing characteristics.

The design criteria for linear and annular hollow cathodes (Figs. 9 and 5 respectively) differ from that of the axial configurations. In particular, it has been found that for cathodes with extended apertures, stable operation can be achieved only when the height of the aperture is approximately equal to the corresponding inner dimension of the cathode, as shown in Fig. 5. Cathodes in which the size of the aperture is significantly less than the height of the cathodes are susceptible to arcing or spoke-type emission except over a limited current and voltage operating range. Voltages of more than 2 or 3 kV can be sustained only at pressure levels of less than 15 microns; at these pressures the current is very low (on the order of one milliamp/linear inch). However, as long as the height of the cathode is not significantly larger than the aperture dimension, stable operation can be achieved over a wide range of operating conditions, even with small apertures,

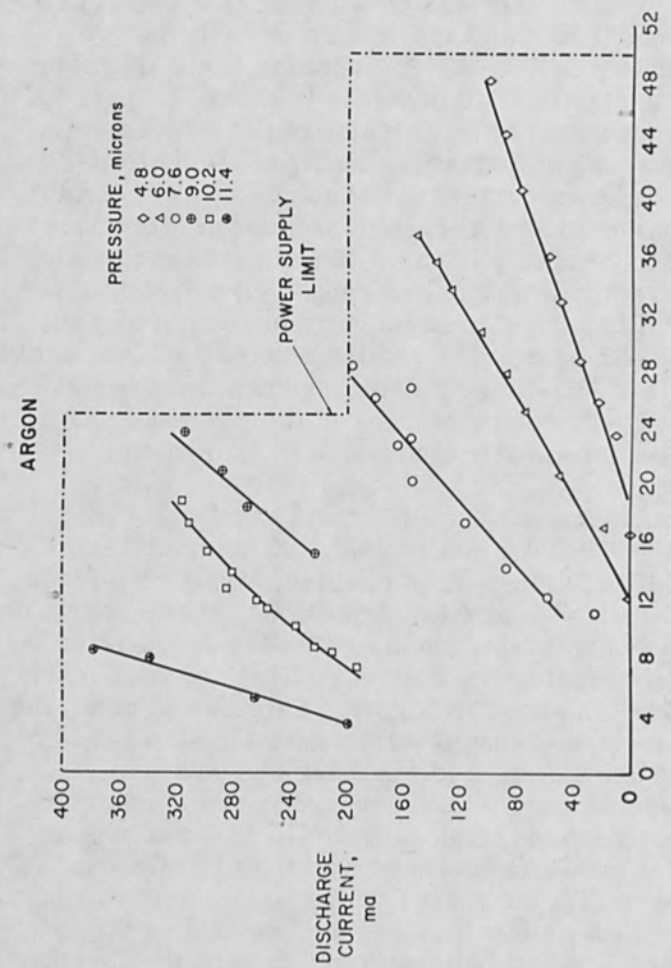

Figure 12. Voltage-current Characteristics of Axial-Beam Hollow Cathode.

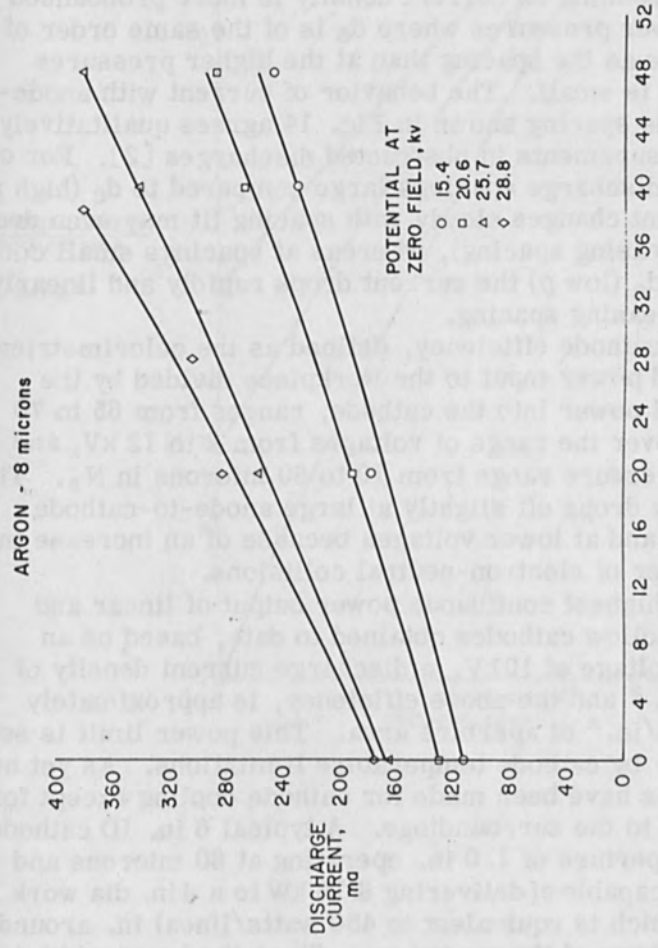

Figure 13. Effect of Magnetic Control on Cathode Current.

1/4 inch or less. In this case the thickness of the electron beam is approximately equal to the size of the aperture.

Typical discharge current characteristics in nitrogen of linear and annular hollow cathodes, ranging in diameter from 2.75 to 6 in. ID, are summarized in Fig. 14. The discharge current density (ratio of discharge current to aperture area) at a given anode-to-cathode spacing is essentially independent of cathode size. It is apparent from Fig. 14 that the discharge current increases with both anode-to-cathode spacing and ambient pressure. The effect of spacing on current density is more pronounced at the lower pressures where d_c is of the same order of magnitude as the spacing than at the higher pressures where d_c is small. The behavior of current with anode-to-cathode spacing shown in Fig. 14 agrees qualitatively with measurements in obstructed discharges [2]. For obstructed discharge spacings large compared to d_c (high p) the current changes slowly with spacing (it may even drop with increasing spacing), whereas at spacings small compared to d_c (low p) the current drops rapidly and linearly with decreasing spacing.

The cathode efficiency, defined as the calorimetrically measured power input to the workpiece divided by the electrical power into the cathode, ranges from 65 to 70 percent over the range of voltages from 8 to 12 kV, and over a pressure range from 10 to 60 microns in N_2. The efficiency drops off slightly at large anode-to-cathode spacings and at lower voltages because of an increase in the number of electron-neutral collisions.

The highest continuous power output of linear and annular hollow cathodes obtained to date, based on an applied voltage of 10 kV, a discharge current density of 45 ma/in.^{2} and the above efficiency, is approximately 300 watts/in.^{2} of aperture area. This power limit is set primarily by cathode temperature limitations. As yet no provisions have been made for cathode cooling except for radiation to the surroundings. A typical 6 in. ID cathode with an aperture of 1.0 in. operating at 60 microns and 10 kV is capable of delivering 3.76 kW to a 4 in. dia work piece, which is equivalent to 450 watts/lineal in. around the periphery of the workpiece. Since the beam width is approximately equal to the cathode height of 1.0 in., the

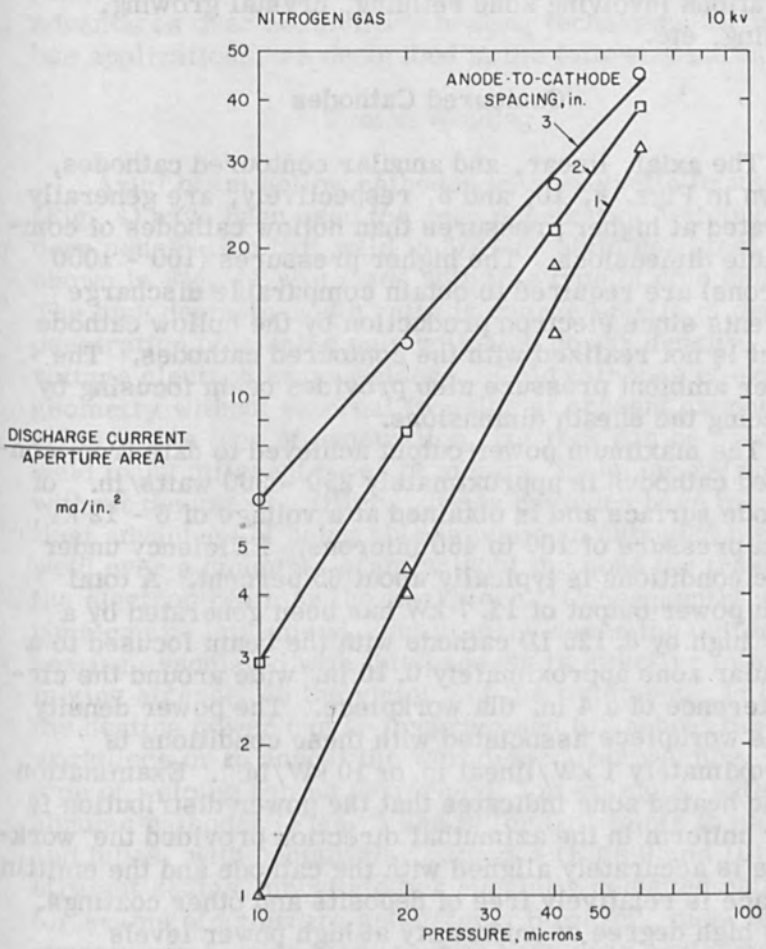

Figure 14. Annular Hollow Cathode Operating Characteristics.

power density at the workpiece is 450 watts/in.^{2}. Accordingly, the hollow cathodes are ideally suited to applications requiring uniform heating over an extended zone, such as operations involving zone refining, crystal growing, brazing, etc.

Contoured Cathodes

The axial, linear, and annular contoured cathodes, shown in Figs. 8, 10, and 6, respectively, are generally operated at higher pressures than hollow cathodes of comparable dimensions. The higher pressures (100 - 1000 microns) are required to obtain comparable discharge currents since electron production by the hollow cathode effect is not realized with the contoured cathodes. The higher ambient pressure also provides beam focusing by reducing the sheath dimensions.

The maximum power output achieved to date from contoured cathodes is approximately 250 - 300 watts/in.^{2} of cathode surface and is obtained at a voltage of 6 - 12 kV, and a pressure of 100 to 450 microns. Efficiency under these conditions is typically about 65 percent. A total beam power output of 13.7 kW has been generated by a 2 in. high by 8.125 ID cathode with the beam focused to a circular zone approximately 0.10 in. wide around the circumference of a 4 in. dia workpiece. The power density at the workpiece associated with these conditions is approximately 1 kW/lineal in. or 10 kW/in.^{2}. Examination of the heated zone indicates that the power distribution is very uniform in the azimuthal direction provided the workpiece is accurately aligned with the cathode and the emitting surface is relatively free of deposits and other coatings. This high degree of uniformity at high power levels permits fusion welding and bonding of a pipe or tube joint everywhere simultaneously along the periphery, thus obviating the need for rotating a gun or cathode relative to the workpiece.

APPLICATIONS

Advantages of cold cathodes include (1) ruggedness and durability, (2) stable operation at pressures up to 1 torr

with a wide variety of gases, (3) excellent uniformity of electron beam power density over extended areas, (4) operation at moderate voltages and currents and (5) simplicity. These features provide cold cathodes with certain advantages over competitive heating techniques for numerous applications, as described in the following paragraphs.

Fusion Welding

Axial beam hollow cathodes with magnetic focusing (Fig. 4) have been used for deep penetration welding. The deep penetration butt weld in 3/4-in. stainless steel plate shown in Fig. 11 was made with this type of cold cathode. The high depth-to-width ratio is characteristic of deep penetration obtainable only with high power density, high voltage electron beam welders. Cold cathodes of extended geometry without external focusing at present cannot achieve this type of penetration, but they can be used to weld many different types of metals, including refractories, without the use of a filler. These cathodes have the distinct advantage of being able to make an extended fusion weld over a complete seam without the need for traversing the electron beam or the workpiece. Consequently welding time can be minimized, and in many cases the uniform heating associated with this process is effective in minimizing stresses in the vicinity of the weldment. In fact, the heating power can be programmed to preheat the workpiece or to anneal the workpiece after welding. This type of welding can be performed, for example, with annular cathodes (Figs. 5 and 6) for butt joints in pipes and tubes, with rectangular cathodes (Figs 9 and 10) for straight seams, or with other specially designed cathodes for seams of arbitrary geometry. However, most of the experimental welds made to date have been performed with annular cathodes. Butt welds have been made in tubes and pipes of different materials ranging in diameter from 1/4 in. to 4 inches, as illustrated by the samples shown in Fig. 16. There is no apparent limit to the diameter of pipes that can be welded using this process. The heaviest gage material that has been welded to date is 1/4-in. thick stainless steel. The coupons shown in Fig. 17 were cut from a butt-welded 4-in. dia x 1/8-in. wall stainless steel

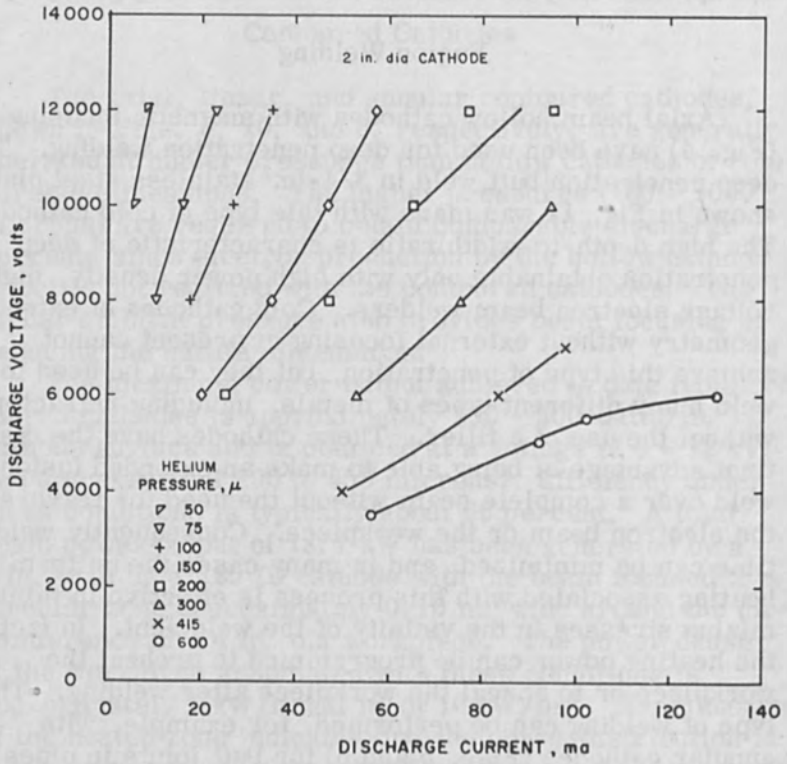

Figure 15. Contoured Cathode Operating Characteristics.

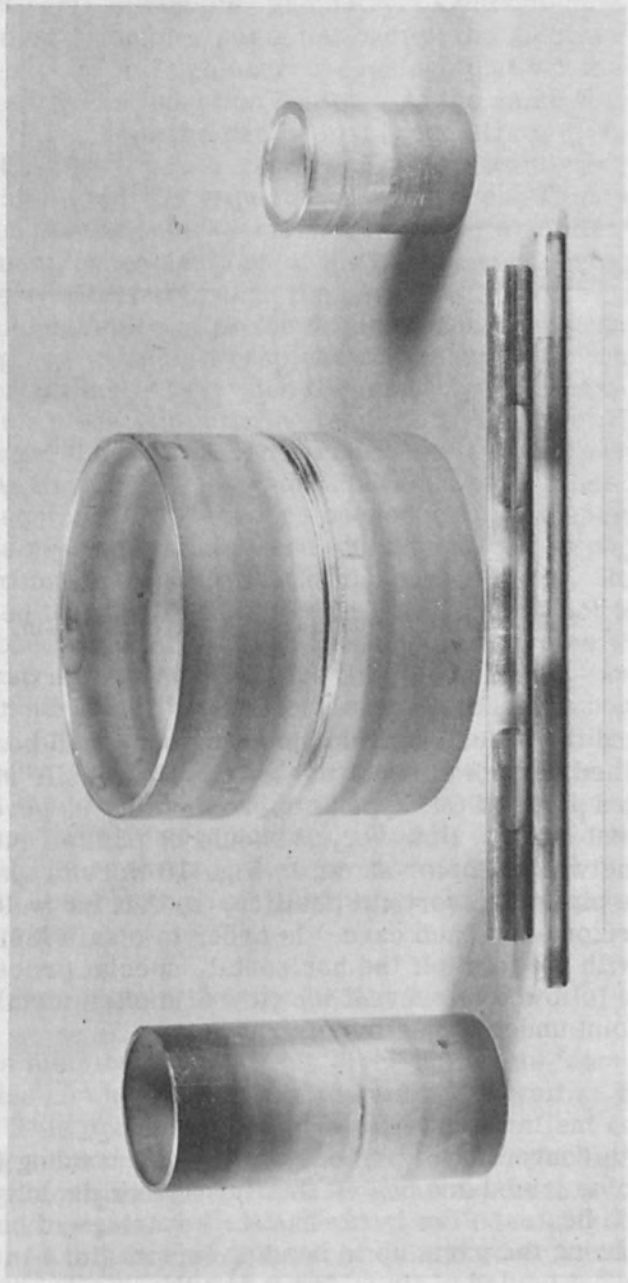

Figure 16. Tube and Pipe Welds Made with Annular Cathodes.

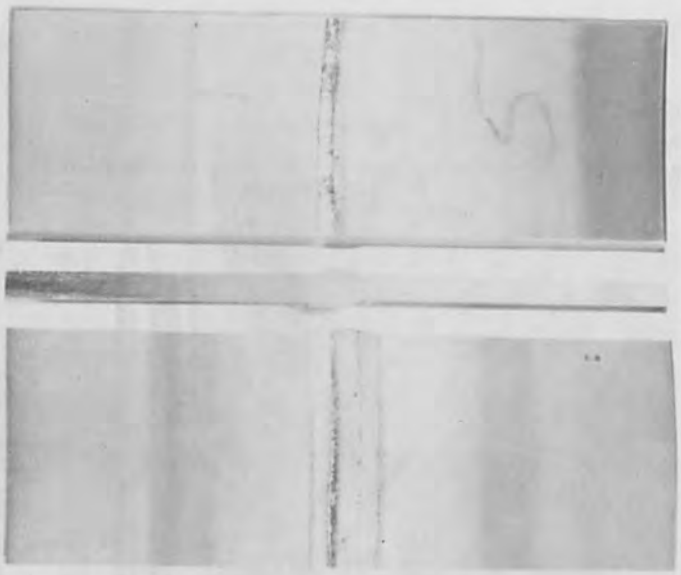

Figure 17. Weld Sample Coupons from 4-in. dia x 1/8-in. wall SS Pipe.

pipe, and they illustrate the type of smooth weld bead that is obtained on both sides of the joint. The tensile strength of welded pipes of this type is approximately 90 percent of the parent metal. However, it should be pointed out that all of the weld samples shown in Fig. 16 were prepared with the pipes in a vertical position, so that the weld plane was horizontal in each case. In order to obtain fusion welds with the joint off the horizontal, special procedures must be followed to prevent the flow of molten metal out of the joint under the action of gravity.

Diffusion Bonding

With conventional methods of diffusion bonding the parts to be joined are heated in a furnace or directly by an induction heater. The latter has the advantage of being able to bring the parts up to bonding temperature in a relatively short period of time, but it has the disadvantage of

not being able to maintain a uniform temperature at the joint of parts of complex geometry. Cold cathodes can be used to heat complex parts uniformly; the electron beam can penetrate through narrow openings that would effectively shield an induction heater. At the same time the extent of the hot zone can be highly localized, if desired, so that the total power required is significantly less than that which would be required by a furnace. This type of heat localization is especially desirable, and often a requirement, when sections of the parts to be bonded are adversely affected by high temperature. Another advantage that cold cathodes offer for diffusion bonding is that the heating power to the workpiece can be accurately measured and controlled. Thus when the metallurgical properties of the parts allow, the bonding temperature can be maintained just below the melting temperature so that only very short bonding times are required. Stainless steel tubes such as those shown in Fig. 18 were bonded at high temperature, and the resulting joints were found to have a strength approximately equal to that of the parent metal. It should be noted that the tubes shown in Fig. 18 were not touched after bonding, i. e., the as-bonded parts have no weld bead or constriction which require finish machining. One further advantage of high temperature diffusion bonding is that the joints do not require meticulous preparation prior to bonding, because at high temperature, plastic deformation at the joint, even with minimal pressure, is sufficient to offset initially poor contact. Finally it should be pointed out that, since there is no flow or molten metal in diffusion bonding, problems associated with weld-plane orientation do not exist.

Joining Nonconducting Materials

As mentioned previously electron beams from cold cathodes can heat electrical insulators as well as conductors. This property combined with the excellent control of heating power provides a technique that is, perhaps unexcelled for joining nonconducting materials in a low pressure environment. Annular hollow cathodes (Fig. 5) have been used to join alumina, zirconia and other nonconducting refractory ceramics. A promising application is the

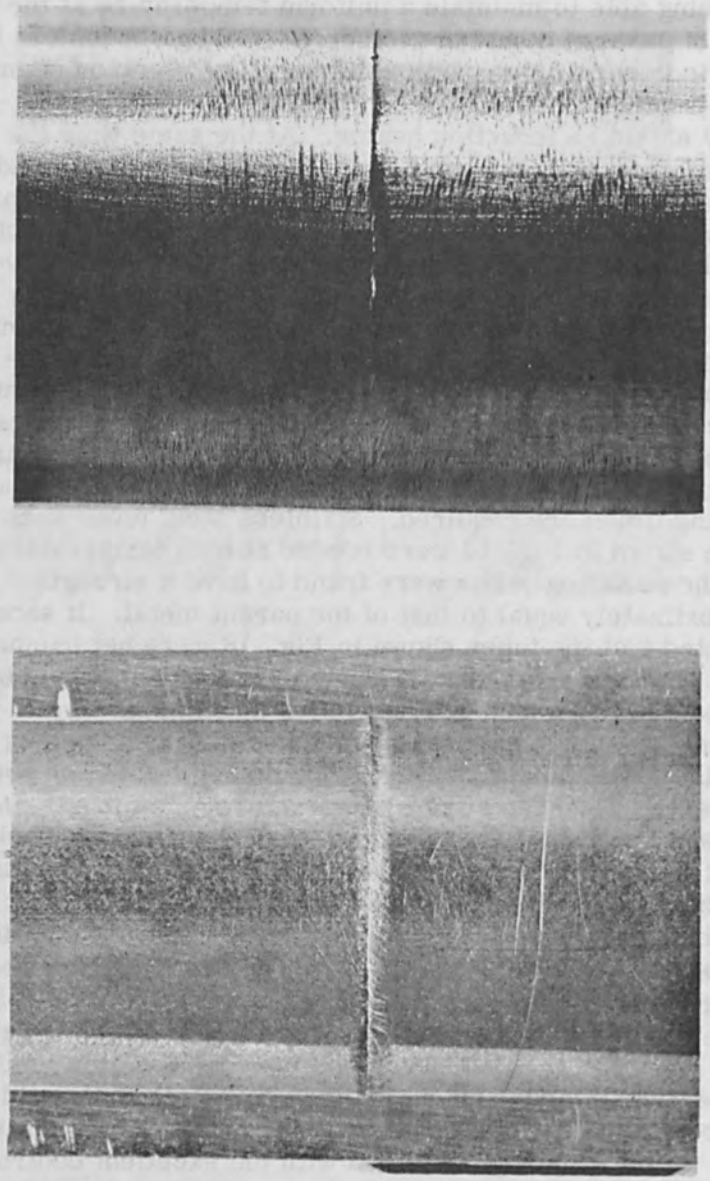

Figure 18. Diffusion Bond of 5/8-in. dia x 0.060-in. Wall SS Tube made with Annular Hollow Cathode.

joining of fused silica (quartz) parts, as illustrated in Fig. 19 which shows two 1-in. dia quartz tubes being fused together in an annular cathode discharge.

Vacuum Brazing

In many applications cold cathodes can be used to advantage as heat sources for vacuum furnaces or for applying heat directly to the workpiece to be brazed. In the former application the electron beam is used to heat a large susceptor of thin-walled refractory metal to provide a high temperature furnace with a short response time. The electron beam is spread out to heat the entire area of the susceptor uniformly. For heating a workpiece directly, cold cathodes again have advantages over induction heaters because a cold cathode can rapidly provide heat in a highly localized zone with well-controlled, uniform temperature at the joint of a complex assembly. Such assemblies may have sub-assemblies with temperature limits which ordinarily might preclude furnace brazing operations. Furthermore for brazing axisymmetric pieces, such as tubes and pipes, a single cathode can be used over a wide range of workpiece sizes. There is no problem of coupling the power into the workpiece with rapid spacial and temporal changes in electrical conductivity. Annular cathodes have been used successfully to make numerous types of inert atmosphere or hydrogen brazes in tubes and to braze ceramics to metals. The latter is a particularly attractive application because the electron beam heats the ceramic as well as the metal. In fact, it has been found that in most cases it is preferable to heat the ceramic and let the heat conduct to the metal, thus assuring that the ceramic is "up to temperature" when the braze material starts to flow.

Zone Refining

Conventional electron beam devices for zone refining have been in use for some time. The "floating zone" method, in which a narrow melted zone supported by surface tension forces is continuously traversed up an ingot, is a particularly attractive method of refining because no

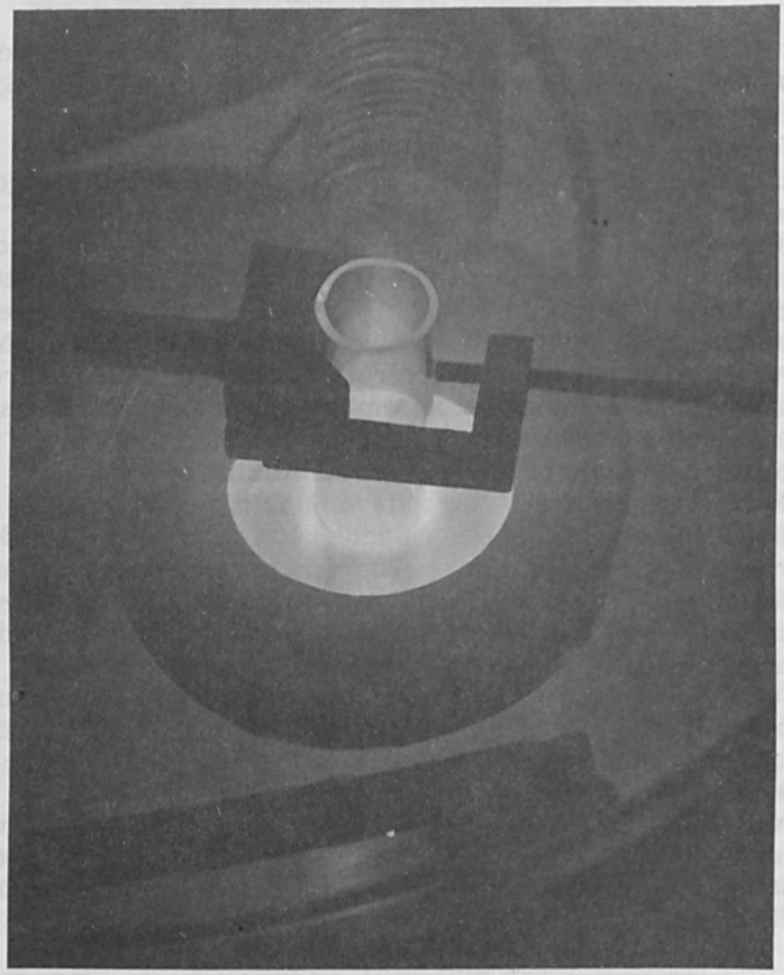

Figure 19. Joining 1-in. dia Fused Silica Tubes in an Annular Hollow Cathode Discharge.

foreign material comes in contact with the melt. The degree of refinement per "pass" is in part a function of the ambient pressure, with greater refinement achieved at lower pressures. Thus, as far as refinement capability is concerned, conventional electron beams appear well suited to this application since they can operate in a hard vacuum. However, outgassing from the heated ingots can cause arcing and unstable operation. In contrast, cold cathodes can be operated at sufficiently high ambient pressure levels, say several hundred microns, so that the partial pressure due to outgassing is a small fraction of the total ambient pressure. Under this condition outgassing does not have a significant effect on the stability of operation. Another advantage of cold cathodes is that they can be used to refine electrical insulators as well as metals. In this application it is often essential to operate with a partial pressure of a particular gas to prevent chemical change of the ingot. More specifically, certain metallic oxides are reduced when heated in a vacuum, but by heating them in an oxygen atmosphere proper stoichiometry can be maintained.

Crystal Growing

Cold cathodes have been used successfully to grow single crystals of alumina (sapphire) as well as several of the rare earth oxides. In this process a rod of commercial grade alumina is located on the centerline of an annular cathode, and a narrow melted zone is maintained in the rod which is traversed down through the cathode (i. e., floating the zone upward) at a rate of several centimeters per hour. A seed crystal may be used if desired, but it is not necessary. The molten zone solidifies in crystalline form with the crystals oriented in a preferred direction to form a long single crystal. A sample of a sapphire crystal grown by this technique is shown in Fig. 20. Some additional heating of the newly formed crystal is required to reduce the thermal gradients in the rod and thereby prevent stressing and ultimate cracking. This heating can be accomplished either by a simple resistance furnace or by a second cathode. Crystals can also be grown by floating

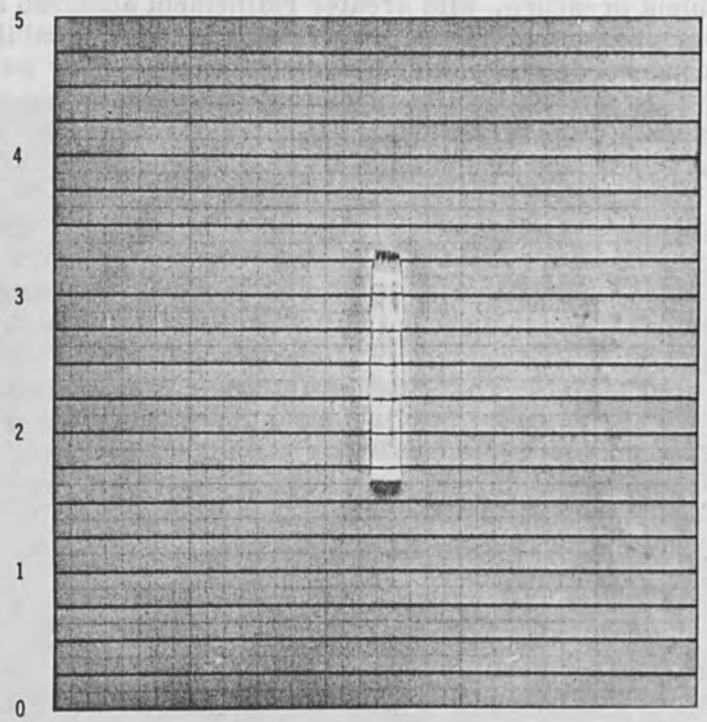

Figure 20. Sapphire Crystal Grown by Annular Hollow Cathode Floating-Zone Technique.

the zone in a downward direction. Regardless of the direction of traverse cold cathodes again have the advantage over conventional electron beam devices in that they operate stably at considerably higher pressure levels. In crystal growing especially, it is often necessary to operate with high partial pressures of certain gases to preserve stoichiometry, not only of the crystal itself but often that of special dopants.

Materials Processing

In addition to the foregoing applications a number of other processes have been considered as suitable candidates for cold cathodes but have not yet been investigated experimentally. In fact, any process which requires the controlled and selective application of high power in a moderate vacuum is a potential candidate. Among these are the following:

1. Annealing - special cathodes can be readily designed to anneal strip, rod, tube, wire, etc. This method of annealing could be used for any type of metal, including refractory metals, and would offer fast rates of annealing with very close programmed control of temperature. Spot annealing on large assemblies would be feasible.
2. Surface coating - cold cathodes can be used for heating substrates for vapor deposition such as in applying polymer coatings. Cathodes can be designed to heat large areas, especially desirable for bulk processing, or to heat other geometries such as wires to apply insulating coatings. Cold cathodes can, of course, be used as heaters in vapor deposition processes.
3. Surface hardening - cold cathodes can be designed to heat pieces of arbitrary geometry for surface hardening. In one method that has been suggested, the electron beam would melt a surface layer which would react with a coating material to form a hard surface with exceptional adhesion properties.

ACKNOWLEDGMENTS

This work was sponsored in part by the United Aircraft Research Laboratories and in part by the Hamilton Standard Division.

The authors wish to acknowledge the contributions of several members of the United Aircraft Research Laboratories staff, in particular, Messrs. C. M. Banas and C. O. Brown for their work in the axial beam hollow cathode and its magnetic current control and Mr. F. J. Ferreira for his original concept and work on the annular hollow cathode.

REFERENCES

1. Cobine, J. D.: "Gaseous Conductors," Dover Publications, New York (1958).
2. Francis, G.: "The Glow Discharge at Low Pressure," Handbuch der Physik, 32, Springer Verlag (1956).
3. Von Engel, A.: "Ionized Gases," Second Edition, Oxford University Press (1965).
4. Brewer, A. K. and J. W. Westhaver: J. Appl. Phys., 8, 779 (1937).
5. Swinton, A. A. C. "Proceedings of the Royal Society," 61, 79 (1897).
6. Von Pirani, M.: U. S. Patent 848,600 (1907).
7. Van Passen, H. L. L. and R. J. Allen: Bull. Am. Phys. Soc. 7, 69 (1962).
8. Boring, K. L. and L. H. Stauffer: Proc. National Electronics Conf. 19, 535 (1963).
9. Muly, E. C. and J. Litton, Jr.: "First Int. Conf. on Electron and Ion Beam Sci. and Tech." (R. Bakish, Ed.), p. 133, John Wiley & Sons, New York (1965).

Laser Welding for Aerospace and Commercial Applications-1970

K. J. Miller

Metals Joining Corporation
Redondo Beach, California

INTRODUCTION

Man has known of light and has used this phenomena of nature since the beginning of time. Today, in our modern civilization, light controls many of our social patterns and has established some traditional mores adhered to throughout the world. However, even though this one very important commodity is widely used by modern day civilization, much is still to be learned about it.

Children have, at some time during their inquisitive formative years discovered the phenomena of light. Light, when directed through a convex glass lens, has been used by many a Boy Scout to start a camp fire. Other children, using the same concept, have discovered that holes may be burned into paper. On occasion, this "discovery" has led to catastrophic results such as the loss of a family home and even loss of life. Broken bottles, deposited by careless campers or tourists, is known to have started many of our forest fires, destroying one of man's vital natural resources. All of the aforementioned is uncontrolled use of light.

Many articles have been published in technical magazines about the use of light as a metallurgical joining tool and as a metal removal process. Some of these technical articles present excellent data for utilizing this phenomena in the metal working field. In some instances, there are conflicting predictions, relative to applying light, to the extent that some learned researchers imply

that it will be many years before this process moves from laboratory experimentations to full production use on an economical basis.

This paper is presented in an effort to acquaint the industrial world with past efforts of using light as a metal working tool, present day status of the process, and its predicted use as a metal working tool by the year 1970.

THE TIG WELDING PROCESS

Tungsten inert gas shielded arc welding establishes an electric arc between the end of the non-consumable tungsten electrode and the surface of the object being welded. This process can melt and weld most of the engineering materials used by modern day joining fabricators in both the aerospace and nuclear fields. In essence, the arc is shielded by an inert gas consisting of argon, helium, or mixtures of these two gases. In using this inert gas, it (the g. s) also provides a known ionization factor which tends to generate very high temperatures, (approximately 11,000°F) and in doing so does not melt the tip of the tungsten electrode. This phenomena is partially due to the ionization factor and partly due to the cooling provisions designed within the torch itself, to transfer heat from the contacting portions of the tungsten electrode with the cooling media.

In applying the process to fusion weld various metals and alloys, the inert gas being used also shields the object being welded at the point of local fusion, as the weld puddle progresses. When the process is used manually, weld deposition rates are nominally based upon 3 inches per minute. This welding rate, however, varies, depending upon material thickness and operator technique. When used automatically, welding speeds are approximately twelve inches per minute but again, based primarily on thickness being welded, this deposition rate can vary appreciably.

Typical TIG weld cross sections show that weld depth to width ratios are approximately 1 to 1. This is true on material thickness which does not require chamfering or beveling. However, due to the somewhat limited pene-

trating characteristics of the process, chamfering or beveling of thicker members is required. Thick members which are chamfered or beveled would require the multi-pass welding technique to fill the prepared joint.

When looking at TIG welded cross sections under the microscope, relatively large heat affected zone areas are observed which start at the weld nugget parent metal boundary line and extend outward into the parent metal. In this respect, the weld sometimes is stronger than the heat affected zone area. For some alloys, annealing of the weldment removes this change in crystalline structure, and further heat treatment would provide properties throughout the weld and weld heat affected areas. Other metals do not respond metallurgically to this post-weld heat treat processing and, therefore, strengths less than 100% joint efficiency will have to be used by the designer when designing for welding.

The foregoing is a very basic and brief summary of this joining process. Although some points inherent of the process appear to be undesirable, when the processes capabilities and deficiencies are understood by the user, no problems will result from its use. As a matter of fact, it is still the principal metallurgical joining process being used by modern day joining fabricators, and were it not for this process our space exploration accomplishments we now accept as commonplace would not have been possible.

THE ELECTRON BEAM WELDING PROCESS

Both the aerospace and nuclear industries have been largely responsible for moving this process from the laboratory into full scale production. The scientist and physicist have been fully aware of electron movements for many years, but this knowledge was not converted to practical use relative to metallurgical joining until late in the 1950's. Since the first successful electron beam weld was made, the metallurgist and the welding engineer quickly realized its potential, and the process is now moving rapidly into many production areas.

The basic requirements for a production electron beam welding system consists of a vacuum chamber to contain the object being welded and also, the electron beam gun must be operated in a vacuum. (Some major breakthroughs have been made recently relative to out-of-vacuum electron beam welding which is being reported upon by the developer). In addition to the work chamber, diffusion, roughing, and holding evacuation pumps are required to obtain a welding vacuum of 10^{-4} to 10^{-5} mm of Hg. The welding system is completed with a power source (30,000 up to 200,000 volts), a control cabinet, operator control console, electron gun, some means of viewing the weld as it progresses, and manipulative means to provide either part movement beneath the electron gun or gun movement over or around the object being welded.

The actual weld is made by a stream of fast moving electrons which strike the object to be welded and when impact is made, electron energy bombardment is converted to kinetic energy to create the heat of fusion in any metal known to man. In essence, the electrons actually pierce the object being welded (even in ferrous and non-ferrous metals at least six inches in thickness) and by control of the energy, the molten metal being displaced by the electron piercing action swirls around and refills the hole as the weld progresses.

The process accomplishes the above by resistance heating of a filament (generally tungsten or tantalum) to its most effective electron emission temperature (around 4000° F) and by superimposing a high voltage field from anode to cathode, the electrons are given a forward push. The speed at which these electrons travel has been calculated to be .67 times that of the speed of light. By passing this now rapidly moving stream of electrons through an electro magnetic focussing coil, they are focussed down into a very small spot diameter. Special focussing methods can maintain approximately a fifteen inch focal length, permitting welding into deep narrow channels or into small holes. The end product of this type of welding is a very deeply penetrated weld cross section with a very narrow weld bead width. As a matter of fact, weld depth to widths are readily obtainable wherein weld depth is much

greater than 20 times that of weld width. The weld is of vacuum melted quality, and because of the high depth to width ratios obtainable, weld heat affected zones are practically non-existent in many engineering materials.

Based upon the fact that extremely narrow welds are produced, even in very thick metals, and weld heat affected zones are negligible and in some cases non-existent, dissimilar metal joining is greatly enhanced. When metal constituents are permitted great freedom to move and to interalloy with all other constituents present, alloy compatibility is of prime importance. This is particularly true when two different alloys are fusion welded and the by-products of some of the alloy ingredients, present in either or both unlike metals, form brittle intermetallic compounds. These undesirable formations are much more likely to occur with the TIG fusion welding process. It is also true that high temperature reaction products occur in joining processes comparable to the long heat soak times inherent of TIG and other "long" time at molten temperature fusion welding processes. When this "long" heat soak time keeps metals at their liquidus for relatively (to EB) long periods of time, dissimilar alloy joining becomes more difficult because of high temperature/time reaction products, formations of brittle intermetallic compounds, excessive alloying and re-alloying, excessive constituent losses, and very large heat affected weld zones. Most of these undesirable metallurgical characteristics are avoided with electron beam welding.

WHY LASER WELD

The metallurgical joining industry in general and the aerospace industry in particular can draw upon many fusion welding processes to weld fabricate various components. For example, we mention resistance welding, (limited because, generally speaking, overlapping joints are required) tungsten inert gas welding (limited because of gross heat distribution into the surrounding areas of the configuration as well as in the weld/heat affected zone) electron beam welding (limited because of the reason stated for tungsten inert gas welding, but on a

lesser scale, plus the usually additional requirement of a vacuum welding chamber) and others.

Of all the fusion welding processes mentioned above, the electron beam process most closely resembles the laser process in that both processes use a stream of almost invisible energy to accomplish the welding operation. (The electron beam process emits a finely focussed invisible stream of electrons which produces the weld by converting electron particle bombardment to kinetic energy and the laser beam acquires its kinetic energy by the conversion of light wave bombardment.) For further comparison the average electron beam energy stream moves at approximately .63 times the speed of light (faster than any other fusion welding process except the laser process) and of course, the light beam moves at the speed of light.

Having established such a close working relationship between the two processes the reader would most certainly question the need for both processes. Looking at the inherent characteristics of each process, we will list the traits of each in check off list form shown in Table I.

The items shown in Table I begin to establish differences between the two processes. Not shown in the table is the fact that the electron beam welding processes have been used in production, producing production welded configurations for approximately five years, as opposed to no reported production welding applications for the laser welding process. Also, equipment development is a very fertile area in laser welding to advance this equipment to the energy level already expended in the electron beam equipment field.

Of further interest is the fact that at any time during a laser welding operation, one can touch the object being welded upon and detect no temperature rise in the part. Not true with the electron beam process. This feature points to one very realistic capability which places the laser process a step beyond the electron beam welding capability. That is, it is possible to weld within very close proximity to glass or ceramic seal areas without cracking the glass or ceramic sealed area. Also, it is possible to weld in very close proximity to insulating

Table I.

Factors	Electron Beam	Laser
Vacuum Chamber Required	Usually	No
Inert Gas Required	No	No
Tooling Costs	Moderate to High	Low to Moderate
Welding Speed	High	High
Initial Equipment Cost	High	Low to Moderate
Equipment Maintenance - Time	Moderate	Low
Equipment Maintenance - Cost	Moderate	Low
Versatility - Metal Thickness	Wide Range	Limited in Thickness
Versatility - Joint Designs	Wide Range	Wide Range
Versatility - Dissimilar Alloys	Excellent	Excellent
Operating Costs	Moderate	Low to Moderate
Operator Skill Dependency	Low	Low
Ease of Automation	Excellent	Excellent
Set Up Time - Job to Job	Moderate	Low
Welding Precision Control	Very Good	Excellent
Training Period - Time	Moderate	Low
Subminiature Components - Size	Limited	No Limitations

wires (varnish coated fine wire) without destroying the insulating characteristics of the wire. In addition, laser welds have been produced in heat treatable alloys in their heat treated condition without affecting the heat treated condition . 010 inch away from the weld zone. These capabilities are not possible by any other fusion welding process without chilling devices which, to date, is not found to be necessary for laser welded components.

The electron beam welding process has definite advantages over other fusion welding processes in that dissimilar alloys can be joined by the process which cannot be accomplished by the other fusion welding processes. As a matter of fact, this is one of the oustanding features of the electron beam welding process. The laser process possesses this same dissimilar alloy joining capability, but even to a greater extent. Specifically, high sulphur bearing alloys such as A. I. S. I. 303 stainless steel or A. I. S. I B1113 steel has been successfully welded by the laser process. Even though sulphur stringers were found in the microsection through the welds, there was no evidence of cracks extending from the sulphur stringers. This would not be true with electron beam welds in this material as high magnification micro-analysis will show micro-cracks in the high sulphur bearing areas.

BASIC OPERATION OF THE LASER WELDER

The operating characteristics of a basic welding system would involve establishing the main welding parameters which controls and defines the energy output wherein welding occurs rather than cutting. To accomplish this, flat test panels are used which represent the same material and thickness exactly simulating the material and thickness of the configuration to be welded. The main controls of the laser consists of (a) pulses per second, (b) energy per pulse, (c) rate or time between pulses, (d) adjustment of point of focus (this may involve changing focal lenses), (e) establishing and adjusting welding travel speed, and, (f) control of cooling parameters. Also, of importance is uniformity of welding travel speed. This factor is not critical when welding a complete joint with

one single burst of light energy at extremely high travel speeds. When the pulse welding technique is used, however, the overlap resulting from the multi-pulse traversing method is directly proportional to uniform travel speed.

Considering that a laser light beam can be focussed to less than a 100 micron spot diameter, the object being welded must be tooled to track with a high degree of precision. When welding on members which are in excess of .001 inch thick, (.010 inch to .020 inch) precision tracking can be somewhat relaxed simply by changing the focal lens to a larger spot diameter. The thinner material, particularly in the .001 inch to .005 inch thickness range would require the smaller focal diameter and precision tracking. If the laser welding technique is such that the entire length of the weld is made by one single burst of light energy, then both the configuration and the metal thickness should be within the nominal thickness range wherein the focal spot would be large enough so that critical seam tracking is not a factor.

When all of the welding parameters have been established and a reproducible schedule has been developed, the production configurations are weld fabricated. Since the process produces a weld by a focussed beam of light, distance of the welding head to the work is not critical. Also, if a weld configuration is located in a deep cavity, change of focal lenses can be made to focus the beam down into a deep cavity. The process lends itself to welding in straight lines, longitudinally, transversely, or at any point in a straight line starting at any tangent point from a 360° circle. Circumferential welds on cylindrical configurations are easily adapted to the laser welding process. Of further interest is the fact that a non linear weld joint or weld joints which enclose a part, such as a lid on a square container, can be indexed beneath the laser head or index the head around the part to make the closeout weld.

When we select any metallurgical joining process to apply on pre-production hardware with quantity production to follow, cost of the joining process to be used is a very important consideration. The cost factor between the

laser welding system and its most closely related joining process (electron beam) is somewhat difficult to attain, because of the present limited thickness welding capability of the laser process. Therefore, to make this cost analysis we will assume that the material thickness maximum to fusion weld by a fabricator is .020 inch in thickness. However, regardless of metal thickness, the initial equipment costs for a laser system will be somewhat less than for an electron beam system, particularly if we confine the processes to the aforementioned thickness maximum. The reasons for this cost difference is quite obvious by referring to Table II.

Table II. Equipment Requirement Analysis

	Electron Beam Welding System	Laser Welding System
Inert Gas Required	-	-
Flashtubes	-	X
Filaments	X	-
Workpiece Manipulator	X	X
Water Cooling System	X	X
Power Source	X	X
Welding Head	X	X
Vacuum Chamber	X	-
Diffusion Pump	X	-
Holding Pump	X	-
Roughing Pump	X	-

Referring to Table II, we see that neither process requires inert gas provisions although both processes sometimes can use this feature to advantage. The laser process could use inert gas coverage when an entire weld length is made by a single burst of light energy. In this case, the inert gas protection would be principally an insurance factor, as present technology with the lower power level operating machines does not require this protection. The electron beam vacuum process often uses inert gas when refractory alloys are welded. The technique is to evacuate the chamber, backfill with the

inert gas and re-evacuate from the inert atmosphere chamber to eliminate all possibility of atmospheric contamination before electron beam welding refractory alloy part.

The second feature noted in Table II is flash tubes. The laser process uses these and a life of approximately 50, 000 flashes is considered good for the flash tubes. These tubes are not used by the electron beam process. The latter process uses filaments whereas the laser process does not and on a life expectancy replacement basis, these two items would balance out from a cost standpoint.

Workpiece manipulation and water cooling are requirements of both processes. The laser uses water cooling or possibly other cooling means for laser head cooling (ruby rod and flash tube) whereas the electron beam process uses water cooling for the diffusion pump. The latter cooling feature would require a greater flow rate of water but if both systems recirculated the water, costs would be about equal for water cooling requirements. The workpiece manipulation factor would be comparable from a cost standpoint for both processes relative to precision tracking but costs would be greater for the electron beam process relative to actual part holding fixtures because of greater distortion tendencies because of the higher heat input. As a matter of fact, wood or other non-metallic substances have been used for laser welding tooling quite satisfactorily because of the low heat dissipation factor inherent in laser welding.

Continuing with the comparison between laser welding and its closest related process, electron beam welding, the power sources are quite different. The electron beam welding process requires power sources in the 20, 000 to 60, 000 volts range for low voltage systems and from 60, 000 to 200, 000 volts for the high voltage electron beam system. Amperages for both high and low voltage electron beam systems range from 250 M. A. up to, and including, one amp. When we are talking about power sources in this voltage magnitude range we are, of necessity, talking about power sources which are relatively expensive when comparing same to laser power sources. The average

laser power source is a somewhat more conventional capacitor discharge type of power source. Although the welding point of energy of the light beam can reach a power density level of one billion watts per square centimeter or more, the power source to produce this type of energy still is, as stated before; a conventional capacitor discharge stored energy system. Based on the power source requirements for both welding processes, an average cost estimate for both processes would be that laser power sources would only be approximately 30% of the cost for an electron beam welding power source system.

Welding heads for both processes, although comparable in that both produce a beam of energy to produce a weld, are quite different from a design standpoint because the electron beam process uses a fast moving stream of electrons to generate kinetic energy, whereas the laser process uses a light beam to acquire heat of fusion. The electron beam gun is simply a matter of placing a cathode or anode in proper relationship to, again, a cathode or anode. By inducing accelerating voltage to a heated filament and forcing the electrons through a magnetic focussing coil the welding energy beam is made. The principal feature of the electron beam welding gun is, therefore, good mechanical engineering design in placing these configurations in their proper relationships. In comparing this gun with a laser gun, the laser, generally speaking, uses a roby rod of high purity, which is excited by a high intensity light flash and when the rod absorbs enough of these light waves the absorbed energy is "dumped" towards and upon the object to be welded. In this case focussing is accomplished by an optical lens as compared to electron beam focussing with a magnetic coil. From a cost standpoint an average electron beam welding gun would approximate the cost of an average laser head; except for the ruby rod in the head, which if destroyed through improper operation would cost in excess of $1,000.00 to replace. Also, of consideration is the fact that when comparing the laser to the electron beam process the exciting energy for the laser head is a quartz flash tube, which would cost an average of $100.00 to replace when blown, in comparison to a refractory alloy filament used in the electron beam

gun which costs an average of $3.00 to replace. However, the life expectancy of a flash tube would be at least in the order of 30 times longer than for a filament, and therefore flash tube to filament cost comparison would probably balance out.

When comparing necessary backup equipment to make these two processes work, as a general rule the electron beam welding process requires a complete evacuation system consisting of a diffusion pump, a roughing pump, and holding pumps. As stated before, the laser process produces a weld so rapidly that vacuum chambers and associated equipment is not required and, therefore, completely unbalances costing analysis when comparing the two processes. When considering this cost and considering that the laser process has no cost in this area, the size of the electron beam welding chamber would dictate the cost of the evacuation system. An average cost for this system would be approximately $10,000.00.

MATERIALS

Both the electron beam welding process and the laser welding process have demonstrated outstanding capabilities when joining a wide range of materials. It would be extremely time consuming to list all of the weldable alloys which can be welded by each process and rather than do so we will put all of the alloys into general groups.

Aluminum and aluminum alloys are readily weldable by both processes, including the 7000 and 2000 series aluminum alloys. Types 7075 and 2024 aluminum alloys are considered as not readily weldable alloys by the most widely used joining processes, which is the tungsten inert arc welding process for aerospace use. All of the 300 series stainless steels appear to be readily weldable by both processes, except type 303 stainless steel, which contains either sulphur or selenium (for free machining). When this alloy is welded by either of these processes stringers are noted in micro-sectioned areas of the weld, particularly when welding on thin sections. Other than this exception, none of the 300 series stainless steels

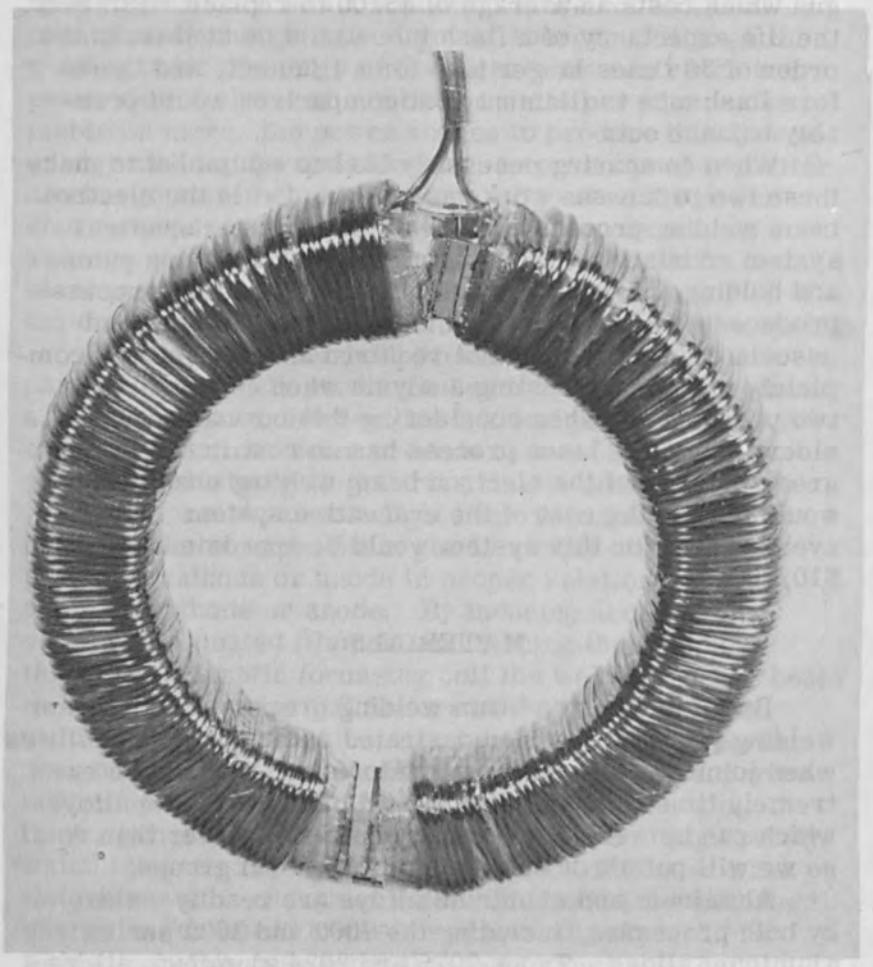

Figure 1. Shows an electrical coil which has been wound into two half segments, fully insulated, and then Laser welded together as the final operation. The two laminated half segments were Laser welded together at the two connecting interfaces by welding mild steel strips around the iron core laminated stacks. The strips and Laser welds can be seen in the upper and lower portions of Fig. 1.

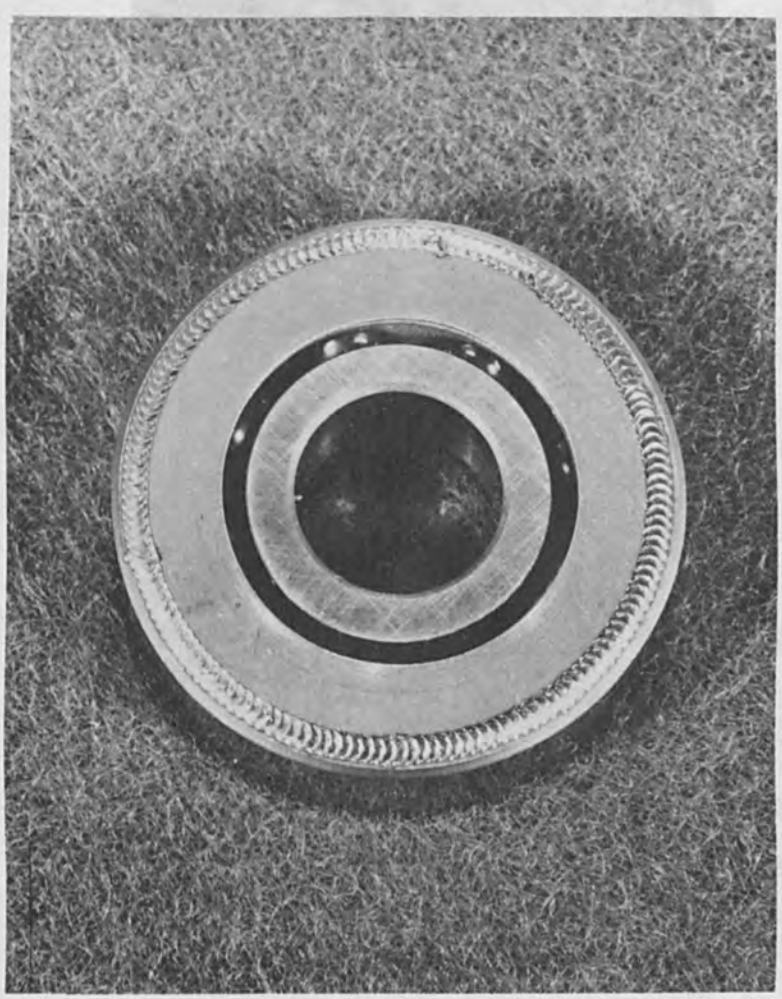

Figure 2. Shows a Laser welded retainer ring to a standard ball bearing. The retainer ring, made of 321 stainless steel is welded to the outer race 440 C bearing material. The weld had to be accomplished without softening the fully heat treated 440 C material in the ball race area.

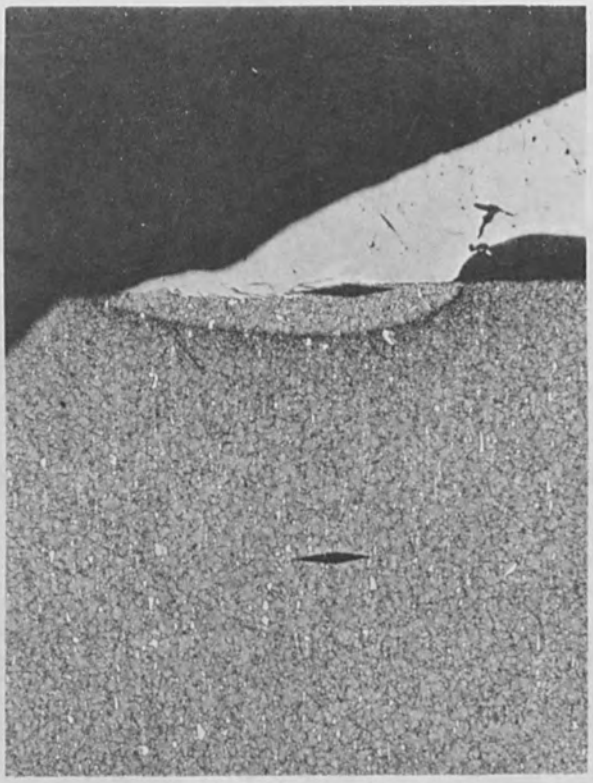

Figure 3. Is a photomicrograph of the retainer ring to bearing weld. It can be seen that extent of heat affected zone is extremely small.

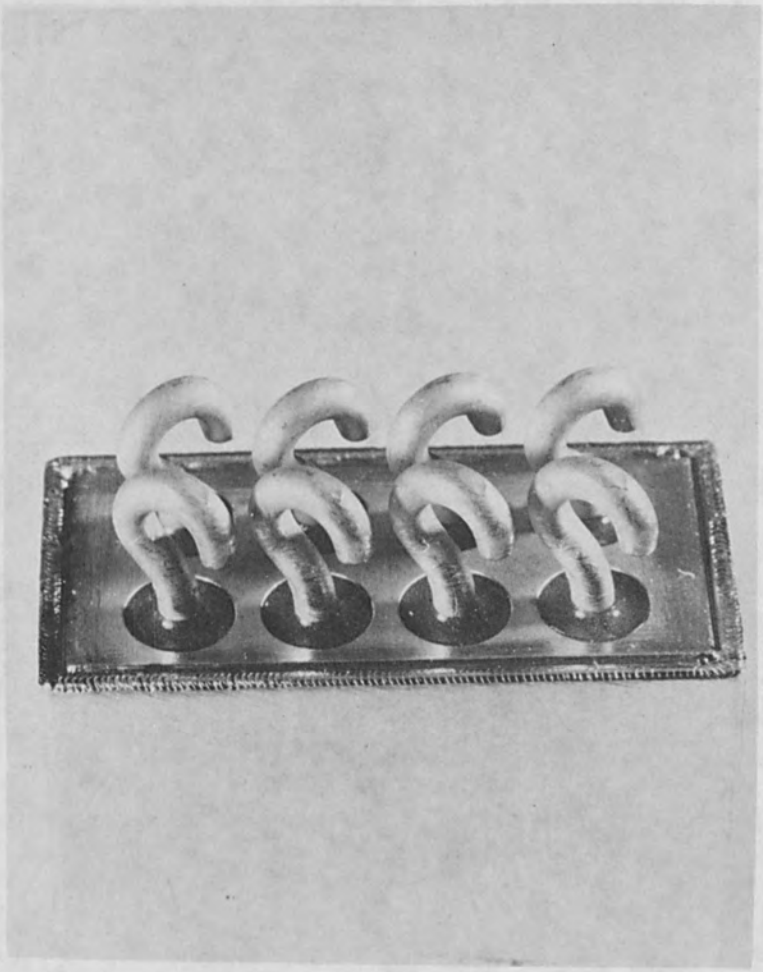

Figure 4. Shows a relay case which has been Laser welded to the heater. In this application, heat build up from the Laser process could not possibly cause cracking of the glass or ceramic insulator material.

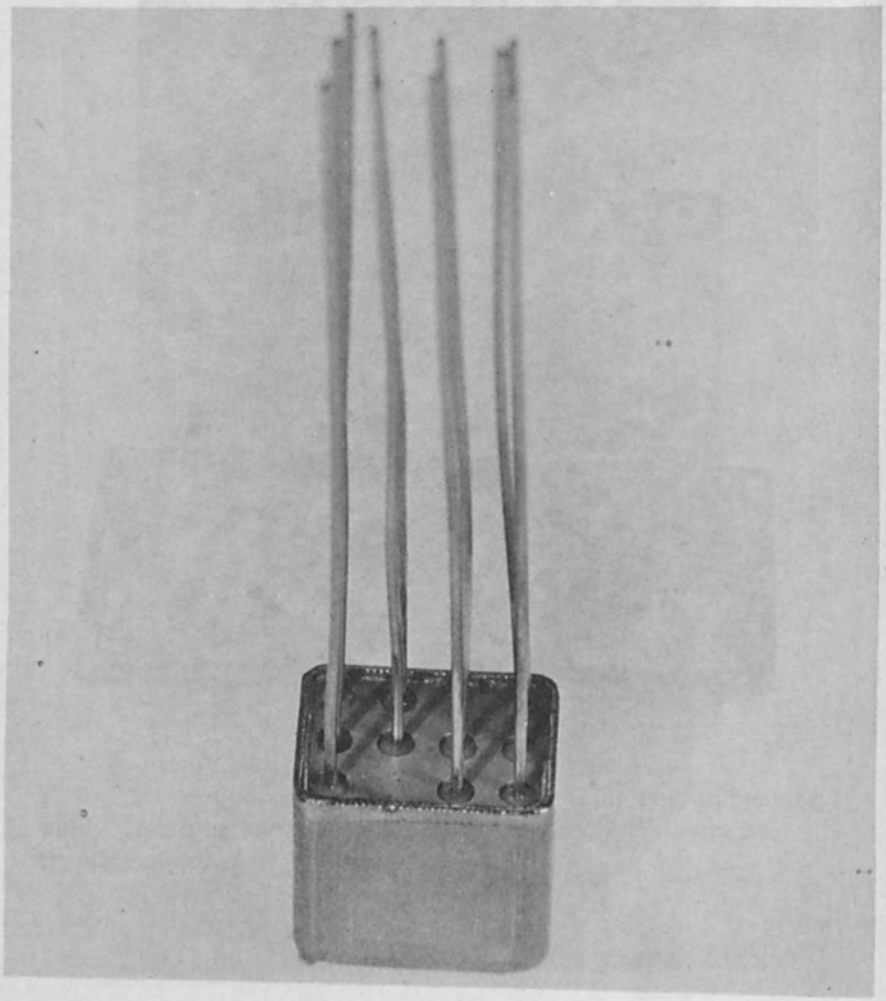

Figure 5. Is another relay case Laser welded but with the weld much closer to the insulator material than the assembly shown in Fig. 4.

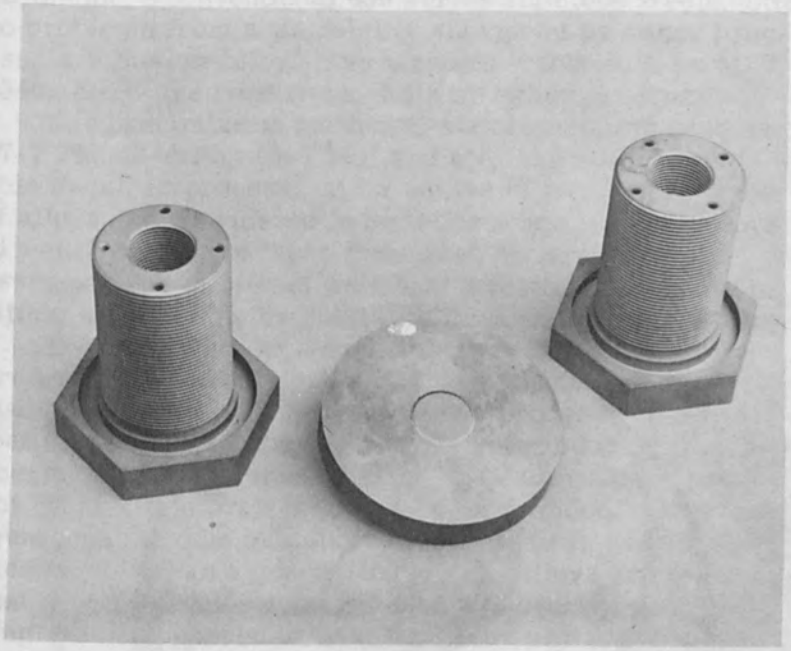

Figure 6. Illustrates the Laser welding capability of joining very thin metal to very thick material. The burst disc is made of type 316 stainless steel simply lap welded to the type 321 3/8" thick heavy block. The center member is the simulated test piece used to develop the Laser welding schedule. The two production units shown on each side depicts the capability of the light beam to weld into deep holes.

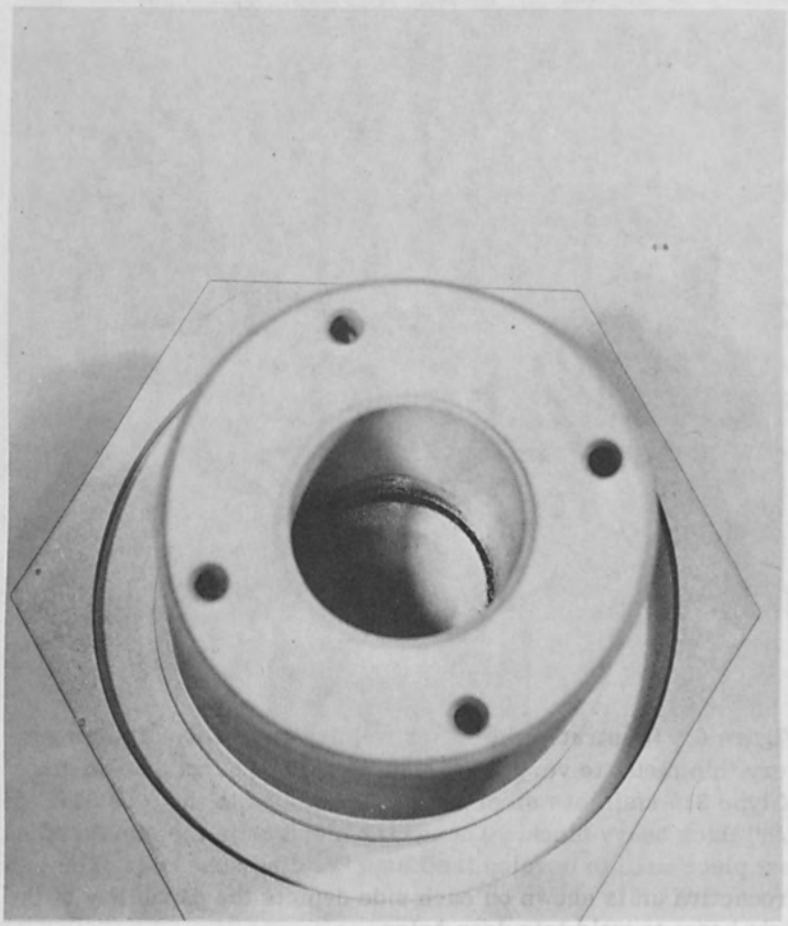

Figure 7. Is a close up of one of the burst disc weldments looking down into the cavity.

appear to offer any particular problems from a weldability standpoint.

The 400 series stainless steels, or more particularly, all the more conventional 400 series stainless steels, offer no problems from a weldability standpoint by either process, and the low alloy, high strength steels such as 4130, 4340, etc., are readily weldable by either process.

The precipitation hardening stainless steels such as 17-7 Ph, 17-4 Ph, 15-7 Mo, and etc, are readily weldable by either process. As a matter of fact, these types of alloys are considered to be tailor made types of alloys to weld by either of these processes because both processes portray minimum weld heat affected zone characteristics, which is highly desirable when welding these alloys.

The reactive alloys such as titanium and zirconium are again, readily weldable by this process, but the outstanding differences between the two processes here is that these types of alloys must be protected from atmospheric contamination when electron beam welded, but do not require this protection when laser welded. This statement must also be made for all of the alloys previously mentioned and as a general rule these alloys are welded inside of a chamber when the electron beam process is employed as opposed to no chamber or protective atmosphere when the laser process is employed.

Other non-ferrous alloys such as copper, monel, brass, bronze, etc., are readily welded by both processes and again, speaking specifically of the more common non-ferrous alloys from each of these groups.

The refractory alloys such as alloys of molybdenum, tungsten, columbium, and etc. are readily weldable by both processes. Again pointing out that the electron beam welding process would require protection from atmospheric contamination during the welding cycle as opposed to no protection for laser welding. The reader is again reminded that the laser process is extremely limited in material thickness welding capabilities as opposed to no limitations regarding material thickness capabilities for the electron beam welding process.

CONCLUSIONS

The Laser welding process is rapidly "coming of age" to take its place alongside other fusion welding processes. By the year 1970 it will have established itself as an irreplaceable space and nuclear age metallurgical joining process. As a matter of fact, when we speak of welding in space, what processes used and known today could be more readily adapted for this application than a Laser "gun".

REFERENCES

1. Anderson, J. E. and Jackson, J. E., "Laser Welding-Where it Stands Today," Materials in Design Engineering (February 1965).
2. American Engineering Magazine Staff Writers, "Laser Light: From Mars to Microwelding" (February 1966).
3. Irving, R. R., "Energy Beams Unleashed on Metals", The Iron Age, (July 15, 1965).
4. Miller, K. J., and Nunnikhoven, J. D., "Laser - A Space Age Welding Process," Laser Focus Magazine (December 1, 1965).
5. Miller, K. J., and Nunnikhoven, J. D., "Laser Welding," Machine Design (August 5, 1965).
6. Miller, K. J., and Nunnikhoven, J. D., "Production Laser Welding", Welding Journal (June 1965).
7. Miller, K. J., and James R. Early, "An Analysis of Modern Fusion Welding Processes: Past, Present and Future", Western Machinery and Steel World (May 1966).

VOLUME 46

WORK HARDENING

Edited by J. P. HIRTH and J. WEERTMAN

Based on a Symposium Sponsored by the Chemistry and Physics Committee of the Institute of Metals Division of the American Institute of Mining, Metallurgical, and Petroleum Engineers

VOLUME 43

MAGNETIC AND INELASTIC SCATTERING OF NEUTRONS BY METALS

Edited by T. J. Rowland and Paul A. Beck

Based on a Symposium Sponsored by the Alloy Phases Committee of the Institute of Metals Division, The Metallurgical Society of the American Institute of Mining, Metallurgical, and Petroleum Engineers

VOLUME 45

ENERGY BANDS IN METALS AND ALLOYS

Edited by L. H. Bennett and J. T. Waber

Based on a Symposium Sponsored by the Committee on Alloy Phases of the Institute of Metals Division of the American Institute of Mining, Metallurgical, and Petroleum Engineers

Printed in the United States of America

METALLURGICAL SOCIETY CONFERENCE VOLUMES

MECHANICAL WORKING OF STEEL 1 (Pittsburgh, January 1963) Phillip H. Smith, editor

MECHANICAL WORKING OF STEEL 2 (Chicago, January 1964) T. G. Bradbury, editor

METALLURGY AT HIGH PRESSURES AND HIGH TEMPERATURES (Dallas, February 1963) K. Gschneidner, Jr., N.A.D. Parlee and M. T. Hepworth, editors

UNIT PROCESSES IN HYDROMETALLURGY (Dallas, February 1963) M. E. Wadsworth and F. T. Davis, editors

DEFORMATION TWINNING (Gainesville, March 1963) R. E. Reed-Hill, J. P. Hirth and Harry Rogers, editors

NEW TYPES OF METAL POWDERS (Cleveland, October 1963) Henry H. Hausner, editor

IRONMAKING 1963 (Buffalo, April 1963) D. H. Regelin and W. D. Gifford, editors

IRONMAKING 1964 (Pittsburgh, April 1964) D. J. Enochs and W. D. Gifford, editors

THE SORBY CENTENNIAL SYMPOSIUM ON THE HISTORY OF METALLURGY (Cleveland, October 1963) Cyril S. Smith, editor

PRECIPITATION FROM IRON-BASE ALLOYS (Cleveland, October 1963) G. R. Speich and J. B. Clark, editors

ALLOYING BEHAVIOR AND EFFECTS IN CONCENTRATED SOLID SOLUTIONS (Cleveland, October 1963) T. B. Massalski, editor

REFRACTORY METALS AND ALLOYS 3: APPLIED ASPECTS (Los Angeles, December 1963) R. I. Jaffee, editor

THE BLAST FURNACE: THEORY AND PRACTICE (Pittsburgh, June 1963) J. H. Strassburger, et al., editors

HIGH TEMPERATURE REFRACTORY METALS (New York, February 1964) W. A. Krivsky, et al., editors

PROCESS SIMULATION AND CONTROL (New York, February 1964) H. L. Bishop and J. M. Uys, editors

APPLICATIONS OF FRACTURE TOUGNESS PARAMETERS TO STRUCTURAL METALS (Philadelphia, October 1964) H. Greenberg, editor

BERYLLIUM METALLURGY AND TECHNOLOGY (Philadelphia, October 1964) L. McD. Schetky and H. Johnson, editors

ENVIRONMENT-SENSITIVE MECHANICAL BEHAVIOR OF MATERIALS (Baltimore, June 1965) A. R. C. Westwood and N. S. Stoloff, editors

LOCAL ATOMIC ARRANGEMENTS STUDIED BY X-RAY DIFFRACTION (Chicago, February 1965) J. B. Cohen and J. E. Hilliard, editors

PHYSICAL METALLURGY OF REFRACTORY METALS (French Lick, October 1965) Joseph Maltz, editor

RADIATION EFFECTS (Asheville, September 1965) W. F. Sheely, editor

MECHANICAL WORKING OF STEEL 3 (Pittsburgh, November-December 1965) D. E. Edgecombe, editor

ELECTRON AND ION BEAM SCIENCE AND TECHNOLOGY (New York, April 1966) Robert Bakish, editor

OXIDE DISPERSION STRENGTHENING (New York, June 1966) George S. Ansell, editor

HIGH TEMPERATURE NUCLEAR FUELS (Delavan, October 1966) A. N. Holden, editor

GORDON AND BREACH, SCIENCE PUBLISHERS

150 FIFTH AVENUE NEW YORK CITY 10011